Open Research Online

The Open University's repository of research publications
and other research outputs

MESSENGER Observations of Volcanism on Mercury: From Hokusai Quadrangle Down to Small Cones

Thesis

oro.open.ac.uk

MESSENGER Observations of Volcanism on Mercury: From Hokusai Quadrangle Down to Small Cones

Jack Wright

MSci (Hons) June 2015, MA (Cantab) April 2018

"Time passes, people move. Like a river's flow, it never ends. A childish mind will turn to noble ambition."

Sheik, The Legend of Zelda: Ocarina of Time, 1998.

ABSTRACT

This thesis addresses the regional geology of the planet Mercury as seen by the MErcury Surface, Space ENvironment, and Ranging (MESSENGER) mission. I aimed to investigate the existence and origin of volcanic photogeological units and landforms on Mercury not mappable at the global scale.

Using MESSENGER images, I have made the first 1:3,000,000-scale geological map of the Hokusai (H05) quadrangle. My map shows that this region has a similar history of effusive volcanism to the rest of Mercury, with widespread plains formation having given way to lower volume effusions that were ultimately confined to impact craters. However, I found that H05 contains plains that do not conform to the definitions of the two globally recognised plains units on Mercury, intercrater plains and smooth plains, which are thought to be volcanic in origin. I mapped such plains as intermediate plains, due to their intermediate roughness between the two global plains types, and I suggest that they represent incompletely volcanically resurfaced regions of Mercury's crust.

The apparent absence of even small volcanic constructs on Mercury, emphasised to me during my mapping of the volcanologically diverse H05, led me to search for such constructs across Mercury. The two candidates I found, if volcanic, were probably built by low-volume eruptions that were uncharacteristic of most of Mercury's volcanic history.

During my search for volcanoes, I investigated the circum-Caloris knobs. Through mapping, photogeological observations and topographic measurements, I have shown that these small (<15 km across) landforms are not volcanoes, but instead are Caloris ejecta blocks that have undergone long-lived, or even recent, modification into cones. My observations suggest that volatile-loss might have driven modification of the blocks.

The intermediate plains, candidate volcanoes, and circum-Caloris knobs will be important targets for the BepiColombo mission, which launched during the preparation of this thesis.

Acknowledgements

Firstly, I owe a great debt of gratitude to my supervisors. I am grateful to Dave for being ever-present and ever-reliable, while also giving me the intellectual freedom to make my project my own. I thank Matt for his role as a sceptical, non-Mercury specialist who made me fight for every conclusion I could draw, and made me a better scientist for it. Without Susan, the ArcSage, I could have spent years wandering in a GIS abyss. I extend my sincerest gratitude to all three for offering me this opportunity, being enthusiastic about my work, and giving me encouragement. There would be no thesis without their support.

Many friends made before and during my PhD have in their own way helped me. School friends, who have always been tolerant of my talk of rocks since having left home. Undergraduate friends, who endured with me the same trial by rain, midges, and SedgCo practicals. My PhD officemates Alex, Candice, Peter, Costanza, Laura, Kaspar, Zoë, Paul, Melissa, Zoe, and Rachael made every day I came in a pleasure. I thank Rhian in particular for going the extra mile in looking after me. I am grateful for help and advice from fellow Mercury students Rebecca and Emma. I hope I will have been as helpful to Chris and Pegg. I thank many beyond K-Block for their friendship: Stacy (my hero), Shannon, both Hannahs, Leanne, and everyone who had lunch with me, so that I could meet the second half of each day. I look forward to visiting Valentina in Italy, so that we can stitch Mercury's clothing together.

I give my deepest personal thanks to my family. My parents, Mark and Jenny, for raising me in a nurturing environment, letting me go off into the world, and for keeping a room at home for when I return. My brothers Harry and Sam, two serial over-achievers who spurred me to make something of myself, as they have of themselves. Granny Pearl, whose phone calls were therapy as much for me as they were for her. Reggie, Lily and Rose, for bringing us all joy.

My final thanks go to Frances, for walking this path with me, for giving me self-belief, and for sharing the life experiences with me that make everything worthwhile. If I have done the same for her, then I know that we'll both be fine.

I hope that I have made everyone proud.

TABLE OF CONTENTS

Contents

Contents

LIST OF FIGURES

Contents

Contents

LIST OF TABLES

LIST OF EQUATIONS

LIST OF ABBREVIATIONS

.csv	Comma-Separated Variable file
.cub	ISIS 3 Image Cube file
.tab	Tab-Separated Value file
ASTER	Advanced Spaceborne Thermal Emission and Reflection
AU	Astronomical Unit
BDR	Basemap Reduced Data Record
BELA	BepiColombo Laser Altimeter
CV1, CV2	Candidate Volcano 1, Candidate Volcano 2
DEM	Digital Elevation Model
ELENA	Emitted Low-Energy Neutral Atoms
ESA	European Space Agency
Esri	Environmental Systems Research Institute
Ga	Giga-annum (refers to a point in time billions of years ago)
GIS	Geographic Information System
Gyr	Giga-year (refers to a stretch of time in billions of years)
HIE	High-Incidence angle mosaic (eastern illumination)
HIW	High-Incidence angle mosaic (western illumination)
HRIC	High Spatial Resolution imaging Channel
IAU	International Astronomical Union
ISIS3	Integrated Software for Imagers and Spectrometers
JAXA	Japan Aerospace Exploration Agency
kyr	Kilo-year (refers to a stretch of time in thousands of years)
LIP	Large Igneous Province
LOI	Low-Incidence angle mosaic
LOLA	Lunar Orbiter Laser Altimeter
LRM	Low-Reflectance Material
LRO	Lunar Reconnaissance Orbiter
LROC	Lunar Reconnaissance Orbiter Camera
MDIS	MESSENGER Dual Imaging System
MERTIS	Mercury Radiometer and Thermal Imaging Spectrometer

Contents

MESSENGER   MErcury Surface, Space ENvironment, GEochemistry, and Ranging

MIPA   Miniature Ion Precipitation Analyser

MLA   Mercury Laser Altimeter

MMO   Mercury Magnetospheric Orbiter

MOSIF   MMO Sunshield and Interface Structure

MPO   Mercury Planetary Orbiter

MTM   Mercury Transfer Module

NAC   Narrow-Angle Camera

NASA   National Aeronautics and Space Administration

PC1, PC2   First principal component, second principal component

PDS   Planetary Data System

PICAM   Planetary Ion Camera

PILOT   Planetary Image Locator Tool

RDR   Reduced Data Record

SERENA   Search for Exosphere Refilling and Emitted Neutral Abundance

STC   Stereo Channel

STROFIO   Start from a Rotating Field Mass Spectrometer

SYMBIO-SYS   Spectrometers and Imagers for MPO BepiColombo Integrated Observatory System

VIHI   Visible and near-Infrared Hyperspectral Imaging channel

WAC   Wide-Angle Camera

1:3M   1:3,000,000 (one-to-three million)

1:400k   1:400,000 (one-to-four hundred thousand)

LIST OF APPENDICES

Appendix 1   Geological map of the Hokusai Quadrangle (H05), Mercury (three crater classes, hardcopy)

Appendix 2   Geological map of the Hokusai Quadrangle (H05), Mercury (five crater classes, hardcopy)

LIST OF SUPPORTING DIGITAL MEDIA

Media	Folder/Filename	Description
DVD (JW_THESIS_SDM)	Chapter_6	Folder containing shapefile catalogues of the circum-Caloris and lunar knobs discussed in Chapter 6 of this thesis
	H05	Folder containing shapefiles for the geological maps of H05
	README.txt	File describing the contents of the Supporting Digital Media

CHAPTER 1
INTRODUCTION

1.1   Thesis overview

1.1.1   Geological mapping

This thesis contains a geological study of Mercury using data from NASA's MErcury Surface, Space ENvironment, GEochemistry, and Ranging (MESSENGER) mission. The aim of this work was to use MESSENGER data to provide science context and targets for the joint ESA-JAXA BepiColombo mission to that planet, which launched on 20th October 2018. To that end, the primary objective of this work, as defined from the outset, was to produce a 1:3 million (1:3M) scale geological map of one of Mercury's quadrangles. This would contribute to an international effort to map the entire planet at this scale before the arrival of BepiColombo in December 2025.

1.1.2   Ancillary science

From the beginning of this work, it was known that the construction of the quadrangle geological map would involve the systematic study of a whole region at a higher level of detail than previously conducted. It was anticipated that such detailed observations within the quadrangle could lead to ancillary studies concerned with geology beyond the boundaries of the chosen quadrangle. For example, MESSENGER produced the first global image dataset of Mercury, which led to many immediate geological discoveries before the end of the mission in April 2015, including large impact basins, widespread volcanic plains, explosive volcanism, and hollows. The quadrangle maps are being produced at a finer scale than has ever been employed before on Mercury, which means that subtler, previously unidentified geological features might be observed. An obvious follow-up study would be to investigate the global distribution of such features. Such an ancillary study would serve to enrich the thesis, which might otherwise be impoverished if it contained a regional map only with no wider results. Therefore, studies inspired by, but not strictly related to, the quadrangle geological map

would be regarded as equally important as the map itself. Naturally, this ancillary science could not be defined until after I had made considerable headway into making my map.

1.1.3   Methodology

To complete the objectives of this thesis, I employed photogeological methods commonly employed in planetary science. I observed landforms using MESSENGER monochrome and enhanced colour image products and topographic data derived from laser altimetry and stereophotogrammetry. I combined information about landform shapes and textures (geomorphology) with colour information (pertaining to surface composition and maturity) to ascertain the geological processes that operated to generate the observed landscape in my quadrangle. I interpreted the geology of Mercury cognizant of potential analogues on Earth, which is more directly and completely understood thanks to centuries of field observations. The Moon also proved to be a useful comparison, due to it being an airless body like Mercury. As Earth's nearest neighbour, it has a more extensive history of photogeological observation for comparison with Mercury, and it has the benefit of field observations and sampling due to the Apollo and Luna programs.

Nevertheless, any conclusions drawn based on remote sensing must be treated with caution due to the lack of ground truth. This is particularly true of Mercury, which has not had any landed missions. Remote sensing geological observations are particularly addled by convergence of form, whereby landforms with similar appearances (e.g. lava flow fronts and fault scarps) can arise from completely unrelated processes. As a result, despite using multiple strands of evidence, the interpretations presented in this thesis should be treated as working hypotheses. New observational evidence from BepiColombo could corroborate or falsify these interpretations, or indeed shed no further light on them. In the future, in-situ observations or samples might provide definitive answers, but until then my conclusions reflect the currently available balance of evidence.

1.2   Thesis structure

This thesis is divided into eight chapters, including this introductory chapter. Chapter 2 contains a chronological account of the planetary science of Mercury. It

concludes with a summary of the state of knowledge of Mercury's geology following the end of the MESSENGER mission, and statements of the research questions addressed throughout the rest of this thesis.

Chapters 3 and 4 pertain to my geological mapping of Mercury. Chapter 3 describes why I selected the Hokusai quadrangle for mapping and how I constructed its map. Chapter 4 describes and discusses the geological history of the Hokusai quadrangle as a whole, and additional case studies of special interest localities.

Chapter 5 describes two candidate small volcanic constructs I have identified on Mercury. I also discuss how these constructs might have been built in a way that is consistent with Mercury's general paucity of volcanic constructs. This chapter has been published separately as a peer-reviewed paper *(WRIGHT ET AL., 2018)*. The narrative of the paper remains largely unchanged in the chapter except that supporting information for the paper has been included in the main body of the chapter.

Chapter 6 is a study of the circum-Caloris knobs, which are conical landforms that are probably ejecta blocks, rather than volcanic constructs. My observations show that these knobs have undergone long-lived, post-formation modification that could be volatile-driven. If so, then these knobs represent a new landform type, generated by a hitherto undescribed process, on Mercury. These knobs may be analogous to landforms on Earth called 'molards'.

Chapter 7 synthesises the findings from this thesis and suggests future work to be carried out before and after the arrival of the BepiColombo spacecraft at Mercury. The conclusions of this thesis are briefly summarised in Chapter 8.

The research that makes up every chapter in this thesis was led by me. I completed my work in collaboration with my supervisors, Professor David Rothery, Dr Matthew Balme and Dr Susan Conway, who provided guidance and discussion throughout the preparation of this thesis. The geological mapping strategy outlined in Chapter 3 is based on that of Valentina Galluzzi, but I enacted the strategy myself and modified it for the specific needs of my map. Naturally, I created my map in the image of the other published MESSENGER-era quadrangle maps of Mercury so that these maps could be integrated easily in the future.

CHAPTER 2
PLANET MERCURY

2.1   Introduction

In this Chapter, I outline our current understanding of the planet Mercury. I present this background information in an approximately chronological narrative from pre-spacecraft observations of the planet, through to the present day. My review is focussed on discoveries and observations pertinent to the surface geology and geological processes of the planet.

2.2   Pre-spacecraft observations of Mercury

2.2.1   Early observations

As a classical planet, Mercury has been known since antiquity. It is the fastest moving planet in the night sky, which is why it is associated with fleet-footed messenger gods in many world religions. With the advent of telescopic astronomy *(GALILEI, 1610)*, and the widespread acceptance of the heliocentric model of the solar system, it became apparent that Mercury is the innermost planet with an orbital period of ~88 Earth days.

2.2.2   Transits

In 1677, Edmond Halley observed a transit of Mercury across the Sun's disc *(HALLEY, 1679)*. He realised that solar transits could be used to estimate the absolute diameter of the Sun, which could then be used to calculate the absolute distances between the planets and the Sun, and the absolute diameters of the planets *(HALLEY, 1679)*. Indeed, the 1769 transit of Venus yielded the first useful determination of the Earth–Sun distance, the astronomical unit (AU). The scale of the solar system allowed the angular size of Mercury apparent in telescopes to be converted into its absolute diameter. When this was done, it was found that Mercury was the smallest planet in the solar system, an observation that would endure the discoveries of Uranus and Neptune, and be reinstated after the reclassification of Pluto as a dwarf planet.

In 1769, astronomer Charles Green observed, during a transit of Mercury, that the planet has a crisper outline than Venus, and inferred that Mercury has little or no atmosphere *(HERDENDORF, 1986)*.

2.2.3 Telescopic observations

2.2.3.1 Early mass estimates

Mercury's mass was estimated using several methods through the 19th and 20th centuries, for example by measuring its perturbations of the comet Encke *(LYTTLETON, 1980)*. Although each method produced a different result, the fact remained that Mercury's mass was very high, given its small size, which meant the planet contained a lot of dense material. This could only be explained by the planet having a large metal core *(HUTTON, 1778)*.

2.2.3.2 Direct surface observation

Mercury's angular separation from the Sun as seen from Earth (elongation) never exceeds 28°, which makes telescopic observations of the planet from Earth very difficult. Early pioneers in this field include Giovanni Schiaparelli, who attempted to map Mercury's surface features and in so doing judged that Mercury's rotational period matched its orbital period of 88 days *(SCHIAPPARELLI, 1889)*. This state is called 'synchronous rotation', where the celestial body is locked in a 1:1 spin:orbit resonance. This view prevailed into the second half of the 20th century.

2.2.3.3 Ground-based radar

In more recent history, the most informative telescopic observations of Mercury have been made by radar. A very important discovery was that Mercury's rotational period is in fact ~59 days *(PETTENGILL AND DYCE, 1965)*, meaning that the planet is not synchronously rotating. Giuseppe Colombo subsequently theorised that Mercury was locked in a 3:2 spin:orbit resonance, since 59 is approximately 2/3 of 88 *(COLOMBO, 1965)*. One consequence of this is that a solar day on Mercury (i.e. sunrise to sunrise) lasts two Mercury years (i.e. 176 Earth days; see Fig. 2.1). Furthermore, this means Mercury has two points on its surface separated by 180° longitude that are sub-solar on alternate orbits at perihelion *(SOTER AND ULRICHS, 1967)*. These points were termed Mercury's 'hot poles'. There are also two points separated by 180° longitude on Mercury's surface that are sub-solar on alternate

orbits at aphelion. These are separated by 90° longitude from the hot poles and are called the 'warm poles'. *SOTER AND ULRICHS (1967)* estimated that the maximum daytime temperature of a hot pole would be 130 K above that of a warm pole.
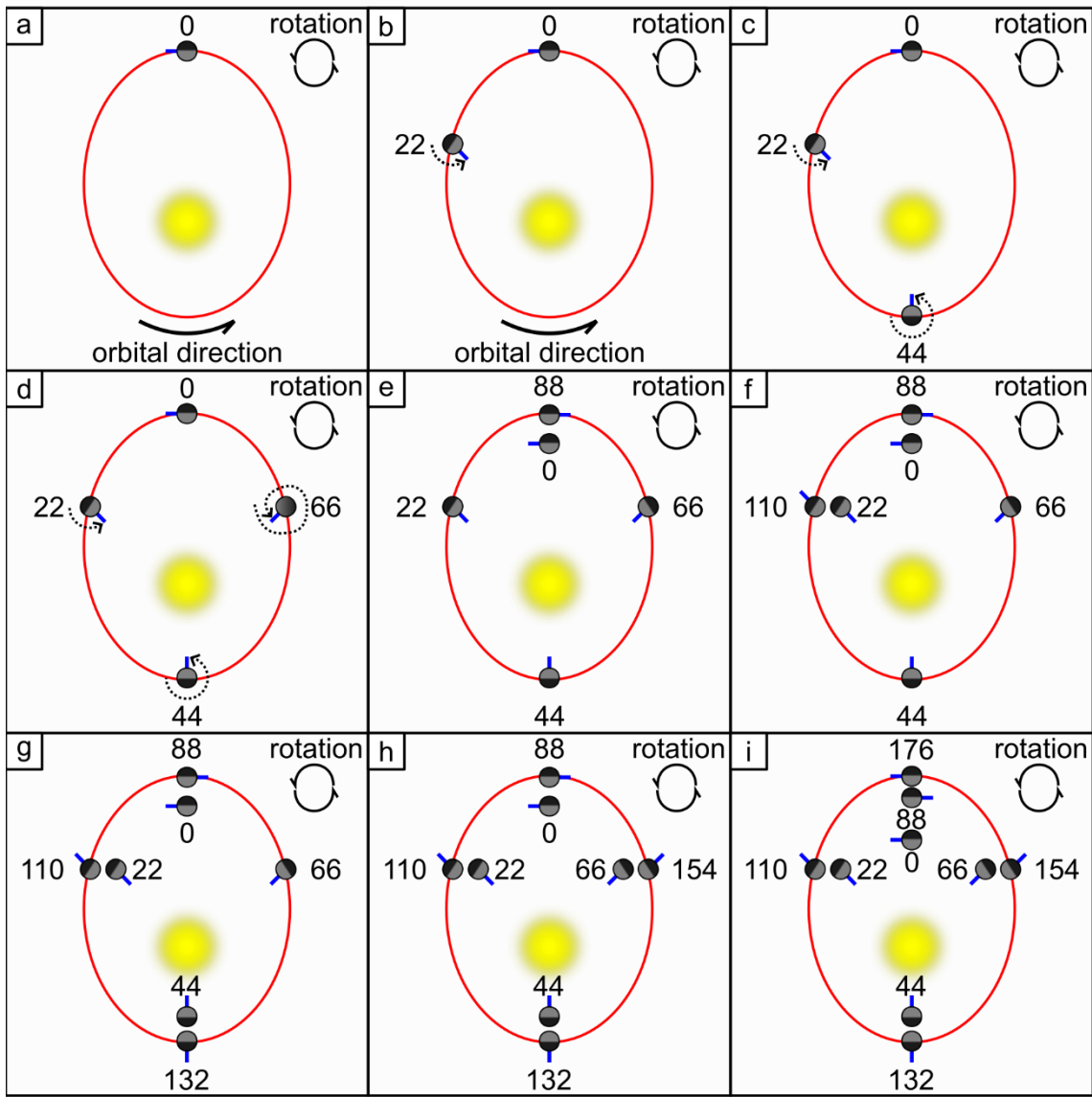
Fig. 2.1 Cartoon illustrating Mercury's 3:2 spin:orbital resonance. In each panel, Mercury's position in its orbit (red ellipse) is indicated by a two-tone grey circle. The illuminated and shadowed hemispheres of Mercury are coloured light and dark grey, respectively. The blue marker indicates a point on the planet's surface that will be tracked in each panel and be demonstrated to be one of Mercury's hot poles. Mercury rotates in a prograde fashion as indicated. Each panel is separated in time by 22 Earth days, equivalent to one quarter of a Mercury year. (a) Arbitrary initial configuration (Day 0). Mercury is at aphelion. The location indicated by the blue marker is experiencing sunrise. (b) Day 22. Mercury has moved less than a quarter of the way around its orbit due to its low orbital speed near aphelion. Mercury has rotated through ~135° on its axis. The Sun has not yet moved overhead at the blue marker point. (c) Day 44. Half a Mercury year has passed, and the planet is at perihelion. The planet has rotated through 270°. The Sun is directly overhead the blue marker point. (d) Day 66. Mercury has rotated through 405°, i.e. ~1.1 axial rotations have taken place since Day 0. (e) Day 88. Mercury has returned to aphelion and has completed one full orbit and made 1.5 axial rotations. The blue marker point is passing into the shadowed side of Mercury for the first time. (f–h) During Mercury's second year, Mercury completes a second axial rotation, but the blue marker point remains unilluminated. (i) Day 176. On this day, Mercury has completed a second orbit of the Sun and its third axial rotation (3:2 spin:orbit ratio). This configuration is identical to Day 0. The blue marker point is experiencing sunrise again, which means that a solar day (sunrise-to-sunrise) on Mercury lasts two Mercury years. The blue marker point is subsolar at alternate perihelions, making it one of the two hot poles. The subsolar point at Day 0 is one of the two warm poles. Cartoon not to scale.

2.2.4   Formation

Several hypotheses for how Mercury could form, with a large iron core, from the same material found in the solar nebula as the other terrestrial planets were suggested. One suggestion was that as Mercury formed close to the Sun, thermal-driven physical fractionation of metal and silicate material caused the planet to accrete dense, refractory elements, such as iron, preferentially, while lighter materials were distributed farther from the Sun *(WEIDENSCHILLING, 1978)*. Another suggestion was that proto-Mercury was a larger planet with an Earth-like composition and internal structure, but soon after its formation its silicate material

was vaporised, due to high solar activity, leaving a diminished silicate portion and a disproportionately large core *(CAMERON, 1985)*. A third alternative considered that proto-Mercury suffered a giant impact after its formation that stripped away most of its silicate material *(BENZ ET AL., 1988)*. Both the last two mechanisms require that the stripped silicate material is not re-accreted, and require Mercury's silicates to have endured intense heating.

2.2.5   Expectations for spacecraft observations

Based on the observations that Mercury is a small planet with a thin or absent atmosphere, exploration of the planet was expected to reveal a geologically dead planet with a cold interior, no magnetic field, a volatile-depleted composition, and a cratered, Moon-like surface.

2.3   Mariner 10 flybys of Mercury

Mariner 10 (Fig. 2.2) was the first spacecraft to fly past Mercury *(DUNNE AND BURGESS, 1978)*. Giuseppe Colombo derived a trajectory that put Mariner 10 into a heliocentric orbit that allowed the spacecraft to fly past Mercury multiple times. Mariner 10 made three flybys of Mercury (1974–1975) before it ran out of fuel *(DUNNE AND BURGESS, 1978)*.

The spacecraft's heliocentric orbital period was 176 Earth days, or twice Mercury's orbital period (88 Earth days). This meant that Mercury completed two orbits between each Mariner 10 flyby. Due to Mercury's 3:2 spin:orbit resonance (Fig. 2.1), Mercury completed exactly three axial rotations in the time between Mariner 10 flybys. An unfortunate consequence of this, from a planetary surface imaging perspective, was that Mariner 10 viewed the same illuminated hemisphere of Mercury during each of its flybys. As a result, Mariner 10 imaged ~45% of the planet's surface (Fig. 2.3; *DAVIES ET AL., 1978*).
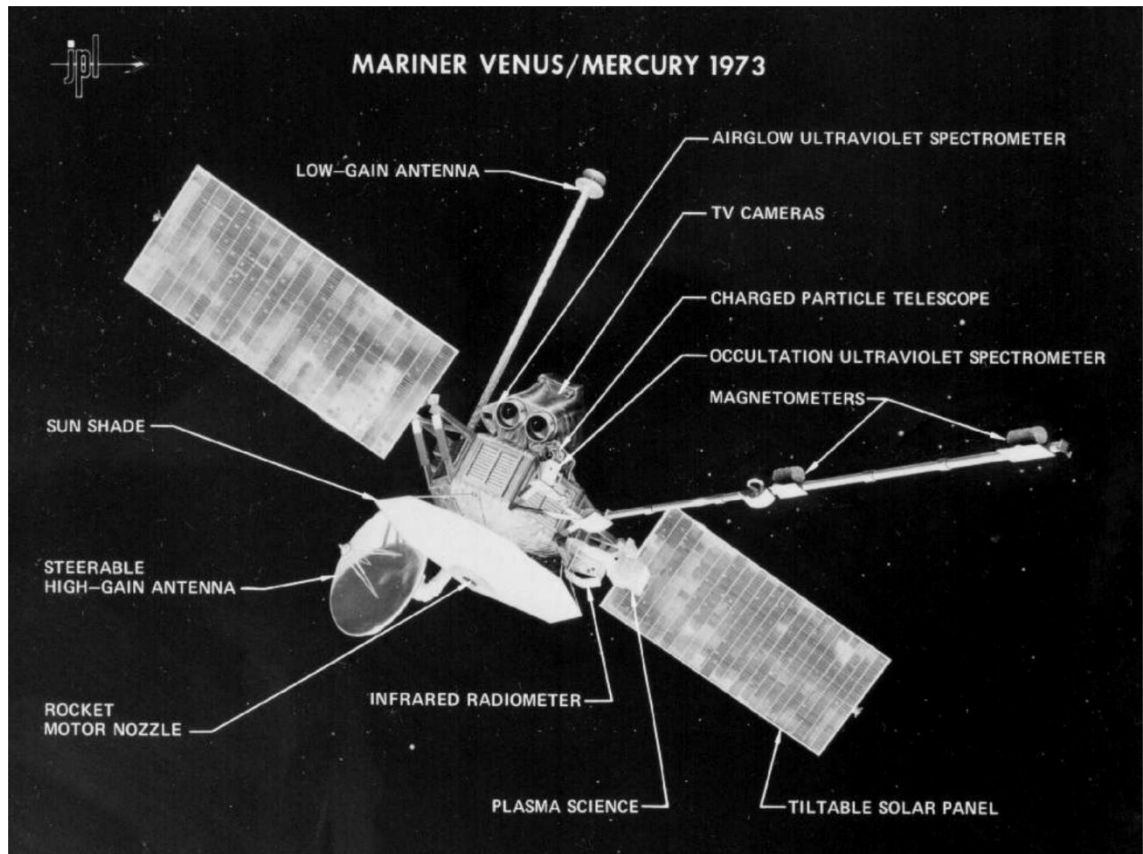
Fig. 2.2 Mariner 10. *Instruments labelled. Image credit: NASA/Jet Propulsion Laboratory.*
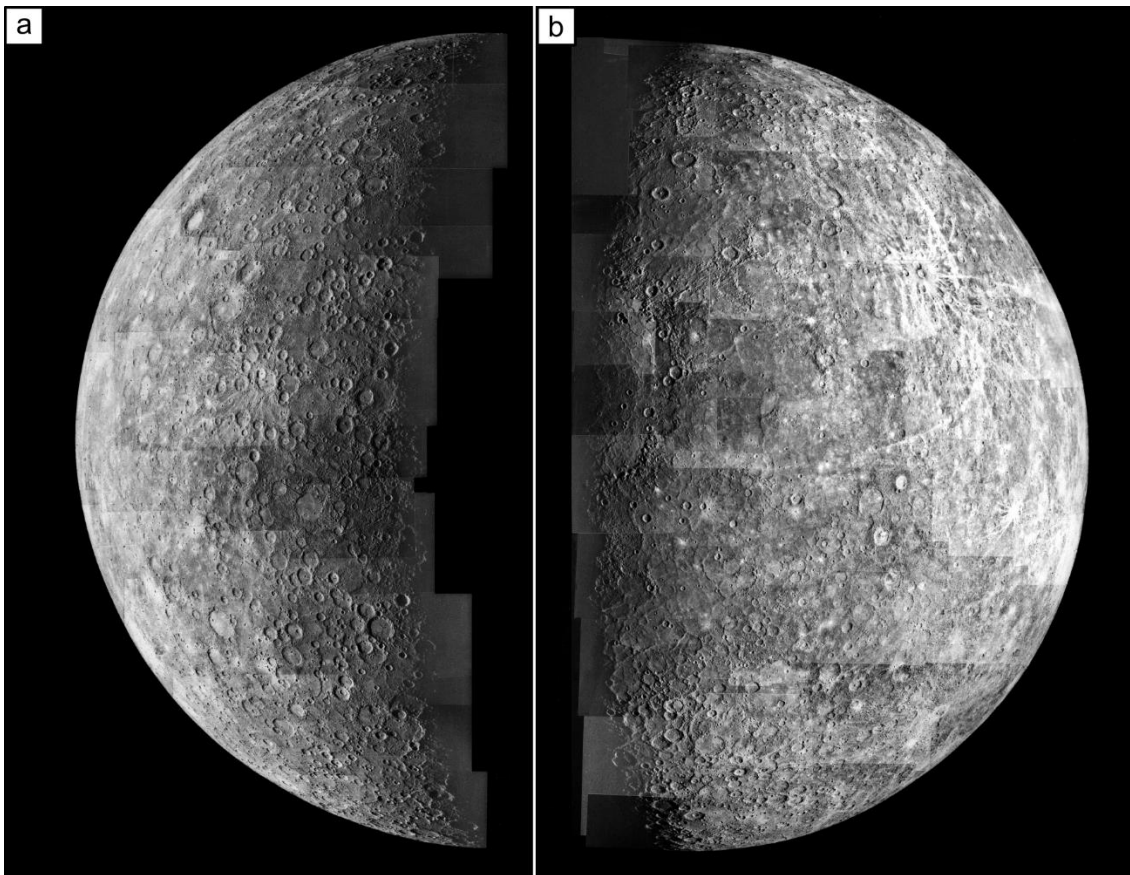
Fig. 2.3 Mercury as imaged by Mariner 10. *(a) Mosaic of images captured during the approach of the first flyby. (b) Mosaic of images captured during the departure after the first flyby. The eastern portion of the Caloris impact basin is visible on the terminator. Image credit: NASA.*

2.3.1 Magnetic field

Perhaps the most unexpected result from the Mariner 10 mission was that Mercury has a magnetic field *(NESS ET AL., 1974)*. Based on the data from the first and third flybys, it was determined that this magnetic field is most likely being generated internally by the planet *(CONNERNEY AND NESS, 1988)*. Internal magnetic fields are generated by fluid motion of an electrically conducting layer within a planet, such as a liquid iron core *(JACOBS, 1979)*. Contemporary models of Mercury's thermal evolution implied that its core would be completely solid *(SOLOMON, 1976)*. The observation of an intrinsic magnetic field at Mercury therefore required an unaccounted for internal heat source, an unexpectedly low rate of planetary heat loss, or a lower melting temperature of iron in order for the core to remain liquid and mobile in the present day *(CONNERNEY AND NESS, 1988)*.

2.3.2 Geology

Mariner 10 also returned the first images of the surface geology of Mercury (*MURRAY ET AL., 1974*). As predicted, in these images Mercury superficially resembled the Moon, in that they showed a surface dominated by impact craters. The largest impact feature imaged was the Caloris basin (Fig. 2.3b), which, based on its visible eastern portion, had an estimated diameter of ~1,300 km (*MURRAY ET AL., 1974*). No evidence of atmosphere-driven processes was observed, which suggested that at no point during the planet's history did it possess a dense atmosphere (*MURRAY ET AL., 1974*).

Mariner 10 showed that Mercury had at least two photogeological units of global extent: intercrater plains and smooth plains (*TRASK AND GUEST, 1975*). Intercrater plains were the most widespread plains and were defined as "level to gently rolling ground between and around large craters and basins [with a] high density of superposed small craters in the size range 5–10 km" (*TRASK AND GUEST, 1975*). The high density of superposing craters implies that the intercrater plains represent an older surface than the smooth plains (*ÖPIK, 1960*). The smooth plains have a low crater density, consistent with an age of formation postdating the end of the Late Heavy Bombardment of the inner solar system (~4.1–3.8 Ga; *STROM ET AL., 1975*). The most extensive smooth plains seen by Mariner 10 were associated with the Caloris basin (*MURRAY ET AL., 1974*), the interior of which constitutes Caloris Planitia.

The origin of the intercrater plains and the smooth plains on Mercury was a topic of much debate during and after the Mariner 10 mission. At this time, the lunar maria were known to be composed of basaltic lavas (*ANDERSON ET AL., 1969*) but lunar light plains, or 'Cayley Formation' type plains, had recently been discovered to be basin ejecta material (*EGGLETON AND SCHABER, 1972*). The widespread occurrence of the intercrater plains and the absence of obvious source impact basins was used as evidence that these plains originated during volcanic resurfacing of Mercury during its early history (*STROM ET AL., 1975*). Photogeologically, the smooth plains resemble the lunar maria (*STROM ET AL., 1975*), which are demonstrably volcanic in origin (*ANDERSON ET AL., 1969*). However, the lack of source vents, flow fronts and other indicative volcanic landforms within

both the intercrater plains and the smooth plains meant that volcanism on Mercury remained unconfirmed *(WILHELMS, 1976)*. The lack of strong colour signatures coincident with photogeological units in early Mariner 10 studies also cast doubt on a volcanic interpretation of Mercury's plains *(RAVA AND HAPKE, 1987)*, since volcanic materials are often spectrally distinct from their non-volcanic surroundings, such as the contrast between the volcanic lunar maria and the non-volcanic lunar highlands.

Some geological mappers of Mercury included a third plains unit, often termed 'intermediate plains', which was variously described as being intermediate in roughness or crater density between the intercrater and smooth plains *(SCHABER AND MCCAULEY, 1980; GUEST AND GREELEY, 1983; MCGILL AND KING, 1983; GROLIER AND BOYCE, 1984; SPUDIS AND PROSSER, 1984; TRASK AND DZURISIN, 1984; KING AND SCOTT, 1990; STROM ET AL., 1990)*. Most of these mappers suggested a volcanic origin for the intermediate plains, but with the same caveats as faced by the volcanic interpretation of the other plains on Mercury.

2.3.3   Stratigraphy

Following photogeological unit definition, geologists devised a chronostratigraphy for Mercury to correlate geological events across the planet. Based on the established chronostratigraphy of the Moon *(WILHELMS ET AL., 1987)*, Spudis and Guest (1988) used the stratigraphic relationships between the Tolstoj, Caloris, Mansur, and Kuiper impact features to define five time systems for Mercury: the Pre-Tolstojan, the Tolstojan, the Calorian, the Mansurian, and the Kuiperian (Fig. 2.4).

Lunar time system	Hermean time system	Time before present (Ga)
Copernican	Kuiperian	0.0 — 0.5 — 1.0
Eratosthenian	Mansurian	1.5 — 2.0 — 2.5 — 3.0
Imbrian	Calorian	3.5
Nectarian	Tolstojan	4.0
Pre-Nectarian	Pre-Tolstojan	4.5
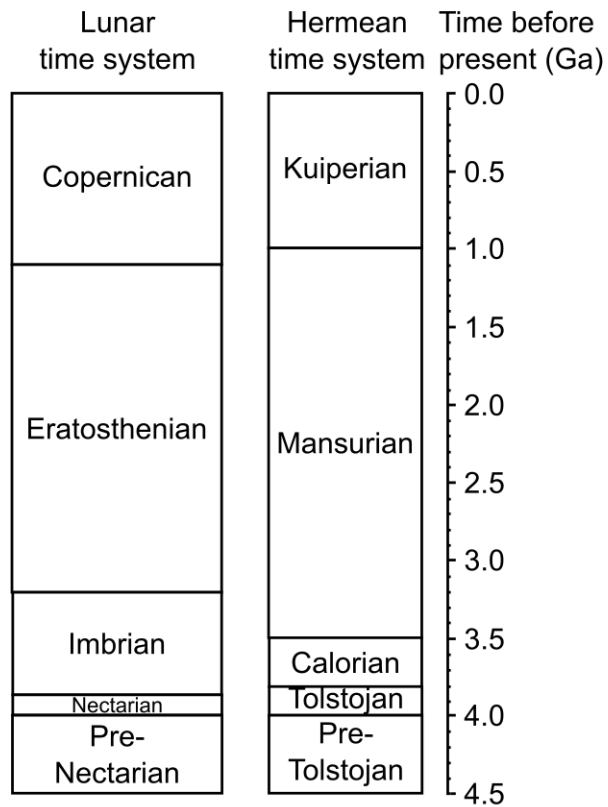
Fig. 2.4 Mariner 10-derived chronology for Mercury with lunar chronology for comparison. The Hermean chronology on the right was devised by SPUDIS AND GUEST (1988) based on the lunar chronology of WILHELMS ET AL. (1987) on the left. The absolute ages of the Hermean time systems were scaled from absolute age estimates from lunar samples, and are therefore highly approximate.

The impact features that define these time systems are in different states of degradation. Under the assumption that impact craters in similar degradation states formed at similar times, and that craters degrade at the same rate, a crater-based morphostratigraphy could be extrapolated over the entire planet. Geological mappers of Mercury from Mariner 10 data classified impact crater materials according to their degradation *(SCHABER AND MCCAULEY, 1980; DEHON ET AL., 1981; GUEST AND GREELEY, 1983; MCGILL AND KING, 1983; GROLIER AND BOYCE, 1984; SPUDIS AND PROSSER, 1984; TRASK AND DZURISIN, 1984; KING AND SCOTT, 1990; STROM ET AL., 1990)*. The Calorian time system is bracketed by the Caloris and Mansur impact events. Craters superposing Caloris that appear more degraded than Mansur formed during the Calorian. Craters with a similar appearance elsewhere on the planet probably also formed in the Calorian. Similarly, craters more degraded than Kuiper and less degraded than Mansur formed during the Mansurian, etc.

2.3.4   Tectonics

Mariner 10 also revealed abundant, widespread, shortening tectonic features with various orientations, but no similarly distributed extensional features. The most widely distributed tectonic features were 'lobate scarps' (Fig. 2.5). Smaller 'wrinkle ridges' appeared to be characteristic of the smooth plains and resembled similar features in the lunar maria *(MURRAY ET AL., 1974)*. The least common tectonic landforms were high-relief ridges *(WATTERS ET AL., 2004)*. Extensional features, such as grabens, appeared to be restricted to Caloris Planitia *(MURRAY ET AL., 1974)*. The dominance of crustal shortening structures suggested that Mercury had undergone global contraction, most likely due to secular cooling of the planet's interior (Fig. 2.6; *SOLOMON, 1978*). The original estimate of cumulative crustal shortening due to the lobate scarps corresponded to a planetary radius decrease of ~2 km *(STROM ET AL., 1975)*. This placed constraints on the rate of internal heat loss, which informed attempts to explain the apparent presence of a core dynamo in Mercury *(CONNERNEY AND NESS, 1988)*.
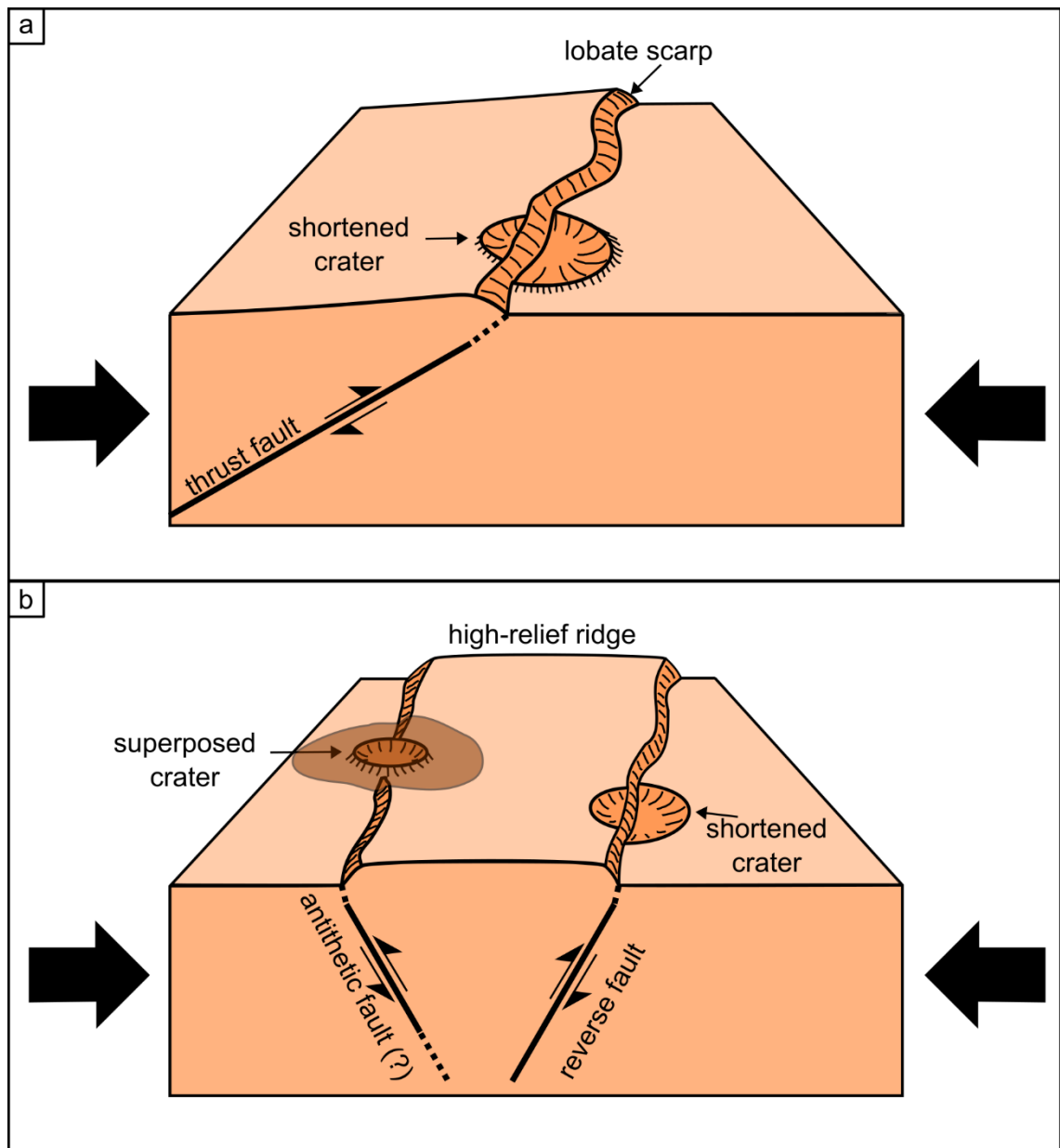
Fig. 2.5 Shortening tectonic structures on Mercury. *(a) Cartoon of a lobate scarp. Impact craters cross-cut by a lobate scarp appear shortened, indicating that scarps accommodate strain due to compression (black arrows). The curvilinear trace of the scarp, which probably represents a fault surface break, indicates that the fault is shallowly dipping (i.e. a thrust fault). (b) Cartoon of a high-relief ridge, another shortening structure. High-relief ridges are much less abundant than lobate scarps on Mercury and are more linear. This suggests that the faults bounding the structure are more steeply dipping (i.e. reverse faults).*

An alternative, but not mutually exclusive, hypothesis for the lobate scarps was tectonism due to tidal despinning (Fig. 2.6). The tidal despinning hypothesis suggested that Mercury achieved its present-day 3:2 spin:orbit resonance by tidal braking from an original, shorter rotational period *(MELOSH AND DZURISIN, 1978)*.

When the planet was rotating faster, it would have had an equatorial bulge. As the planet's rotation rate decreased, this bulge would have relaxed, causing equatorial compression and polar extension. The tidal spinning hypothesis predicted predominantly north–south oriented equatorial thrust faults, with circum-polar normal faults and mid-latitude strike-slip faults *(MELOSH, 1977)*. This pattern of faulting, particularly circum-polar normal faulting, was not observed but ambiguity remained since Mariner 10 images covered only 45% of the surface of Mercury.
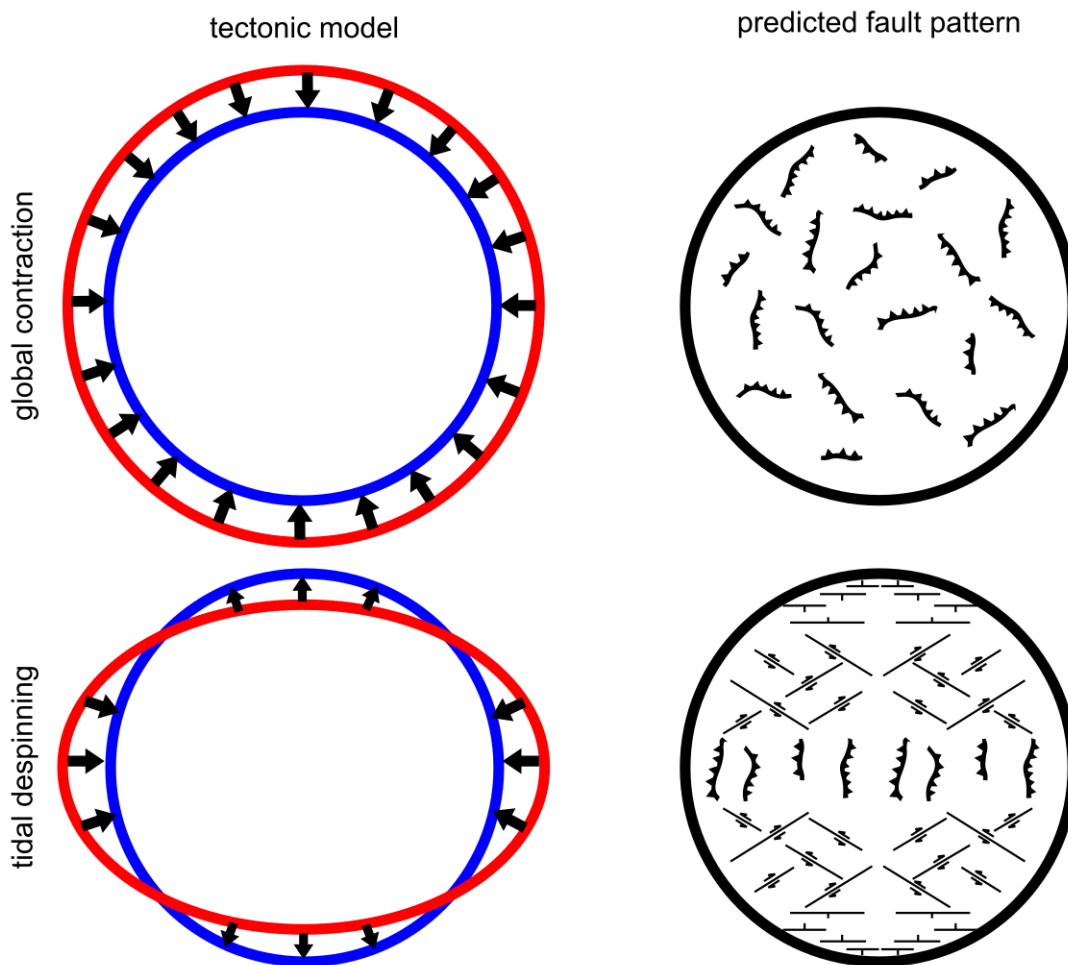
Fig. 2.6 Comparison of global contraction and tidal despinning tectonic models for Mercury. Global contraction due to secular cooling predicts globally distributed, randomly oriented thrust faults. Tidal despinning predicts latitudinal bands of thrust, strike-slip, and normal faults with preferred orientations. Modified from MELOSH (1977).

The wrinkle ridges in the lunar maria appear to be strongly controlled by the geometry of the basin hosting the maria, and so are thought to have formed in response to compressional stresses due to volcanic loading of the lithosphere

(SOLOMON AND HEAD, 1980). It was unclear in Mariner 10 data if Mercury's wrinkle ridges formed chiefly due to lithospheric loading or in response to the global tectonic regime. This uncertainty partially arose out of the limited extent of smooth plains, which hosts wrinkle ridges, in the Mariner 10 hemisphere. *PLESCIA AND GOLOMBEK (1986)* reviewed planetary wrinkle ridges and their terrestrial analogues and favoured a tectonic origin for wrinkle ridges.

2.4 Between Mariner 10 and MESSENGER

2.4.1 Liquid core confirmation

After Mariner 10, more than 30 years passed before the next spacecraft visited Mercury. However, several important advances in Mercury science were made during this time. For example, using radar, *MARGOT ET AL. (2007)* measured the libration of Mercury, which indicated that the rotation of the planet's silicate layer is decoupled from the solid inner core by a liquid outer core. This raised the likelihood that core freezing could be driving compositional convection in the liquid core, which could generate Mercury's magnetic field. Furthermore, core freezing could still be decreasing the volume of the planet such that global contraction is ongoing *(MARGOT ET AL., 2007)*.

2.4.2 Volcanic origin for smooth plains

Improved colour calibration of Mariner 10 images allowed colour relationships to be reassessed. *ROBINSON AND LUCEY (1997)* found that colour did correlate with previously mapped photogeological units. For example, smooth plains near the crater Rudaki were observed to be redder than the Mercury average. They also exhibited sharp embayment relationships with the surrounding high-standing topography. Conversely, fresh impact ejecta was found to be bluer and insensitive to topographic undulations *(ROBINSON AND LUCEY, 1997)*. These observations provided evidence that Mercury's smooth plains are volcanic in origin, since volcanics are expected to have spectral contrasts with their non-volcanic surroundings.

2.5 MESSENGER at Mercury

MESSENGER made three flybys of Mercury between 2008 and 2009 before becoming the first spacecraft to orbit Mercury in 2011 (the mission ended on 30th April 2015). It carried a suite of instruments designed to address the questions still surrounding Mercury after the end of the Mariner 10 mission *(SOLOMON ET AL., 2001, 2007)*. This mission imaged the entire surface of Mercury under varying illumination conditions, which allowed the geology and geochemistry to be studied in greater detail than ever before.
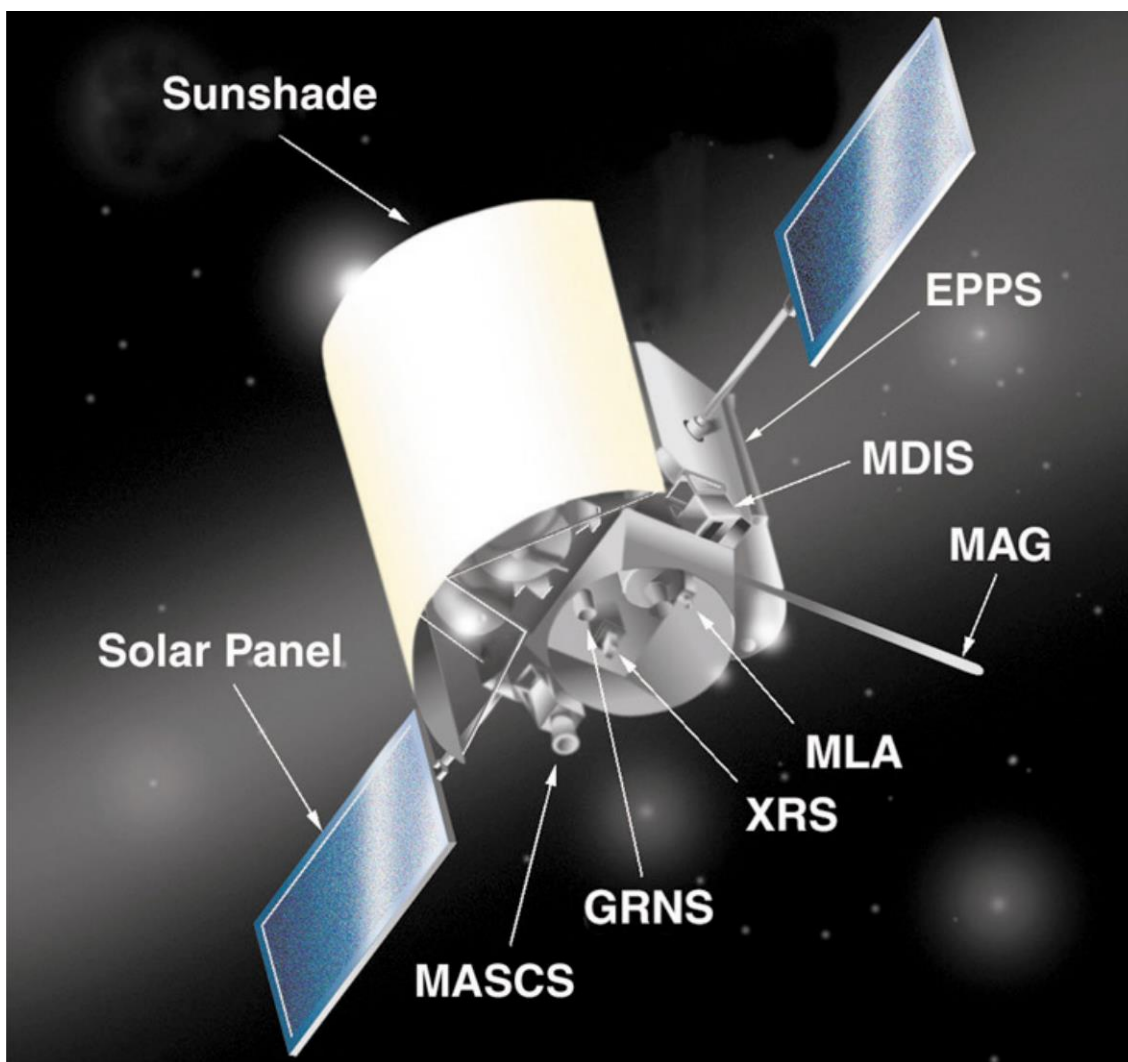
Fig. 2.7 Labelled artist's conception of the MESSENGER spacecraft and its instruments. EPPS: Energetic Particle and Plasma Spectrometer, for measuring the charged particles in the magnetosphere. MDIS: Mercury Dual Imaging System, including the monochrome narrow-angle camera (NAC) and the multispectral wide-angle camera (WAC), for imaging the surface of Mercury. MAG: Magnetometer, for measuring Mercury's magnetic field. MLA: Mercury Laser Altimeter, for measuring Mercury's topography and overall shape. XRS: X-Ray Spectrometer, for measuring the elemental composition within the top millimetre of Mercury's surface. GRNS: Gamma-Ray and Neutron Spectrometer, for measuring elemental composition to a depth of 10 cm using gamma-ray spectroscopy and hydrogen mineral composition from emitted low-energy neutrons. MASCS: Mercury Atmospheric and Surface Composition Spectrometer, for measuring the composition of the exosphere and surface using infrared light. To survive in the harsh thermal environment around Mercury, the instruments were protected by a Sun-facing ceramic sunshade. Image credit: NASA/Johns Hopkins University Applied Physics Laboratory/Carnegie Institute of Washington.

Important results from the global surface mapping campaign included: complete imaging of the Caloris basin (and the circum-Caloris plains), which was confirmed as the largest, well-preserved impact structure on Mercury *(FASSETT ET AL., 2009)*; the discovery of the full extent of the northern smooth plains (Borealis Planitia), which cover ~7% of the planet's surface *(HEAD ET AL., 2011; OSTRACH ET AL., 2015)*; measurement of a relatively high abundance of volatile sulfur (~4 wt %) and low abundances of surface-darkening titanium (~0.8 wt %) and iron (~4 wt %; *NITTLER ET AL., 2011*); new model ages for the Kuiperian and Mansurian time systems *(BANKS ET AL., 2017)*; a revised crater degradation classification scheme *(KINCZYK ET AL., 2016)*; the first global geological map of Mercury *(PROCKTER ET AL., 2016; KINCZYK ET AL., 2018B)*; the discovery of impact-delivered water ice in the permanently shadowed regions at Mercury's poles *(D. J. LAWRENCE ET AL., 2013)*, and new measurements of Mercury's physical parameters (see Section 2.5.5, Table 2.1: *MAZARICO ET AL., 2014; PERRY ET AL., 2015*). In the sections that follow, I discuss in more detail the advances made so far during the MESSENGER-era of Mercury exploration that have a bearing on the following chapters of my thesis.
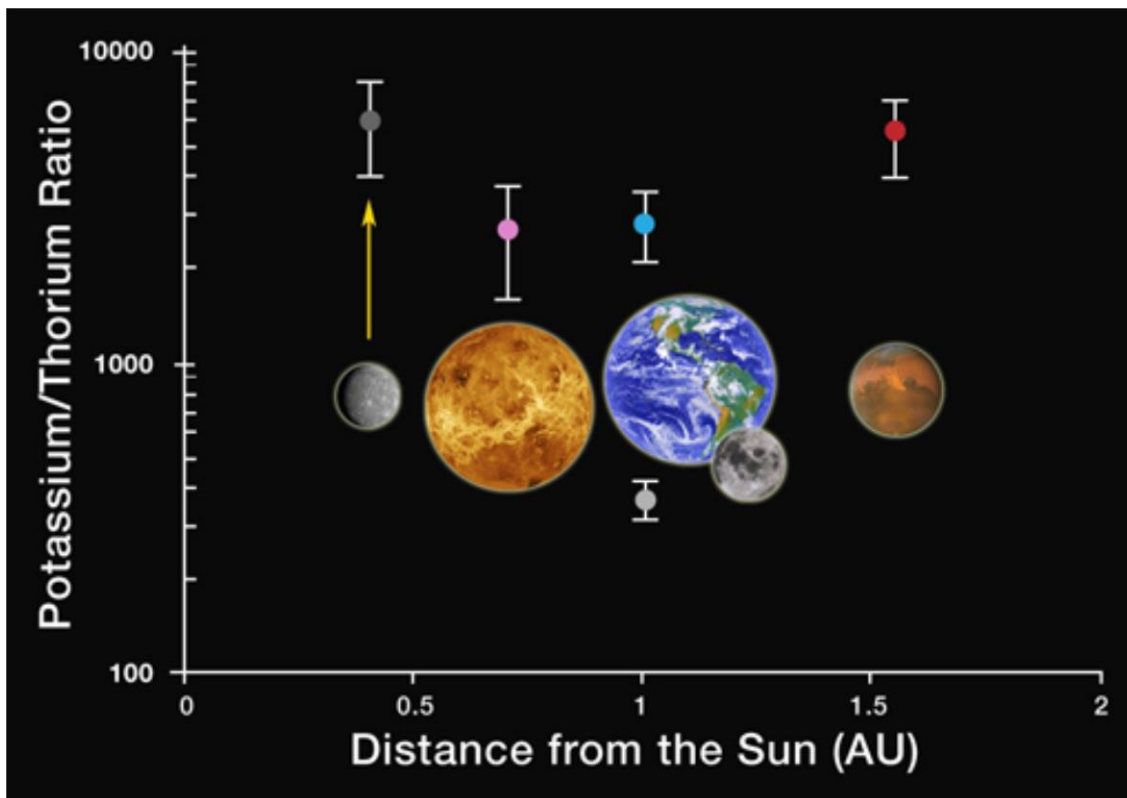
Fig. 2.8 Potassium/thorium ratios of the major rocky bodies of the inner solar system. *Potassium is a more volatile element than thorium, which is refractory. Therefore, planets with high potassium/thorium ratios are generally enriched in volatile species. Earth and Venus have very similar potassium/thorium ratios. Mars has a higher potassium/thorium ratio, which likely reflects a higher volatile content due to it having accreted farther from the Sun than Earth and Venus. The Moon has a lower potassium/thorium ratio than the Earth, despite its identical distance from the Sun, most likely due to it having been formed during an energetic giant impact, which would have driven off its volatile species. Mercury has a high potassium/thorium ratio, indicative of an overall volatile-rich composition. Image credit: NASA/Johns Hopkins University Applied Physics Laboratory/Carnegie Institute of Washington.*

2.5.1   Crustal formation

2.5.1.1 Effusive volcanism

Multiple lines of evidence from MESSENGER data indicate that most of Mercury's crust was formed by voluminous effusive volcanic eruptions. The correlation between photogeological units and colour originally identified by ROBINSON AND LUCEY (1997) in Mariner 10 data was reaffirmed strongly by MESSENGER (ROBINSON ET AL., 2008; DENEVI ET AL., 2009). In particular, most smooth plains of Mercury

were coincident with a colour unit termed 'high-reflectance red plains' *(DENEVI ET AL., 2009)*. High-reflectance red plains embay their surroundings with sharp contacts and have a strong colour contrast with 'intermediate terrain', which corresponds to Mercury's 'average' colour *(DENEVI ET AL., 2009)*. The smooth plains of Borealis and Caloris Planitiae mostly consist of high-reflectance red plains *(DENEVI ET AL., 2013; OSTRACH ET AL., 2015)*, although the colour unit of the circum-Caloris plains is 'low-reflectance blue plains'. Low-reflectance blue plains also have sharp contacts and embayment relationships, which suggest that they are at least partly volcanic. The colour difference could therefore indicate a different composition from the high-reflectance red plains *(DENEVI ET AL., 2009)*.

Major element data from MESSENGER's X-Ray Spectrometer (XRS) are consistent with the high-reflectance red plains having a low-iron, basaltic composition, whereas low-reflectance regions were consistent with a more ultramafic composition *(NITTLER ET AL., 2011; WEIDER ET AL., 2012)*.
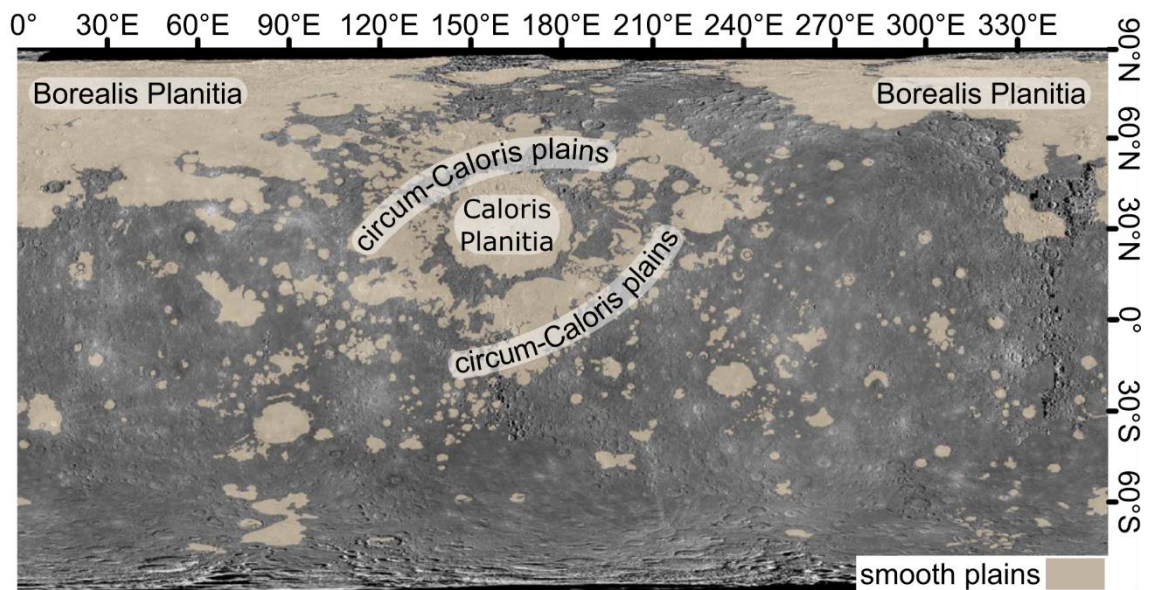
Fig. 2.9 Global map of Mercury's smooth plains deposits. *Smooth plains mapped by DENEVI ET AL. (2013) at 1:1.25M.*

Important photogeological evidence for a volcanic origin for at least some smooth plains on Mercury includes the observation of possible lava channels and source vents northwest of Caloris *(BYRNE ET AL., 2013)*, and a candidate shield volcano in Caloris Planitia *(HEAD ET AL., 2008*, but see Chapter 5 and *ROTHERY ET AL., 2014)*. With the full extent of the smooth plains revealed, the observation that there are

no impact basins whose ejecta could have formed the smooth plains made during the Mariner 10 era was corroborated by MESSENGER *(DENEVI ET AL., 2013)*.
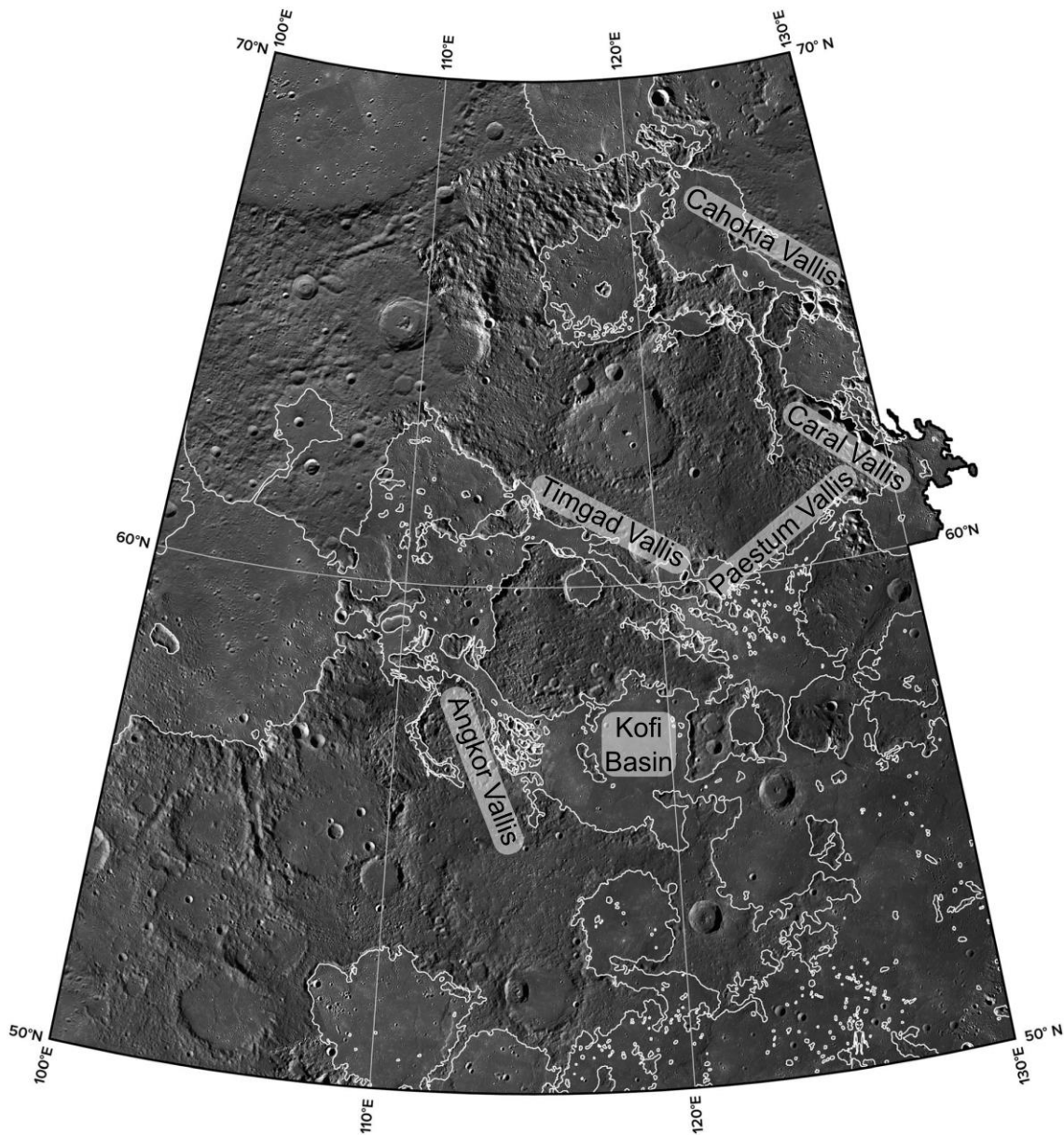
Fig. 2.10 An assemblage of volcanic features northwest of Caloris described by BYRNE ET AL. (2013). *Several elongate, smooth plains-floored (white outlines) depressions are interpreted as lava flow-modified channels ('valles', sing. 'vallis'). High-standing materials surrounded by smooth plains are interpreted as kipukas. Several kipukas within the valles are elongate along the vallis axis, which is interpreted to be a result of streamlining due to mechanical and thermal erosion by channel-confined lavas. Modified from BYRNE ET AL. (2013). Orthographic projection of the ~250 m/pixel global monochrome basemap centred on 115°E, 60°N.*

MESSENGER-era crater counts of the smooth plains support a volcanic interpretation for their origin. Multiple independently conducted crater size-frequency distribution studies of Caloris Planitia and the circum-Caloris plains indicate that they are younger than the Caloris impact itself by ~100 Myr (*FASSETT ET AL., 2009; DENEVI ET AL., 2013; MANCINELLI ET AL., 2016*). This means that at least some of these plains must have formed due to volcanism following the impact.

BYRNE ET AL. (2016) measured the crater size-frequency distribution of several smaller smooth plains deposits across Mercury. They found that no smooth plains deposit unconfined by impact craters >~6.5×10^4 km^2 has a model age <3.5 Ga. They conclude that large-volume effusive eruptions on Mercury ceased around 3.5 Ga. However, small-volume effusive eruptions appear to have endured within impact craters for at least one billion years after this. For example, the crater size-frequency distribution of the smooth plains with a distinct colour signature within the crater Rachmaninoff have a crater retention model age of ~1–2 Ga, much younger than the formation of the impact itself (~3.5 Ga: *PROCKTER ET AL., 2010; CHAPMAN ET AL., 2012*). *BYRNE ET AL. (2016)* concluded that large-volume effusive eruptions ceased in response to the horizontally compressive stress regime imposed by Mercury's global contraction. The occurrence of small volumes of younger volcanic smooth plains within impact craters seems to support this hypothesis, since impacts 'reset' the local stress regime and propagate fractures that could be exploited by magma that had otherwise stalled in the subsurface (*BYRNE ET AL., 2016*).

The origin of the intercrater plains is more difficult to ascertain. *WHITTEN ET AL. (2014)* noted that multiple overlapping secondary crater fields superposed on smooth plains can replicate the appearance of the intercrater plains. This means that it is possible that intercrater plains are merely older volcanic plains than the smooth plains observable today. This hypothesis is corroborated by the observation that the intercrater plains conceivably represented an approximately level surface before it was heavily cratered and tectonised (*WHITTEN ET AL., 2014*). Furthermore, the areal density of superposed impact craters on both the smooth and intercrater plains of Mercury, arranged from most-cratered to least-cratered, show a smooth and continuous increasing density progression from intercrater

plains, to overlapping intercrater and smooth plains, to smooth plains *(WHITTEN ET AL., 2014)*. In the global map of Mercury, intercrater plains cover >70% of the planet *(PROCKTER ET AL., 2016; KINCZYK ET AL., 2018B)*, and do not appear to be controlled by the limited extents of basin ejecta deposits *(WHITTEN ET AL., 2014)*. Nevertheless, no definitive volcanic landforms have been observed in the intercrater plains *(WHITTEN ET AL., 2014)*.

WHITTEN ET AL. (2014) judged that the regions mapped as intermediate plains on the basis of Mariner 10 data should be remapped as either intercrater plains or smooth plains using MESSENGER data. As a result, the global geological map of Mercury contains the smooth and intercrater plains units but not intermediate plains units *(PROCKTER ET AL., 2016; KINCZYK ET AL., 2018B)*.

2.5.1.2 Flotation crust

Mercury's surface composition as measured by MESSENGER is inconsistent with the planet having an anorthitic flotation crust akin to the Moon's *(NITTLER ET AL., 2011)*. Instead, Mercury's surface appears to be mostly secondary volcanic crust, most likely generated by high degrees of partial melting of the mantle. Eruptions would have been enhanced in the absence of a low-density flotation crust *(HEAD AND WILSON, 1992)*. The limited surface elevation range on Mercury measured by MLA *(ZUBER ET AL., 2012)* and stereo-derived topography *(BECKER ET AL., 2016)* corroborates the absence of a buoyant flotation crust.

Mercury is a fully differentiated planetary body, and so the planet will have gone through a magma ocean stage during its development *(BROWN AND ELKINS-TANTON, 2009)*. This begs the question: why did a planet-wide flotation crust not form at that time? An important clue is that MESSENGER measured a very low iron concentration on Mercury's surface *(NITTLER ET AL., 2011)*. Since Mercury's crust appears to have formed from partial melting of the mantle, it follows that Mercury's mantle is also low in iron *(NITTLER ET AL., 2011)*. This means that the bulk silicate fraction of Mercury has a low density. It follows that any magma ocean that developed on Mercury would also have had a low density, which would prevent crystallising anorthite from being buoyant enough to form a flotation crust *(NITTLER ET AL., 2011)*.

Experimental melts simulating Mercury's silicate composition show that nearly all rock-forming minerals, apart from graphite, are prohibited from forming a flotation crust by the low iron content of Mercury's mantle *(VANDER KAADEN AND MCCUBBIN, 2015)*. By using estimates of the carbon content in Earth's mantle as a proxy for Mercury's mantle carbon content, *VANDER KAADEN AND MCCUBBIN (2015)* estimated that the global thickness of Mercury's flotation crust would have been 1–100 m. This thickness estimate is highly uncertain due to uncertainties in the carbon content of Mercury's mantle and the efficiency of graphite flotation *(VANDER KAADEN AND MCCUBBIN, 2015)*. Nevertheless, data from MESSENGER's Neutron Spectrometer (NS), gathered during the spacecraft's terminal low-orbital campaign, are consistent with up to ~5 wt % carbon in Mercury's low-reflectance material and ~1 wt % carbon elsewhere *(PEPLOWSKI ET AL., 2016)*. The low stratigraphic position of Mercury's low-reflectance material *(ERNST ET AL., 2015)* is consistent with this material being a remnant of the planet's primary graphite flotation crust *(PEPLOWSKI ET AL., 2016)*. It is possible that continual impact bombardment of Mercury has distributed carbon from the lower crust over the surface of the planet, thus darkening it (Fig. 2.11).
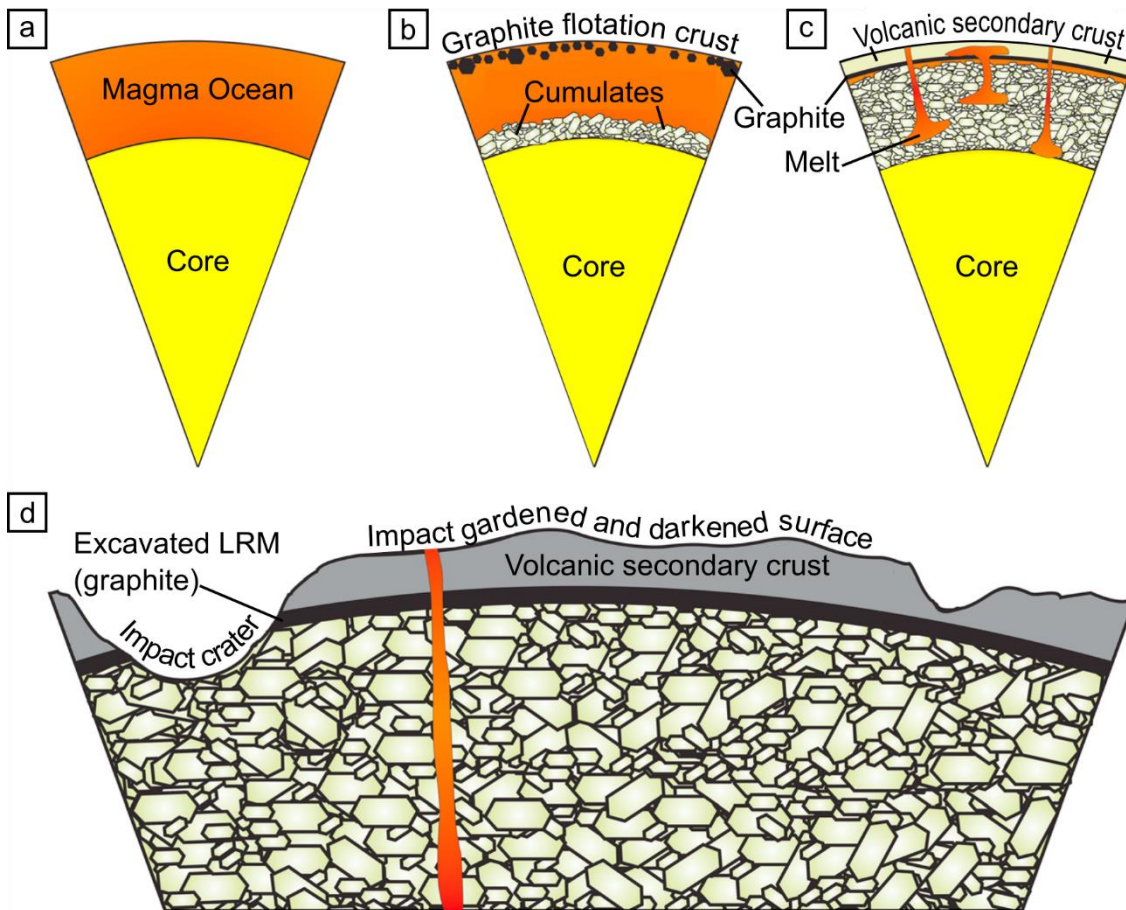
Fig. 2.11 Model for the formation of Mercury's early crust proposed by VANDER KAADEN AND MCCUBBIN (2015). *(a) Following the formation of Mercury's metal-rich core, the planet's silicate fraction formed a metal-poor magma ocean. (b) As Mercury's magma ocean cooled, it began to crystallise. Due to the low density of the residual melt, most crystallised minerals (plagioclase, olivine, pyroxene) formed cumulates at the core-mantle boundary. Carbon, which is not incorporated as a major component of most rock-forming minerals, would have crystallised under Hermean conditions as graphite and been sufficiently buoyant to form a thin flotation crust. Note that the thickness of this graphite crust is vertically exaggerated for clarity in this cartoon. (c) After solidification of the magma ocean, heat from the core would have driven partial melting of the planet's mantle, leading to secondary crust formation by volcanic plains emplacement stratigraphically above the graphite primary flotation crust. (d) Subsequent impact cratering exhumed lower crustal graphite and distributed it over Mercury's surface, thus darkening it. This model, explanation, and cartoon have been adapted from VANDER KAADEN AND MCCUBBIN (2015).*

2.5.2 Volatile-rich planet
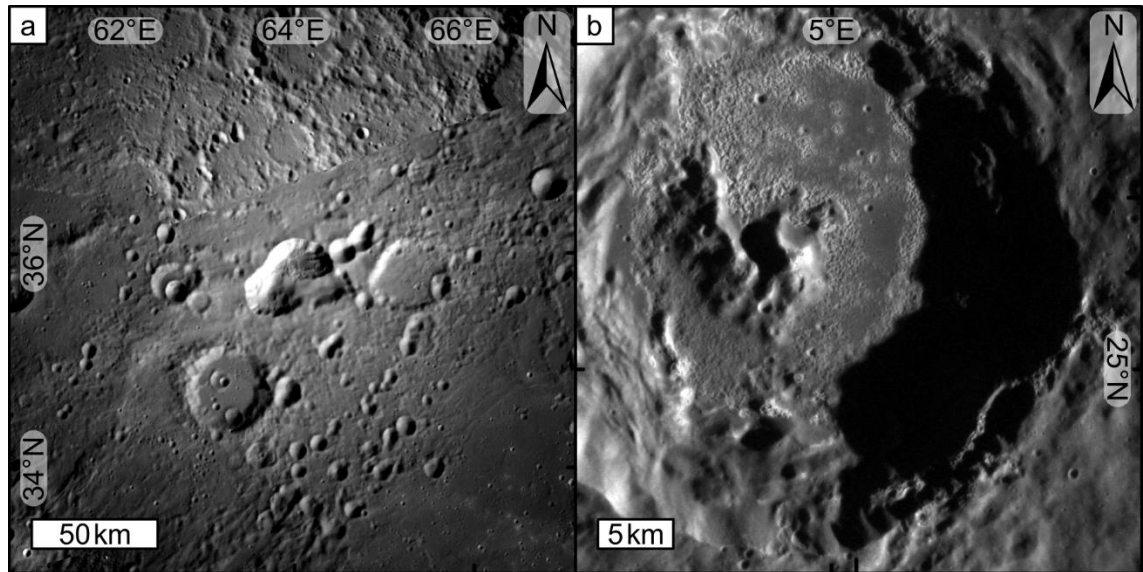
Fig. 2.12 Evidence for volatile-driven activity on Mercury. *(a) Putative explosive volcanic deposit (bright material) called Nathair Facula and central, irregular depression interpreted as an explosively excavated volcanic vent. Orthographic projection centred on 63.8°E, 35.8°N of the ~166 m/pixel global MDIS monochrome mosaic. (b) Hollows in Kyōsai crater give its floor a moth-eaten appearance. Sinusoidal projection centred on 5.1°E, 25.1°N of NAC frame EN0250852067M.*

2.5.2.1 Explosive volcanism

Perhaps the most convincing photogeological evidence that volcanism of some form occurred during Mercury's history is the observation of irregular, rimless depressions several tens of kilometres across *(HEAD ET AL., 2008)* distributed across Mercury (e.g. Fig. 2.12a) that are often accompanied by high-albedo, diffuse red spots centred on, and extending beyond, the depression *(MURCHIE ET AL., 2008).* The irregular depressions are interpreted as explosively excavated volcanic craters, since, unlike impact craters, they can be highly non-circular and lack uplifted rims, and the red spots (now named 'faculae', *sing.* 'facula') are interpreted as explosive volcanic deposits *(HEAD ET AL., 2008; KERBER ET AL., 2009, 2011; GOUDGE ET AL., 2014; THOMAS ET AL., 2014A; JOZWIAK ET AL., 2018).*

Most putative volcanic craters are located within impact craters *(THOMAS ET AL., 2014A; JOZWIAK ET AL., 2018).* This suggests that impact craters facilitated these volcanic eruptions somehow, possibly by propagating fractures that could then be

exploited by ascending magmas, or by removing a thickness of overburden that posed a barrier to magma ascent *(THOMAS ET AL., 2014A; BYRNE ET AL., 2016; JOZWIAK ET AL., 2018)*.

The discovery of explosive volcanism on Mercury was surprising since the exsolution of volatile species in a magma is required to drive the explosion *(CASHMAN ET AL., 2000)*. As explained in Section 2.2.4, the planetary formation mechanisms that allow Mercury to retain a large iron core would have exposed the planet's materials to high temperatures. This would have driven-off volatiles, leaving Mercury's interior depleted in such species *(NITTLER ET AL., 2011)*. The surface geochemistry of Mercury appears volatile-rich, but this conceivably could be an exogenic veneer, however the observation of explosive volcanism on Mercury provides evidence that volatiles are present in Mercury's interior, which suggests that they are endogenic.

As an airless body, pyroclasts from explosive eruptions on Mercury would have followed essentially ballistic trajectories *(WILSON AND HEAD, 1981)*. Furthermore, even a modest magma volatile content would have caused violent explosion eruptions *(WILSON AND HEAD, 1981)*. *KERBER ET AL. (2009)* calculated that ~5,500 ppm of CO (an important lunar magmatic volatile) would be required to ejecta pyroclasts from a prominent pit in southwestern Caloris Planitia with sufficient velocity to reach the outermost extent of its putative deposit, Agwo Facula (range 24 km). For comparison, basalts erupted from Kilauea, Hawai'i indicate ~1,300–6,500 ppm (H_2O, CO_2, S) for their mantle source *(GERLACH, 1986)*. The volatile content inferred for Mercury is far greater than that of the Moon *(WILSON AND HEAD, 1981)*, which is volatile-depleted as a result of a giant impact *(TAYLOR, 1987)*. Therefore, the discovery that Mercury is not volatile-depleted calls into doubt many older hypotheses for the planet's formation (see Section 2.5.4).

More recent studies have suggested that the volatile species driving explosive volcanism on Mercury is sulfur, carbon, or some combination of the two *(WEIDER ET AL., 2016)*. This is because MESSENGER XRS and NS data suggest that the largest putative explosive volcanic deposit on Mercury, Nathair Facula, is depleted in sulfur and carbon compared with the rest of Mercury's surface *(NITTLER ET AL., 2011; PEPLOWSKI ET AL., 2016)*. Whether these volatile species come from a mantle source

or are imbued in the magma by assimilation from the crust during ascent remains uncertain *(JOZWIAK ET AL., 2018)*, since no direct evidence of mantle volatiles has been found so far.

Where smooth plains and putative explosive volcanic deposits are in contact, the explosive deposits always superpose the smooth plains *(HEAD ET AL., 2009; ROTHERY ET AL., 2014)*. No observations of a facula partially obscured by smooth plains have been made. This suggests that explosive volcanism on Mercury outlasted large-volume effusive volcanism. The limited lateral extent and thickness of Mercury's putative pyroclastic deposits means that they are not good targets for crater size-frequency distribution studies, but, cognisant of the difficulties in employing this method, *THOMAS ET AL. (2014C)* found tentative model ages for five explosive volcanic deposits on Mercury that suggest they formed 3.9–3.3 Ga. It is possible that global contraction inhibited magma ascent within Mercury in general, but explosive volcanism was able to continue for longer as a result of the buoyancy imparted to such magmas by their volatile content *(THOMAS ET AL., 2015)*.

2.5.2.2 Hollows

Hollows provide further evidence of volatiles species within Mercury's crust *(BLEWETT ET AL., 2011, 2013; THOMAS ET AL., 2014C)*. Hollows are depressions typically up to several hundred metres across and up to tens of metres deep, which makes them smaller than typical putative explosive volcanic vents on Mercury (e.g. Fig. 2.12b). They have steep sides and flat, uncratered floors. This crisp morphology implies that they are geologically young and/or actively forming. They have irregular, but typically rounded outlines, but they lack raised rims. Hollows often occur in close proximity to one another, and large hollows appear to have formed when smaller, clustered hollows coalesced *(BLEWETT ET AL., 2011)*. They appear relatively bright and blue in enhanced colour compared with intermediate terrain on Mercury *(BLEWETT ET AL., 2011)*.

Hollows typically occur on the floors of impact craters, or on crater peaks, walls, or proximal ejecta *(BLEWETT ET AL., 2011)*. Most craters with hollows developing within their materials have exhumed low-reflectance material *(DENEVI ET AL., 2009; BLEWETT ET AL., 2013)*. Hollows that exist outside impact craters still appear to form

in low-reflectance material, although the origin of such low-reflectance material itself is not clear *(XIAO ET AL., 2013)*. Hollows appear to be anti-correlated with the high-reflectance red plains *(BLEWETT ET AL., 2013; THOMAS ET AL., 2014C)*, which suggests that these plains lack the necessary materials for hollow formation. Therefore, it has been suggested that they form by the loss of a surface darkening agent in the low-reflectance material, leaving the resultant hollow with a characteristically bright appearance *(BLEWETT ET AL., 2013)*.

When hollows were first discovered, several ideas about how they formed were discussed. Volcanism can produce depressions by caldera and pit collapse, but hollows are much smaller than the explosive volcanic vents elsewhere on Mercury *(ROTHERY ET AL., 2014; THOMAS ET AL., 2014B, 2014A; JOZWIAK ET AL., 2018)* and have very different colour signatures *(BLEWETT ET AL., 2011)*, most noticeable where hollows and explosive vents occur alongside each other. Furthermore, hollows appear to occur, among other places, on crater ejecta, which is an unlikely location for volcanic eruptions *(BLEWETT ET AL., 2011)*.

The most likely formation mechanism for hollows is that Mercury's interior contains materials that volatilise when exposed to surface conditions *(BLEWETT ET AL., 2011)*. This explains why hollows are associated with impact craters, which exhume material from pressure-temperature conditions in the subsurface where they are stable, and deposit them at the surface where they become susceptible to volatilisation. The existence of volatiles in the subsurface of Mercury is already established by the widespread explosive volcanic vents *(THOMAS ET AL., 2014A; JOZWIAK ET AL., 2018)*. The exact mechanism of volatile-loss is still debated. Some studies have found some evidence that hollows occur more commonly on Sun-facing slopes within impact craters *(BLEWETT ET AL., 2013; THOMAS ET AL., 2014C)*, which suggests that volatile-loss could be an insolation-driven process, such as sublimation, thermal desorption, or photon-stimulated desorption *(PIETERS AND NOBLE, 2016)*. If sublimation is responsible, then that would make the hollows analogous to the Swiss-cheese terrain at the south pole of Mars *(THOMAS ET AL., 2000; MALIN ET AL., 2001)*. Alternatively, micrometeorite bombardment might provide the energy for volatile release, but this mechanism would operate equally well on anti-Sun slopes, so it is not presently favoured.

If hollows formed by the loss of a volatile component from the low-reflectance material, then the question remains as to what the lost volatile component is. High-resolution multispectral images of hollows were examined by *THOMAS ET AL. (2016)* to measure the reflectance spectra of hollows walls, where hollow growth appears to be ongoing, and hollow floors, where the inert lag deposit gathers and hollow formation is not ongoing. They found that the final lag after hollow formation has a flatter spectral slope than that of any other previously measured surface unit (see *DENEVI ET AL., 2009*). This means that the lost volatile component must have a redder spectral slope and a higher reflectance than the parent low-reflectance material. This is consistent with the volatile component being calcium or magnesium sulfides *(THOMAS ET AL., 2016)*. The low iron abundance of Mercury's surface means that most sulfur on Mercury is in calcium and magnesium sulfides *(NITTLER ET AL., 2011)*. *THOMAS ET AL. (2016)* also found that carbon is not lost during hollow formation, which means that it must be inert. This is consistent with graphite being the darkening agent of the low-reflectance material and Mercury's surface in general *(MURCHIE ET AL., 2015)*. This does not preclude carbon from acting as a volatile within magmas, due to their high temperatures.

2.5.3   Tectonics

MESSENGER's complete imaging of Mercury's surface allowed several studies of global tectonics. *BYRNE ET AL. (2014)* mapped shortening tectonic features across the whole globe. They calculated that Mercury has lost ~7 km of its planetary radius since its formation. This brought the amount of global contraction in line with thermophysical models of Mercury's cooling, which were in conflict with the ~2 km of planetary radius loss based on Mariner 10 data *(DOMBARD AND HAUCK, 2008)*.

WATTERS ET AL. (2015) mapped lobate scarps >50 km in length and found that their distribution and density are non-uniform (Fig. 2.13). They report that contractional landforms are concentrated in longitudinal bands and are generally oriented north–south at low latitudes and east–west at high latitudes, although they offer no explanation about how their observations are not influenced by illumination bias *(FEGAN ET AL., 2017)*. If these observations are real, then they cannot be explained by global contraction alone (Fig. 2.6). The observed preferred

orientation of lobate scarps is consistent with the pattern of faulting predicted by the tectonics of a tidally despun planet *(MELOSH, 1977)*, particularly if high-latitude lobate scarps were reactivated structures exploiting earlier normal faults *(DOMBARD AND HAUCK, 2008)*. A later study using artificially illuminated MLA digital elevation models of Borealis Planitia, an approach that mitigates the problems of illumination bias, also found predominantly east–west trending polar faults and north–south trending mid-latitude faults *(CRANE AND KLIMCZAK, 2019)*.

A combination of global contraction and tidal despinning still cannot account for the spatial concentration of lobate scarps *(WATTERS ET AL., 2015)*. It appears that where the faults are concentrated, Mercury's crust has been thickened by mantle downwelling *(JAMES ET AL., 2015)*, which would accentuate compressional stresses, as has been shown to be the case on Earth *(NEIL AND HOUSEMAN, 1999)*. So it appears that Mercury's global tectonics is best explained by tidal despinning before the end of the Late Heavy Bombardment, so that impacts and volcanism could remove any traces of polar normal faults, followed by global contraction that exploited pre-existing lithospheric weaknesses inherited from tidal despinning. In addition, mantle dynamics played a role in spatially concentrating faults throughout the planet's history *(KING, 2008; WATTERS ET AL., 2015)*.

The cross-cutting relationships between lobate scarps and impact craters in different states of degradation suggest that lobate scarp activity has occurred over much of the last 3–4 Gyr *(BANKS ET AL., 2015)*, but crater size-frequency distributions suggest the largest lobate scarps observed today had reached their present day size ~3.5 Ga *(GIACOMINI ET AL., 2015)*. Lobate scarp formation has been shown to have been active in Mercury's geologically recent past *(WATTERS ET AL., 2016)*, which suggests global contraction is ongoing today, albeit at a slower rate than occurred during the Late Heavy Bombardment *(BANKS ET AL., 2015)*.

MESSENGER also revealed long-wavelength undulations in Mercury's surface elevation *(ZUBER ET AL., 2012)* that are unrelated to crustal thickness variations *(SMITH ET AL., 2012)* or faulting *(BYRNE ET AL., 2014)*. Three approximately east-northeast–west-southwest trending undulations (two crests and a medial trough) appear to have warped Caloris Planitia, which requires the warping to postdate smooth plains emplacement within Caloris *(FASSETT ET AL., 2009; DENEVI ET AL.,*

2013; BYRNE ET AL., 2014; MANCINELLI ET AL., 2016). In Borealis Planitia, a broad, circular topographic rise (the 'northern rise') also appears to postdate regional smooth plains emplacement *(ZUBER ET AL., 2012).* It has been suggested that these undulations have been caused by lithospheric folding or dynamic mantle processes *(BYRNE ET AL., 2014).* However, recent finite-element models have suggested that the compression required to fold Mercury's lithosphere to generate the observed undulations would be equivalent to hundreds of kilometres of planetary radius loss (rather than ~7 km), making it highly unlikely that lithospheric folding played a substantial role in forming the undulations *(KAY AND DOMBARD, 2019).* Furthermore, the amplitude of dynamic topography predicted by convective mantle support *(KING, 2008)* is one to two orders of magnitude below that of the undulations *(KLIMCZAK ET AL., 2013).* Therefore, the problem of the source of these topographic undulations remains unsolved.

2.5.4   Formation of Mercury

The discovery that Mercury is relatively enriched in volatiles has meant that the formation of the planet has had to be reconsidered *(PEPLOWSKI ET AL., 2011).* The partial vaporisation and giant impact formation mechanisms introduced in Section 2.2, which were put forward to explain the presence of a disproportionately large iron core within Mercury, are no longer viable since they would involve a short period of intense heating of the planet, which would be expected to leave the planet depleted in volatile species *(PEPLOWSKI ET AL., 2011).*

Longitudinal Distribution of Prominent Faults
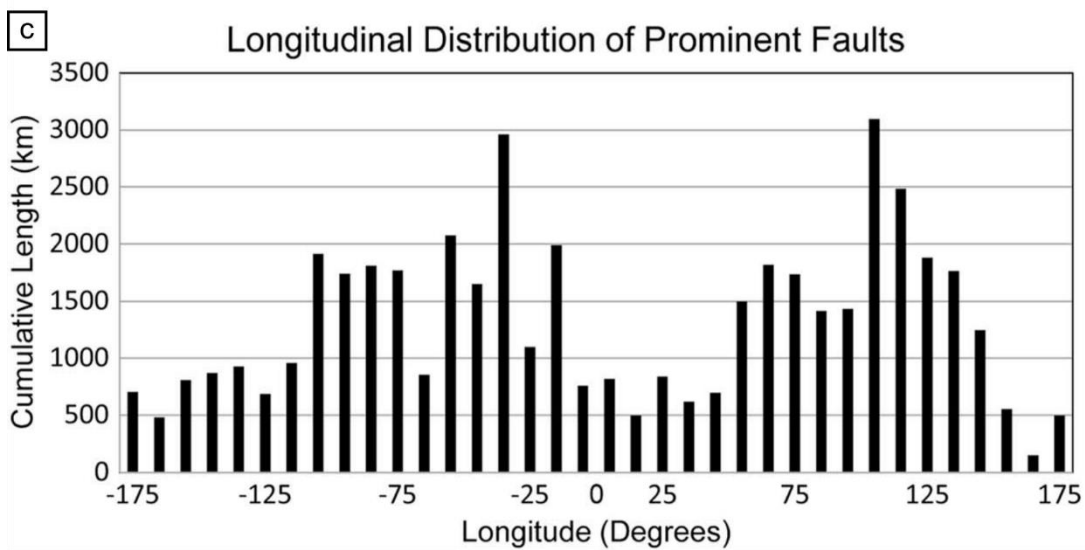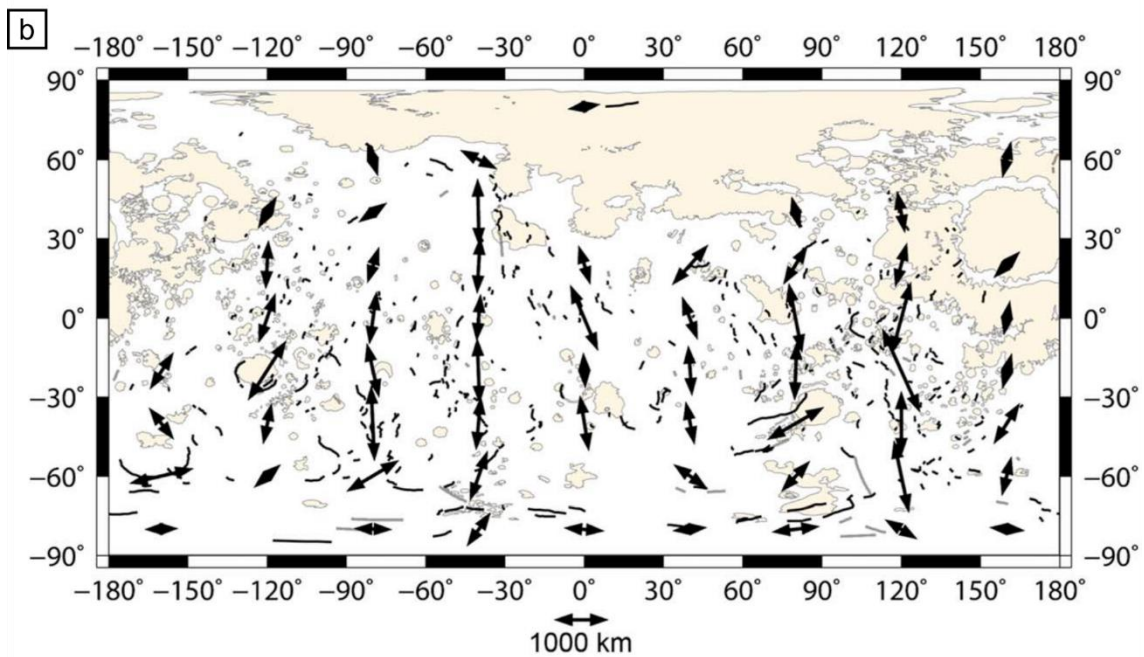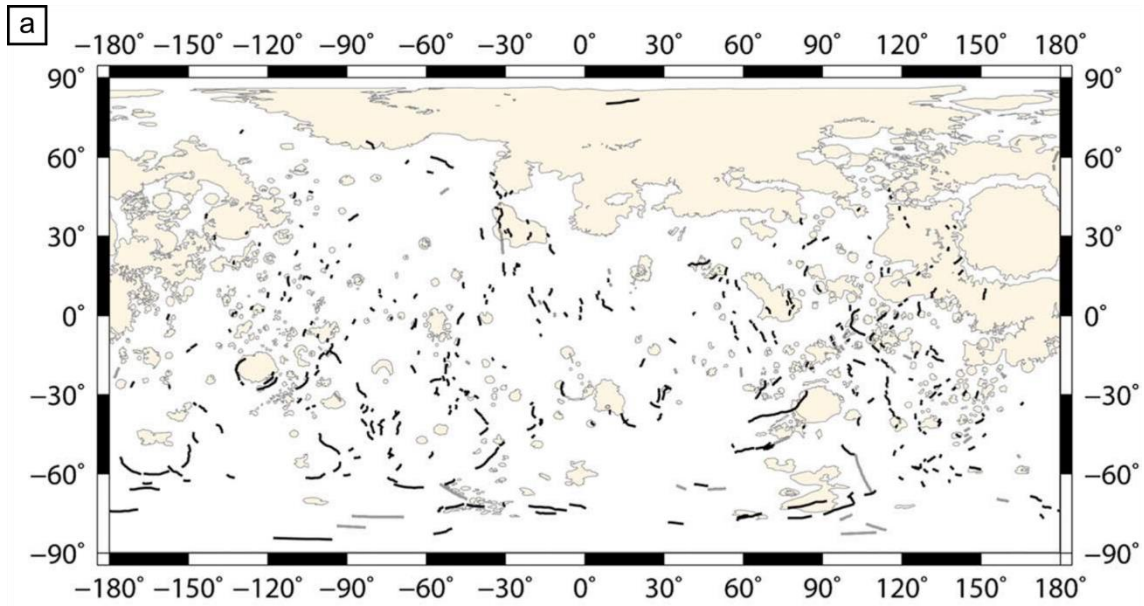
Fig. 2.13 Distribution and orientation of lobate scarps on Mercury mapped by WATTERS ET AL. (2015). *(a) Map of lobate scarps >50 km in length superimposed on a map of smooth plains (light yellow) by* DENEVI ET AL. (2013). *(b) Double-headed arrows indicate local fault orientation and are scaled to reflect total local fault length. Equatorial lobate scarps are generally north–south, whereas higher latitude scarps are more often east–west. (c) Histogram of total fault length binned by longitude. There is an apparent marked decrease in lobate scarp length between 0–60°E and 150–240°E, probably due to smooth plains from Borealis Planitia and the Caloris smooth plains. From* WATTERS ET AL. (2015).

One new suggestion is that Mercury was a hit-and-run impactor whose core was not catastrophically disrupted by the collision and instead migrated away from the collision site *(ASPHAUG AND REUFER, 2014)*. If Mercury formed farther out in the solar system from its present day orbit then it might have accreted a volatile-rich silicate shell larger than it currently possesses. Many numerical simulations of planetary formation predict hit-and-run collisions between proto-planets and proto-planetary migration *(ASPHAUG AND REUFER, 2014)*. It is possible that a larger, naturally volatile-rich Mercury, which formed farther out in the solar system, migrated inward and was involved in a hit-and-run collision. By having Mercury move away from the site of the giant impact, it could not reaccrete much of its silicates stripped by the collision, explaining how the planet has a large core but only a thin mantle *(ASPHAUG AND REUFER, 2014)*. However, it would seem that this model would cause heating of Mercury that would drive off the planet's volatiles. Whether more volatiles could be retained during multiple, low-energy hit-and-run collisions is unclear.

Currently, the most favoured formation model for Mercury is the iron-rich accretion model of *WEIDENSCHILLING (1978)*. Recently, it has been suggested that the solar magnetic field in the protoplanetary disk aided rapid accretion of iron-rich aggregates at Mercury's present-day orbit *(KRUSS AND WURM, 2018)*. After the iron-rich proto-Mercury reached a sufficient size, it would be able to accrete and retain chondritic material that would endow it with the volatile-rich crust observed today *(PEPLOWSKI ET AL., 2011)*.

2.5.5   Summary

In summation, MESSENGER has shown that Mercury is a unique planet in the solar system. Its bulk composition (volatile- and metal-rich) means that the planet had a formation and early development unlike any of the other terrestrial planets. Furthermore, the cooling of the relatively large core means that Mercury's lithosphere has been in compression for most of the planet's history, which has dominated the planet's tectonics and influenced the expression of its volcanism. The volatile content of Mercury is demonstrated by hollows probably active today and explosive volcanism that has persisted through Mercury's geological history, and it remains to be seen what further unexpected landforms and processes these volatiles could have contributed to. A graphical summary of the geological history of Mercury based on MESSENGER data is shown in Fig. 2.14.
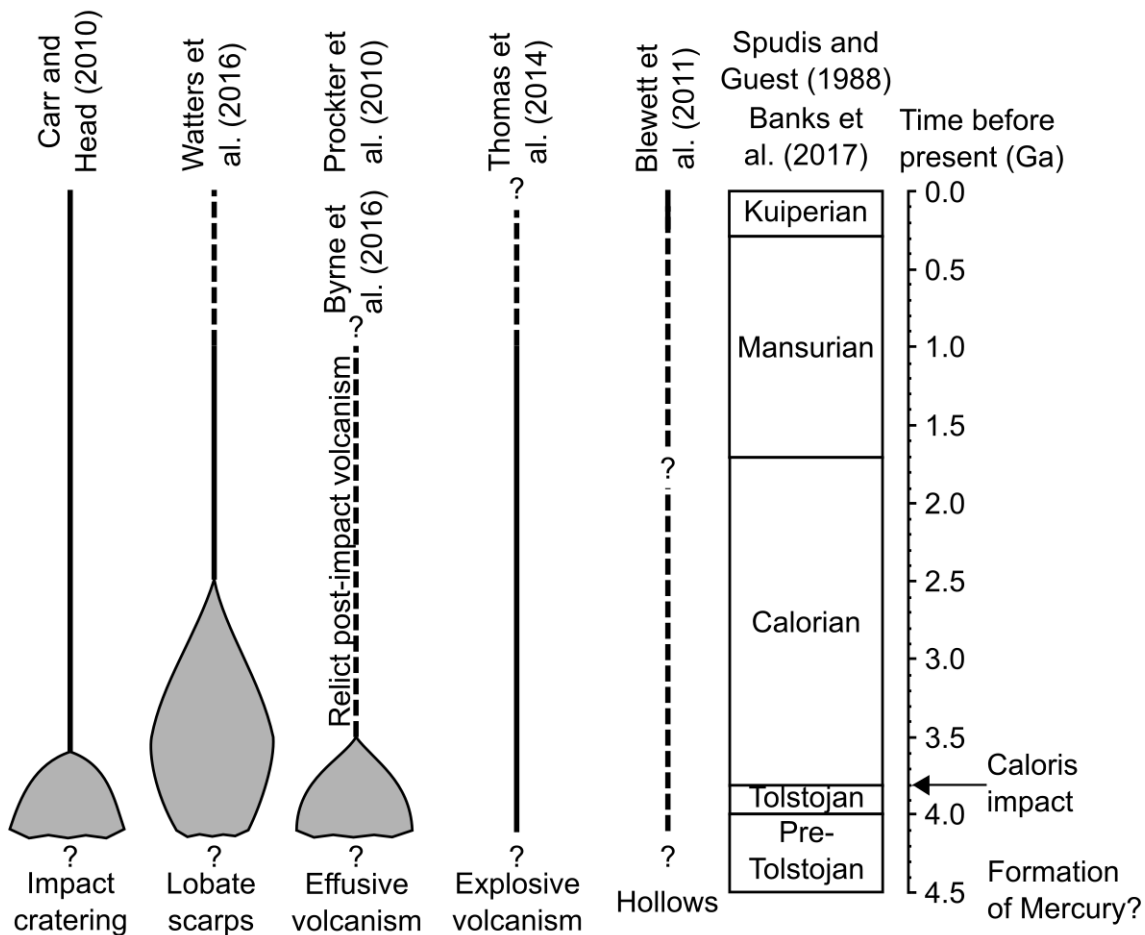
Fig. 2.14 Summary of the geological history of Mercury. On the right is an absolute timescale. The time systems of Mercury are shown to the left of the absolute time scale. The basal ages of the Kuiperian and the Mansurian are taken from (BANKS ET AL., 2017). Approximate basal ages for the Calorian and Tolstojan are taken from (SPUDIS AND GUEST, 1988). The base of the Pre-Tolstojan is undefined. To the left of the Hermean time systems are graphical representations of the prevalence and duration of various geological processes during Mercury's history. References containing the absolute ages indicated in this figure are labelled appropriately. Impact cratering is thought to have been very intense on Mercury before the end of the Late Heavy Bombardment of the inner solar system ~3.8 Ga. As an airless body, impact cratering remained an important geological process throughout Mercury's history, albeit at a reduced rate. Lobate scarps are thought to have increased in activity following an initial stage of planetary expansion (for which there is no observable geological evidence) during core formation and reached peak activity ~3.5 Ga. After this, lobate scarp activity declined due to the decrease in the rate of secular cooling, but new, young lobate scarps continued to be formed until the relatively recent past. Effusive volcanism, which generated the widespread intercrater plains, was most active before the onset of global contraction. The last large-volume effusive eruptions formed the smooth plains, and these eruptions ceased at around the time lobate scarp activity reached its peak. Explosive volcanism was presumably active during the same interval as effusive volcanism, however there is no evidence that it resurfaced substantial areas of Mercury's surface, so it must be assumed that this process has always been much less dominant than effusive volcanism when both eruptive styles were active together. However, the superposition of putative explosive volcanic deposits on smooth plains suggests that explosive volcanism outlasted effusive volcanism. Evidence for Kuiperian explosive volcanic activity has been reported, but most volcanic activity appears to have ceased before this. All hollows appear geologically recent, but the materials for their formation appear to be endogenic, which suggests that hollow formation could have occurred throughout Mercury's history.

In Table 2.1 I summarise MESSENGER-derived properties of Mercury as a reference for the reader.

Physical properties	
Mass	3.30×10^{23} kg *(MAZARICO ET AL., 2014)* 0.055 Earth masses
Mean radius	2439.36 km *(PERRY ET AL., 2015)* 0.38 Earth radii
Surface gravity	3.70 ms^{-2} *(MAZARICO ET AL., 2014; PERRY ET AL., 2015)* 0.38g
Axial tilt (relative to the normal of the orbital plane)	2.06' (0.034°) *(MAZARICO ET AL., 2014)*
Rotational period	58.6 Earth days *(MAZARICO ET AL., 2014)*
Orbital characteristics	
Aphelion	0.47 AU
Perihelion	0.31 AU
Orbital period	88 Earth days

Table 2.1 Mercury planetary properties measured by MESSENGER.

2.5.6 BepiColombo

BepiColombo *(BENKHOFF ET AL., 2010)*, the next spacecraft mission to Mercury, launched on 20th October 2018. It is a joint European Space Agency (ESA) and Japan Aerospace Exploration Agency (JAXA) mission comprising two spacecraft with scientific payloads, the Mercury Planetary Orbiter (MPO) and the Mercury Magnetospheric Orbiter (MMO), designed to study Mercury after orbital insertion on 5th December 2025. ESA delivered MPO, which will focus on studying the surface of the planet *(ROTHERY ET AL., 2010)*.

Before BepiColombo arrives, it is important that as much as possible is known about Mercury based on MESSENGER data. From a planetary geology standpoint, the most valuable tools for generating science targets and objectives for a new spacecraft mission are detailed geological maps. As stated previously, MESSENGER data have been used to create the first global geological map of Mercury *(PROCKTER*

ET AL., 2016; KINCZYK ET AL., 2018B). This map is being produced at a small map scale (1:15M), which is useful for a global picture of the planet, but it does not exploit the maximum resolution of MESSENGER data. Larger scale quadrangle geological maps are being produced using MESSENGER data to provide science context and targets for BepiColombo *(GALLUZZI ET AL., 2019).* These maps are being produced for publication at the 1:3M-scale, which allows greater detail to be shown on each quadrangle map than can be shown on the global map. MESSENGER-era quadrangle geological maps of three quadrangles have been published so far *(GALLUZZI ET AL., 2016; MANCINELLI ET AL., 2016; GUZZETTA ET AL., 2017)* and the maps of the remaining quadrangles are to be published before the arrival of BepiColombo *(GALLUZZI ET AL., 2019).*

MMO

MOSIF

MPO

MTM

SYMBIO-SYS
(spectrometer)

SERENA-ELENA

SERENA-PICAM

SERENA-MIPA

MIXS-T

MIXS-C

MERTIS

SIMBIO-SYS
(high resolution camera)

SERENA-STROFIO

BELA
(receiver)

BELA
(transmitter)

SIMBIO-SYS
(stereo camera)
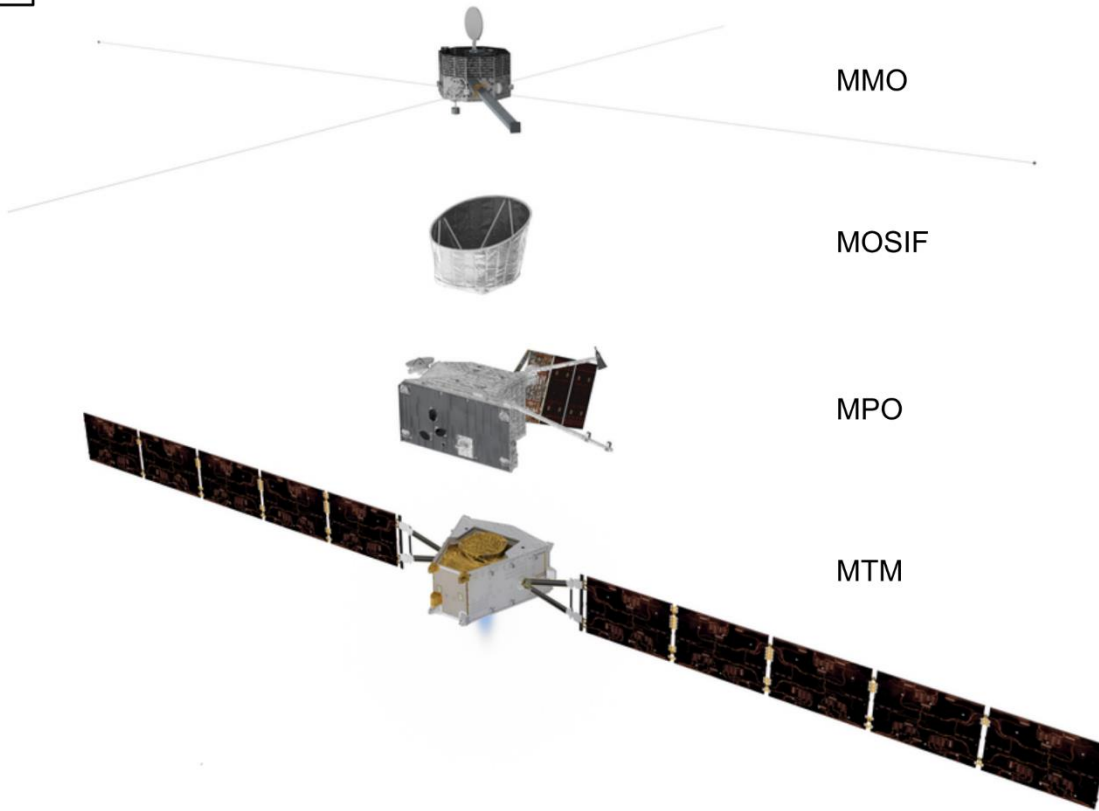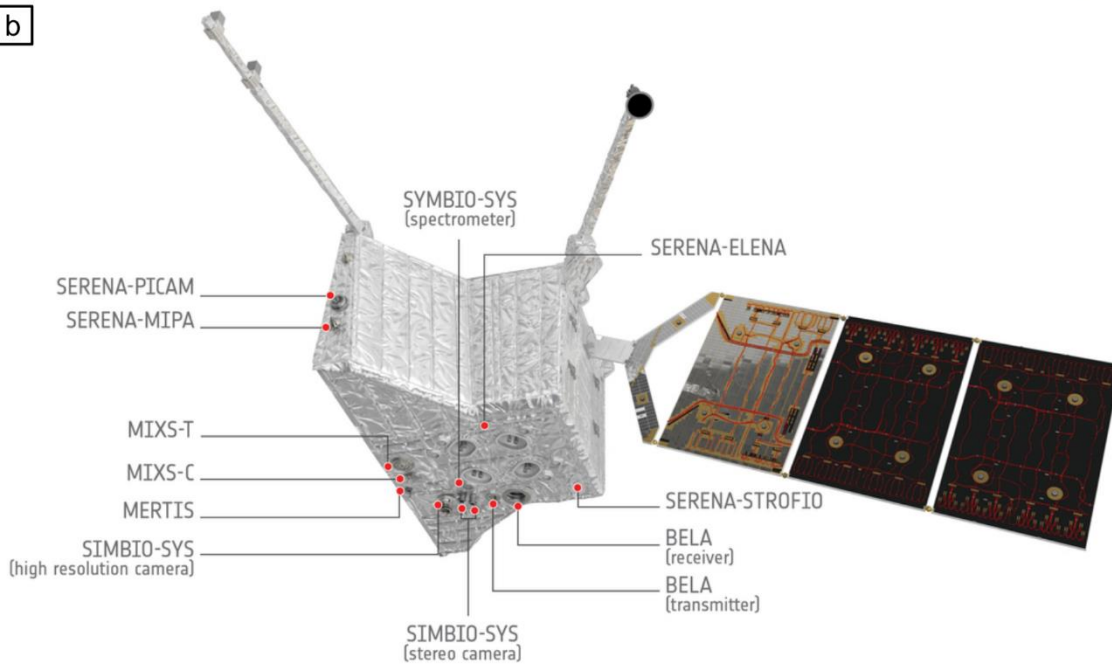
Fig. 2.15 The BepiColombo spacecraft and the instruments that will study Mercury's geology. *(a) Exploded artist's conception of the BepiColombo spacecraft stack. MMO: Mercury Magnetospheric Orbiter. MOSIF: MMO Sunshield and Interface Structure. MPO: Mercury Planetary Orbiter. MTM: Mercury Transfer Module. (b) The instruments of MPO. SYMBIO-SYS: Spectrometers and Imagers for MPO BepiColombo Integrated Observatory System. Encompasses: Stereo Channel (STC) for colour and monochrome imaging of the whole planet at 50 m/pixel resolution or better; the High Spatial Resolution Imaging Channel (HRIC) for 5 m/pixel colour and monochrome imaging, and; Visible and near-Infrared Hyperspectral Imaging channel (VIHI) for imaging in 256 narrow channels (400–2,000 nm) at up to 100 m/pixel. BELA: BepiColombo Laser Altimeter for measuring the topography of Mercury at all latitudes. MERTIS: Mercury Radiometer and Thermal Infrared Spectrometer for mineralogical, temperature, and thermal inertia mapping. MIXS: Mercury Imaging X-ray Spectrometer for element mapping, including Si, Ti, Al. Fe, Mg, Na, Ca, P, Mn, K, S, Cr, Ni, and O. SERENA: Search for Exosphere Refilling and Emitted Neutral Abundance. Encompasses Emitted Low-Energy Neutral Atoms (ELENA), Start from a Rotating Field Mass Spectrometer (STROFIO), Miniature Ion Precipitation Analyser (MIPA), and Planetary Ion Camera (PICAM). Together these instruments will identify the sources, sinks and compositions of exospheric atoms and ions.*

2.6   Research questions

The MESSENGER mission has answered many questions about the geology of Mercury, but as I have highlighted in the previous sections, work remains to be done, some of which can be achieved before the arrival of BepiColombo.

As part of this thesis, I have constructed a geological map of the Hokusai quadrangle (H05) of Mercury. In Chapter 3 I explain why I selected this quadrangle for mapping and in Chapter 4 I discuss the geological history of the region that my map (Appendices 1 and 2) records.

While I constructed my map, I studied the global context of H05 and I became particularly interested in the history and modes of volcanism on Mercury and the various volatile-driven processes on the planet. I set out to investigate the following research questions:

- What is the geological history of the Hokusai quadrangle? Are there any photogeological units of regional extent that have not been demarcated in the global geological map of Mercury? If there are, what are the probable provenances of such units?

- Are volcanic plains the only expressions of effusive volcanism on Mercury? For example, small shield volcanoes have been observed on the Moon, Mars and Io. Are there small volcanic constructs on Mercury? If so, under what circumstances are they likely to have formed? If not, what has inhibited volcanic construction?

CHAPTER 3
GEOLOGICAL MAPPING OF THE HOKUSAI (H05) QUADRANGLE OF MERCURY

3.1   Selection of H05 as the mapping area

3.1.1   Mariner 10 quadrangle maps
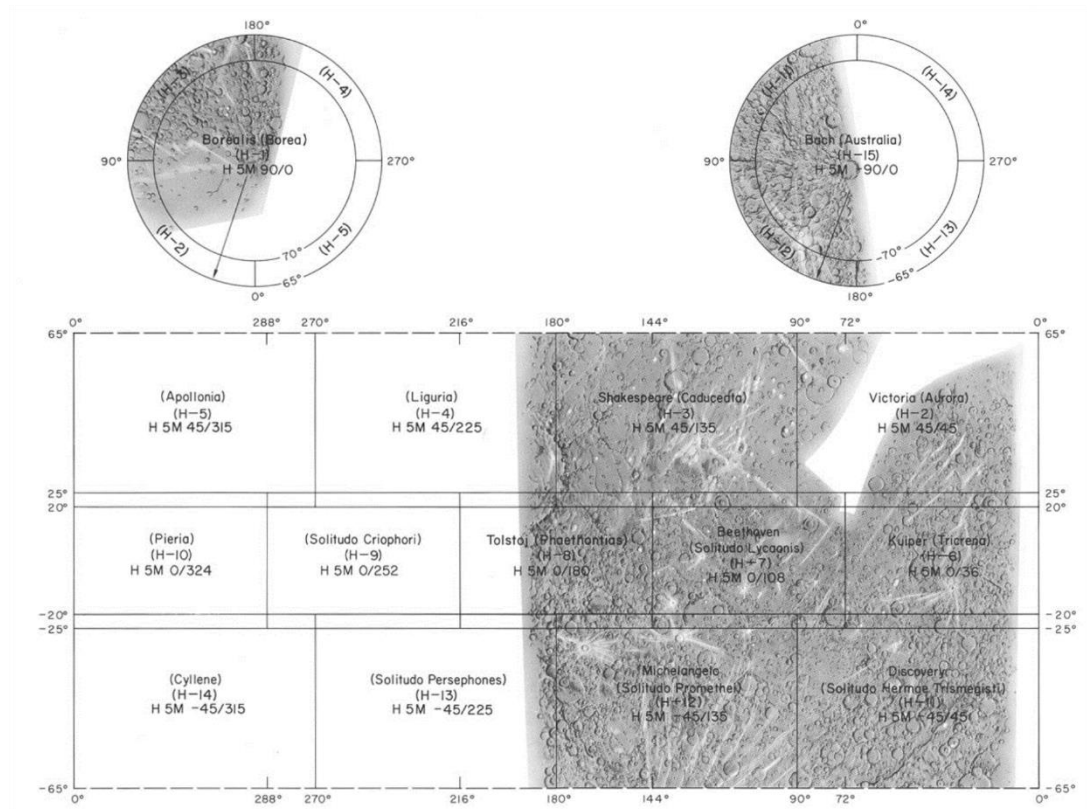
Fig. 3.1 Mariner 10-era quadrangles of Mercury. *Longitudes are given in degrees west. Western hemisphere quadrangles are shown with shaded relief maps and bright crater rays. The shaded relief maps indicate the image coverage of Mercury provided by Mariner 10. Note how western hemisphere quadrangles have primary names based on prominent topographic features contained within them, as well as subsidiary names (in brackets) that come from albedo features seen in Earth-based radar images. Quadrangles unimaged by Mariner have albedo names only. From DAVIES ET AL. (1978).*

Before the arrival of Mariner 10 in 1974, Mercury was divided into 15 latitudinally and longitudinally defined 'quadrangles' in preparation for studies of its surface *(DAVIES ET AL., 1978)*. The arrangement of those quadrangles is shown in Fig. 3.1.

By conducting photogeological interpretation of Mariner 10 data, geological maps of H01 (GROLIER AND BOYCE, 1984), H02 (MCGILL AND KING, 1983), H03 (GUEST AND GREELEY, 1983), H06 (DEHON ET AL., 1981), H07 (KING AND SCOTT, 1990), H08 (SCHABER AND MCCAULEY, 1980), H11 (TRASK AND DZURISIN, 1984), H12 (SPUDIS AND PROSSER, 1984) and H15 (STROM ET AL., 1990) were made at the 1:5M-scale. Due to the lack of Mariner 10 data, no maps of the eastern hemisphere of Mercury were produced. The extent of Mariner 10 1:5M-scale geological mapping of Mercury is shown in Fig. 3.2.
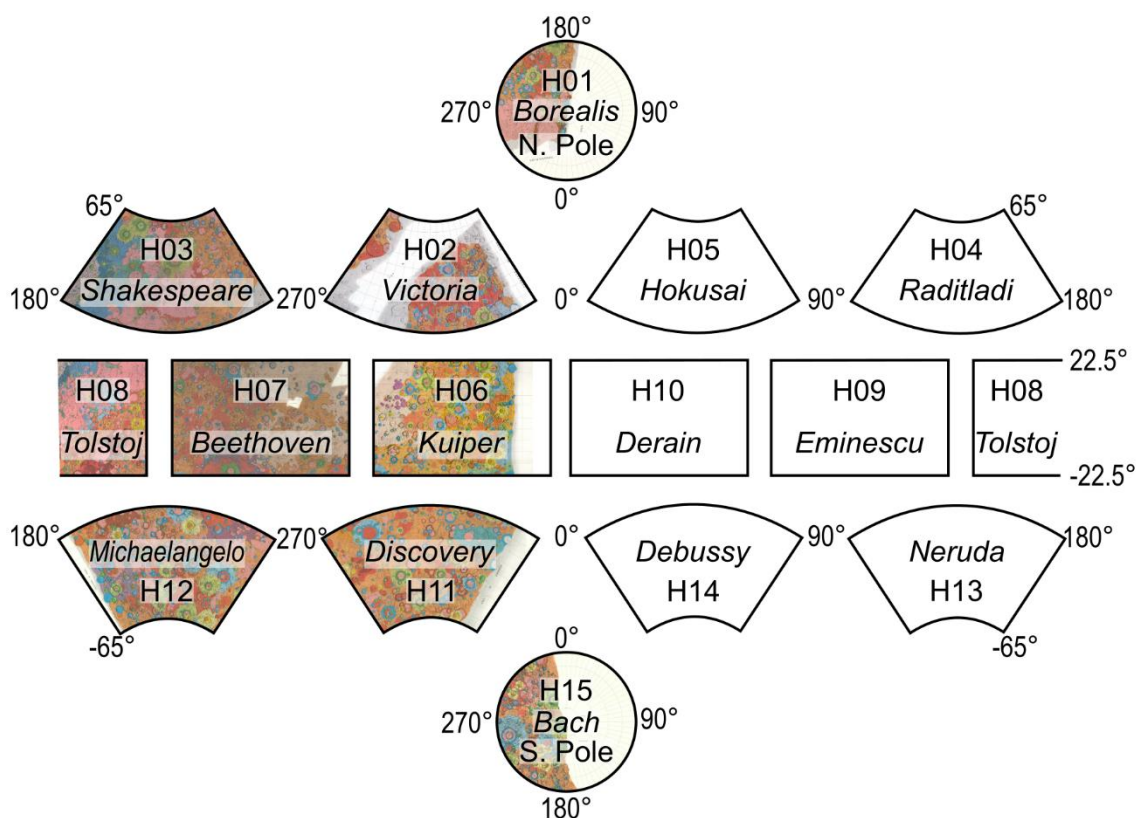
Fig. 3.2 Mercury geological mapping coverage at the beginning of the MESSENGER mission. *The 1:5M scale quadrangle geological maps of Mercury based on Mariner 10 data are shown (SCHABER AND MCCAULEY, 1980; DEHON ET AL., 1981; GUEST AND GREELEY, 1983; MCGILL AND KING, 1983; GROLIER AND BOYCE, 1984; SPUDIS AND PROSSER, 1984; TRASK AND DZURISIN, 1984; KING AND SCOTT, 1990; STROM ET AL., 1990). Note that eastern hemisphere quadrangles are labelled here with their topographic feature names given to them during the early stages of the MESSENGER mission. This figure is an updated version of Fig. 3.1, with Mercury's prime meridian in the centre and positive east degrees of longitude, which is the convention of this thesis. During the MESSENGER mission, quadrangle boundaries were modified so that northern and southern boundaries of the equatorial quadrangles are at 21.5° north and south, respectively. After DAVIES ET AL. (1978).*

3.1.2   MESSENGER quadrangle maps

By the end of the mission, the MESSENGER spacecraft had achieved imaging with a global coverage and higher resolution than Mariner 10. This has allowed for the first quadrangle geological maps based on MESSENGER data to be produced *(GALLUZZI ET AL., 2016; MANCINELLI ET AL., 2016; GUZZETTA ET AL., 2017)*, including regions unseen by Mariner 10 *(GALLUZZI ET AL., 2016; MANCINELLI ET AL., 2016)*. The boundaries of the quadrangles were slightly redefined after the arrival of MESSENGER, as shown in Fig. 3.2. MESSENGER-era quadrangle maps are being produced at the 1:3M-scale (Fig. 3.3; *GALLUZZI ET AL., 2019*). These maps are being produced as part of an international effort to have 1:3M-scale maps covering all of Mercury in time for the arrival of the BepiColombo mission *(BENKHOFF ET AL., 2010)*. The map I produced as part of this thesis was intended from the beginning of my project to contribute to this international Mercury quadrangle mapping effort.
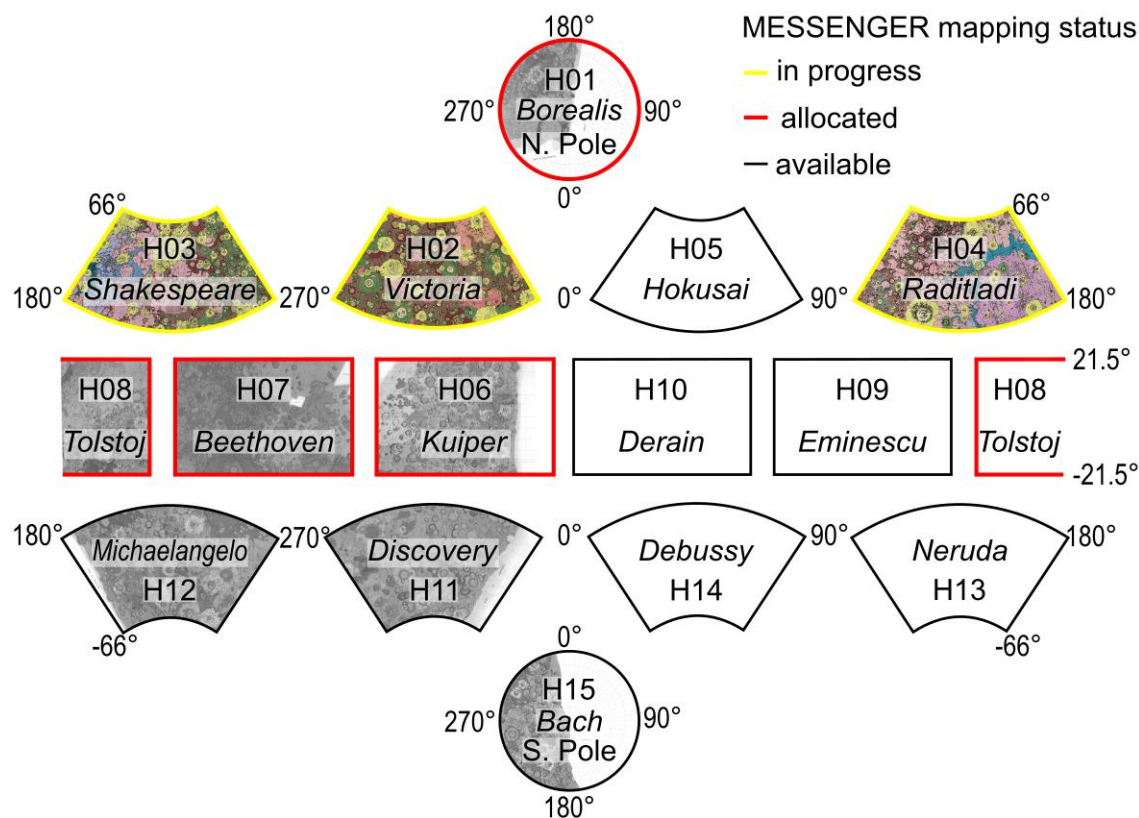
Fig. 3.3 Status of MESSENGER quadrangle geological maps when this work was beginning. *Mercury quadrangles with MESSENGER-era geological maps are highlighted in yellow and the maps are shown in colour. At the beginning of this work, these maps were unpublished but in an advanced state of preparation (GALLUZZI ET AL., 2016; MANCINELLI ET AL., 2016; GUZZETTA ET AL., 2017). Where only Mariner 10 maps were available, these are shown in greyscale. Quadrangles highlighted in red were known to be the subject of studies by other workers and I did not consider mapping them. The remaining quadrangles, outlined in black, were considered for mapping. After DAVIES ET AL. (1978).*

3.1.3   Selection process

The quadrangles available to map during my PhD were H05 (Hokusai), H09 (Eminescu), H10 (Derain), H11 (Discovery), H12 (Michaelangelo), H13 (Neruda), H14 (Debussy) and H15 (Bach). I evaluated each of these using the following criteria:

1. Does a Mariner 10 geological map of the quadrangle exist?
2. What is the mapping status of adjacent quadrangles?
3. What MESSENGER datasets and resolution are available for the quadrangle?
4. What known features of interest exist within the quadrangle?

5. What possible science questions could be investigated by making a geological map of the quadrangle?

Here, I summarise my reasoning for selecting the H05 quadrangle.

3.1.3.1 Previous maps of H05

As stated previously, H05 was not imaged by Mariner 10 so the quadrangle has no pre-existing geological maps. This formed an important part of my decision to select H05 for mapping, since I would be producing the first geological map of the region.

3.1.3.2 Quadrangles adjacent to H05

H05 is bordered by H01 in the north, H02 in the west, H04 in the east, H06 in the southwest, H10 in the south and H09 in the southeast (Fig. 3.4).

When I was evaluating quadrangles for mapping at the start of my work in October 2015, there were no published MESSENGER-era geological maps of any Mercury quadrangles. At that time, I was aware that the maps of H02 *(GALLUZZI ET AL., 2016)* and H04 *(MANCINELLI ET AL., 2016)*, the quadrangles to the west and east of H05, were in the final stages of preparation for publication. This information was important during my decision making process, since by mapping H05 I would be able to collaborate with the mappers of its adjacent quadrangles to fix the boundaries between our quadrangles. Furthermore, I was aware that a map of H03 (non-adjacent to H05) was underway at that time *(GUZZETTA ET AL., 2017)*. By mapping H05, I would be completing geological mapping coverage of the mid-northern latitudes of Mercury. Finally, I was aware that other workers, operating outside the European Mercury quadrangle mapping effort *(GALLUZZI ET AL., 2019)*, were seeking to prepare a geological map of H01 using MESSENGER data *(OSTRACH ET AL., 2018)*.
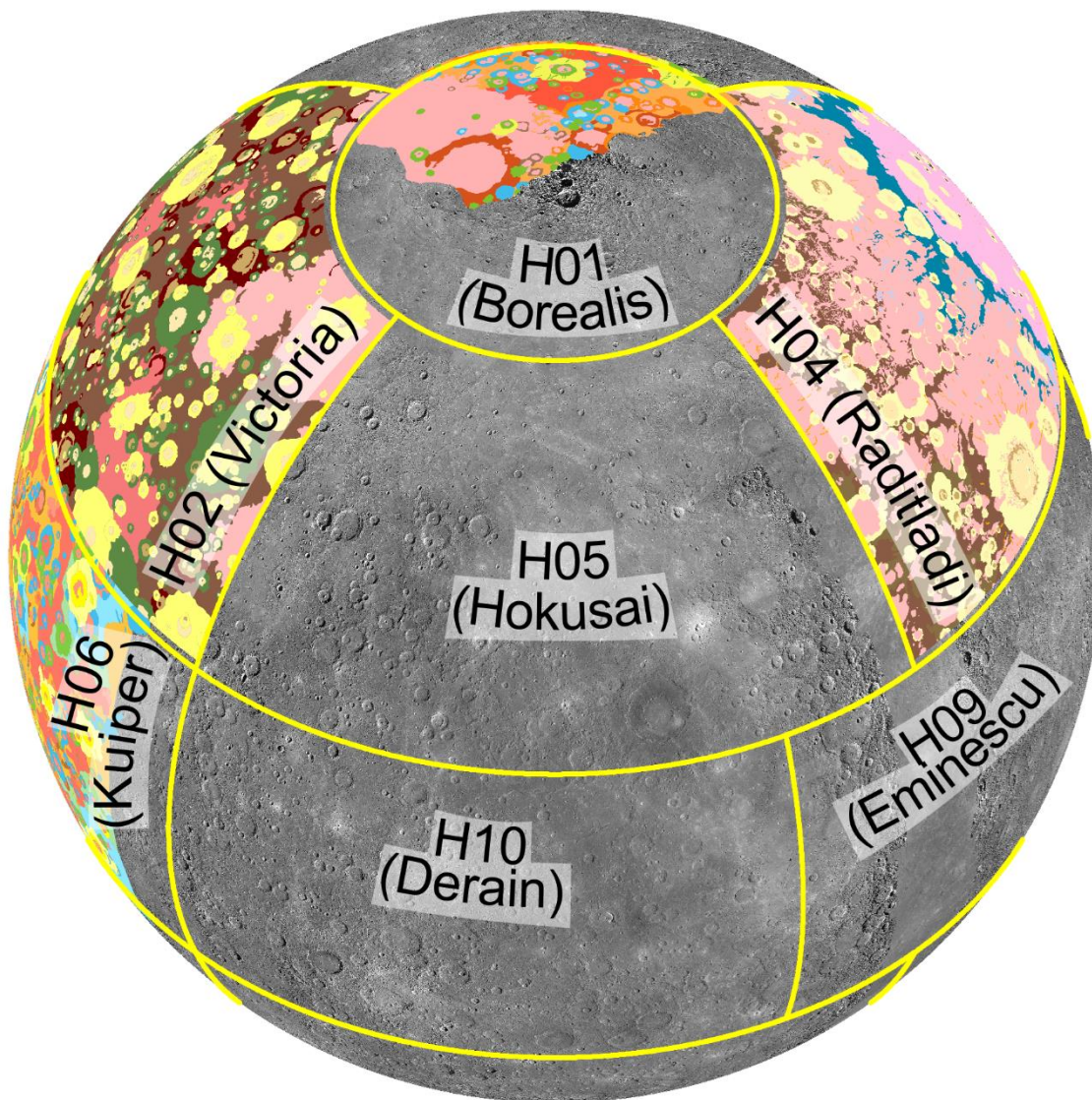
Fig. 3.4 Quadrangles adjacent to H05. *Quadrangle boundaries are marked in yellow. MESSENGER-era geological maps are shown for H02 (GALLUZZI ET AL., 2016) and H04 (MANCINELLI ET AL., 2016). Mariner 10 maps are shown for H01 (GROLIER AND BOYCE, 1984) and H06 (DEHON ET AL., 1981). Orthographic projection of the~166 m/pixel global basemap centred on H05 (CHABOT ET AL., 2016). Mariner 10 mapping shapefiles are publicly available at https://tinyurl.com/y8nejo2p. H02 and H04 shapefiles are reproduced with kind permission of the authors.*

At the time of selection, no other quadrangles had MESSENGER-era geological maps bordering H05. Furthermore, the partial maps of H01 *(GROLIER AND BOYCE, 1984)* and H06 *(DEHON ET AL., 1981)*, made using Mariner 10 data, do not extend to the shared boundaries of those quadrangles with H05 (Fig. 3.4). As eastern hemisphere quadrangles, no Mariner 10 maps of H09 or H10 existed at the time of

quadrangle selection. Therefore, during the course of my work, my map of H05 would could be checked against the MESSENGER maps of H02 and H04 only.

3.1.3.3 Availability of MESSENGER data for H05

Due to MESSENGER's highly elliptical orbit, with its periherm latitude drifting between 55.7°N and 84.1°N over the course of the mission (Fig. 3.5), dataset availability and spatial resolution are generally better in the northern hemisphere than the southern hemisphere. This was an important factor in my decision to map H05, since it was the last quadrangle available for me to map in the northern hemisphere.
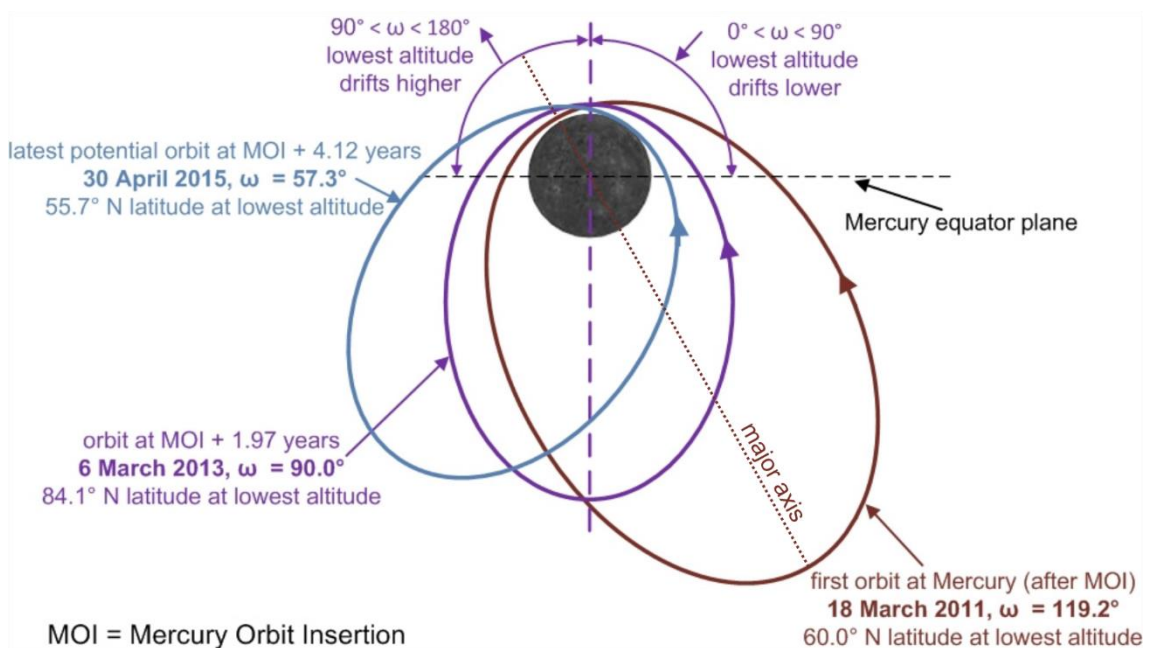
Fig. 3.5 MESSENGER orbital configurations at Mercury. MESSENGER's initial orbit after capture is shown in brown. Over the course of the mission, MESSENGER's orbital major axis rotated clockwise, in response to gravitational forcing by the Sun and Mercury, causing MESSENGER's 'argument of apoapis' (ω) to decrease from its original value of 119.2°. While 90° < ω < 180°, MESSENGER's periherm latitude drifted north toward 84.1°N and the periherm altitude drifted upward. Several orbital correction manoeuvres during the mission prevented the periherm altitude from drifting high enough to compromise data resolution. When ω became less than 90°, MESSENGER's periherm latitude began to drift south and its periherm altitude began to fall. Several orbital correction manoeuvres delayed the deorbiting of the spacecraft, until its fuel supply was exhausted. MESSENGER impacted onto Mercury on 30th April 2015. Image credit: NASA/Johns Hopkins University Applied Physics Laboratory/Carnegie Institute of Washington.

Certain MESSENGER instruments, including the Mercury Laser Altimeter (MLA; *CAVANAUGH ET AL., 2007*), were within operational range of Mercury over the northern hemisphere. Fig. 3.6 shows all the MLA data tracks available for H05. MLA data are sparse south of 5°S and unavailable south of 20°S. Therefore, even equatorial quadrangles have only partial MLA data coverage. As the northernmost quadrangle available to map, H05 had the best MLA data coverage.
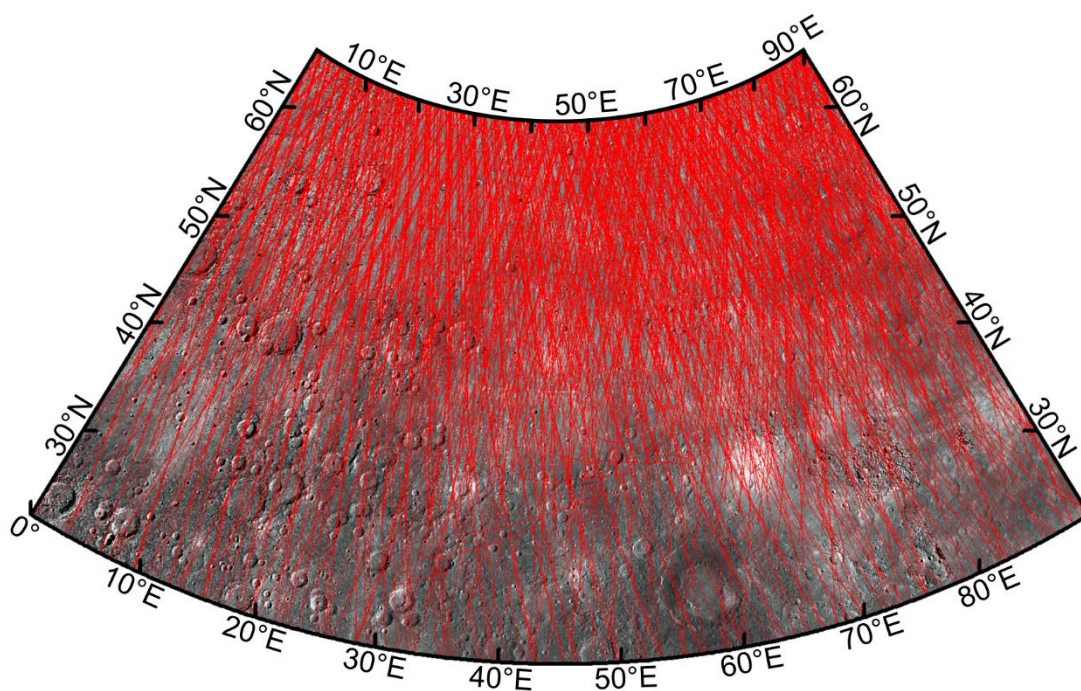
Fig. 3.6 Mercury Laser Altimeter (MLA) coverage of H05. *Red lines indicate individual MLA data tracks. Note how MLA has denser track spacing in the north than the south. Lambert conformal conic projection (central meridian 45°E, standard parallels 30°N and 58°N) of the ~166 m/pixel global monochrome mosaic.*

In the case of the Mercury Dual Imaging System (MDIS; *HAWKINS ET AL., 2007*), MESSENGER's highly elliptical orbit resulted in a trade-off between data coverage and resolution. Fig. 3.7 shows all the individual monochrome narrow-angle camera (NAC) frames from MDIS for H05. At higher northern latitudes, the spacecraft was at lower altitudes, allowing NAC to capture images of the planet's surface with higher spatial resolution. However, the instrument's footprint on the surface was smaller at lower altitudes, meaning data coverage was sparser. Nevertheless, the availability of high-resolution NAC images permits more accurate mapping of unit contacts and more detailed unit descriptions. Furthermore, poor NAC coverage at H05 is supplemented by complete coverage of the quadrangle by the multispectral

wide-angle camera (WAC) of MDIS. As a result, H05 was the quadrangle best characterised by MESSENGER data available to map at the time of mapping area selection.
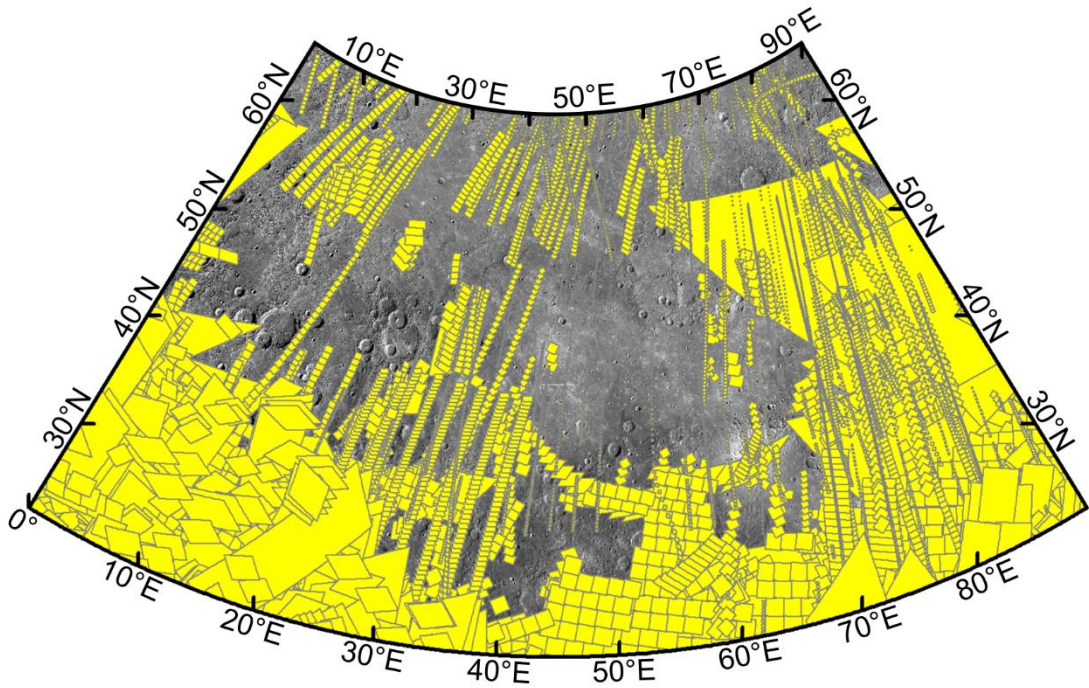
Fig. 3.7 Mercury Dual Imaging System (MDIS) narrow-angle camera (NAC) coverage of H05. *Yellow polygons show the extent of individual NAC frames. Same projection and background as in Fig. 3.6.*

3.1.3.4 Known features of interest within H05
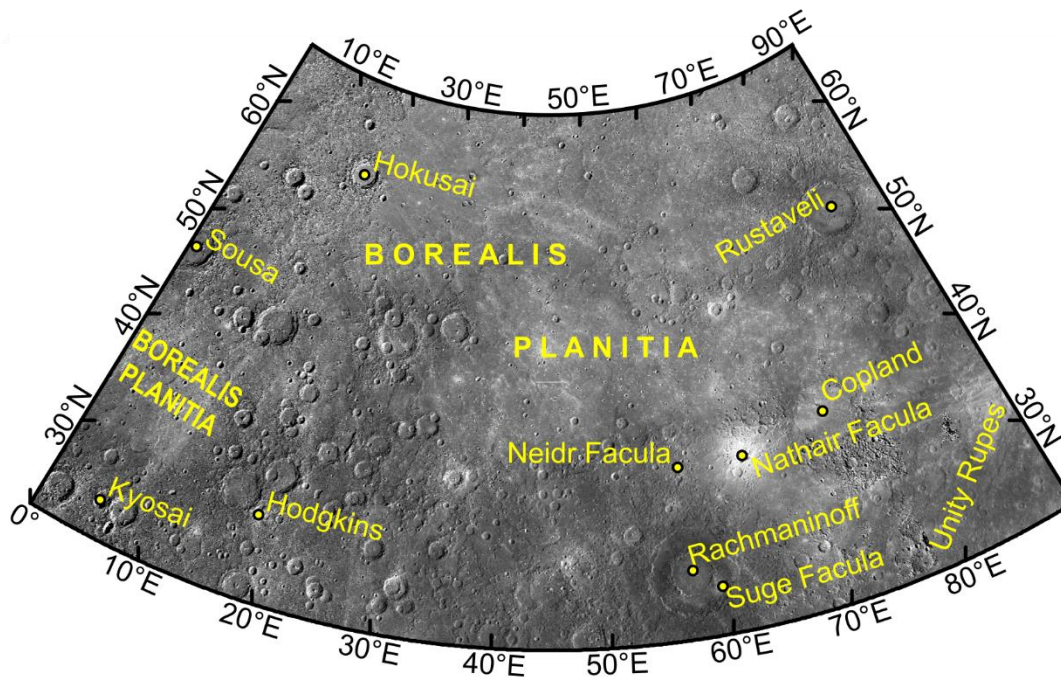
Fig. 3.8 Nomenclature of H05. _Named features within H05 as of 14/01/2019. It should be noted that several features within H05 received their official names after I began this work. Unity Rupes received its name on 30/01/2016. The naming scheme for 'faculae' on Mercury was implemented on 27/02/2018 and Nathair, Neidr, and Suge Faculae received their names on 06/04/2018. Same projection and background as in Fig. 3.6._

H05 is dominated by Borealis Planitia (Fig. 3.8), the 'northern smooth plains' of Mercury _(HEAD ET AL., 2011)._ These smooth plains are broadly interpreted to be volcanic in origin _(DENEVI ET AL., 2013)_ and probably represent multiple extensive lava flows stacked to a maximum thickness of ~2 km in places _(OSTRACH ET AL., 2015)._ Previous studies of Borealis Planitia have focussed on latitudes above ~50°N _(HEAD ET AL., 2011; OSTRACH ET AL., 2015),_ however H05 contains the southernmost extent of Borealis Planitia, which appears to exhibit different colour properties compared with the majority of the plains (see Fig. 3.18 in Section 3.2.1.2). This observation could be explained by lateral heterogeneities in mantle source compositions for erupted lavas, or by impact gardening mixing surface volcanic colour signatures with the colours of underlying units, or a non-volcanic origin for smooth plains in southern Borealis Planitia. These hypotheses could be tested by high-resolution mapping, such as would be carried out during my quadrangle map

production (see Section 3.3.3). Until now, the highest resolution study of Borealis Planitia was conducted at a scale of 1:1.25M *(DENEVI ET AL., 2013)*.

The Rachmaninoff impact basin was first imaged during the third MESSENGER flyby (Fig. 3.9; *PROCKTER ET AL., 2010*). This young impact feature, suggested to postdate the Late Heavy Bombardment of the inner solar system ~3.8 Ga *(PROCKTER ET AL., 2010)*, contains the lowest surface elevation on Mercury *(BECKER ET AL., 2016; STARK ET AL., 2017)*. Depending on the crustal thickness in the region *(SORI, 2018)*, it is possible that Rachmaninoff has excavated lower crustal or even uppermost mantle material. Furthermore, a diversity of colour units that correlate with photogeological units is suggestive of a basin with a rich geological history. Rachmaninoff contains high-reflectance red plains that contrast with the surrounding low-reflectance blue material and appear to have a crater retention age resolvably younger than the basin itself *(PROCKTER ET AL., 2010; CHAPMAN ET AL., 2012)*. This probably requires a volcanic origin for the relatively young interior red plains of Rachmaninoff, and this volcanism could represent some of the most recent plains formation on Mercury *(PROCKTER ET AL., 2010; CHAPMAN ET AL., 2012)*. Furthermore, Rachmaninoff contains Suge Facula, a prominent bright, red spot with diffuse boundaries. Elsewhere on Mercury, such faculae (formerly 'red spots'; *MURCHIE ET AL., 2008*), contain irregularly shaped, rimless depressions, which are interpreted as explosively excavated volcanic craters. The bright spots are interpreted as deposits of ballistically emplaced pyroclasts. However, the basin floor of Rachmaninoff encompassing Suge Facula has no obvious vent structure, but instead has a pitted appearance *(THOMAS ET AL., 2014A; JOZWIAK ET AL., 2018)*. This texture is believed to arise from the sublimation of a volatile species within a young volcanic unit, rather than a primary volcanic explosion *(THOMAS ET AL., 2014A; JOZWIAK ET AL., 2018)*. Detailed mapping of Rachmaninoff, so far carried out using only flyby MESSENGER data *(PROCKTER ET AL., 2010)*, can test this hypothesis and reveal the evolution of this intriguing basin.

The region immediately to the north of Rachmaninoff contains other prominent faculae, including Nathair Facula, the largest bright spot on Mercury, and Neidr Facula (Fig. 3.9). Whereas 82% of volcanic vents on Mercury occur within impact craters *(JOZWIAK ET AL., 2018)*, the two large vents associated with these faculae

appear to have formed directly on Mercury's plains. Mapping of the surrounding region may shed light on how these vents and deposits formed.
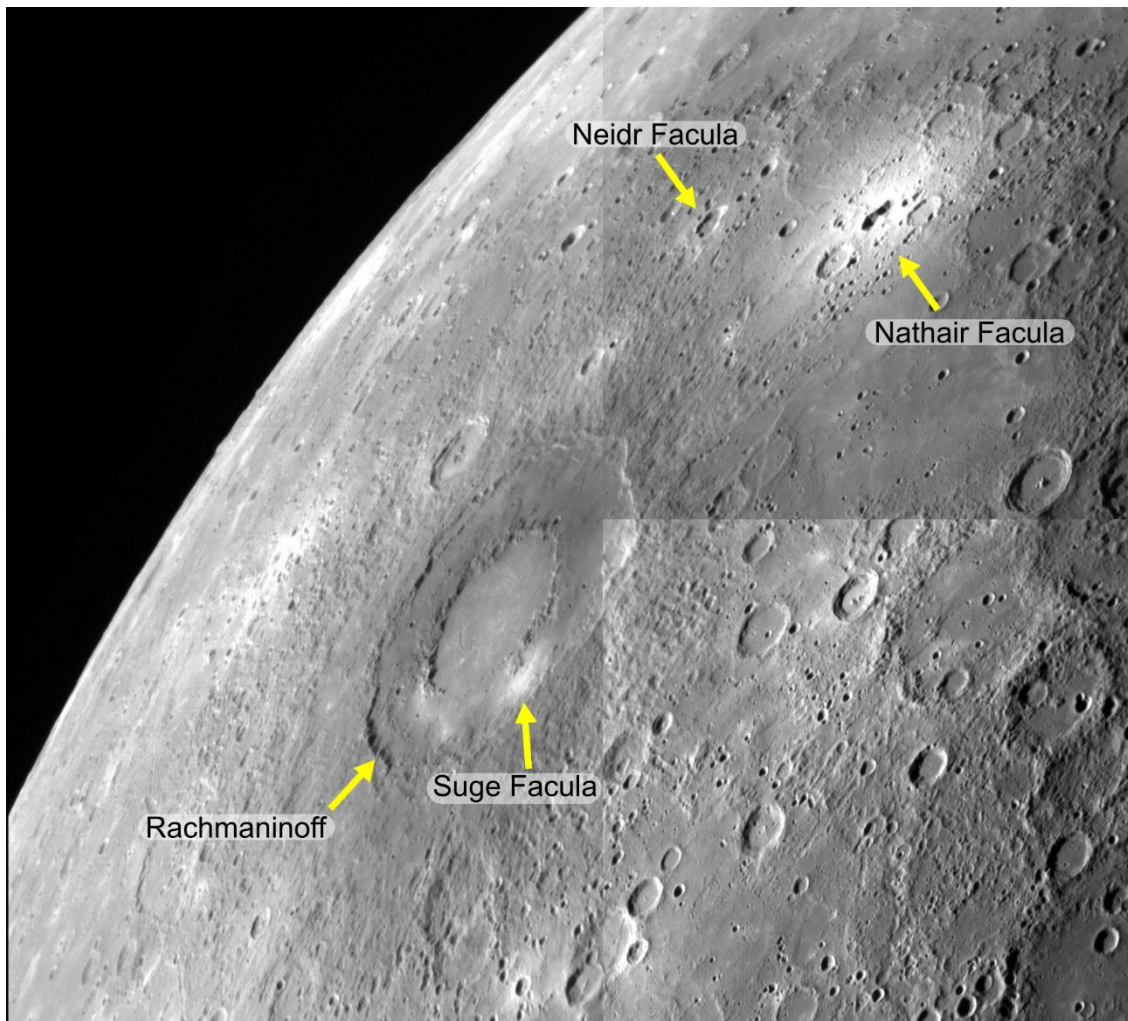
Fig. 3.9 Rachmaninoff basin setting. *Rachmaninoff and the surrounding region were first imaged during MESSENGER'S third flyby. Mosaic of NAC frames EN0162744123M, EN0162744150M, EN0162744128M, and EN0162744155M. Mean ground resolution ~446 m/pixel.*

Hokusai crater is another interesting impact structure, and it gives its name to the whole H05 quadrangle. Hokusai is a 114 km-diameter ringed peak-cluster basin *(BAKER ET AL., 2011)* with crater rays that extend thousands of kilometres from the impact site *(XIAO ET AL., 2016)*. Bright crater rays are understood to be possessed by only the youngest impact structures on planetary surfaces *(OBERBECK, 1971)*, and are known on the Moon *(OBERBECK, 1971)* and Mars *(MCEWEN ET AL., 2005)*, as well as Mercury *(HAPKE ET AL., 1975)*. As well as being brighter than their surroundings, rays on Mercury are typically bluer than surrounding terrain *(HAPKE ET AL., 1975;*

BLEWETT ET AL., 2009). As an airless body in the innermost solar system, space weathering is thought to be very efficient on Mercury, and exposed surfaces are believed to darken and redden with age *(BRADEN AND ROBINSON, 2013)*. Thus, craters with blue rays are believed to be among the youngest geological features on Mercury *(BANKS ET AL., 2017)*. It is therefore important for detailed maps of Hokusai's rays to be made, as they could be used as global stratigraphic markers for the youngest surface processes operating on Mercury's surface. Recent research focussing on Hokusai has considered whether the crater is a candidate rampart crater (see *CARR ET AL., 1977*) formed by fluidisation of its impact ejecta by large volumes of impact melt *(KINCZYK ET AL., 2018A)* and whether the Hokusai impact could have delivered the water that forms the ice deposits in the permanently shadowed regions of Mercury's north pole *(ERNST ET AL., 2018)*.
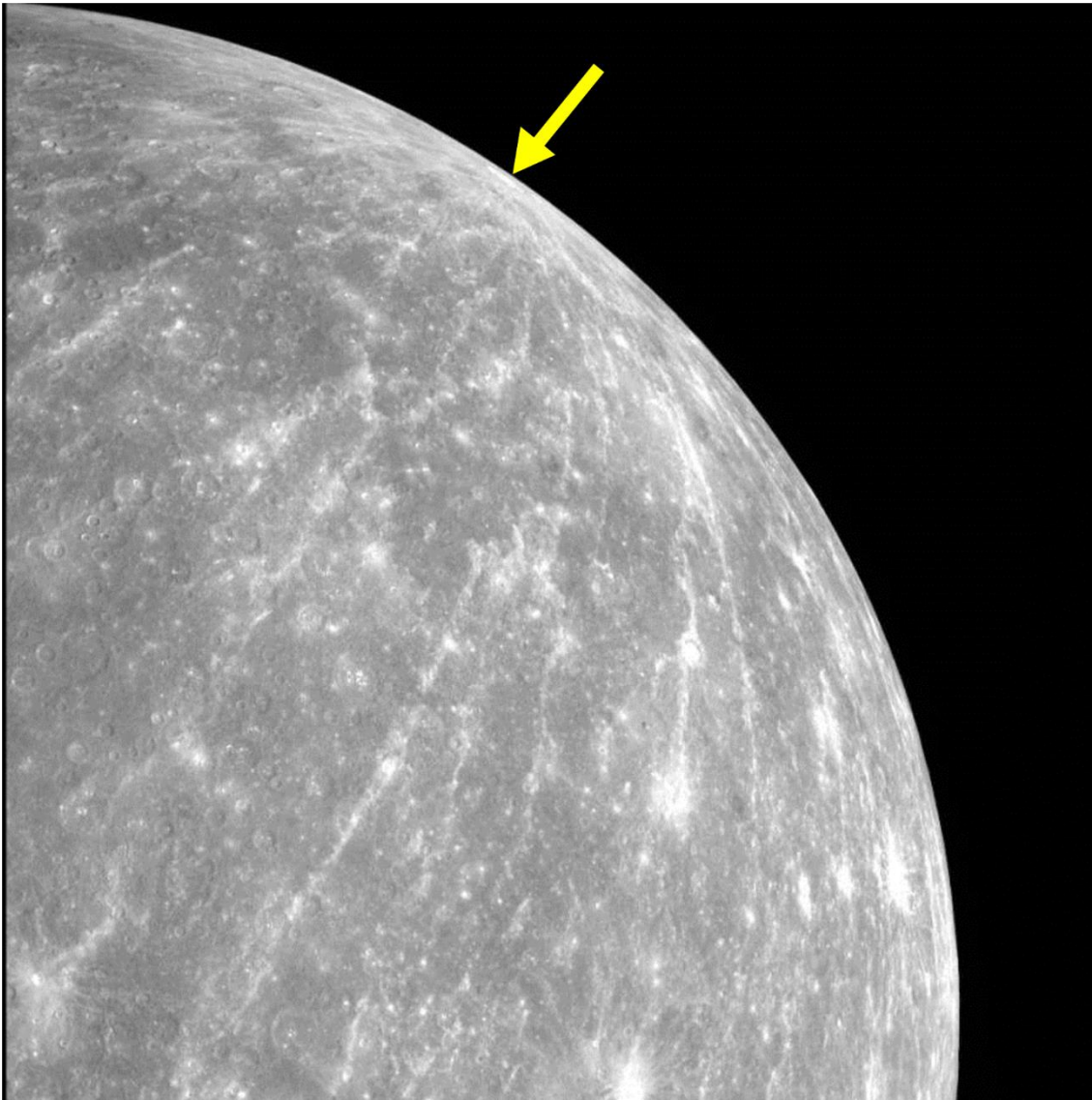
Fig. 3.10 Ray system of Hokusai crater. *One of the earliest MESSENGER images that resolves Hokusai crater (yellow arrow), captured during MESSENGER's second flyby. WAC frame EW0131772403C. Mean ground resolution ~2.4 km/pixel.*

3.1.3.5 Summary

I chose H05 as the quadrangle that I would produce a geological map of as part of my research for the following reasons:

1. H05 has no pre-existing geological maps, therefore producing a geological map of the quadrangle would be a unique and valuable contribution to Mercury science.
2. MESSENGER-era geological maps are available for some of the adjoining quadrangles. This will allow the boundary interpretations of my map of H05 to be checked against the results of independent workers.

3. H05, as the last remaining quadrangle available for mapping in the northern hemisphere of Mercury, has good MDIS and MLA coverage, the two most important MESSENGER datasets for geological mapping.

4. At the time of mapping quadrangle selection, H05 was already known to contain several features of interest, including extensive smooth plains, Rachmaninoff basin and its associated volcanic features, and Hokusai crater itself.

3.2 Data

All the data I used to make the geological map of H05 are publicly available for download from the Planetary Data System. All of these data are products of NASA's MESSENGER mission.

3.2.1 Basemaps

3.2.1.1 Monochrome

The primary data for photogeological mapping of planetary surfaces are monochrome image mosaics for use as basemaps. The abundance of MESSENGER data allowed the construction of several regional and global mosaics during and after the mission with different illumination conditions (Fig. 3.11). I have consulted each of the basemaps discussed below during my mapping, since they convey different geological information, however I chose a primary basemap on which I digitised the map. The primary basemaps for geological mapping of H05 are the Basemap Reduced Data Record (BDR) tiles produced by the MESSENGER team during the spacecraft's orbital imaging campaign (Fig. 3.12). These basemap tiles have a mean ground resolution of 166 m/pixel and are mosaics of MDIS WAC and NAC frames with solar incidence angles of ~68°, which is optimal for photogeological interpretation *(CHABOT ET AL., 2016)*. This basemap has 100% coverage over H05.
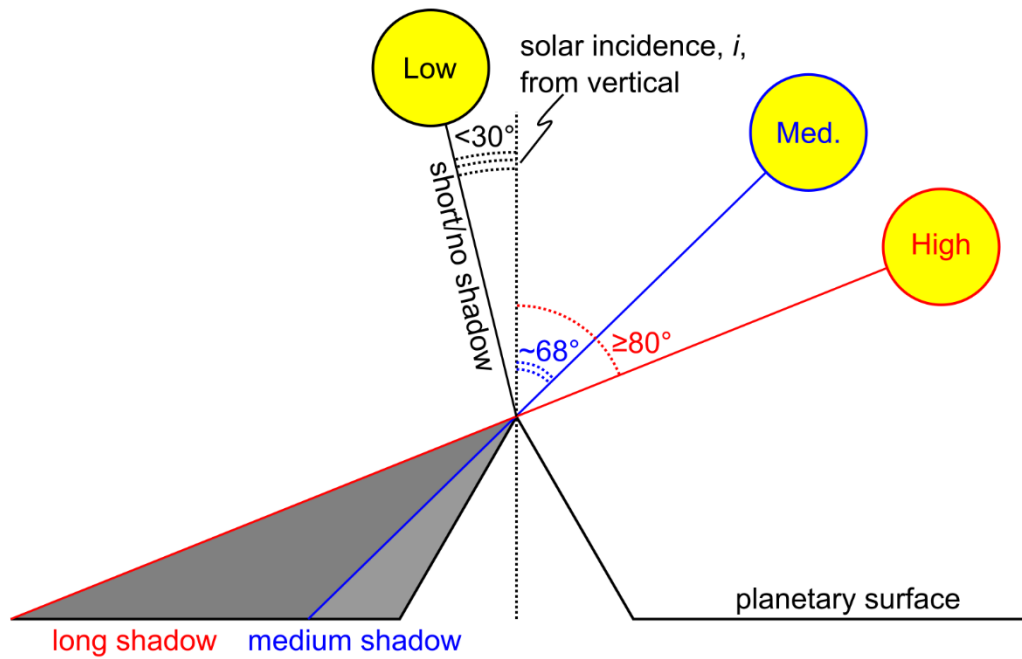
Fig. 3.11 Cartoon of shadows and solar incidence angles. *This cartoon illustrates the convention used in this thesis when referring to solar incidence angle. Solar incidence, i, is measured from the vertical (i.e. perpendicular to the planetary surface). 'High' solar incidence angle MDIS frames are captured when the Sun is close to the local horizon; long shadows are cast. 'Low' solar incidence refers to when the local solar time is close to midday; short shadows are cast.*
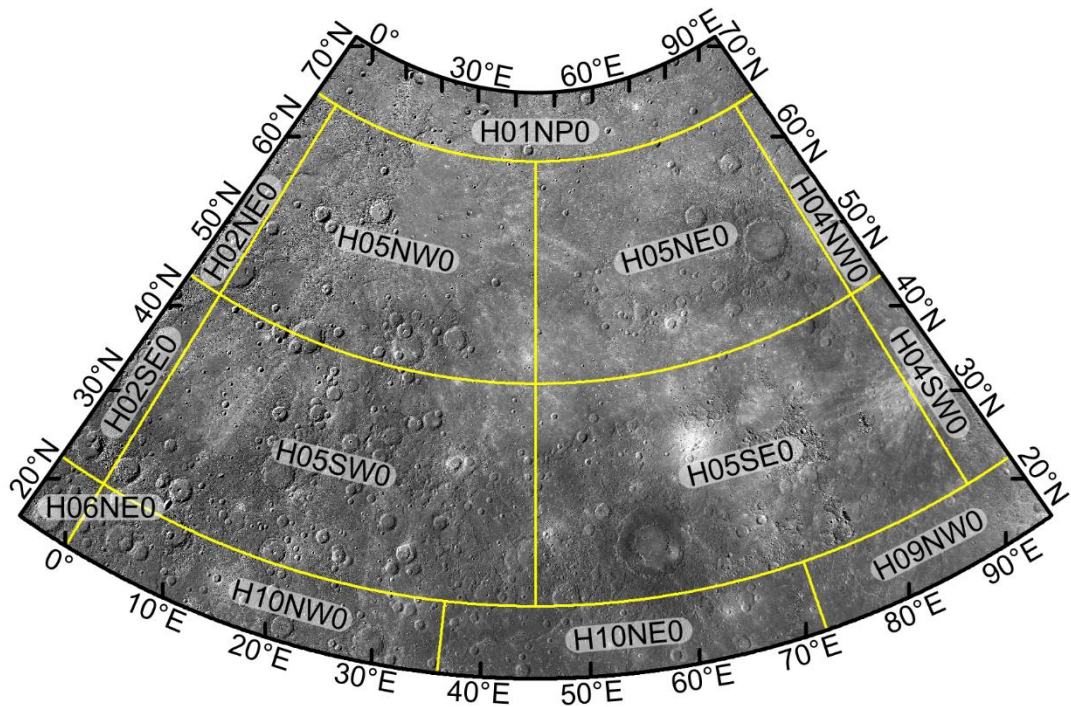
Fig. 3.12 Primary H05 basemap. *This is the primary basemap I used to make the geological map of H05. Individual basemap tiles are labelled and outlined in yellow. The tiles H05NW0, H05NE0, H05SW0 and H05SE0 make up the H05 quadrangle. 5° of latitude and longitude overlap is included in the basemap to allow boundary checking with the adjacent quadrangles after completion of the map. Illumination is primarily from the east, but is variable in solar incidence angle across the basemap. ~166 m/pixel. Lambert conformal conic projection (central meridian 45°E, standard parallels 30°N and 58°N).*

Other basemaps became available for mapping during my PhD. These include basemaps with low solar incidence angles (Fig. 3.13), suitable for investigating surface reflectance variations, and basemaps with high solar incidence angles, from both west and east, useful for enhancing low topographic features (Fig. 3.14 and Fig. 3.15).
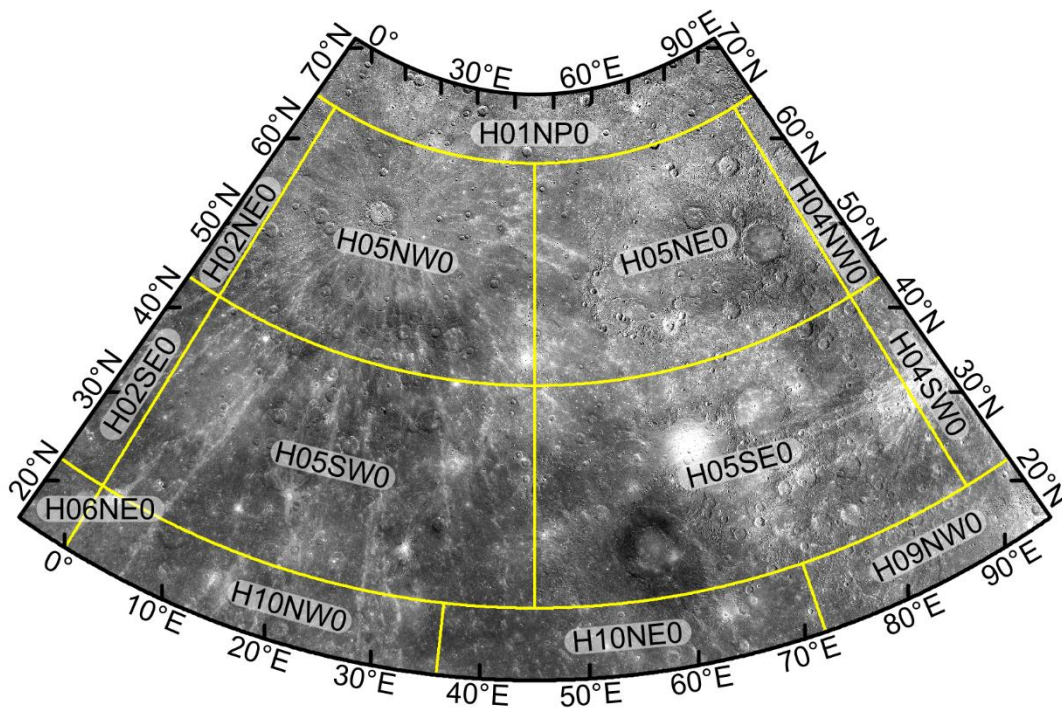
Fig. 3.13 H05 basemap with low solar incidence. *Mosaic of MDIS WAC and NAC frames optimised for minimal solar incidence. Individual basemap tiles are labelled and outlined in yellow. Note how desired illumination conditions are available in the west only. ~166 m/pixel. Same projection as in Fig. 3.12.*
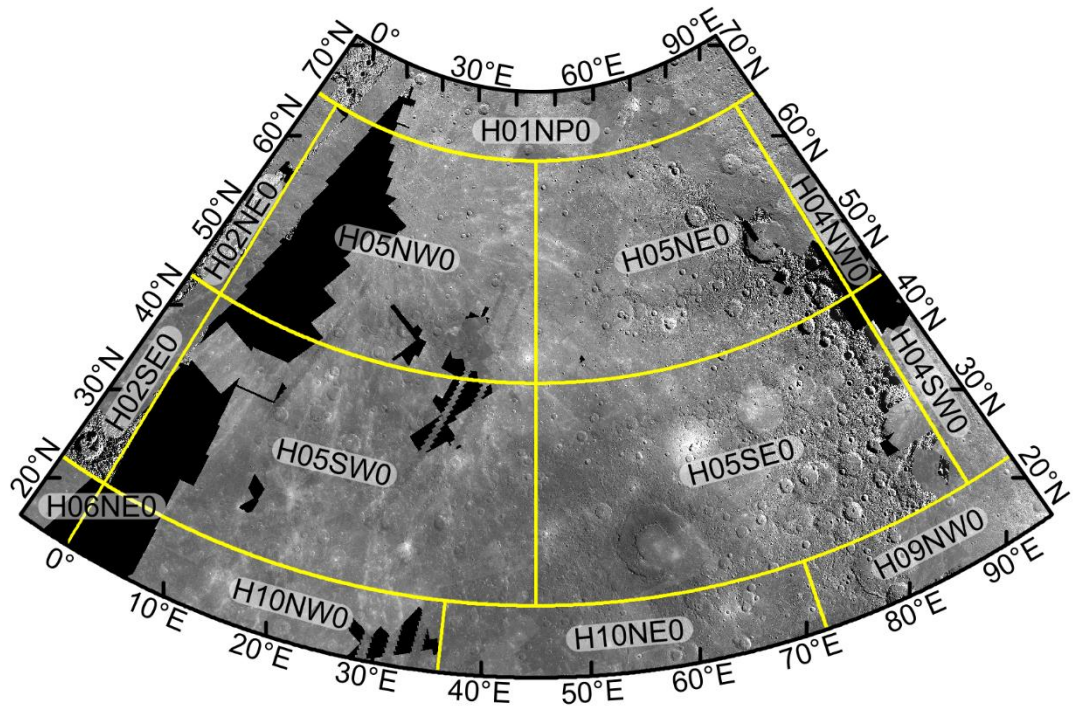
Fig. 3.14 Western illumination H05 basemap with high solar incidence. *Mosaic of MDIS WAC and NAC frames with western illumination. Individual basemap tiles are labelled and outlined in yellow. Frames with solar incidence close to 80° are incorporated where available. Note how the desired illumination conditions are available in the east only. Solar incidence steadily decreases from east to west across the basemap. At the westernmost edge of H05, areas with no western illumination data of sufficient resolution are shown in black. ~166 m/pixel. Same projection as in Fig. 3.12.*
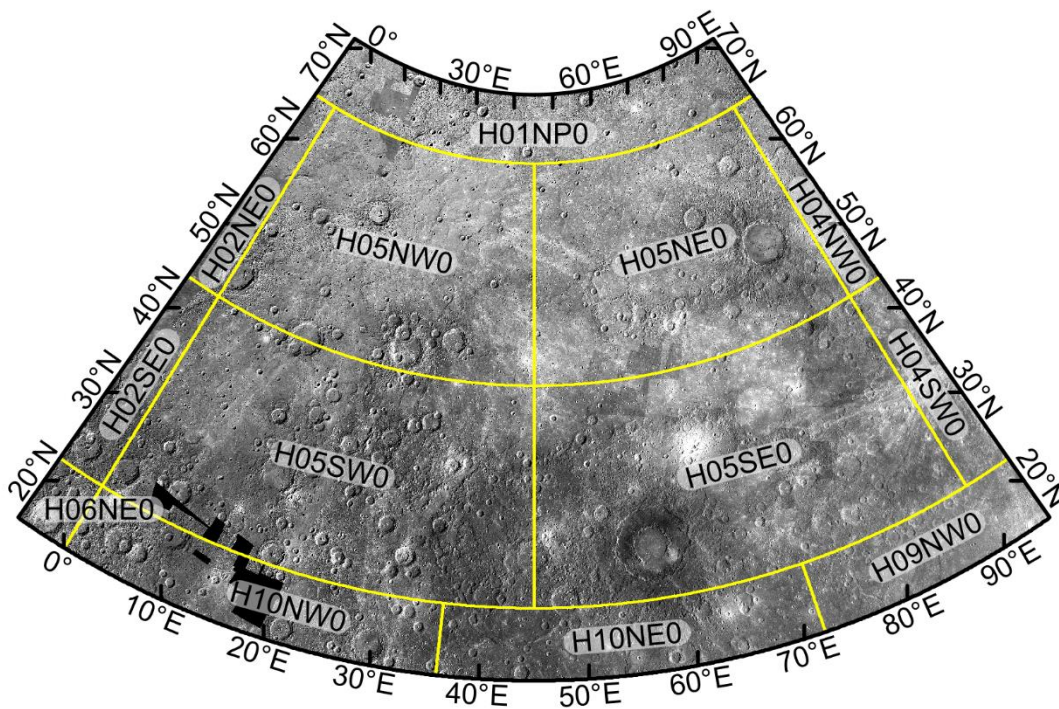
Fig. 3.15 Eastern illumination H05 basemap with high solar incidence. *Mosaic of MDIS WAC and NAC frames with eastern illumination. Individual basemap tiles are labelled and outlined in yellow. Frames with solar incidence close to 80° are incorporated where available. Most of this basemap is composed of high-incidence angle frames, except the southeast corner. Small areas of no coverage are shown in black and are limited to the south west. ~166 m/pixel. Same projection as in Fig. 3.12.*

Before the ~166 m/pixel mosaics were released by the MESSENGER team, global mosaics with lower resolution were available. I referred to these occasionally while mapping, and so they are included here for completeness. These include a global mosaic of Mercury with ~250 m/pixel resolution (Fig. 3.16) and the M1M2M3M10 mosaic composed of MESSENGER's flyby data combined with Mariner 10 data (Fig. 3.17).
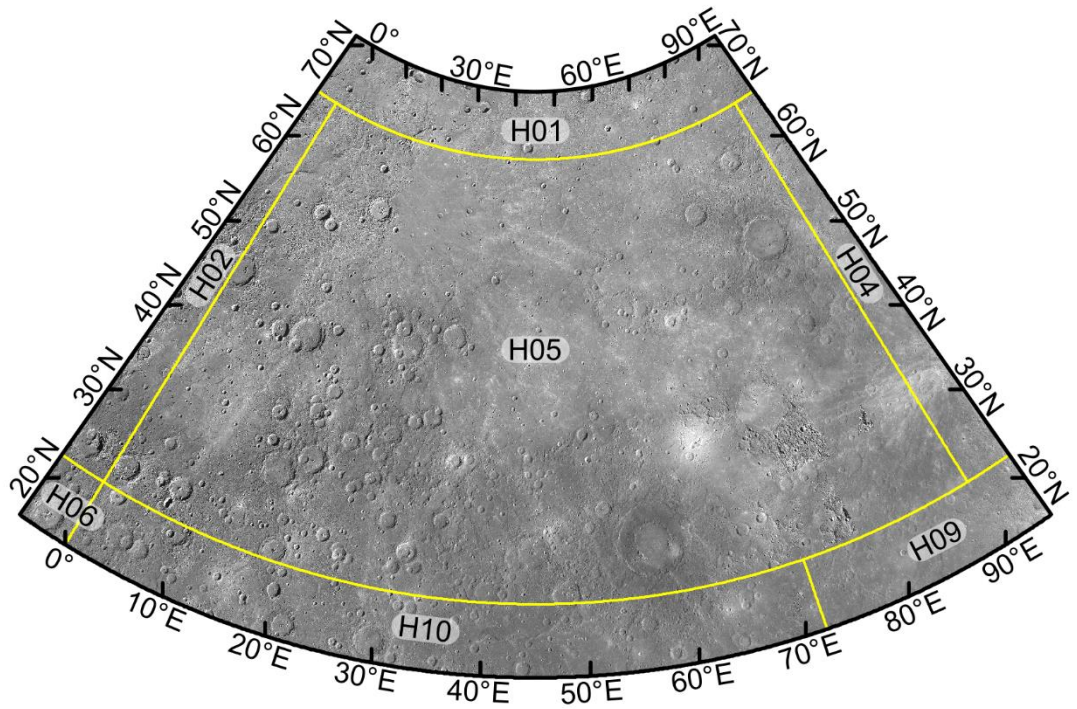
Fig. 3.16 250 m/pixel basemap. *A secondary basemap with lower resolution. Useful because it has fewer seams between different regions of the mosaic. Quadrangles are labelled and outlined in yellow. Same projection as in Fig. 3.12.*
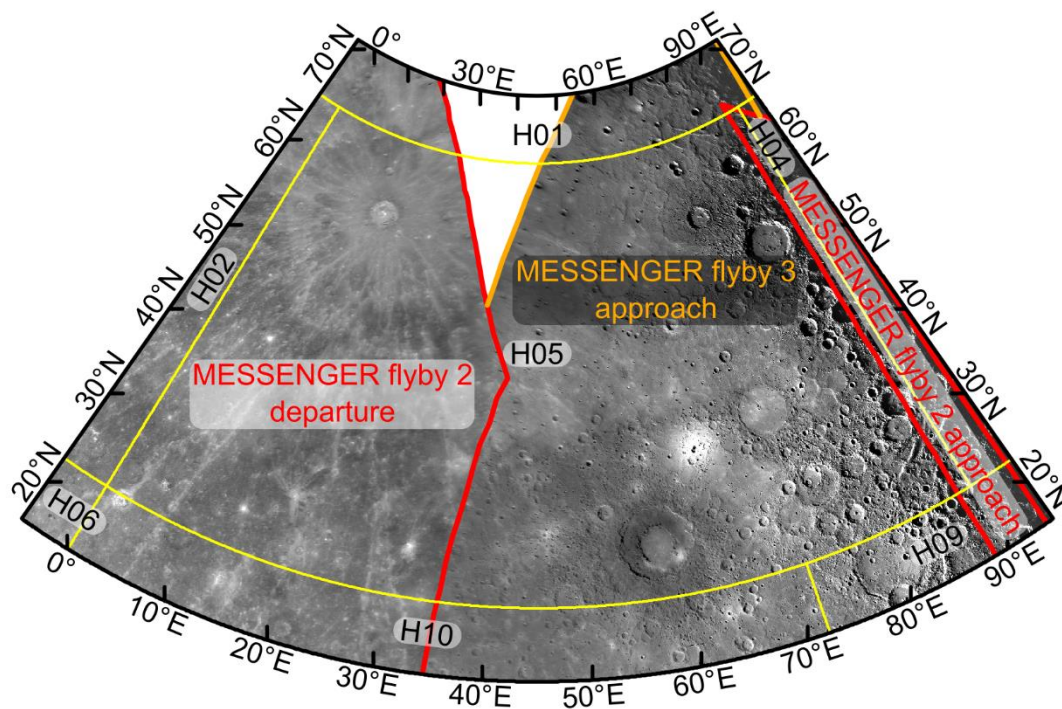
Fig. 3.17 H05 MESSENGER flyby data basemap. *MESSENGER flyby data generally have poorer spatial resolution than orbital data (~500 m/pixel), however the extremely high solar incidence in the east of the basemap enhances topographic features thus assisting photogeological interpretation. Quadrangles are labelled and outlined in yellow. Regions of the mosaic covered by MESSENGER flybys 2 and 3 are labelled and outlined in red and orange, respectively. Same projection as in Fig. 3.12.*

3.2.1.2 Colour

The most important colour dataset for assisting photogeological interpretation was the enhanced colour MESSENGER global mosaic (Fig. 3.18). This mosaic was constructed using MDIS WAC frames captured with the 430, 750, and 1,000 nm bands. Principal component analyses were conducted by the MESSENGER team in this spectral space and they created the enhanced colour mosaic by placing the second principal component (PC2), the first principal component (PC1) and the 430/1,000 ratio in the red, green and blue channels respectively *(DENEVI ET AL., 2009, 2016)*. PC1 corresponds closely to standard reflectance. PC2 represents the spectral slope from short-to-long wavelengths. Such slopes are positive for all terrains on Mercury, meaning the planet is generally red, but terrains with shallower spectral slopes (low PC2) are 'blue' in a relative sense. Similarly, the 430/1,000 ratio measures 'blueness' since it is a ratio of reflectance at blue

wavelength to reflectance at the near-infrared. Why these particular spectral parameters have been selected by the MESSENGER team has not been released publicly. Given the spectral parameters used, it is obvious that PC2, which measures 'redness', should be assigned to the R-channel, and that the 430/1,000 ratio, which measures 'blueness', should be assigned to the B-channel. As a result, in this mosaic, regions that appear redder or bluer really are redder or bluer than intermediate terrains on Mercury. This mosaic has a mean ground resolution of ~665 m/pixel.
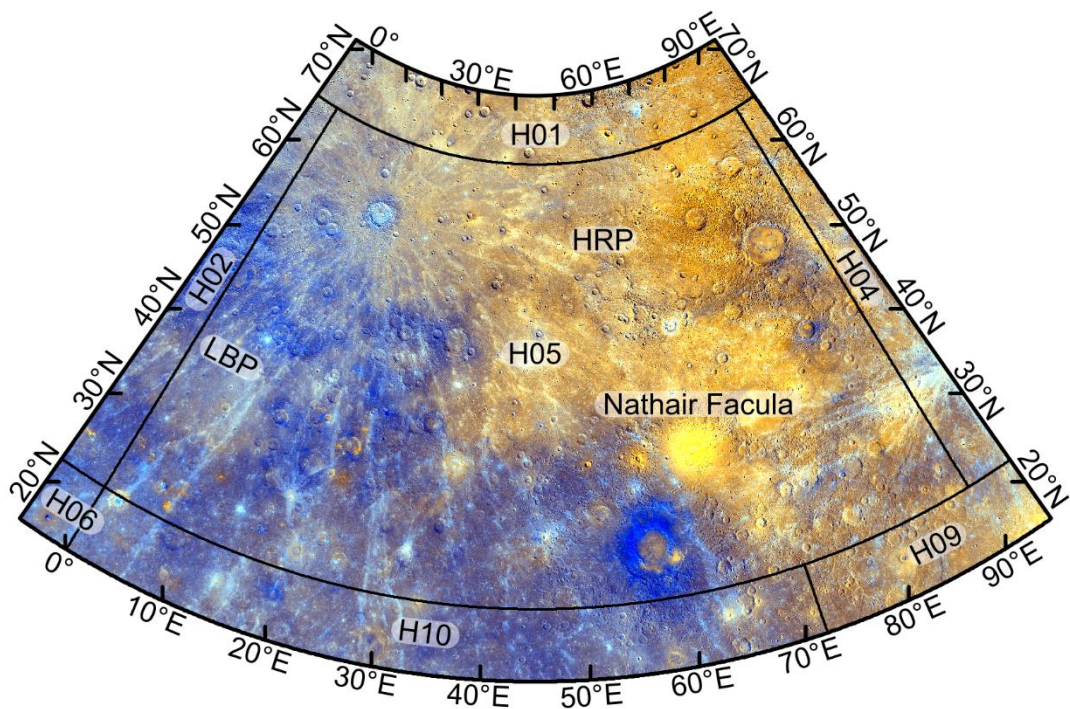
Fig. 3.18 MESSENGER enhanced colour H05 basemap. *The most prominent bright spot, Nathair Facula, is labelled. HRP indicates a region of Borealis Planitia that exhibits the colour terrain unit high-reflectance red plains. LBP indicates a region in southern Borealis Planitia that instead exhibits low-reflectance blue plains. The regions labelled HRP and LBP are contiguous and the colour change between them is gradational. Quadrangles are labelled and outlined in black. ~665 m/pixel. Same projection as in Fig. 3.12. See DENEVI ET AL. (2009).*

Higher spatial resolution colour data are available for H05 in the form of the MD3 colour basemap tiles (Fig. 3.19). These three colour tiles place the 1,000, 750, and 430 nm bands in the red, green and blue channels, respectively, and have a ground resolution of ~333 m/pixel.
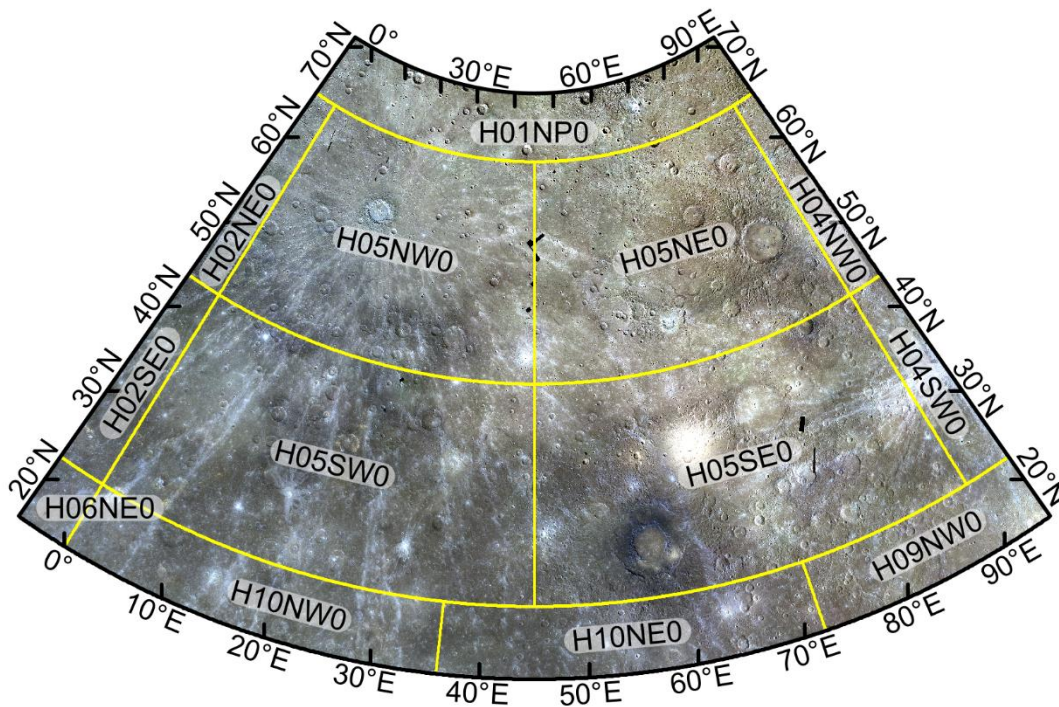
Fig. 3.19 MESSENGER MD3 colour tile basemap of H05. *Individual basemap tiles are labelled and outlined in yellow. ~333 m/pixel. Same projection as in Fig. 3.12.*

3.2.2 Topography

Topographic data were also used during mapping. At the beginning of my work, the only digital elevation model (DEM) available for H05 was the gridded MLA DEM (Fig. 3.20; ZUBER ET AL., *2012*). In October 2016, one year after beginning my work, a global stereo-derived DEM of Mercury was released (Fig. 3.21; BECKER ET AL., *2016*). In March 2017, a quadrangle DEM of H05 with higher spatial resolution was released (Fig. 3.22; STARK ET AL., *2017*). Once available, this DEM became the primary source of topographic information used when mapping H05.
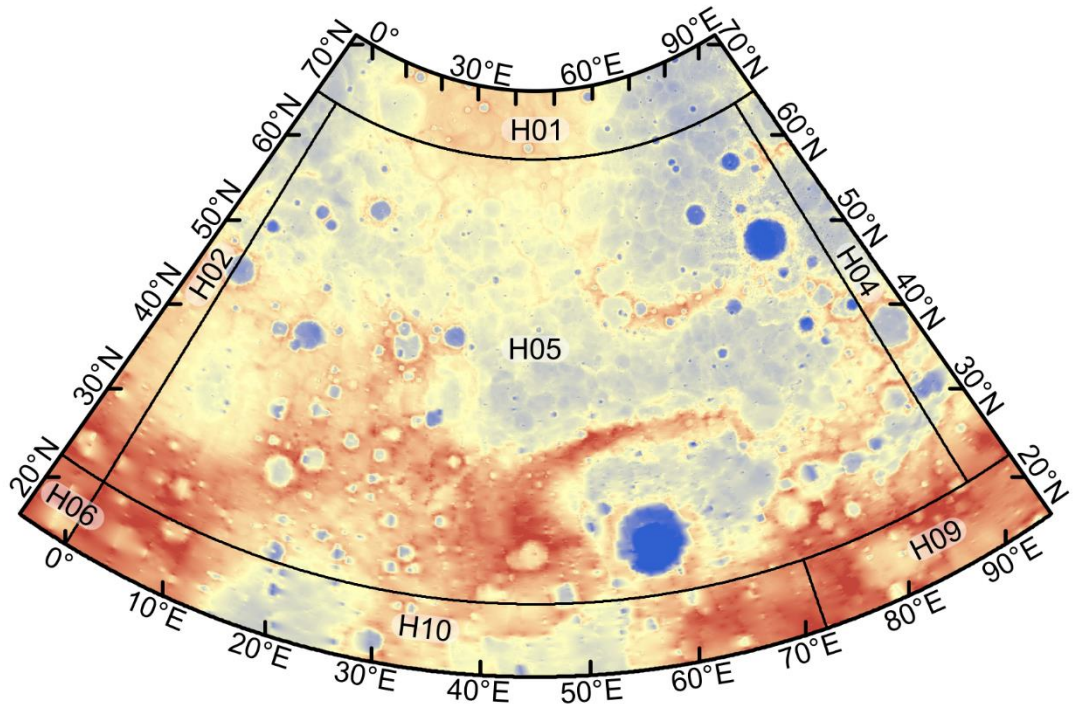
Fig. 3.20 MLA gridded topography of H05 and the surrounding quadrangles. *This DEM was constructed using MLA data tracks. The topography between tracks has been interpolated (ZUBER ET AL., 2012). As shown in Fig. 3.6, MLA data tracks are more widely spaced in southern H05, resulting in a higher degree of interpolation uncertainty. Furthermore, publicly available pixel values for this DEM do not correspond to surface elevation values, hence no vertical scale is shown. Quadrangles are labelled and outlined in black. ~665 m/pixel. Same projection as in Fig. 3.12.*
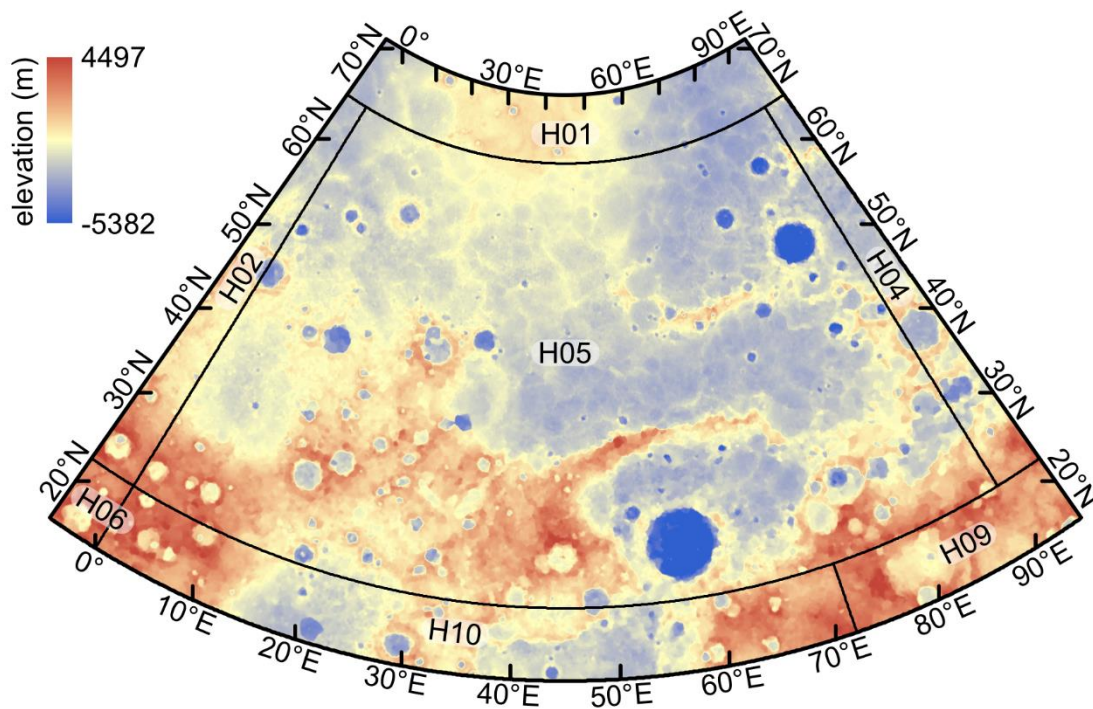
Fig. 3.21 Stereo-topography DEM of H05 and the surrounding quadrangles. *Quadrangles are labelled and outlined in black. ~665 m/pixel. Same projection as in Fig. 3.12. By BECKER ET AL. (2016).*
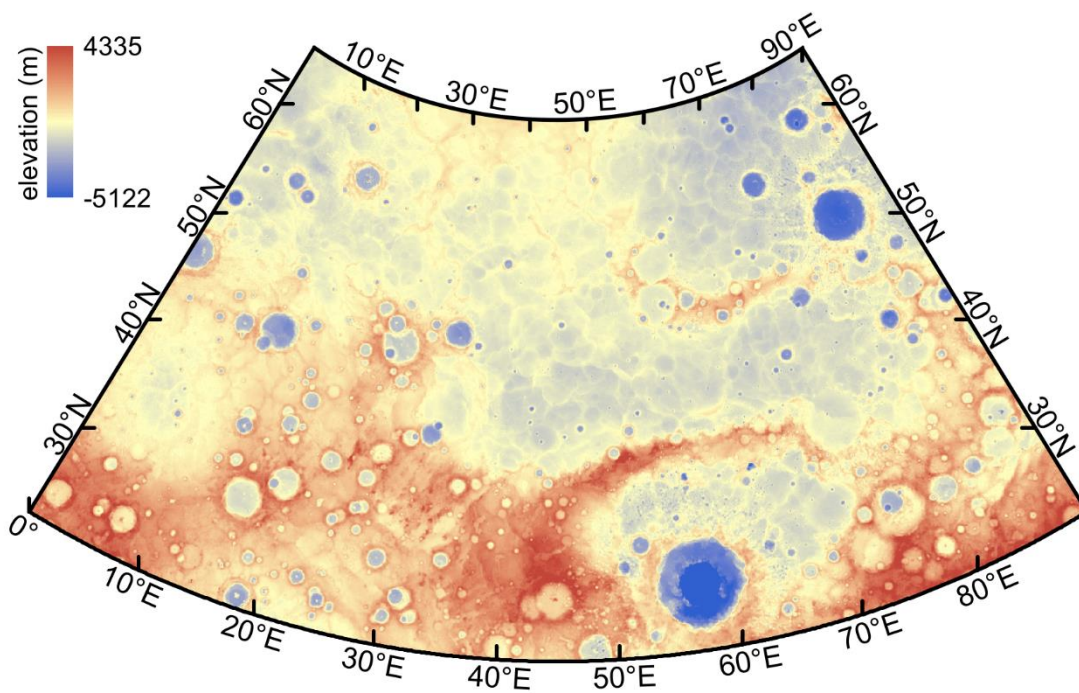
Fig. 3.22 Stereo-topography DEM of H05. *No overlap with the surrounding quadrangles is shown. ~222 m/pixel. Same projection as in Fig. 3.6. By STARK ET AL. (2017).*

3.3 Methods

3.3.1 Software

3.3.1.1 Data processing

Unless otherwise stated, all basemap, MDIS NAC and WAC frames, and DEMs presented in this work were downloaded from the PDS and processed for ingestion into a Geographic Information System (GIS) using the United States Geological Survey (USGS) Integrated Software for Imagers and Spectrometers version 3 (ISIS3). The native format of MESSENGER data (.IMG) on the PDS cannot be projected within a GIS. The data processing steps for converting raw .IMG files to GIS-ready products are shown in Fig. 3.23. In general, raw data were first converted from their native .IMG format to a .cub format that can be further manipulated by ISIS3. Derived products, such as basemaps, generally required map projection only, whereas MDIS frames also required radiometric and photometric calibration.
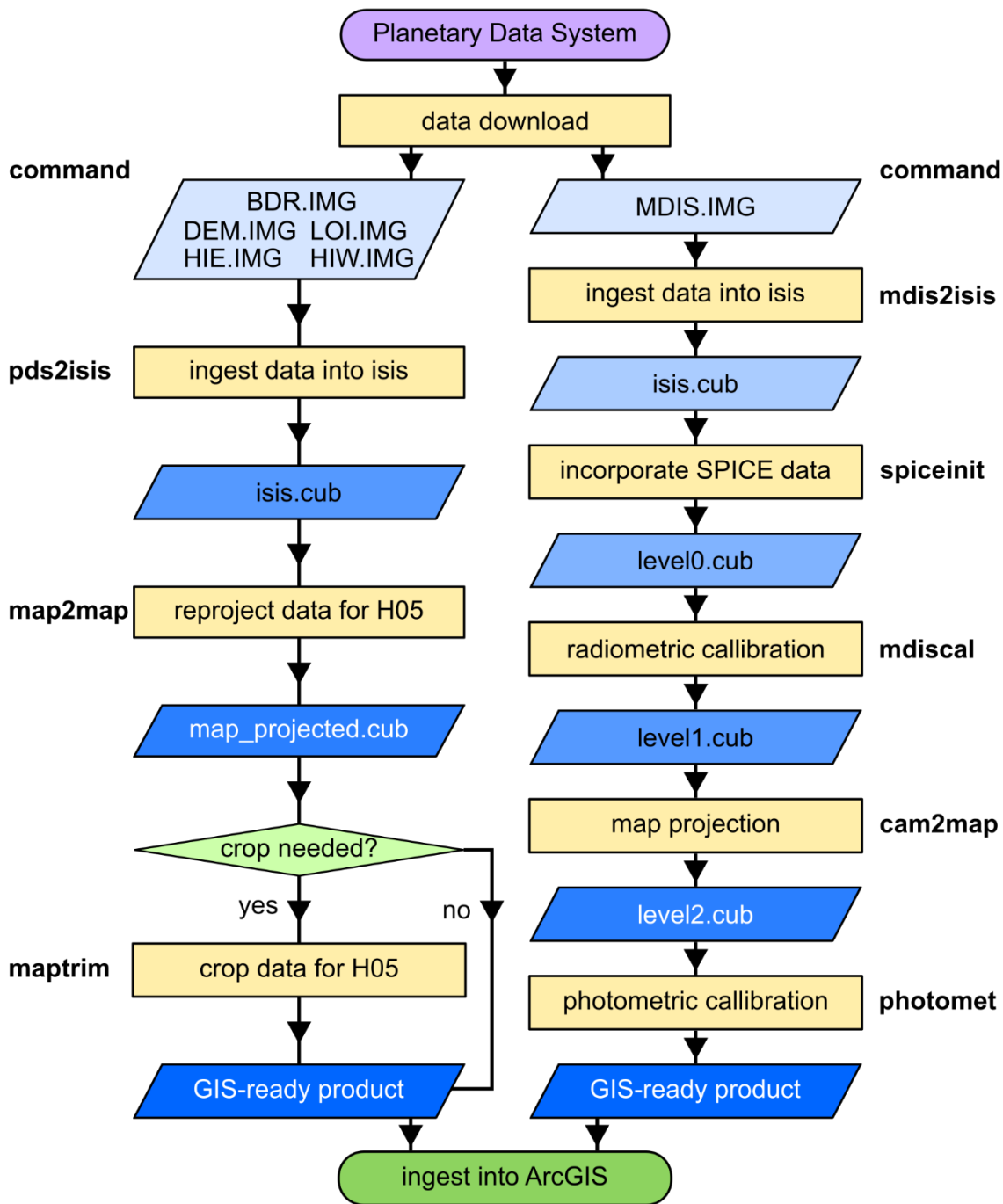
Fig. 3.23 Flowchart of ISIS3 data processing. *MESSENGER data were downloaded from the PDS. Raw MDIS frames ('MDIS.IMG') were processed using the steps on the right path. Derived MESSENGER products, such as basemap tiles or DEMs, were processed using the steps on the left path. 'BDR.IMG' represents raw BDR basemap tiles. 'LOI.IMG' represents low-incidence angle basemap tiles. 'HIE.IMG' and 'HIW.IMG' represent eastern and western illumination high-incidence angle basemap tiles, respectively. 'DEM.IMG' represents raw DEM products.*

3.3.1.2 Geological mapping

All map work presented in my thesis was conducted within the Esri ArcGIS 10.1 GIS software package.

3.3.2 Projection

H05 is a mid-northern-latitude quadrangle. These are conventionally mapped in a Lambert Conformal Conic (LCC) projection *(DAVIES ET AL., 1978)*. Conceptually, the surface of a globe is projected onto the curved surface of a cone; the curved surface of the cone is then 'unrolled' to make the flat, projected coordinated system. Two standard parallels represent the intersections between the globe and the cone of projection (Fig. 3.24). The latitudes of the first and second standard parallels are chosen to lie at 1/6 and 5/6 of the latitudinal range of the map to minimise distortion across it *(DEETZ AND ADAMS, 1935)*. Since the latitudinal bounds of H05 are 22.5°N and 65°N, the first and second parallels for its LCC projection were set at 30°N and 58°N, respectively. Throughout the remainder of this thesis, this projection is referred to as the native LCC of H05.
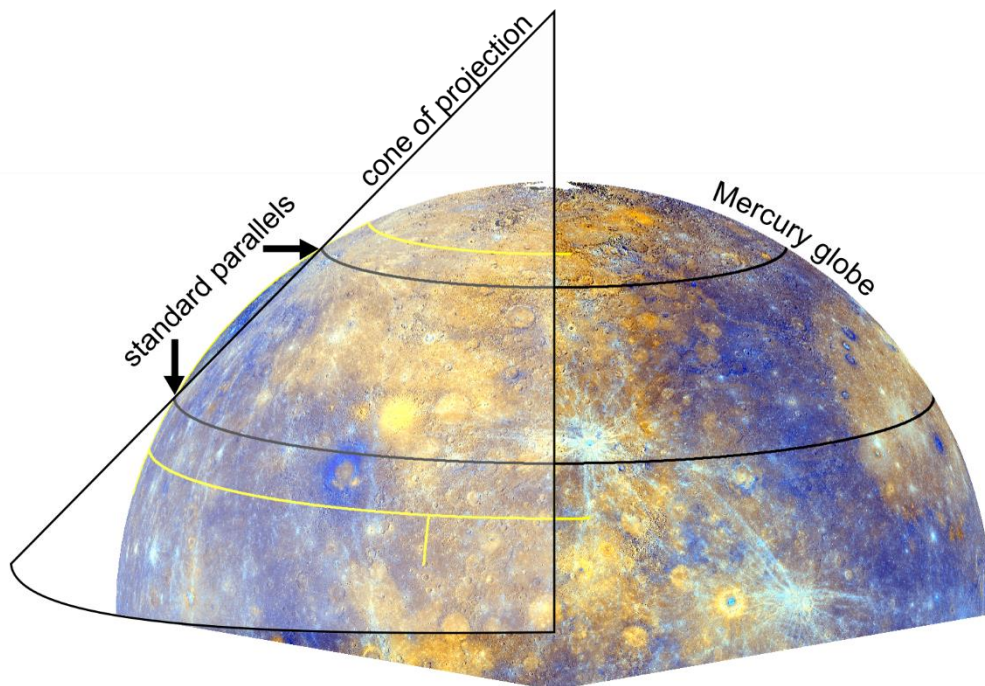
Fig. 3.24 Construction of a Lambert Conformal Conic Projection for H05. *The 'cone of projection' is the transparent shape that intersects the globe along the labelled standards parallels shown as black lines. Quadrangle boundaries are shown as yellow lines. Orthographic projection of Mercury's northern hemisphere centred on 90°E, 10°N.*

LCC projections preserve angles locally. As a result, the general shapes of geographic features are preserved. For example, circular impact craters on a planetary surface appear circular over the entirety of a map projected as a LCC. However, distances are distorted such that the map scale is true along the standard parallels only. Between the standard parallels the scale is compressed and outside them the scale is expanded (Fig. 3.25). For example, an impact crater that is 200 km in diameter within H05 on Mercury will measure ~6.67 cm in diameter on the map at a publication scale of 1:3M. However, on the same map, a 200 km diameter crater located at 44°N (i.e. between the standard parallels) will measure ~6.60 cm in diameter (~0.99× true scale). A 200 km-diameter crater at the edge of the H05 basemap at 71°N would measure ~6.73 cm across (~1.01× true scale; *DEETZ AND ADAMS, 1935*).
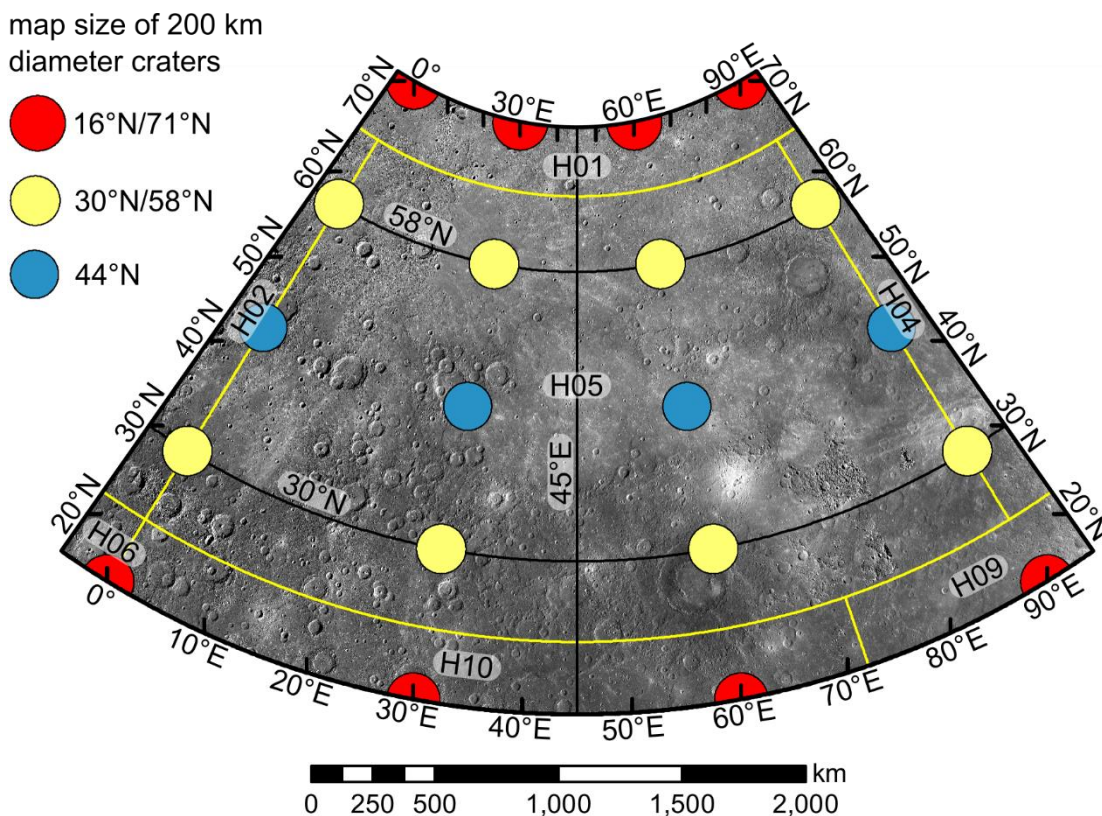
Fig. 3.25 Tissot's Indicatrices of deformation for the Lambert Conformal Conic projection of the H05 basemap. *The central meridian (45°E) and first (30°N) and second (58°N) standard parallels that define the projection are labelled and shown as black lines. Red, yellow, and blue shapes illustrate the distortion caused by the projection. Quadrangle boundaries are shown by yellow lines. ~166 m/pixel monochrome basemap in the native projection of H05.*

Nevertheless, a LCC is a suitable projection in which to conduct geological mapping of H05. The preservation of landform shapes across the entirety of the basemap will ward against misinterpretation of geological structures. Furthermore, the distortion of landform sizes caused by the projection is small and therefore unlikely to affect geological interpretations significantly.

3.3.3   Scale

As stated previously, my map of H05 was intended from the beginning of my work to be compatible with the other MESSENGER-era quadrangle geological maps of Mercury being produced *(GALLUZZI ET AL., 2016; MANCINELLI ET AL., 2016; GUZZETTA ET AL., 2017)*. Therefore, the final publication scale of my geological map of H05 was set as 1:3M-scale. To make the mapping linework as accurate as possible and to make it appear 'smooth', digitisation needed to be carried out at a larger scale than the final publication scale. The other MESSENGER-era mappers *(GALLUZZI ET AL., 2016; MANCINELLI ET AL., 2016; GUZZETTA ET AL., 2017)* were cognisant of USGS guidance for planetary mappers that the digitisation scale should be two to five times larger than the publication scale *(TANAKA ET AL., 2011)*. Furthermore, the USGS recommends that the scale of digitisation be held constant. Following this 'top-down' recommendation, a map to be published at 1:3M-scale should be digitised at a scale between 1:1.5M and 1:600k. An alternative 'bottom-up' solution to the problem of digitisation scale suggests that it should be 2,000 times the raster resolution *(TOBLER, 1987)*. By this rationale, the recommended digitisation scale would be ~1:300k, since the resolution of my basemaps is ~166 m/pixel. Bearing both these recommended constraints in mind, I elected to map H05 at a constant scale of 1:400k.

3.3.4   Mapping

I created my geological map of H05 by digitising vector layers on top of basemap raster layers in ArcMap 10.1. All these digitisations belong to one of the three feature classes, contained within my geodatabase:

1. Geological contacts (polylines).
2. Linear features (polylines).
3. Surface features (polygons).

Polylines are composed of geographically located vertices linked by vector line segments. As explained in Section 3.3.3, digitisation was completed at a constant scale of 1:400k, in order for mapping detail to be equal over the entirety of the map. To this end, polyline digitisation was conducted in vertex streaming mode, whereby polyline vertices were created automatically at regular intervals (known as the 'stream tolerance') as the cursor is moved over the map. I set the stream tolerance to 300 m, roughly two times the ground resolution of my basemaps (~166 m/pixel). This is because the pixel size represents the absolute limit of MESSENGER data resolution. No features smaller than the pixel size can be resolved, therefore it would be meaningless, or even misleading, for the 'resolution' of geological mapping to be higher than this.

All linework was drawn such that intersecting geological features were digitised by line segments that intersect at a common vertex, rather than line segments overlapping.

3.3.4.1 Contacts

Geological contacts mark the location of a physical boundary between geological units. In the case of Mercury, there is evidence that a thick regolith has developed over the course of several billion years due to impact bombardment *(KRESLAVSKY ET AL., 2014)*, such that little or no bedrock geology is visible in MESSENGER data for conventional photogeological interpretation. Instead, and in keeping with the previous geological maps of Mercury *(TRASK AND GUEST, 1975; GALLUZZI ET AL., 2016; MANCINELLI ET AL., 2016; GUZZETTA ET AL., 2017)*, the contacts I digitised show the boundaries between different surface geomorphic provinces and impact crater materials. A more detailed explanation of crater material contacts is given in Section 3.3.5.

I have mapped two ordinary types of geological contact: (1) certain, where there is a sharp and easily located boundary between geomorphic units, and (2) approximate, where my interpretation is that a contact between geomorphic units must exist, but that its exact location is uncertain.

I have also included geological faults within the contact feature class. I chose to do this in anticipation of different geomorphic units appearing on opposite sides of a

fault (i.e. a faulted contact). I originally included the possibility of four different fault types within my map: (1) thrust (certain), where a clearly defined fault break exists with obvious shortening kinematics; (2) thrust (uncertain), where a feature resembling a thrust is present, but this identification is ambiguous; (3) fault (certain), where a clearly defined fault break exists, but the kinematics of the fault are unclear, and; (4) fault (uncertain), for faults of uncertain existence. As mapping progressed, fault identification improved until only thrust (certain) and thrust (uncertain) were required.

3.3.4.2 Linear features

All non-contact linear features, such as crater rims, ridges and grabens, are included within this feature class.

I digitised the crater rims of all superposing impact craters ≥5 km in diameter. Craters ≥20 km in diameter are shown with a black polyline with a double-hachure that points into the crater interior. Craters ≥5 km and <20 km in diameter are shown with an unornamented black line. Craters rim segments that have been buried by superposing impact ejecta or plains material are shown with a black dot-dash line. For further information about impact crater mapping, see Section 3.3.5.

I have mapped two classes of wrinkle ridges in H05. Ordinary wrinkle ridges have no obvious control on their orientation and are marked with an unornamented magenta line digitised along the surface break of the wrinkle ridge. Wrinkle ridge rings appear to occur in circular segments and their orientation is obviously controlled by impact craters buried directly underneath them. These are marked with an orange line digitised in the same manner as ordinary wrinkle ridges.

Other mapped linear features include networks of small ridges and grabens within smooth plains hosted inside impact craters. Although these features are almost certainly fault bounded, these bounding faults, often too small to be resolved in the basemap, are too closely spaced to appear distinct at the publication scale of the map. I have digitised the medial lines of these small ridges and grabens.

The brinks of irregular pits, interpreted to be explosively excavated volcanic craters, are the final class of linear feature. I have marked these with a black single-hachured line where the hachure points down into the pit.

3.3.4.3 Surface features

Surface features include faculae, hollow fields and secondary impact crater clusters and chains. They are digitised originally as polygons, rather than being created as polygons from their digitised outlines. They are rendered as transparent ornaments on the map to allow the underlying geological units and contacts to show through. This is to maximise the geological information apparent in the map and to reflect the surficial nature of these features: faculae are thought to be thin deposits of pyroclasts, and hollows and secondary impact craters are merely depressions in the surrounding geological units.

3.3.4.4 Geological unit production

To generate the geological units polygon feature class, I used the ArcMap tool 'Feature To Polygon' with the entire finalised contacts feature class as the input.

3.3.5   Crater classification

Impact crater deposits are too numerous at the quadrangle scale on Mercury for them to be mapped as unique units. Instead, since impact craters degrade over geological time, they are grouped according to their morphological degradation class *(MCCAULEY ET AL., 1981)*. In theory, this will convey information about the relative ages of non-overlapping impact craters in the mapping region. This is based on the assumption that craters in the same degradation state originally formed at similar times and advance in degradation at a similar rate, as explained in Chapter 2. Crater materials in the same degradation class that are in contact with each other have this contact marked. This makes it clear to the reader which crater superposes which. The presence or absence of several morphological features (bright rays, secondary crater field, textured distal ejecta, crisp rim, wall terraces, internal peak/ring) are used to assign an individual crater to a degradation class. However, it should be noted that, all other factors being equal, smaller craters will degrade faster on Mercury than larger ones *(GALLUZZI ET AL., 2016)*. Furthermore, given the qualitative nature of crater degradation, assigning a crater to a degradation class is highly subjective and the more classes that are available for assignment the less reproducible a classification can be. Nevertheless, if a classification scheme with more classes can be properly implemented, the

resultant map would have higher temporal resolution and contain more geological information than a map with fewer degradation classes.

Mariner 10-era geological mappers of Mercury classified large impact craters into one of five crater degradation classes. These were named c_1 (most degraded), c_2, c_3, c_4 and c_5 (very fresh; *MCCAULEY ET AL., 1981*). This numbering suggests the stratigraphic order that the c_1 craters generally formed early in Mercury's history, the c_2 craters formed more recently, and so on. Originally, the 1:15M scale global geological map of Mercury *(PROCKTER ET AL., 2016)* being produced by the MESSENGER team reversed this numbering scheme, however more recent conference abstracts of this map have the original stratigraphic crater degradation class numbering scheme *(KINCZYK ET AL., 2018B)*. All craters ≥40 km in diameter have been assigned a degradation class in the global map.

The MESSENGER-era quadrangle mappers of Mercury have adopted a three-class crater classification scheme *(GALLUZZI ET AL., 2016; MANCINELLI ET AL., 2016; GUZZETTA ET AL., 2017)*. This is because these mappers wanted to construct a morphostratigraphy for their quadrangles, where all craters in a fresher degradation class were also stratigraphically younger than any crater in a more degraded class. Since the quadrangle maps were produced at a larger scale than the global map, they classify all craters ≥20 km in diameter. Some examples of degraded craters at the lower size limit of classification were found superposing apparently fresher large impact crater materials. In order to reconcile the apparent contradiction between crater morphology and stratigraphy, the three-class crater classification scheme was created. Classes C_3 and C_1 are reserved for the freshest and most degraded craters, respectively, and craters intermediate in appearance are classified as C_2. Reducing the number of classes made the classification more reproducible, allowing for successful merging of quadrangle maps *(GALLUZZI ET AL., 2019)*, and also eliminated examples of small craters in degraded classes overlying large craters in fresher classes by reclassifiying them both into C_2 materials.

In this work, I have used both classification systems simultaneously on all impact craters ≥20 km in diameter. I have done this so that digital versions of my map can be compared with both the global geological map of Mercury *(PROCKTER ET AL., 2016; KINCZYK ET AL., 2018B)* and the MESSENGER-era quadrangle maps *(GALLUZZI*

ET AL., 2016; MANCINELLI ET AL., 2016; GUZZETTA ET AL., 2017). For clarity in what follows, throughout the remainder of this thesis I refer to the classes of the three-class scheme with uppercase lettering (i.e. C_1, C_2, C_3) and the classes of the five-class scheme with lowercase lettering (i.e. c_1, c_2, c_3, c_4, c_5). In all other respects, I have mapped craters in the style of the MESSENGER-era quadrangle maps *(GALLUZZI ET AL., 2016; MANCINELLI ET AL., 2016; GUZZETTA ET AL., 2017).* Craters large enough to be assigned a degradation class also had their floor contacts digitised and their floor materials categorised as either smooth or hummocky (see Sections 3.4.3.2 and 3.4.3.3). No contact between the proximal and distal ejecta of classified craters was digitised.
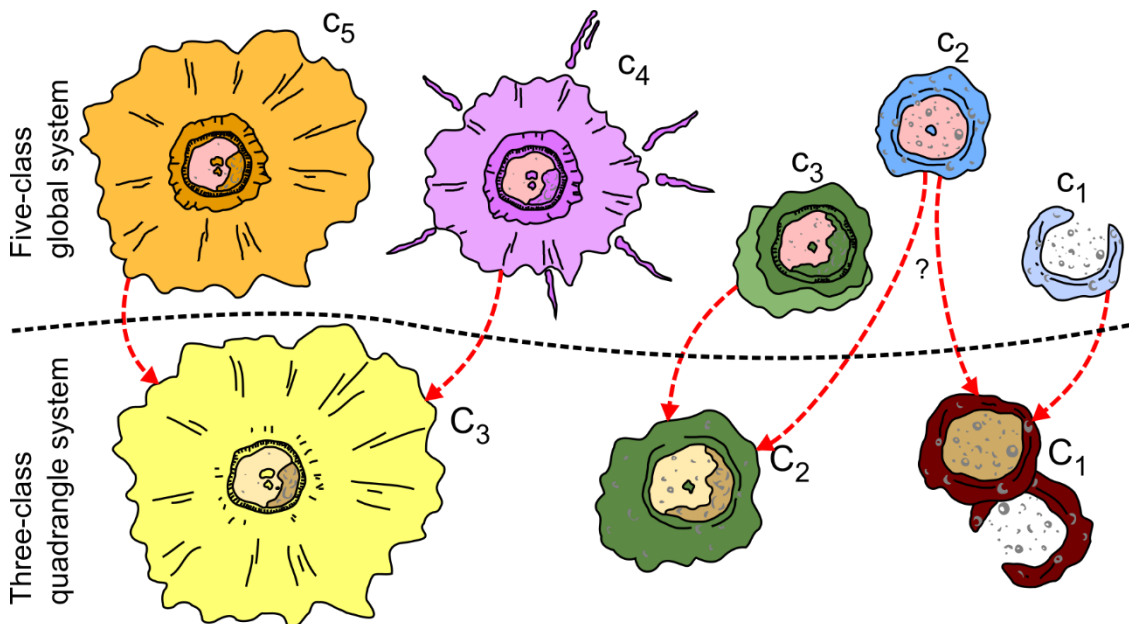
Fig. 3.26 Crater degradation classification schemes employed in H05. *The red arrows show the approximate correspondence between classes in the five-class scheme (KINCZYK ET AL., 2018B) used on all craters ≥40 km in diameter and the three-class scheme (GALLUZZI ET AL., 2016; MANCINELLI ET AL., 2016; GUZZETTA ET AL., 2017) used on all craters ≥20 km in diameter. Note that in the three-class scheme, no contact or distinction is made between the proximal and distal crater ejecta. Cartoon modified after GALLUZZI (2015).*

3.4   Unit descriptions and interpretations

In this section, I introduce the various mapped units within H05 that were defined before mapping commenced. For a discussion of the geological history of H05, see Chapter 4.

3.4.1   Intercrater plains

The most widespread geomorphic unit on Mercury *(TRASK AND GUEST, 1975; WHITTEN ET AL., 2014; PROCKTER ET AL., 2016)*, the intercrater plains have been described as 'level to gently rolling ground between and around large craters and basins' *(TRASK AND GUEST, 1975)*. Intercrater plains host large, degraded craters, as well as fresher craters. These plains are characterised by a high density of degraded secondary impact craters that can no longer be associated with a primary impact crater. These craters have different morphologies in different regions of H05, either being immature and bowl-shaped, or mature with flat floors and subdued rims. Intercrater plains have no striking colour properties and generally coincide with the intermediate terrain colour unit *(DENEVI ET AL., 2009)*.

The intercrater plains probably represent the remains of extensive lava flows that erupted before the end of the Late Heavy Bombardment of the inner Solar System *(WHITTEN ET AL., 2014)*. They have been substantially reworked by impact bombardment and incorporate distal ejecta from many degraded impact craters. This explains the poor correspondence between the geomorphically defined intercrater plains and colour terrain units on Mercury.

3.4.2   Smooth plains

Smooth plains are abundant in H05 due to its inclusion of a substantial portion of Borealis Planitia (Fig. 3.8). In Borealis Planitia, smooth plains are characterised by a low density of superposing impact craters and an abundance of wrinkle ridges (Fig. 3.27). Superposing craters generally have textured ejecta blankets that appear to thin toward their contacts with the surrounding smooth plains. Wrinkle ridges that do not form rings overlying impact craters appear to be randomly oriented, except where they intercept wrinkle ridge rings; here, they tend to intersect perpendicular to the ring. Wrinkle ridges form linked networks that extend across much of Borealis Planitia. Borealis Planitia generally has a sharp contact with adjacent units. In colour data, Borealis Planitia generally corresponds to the colour terrain unit high-reflectance red plains *(DENEVI ET AL., 2009)*, except in the southwest of H05 where instead it appears to be low-reflectance blue plains *(DENEVI ET AL., 2009)*.
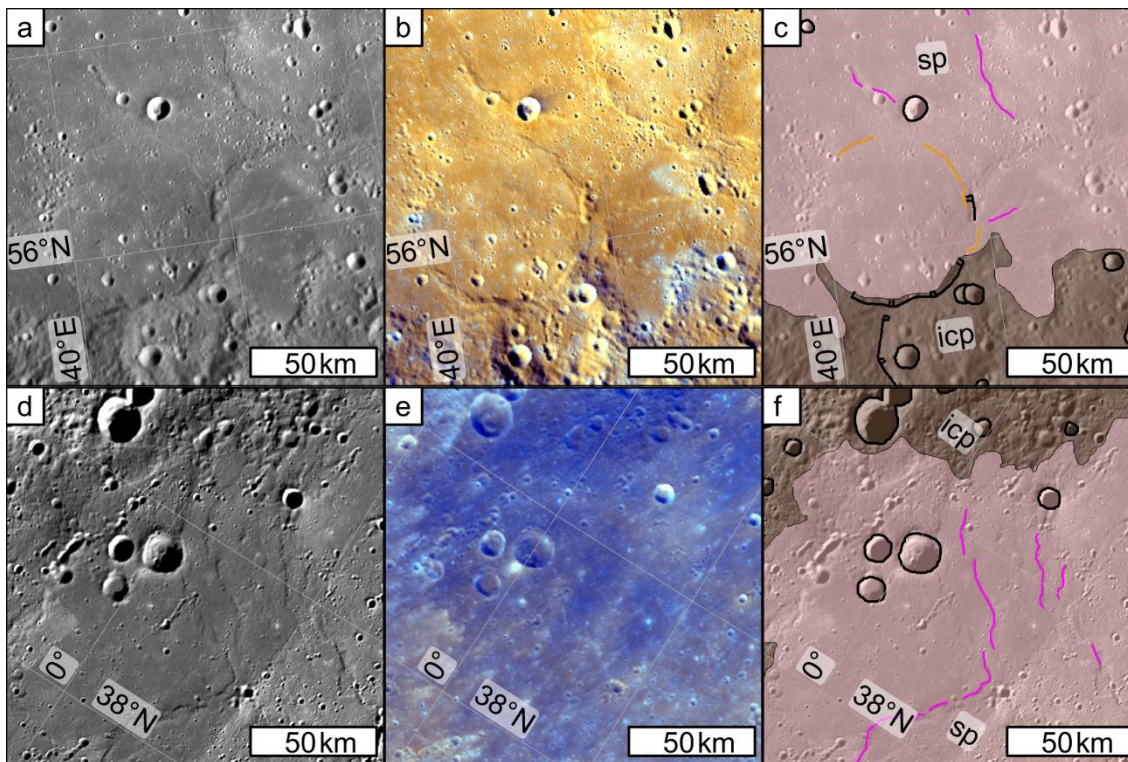
Fig. 3.27 Expressions of the smooth plains of Borealis Planitia in H05. *(a–c) High-reflectance red plains material in Borealis Planitia. (a) ~166 m/pixel BDR basemap. (b) ~665 m/pixel enhanced colour basemap. (c) Mapped units. The contact between the geomorphic units smooth plains (sp) and intercrater plains (icp) is sharp. In the centre of the view, an impact crater has a mixed surface expression as a partial rim (black hachured line) and a wrinkle ridge ring (orange line). (d–f) Low-reflectance blue plains material in Borealis Planitia. (d) ~166 m/pixel BDR basemap. (e) ~665 m/pixel enhanced colour basemap. (f) Mapped units. As in (c), a sharp geomorphic contact exists between the smooth plains (sp) and the intercrater plains (icp). All panels are shown at the publication scale of 1:3M, in the map's native LCC, with graticules showing 2° intervals of latitude and longitude.*

Away from Borealis Planitia, smooth plains exist in small patches within the other plains units of H05, such as the floors of degraded secondary crater chains or volcanic vents. Here, the contact between the smooth plains and the surrounding units is often less clear. Smooth plains are also found in patches perched in the proximal ejecta of geomorphically fresh craters, such as Rachmaninoff and Rustaveli (Fig. 3.28). These smooth patches have sharply defined boundaries.
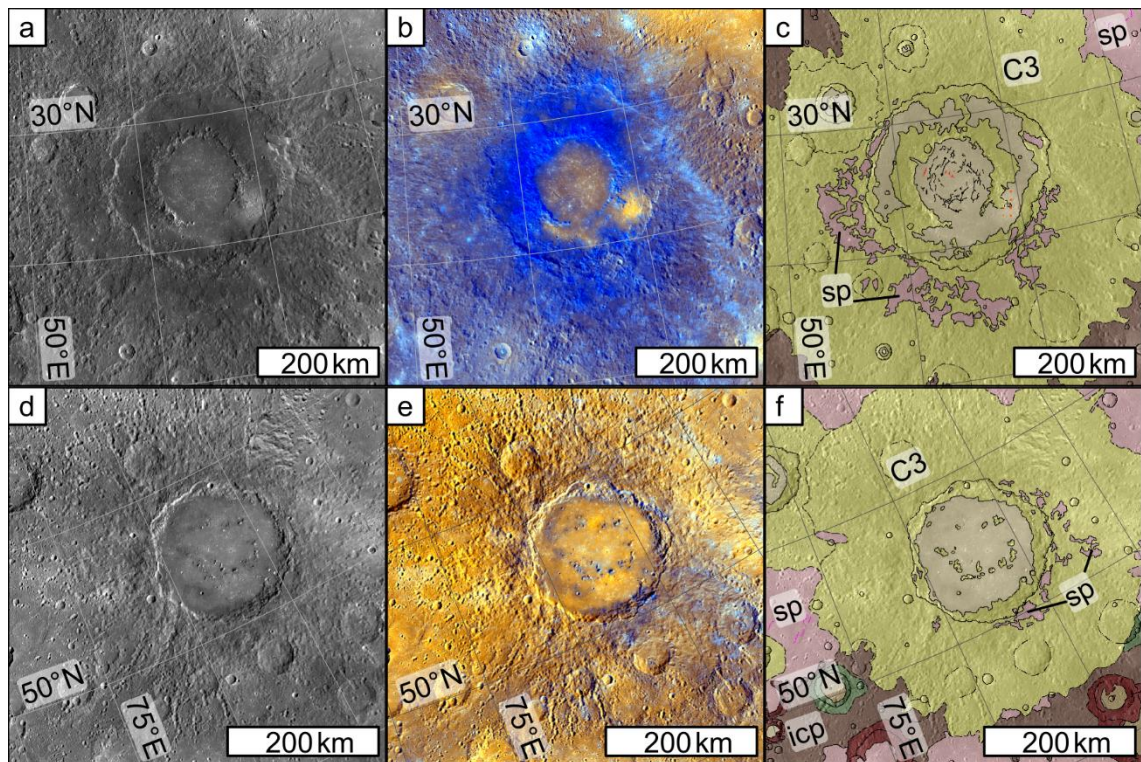
Fig. 3.28 Comparison of Rachmaninoff and Rustaveli in H05. *(a–c) Rachmaninoff basin. 1:12.5M-scale. (a) ~166 m/pixel BDR basemap. (b) ~665 m/pixel enhanced colour basemap. (c) Mapped units. Perched patches of smooth plains are indicated (sp). (d–f) Rustaveli crater. 1:10M-scale. (d) ~166 m/pixel BDR basemap. (e) ~665 m/pixel enhanced colour mosaic. (f) Mapped units. Perched patches of smooth plains are indicated (sp). Graticules in all panels show 5° intervals of latitude and longitude. All panels show the native LCC of H05.*

The smooth plains constituting Borealis Planitia are probably the remains of the last large-volume effusive eruptions on Mercury *(DENEVI ET AL., 2013; OSTRACH ET AL., 2015; BYRNE ET AL., 2016)*. The fact that wrinkle ridge rings of different diameters occur alongside each other in Borealis Planitia requires multiple emplacement events *(OSTRACH ET AL., 2015)*, which argues for multiple effusions and against a basin ejecta origin, such as was the case for the Cayley Plains on the Moon *(EGGLETON AND SCHABER, 1972)*, for these smooth plains on Mercury.

Small patches of smooth plains perched on the proximal ejecta of impact basins are interpreted as ponds of fluidised impact ejecta and/or impact melt, as is well documented on the Moon *(HOWARD AND WILSHIRE, 1975)*. Small patches within low-lying regions of the other plains units of H05 could either represent small-

scale effusions *(MALLIBAND ET AL., 2018)* or ponds of impact melt or ejecta *(WHITTEN ET AL., 2014)*.

3.4.3 Crater materials

Craters ≥20 km in diameter had their floor contacts and the extent of their continuous distal ejecta digitised. Ejecta, walls, and internal uplift (central peaks/rings) of each classifiable crater were assigned a common degradation class based on their morphology. As I have used both the three-class and the five-class crater classification schemes, I describe here the characteristics of the three-class system and then state any further characteristics that would allow a classification in the five-class system.

3.4.3.1 Crater degradation classes

Fresh craters are assigned the C_3 degradation state in the three-class system. C_3 craters have sharp crater rims, and where terraces are present these are well-organised. Any internal uplift (central peaks/rings) has a fresh appearance. The contacts between the crater wall, floor, and internal uplift are distinct. C_3 craters have radially textured ejecta that extends approximately one crater diameter away from the crater rim. Often secondary crater chains and clusters can be attributed to primary craters in this degradation class. The crater and its ejecta typically have few superposing impact craters, unless these are obvious self-secondaries. The contact between the crater's distal ejecta and the surrounding material is relatively well-defined. In the five-class system, craters satisfying these criteria are classified as c_4 craters. If a crater also possesses bright crater rays, then it is classified as c_5.

Moderately degraded craters are assigned the C_2 degradation state in the three-class system. C_2 craters have easily identified crater rims but crater terraces are not pristine. Original internal uplift is still present but may have been modified by subsequent impacts. The crater's ejecta is less obviously textured and the contact with the surrounding materials, particularly if they are intercrater plains, is difficult to discern. C_2 craters and their ejecta often have multiple superposing C_3 and other C_2 impact craters. In the five-class system, craters satisfying these criteria are classified as c_3 if obvious distal ejecta is still present, or c_2 if it is missing or greatly subdued.

The most degraded craters are assigned the C_1 degradation state in the three-class system. C_1 craters have rims that have been partially or totally overprinted by subsequent impacts and often the best indication that a crater of this class is present is by consulting topographical data. Crater terraces are both highly disorganised and incomplete, or obliterated altogether and the contact with the floor material is unclear. Any original internal uplift has been greatly subdued if it has not been entirely overprinted. No distal ejecta is discernible. These craters may be classified as c_2 craters in the five-class system, unless their walls have been breached by the surrounding plains, in which case they are classified as c_1 craters.

3.4.3.2 Smooth crater floors

This is one category of crater floor material mapped in craters $\geq$20 km in diameter, characterised by a smooth and level surface and few superposing impact craters.

This material may represent solidified impact melt retained within the impact cavity. Alternatively, it could be post-impact volcanic plains that erupted directly from the crater floor. It is not always possible to distinguish between these two possibilities, so such interpretations are left off the map. In degraded craters, post-impact volcanic resurfacing is more likely to be responsible for smooth material on the crater floor. This problem is discussed further in Chapters 4 and 5.

3.4.3.3 Hummocky crater floors

This is the other category of crater floor material mapped in craters $\geq$20 km in diameter. It is rough-textured or rolling material found within craters.

When found in fresh craters this can often be ascribed to crater wall debris or a crisp original floor morphology. In more degraded craters, this texture formed as a result of impact bombardment of the original crater floor.

3.5   Geology of H05

In the following chapter, I outline the geological history of H05 as determined by mapping the units described in this chapter.

CHAPTER 4
GEOLOGICAL HISTORY OF THE HOKUSAI QUADRANGLE

4.1 Introduction

In this chapter, I present my geological map of the Hokusai quadrangle (H05) of Mercury, which was to be a major product of my thesis research as defined from the outset. Appendices 1 and 2 contain publication-scale versions of the map with the three- and five-class degradation systems, respectively. In Section 4.2.1, I report the results of my classification of impact crater materials into two different degradation state schemes. In Section 4.2.2, I describe the 'intermediate plains' unit that I mapped in H05, alongside the established smooth plains and intercrater plains units described in Chapter 3. In Section 4.2.3, I outline the major geological unit-forming events that affected H05 to produce its present-day photogeological units and I present my interpretation of the quadrangle's general stratigraphy in Section 4.2.4. In Section 4.2.5, I discuss the tectonic features of the quadrangle. Following this quadrangle overview, I describe in more detail the geology of two regions of particular interest in H05: the impact crater Rachmaninoff and the surrounding region (Section 4.3.1); and the southwestern region of H05 where I mapped evidence of ancient impact basins (Section 4.3.2).

4.2 Mapping results

The major geological units in H05 were mapped in accordance with the unit descriptions given in Chapter 3, which are based on the map units of the other MESSENGER-era quadrangle geological maps of Mercury *(GALLUZZI ET AL., 2016; MANCINELLI ET AL., 2016; GUZZETTA ET AL., 2017)*. This map is shown in Fig. 4.1 and included at its full publication scale in Appendix 1. However, during my mapping I found that the geology of H05 cannot be represented adequately with the provisions from the other quadrangle maps. This followed from my simultaneous use of the 3-class quadrangle *(GALLUZZI ET AL., 2016; MANCINELLI ET AL., 2016; GUZZETTA ET AL., 2017)* and 5-class MESSENGER team *(KINCZYK ET AL., 2018B)* crater

degradation systems and my discovery of plains in H05 that do not conform to the strict definitions of smooth plains or intercrater plains *(GALLUZZI ET AL., 2016; MANCINELLI ET AL., 2016; GUZZETTA ET AL., 2017).*

Surface features
☐ crater rays
▥ pyroclastic deposits

Crater materials
▥ C₃ crater
▥ C₂ crater
▥ C₁ crater
▥ smooth crater floor
▥ hummocky crater floor

Geological units
▥ smooth plains
▥ intermediate plains
▥ intercrater plains

Crater rims
crest of crater rim (diam. ≥ 20 km)
crest of crater rim (5 < diam. < 20 km)
crater of subdued or buried crater
vent

Structures
graben
ridge
wrinkle ridge
wrinkle ridge ring

Faults
thrust, certain
thrust, uncertain

Contacts
certain
approximate

Fig. 4.1 Geological map of H05 using three crater degradation state classes. This small-scale map figure is included in this chapter to illustrate the types of features that were digitised. ~1:26M-scale. The 1:3M-scale publication version of the map with the finalised symbology is in Appendix 1 of this thesis. No overlap with the surrounding quadrangles is shown. This projection is the native Lambert Conformation Conic (LCC) projection of H05.

4.2.1 Crater classification

As explained in Chapter 3, I classified all impact crater materials according to their degradation state. I used two systems in parallel: the 3-class system used in the MESSENGER-era quadrangle maps *(GALLUZZI ET AL., 2016; MANCINELLI ET AL., 2016; GUZZETTA ET AL., 2017)*, where crater materials are classified as C_1 (very degraded), C_2 (degraded), or C_3 (fresh); and the 5-class system used in the MESSENGER global map *(KINCZYK ET AL., 2018B)*, where crater materials are classified as c_1–c_5 (degraded–fresh). The 3-class system was easier to implement and I believe that my classifications are robust. Classifying craters into the 5-class system was more difficult because of the increased number of intermediate degradation states between well-defined end-members. I followed the class definitions of *KINCZYK ET AL. (2016)*, which have slightly different criteria for classification depending on the original morphology (simple, complex, peak-ring, etc.) of each crater. Classes c_1, c_4 and c_5 are well-defined, such that I believe all of my classifications into these classes are robust and reproducible by other mappers. Classes c_2 and c_3 are more nebulously defined, such that other mappers might classify some moderately degraded craters in H05 differently from me.

Despite a lower classification confidence when implementing the 5-class system, it offers the opportunity for higher temporal resolution when interpreting the geological history of H05 from its map. This is true only if all craters of a relatively undegraded class formed after craters of a more-degraded class. When *GALLUZZI ET AL. (2016)* attempted to implement the 5-class system, they found instances of degraded craters superposing relatively fresh craters. This prevented them from using the five crater class system to construct a coherent morphostratigraphy, as explained in Chapter 3. This apparent contradiction of the principle of superposition is most likely explained by the observation that smaller craters degrade more rapidly than larger impact craters *(KINCZYK ET AL., 2016)*. Therefore they devised the 3-class system. However, I found no instances of degraded craters superposing fresher craters in H05 using either system. The most likely explanation for the good correlation between crater degradation and stratigraphy in H05, compared with H02, is that H05 contains abundant smooth plains, which are superposed by the freshest craters only. The reduced extent of older surfaces

in H05 means that it contains fewer degraded impact craters than H02, which means that the likelihood of crater degradation contradicting stratigraphy in H05 is lower. This means that if my classifications shown in Fig. 4.2 are reliable, then a coherent geological history across the whole of H05 can be reconstructed using the 5-class system. This geological history would have higher temporal resolution than is afforded by the 3-class system for the other MESSENGER-era quadrangle maps of Mercury. I detail the major H05 unit-forming events in Section 4.2.3 using the 5-class crater system. Furthermore, I would recommend that future quadrangle geological mappers of Mercury also employ the 5-class crater classification system, in the first instance, to maximise the amount of geological information displayed on their maps, before having to revert to the 3-class system if necessary.

Surface features
- crater rays
- pyroclastic deposits

Crater materials
- c_5 crater
- c_4 crater
- c_3 crater
- c_2 crater
- c_1 crater
- smooth crater floor
- hummocky crater floor

Geological units
- smooth plains
- intermediate plains
- intercrater plains

Crater rims
- crest of crater rim (diam. ≥ 20 km)
- crest of crater rim (5 < diam. < 20 km)
- crater of subdued or buried crater
- vent

Structures
- graben
- ridge
- wrinkle ridge
- wrinkle ridge ring

Faults
- thrust, certain
- thrust, uncertain

Contacts
- certain
- approximate

Fig. 4.2 Geological map of H05 using five crater degradation state classes. This map figure shows a small amount of detail as it is only ~1:26M-scale. A 1:3M-scale version of the map is in Appendix 2 of this thesis. No overlap with the surrounding quadrangles is shown. Native LCC projection of H05.

4.2.2 Intermediate plains

In addition to smooth plains and intercrater plains, Mariner 10-era quadrangle geological maps had additional plains units, including 'intermediate plains' *(SCHABER AND MCCAULEY, 1980; GUEST AND GREELEY, 1983; MCGILL AND KING, 1983; GROLIER AND BOYCE, 1984; SPUDIS AND PROSSER, 1984; TRASK AND DZURISIN, 1984; KING AND SCOTT, 1990; STROM ET AL., 1990).* The exact definitions and interpretations of

intermediate plains vary between maps, but generally these plains appear to have a surface texture intermediate in roughness between smooth plains and intercrater plains mapped elsewhere in a given quadrangle. However, following their study using MESSENGER data, *WHITTEN ET AL. (2014)* recommended that all occurrences of intermediate plains in the Mariner 10 maps could be remapped as either smooth plains or intercrater plains. To achieve this, smooth patches within intermediate plains regions would be remapped as smooth plains and the remaining regions (encompassing a variety of textures) are included in the intercrater plains *(WHITTEN ET AL., 2014)*. Thus, these two are the only plains units included in the first global geological map of Mercury *(KINCZYK ET AL., 2018B)*.

However, some MESSENGER-era quadrangle mappers have included an intermediate plains unit in their maps *(GALLUZZI ET AL., 2016; GUZZETTA ET AL., 2017)*. An important result of geological mapping of H05 is that the distinction between the plains units on Mercury recognisable at a global scale (i.e. smooth plains and intercrater plains) is not so clearly defined at the quadrangle scale, and that a consistently mappable intermediate plains unit is a useful geomorphic designation. Furthermore, while the different sub-types of the intercrater plains defined by *WHITTEN ET AL. (2014)* may not be important to distinguish at the 1:15M-scale of the global map *(KINCZYK ET AL., 2018B)*, these different sub-types are worth splitting into separate formal units at the quadrangle-scale, particularly if a plausible provenance for each can be found.

4.2.2.1 Description

The regions I have designated as 'intermediate plains' in H05 were all mapped as intercrater plains in the global geological map of Mercury *(KINCZYK ET AL., 2018B)*. I use the name intermediate plains merely to reflect the observation that these plains have a texture intermediate in roughness between the intercrater plains and the smooth plains in H05 (Fig. 4.3). I do not suggest at this stage that the intermediate plains are necessarily intermediate in age between the intercrater plains and the smooth plains. Intermediate plains are characterised by hummocky terrain composed of degraded impact crater rims. The intervening low-lying regions are often topographically level and have smooth surfaces. These smooth patches are a significant defining character of the intermediate plains unit, making

up ~50% of its total area, which is a substantially larger percentage of smooth material than that contained within the intercrater plains *(WHITTEN ET AL., 2014)*. In many instances, it is obvious that the locations of the smooth patches are delimited by depressions formed by underlying impact craters. While the hummocky and smooth regions are separable on the basis of texture, they have indistinguishable albedo and colour for the most part. Intermediate plains generally resemble intercrater plains in terms of colour and albedo, in that they are blue and have low reflectance. The smooth patches qualitatively appear to have a similar superposing crater density to the smooth plains, however these patches do not have a sufficient area to test this observation with a statistically robust crater size-frequency distribution study since they typically occupy several hundred square kilometres only. I have mapped some larger smooth patches that occupy obvious crater interiors, and are fully topographically confined, as smooth plains instead of intermediate plains. Nevertheless, many smooth patches are interconnected in networks such that contacts separating them from more hummocky regions would approach fractal complexity and could not be meaningfully displayed at the map publication scale of 1:3M. Thus, I decided to map the intermediate plains as a single unit defined by degraded crater controlled-hummocky plains with intervening smooth patches.
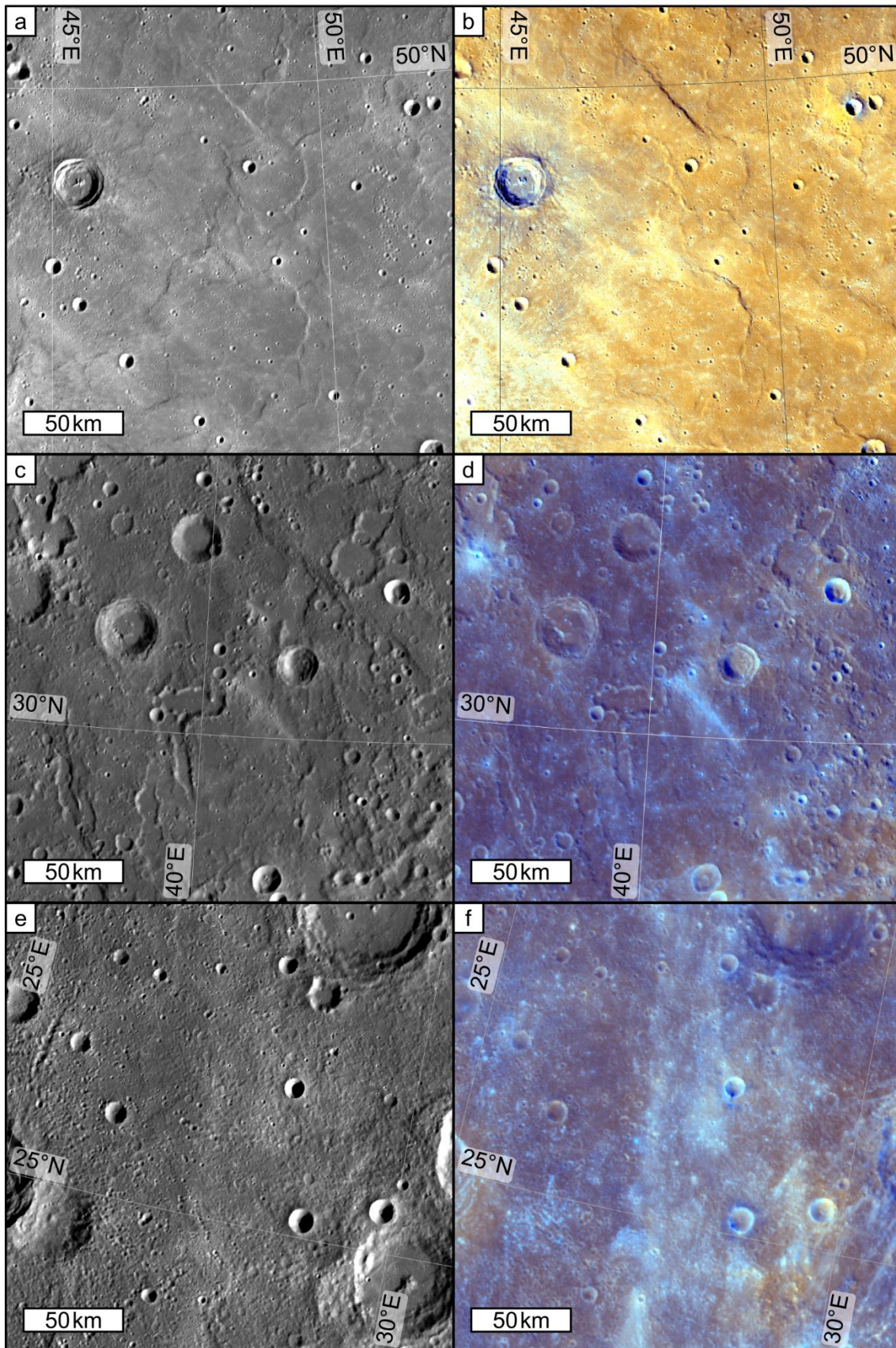
Fig. 4.3 Comparison of plains units within H05. (a) Smooth plains in monochrome. Smooth plains are characterised by a low spatial density of superposing impact craters. Any superposing impact craters are generally in a relatively undegraded state. Wrinkle ridges are abundant. ~166 m/pixel BDR basemap. (b) Smooth plains in enhanced colour. The geomorphic unit smooth plains typically corresponds to the colour-composition unit high-reflectance red plains, as shown here. Same view as (a). ~665 m/pixel enhanced colour basemap. (c) Intermediate plains in monochrome. Intermediate plains have a variable texture that is intermediate in roughness between smooth plains and intercrater plains. ~166 m/pixel BDR basemap. (d) Intermediate plains in enhanced colour. Intermediate plains albedo and colour typically correspond to those of the intercrater plains. ~665 m/pixel enhanced colour basemap. (e) Intercrater plains in monochrome. Intercrater plains in H05 have a high density of superposing impact craters in all states of degradation. ~166 m/pixel BDR basemap. (f) Intercrater plains in enhanced colour. Intercrater plains are generally bluer than smooth plains and correspond to the intermediate terrain, low-reflectance blue plains, and low-reflectance material colour units. ~665 m/pixel enhanced colour basemap. All panels are shown at the publication scale of 1:3M, in the map's native LCC projection, with graticules showing 5° intervals of latitude and longitude.

Intermediate plains in H05 are generally in contact with both smooth plains and intercrater plains, rather than being entirely contained within either unit (Fig. 4.4). This suggests that the formation of the intermediate plains is closely linked to the formation and extent of the smooth and intercrater plains. Intermediate plains contacts with smooth plains are typically sharp, whereas contacts with intercrater plains are more uncertain in their location, particularly where the intermediate plains exhibit their hummocky, rather than smooth, texture. I have found two putative volcanic vents within the intermediate plains (See Section 4.3.2 for further discussion).
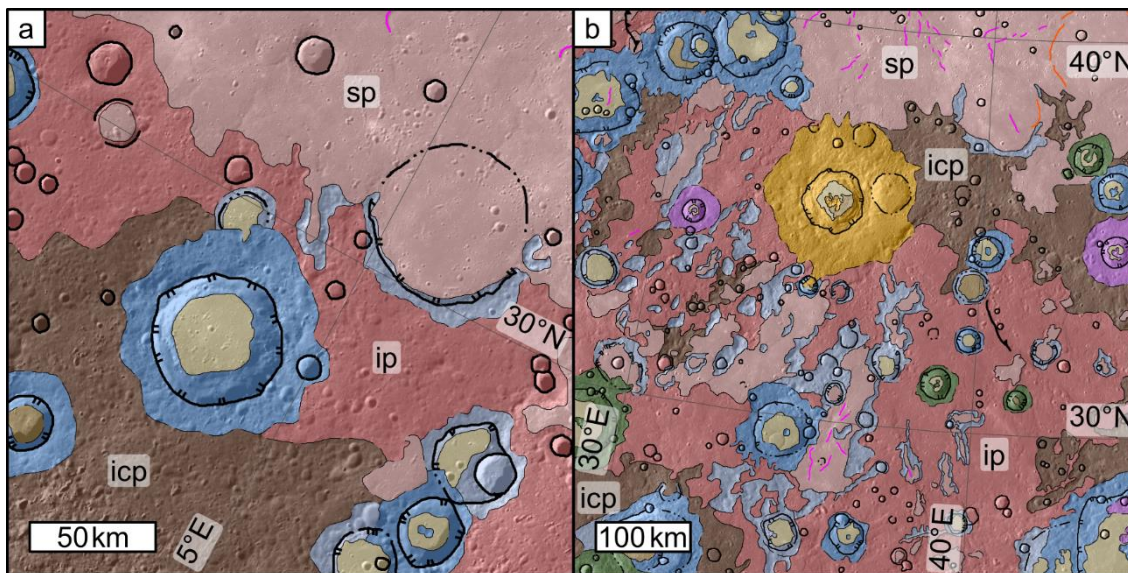
Fig. 4.4 Spatial relationship between the intermediate plains, smooth plains, and intercrater plains in H05. *(a) In western H05, intermediate plains (ip) are located directly between the smooth plains (sp) of Borealis Planitia in the north and the intercrater plains (icp) in the south. The contact with the smooth plains is sharply defined, whereas the intercrater plains contact is much less certain. (b) Part of the most extensive region of intermediate plains in H05 shown. This intermediate plains unit has a more complex spatial relationship with smooth and intercrater plains than in (a), as it is bordered by and contains both. The colours of the geological units in both panels match those in the legend of Fig. 4.2. Semi-transparent geological units are overlain on the ~166 m/pixel monochrome basemap. Native LCC projection of the H05 map.*

4.2.2.2 Interpretation

Based on my observations that the smooth patches within the intermediate plains pond in topographic lows, form interconnected networks in places, and geomorphologically resemble and are typically in contact with the smooth plains, I suggest that these smooth patches were emplaced as lava flows. Some smooth patches may be due to ponds of impact melt, however the locations of the smooth patches are not obviously colocated with craters that could have distributed impact melt, which means this alternative explanation is unlikely in most cases. I suggest that the lava flows were of insufficient volume to achieve the thickness required to mask the hummocky texture from the underlying intercrater plains completely. As a result, intermediate plains cannot be mapped as smooth plains, because it is not sufficiently smooth, nor is it satisfactory for it to be mapped as intercrater plains

because that would remove visualisation of the proposed small-volume effusions from the map.

There is already a precedent for smooth plains material 'flooding' surrounding terrain on Mercury. BYRNE ET AL. (2013) describe a landscape northwest of the Caloris basin that contains volcanically flooded impact features, valleys with smooth plains on their floors (which they interpret as lava channels), and they also observe areas where the intercrater plains material surrounding these volcanically flooded regions has a muted topographic expression. They interpret this 'graded terrain', that is in contact with smooth plains, as intercrater plains that has been inundated by a volume of lava, in the same way that I interpret the intermediate plains in H05.

It is difficult to tell whether effusions in southwestern H05 occurred in either the early or late stages of smooth plains formation in Borealis Planitia. If the interpretation of the intermediate plains as intercrater plains with a thin infilling of superposing lavas is correct, then age dating by measuring the crater size-frequency distribution of the intermediate plains would be problematic since it would be difficult in many cases to determine if a crater superposes the intermediate plains or is a crater 'inherited' from the underlying intercrater plains. Instead, I made several observations along the intermediate plains-Borealis Planitia contact to establish the stratigraphic relationship between the two (Fig. 4.5). I tried to make similar observations to ROTHERY ET AL. (2017), who examined the relationship between the circum-Caloris plains and Caloris Planitia. Unfortunately, MESSENGER data are of insufficient resolution to distinguish between the three possible relationships outlined in Fig. 4.5. This means the intermediate plains could be the same age as much of the smooth plains (Fig. 4.5a), older (Fig. 4.5b), or younger than most of the smooth plains in H05 (Fig. 4.5c). In Sections 4.2.3 and 4.3.2 I discuss observations that suggest that at least some of the intermediate plains formed after most of the smooth plains in H05 were emplaced.
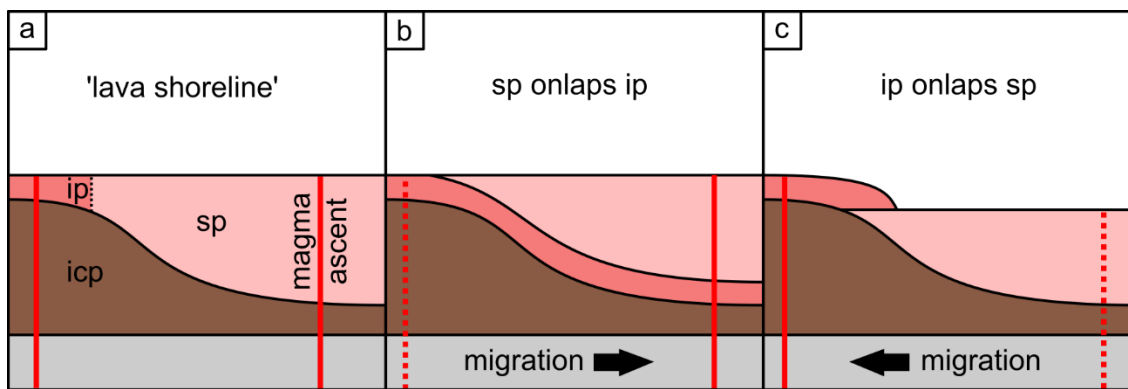
Fig. 4.5 Possible stratigraphic relationships between the smooth and intermediate plains. *(a) Smooth and intermediate plains formed due to effusions from distributed centres simultaneously, making both surfaces similar in age. sp = smooth plains, ip = intermediate plains, and icp = intercrater plains. (b) Intermediate plains formed early during distributed effusions. In time, perhaps due to global contraction (BYRNE ET AL., 2016), eruption centres migrated away from where intermediate plains are observed today to where smooth plains have accumulated in greater thickness. Intermediate plains are stratigraphically older than, and are onlapped by, smooth plains. (c) Smooth plains accumulated in global lows, such as Borealis Planitia. In response to the growing thickness of lava, eruption centres migrated away from the centre of the thick volcanic pile to the edge (MCGOVERN AND LITHERLAND, 2011). Intermediate plains formed due to late-stage, low-volume effusions that did not reach the required thickness to mask the texture of the underlying intercrater plains entirely.*

4.2.3   Main unit formation

Here I outline the geological history of H05, based on my map shown in Fig. 4.2. Several figures throughout this section (Fig. 4.8, Fig. 4.9, Fig. 4.10, Fig. 4.13, Fig. 4.14, and Fig. 4.15) show the major unit-forming epochs as determined from the complete map.

The oldest geological events that occurred in H05, for which observable evidence exists in MESSENGER data, are the formations of three candidate ancient impact basins. *FASSETT ET AL. (2012)* proposed numerous large (≥300 km) basins across the whole of Mercury, including the three they informally refer to as 'b30', 'b31', and 'b45', which extend into H05 (Fig. 4.6). b30 and b31 were first identified as circular topographic depressions in a stereo DEM constructed from MESSENGER flyby data by *PREUSKER ET AL. (2011)*. b45 was subsequently proposed on the basis of orbital stereo DEM data. *FASSETT ET AL. (2012)* deemed the existence of each of these candidate ancient basins to be 'probable', rather than 'certain', on the basis that

each has only ~20% of its rim present. A updated version of the *FASSETT ET AL. (2012)* catalogue of ancient basins has upgraded the confidence of the existence of b30 and b31 from probable to certain *(ORGEL ET AL., 2019)*.
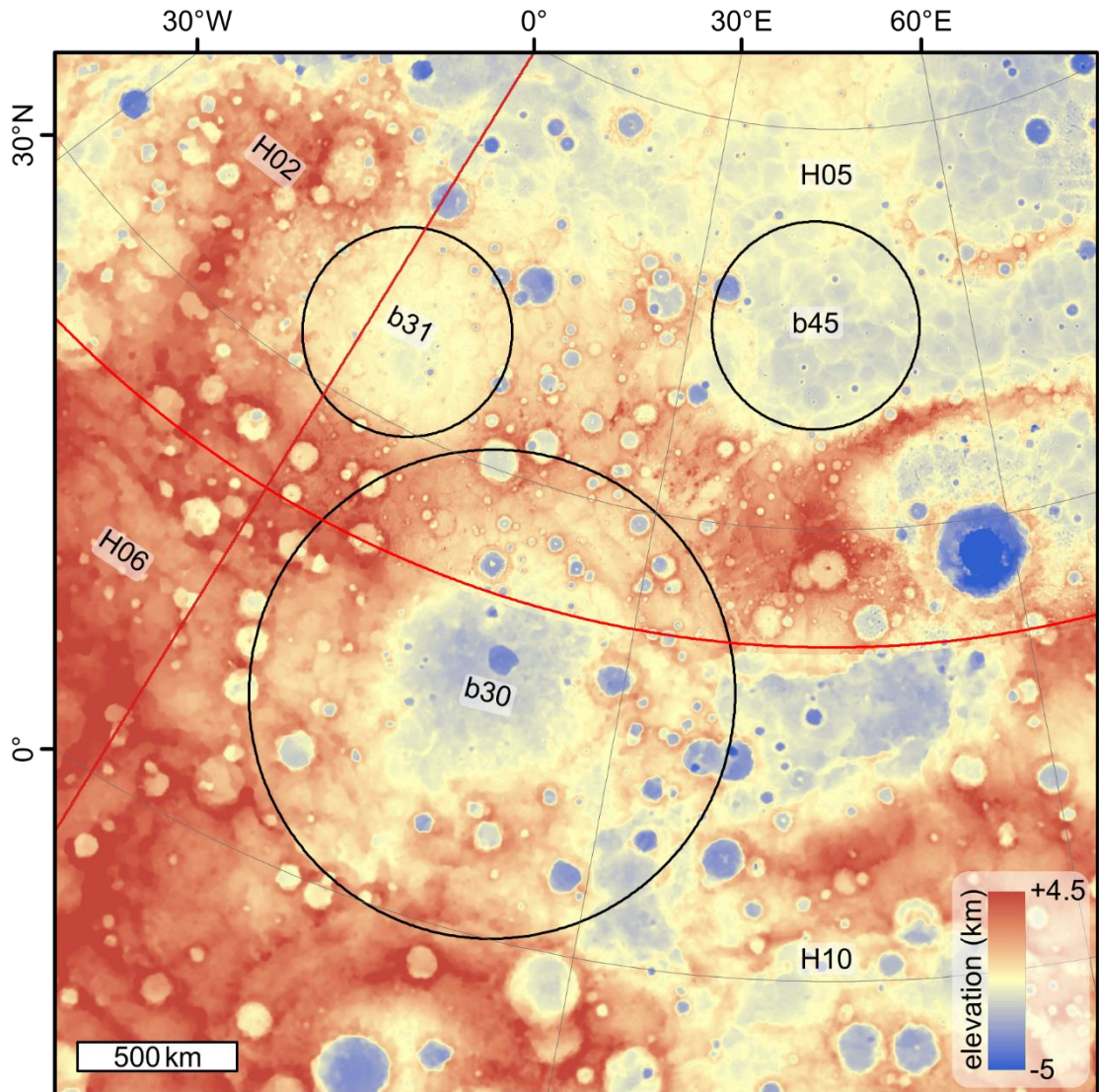
Fig. 4.6 Topography of locations of candidate ancient basins that extend into H05. *The basins are labelled and the approximate locations of their rims are marked in black according to the basin centre coordinates and diameters measured by FASSETT ET AL. (2012). Quadrangles are labelled and their boundaries are shown in red. The topography dataset for H05 is the stereo-derived, ~222 m/pixel DEM of STARK ET AL. (2017), whereas the remainder of the figure uses the global 665 m/pixel DEM (BECKER ET AL., 2016). Higher resolution DEMs of H02, H06 and H10 were not available at the time of writing. Native LCC projection of the H05 map.*

In H05, I found additional geological evidence supporting the existence of the ~1,390 km diameter basin, b30. A series of narrow (~20 km across), linear raised ridges (up to ~1 km of relief) with wide (30–50 km across), intervening troughs radiate from the basin centre beyond the approximate location of the north-eastern rim of b30. The ridges do not appear to be fault-bounded, which suggests that they are not lobate scarps. Instead, I suggest that these ridges and troughs are impact sculpture (see *FASSETT ET AL., 2009*) due to radial scouring of, and secondary crater chain (catena) formation in, the terrain to the northeast of the b30 impact site. This is the same as the proposed formation mechanism for the Van Eyck Formation in the Caloris Group *(MCCAULEY ET AL., 1981; FASSETT ET AL., 2009)*, and a comparison of the Van Eyck Formation with the region north-east of b30 shows that they are very similar in appearance (Fig. 4.7). The somewhat more degraded appearance of the impact sculpture around b30 compared with that of Caloris most likely reflects the older age of the b30 impact.
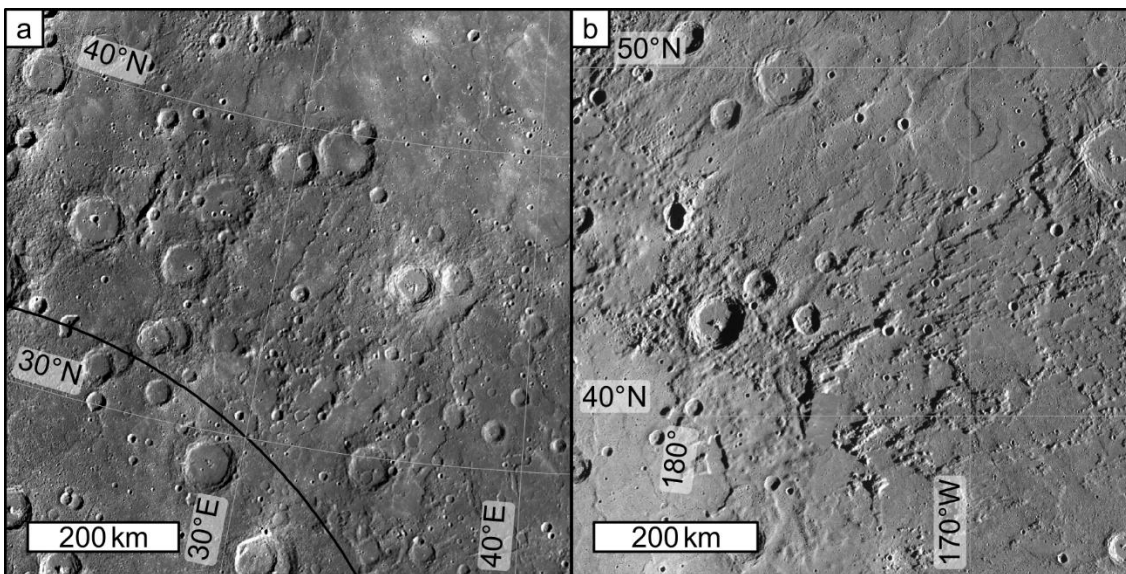
Fig. 4.7 Comparison of terrain associated with candidate ancient basin, b30, and the Caloris Group Van Eyck Formation. *(a) Linear ridges and troughs radiating away from the northeastern rim of b30 (black line). H05 mapping LCC projection. (b) View of the Van Eyck Formation northeast of the Caloris basin rim. Sinusoidal projection centred on 170°W. Both panels show the ~166 m/pixel monochrome basemap.*

If the linear troughs and valleys that appear to radiate from the candidate ancient basin b30 are correctly interpreted as radial scour and catenae, then it must be explained why such impact sculpture is found in only a small azimuthal interval

around the basin. The full extent of radial troughs and ridges is shown in Fig. 4.7 and this region is completely contained within H05. I observed no obvious radial troughs or ridges in the adjoining quadrangles occupied by b30 (H02, H06 and H10). I suggest that this is primarily due to preservation bias, rather than an originally asymmetric distribution of impact sculpture around b30. Much of the Van Eyck Formation is embayed by smooth plains, suggesting that the Van Eyck Formation could have been more extensive immediately after the Caloris impact but has since been buried in places by smooth plains material. b30 is certainly older than both the smooth plains and the intercrater plains, which suggests that much of the original extent of its impact sculpture could have been buried by both of these plains units in combination. This hypothesis is corroborated by the fact that the radial ridges represent not only locally high relief, but are also generally elevated 1–2 km above datum, allowing them to escape burial since plains preferentially infill low-lying regions. The troughs between the ridges are infilled by smooth and intermediate plains, which I interpret to reflect deeper and shallower degrees of floor burial by lava flows, respectively. Any additional original sculpture associated with b30 might have been buried by so great a combined thickness of intercrater and smooth plains material that no surface expression of it remains except that which I have outlined in Fig. 4.8.
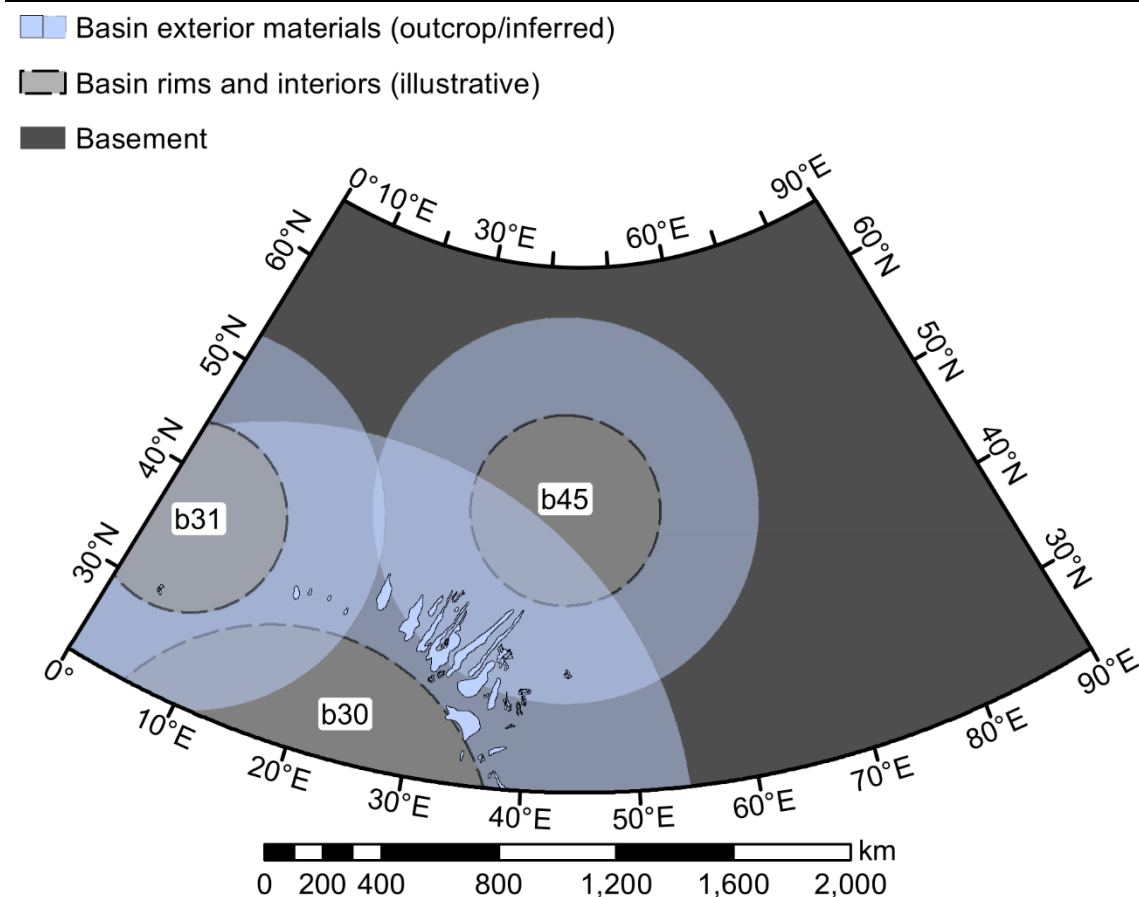
Fig. 4.8 Illustration showing the oldest geological units within H05 for which there is observable evidence. Geological basement of uncertain origin and composition is shown in dark grey. The original locations of the rims of candidate ancient basins (FASSETT ET AL., 2012) are shown as dashed black lines. Ancient basin interiors are light grey. Hypothetical original extents of basin ejecta are shown in transparent light blue. Geological evidence for these ancient basins, in the form of radiating ridges and other high-standing topography, is shown with a black outline in opaque light blue. Based on the apparent differential preservation of basin sculpture around b30, I tentatively suggest that basin b45 formed first, followed by b30, then b31. Native LCC projection of H05.

Subsequent overprinting or obliteration of impact sculpture by impacts and their ejecta could be a further erosional agent. Since the three ancient basins in H05 are closely colocated, it may be possible to suggest the order in which they formed. On the basis of the extent of geological evidence for all three candidate ancient basins in H05, I tentatively suggest the order of formation described in Fig. 4.8. Since b30 is the only candidate basin with a substantial geological expression, its spatially differential preservation is the most important line of evidence I used to suggest a formation order for the basins. In Fig. 4.8, I show conservative estimates for the

original extent of the basins' ejecta, i.e. one basin radius beyond the presumed location of their rims. The linear ridges and troughs, that appear to radiate from b30, are well expressed in the region where the b30 and b45 ejecta blankets might be expected to interact. However, ridges and troughs are greatly subdued or absent in the region where b30 and b31 materials might have interacted. This provides some evidence that b45 formed first, b30 formed second, creating sculpture potentially more extensive than observable today, and b31 formed last, partially removing sculpture in the region to the northwest of the rim of b30.

Regardless of the formation order of the basins, they are the earliest geological events with any direct visible evidence for their occurrence in H05. The basins in turn provide evidence for the original crust of Mercury into which their impactors collided. This basement is of uncertain origin and composition, and is not unambiguously expressed at the present-day surface of H05. As mentioned in Chapter 2, it has been suggested that Mercury had a very thin (~100 m thick), perhaps laterally discontinuous, flotation crust of graphite *(VANDER KAADEN AND MCCUBBIN, 2015)*. It has also been suggested that graphite might be the surface darkening agent that contributes to the low albedo of the low-reflectance material (LRM) distributed across the surface of Mercury, and hence that LRM forms the remains of the primary crust *(PEPLOWSKI ET AL., 2016)*. LRM does not appear to be associated with the raised ridges radiating from b30, which might be expected to contain remnants of the ejecta of that basin. Therefore, it is not clear whether b30, or any of the other candidate ancient basins, formed in a primary crust of graphite. However, a much younger impact crater, Rachmaninoff, has exhumed a substantial amount of LRM. Rachmaninoff contains the lowest surface elevation on Mercury and overlies thin crust *(SORI, 2018)*. Therefore, the LRM exhumed by this impact might be representative to some degree of the basement at the bottom of the H05 stratigraphy. Rachmaninoff is discussed in detail in Section 4.3.1.

Following the formation of the basement and the subsequent formation of the ancient basins, many smaller impact craters formed that are still observable today, despite heavy degradation. The remains of these impact craters are classified as c_1 material. Since fresh observable impact craters on Mercury generally have ejecta blankets that extend approximately one crater diameter beyond their respective

crater rims, in Fig. 4.9 I show present-day c_1 crater material in opaque light blue, surrounded by an annulus extending one crater diameter beyond each crater rim in transparent light blue, indicating the possible original extent of each crater's impact ejecta. This is to illustrate, to a first approximation, the fraction of the impact ejecta that survives from this period of H05's geological history. As Fig. 4.9 illustrates, c_1 crater material has been heavily reworked and overprinted by subsequent geological events.
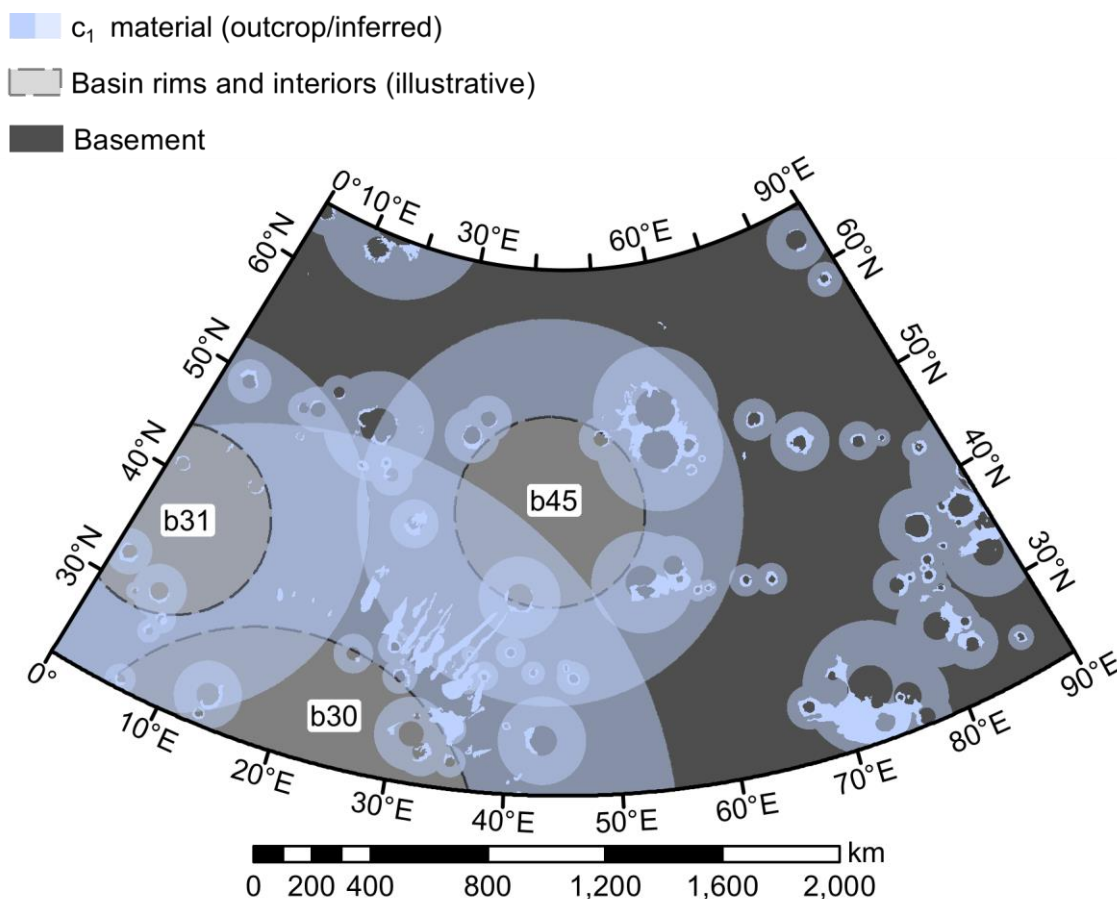
Fig. 4.9 Map of the most degraded impact crater materials in H05. *Observable c_1 degradation state crater materials are shown in opaque light blue. Hypothetical original extents of c_1 crater materials are shown in transparent light blue as an annulus extending one crater diameter beyond the respective crater rim. Here, ancient basin ejecta is interpreted as c_1 crater material and symbolised as such. Native LCC projection of H05.*

The first major secondary crust, for which there is unequivocal geological evidence in H05, is the intercrater plains unit. As can be seen in Fig. 4.10, present-day observable intercrater plains have a strong control on the current extent of c_1 crater material. Intercrater plains appear to have buried the original floor of basin b30 and they embay the rims of most c_1 crater material. The most extensive c_1 crater

104

material is found in topographically high regions, which provides further evidence that the intercrater plains formed primarily as lava flows that infilled low-lying topography and that higher regions escaped burial (Fig. 4.11).
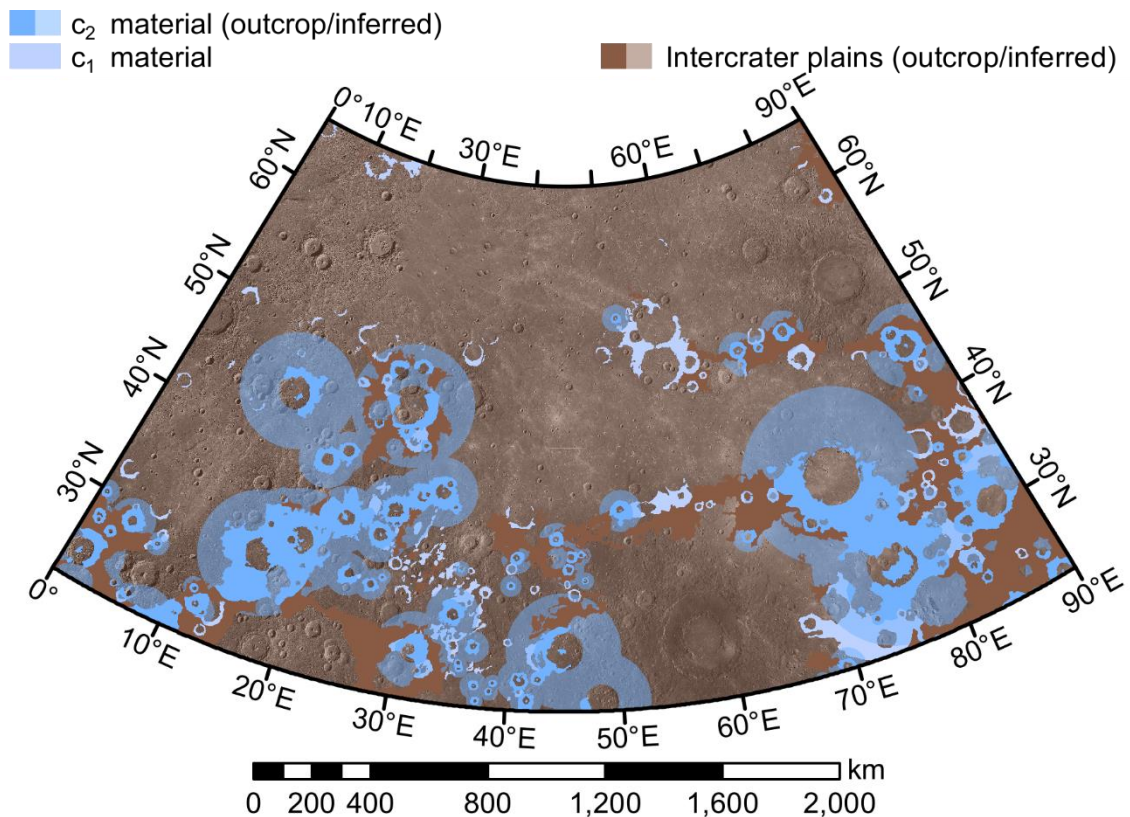
Fig. 4.10 Map showing the present and original (inferred) extent of the intercrater plains in H05. *Intercrater plains (opaque brown) are interpreted (transparent brown) to have buried the original basement in H05 by their formation as effusions of lava. Observable intercrater plains appear to have a strong control on the present-day extent of c_1 crater materials, suggesting that these craters formed before the intercrater plains. Observable c_2 crater materials (opaque blue) are shown with hypothetical original ejecta blanket extents (transparent blue) as in Fig. 4.8. Intercrater plains appear to control the extent of c_2 craters to differing degrees, which suggests that craters in this class formed during and after most of the intercrater plains emplacement. Background is the ~166 m/pixel H05 monochrome basemap. Native LCC projection of H05.*
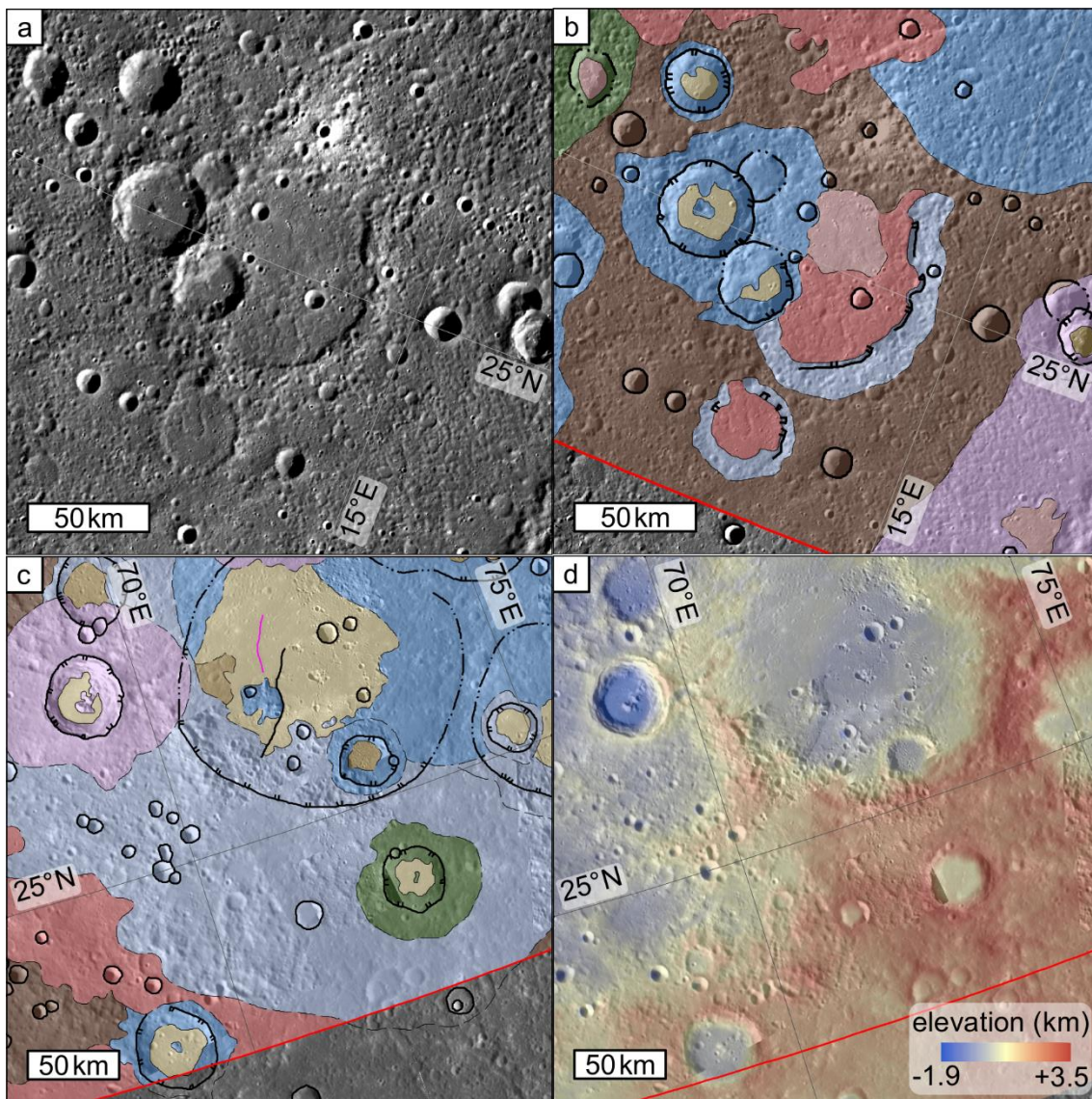
Fig. 4.11 The relationships between plains units and degraded crater materials in H05. (a) A typical c_1 crater. (b) Geological map of the crater shown in (a). Intercrater plains have completely buried the distal ejecta blanket and embay the topographically elevated proximal ejecta. Intercrater plains appear to have buried part of the northern rim of the crater. Later smooth plains material appears to have been emplaced subsequent to infilling of the crater floor by intercrater plains material. c_2 crater material in this view has been embayed to differing degrees, which suggests that craters in this degradation state formed during and after the formation of most intercrater plains. (c) A c_1 crater with more extensive ejecta. This c_1 ejecta appears to have been preserved because it is located on globally high-standing topography (see part (d)). Plains material occupies some of the nearby low-lying areas, but appears to have been unable to flood much of the c_1 material. This, in combination with a coincidental lack of superposing impact craters, appears to be responsible for the uncommon extensiveness of c_1 crater material here. (d) Same view as (c). ~222 m/pixel stereo DEM (STARK ET AL., 2017). Backgrounds of all panels are the ~166 m/pixel H05 monochrome mosaic basemap. Geological units shown in (b) and (c) are coloured as in Fig. 4.2. Red lines indicate the extent of H05. All panels are in the native LCC projection of the H05 map.

By comparing Fig. 4.9 and Fig. 4.10, more original c_2 material is observable today than c_1 material. In Fig. 4.11a and Fig. 4.11b, c_2 crater material that both superposes, and is superposed by, intercrater plains can be seen, suggesting that c_2 crater formation and intercrater plains emplacement were contemporaneous. Furthermore, ejecta from the ~200 km diameter crater, Copland, appears to be buried by intercrater plains, except in the southeast (Fig. 4.12). There does not appear to be a substantial elevation difference between Copland's unburied ejecta and the nearby intercrater plains, which provides some indication that intercrater plains emplacement involved multiple, spatiotemporally distributed eruption centres with lava flow lengths on the order of hundreds, rather than thousands, of kilometres, as has been suggested for smooth plains emplacement elsewhere on Mercury (ROTHERY ET AL., 2017). This could explain why some parts of a crater's ejecta, which effectively formed together in a geological instant, can be buried by plains in some parts and unburied in others that are separated by hundreds of kilometres.
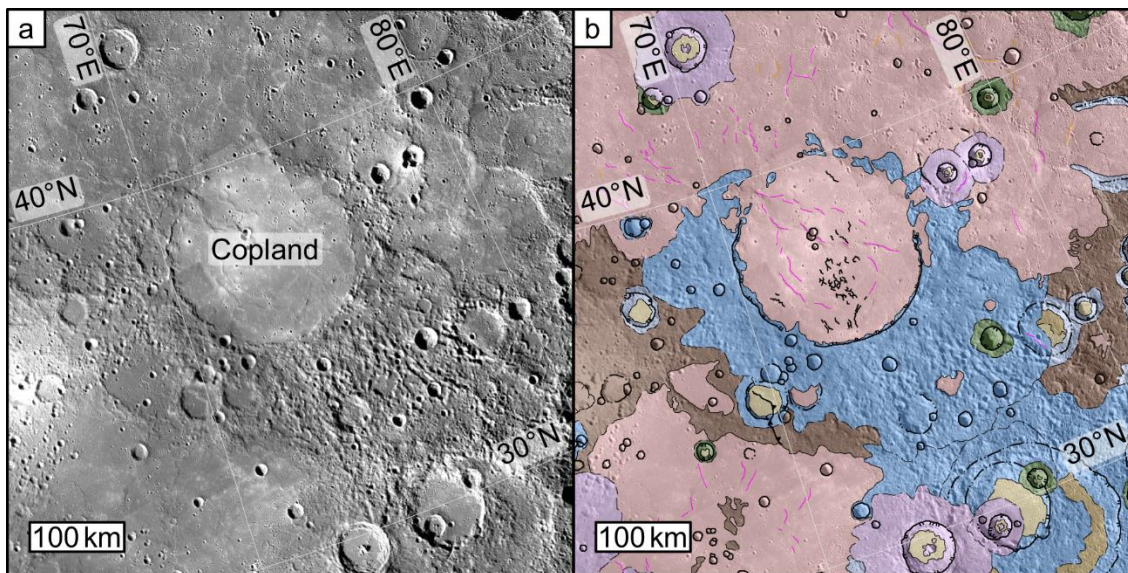
Fig. 4.12 The relationship between c_2 crater material and intercrater plains in H02.
(a) Copland crater (~200 km across). This crater has a sharp rim in places and has a degraded but recognisable distal ejecta blanket that superposes very degraded craters nearby. These observations qualify it for classification as a c_2 crater, rather than a c_1 crater. (b) Detail of the geological map of H05, focussed on Copland. Copland's western ejecta blanket is buried by intercrater plains but the southeastern ejecta blanket is unburied. The colours of the geological units match those in the legend on Fig. 4.2. Both panels show the ~166 m/pixel high-incidence western illumination mosaic tiles in the native LCC projection of the H05 map.

The emplacement of the smooth plains as effusions of lava was the next major geological event that took place in H05 (Fig. 4.13). The smooth plains of Borealis Planitia dominate the geology of H05. Smooth plains are interpreted as the remains of the most recent large volume effusions of lava on Mercury *(BYRNE ET AL., 2016)*. As such, they embay all c_1 and c_2 craters with which they are in contact. c_3 craters appear to have formed during and immediately after the emplacement of the smooth plains, since some small c_3 craters appear to superpose them. Away from the smooth plains, c_3 crater ejecta extends substantially closer to estimated original ejecta extents, as illustrated in Fig. 4.13. This suggests that all c_3 craters formed after the end of intercrater plains formation.

The smooth plains in most of Borealis Planitia correspond to the high-reflectance red plains colour unit, however the smooth plains in southwestern H05, at the location of b31, correspond to low-reflectance blue plains *(DENEVI ET AL., 2009)*. Therefore, it is possible that the relatively small extent of low-reflectance blue

108

plains smooth plains associated with b31 is merely due to impact craters depositing blue material on top of them. However, most of the impact craters in this region are embayed by the smooth plains, and therefore predate them. It is more likely that the colour difference between the smooth plains associated with b31 and those elsewhere in H05 is due to an original compositional difference between the lavas. For example, there could be lateral compositional heterogeneity in the mantle source region beneath b31 and the rest of Borealis Planitia. Alternatively, the compositional difference could be due differences in the residence times in the magmatic plumbing systems at b31 and the rest of Borealis Planitia, such that the erupted lavas at one location were more evolved than at the other. A similar contrast between the smooth plains inside and outside of an impact basin is seen at Caloris. The interior plains, Caloris Planitia, correspond to high-reflectance red plains, whereas the exterior plains correspond to low-reflectance blue plains *(DENEVI ET AL., 2009)*.

Intermediate plains do appear to embay c_3 crater material, which supports my interpretation that this plains unit formed close in geological time to the smooth plains and could be smooth plains material of insufficient thickness to bury the underlying hummocky texture of the intercrater plains. If both intermediate and smooth plains represent the remains of effusions of lava, then the geological history of H05 could be reconstructed in more detail if the relative ages of the smooth plains and the intermediate plains could be determined. As explained earlier in Section 4.2.2.2, if the intermediate plains are younger than the smooth plains, then the intermediate plains might represent small volume, terminal effusions in H05, which would explain why they are of insufficient thickness to bury the intercrater plains to a sufficient depth to appear as smooth plains. Alternatively, if eruption centres migrated from where the intermediate plains exist to smooth plains areas, then intermediate plains could be older lava flows. It will take high-resolution observations of the intermediate plains by BepiColombo to determine their stratigraphic position and characterise the geological history of H05 further.

Smooth plains contain wrinkle ridge rings, which indicate buried impact craters. Based on the observations outlined earlier in Section 4.2.3, I suggest that most of

these buried impact craters originally impacted into either intercrater plains material or H05 basement, and formed at a time when c_1, c_2 or early c_3 craters were formed.
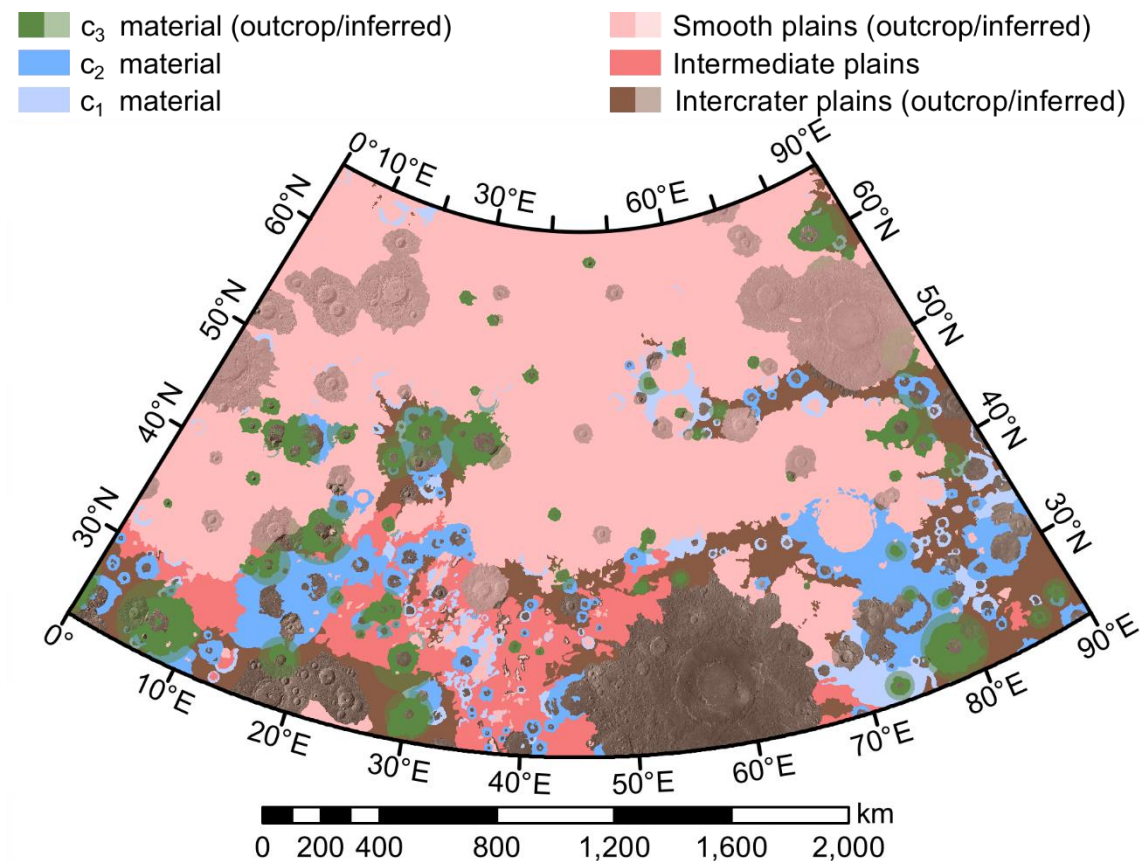
Fig. 4.13 Map showing the present and original (inferred) extent of the smooth plains in H05. *Smooth plains (light pink) probably represent the most recent large-volume effusions of lava on Mercury. All c_2 craters in contact with smooth plains material are embayed by it, which suggests that most of these craters formed before the end of smooth plains emplacement. Observable c_3 crater materials (green) are shown with hypothetical original ejecta extents (transparent green) as in Fig. 4.8. Smooth plains do appear to control the extent of c_3 ejecta in places, whereas intercrater plains do not, which suggests that c_3 craters formed before, during, and after the emplacement of the smooth plains. Intermediate plains appear to have a similar effect on the extent of c_3 crater materials, which suggests that intermediate plains are closer in age to smooth plains than intercrater plains. Background is the ~166 m/pixel H05 monochrome basemap. Native LCC projection of H05.*

c_4 craters formed following the end of large-volume smooth plains emplacement. While I found no examples of crater materials in this degradation state that are embayed by volcanic smooth plains, the large craters Rachmaninoff and Rustaveli have small patches of smooth plains on their proximal ejecta that I interpret as

ponds of impact melt. Textured c_4 crater ejecta extends approximately one crater diameter beyond the rim of its respective crater regardless of the target material (Fig. 4.14). This suggests that all major plains formation in H05 had ceased by the time these craters formed.
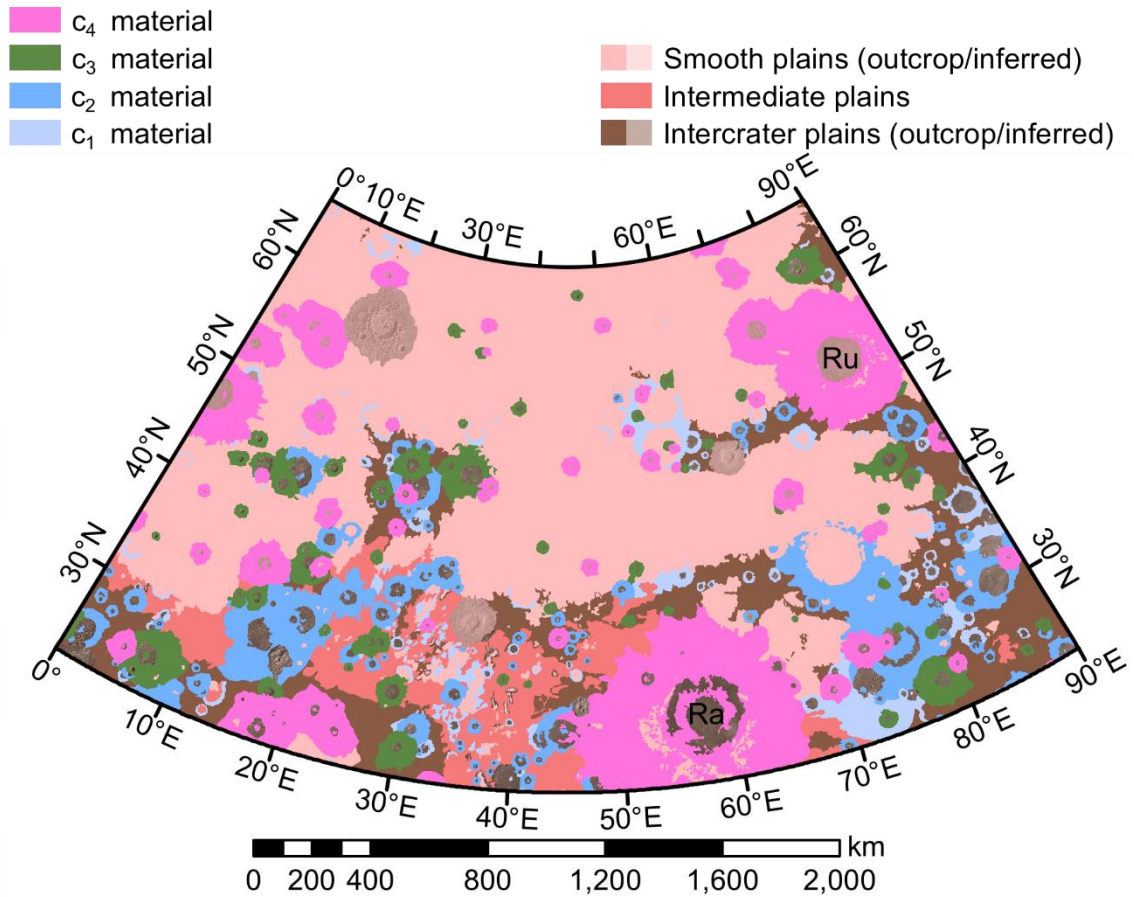
Fig. 4.14 Map showing the ejecta of all mapped impact craters in H05, except those with bright crater rays. c_4 *craters (heliotrope) have textured ejecta blankets that extend approximately one crater diameter beyond their crater rims irrespective of whether surrounding material is intercrater, intermediate, or smooth plains, which suggests that all these craters formed after the end large-scale volcanic plains formation. Rachmaninoff (Ra) and Rustaveli (Ru), c4 craters with prominent patches of superposing smooth plains, are labelled. Background is the ~166 m/pixel H05 monochrome basemap. Native LCC projection of H05.*

A small number of rayed c_5 craters are the most recent impact craters to have formed in H05 (Fig. 4.15). Rays from these craters always superpose c_4 craters where they are in contact, which suggests that all c_5 craters in H05 formed after c_4 craters. The putative explosive volcanic deposits Nathair and Neidr Faculae both

appear to superpose the distal ejecta of the c_4 crater Rachmaninoff, which would imply that at least the most recent explosive volcanic eruptions at these sites occurred after many c_4 craters formed.
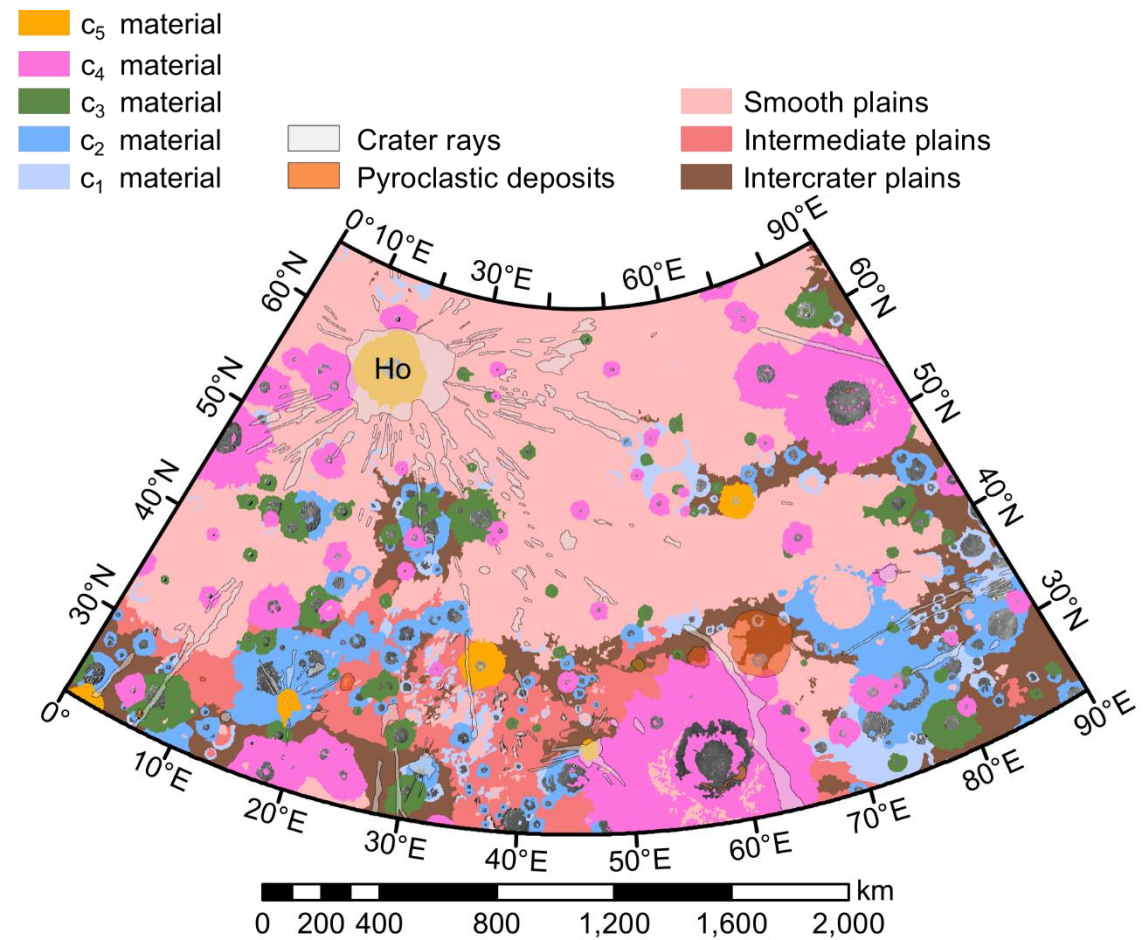
Fig. 4.15 Map showing the most recent geological features within H05. *c_5 craters have bright crater rays (semi-transparent white polygons). Hokusai (Ho) is surrounded by bright rays, which means that it appears paler than other c_5 craters in the map. Crater rays are not embayed by any plains materials, which confirms that rayed craters formed after the end of large-volume effusive eruptions in H05. Major pyroclastic deposits in H05 superpose c_4 crater materials, which suggest that the most recent faculae formed after the beginning of c_4 crater formation, or perhaps even more recently. Native LCC projection of H05.*

4.2.4 Correlation of main units

Based on the geological history outlined in the previous section, I have constructed a schematic chronostratigraphy for H05 (Fig. 4.16). Following the advice of GALLUZZI ET AL. (2016), the simple formation order of the crater materials is shown, rather than all possible superposition relationships (e.g. mapped c_4 material does superpose c_1 material in some places, but is not illustrated in Fig. 4.16).
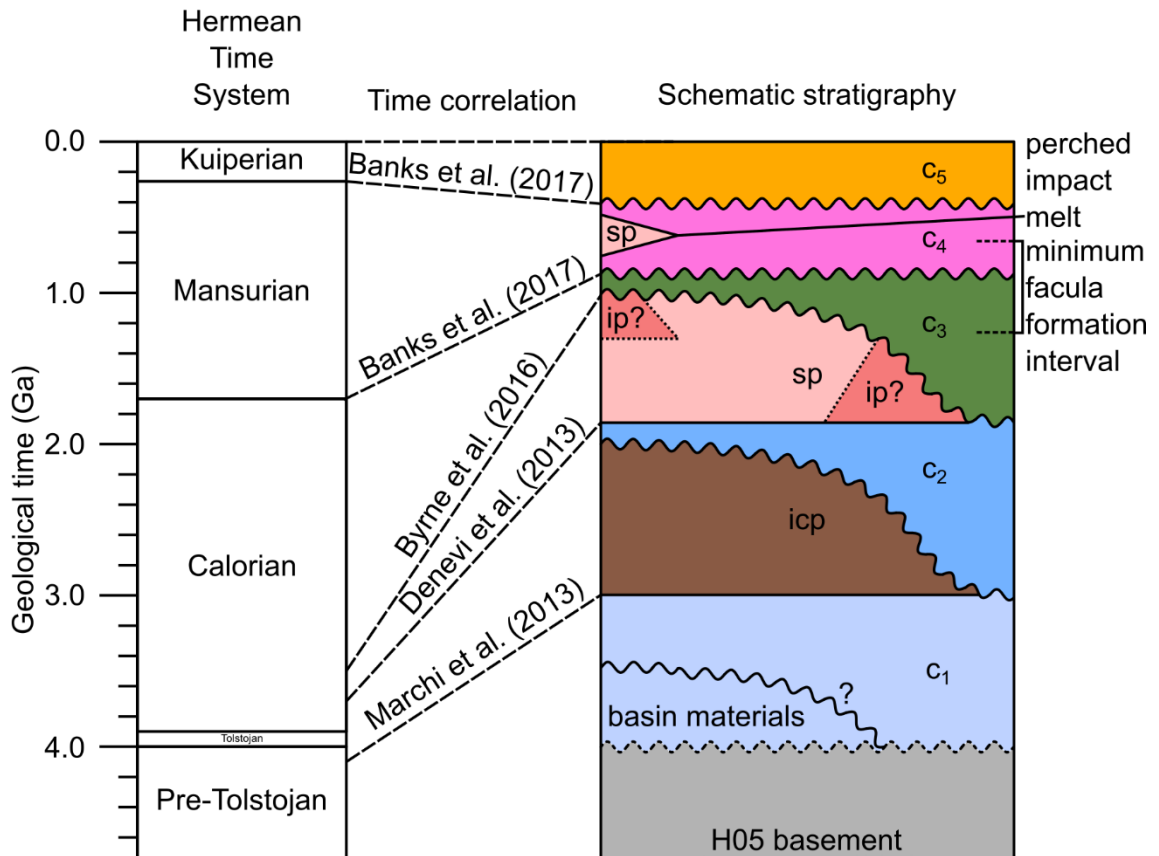
Fig. 4.16 Approximate chronostratigraphy of H05. *On the right, a schematic stratigraphy shows the relative order of formation of the major geological units based on the main superposition relationships observed in the map. Undulating boundaries between units indicate that the overlying unit has an erosional relationship with the underlying unit. Question marks indicate an ambiguity in the placement of a unit in the stratigraphy. Dotted lines represent inferred, but unobserved, unit relationships. On the left, a geological timescale shows the extents of the time systems of Mercury. The bases of the Tolstojan and Calorian shown here were determined by SPUDIS AND GUEST (1988). The bases of the Mansurian and Kuiperian shown here were determined by BANKS ET AL. (2017). Approximate bounding absolute model ages for the major geological units are taken from the literature and tied to the geological timescale. Based on a similar figure in GALLUZZI ET AL. (2016).*

4.2.4.1 Summary of H05 geological evolution

1. H05 basement of speculative origin formed.
2. Early c_1 craters and ancient impact basins formed, followed by the remainder of c_1 craters.
3. c_2 craters and the intercrater plains formed, however c_2 crater formation appears to have outlasted intercrater plains formation in H05.

4. c_3 craters and smooth plains predominantly of volcanic origin formed. Intermediate plains formed alongside smooth plains. c_3 crater formation appears to have outlasted smooth and intermediate plains formation. Some explosive volcanic vents and deposits may date from this time.

5. c_4 craters formed. Some smooth plains, of probable impact melt origin, superpose c_4 crater proximal ejecta. This is the oldest stratigraphic age that can be ascribed to explosive volcanic vents and deposits in H05.

6. c_5 craters formed. Explosive volcanic vents and deposits might also have formed at this time.

4.2.5 Tectonics

Here I describe the formation and development of the tectonic structures in H05 (Fig. 4.17) separately from the formation of the main map units.
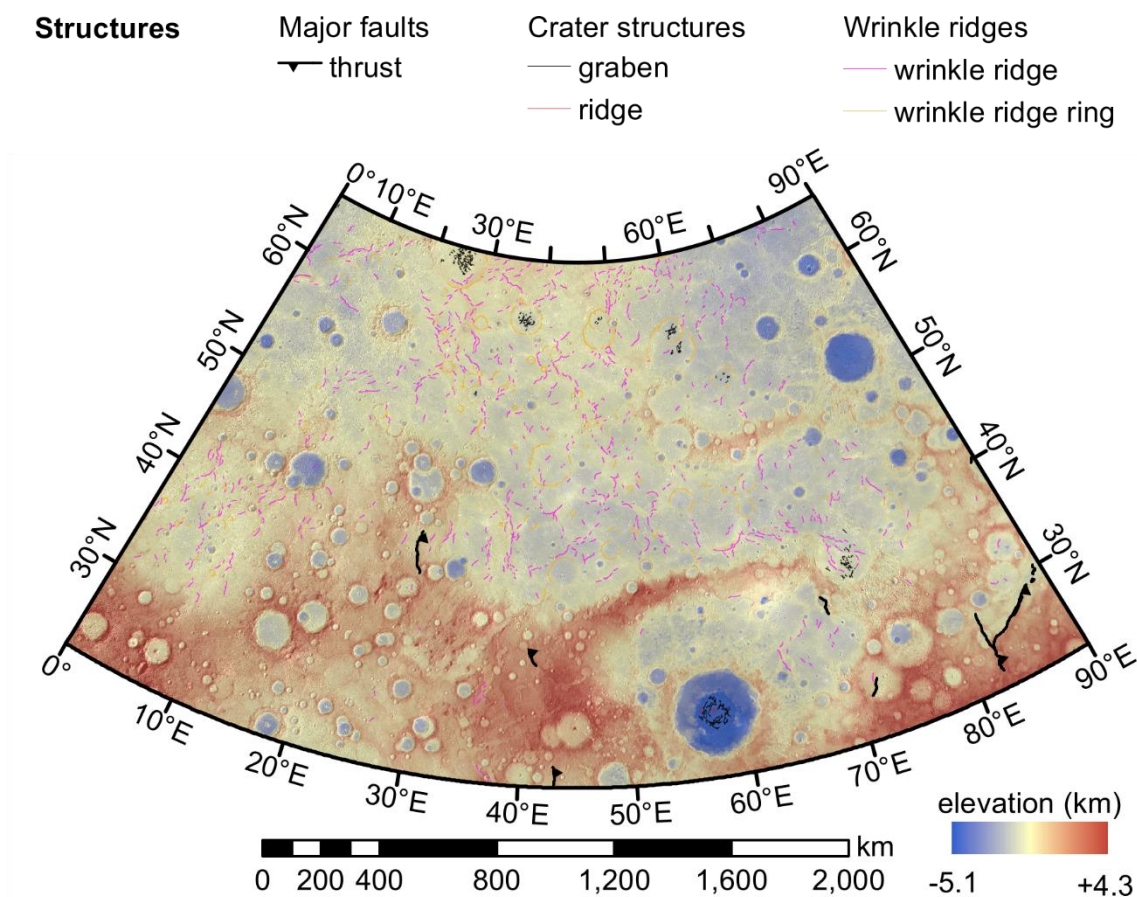
Fig. 4.17 Map of tectonic structures in H05 overlain on colourised topography.
~1:26M-scale. Background is the ~222 m/pixel stereo-DEM (STARK ET AL., 2017), overlain on the H05 ~166 m/pixel basemap. Native LCC projection of H05.

The most abundant tectonic features within H05 are the wrinkle ridges in Borealis Planitia (Fig. 4.18). Wrinkle ridges are thought to form in compressive stress regimes and appear to be the surface expressions of thrust faults *(BYRNE ET AL., 2014)*. As explained in Chapter 3, they come in two mapped forms: common wrinkle ridges and wrinkle ridge rings. Both wrinkle ridge types have indistinguishable appearances, except that wrinkle ridge rings form closed or nearly closed loops that appear to overlie impact craters rims that have been buried by the smooth plains hosting the wrinkle ridges. This observation argues that aside from the control on the orientations of the wrinkle ridge rings by buried impact craters, both common and ring wrinkle ridges are formed as a result of folding in response to reverse faulting at shallow depth with very similar fault parameters. The orientations of common wrinkle ridges are not obviously controlled by the margins of Borealis Planitia, which distinguishes them from the wrinkle ridges elsewhere on Mercury. The wrinkle ridges in the Caloris *(MURCHIE ET AL., 2008)* and Rembrandt *(WATTERS ET AL., 2009)* basins are obviously radial or concentric to the basin rims, similar to the wrinkle ridges in the lunar maria *(SOLOMON AND HEAD, 1980)*. Since wrinkle ridge orientations in H05 do not appear to be controlled by the margins of the lavas that host them, then the compression that generated them probably had some influence stronger than that of volcanic loading, such as global contraction *(BYRNE ET AL., 2014)*. A recent study of the wrinkle ridges throughout the whole of Borealis Planitia suggests that structures are predominantly oriented east–west north of 70°N and north–south south of 50°N *(CRANE AND KLIMCZAK, 2019)*. Their study utilised the MLA DEM *(ZUBER ET AL., 2012)* to map structures, which mitigates against illumination bias when mapping linear features *(FEGAN ET AL., 2016)*. Therefore the latitude dependent orientation of wrinkle ridges in Borealis Planitia seems real, which means the wrinkle ridges cannot have formed solely in response to global contraction, which would yield randomly oriented structures *(STROM ET AL., 1975)*. Instead, some wrinkle ridges may be exploiting and reactivating buried structures related to the tidal despinning of the planet *(MELOSH, 1977; CRANE AND KLIMCZAK, 2019)*.
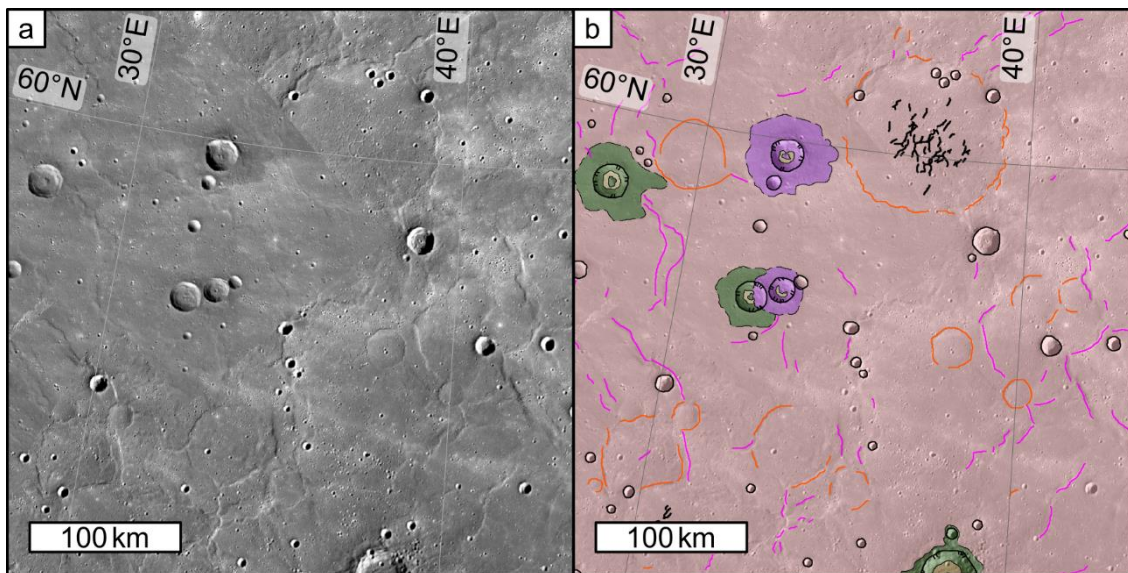
Fig. 4.18 Wrinkle ridges in H05. *(a) Smooth plains with abundant wrinkle ridges. ~166 m/pixel monochrome mosaic. Note how wrinkle ridge rings of different diameters are closely colocated. (b) Same view as (a). Transparent geological units are coloured as shown in the legend of Fig. 4.2. Common wrinkle ridges (magenta lines), wrinkle ridge rings (orange lines), and grabens (black lines) are shown. Background is the ~166 m/pixel monochrome mosaic. Both panels are in the native LCC projection of the H05 map.*

Since wrinkle ridge rings form due to thrust faults that have propagated along the structural discontinuity between crater walls and their infills, this geometry suggests that wrinkle ridge rings lie above shallowly rooted faults. Numerical dislocation models, where fault parameters are derived from measured fault-induced topography, suggest that wrinkle ridge faults penetrate to a depth of ~25 km *(PETERSON ET AL., 2017)*, but this depth is far below the base of Borealis Planitia, where the wrinkle ridges are found, which is 1–3 km thick *(OSTRACH ET AL., 2015)*. These fault penetration depths seem inconsistent with the geometry of wrinkle ridge rings as deep-penetrating faults arranged in a ring could intersect at depth. Geological studies of fault-bounded landforms in Borealis Planitia suggest that wrinkle ridge faults are shallowly rooted *(CRANE AND KLIMCZAK, 2019)*. This is more consistent with my observation that common wrinkle ridges closely resemble wrinkle ridge rings. Therefore, I tentatively suggest that all wrinkle ridge landforms are probably shallowly rooted to a basal décollement, probably at the interface between the volcanic unit in which the wrinkle ridges are found and the underlying basement (Fig. 4.19). This basement was probably modified by impact cratering, such that its regolith could act as the decoupling layer between the volcanic plains

and the basement, forming the décollement. This is the same mechanism by which basin-edge lobate scarps are proposed to have formed *(FEGAN ET AL., 2017).*
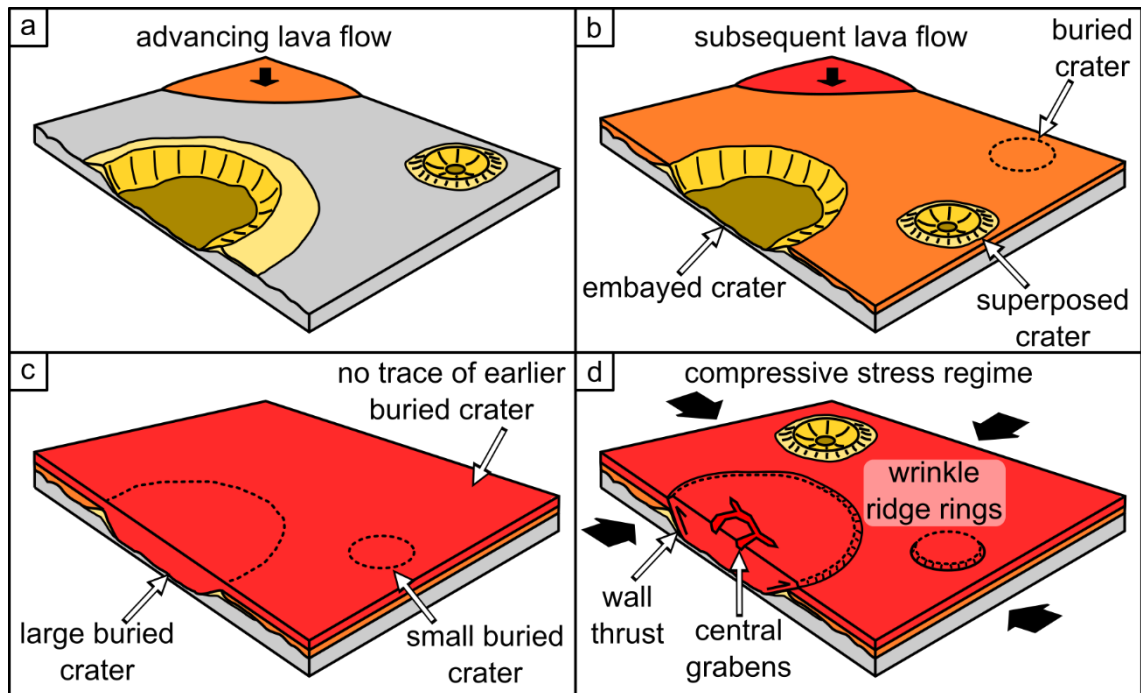
Fig. 4.19 Cartoon showing how wrinkle ridge rings formed. *(a) In this model, a lava flow field (orange) advanced over a substantially older, regolith-covered plains unit (grey) that is superposed by impact craters of different sizes (yellow). (b) The first lava flow field buried smaller craters in its path, but only embayed larger craters. Smaller craters may have topographic signature as a depression in the smooth plains, if not a morphological expression, due to volcanic sagging. Later, new impact craters formed. A second lava flow field advanced over the first. (c) The second lava flow completely infilled topographic depressions from small impact craters buried by the first lava flow field. Smaller craters that superposed the first lava flow are now buried by the second lava flow. Larger craters that were superposed on the original plains were buried by the second lava flow field. (d) Large-volume effusions ceased due to global contraction (BYRNE ET AL., 2016). The weak regolith layer between the basement plains and the lavas acted as a decoupling layer, focussing fault development along the boundary between walls of buried craters and their infilling lavas. These faults thrusted the lava units up and out of their host craters, to form outwardly verging folds observable today as wrinkle-ridge rings. Circumferential wrinkle ridges shielded the interiors of large buried craters from the compressive stress regime, allowing networks of grabens to form within some examples (FREED ET AL., 2012). Multiple lava flow events are required for wrinkle ridge rings of different sizes to exist alongside each other within the smooth plains (OSTRACH ET AL., 2015) as shown here and observed in my map of H05.*

Lobate scarps, which are the most important tectonic features on Mercury, are not abundant in H05. This appears to be due to the widespread smooth plains in H05 compared to most other quadrangles. Lobate scarps occur more commonly in the intercrater plains *(Strom et al., 1975)*. The most prominent lobate scarp in H05 is Unity Rupes, in the southeast of the quadrangle (Fig. 4.20). This lobate scarp was unnamed when I started my mapping, but since it was the largest tectonic feature in H05, I applied to the IAU for it to be named. Lobate scarps on Mercury are named after ships used during expeditions of scientific discovery. The *Unity* was an East Indiaman that conveyed Edmond Halley to St Helena where he observed a transit of Mercury in 1677 *(Cook, 1998)*, making 'Unity' a fitting name for a lobate scarp on the planet. Unity Rupes was officially named on 31st January 2016.

Unity Rupes has been interpreted as a right-lateral ramp at the northernmost extent of a system of lobate scarps extending ~2,000 km south of it containing Blossom Rupes *(Massironi et al., 2015)*. The southernmost extent of the system has a corresponding left-lateral ramp. This system indicates broad east-to-west movement of Mercury's crust by thrust faulting. The importance of strike slip tectonics at Unity Rupes separates it from most other lobate scarps on Mercury, which appear to be chiefly compressional. Beagle Rupes is an important example of a well-studied lobate scarp on Mercury that exhibits transpressional lateral ramps similar to Unity Rupes. It served as a useful comparison when I attempted to determine the sequence of faulting that formed the Unity Rupes system.
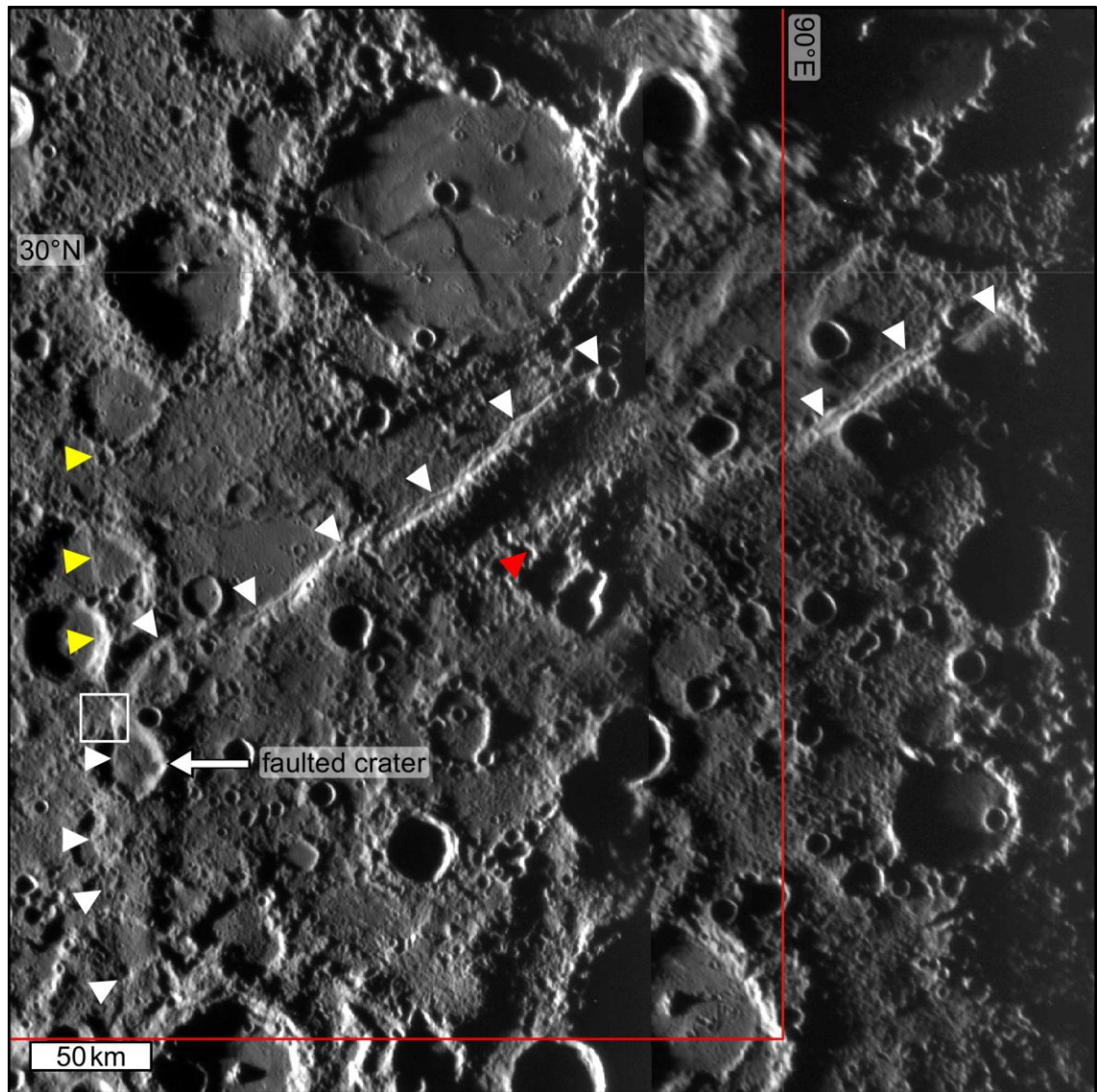
Fig. 4.20 Unity Rupes. *White triangles indicate the main Unity Rupes fault surface break. Yellow triangles indicate a small fault break that intersects with the prominent bend in Unity Rupes and trends northward. A red triangle indicates a linear rise similar to that associated with lobate scarps that does not have an obvious fault break. A crater that is cross cut by Unity Rupes, and used to estimate the movement on the fault, is indicated with a white arrow. The white box indicates the extent of Fig. 4.21. ~500 m/pixel M1M2M3MI0 mosaic. Red line shows the extent of H05. Mercator projection centred on 85°E, 27°N.*

I have made one key observation of Unity Rupes that narrows down the possible sequences of faulting that led to the present landscape. Upon close inspection of the junction between the main Unity Rupes fault break and the smaller, northward spur, it appears that the northward spur has been cross-cut by the main fault break, and so the spur is older than the rest of Unity Rupes (Fig. 4.21). This means that originally the Unity Rupes fault was generally north–south trending, until the bend

developed, at which point movement on the northward spur ceased. The more recent fault developed in the hinterland of the northward spur and appears to have been active for longer as it has attained much greater relief. Thrust propagation into the hinterland is sometimes referred to as 'out-of-sequence' thrusting since on Earth propagation of thrusts into the foreland has been documented more widely (*MORLEY, 1988*).
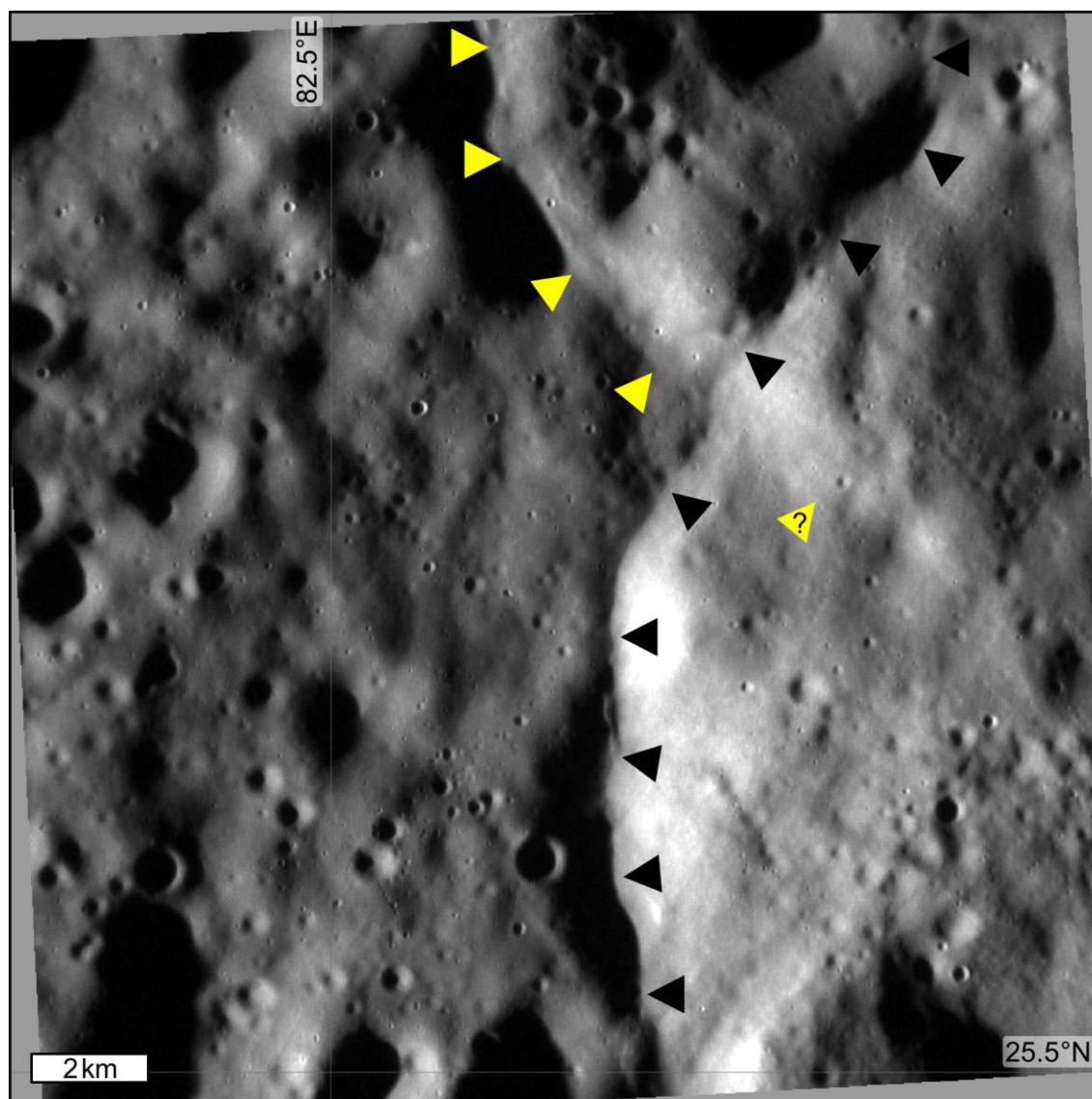
Fig. 4.21 Interacting faults at Unity Rupes. *The main continuous Unity Rupes fault break (black triangles) cross-cuts the apparently earlier northward spur (yellow triangles). A possible hint of the abandoned northward spur fault break and uplift behind the main Unity Rupes fault (question mark). Sinusoidal projection centred on 82.6°E, 25.7°N. MDIS NAC frame EN1033975119M. ~18 m/pixel.*

Out-of-sequence thrusting has been reported at Beagle Rupes on Mercury (*ROTHERY AND MASSIRONI, 2010*), where a fault geometry was described very similar

to that observed at Unity Rupes (Fig. 4.22). The faults labelled 2 and 3 in Fig. 4.22 form a junction that resembles the junction at Unity Rupes. Fault 3 cross-cuts fault 2, and so it is the younger of the two. Both these faults are interpreted to be part of the Beagle Rupes system and they lie in its hinterland. The fault geometry at Beagle Rupes led *ROTHERY AND MASSIRONI (2010)* to suggest the whole fault system bottoms out into a regional décollement at a depth of ~30 km. It is possible that the Unity Rupes system also links into a décollement. The nature of this décollement, and whether or not it could be the same as the Beagle Rupes one, can only be speculated upon at this stage. Unity Rupes and Beagle Rupes are ~1,500 km apart. Given the higher relief of lobate scarps (~2 km), compared with wrinkle ridges (~400 m), it seems likely that the décollements for both Beagle Rupes and Unity Rupes lie at an interface at a greater depth than the base of the volcanic plains that host the wrinkle ridges. A deeper interface is required to allow faults with greater down-dip widths, which build higher topography, to propagate. Therefore, the décollement could be the base of the crust, the brittle-ductile transition within the lithosphere *(PACHECO ET AL., 1992)*, or a crustal discontinuity such as the buried floor of an ancient basin *(WATTERS ET AL., 2004)*. The candidate ancient basin 'b44' (102.6°E, 10.3°S, diameter ~450 km; *FASSETT ET AL, 2012*) may have provided a decollement for Beagle Rupes, but no ancient basins are currently suggested to lie underneath or close to Unity Rupes.

There are other similarities between Beagle Rupes and Unity Rupes. At the northernmost extent of Beagle Rupes there are fault segments detached from, but parallel to, the main fault break (I have marked one at the top-centre of Fig. 4.22). Unity Rupes has a very similar arrangement, although it has a linear topographic rise between its main break and the detached fault segment. Since this linear rise has no obvious surface break it might be pre-existing topography unrelated to Unity Rupes or it could be due to folding directly due to the compression responsible for forming the Unity Rupes system (see *CRANE AND KLIMCZAK, 2019*) related to hinterland fault propagation.
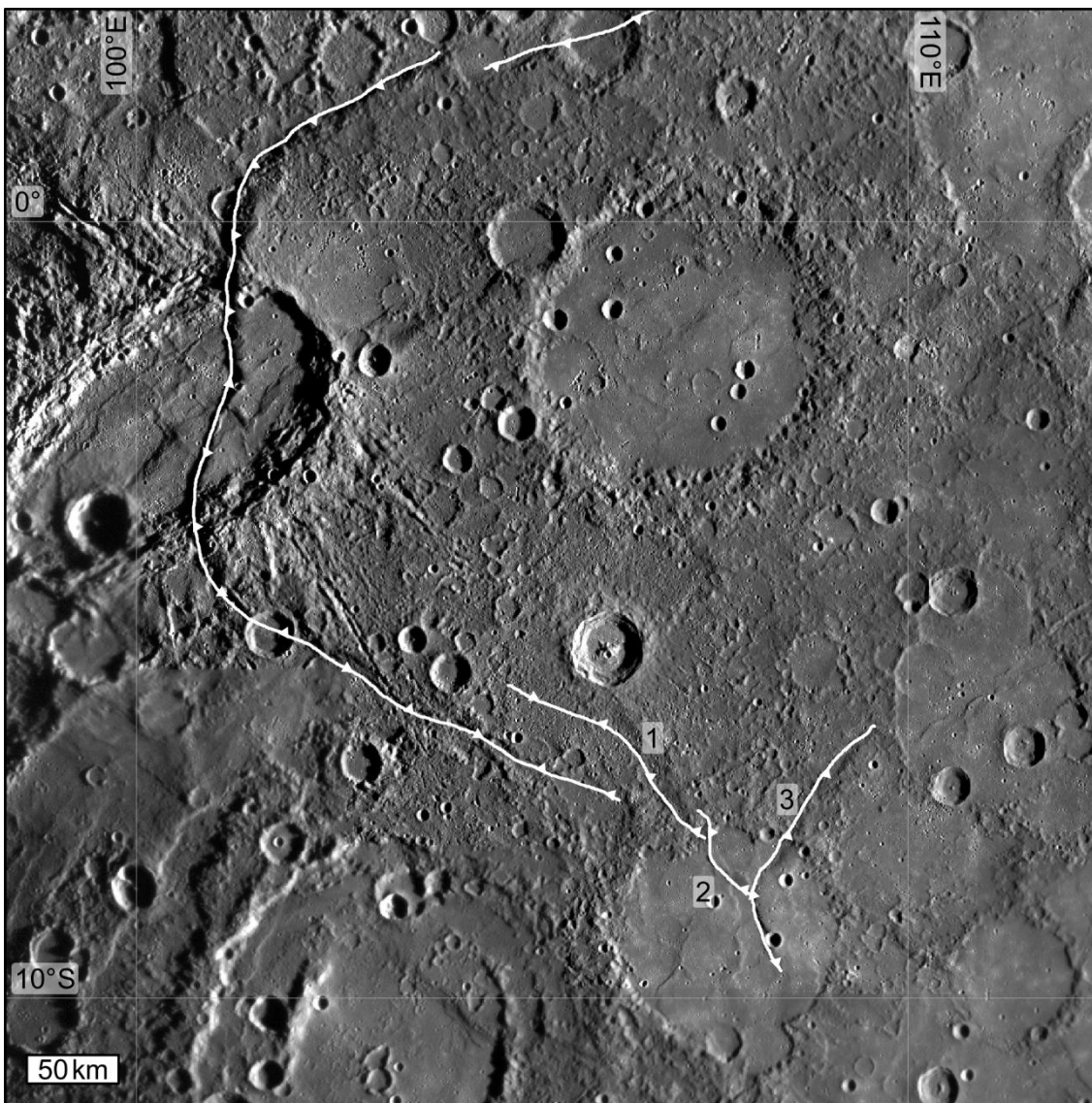
Fig. 4.22 Beagle Rupes. *This lobate scarp has many fault break geometries similar to those that I have observed at Unity Rupes. The north–south trending main fault break of Beagle Rupes becomes a right-lateral ramp at fault's northernmost extent, which resembles Unity Rupes closely. The small fault segment at the top of the figure sits behind a continuation of the main thrust front of Beagle Rupes. A similar arrangement appears at Unity Rupes. The faults marked 1, 2, and 3 were interpreted by ROTHERY AND MASSIRONI (2010) to be part of the Beagle Rupes fault system and to have formed after the main fault break in the order that they are numbered in the figure, based on their cross-cutting relationships. The junction between fault breaks 2 and 3 is very similar to the fault junction at Unity Rupes (Fig. 4.21). Also note the elliptical crater Sveinsdóttir at the left of this figure. This crater cannot be used to investigate the kinematics of Beagle Rupes by circle-fitting because the rim did not originally form as a circle (GALLUZZI ET AL., 2015). ~500 m/pixel M1M2M3M10 mosaic. Mercator projection centred on 108°E, 8°S. Simplified from ROTHERY AND MASSIRONI (2010) (their Fig. 1) with kind permission from the authors.*

I estimated the slip vector of Unity Rupes by following the method of GALLUZZI ET AL. (2015). Impact craters that have been deformed by faults can be used to estimate the direction and amount of movement of faults on planetary bodies (GOLOMBEK ET AL., 1996; PAPPALARDO AND COLLINS, 2005). Circles are fitted to the walls of craters cross-cut by a fault (Fig. 4.23). The vector joining the centres of the circle fitted to the crater wall on the footwall side of the fault and the circle fitted to crater wall on the hangingwall side of the fault indicates the slip trend and the horizontal component of movement on the fault (GALLUZZI ET AL., 2015). With additional elevation data, the vertical component of movement can be determined, which would allow the reconstruction of the fault plane (GALLUZZI ET AL., 2015). This is achieved by comparing the elevation of the crater rim or floor on either side of the fault. The circle-fitting method relies on two assumptions: that the faulted craters were circular when they originally formed; and that crater deformation is entirely due to fault movement. Most fresh impact crater rims on Mercury are well approximated by circles (HERRICK ET AL., 2012), and impact craters begin to exhibit ellipticity only when the impact angle is ~10° from the horizontal or less (BOTTKE ET AL., 2000). The second assumption is more difficult to justify. Faulting of craters may conceivably deform them in more ways than by sliding on the fault. For example, faulting may cause collapse of the crater walls. Furthermore, impact craters on Mercury are subject to degradation by regolith gardening and bombardment, which would cause deformation unrelated to fault movement. Nevertheless, GALLUZZI ET AL. (2015) obtained fault plane solutions of 15 lobate scarps on Mercury using this method.

My applications of the GALLUZZI ET AL. (2015) method to Unity Rupes in H05 are illustrated in Fig. 4.23 and the results are recorded in Table 4.1. The faulted crater lies on the north–south trending part of Unity Rupes south of its bend and the junction with the northward spur (Fig. 4.20). As can be seen in Fig. 4.23, the crater is very degraded (I classified it as c_2). The highly degraded state of this crater is not ideal for characterising the activity of Unity Rupes. The degradation means that no meaningful estimate of the vertical component of Unity Rupes' movement can be made, since degradation acts to decrease the original rim-to-floor depth of the crater by eroding the walls and infilling the floor (BAKER AND HEAD, 2013). Crater

wall degradation may result in outward retreat of the crater rim. This would have the effect of increasing the diameters of the fitted circles, but it should not affect the apparent centres of the craters. Thus, the magnitude and direction of horizontal transport determined by the method should remain valid. Furthermore, crater rim retreat has been shown to be insignificant on Mercury *(WOOD ET AL., 1977)*. Therefore, I applied the method to Unity Rupes in order to investigate the contention of *MASSIRONI ET AL. (2015)* that much of it serves as a lateral ramp.
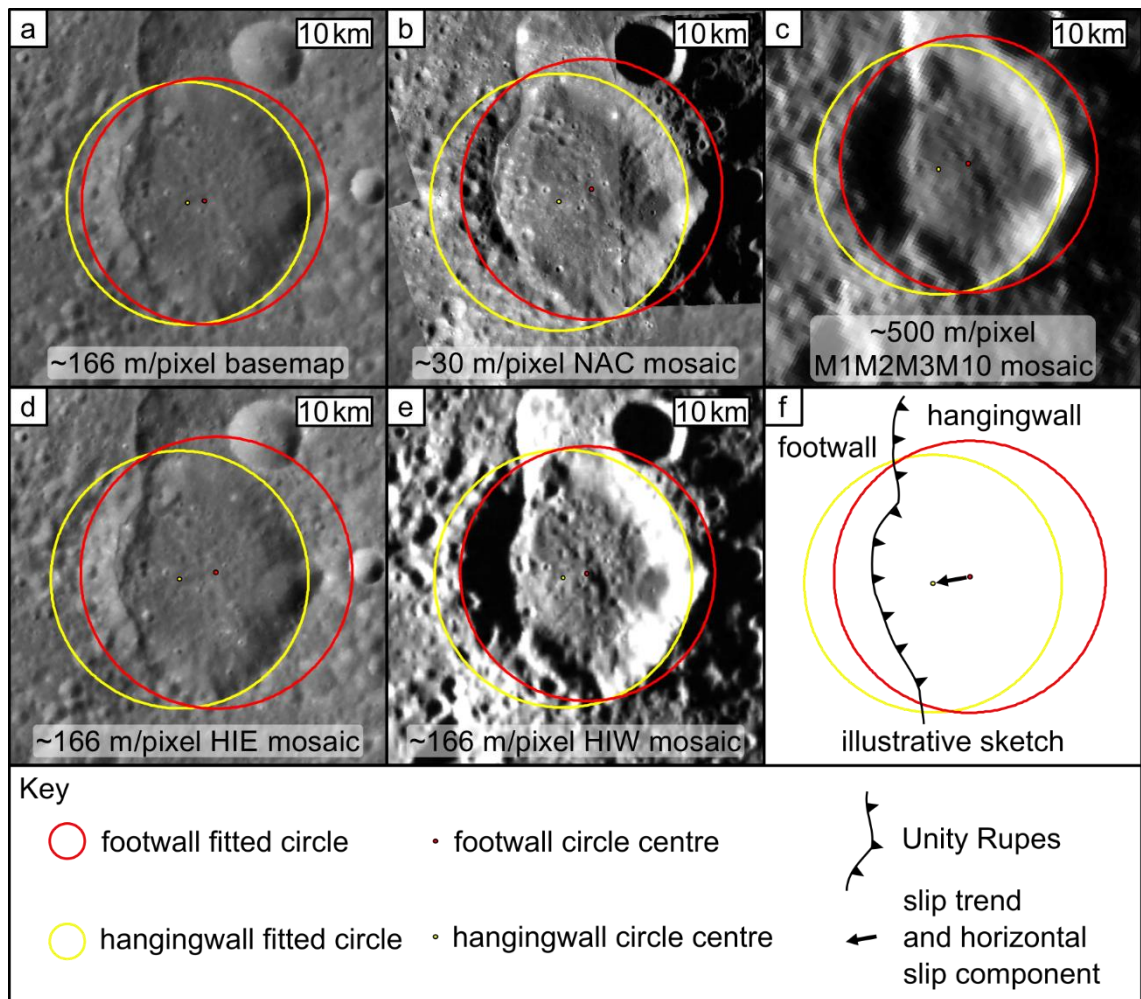
Fig. 4.23 Circle fits to impact crater faulted by Unity Rupes. *(a) ~166 m/pixel BDR basemap circle fit. (b) MDIS NAC mosaic circle fit. NAC frames EN0252092730M (~26 m/pixel), EN0252093741M (~26 m/pixel), and EN0254596575M (~38 m/pixel). (c) ~500 m/pixel M1M2M3M10 mosaic circle fit. (d) ~166 m/pixel high-incidence angle mosaic with eastern illumination circle fit. (e) ~166 m/pixel high-incidence angle mosaic with western illumination circle fit. (f) Illustration of the circle fitting method. Circles are fitted to the impact crater rims on both the hangingwall and footwall sides of Unity Rupes. The bearing from the centre of the footwall circle to the centre of the hangingwall circle gives the direction of transport, or 'slip trend'. The horizontal distance between the centres of the two circles is the amount of horizontal movement on the fault (Δx). Some items in the key are used only in the illustrative sketch in part (f) to reduce visual clutter in the other parts. Parts (a–e) show the same view of the faulted crater indicated in Fig. 4.20. All parts are stereographic projections, which preserve local angles, centred on 85°E, 27°N.*

Fig. 4.23 ref.	Footwall diameter (km)	Hangingwall diameter (km)	Slip trend (°)	Δx (km)
a	32.5	32.1	259	2.3
b	34.5	34.1	247	4.7
c	34.0	33.0	255	4.0
d	36.0	34.0	259	5.0
e	33.7	34.1	257	3.3
mean	**34.1 ± .1.3**	**33.5 ± 0.9**	**255 ± 5**	**3.9 ± 1.1**

Table 4.1 Crater circle fitting measurements for Unity Rupes.

If the slip trend I measured using the circle fitting method (255 ± 5°) is correct, then, at the location of the faulted crater, Unity Rupes exhibits nearly pure thrusting, since the fault break and the slip trend are approximately perpendicular (Fig. 4.23f). If this transport direction is uniform throughout the Unity Rupes system, then, due to the bend in the fault, most of the surface break is sub-parallel to the transport direction. This is consistent with Unity Rupes forming a right-lateral ramp as suggested by MASSIRONI ET AL. (2015).

4.3 Regions of interest

Producing the reginal map of H05 drew my attention to some geologically complex regions of special interest. I address the most important localities in the following subsections.

4.3.1 Rachmaninoff

The Rachmaninoff impact basin (Fig. 4.24) was introduced in Chapter 3 as a feature of interest that led me to select H05 as my mapping quadrangle. Here, I describe the formation and geological evolution of the basin.
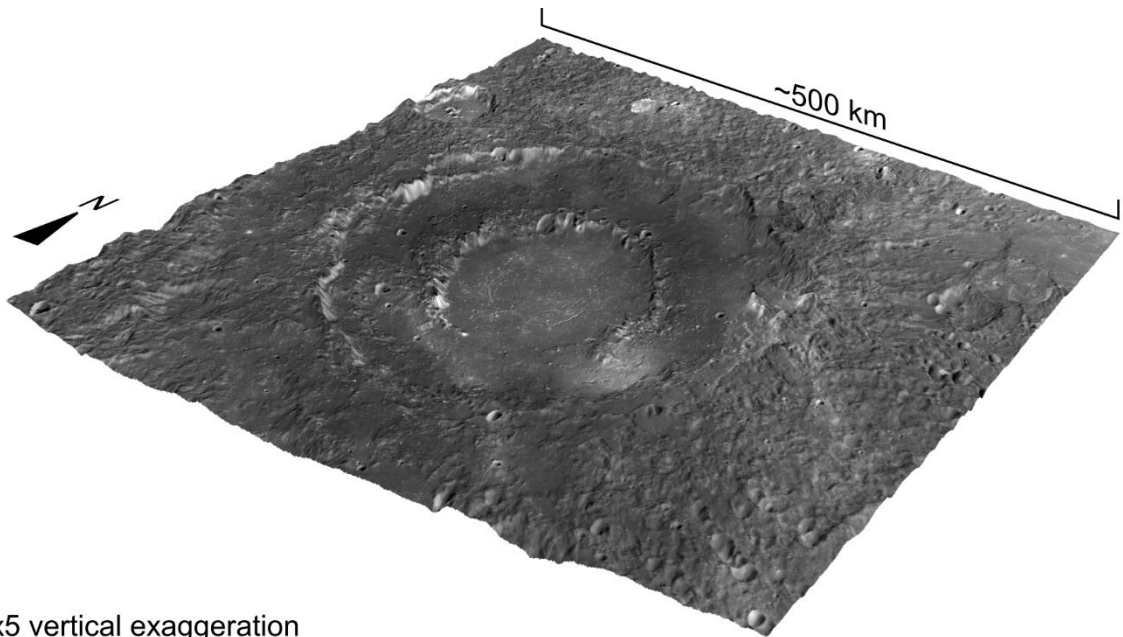
x5 vertical exaggeration

Fig. 4.24 Perspective view of Rachmaninoff crater. *This view was created in ArcScene using the ~166 m/pixel basemap overlain on the ~222 m/pixel stereo DEM of H05 by STARK ET AL. (2017). Original image projection was the native LCC projection of H05.*

I have designated Rachmaninoff as a c_4 crater, based on its crisp rim and widespread textured ejecta blanket that dominates the geology of southeast H05. This designation agrees with that of *KINCZYK ET AL. (2016)* on the global geological map of Mercury *(PROCKTER ET AL., 2016; KINCZYK ET AL., 2018B)*. c_4 craters formed during the Mansurian *(KINCZYK ET AL., 2016; BANKS ET AL., 2017)*, long after the end of large-volume effusive eruptions on Mercury *(BYRNE ET AL., 2016)*, and the superposition of distal Rachmaninoff ejecta on smooth plains northeast of the crater supports this interpretation (Fig. 4.24).

The floor of Rachmaninoff has striking colour variations, with a typically rough and low-albedo annulus between the crater wall and the peak-ring, and a smoother and higher albedo region contained within the peak-ring, except in the south where the peak-ring is absent. *PROCKTER ET AL. (2010)* were the first to suggest that the smooth plains that are mostly confined within the peak-ring, and are much redder than the blue, low-reflectance material elsewhere on the basin floor, formed due to post-impact volcanism. This interpretation is supported by crater size-frequency distribution studies, which suggest that the red plains are younger than the blue basin floor and Rachmaninoff's ejecta blanket *(PROCKTER ET AL., 2010; CHAPMAN ET*

AL., 2012). The plains within the peak-ring contain a network of grabens that *BLAIR ET AL. (2013)* attribute to the thermal contraction of a thick volcanic unit.
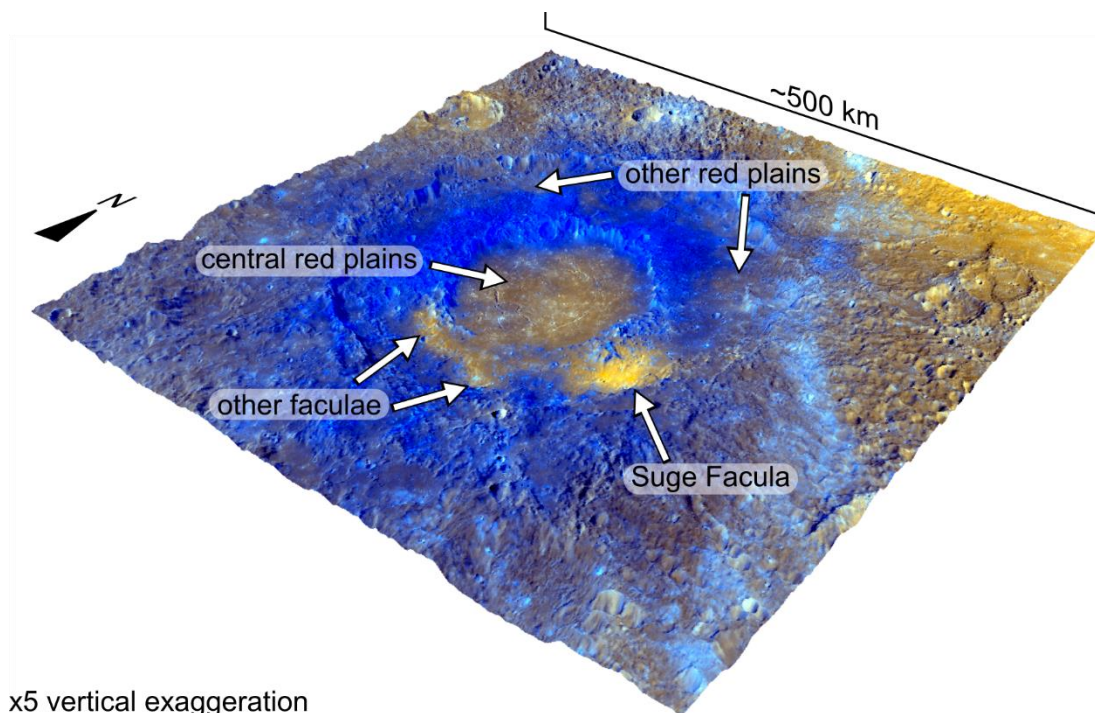
Fig. 4.25 Perspective view of Rachmaninoff in enhanced colour. Important colour variations interpreted in this section are labelled. ~665 m/pixel.

Where the high-albedo red plains lie outside the peak-ring in the south, they terminate in particularly high-albedo spots with diffuse boundaries. Suge Facula is one of these spots. Unlike most other faculae on Mercury, Suge Facula and the others within Rachmaninoff do not contain rimless depressions that are interpreted as the explosive volcanic vents responsible for depositing pyroclasts to form the high albedo region (a facula). This suggests that faculae can be created by means other than deep-seated, centralised explosive volcanic eruptions. Rachmaninoff's crater floor within Suge Facula has a somewhat pitted appearance, leading *THOMAS ET AL. (2014A)* to classify it as 'pitted ground', rather than a vent deposit. *THOMAS ET AL. (2014B)* suggested that pitted ground formed due to volatile loss from the substrate disturbing an overlying cooling lava; an interpretation that remains generally accepted *(JOZWIAK ET AL., 2018).*

Due to the complex geological history of this basin, I have made several reconstructions of Rachmaninoff at different stages of its development based on my own observations (Fig. 4.26–Fig. 4.28 and Fig. 4.31).

Legend

Linework

~ contact

~ crater rim

~ peak-ring crest

Rachmaninoff units

■ exterior impact melt

□ impact ejecta

▨ crater wall material

■ peak-ring material

■■ interior impact melt (outcrop/inferred)

■■ rough crater floor (outcrop/inferred)

Other units

■ smooth volcanic plains
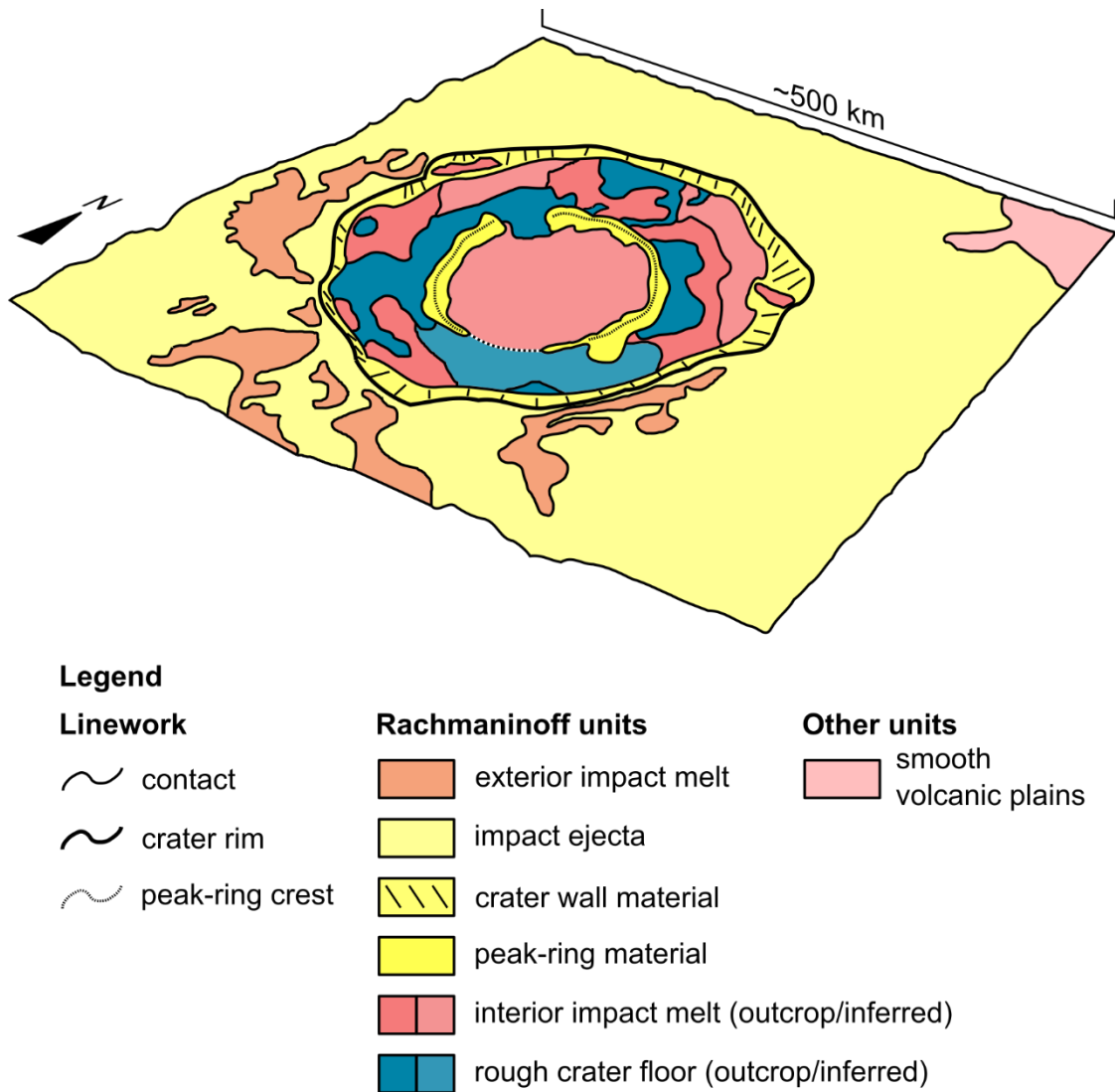
Fig. 4.26 Illustration of the geology of Rachmaninoff immediately following its formation. Assuming the red plains in the crater are volcanic in origin, I show my inferences of the original extent of rough crater floor and impact melt. Drawn from the perspective view shown in Fig. 4.24.

Rachmaninoff probably formed after the end of large-volume volcanic eruptions on Mercury due to global contraction *(BYRNE ET AL., 2016)*, since it is a c_4 crater with ejecta superposing nearby smooth plains, yet the presence of volcanic plains within the crater suggests that the impact took place when subsurface magma storage was still occurring. The interior of Rachmaninoff contains the lowest surface elevation on Mercury *(BECKER ET AL., 2016; STARK ET AL., 2017)* and the underlying crust is also the thinnest on the planet *(SORI, 2018)*. Therefore, it is probable that material excavated by Rachmaninoff originally came from the lowermost crust or uppermost mantle. Rough Rachmaninoff floor materials are made of low-

reflectance material (LRM), which is believed to be dark due to its graphite content (*PEPLOWSKI ET AL., 2016*). Since Rachmaninoff has exhumed material from deep within the stratigraphy of H05 it appears consistent that this basal material should be the carbon-rich primary flotation crust hypothesised by *VANDER KAADEN AND MCCUBBIN (2015)*. The fact that other impacts in H05 do not appear to have exhumed LRM could be due to the primary graphite crust being laterally discontinuous or buried too deeply away from the thin crust at Rachmaninoff. The carbon on and beneath the crater floor probably played a role as a volatile substance in the volcanic evolution of the crater that followed its formation (*WEIDER ET AL., 2016*).

After the crater's initial formation, several geologically significant effects occurred. The impact removed overburden, promoted uplift, temporarily reset the pre-existing stress regime, propagated fractures, and deposited heat, all of which could have facilitated the generation and extraction of magma from the subsurface (*BYRNE ET AL., 2016*). These effects would have been most strongly felt in the centre of the crater, where the volcanic plains appear to be thickest, based on their colour (thinner volcanic plains would have their red colour signature more readily subdued by mixing with the substrate by impact gardening). Modelling suggests that in order for thermal contraction of a cooling lava to produce the pattern of graben seen in Rachmaninoff, the plains must be ~1 km thick in the centre (*BLAIR ET AL., 2013*). The less pronounced red colour of the northwestern and northeastern plains could be because they have a thickness substantially less than 1 km. If these plains are thinner, this might reflect a general shift from eruption centres distributed throughout the crater in the geological time immediately following the impact, to more eruptions concentrated in the centre of the crater. This would make the outer plains older than the inner plains. Alternatively, the outer plains might have formed after the central plains became critically thick such that magma could no longer ascend to the surface there, and low-volume terminal effusions may have been redirected to outside the peak-ring. Neither hypothesis for the outer plains can be rejected, since the inner and outer plains are not in contact at any location for their stratigraphic relationship to be assessed. Based on Rachmaninoff postdating the smooth plains, the crater likely formed <3.5 Ga. Initial model age estimates of the central red plains in Rachmaninoff suggested

they formed ~1 Ga *(PROCKTER ET AL., 2010)*, although this very young age was since revised to an older age, albeit one that still resolvably postdates the impact (~2 Ga; *CHAPMAN ET AL., 2012*).

Legend

Linework

~ contact

~ crater rim

~ peak-ring crest

Rachmaninoff units

exterior impact melt

impact ejecta

\\\ crater wall material

peak-ring material

interior impact melt

rough crater floor

thin volcanic plains

thick volcanic plains

Other units

smooth volcanic plains

undivided subsurface
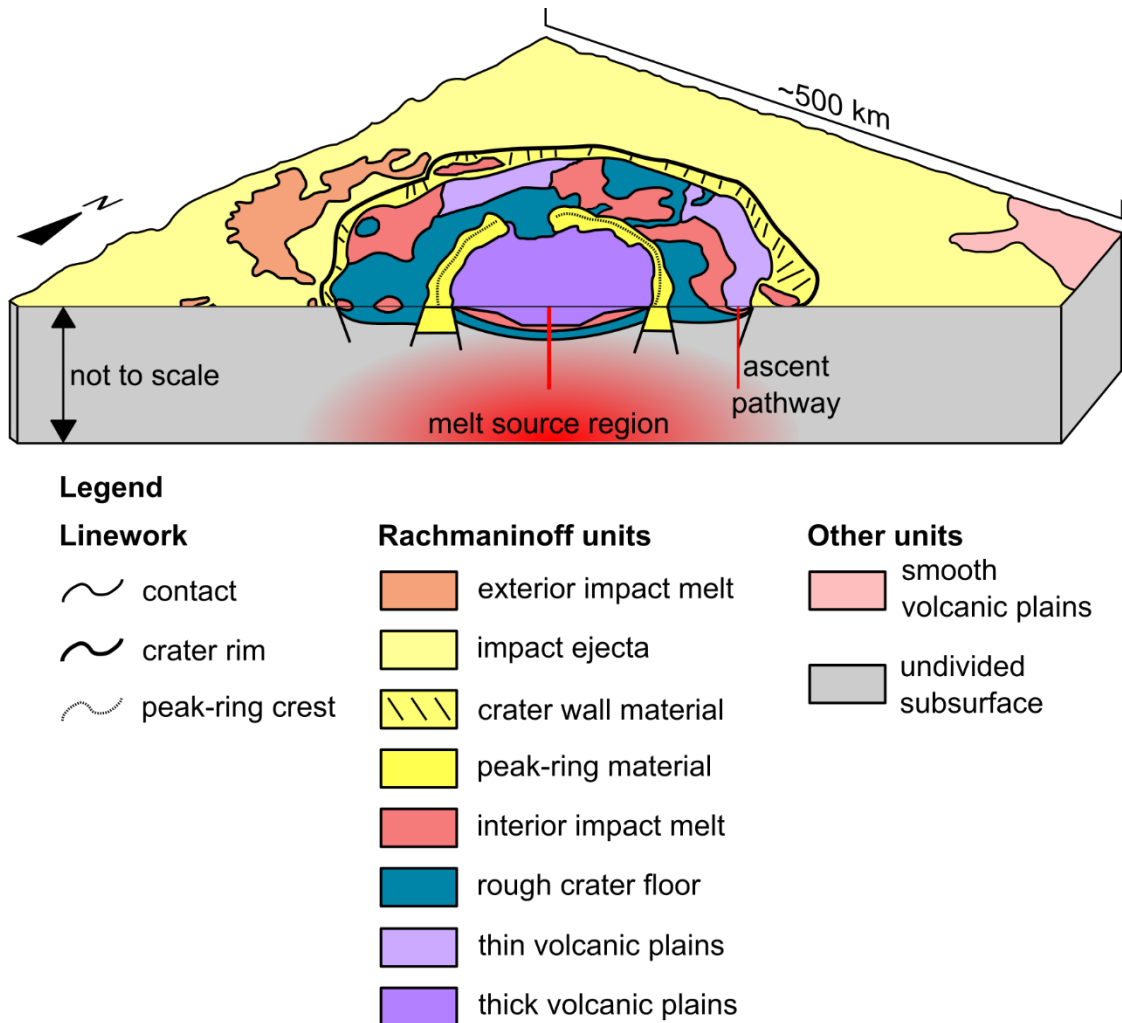
Fig. 4.27 Illustration showing the post-impact volcanism in Rachmaninoff. At least three eruption centres were active during the first stage of post-impact volcanism in Rachmaninoff: one in the northwest, one in the northeast (possible ascent path illustrated) and one in the centre (possible ascent path illustrated). The northwestern and northeastern volcanic plains are interpreted as thinner deposits than the central volcanic plains based on their less pronounced red colour. The basal topography of the central plains is based on that suggested by BLAIR ET AL. (2013).

Suge Facula and the other faculae within Rachmaninoff appear to have formed at the same time as the central lavas in Rachmaninoff, or later (Fig. 4.28). It is interesting that Suge Facula lies at the boundary between smooth volcanic plains in Rachmaninoff and other impact-related units. If Suge Facula formed because

lavas flowed over a volatile–bearing substrate (Fig. 4.29), as suggested by *Thomas et al. (2014a)*, then Suge facula probably does represent the most distal reach of the central Rachmaninoff lavas. Furthermore, if Suge Facula formed in this fashion, then it might yield some insight into the succession of lava flows that took place in Rachmaninoff.

Legend

Linework

~ contact

~ crater rim

⌢ peak-ring crest

~ graben

Ornaments

⌇⌇ pitted ground

Rachmaninoff units

☐ exterior impact melt

☐ impact ejecta

\\\ crater wall material

☐ peak-ring material

☐ interior impact melt

☐ rough crater floor

☐ thin volcanic plains

☐ thick volcanic plains

Other units

☐ smooth volcanic plains
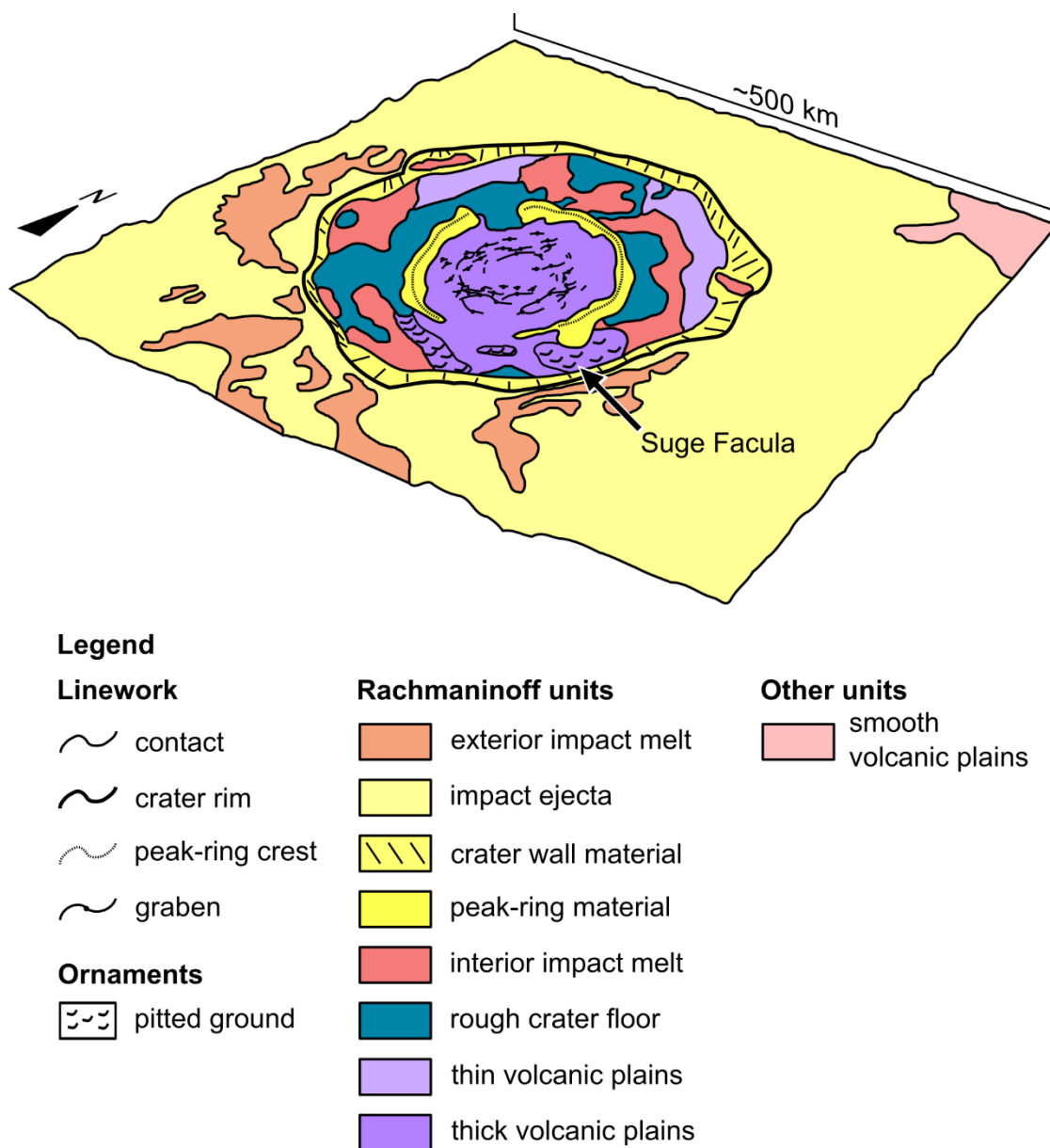
***Fig. 4.28 Illustration showing the extent of early volcanism in Rachmaninoff.** Suge Facula and other regions of pitted ground in Rachmaninoff are interpreted as disrupted lava flows. Following its eruption, thermal contraction of the volcanic pile is believed to be responsible for creating the network of grabens in Rachmaninoff's centre (Blair et al., 2013).*
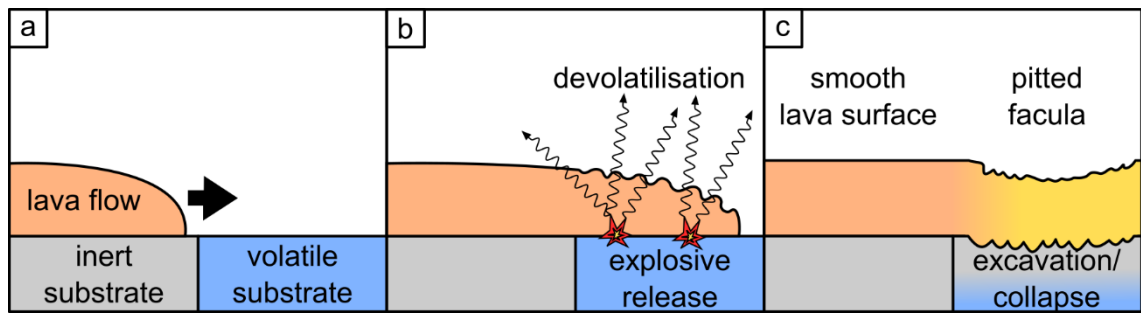
Fig. 4.29 Cartoon illustrating how pitted ground may form due to substrate devolatilisation. *(a) In this model, an advancing lava flow moves undisturbed over a substrate containing an insubstantial quantity of volatile material but approaches a compositionally distinct substrate with a high volatile content. (b) The lava flows over the volatile-bearing substrate. Heat from the lava is conducted into the substrate and vapourises the volatile material. Volatile material explosively propagates through the lava and escapes. The lava surface is disrupted by shallow subsurface explosions and minor fountaining. (c) When devolatilisation has ceased, the lava surface has developed a pitted texture in response to subsurface collapse and excavation.*

I interpret Suge facula and the other faculae in Rachmaninoff with the pitted ground texture as the most distal reaches of centrally sourced lava flows in the crater. Therefore, the thickness of the lava diminishes toward the eastern extent of Suge facula, which I interpret as the approximate location of the flow terminus. In the model where pitted ground formed when a hot lava flowed over a volatile-bearing substrate, the lava must be of some specific thickness such that explosive loss of volatiles in the subsurface creates pits at the surface. Furthermore, for the pitted ground texture to be present today, it must not have been buried too deeply by subsequent lava flows or obliterated by impacts. Therefore, the eastern extent of Suge Facula is controlled by either the lava flow length or the presence of volatiles in the substrate. Given that no 'normal' smooth red plains occur beyond Suge Facula, it appears that the extent of the lava controls the extent of Suge Facula and that the eastern margin of Suge Facula is the approximate location of the flow terminus. The western extent of Suge Facula might have been controlled by the thickness of the lava. Since the lava thickness will increase toward the centre of Rachmaninoff, it will be thicker in the west of Suge Facula compared with the east, where I interpret the lava to terminate. The location of the western margin of Suge Facula might reflect a threshold thickness of lava above which subsurface volatile

loss does not manifest at the surface. Alternatively, as the supply of lava waned following the creation of an originally more extensive region of pitted ground, subsequent lava flows emanating from the centre of Rachmaninoff might not have reached as far as the proposed flow terminus at the eastern margin of Suge Facula, but were of sufficient thickness to bury any pitted ground texture that developed west of Suge Facula. This latter hypothesis is supported by evidence for late-stage flows in the centre of Rachmaninoff discussed below. Both scenarios would produce the observed surface morphologies illustrated in Fig. 4.30.
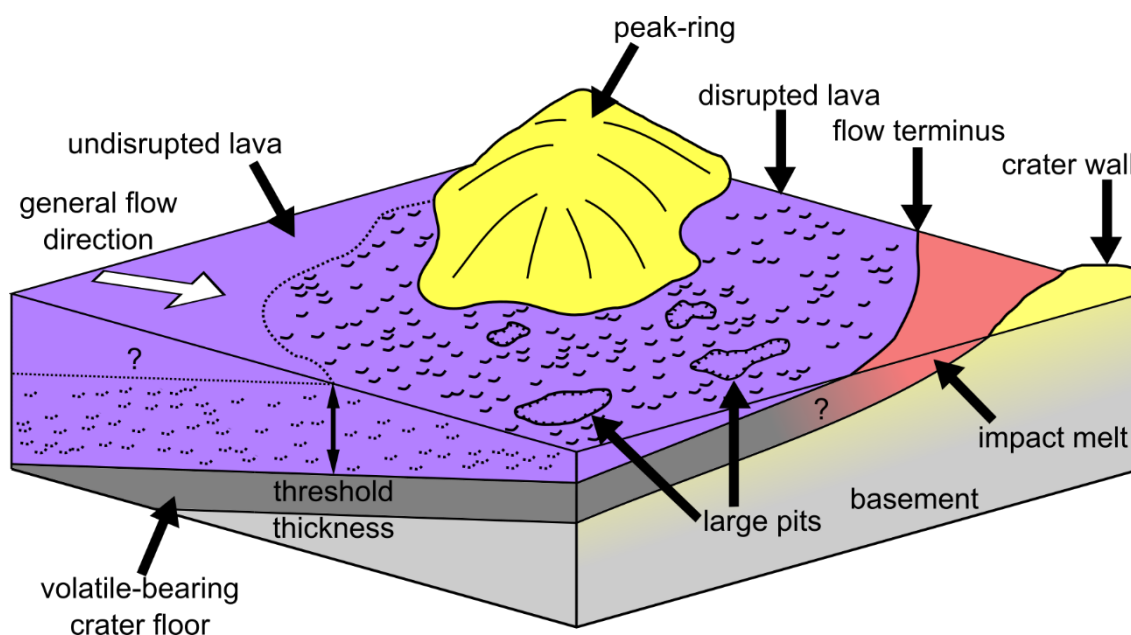
Fig. 4.30 Illustration of the formation of Suge Facula pitted ground. *Lava erupted from the centre of Rachmaninoff and built up until it could flow past the peak-ring. Early lava flows might have flowed over volatile-bearing substrates and developed into pitted ground by the mechanism described in Fig. 4.29. Later flows buried this pitted ground, if it formed, such that most volcanic plains within Rachmaninoff have a smooth surface. The location of Suge Facula represents an example of a distal lava flow in Rachmanininoff that did not have its pitted ground buried. This lava flow was sufficiently thin such that devolatilisation of the substrate disrupted the lava surface giving it a pitted texture to form Suge Facula. Explosions and fire-fountaining must have been sufficiently minor to avoid observable amounts of pyroclastic material accumulating on the peak-ring. This mechanism also applies for the other more minor regions of pitted ground within Rachmaninoff, which also appear to coincide with the most distal reaches of lava flows emanating from the centre of Rachmaninoff. Cartoon not to scale.*

Once the majority of the effusions in the centre of Rachmaninoff ceased, a network of circumferential and radial grabens formed. BLAIR ET AL. (2013) used thermomechanical simulations to model the formation of the grabens in Rachmaninoff. They found that thermal contraction of a thick volcanic pile was the best fit mechanism for their formation. This was the only proposed mechanism that could produce the observed pattern of grabens. Other proposed mechanisms were extension due to uplift of the basin floor and subsidence due to volcanic loading. Models predict that basin floor uplift occurs geologically rapidly after the impact (within 10 kyr to 1 Myr; BLAIR ET AL., 2013). This would require the volcanic plains in Rachmaninoff to have been emplaced and cooled beneath their elastic blocking temperature shortly after the impact. Since the interior smooth plains of Rachmaninoff have a resolvably younger crater-retention age than the basin itself, it seems probable that the most recent eruptions in Rachmaninoff postdate the crater by at least ~100 Myr. Furthermore, uplift models do not induce a stress state that produces the observed pattern of grabens, making graben formation due to uplift unlikely (BLAIR ET AL., 2013). Subsidence due to volcanic loading for all the considered models had flexural wavelengths greater than the extent of the central smooth plains (BLAIR ET AL., 2013). For a range of elastic thicknesses of the lithosphere, crustal thicknesses and volcanic load thicknesses, all models predicted that the entirety of the volcanic plains in Rachmaninoff would be in compression due to volcanic loading (BLAIR ET AL., 2013). This would preclude the formation of the observed grabens, requiring another process, such as thermal contraction of a thick volcanic pile to dominate over flexure due to loading.

However, the thermal contraction model also predicts grabens that extend into the very centre of Rachmaninoff (BLAIR ET AL., 2013). No grabens are observed within a radial distance of ~10 km from the crater's centre. Instead, small ridges are observed (Fig. 4.31). Modelling suggests that the compressional stresses required to generate these ridges would not have been sufficient to preclude or reverse the generation of grabens at the centre of Rachmaninoff (BLAIR ET AL., 2013). This supposition is supported by observations of cross-cutting systems of grabens and ridges elsewhere on Mercury (WATTERS ET AL., 2009). It has been suggested that the central graben have been buried by a late-stage lava flow (BLAIR ET AL., 2013). This

hypothesis is corroborated by the shallower grabens occurring at the inner edge of the observable network. It is possible that they have been partially infilled by this late-stage flow. Ridge formation, probably due to volcanic loading, might have occurred before and during late-stage flow emplacement, but the ridges observable today could entirely postdate late-stage flows *(BLAIR ET AL., 2013)*. Ridge formation represents the latest volcano-tectonic event to take place within Rachmaninoff. Further geological activity within the crater is restricted to hollow formation, which is prevalent in the peak ring of the basin.
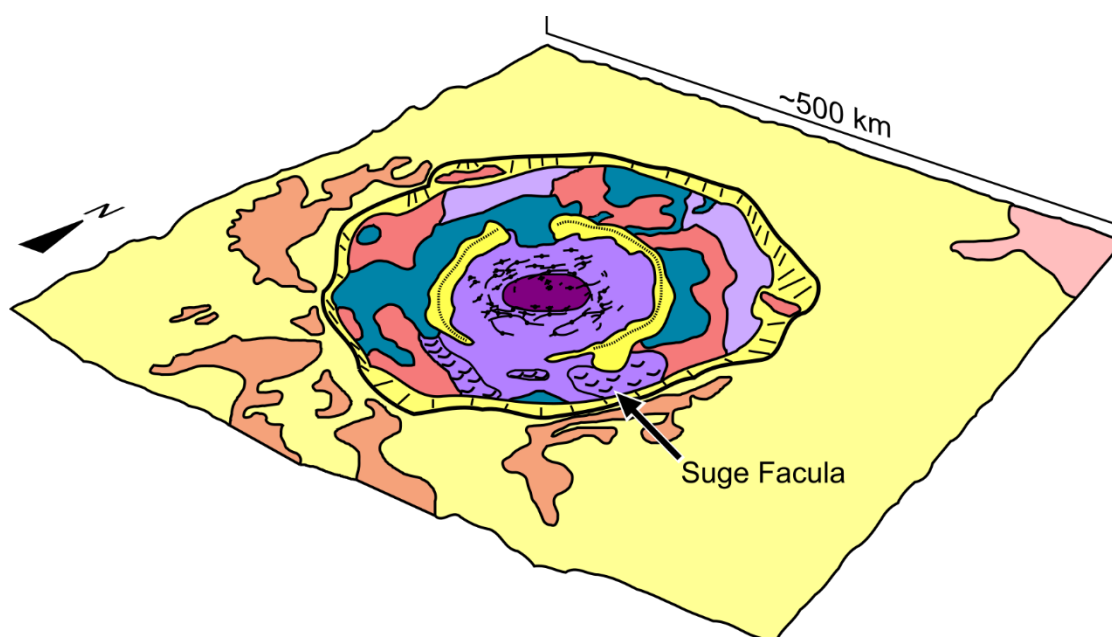
Legend

Linework

~ contact

~ crater rim

~ peak-ring crest

~ graben

~ ridge

Ornaments

pitted ground

Rachmaninoff units

exterior impact melt

impact ejecta

\\\ crater wall material

peak-ring material

interior impact melt

rough crater floor

thin volcanic plains

thick volcanic plains

terminal lava flows

Other units

smooth volcanic plains

Fig. 4.31 Illustration showing the terminal stages of volcanism in Rachmaninoff. A terminal stage of effusive volcanism is corroborated by the embayed appearance of the innermost grabens in the centre of Rachmaninoff. Small ridges formed in the very centre of Rachmaninoff due to subsidence of the basin in response to volcanic loading (BLAIR ET AL., 2013).

4.3.1.1 Volcanic vents exterior to Rachmaninoff

As stated in Chapter 3, an important factor in my decision to map H05 was that this quadrangle contains the largest putative pyroclastic deposit on Mercury (Nathair Facula) and its source vent (Fig. 4.32a). When I mapped this vent I found that its putative pyroclastic deposit superposes Rachmaninoff's distal ejecta (which in turn superposes volcanic smooth plains nearby). This implies that the most recent explosive volcanic eruptions that formed Nathair Facula occurred after the Rachmaninoff impact. Eruptions probably took place at Nathair Facula in the same interval of geological time that post-impact eruptions took place within Rachmaninoff, although these sites of volcanism are so distant from each other that no superposition relationship to establish their relative ages can be observed.

Following the example of *ROTHERY ET AL. (2014)*, who studied the vent formerly known as the 'kidney-shaped depression' *(HEAD ET AL., 2008, 2009; KERBER ET AL., 2009)*, hosted within the bright spot now known as Agwo Facula, I examined the floor of the vent within Nathair Facula to estimate the number of eruptive episodes that took place within the vent. In contrast to the Agwo Facula vent, the Nathair Facula vent lacks the prominent septa between eruption centres that aided *ROTHERY ET AL. (2014)* in their interpretations. I hypothesise that this could be due to the different settings of these two vents. Agwo Facula is located in southwestern Caloris Planitia, and so its vent structure is likely composed of competent smooth plains material. According to my mapping, the Nathair Facula vent is located in intercrater plains, which is more heavily cratered than smooth plains, and therefore likely to possess much less strength *(LE FEUVRE AND WIECZOREK, 2011)*. This may have prevented septa from forming and/or surviving within the Nathair Facula vent. Alternatively, the high inferred volcanic gas concentration at Nathair

Facula *(KERBER ET AL., 2011)* may have made it sufficiently explosive such that septa could not form or were destroyed by subsequent eruptions.
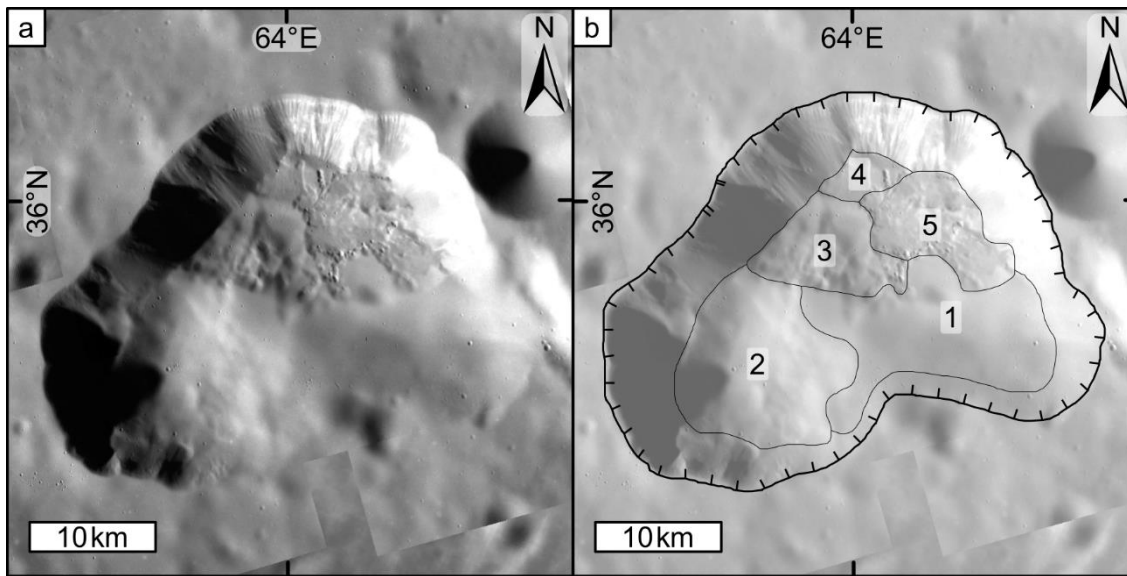
Fig. 4.32 Vent within Nathair Facula. *(a) Note the different floor and wall textures throughout the vent, including gullies on the northern wall. Mosaic of NAC frames EN0224508427M, EN1003815055M, EN1003843856M, and EN1993843866M. ~26 m/pixel. Orthographic projection centred on 63.8° E, 35.8° N. (b) Vent map with labels indicating floor textures from very degraded (1) to very fresh (5). My numbering conveys my interpreted relative order of eruption of the identified eruption centres within the vent: 1 = first, 2 = second, 3 = third, 4 = fourth, and 5 = fifth. Bold, hachured line indicates vent brink. Fine lines indicate boundaries between floor textures.*

Nevertheless, I have identified geomorphic textures on the floor of the Nathair Facula vent (Fig. 4.32b) that suggest that the locus of volcanic eruptions migrated in geological time, similar to what *ROTHERY ET AL. (2014)* observed at the Agwo Facula vent, which they interpret as a compound volcanic vent *(DAVIDSON AND DE SILVA, 2000)*. Similar to my classification of impact crater degradation states, I demarcated distinct floor textures within the Nathair Facula vent and assigned them a number according to how degraded they appear. '1' appears to be the most degraded floor area and has a uniform and featureless texture. I suggest that this is mostly due to its being the oldest eruption centre in the Nathair Facula vent such that regolith gardening and subsequent eruptions and deposition of pyroclasts have largely buried its original floor texture. On the basis of its crisp appearance and apparent cross-cutting relations with its surrounding floor textures, I suggest

that '5' is the youngest eruption centre within the vent. The relative order of the remaining demarcated regions is somewhat more equivocal, but all the floor textures taken together suggest that at least five eruption centres exist within the Nathair Facula vent, making it a 'compound volcano' *(DAVIDSON AND DE SILVA, 2000)*.

The demarcated eruption centres within the Nathair Facula vent are not approximately circular in shape, as might be expected if they were excavated explosively. This possibly reflects that within each demarcated region multiple eruptions took place before the centre of eruption migrated to the next region. Each region likely reflects a composite shape formed by multiple eruptions that occurred within a relatively short interval of geological time, which provides an explanation for the irregular outlines and uniform textures of the larger, older centres (1 and 2). The younger centres (3, 4, and 5) appear to have circular pits within them that could be candidate eruption sites, but I could not confidently determine the relative order of the eruption sites within regions 3, 4, or 5. Younger eruption sites within eruption centres 3 and 5 have likely overprinted eruption centre 1, which would contribute to the convoluted outline of eruption centre 1.

Overall, eruptions from the Nathair Facula vent appear to have migrated from south to north. This is reflected in both an increase in floor texture crispness toward the north of the vent, but also an increase in vent wall geomorphic complexity. The vent walls south of ~36°N are relatively featureless, similar to a wall in an impact crater in an advanced state of degradation. North of ~36°N, the vent walls show evidence of recent mass movement downslope and gully formation *(MALLIBAND ET AL., 2019A)*. This suggests that the southern (older) eruptions in the Nathair Facula vent occurred long enough ago that slope evolution by mass movement has slowed sufficiently such that regolith gardening has become the most important modifying agent of the southern vent slopes. Eruptions at the northern (younger) sites occurred sufficiently recently that evidence of gully formation has yet to be erased by regolith gardening.

The nearby Neidr Facula vent (Fig. 4.33) does not have such a diversity of floor and wall textures as the Nathair Facula vent. The non-circular outline of the Neidr Facula vent suggests that it too was excavated by multiple eruptions, making it

another example of a compound volcanic vent on Mercury. If my interpretations of the Nathair Facula vent are correct, then the absence of distinct floor textures within the Neidr Facula vent suggests that if multiple eruptions did occur, then they did so within a relatively short span of geological time. Furthermore, septum development between individual eruption sites may have been precluded due the vent forming within incompetent intercrater plains material. Rachmaninoff distal ejecta is superposed by Neidr Facula material, which implies that at least the most recent eruptions from this vent postdate the Rachmaninoff impact, as with Nathair Facula. The formation order of the Nathair Facula and Neidr Facula is more difficult to determine as these features do not overlap. I suggest that eruptions at Nathair Facula extended into the more recent past than those at the Neidr Facula vent, since the Neidr Facula vent lacks the same crispness of floor and wall textures (particularly gullies) apparent within the Nathair Facula vent.
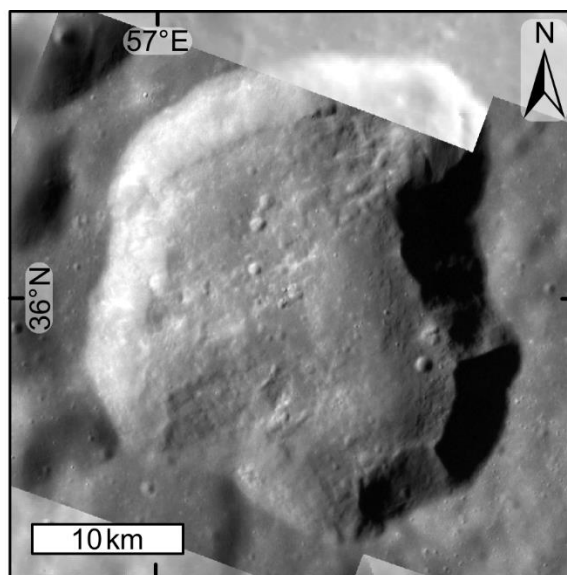
Fig. 4.33 Vent within Neidr Facula. *I did not observe diverse floor or wall textures comparable to those of the Nathair Facula vent (Fig. 4.32) within the Neidr Facula vent. Mosaic of NAC frames EN0249844224M and EN0249844228M, ~30 m/pixel. Orthographic projection centred on 57.4°E, 36.0°N.*

An interesting observation both the Nathair Facula vent and the Neidr Facula vent have in common is that they are large (>>10 km across) vents that occur outside impact features. Volcanism on Mercury seems to have been highly sensitive to the prevailing stress conditions. Large-volume effusive volcanism appears to have ceased in response to the horizontally compressive stress regime induced by global

contraction *(BYRNE ET AL., 2016)*. Most putative explosive volcanic vents on Mercury occur within impact structures *(GOUDGE ET AL., 2014; THOMAS ET AL., 2014A; JOZWIAK ET AL., 2018)*, which temporarily reset preexisting stress fields *(BYRNE ET AL., 2016)*. The vents associated with Nathair Facula and Neidr Facula, located in southeastern H05, appear to be important exceptions to this observation, as they are not obviously associated with any observable or inferred impact structures (Fig. 4.34). However, together with two smaller vents, they form a line that is subparallel to the nearby margin of Borealis Planitia. This is similar to how late-stage volcanism in the lunar maria tends to occur toward mare margins *(HEAD AND GIFFORD, 1980)* due to the stress state induced by the load of mare basalts *(MCGOVERN AND LITHERLAND, 2011)*. The stress field due to loading by Borealis Planitia may have played a role in the location of these vents. This is consistent with these vents postdating smooth plains emplacement.
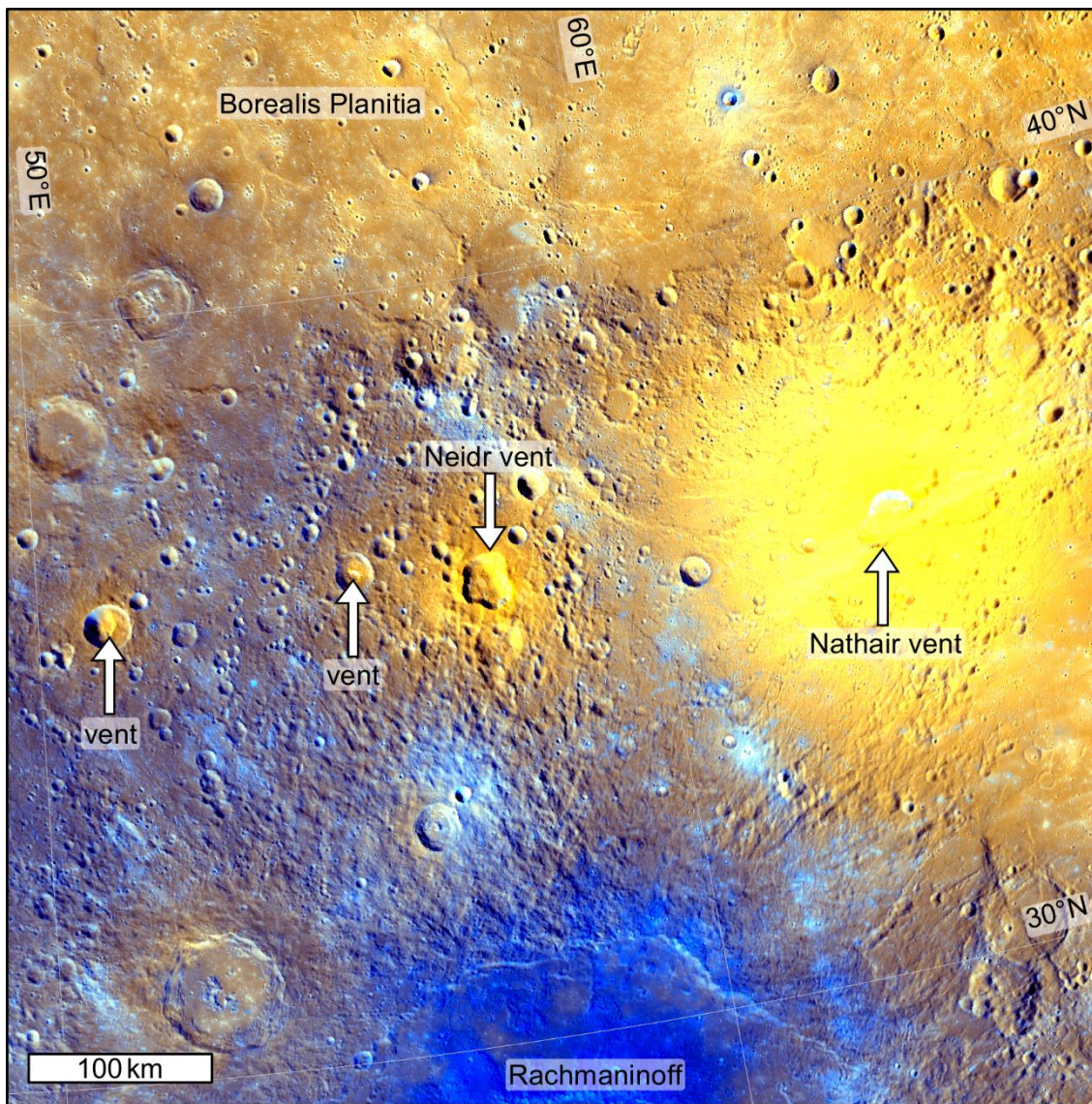
Fig. 4.34 Putative explosive volcanic vents and deposits in southeastern H05. *Four putative volcanic vents are arranged in a line sub-parallel to the margin of Borealis Planitia to the north. The vents within Nathair Facula and Neidr Facula are not located within impact craters. The two small vents in the west are in impact craters. ~665 m/pixel enhanced colour mosaic. Native LCC projection of the H05 map.*

4.3.2 Southwestern H05

As stated in earlier section of this chapter, and in Chapter 3, many interesting geological features in H05 have been studied previously. During my mapping, I found that the geology of southwestern H05 is particularly rich. Here I describe the main features of interest in this region and explain their significance in the wider context Mercury's geology.

The geology of southwestern H05 is dominated by intermediate plains and impact sculpture from the ancient basin b30 (Fig. 4.35; FASSETT ET AL., 2012). The assemblage of landforms in southwestern H05 is similar to that described by BYRNE ET AL. (2013) that lies between Borealis Planitia and the circum-Caloris smooth plains (Fig. 4.36).
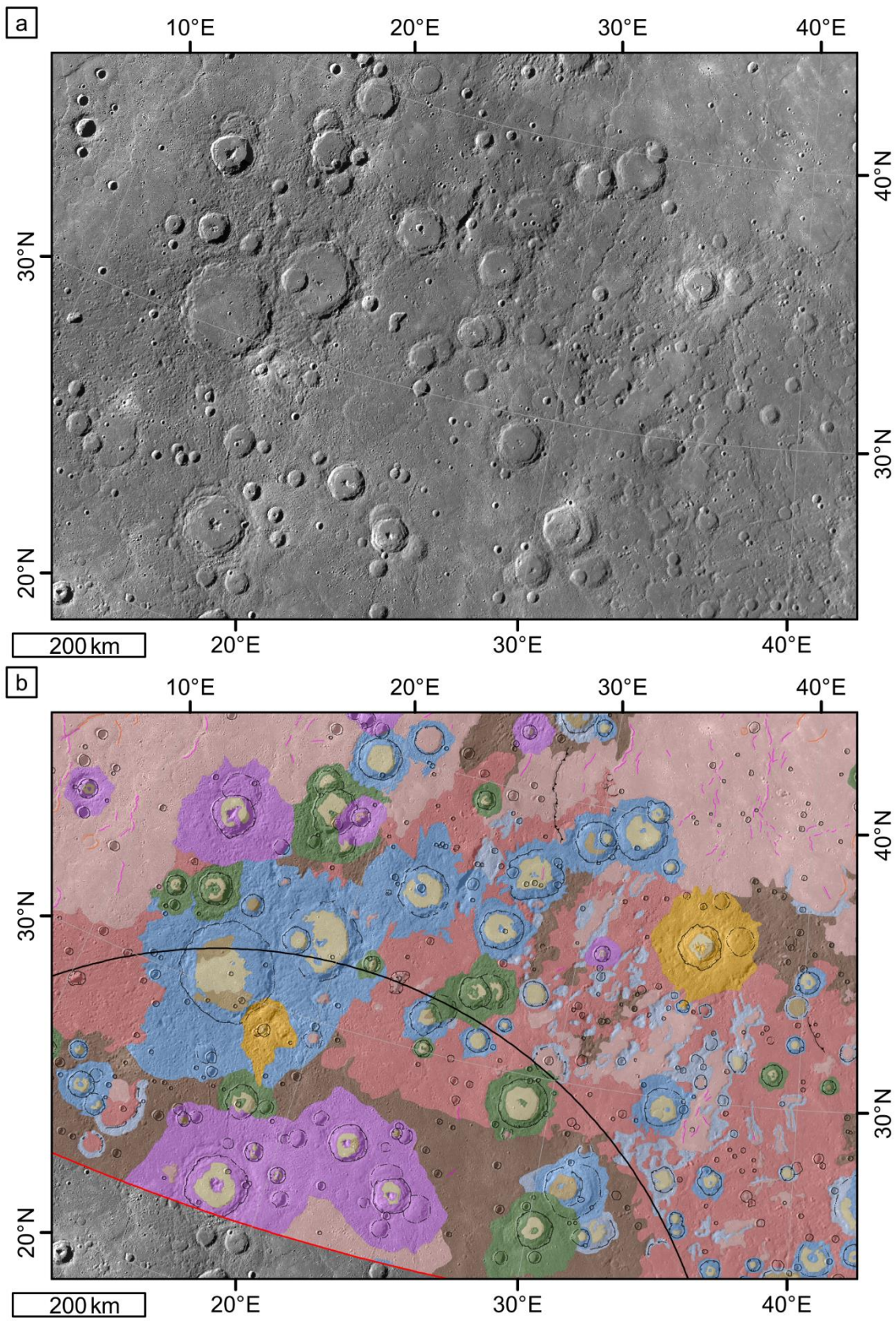
Fig. 4.35 Geology of southwestern H05. *(a) Monochrome mosaic of southwestern H05. The smooth floored troughs radiating from b30 are located in the centre-right of the figure. (b) Transparent geological units are coloured according to the key in Fig. 4.2 and are overlain on the ~166 m/pixel global monochrome mosaic. The red line indicates the extent of H05. The black arc indicates the proposed location of the buried rim of the ancient basin b30 (FASSETT ET AL., 2012). Both panels are in the native LCC projection of H05.*

BYRNE ET AL. (2013) describe smooth plains that occupy valleys and interpret them as volcanically flooded and modified Caloris impact sculpture. This is the same as my interpretation of the troughs radiating from b30 with smooth plains covered floors. Some of the 'broad channels' described by BYRNE ET AL. (2013), such as Paestum Vallis and Angkor Vallis, contain streamlined kipukas, which they interpret to be remnants of the pre-existing terrain before lava inundation. They attribute the streamlined appearance of the kipukas at least in part to thermal and mechanical erosion by low-viscosity lavas. The troughs in southwestern H05 do not contain streamlined kipukas like those observed by BYRNE ET AL. (2013). There is no obvious spectral difference between the smooth plains in Paestum and Angkor Valles and the smooth plains in the radial troughs in H05 that would suggest a compositional (and therefore a viscosity) difference between the lavas. A higher viscosity lava might be expected to erode the surrounding landscape less effectively (BYRNE ET AL., 2013). Therefore, the lack of obvious streamlined kipukas could instead be due to lower velocity lava flows in H05. The broad channels described by BYRNE ET AL. (2013) connect two large expanses of smooth plains, which suggests that the flux of lava along the broad channels was high. The troughs in H05 are at the southernmost extent of Borealis Planitia, and their southern reaches border elevated intermediate plains. Rather than hosting high-velocity channel flow, the troughs in H05 more likely contained slower flowing lavas that were running up against higher terrain.
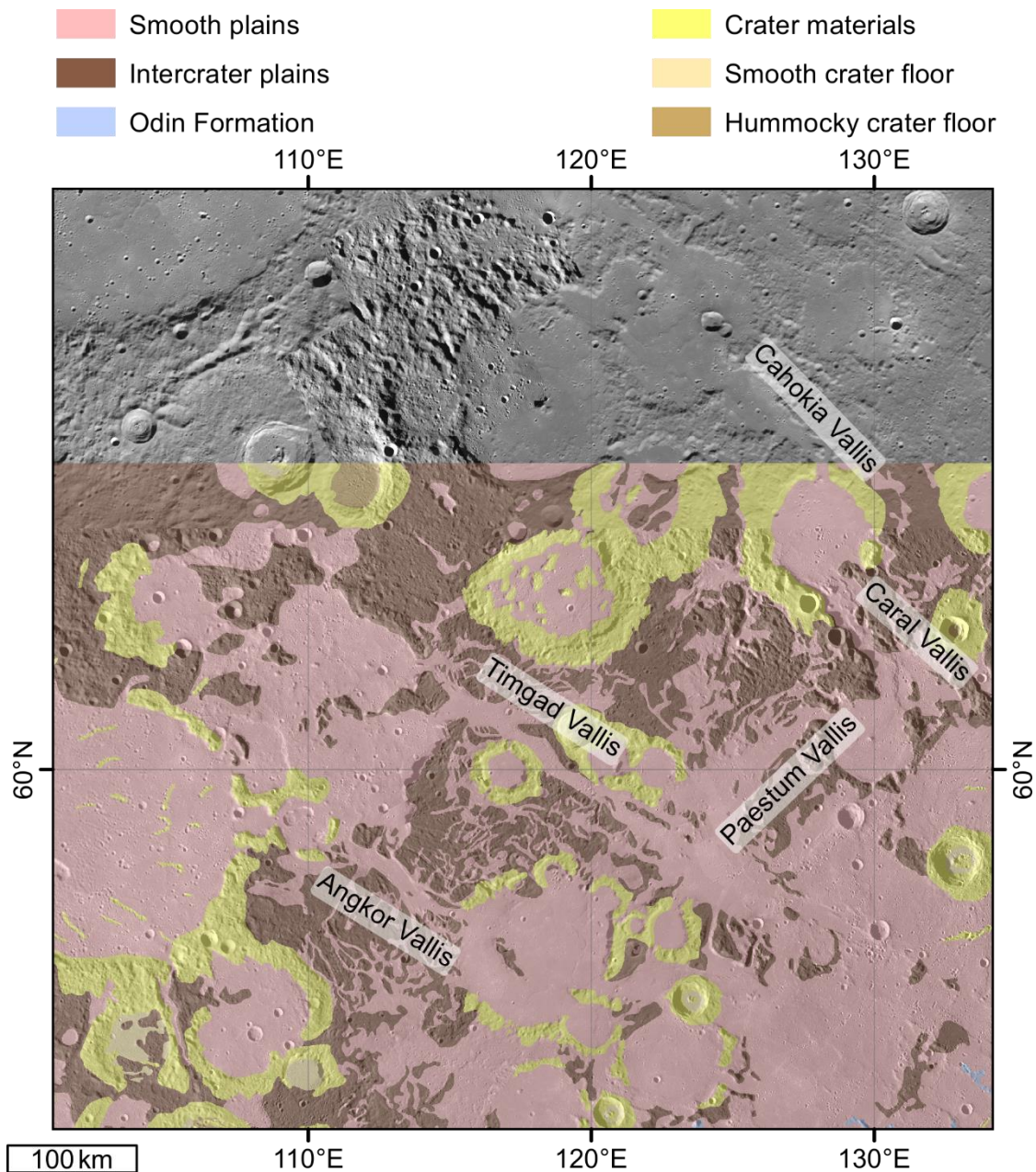
Fig. 4.36 Part of the study region of BYRNE ET AL. (2013). *These authors interpret this as a landscape that has been inundated by low-viscosity lavas. Lava appears to have drained through, and modified in places, several channels (labelled). Transparent geologial units overlain on the ~166 m/pixel global monochrome mosaic. Mercator projection centred on 110.0°E, 59.0°N. Geological shapefiles are those of MANCINELLI ET AL. (2016) and are reproduced here with the kind permission of the authors. Geological units are unavailable north of 65°N as this was the northernmost extent of mapping by MANCINELLI ET AL. (2016).*

The intermediate plains of southwestern H05 also contain two irregularly shaped pits (Fig. 4.37). These have the same red colour signature as putative pyroclastic vents elsewhere on Mercury *(MURCHIE ET AL., 2008, 2015; KERBER ET AL., 2011; GOUDGE ET AL., 2014; THOMAS ET AL., 2014A; JOZWIAK ET AL., 2018)*. These pits are

comparable in size to Nathair Facula's pit. Nathair Facula, the largest putative explosive volcanic vent on Mercury, in southeastern H05. However, pits A and B (named in Fig. 4.37) in southwestern H05 do not have red colour anomalies so extensive or so bright as Nathair Facula. This could be because the explosive volcanic activity that created the red deposits at pits A and B occurred earlier in Mercury's history than that which created Nathair Facula. Pyroclastic deposits probably degrade in time due to space weathering *(JOZWIAK ET AL., 2018)*, which tends to reduce spectral contrasts *(HAPKE, 2001)*. Alternatively, it is possible that the explosions that excavated these pits had a lower volatile content than those at Nathair Facula's vent. It has been suggested that Nathair's Facula's vent was excavated by eruptions with an exceptionally high gas fraction *(KERBER ET AL., 2011)*. If the red colour of the deposit is due to the removal of a relatively blue volatile, then lower volatile-content eruptions might not only have smaller deposits but also deposits with a less intense red colouration.
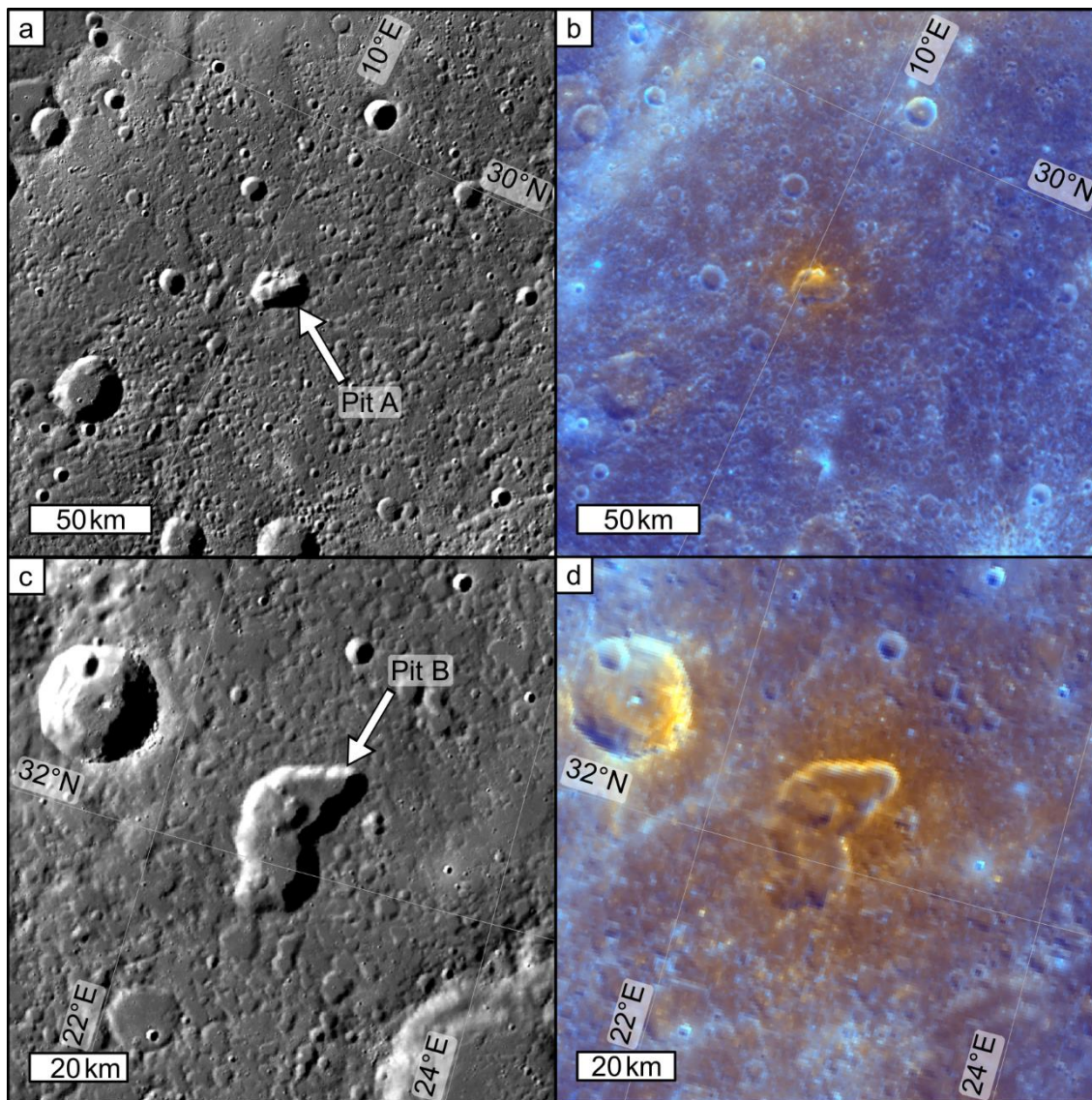
Fig. 4.37 Candidate effusive volcanic vents in H05. *(a) Pit A is located within intermediate plains and close to a contact with the smooth volcanic plains of Borealis Planitia to the north. Smaller superposed pits can be seen on the northern wall of the main pit. ~166 m/pixel basemap. (b) Pit A has a faint red colour anomaly associated with it that appears to be centred on the small superposed pits. ~665 m/pixel enhanced colour mosaic. (c) Pit B is also located in intermediate plains. It has a small internal depression within it. The floor of the pit appears to be smooth plains material. The brink of the pit has an irregular, scalloped outline. ~166 m/pixel basemap. (d) Pit B also has a red colour anomaly. ~665 m/pixel enhanced colour mosaic. All panels are in the native LCC projection of the H05 map.*

However, in the case of Pit A, an alternative explanation for its pyroclastic deposit exists. Pit A has smaller depressions located on its northern brink (Fig. 4.37a). The red colour anomaly appears to be focussed on these northern brink depressions,

rather than the centre of Pit A itself (Fig. 4.37b). This observation suggests that at least the most recent explosive volcanic activity at Pit A was small in volume and concentrated at the pit's northern brink. If my interpretation that the intermediate plains represent shallowly volcanically infilled intercrater plains is correct, then the possibility that significant, and earlier, effusive activity occurred at Pit A is raised. This would help to explain the lack of a large red colour anomaly at Pit A. Further evidence that the pits in southwestern H05 are effusive volcanic vents exists at Pit B. The floor of Pit B is formed of smooth material, as are other low-lying regions in the surrounding intermediate plains (Fig. 4.37c).

BYRNE ET AL. (2013) describe in their study area 'coalesced depressions' that resemble pits A and B in southwestern H05 (Fig. 4.38). Their coalesced depressions, which are of similar scale to pits A and B, are found within smooth plains, lack faculae, and also have smooth floors. BYRNE ET AL. (2013) suggest that the circular pit located within one of their coalesced depressions (Fig. 4.38a) is similar to the nested calderas of the Tharsis Montes region of Mars (BYRNE ET AL., 2012). Similar pits elsewhere on Mercury have been interpreted as collapses above drained magma chambers (GILLIS-DAVIS ET AL., 2009). On the basis of these observations, BYRNE ET AL. (2013) interpret their coalesced depressions as candidate effusive volcanic vents from which relatively minor amounts of smooth plains material within their respective vicinities were sourced. Despite widespread effusive volcanic plains, only a few candidate effusive volcanic vents on Mercury have been suggested (BYRNE ET AL., 2013; JOZWIAK ET AL., 2018). This is probably because the characteristic eruption conditions on Mercury (high volume, high effusion rate, low viscosity; BYRNE ET AL., 2013) caused most effusive vents to bury themselves or each other with their flow fields in the same way that the source vents for large igneous provinces on Earth are seldom exposed due to volcanic burial (WHITE ET AL., 2009). Therefore, due to their rarity, the observation of two candidate effusive volcanic vents in southwestern H05 is important for understanding the emplacement of volcanic plains in that region and on Mercury in general.
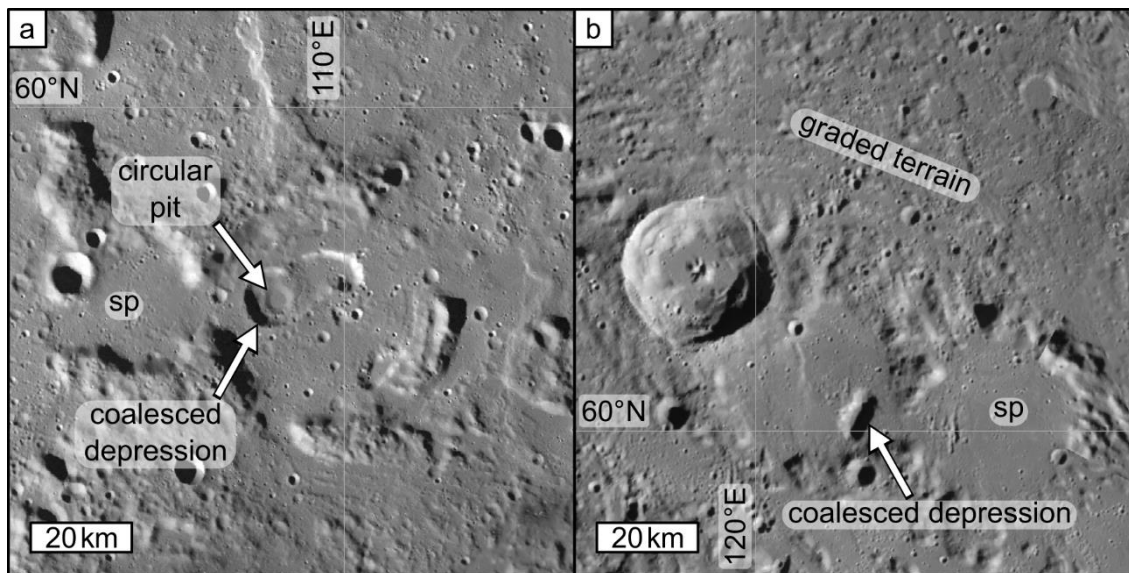
Fig. 4.38 Landforms of probable volcanic origin elsewhere on Mercury that resemble southwestern H05 landforms. *A 'coalesced depression' that is a candidate effusive volcanic vent (BYRNE ET AL., 2013), which appears similar to pit B in H05. One explanation for the circular pit within the coalesced depression could be that it is a nested caldera (BYRNE ET AL., 2013). (b) 'Graded terrain' that is interpreted as intercrater plains that has been inundated but not completely buried by volcanic smooth plains material (BYRNE ET AL., 2013). The origin of the graded terrain shown here is essentially the same as my interpretation of the formation of the intermediate plains unit in H05. A second example of a coalesced depression, identified by BYRNE ET AL. (2013), that is a candidate effusive volcanic vent, more similar to pit A, is indicated. Both panels, ~166 m/pixel global monochrome mosaic. Both panels are Mercator projections centred on 110.0°E, 59.0°N.*

BYRNE ET AL. (2013) also describe 'graded terrain', which lies alongside the smooth plains, and particularly the broad channels, in their study area. This terrain is characterised by a more muted expression of the intercrater plains close to channel confined smooth plains. The graded terrain contains impact craters that despite not having obvious breached perimeters, nevertheless appear to have been volcanically flooded to varying degrees. BYRNE ET AL. (2013) suggest that at least some volume of erupted lavas within the region were not channelised but instead spread out over the surroundings. The 'grading' of the muted intercrater plains into normal intercrater plains with increasing distance from the broad channels suggests that as the lava flux in the region dropped, overland lava flows retreated until they became channel confined. I suggest that the intermediate plains in southwestern H05 formed in a similar manner. These intermediate plains also

contain smooth patches, both within and outside of host impact craters, which are not all obviously connected. I suggest that lavas partially inundated regions where I have mapped intermediate plains in H05 but that effusions ceased before the texture of the underlying intercrater plains was completely buried. Lavas were able to pond deeply within impact craters and other low-lying regions, creating smooth patches. These smooth patches appear as deficient in superposing impact craters as the smooth plains of Borealis Planitia, which suggests that the intermediate plains could have formed alongside it, but this qualitative observation cannot be corroborated by a statistically significant crater count since even their combined area is too small.

The similarities between southwestern H05 and the assemblage of features described by BYRNE ET AL. (2013) suggests that other partially volcanically inundated landscapes could be found elsewhere on Mercury. Furthermore, these two regions demonstrate that the volcanic history of the planet can easily be oversimplified by mapping only smooth and intercrater plains.

Pits A and B lie close to the proposed location of the buried rim of the b30 basin (Fig. 4.39). Putative explosive volcanic vents within the Caloris basin occur very close to its rim (MURCHIE ET AL., 2008), perhaps because their magmas ascended along structural weaknesses associated with the rim (GOUDGE ET AL., 2014; JOZWIAK ET AL., 2018), or because early volcanic loading of the interior of Caloris created a stress field that favoured subsequent eruptions to occur at its edge (MCGOVERN AND LITHERLAND, 2011), or because the thick plains of Caloris Planitia posed a barrier to later eruptions (ROTHERY ET AL., 2014). Whatever combination of these effects led to explosive volcanic vents in Caloris occurring close to its rim, all three of them are equally valid for explaining why pits A and B occur where the rim of b30 is proposed to be buried.
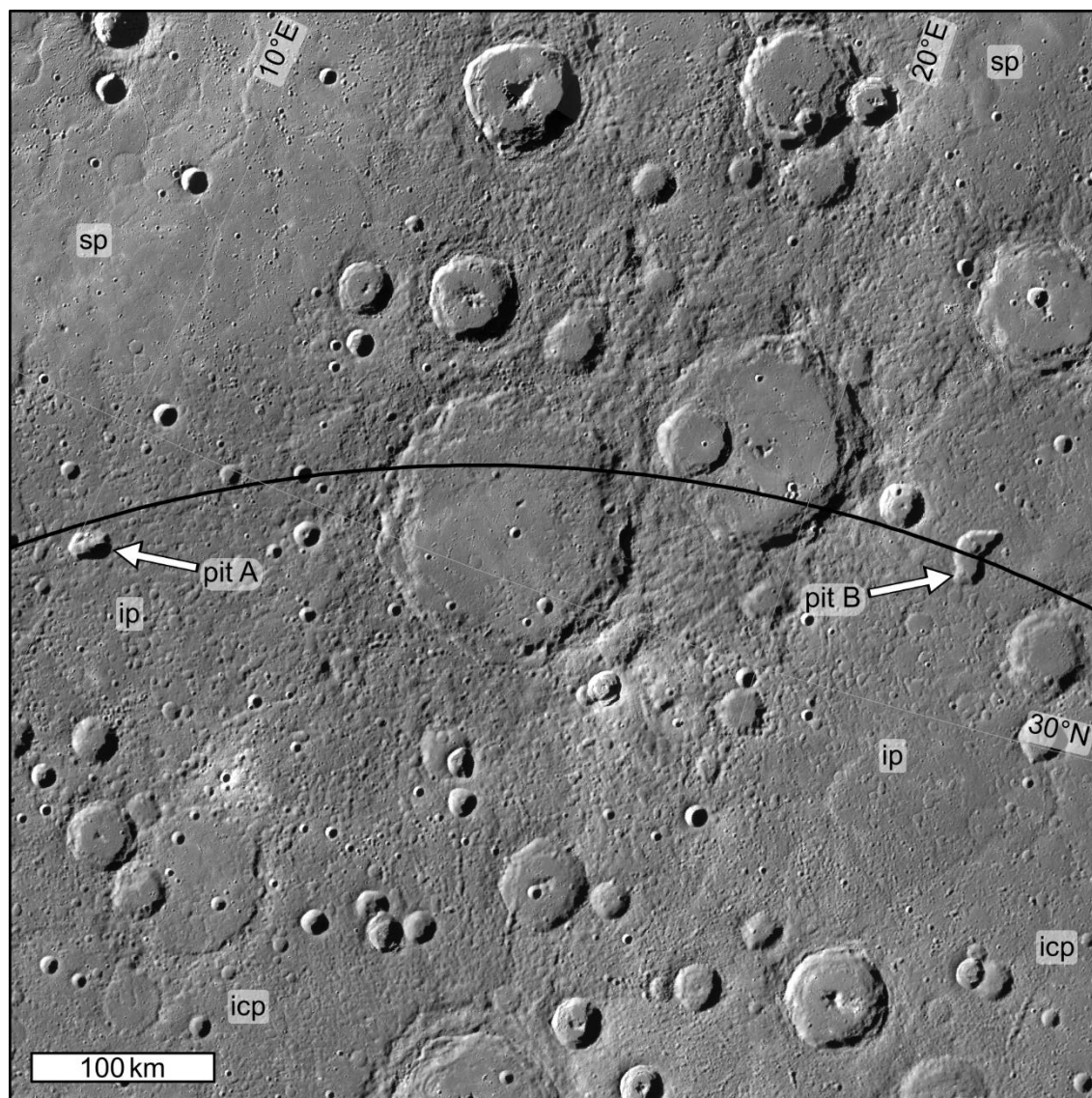
Fig. 4.39 Locations of candidate effusive volcanic vents in H05. *Pits A and B are shown in relation to the location of the rim of the b30 basin proposed by FASSETT ET AL. (2012). The pits lie very close to the predicted location of the buried basin rim and close to the contact with the smooth plains of Borealis Planitia to the north. ~166 m/pixel basemap. Native LCC projection of the H05 map.*

Pits A and B are also located close to the contact between their host intermediate plains and Borealis Planitia to the north. The location of these pits may have been influenced by the volcanic load of Borealis Planitia, in addition to that of b30. If this is the case, then pits A and B must have formed towards the end of smooth plains emplacement in order for the load of Borealis Planitia to concentrate eruptions towards its outer margin. If pits A and B did form after the majority of Borealis Planitia, and were also effusive volcanic vents that supplied some of the lava that created the intermediate plains around them, then that would mean

intermediate plains formation occurred during the later stages of smooth plains emplacement in H05.

4.4 Concluding remarks

My geological mapping of H05 has shown that the quadrangle has had a rich history. Traces of ancient impact basins of comparable scale to the Caloris basin are evident in the quadrangle, and structures related to these basins appear to have influenced the subsequent geological evolution of the quadrangle by affecting magma composition, ascent and eruption. The intercrater plains and smooth plains appear to have been emplaced largely by effusive volcanism. Effusive volcanism persisted after large-volume smooth plains emplacement as intermediate plains formation, within which I have identified candidate source vents, and more locally as post-impact volcanism. Explosive volcanism from pits appears to have outlasted effusive volcanism in H05. Minor surface pitting within Rachmaninoff appears to be linked to post-impact effusive volcanism within that crater, whereas the most recent explosive eruptions from large pits within Nathair and Neidr Faculae certainly postdate Rachmaninoff. The sequence of geological events within H05 corresponds well with the five degradation state classification scheme, unlike in the other Mercury quadrangle maps produced in the MESSENGER era.

CHAPTER 5
CONSTRUCTIONAL VOLCANIC EDIFICES ON MERCURY

5.1   Introduction

The MESSENGER mission has documented abundant evidence for widespread volcanic activity on Mercury, but an enduring curiosity has been the lack of diversity of volcanic forms on the planet, compared with the other rocky bodies in the Solar System. During my research, I serendipitously observed two small (<15 km in diameter) prominences with shallow summit depressions. In this chapter, I investigate the possibility that they are constructional volcanic edifices, a class of volcanic landform that has not been unambiguously identified on Mercury, and discuss how they may have formed due to small-volume, late-stage eruptions. I also discuss the paucity of constructional volcanic edifices on Mercury compared with Earth and the Moon. I suggest that this paucity is because volcanic eruptions with sufficiently low eruption volumes, rates, and flow lengths, suitable for edifice construction, were highly spatiotemporally restricted throughout Mercury's geological history due to the strong influence of global contraction. This chapter of my thesis is adapted from a peer-reviewed, open-access *Journal of Geophysical Research: Planets* paper *(WRIGHT ET AL., 2018)*. In Section 5.2 I outline the previous studies that have described the physical volcanology of Mercury. In Section 5.3 I describe the data and methods I used to search for and study volcanic edifices. In Section 5.4 I describe the candidate volcanic edifices that I found. I discuss the implications of these small edifices in Section 5.5 and state my conclusions in Section 5.6.

5.2   Background

Constructional volcanic edifices, which form from the accumulation of erupted products proximal to their vents *(DAVIDSON AND DE SILVA, 2000)*, have been recognised throughout the Solar System *(SIGURDSSON ET AL., 2000)* but have not been positively identified on Mercury. The morphology of volcanic landforms

reflects the style and environment of eruption, which in turn provides insight into interior processes of planetary bodies. Therefore, characterising the full range of volcanic landforms and their spatiotemporal distributions is required to understand the geological evolution of the body on which they occur.

5.2.1   Smooth plains volcanism

Mercury has abundant smooth plains, first imaged by Mariner 10, most of which are interpreted as effusive lava plains *(STROM ET AL., 1975; HEAD ET AL., 2008; DENEVI ET AL., 2013; OSTRACH ET AL., 2015)*. More recent imaging by MESSENGER shows that smooth plains cover ~27% of the planet's surface (Fig. 5.1; *DENEVI ET AL., 2013*) and suggests that Mercury's intercrater plains are older, more heavily cratered lava plains *(WHITTEN ET AL., 2014)*, indicating that the planet's crust is predominantly volcanic. This volcanic style is analogous to large igneous provinces (LIPs) on Earth, which have high erupted volumes that form thick plains *(BRYAN AND ERNST, 2008)*. The most extensive smooth plains on Mercury are those constituting Borealis Planitia (informally the 'northern smooth plains'; *HEAD ET AL., 2011; OSTRACH ET AL., 2015*) and those smooth plains associated with the Caloris impact basin. The plains interior to the basin are formally 'Caloris Planitia' *(STROM ET AL., 1975)*, and the plains surrounding Caloris have been informally referred to as the 'circum-Caloris' plains *(FASSETT ET AL., 2009; DENEVI ET AL., 2013)*. Observations of the relationships between Caloris Planitia and the circum-Caloris smooth plains *(ROTHERY ET AL., 2017)* and their superposing crater densities *(FASSETT ET AL., 2009; DENEVI ET AL., 2013; OSTRACH ET AL., 2015)* suggest that they formed within a short span of geological time. Absolute ages on Mercury have intrinsically large errors due to uncertainties in the crater production function used to derive them (e.g. *STROM AND NEUKUM, 1988; NEUKUM ET AL., 2001; MARCHI ET AL., 2009; LE FEUVRE AND WIECZOREK, 2011)*. However, both Borealis and Caloris Planitia, and the circum-Caloris plains, are estimated to have formed ~3.7 Ga *(DENEVI ET AL., 2009; HEAD ET AL., 2011; OSTRACH ET AL., 2015)*, and large-volume effusive volcanism is believed to have ceased soon after (i.e. ~3.5 Ga; *BYRNE ET AL., 2016*).
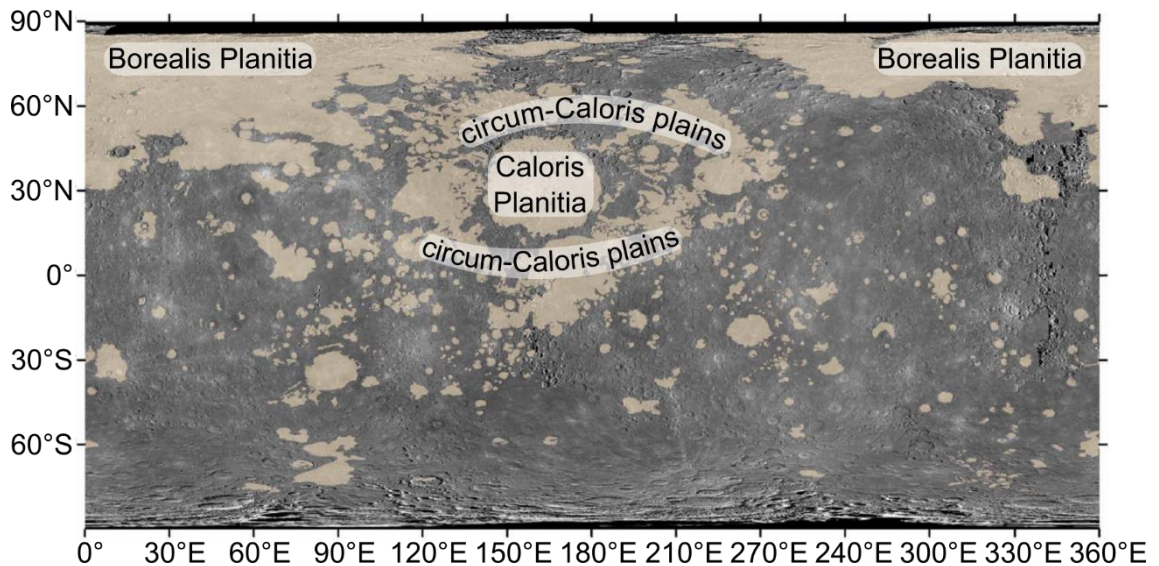
Fig. 5.1 Global map of smooth plains on Mercury. *Modified from DENEVI ET AL. (2013).*

5.2.2   Explosive volcanism

MESSENGER also identified bright, spectrally red spots with diffuse outer boundaries, usually with an irregular depression in their centres. These red spots, now formally termed 'faculae' (*sing.* 'facula'), are interpreted as deposits of ballistically emplaced pyroclasts surrounding explosively excavated volcanic craters *(HEAD ET AL., 2008; MURCHIE ET AL., 2008; KERBER ET AL., 2009, 2011; BARNOUIN ET AL., 2012; GOUDGE ET AL., 2014; THOMAS ET AL., 2014A; JOZWIAK ET AL., 2018)*. The oldest pyroclastic deposit dated by *THOMAS ET AL.(2014B)* using its crater size-frequency distribution was determined to have formed ~3.9 Ga, and explosive volcanism of this kind appears to have been active until at least ~1.0 Ga *(THOMAS ET AL., 2014B; JOZWIAK ET AL., 2018)*, or even ~280 Ma *(BANKS ET AL., 2017)*.

5.2.3   A shield volcano?

A candidate shield volcano was proposed within Caloris Planitia based on images captured during MESSENGER's first flyby *(HEAD ET AL., 2008)*. Shield volcanoes form by effusions of low-viscosity lavas from a point source, along with a relatively minor explosive component and, in addition to those on Earth, have been reported on the Moon, Venus, Mars, and Io *(SIGURDSSON ET AL., 2000)*. Shield volcanism represents an end-member eruptive style that brackets a continuum with LIPs *(GREELEY, 1982)*. Evidence for the shield volcano in Caloris Planitia included apparent embayment of nearby impact craters and an albedo change (now known

as 'Agwo Facula') surrounding a 'kidney-shaped depression' *(HEAD ET AL., 2008)*. However, subsequent orbital data cast doubt on the shield interpretation of this edifice. Higher-resolution images captured under a range of illumination conditions show that impact craters proximal to the Caloris depression are not obviously embayed by flows *(ROTHERY ET AL., 2014)*. Furthermore, detrended MLA data (where long-wavelength slopes are removed from local topography) show that although the excavated depression, regarded as a vent, is more than 1 km deep, its brink is not substantially elevated above its surroundings, and the external flank slopes of the candidate 'shield' are ~0.14° *(ROTHERY ET AL., 2014)*. This slope value is even lower than those typical for low shields on Mars (0.43°; *HAUBER ET AL., 2009*) and at the lowermost bound of the extremely low-angle shields that have been identified on that planet (0.15–0.35°; *VAUCHER ET AL., 2009*). Martian shields have some of the lowest flank slopes in the Solar System, suggesting that the low topographic rise around the Caloris vent could have been constructed by other means. A study that considered 20 additional explosive vents on Mercury, situated on otherwise generally flat plains, found that six of these are associated with little (<1°) or no relief *(THOMAS ET AL., 2014A)*. Therefore, these landforms more likely represent subtle ramps generated by the ballistic emplacement of pyroclasts from the explosive eruption of a compound volcanic vent, rather than a true shield constructed predominantly of lava flows *(ROTHERY ET AL., 2014)*.

These findings suggest that explosive volcanism on Mercury has been chiefly excavational in nature, producing large craters with thin deposits, morphologically resembling those of maar volcanoes *(WHITE AND ROSS, 2011)* or phreatic explosions *(BROWNE AND LAWLESS, 2001)*. Examples of constructional volcanic edifices, where the landform is characterised by a topographic rise, rather than a large crater *(DAVIDSON AND DE SILVA, 2000)*, have hitherto not been observed on Mercury, despite extensive study with orbital MESSENGER observations of Borealis Planitia *(HEAD ET AL., 2011; BYRNE ET AL., 2013; OSTRACH ET AL., 2015)*, the Caloris plains *(DENEVI ET AL., 2013; ROTHERY ET AL., 2017)*, and intercrater plains *(WHITTEN ET AL., 2014)*.

5.2.4 Constructing volcanic edifices

Given the lack of erosional processes that could fully remove evidence of volcanic edifices in the smooth plains, their paucity suggests that Mercury's volcanic eruptions during its early history (>3.5 Ga; BYRNE ET AL., 2016) were somehow unable to build substantial topography. This has been attributed to the planet's erupted lavas having very low viscosities (STOCKSTILL-CAHILL ET AL., 2012). Rare streamlined kipukas and eroded lava channels provide evidence that the widespread smooth plains of Mercury were emplaced at least partly by "voluminous, high-temperature, low-viscosity lavas of mafic to ultramafic composition" (BYRNE ET AL., 2013). However, the typical viscosity of Mercury's lavas is predicted to have increased through time. Decreasing eruption temperatures and degrees of partial melting will have occurred as secular cooling of the planet's interior progressed, forming melts with higher crystal fractions, silica content, and consequently higher viscosities (NAMUR AND CHARLIER, 2017). This suggests that late-stage eruptions may have been more capable of constructing edifices than earlier ones.

Lava viscosity is not the only control on edifice construction. For a given lava viscosity, construction capacity increases with decreasing effusion rate, erupted volume, and flow length, as demonstrated on Earth by the Galápagos shields. These have a break in slope between low-slope flank eruptions and steeper summit eruptions, giving them an 'inverted soup dish' shape, compared with the uniformly shallow flanked Hawaiian shields (NAUMANN AND GEIST, 2000). Since edifice construction on Earth is associated with lower erupted volumes than LIPs in general (BRYAN AND ERNST, 2008), identifying sites of low-volume effusive volcanism on Mercury could be the key to discovering constructional volcanic edifices on its surface.

In this chapter, I describe two small (i.e. <15 km in diameter) positive-relief features with summit depression that are plausibly of volcanic origin. These features were discovered serendipitously but, following a global search of the smooth plains, which represent the last effusions of lava, I found no additional similar features. I compare the morphologies and settings of the candidate volcanic

edifices to volcanoes on Earth and the Moon, and discuss their possible origins, volcanic or otherwise.

5.3   Data and methods

I searched for volcanic edifices using the ~166 m/pixel monochrome MDIS global mosaic *(CHABOT ET AL., 2016)*. Where available, I inspected higher-resolution NAC and WAC images and MLA topographic profiles across candidate volcanic edifices. I made colour observations using the ~665 m/pixel enhanced colour global mosaic *(DENEVI ET AL., 2016)* and RGB-combined WAC images. I used ISIS3 to perform standard radiometric and photometric corrections on the NAC and WAC products. I made RGB-combined mosaics by using 1,000, 750, and 430 nm WAC narrow band filter images in the red, green, and blue channels, respectively *(HAWKINS ET AL., 2007; DENEVI ET AL., 2009)*. The enhanced colour mosaic also uses the 1,000, 750, and 430 nm WAC bands and places the second principal component, the first principal component, and the 430/1,000 ratio in the red, green, and blue channels, respectively *(DENEVI ET AL., 2009, 2016)*. I projected these products into individual sinusoidal projections with central meridians running through their respective geographic centres. This preserves angles and distances at the centre of the projection for small features. I used the 665 m/pixel global stereo digital elevation model (DEM) of Mercury by *BECKER ET AL. (2016)* to investigate the topography of regions of interest, although this dataset has insufficient resolution to characterise features <15 km across well. I analysed these data using Esri ArcMap 10.1 GIS software.

I measured the diameters of my candidate volcanoes using CraterTools *(KNEISSL ET AL., 2011)*, which minimizes projection-related errors when measuring distances. The diameters were calculated from circles that I fitted to the candidate volcanoes using the 3-point method within CraterTools *(KNEISSL ET AL., 2011)*. I measured the height of candidate volcano #1 ('CV1') using shadow-length calculations *(BARNOUIN ET AL., 2012)*. I also derived a profile of CV1 using its shadow shape by employing the method of *BASILEVSKY (2002)* (Fig. 5.2). To do this, I took a NAC frame in which CV1 casts a shadow on an approximately horizontal surface (Fig. 5.2a), rotated the frame by its solar azimuth so that the shadow of CV1 is cast 'up the page' (Fig. 5.2b),

and then I scaled down the image in the direction of the solar azimuth by a factor given by

$$\tan i \pm \tan e \qquad 5.1$$

where *i* and *e* are the solar incidence and spacecraft emission angles, respectively. This expression uses a '+' if the spacecraft is looking back at the surface toward to Sun, or a '–' if the Sun is behind the spacecraft *(BARNOUIN ET AL., 2012)*. In the scaled image (Fig. 5.2c), the distance to the umbral shadow of the candidate volcano cast on a flat surface measured from a point on the terminator of the landform (in the direction of the solar azimuth) returns the elevation at that point (Fig. 5.2d).
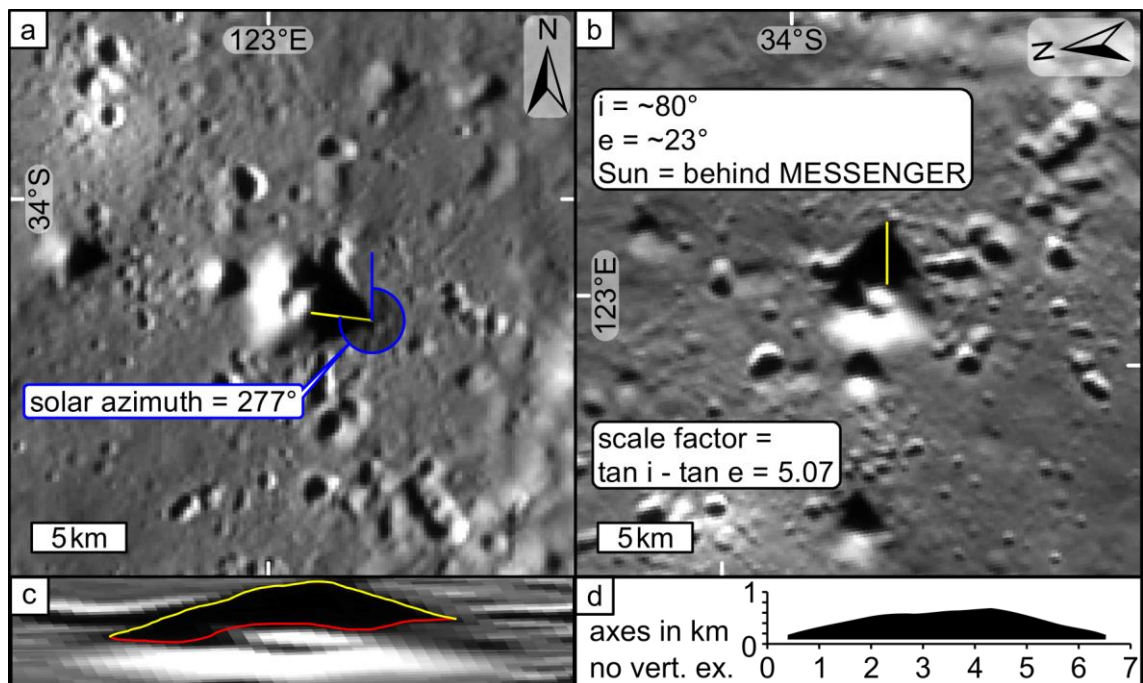
Fig. 5.2 Demonstration of the shadow measurement technique used to make a topographic profile of CV1. (a) MDIS NAC frame EN0251749039M featuring CV1. The solar azimuth (277°) is illustrated with the yellow line. (b) EN0251749039M rotated so that shadows are cast towards the top of the figure (see yellow line). The inputs for equation 5.1 are shown. (c) EN0251749039M after being scaled down vertically by the scale factor given in equation 5.1. The vertical distance between the cast shadow (yellow line) and the corresponding point on the terminator of the landform (red line) returns the elevation at that point on the terminator. (d) Topographic profile of CV1 constructed by measuring the vertical separation between the scaled cast and terminator shadows shown in (c).

MLA data were available to measure the shape of candidate volcano #2 ('CV2'). Following the method used by *KRESLAVSKY AND HEAD (1999)*, I calculated the point-

to-point slopes along the MLA track coincident with the landform. I discarded point-to-point slopes when along profile spacing between the MLA points was more than the normal consecutive shot separation of ~500 m. The calculated flank slope of the landform is the median of the retained point-to-point slopes.

For my comparison with Earth volcanoes, I used Esri World Imagery and the Advanced Spaceborne Thermal Emission and Reflection (ASTER) Global Digital Elevation Map V0002. For the Moon, I used the global Lunar Reconnaissance Orbiter Camera (LROC) WAC 100 m/pixel mosaic, individual LROC NAC frames, and the global Lunar Orbiter Laser Altimeter (LOLA) 60 m/pixel DEM (*CHIN ET AL., 2007; ROBINSON ET AL., 2010; SMITH ET AL., 2010*).

5.4 Results and interpretations

5.4.1 Candidate volcano #1

5.4.1.1 Observations

Candidate volcano #1 ('CV1') is a positive-relief feature, situated within an impact crater (diameter ~125 km; Fig. 5.3a), at 123°02'14"E, 34°07'40"S. When I first observed CV1, its host crater was unnamed, so I applied to the International Astronomical Union for the crater to be named 'Heaney', after the Irish Nobel Laureate, Seamus Heaney. Heaney crater was officially named on 20th March 2017.

CV1 is approximately circular in plan view (Fig. 5.3b) and has a basal diameter of 6.1 km, a height of ~530 m (from shadow calculations), and flank slopes of ~10° (treating it as a simple cone). It is the highest topographic prominence within Heaney and is located 30.5 km from the crater's centre. There is a bowl-shaped depression, 1.7 km across, at the summit of CV1, with a separate depression running up from the base of the northern flank. Based on shadow calculations, the summit depression has a depth-diameter (d/D_{rim}) ratio of 0.14, which is shallower than the d/D_{rim} ratio (0.19) of the fresh impact crater indicated in Fig. 5.3b (see also *FASSETT ET AL., 2017*). The ratio of the summit depression diameter to the basal diameter of CV1 is ~0.28. It is unclear in any existing NAC image whether the summit depression is younger or older than the flank depression. To the west, there are two much smaller knobs that form a straight line with CV1. In enhanced colour (Fig. 5.3c and d), CV1 is surrounded by a diffuse, red colour anomaly, whereas

visible ejecta from impact craters nearby have blue colour signatures. The smaller knobs have no visible colour anomalies.
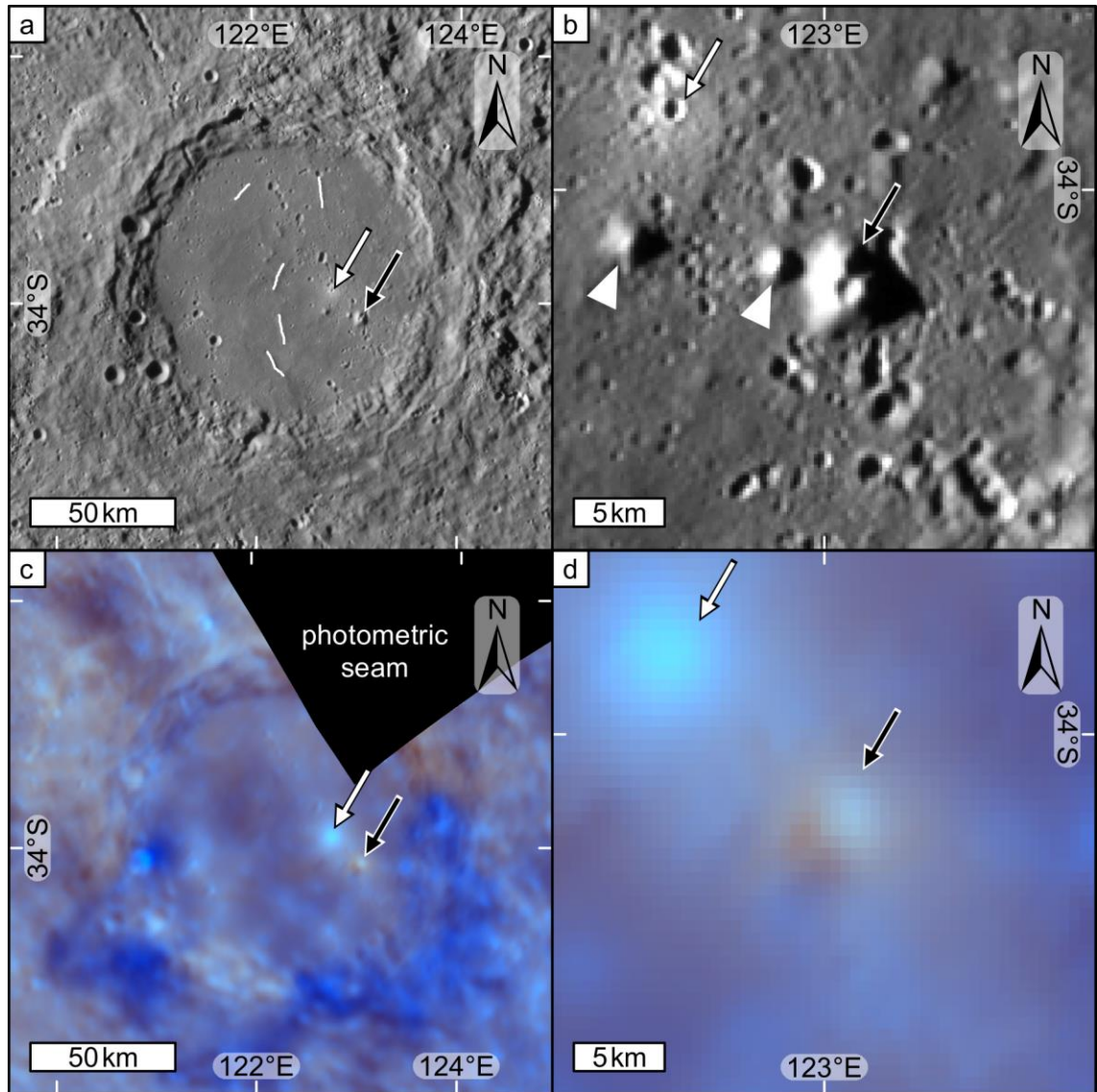
Fig. 5.3 Photogeological and colour observations of CV1. *In all panels, CV1 is indicated with a black arrow, and a nearby, young impact crater is indicated with a white arrow. (a) Location of CV1 within Heaney, a young impact crater nearby, and small wrinkle ridges within the smooth infill (white lines). ~166 m/pixel. (b) Detail of CV1, the young impact crater, and small knobs nearby (white triangles). NAC frame EN0251749039M, 188 m/pixel. (c) Enhanced colour view of Heaney crater. The red colour anomaly associated with CV1. The high-albedo, blue colour anomaly associated with the young impact crater. A portion of the mosaic in the upper-right corner of the figure has been masked out due to a photometric seam. ~665 m/pixel. (d) Detail of the colour anomalies of CV1 and the young impact crater. ~665 m/pixel. All panels show sinusoidal projections centred on 123°E, 34°S.*

Heaney's unburied crater rim is relatively crisp, and the continuous ejecta blanket extends by about one crater diameter beyond the rim, superposing external smooth plains nearby (Fig. 5.4a). Smooth plains with small wrinkle ridges cover the floor of Heaney (Fig. 5.3a), subduing the topographic range within the crater (Fig. 5.4b) compared with craters of this size without smooth plains. There is no evidence that smooth plains material cascaded into the crater from the surroundings. The present-day depth of the crater, measured using the global stereo DEM *(BECKER ET AL., 2016)*, and defined as maximum rim elevation minus minimum floor elevation (ignoring superposing impact craters), is ~3,500 m.

Impact craters on Mercury of the same diameter as Heaney can have a variety of morphologies (Fig. 5.5). Complex craters (50–168 km) have central peaks (Fig. 5.5a), peak-ring basins (84–320 km) have a ring of peaks (Fig. 5.5b), and protobasins (50–195 km) have both a central peak and ring of peaks (Fig. 5.5c; *BAKER AND HEAD, 2013*). Although there is a general trend from complex craters, to protobasins, to peak-ring basins with increasing diameter, the morphologies have overlapping diameter ranges, which requires additional factors during the impact to determine the final crater morphology. Peak-ring basins might form by outward collapse of a transient, gravitationally unstable central peak *(COLLINS ET AL., 2008)*, or by suppression of central peak formation by a thick column of melt nested in the centre of the transient cavity *(CINTALA AND GRIEVE, 1998; BAKER AND HEAD, 2013)*. Protobasins might form when the oversteepened central peak is not large enough to collapse fully, or when the melt volume is insufficient to suppress central peak formation entirely. However, it has been suggested that protobasins form instead when the target substrate is heterogeneous *(HERRICK, 2014)*. The formation of ringed impact basins remains an unsolved issue in planetary science.

The present maximum depth of Heaney (3,500 m) offers some constraint on the crater's original morphology, now obscured by the smooth plains. *BAKER AND HEAD (2013)* showed that the mean d/D_{rim} ratio of complex craters on Mercury (0.034 ± 0.010) is greater than that of protobasins (0.027 ± 0.007), which in turn have a greater mean d/D_{rim} ratio than that of peak-ring basins (0.017 ± 0.006). Using these values and the diameter of Heaney (125 km), its predicted original depth range is 3,000–5,500 m for a complex crater, 2,500–4,250 m for a

protobasin, and 2,050–2,200 m for a peak-ring basin. This suggests that Heaney is too deep to have formed as a peak-ring basin, but it could be a partially infilled protobasin or complex crater. Estimates for maximum thicknesses of the smooth plains in Heaney are 750 and 2,000 m for protobasin and complex crater morphologies, respectively.
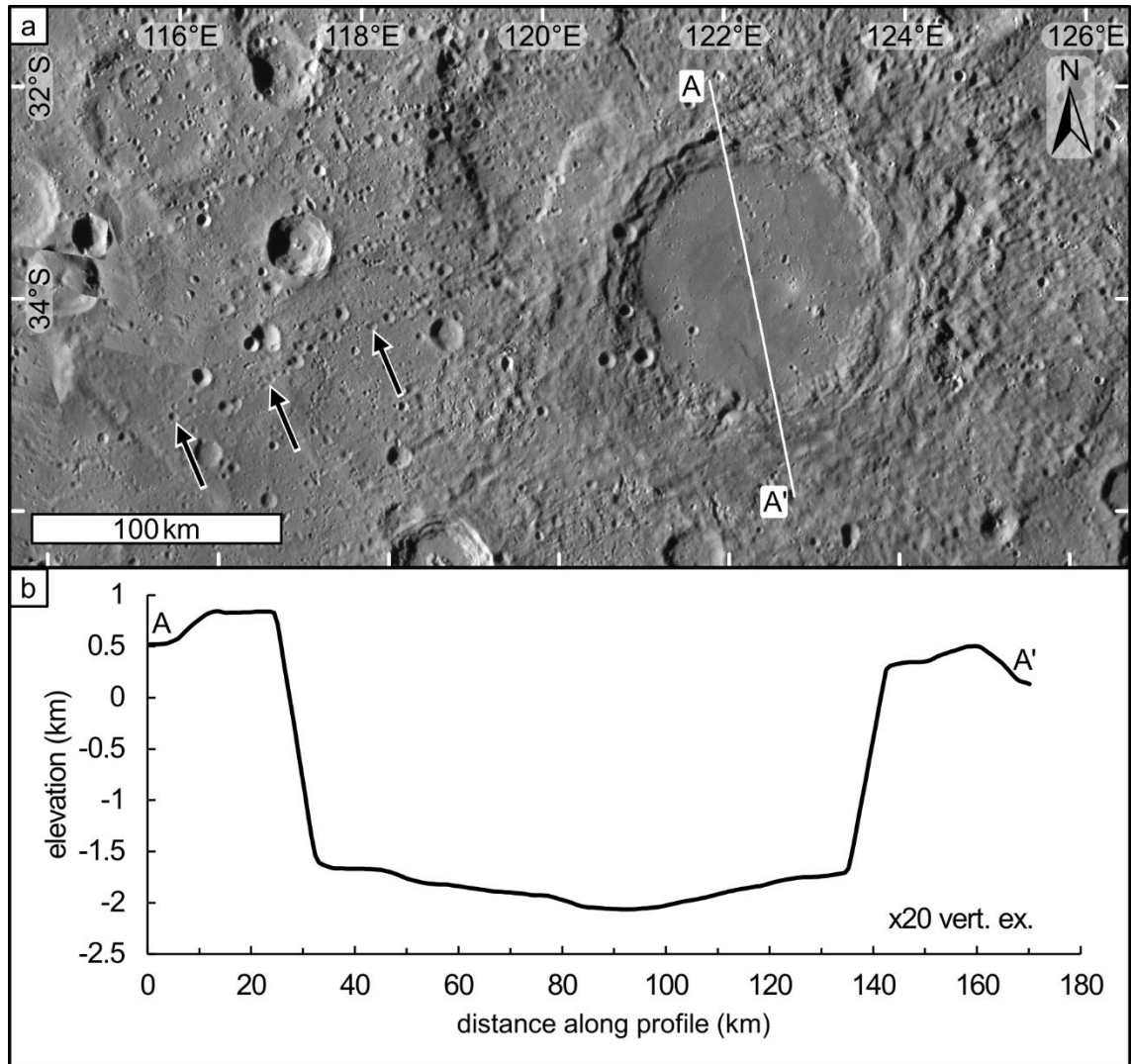
Fig. 5.4 Observations of Heaney crater. (a) Geological setting of the crater. Heaney has a textured ejecta blanket that extends beyond its rim by approximately one crater diameter. The black arrows indicate a secondary impact crater chain attributable to Heaney that superposes nearby smooth plains. The line marked A–A' represents the cross section shown in (b). ~166 m/pixel monochrome mosaic. Sinusoidal projection centred on 123°E, 34°S. (b) The topography of Heaney measured from the global stereo digital elevation of Mercury (BECKER ET AL., 2016). The elevation of the smooth plains monotonically decreases toward the centre of the crater and gives no obvious indication of the presence of any internal uplift (central peak or peak-ring).
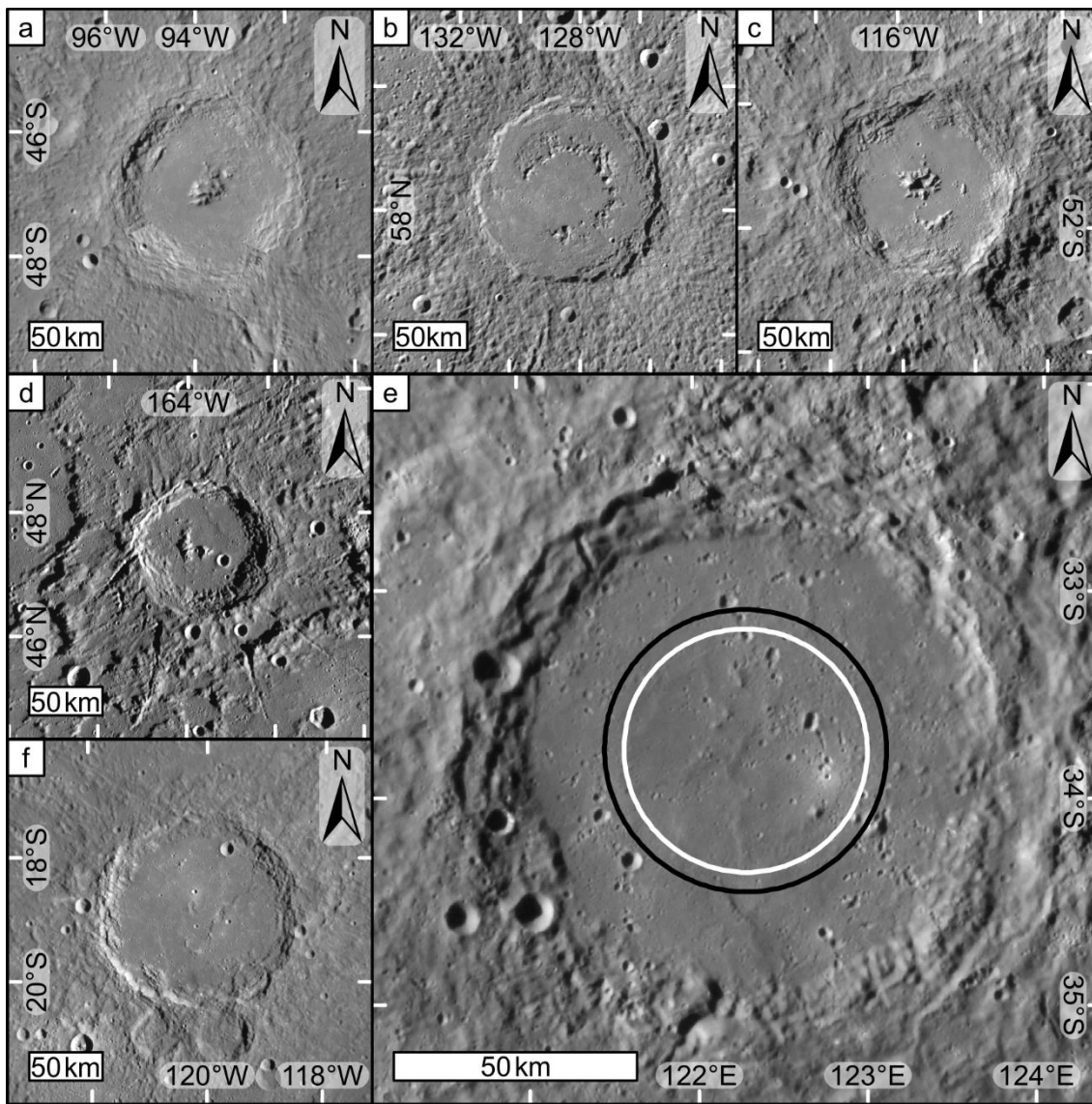
Fig. 5.5 Comparison of Heaney with other impact features on Mercury that are similar in age and size. *(a) Sūr Dās (diameter 131 km), with a central peak rather than a peak-ring. It is therefore possible that Heaney originally had no peak-ring. (b) Ahmad Baba (diameter 126 km), a peak-ring basin. (c) Hawthorne (diameter 120 km), a protobasin. (d) Mansur (diameter 95 km), the degradation state of which defines the base of the Mansurian time system on Mercury. Heaney has a similar degradation state, suggesting that it formed at a similar time. (e) Heaney. The circles represent expected radii of peak-rings for a peak-ring basin (black) and protobasin (white) of similar diameter to Heaney, per equation 5.2. Note that none of the other small knobs in Heaney lie where one would expect to find the highest peak elements. (f) Bello (diameter 139 km), located within Beethoven. Bello has a very similar size, apparent morphology, and degradation state to Heaney. Smooth plains, of probable volcanic origin, obscure any internal peaks that may have been present. All panels are views of the ~166 m/pixel monochrome basemap in individual sinusoidal projections with central meridians through their respective geographic centres.*

In enhanced colour, Heaney crater appears to have exhumed dark blue, low-reflectance material (LRM; *ROBINSON ET AL., 2008*) in its southern rim and ejecta (Fig. 5.3c), whereas its smooth fill corresponds to the surface unit termed low-reflectance blue plains by *DENEVI ET AL. (2009)*. The crater rim is generally blue but appears somewhat redder in the northeast.

5.4.1.2 Impact interpretation

An initial hypothesis for the formation of CV1 is that it is part of Heaney's peak-ring. The relatively undegraded state of the crater and its ejecta superposing smooth plains nearby suggest a late-Calorian/early-Mansurian age for the impact (see Fig. 5.5d; *KINCZYK ET AL., 2016*). The base of the Mansurian is conventionally held to be ~3.5–3.0 Ga *(SPUDIS AND GUEST, 1988)*, although a recent study has revised the base to ~1.7 Ga *(BANKS ET AL., 2017)*. In any case, large-scale effusive volcanism is thought to have ceased long before the Mansurian *(BYRNE ET AL., 2016)*. A crater in this degradation state would ordinarily be expected to host a preserved central peak or peak-ring *(KINCZYK ET AL., 2016)*. If CV1 were a remnant peak-ring element, then its summit depression would merely be a coincidentally superposed impact crater. The northern flank depression can be interpreted as part of a secondary crater chain, of which the summit depression may also be a part. The summit depression's shallow appearance compared with primary craters of similar diameter on the surrounding smooth plains could be due to it being a secondary crater, since these exhibit atypical morphometries compared with primary craters *(STROM ET AL., 2008)*. In addition, the shallowness of the depression might be due to its formation at the apex of a cone, since topographic slopes have been shown to affect impact crater depth *(ASCHAUER AND KENKMANN, 2017)*. If the summit depression is an impact crater, the red colour anomaly associated with the landform could be due to impact ejecta from the summit crater. The smaller knobs to the west of the feature could be other peak-ring elements appearing just above the subsequent infill. The burial of the rest of the presumably once-present peak-ring suggest that the smooth infill is due to flooding by thick volcanic lava, rather than merely the volume of impact melt originally produced *(GRIEVE AND CINTALA, 1992; CINTALA AND GRIEVE, 1998)*. Post-impact volcanism of this kind is a common process that is well-documented on Mercury *(STROM ET AL., 1975; PROCKTER ET AL.,*

2010). Originally, the smooth plains probably had a flat surface, but this will have subsided in the centre, where the fill was originally thickest, producing the concave-up topography within the present-day crater interior *(BLAIR ET AL., 2013)*.

I tested this remnant peak-ring element hypothesis by using the empirical relation between crater rim diameter, D_{rim}, and peak-ring diameter D_{ring}, found by *BAKER ET AL. (2011)* to be given by the relation

$$D_{ring} = AD_{rim}^{p} \qquad\qquad 5.2$$

The values of A and p are empirical constraints that are different for peak-ring basins and protobasins and are given in Table 2 of *BAKER ET AL. (2011)*. Given Heaney's rim diameter of 125 km, its peak-ring radius is predicted by this relation to be ~29 or ~25 km for a peak-ring basin or protobasin morphology, respectively (Fig. 5.5e). Therefore, CV1 is at a radial distance from Heaney's centre (30.5 km) more consistent with the crater being a flooded peak-ring basin than a protobasin.

However, the remnant peak-ring element interpretation is not well supported. As stated previously, my measurements show that Heaney is very deep for it to be an infilled peak-ring basin. Furthermore, it is unclear why the rest of the presumed peak-ring is buried by smooth plains material with no clear surface expression, when CV1 has 530 m of relief. Measurements of the heights of peak-rings on Mercury suggest that it is unlikely that the range of peak element heights in undegraded basins is greater than 500 m *(BAKER AND HEAD, 2013)*. This seems to require: (1) CV1 to be exceptionally tall compared with the rest of the peak-ring, allowing it to have escaped burial; (2) extreme differential erosion of the peak-ring, or; (3) the peak-ring to have been highly incomplete when it formed.

The crater Bello, of comparable diameter, depth, degradation state, and, I therefore interpret, age, also has a floor covered by smooth plains, leaving no trace of any central peak or peak-ring that might once have been present (Fig. 5.5f). This suggests that the floors and peaks of both Heaney and Bello are deeply buried. CV1 is situated toward Heaney's crater wall, where the fill is probably thinnest, yet even the immediately adjacent peak elements that might be expected to be present do not manifest. It seems unlikely that the rest of any peak-ring is buried just beneath the surface, as the wrinkle ridges within the fill do not form a ring marking its

expected location as they can do with buried peak-ring impact craters elsewhere on Mercury *(BAKER ET AL., 2011)*.

After their formation, peak-rings are subject to erosion, which can render them incomplete. Impact craters on Mercury often contain landforms known as 'hollows' that are interpreted to have formed by the loss of a volatile component of the exhumed material to space *(BLEWETT ET AL., 2011)*. There are many examples of impact features on Mercury, similar in age to Heaney, such as Raditladi and Lermontov, that show extensive hollowing *(BLEWETT ET AL., 2013)*. However, it seems unlikely for this process to erode peak-rings entirely since hollows appear to have maximum depths of only several tens of metres *(BLEWETT ET AL., 2011)*, compared with peak elements, which are generally several hundreds of metres high *(BAKER AND HEAD, 2013)*. Furthermore, neither Heaney nor Bello shows evidence of pervasive hollowing in their crater walls (see *THOMAS ET AL., 2014C*), as one might expect if hollowing were responsible for eroding their peak-rings.

The most widespread erosive process on Mercury is impact cratering. In Heaney, there are no impact craters that postdate the smooth plains along the circle where a peak-ring would be expected to be found. Furthermore, it seems unlikely that cratering predating the plains could have removed all but one peak of the ring. There are no 'ghost craters' *(STROM ET AL., 1975)* in the smooth infill suggestive of impact overprinting of an originally complete peak-ring before smooth plains emplacement. Therefore, I believe that erosion of an originally complete peak-ring, by hollowing or impact cratering, is an improbable explanation for the prominence of CV1.

There are other impact crater morphologies, such as protobasin and complex crater, which Heaney could have originally exhibited with implications for the impact interpretation of CV1. The rings of peaks in protobasins on Mercury are lower in height than those of peak-ring basins and are often very incomplete, with no evidence that the missing peak elements were removed after formation *(BAKER AND HEAD, 2013)*, and so could be more easily buried by volcanism. If CV1 is a remnant peak-ring element of an original, incomplete protobasin then, as previously stated, it is at a somewhat greater radial distance from the centre of Heaney than would be expected. Furthermore, the absence of any surface

expression of an accompanying central peak requires the smooth plains to be very thick in the centre of Heaney and much thinner at the edge. The central peaks and peak-rings in protobasins of Heaney's diameter are predicted to be ~1 km high *(BAKER AND HEAD, 2013)*. This would require the smooth plains to be >1 km thick in the centre of Heaney, to bury a central peak, but to be much thinner at the edges, to allow CV1 to remain unburied. This is not inconceivable, given our estimate of the maximum fill thickness for a protobasin (~750 m), but it still requires very specific floor topography and a largely incomplete peak-ring. Finally, as Sūr Dās demonstrates (Fig. 5.5d), it is possible that Heaney did not in fact form with a peak-ring at all, which would require a non-impact-related origin for CV1.

The red colour associated with CV1 could be due to material exhumed from depth as part of a peak-ring. The reddish parts of the crater rim suggest that this is possible. However, if other small knobs within Heaney are interpreted as remnant peak-ring elements, then the fact that they do not appear to have the same colour anomaly would require the peak-ring to be compositionally diverse on short length scales. Furthermore, the colour contact between the low-reflectance blue plains crater infill and the embayed reddish crater rim is sharp, whereas the red colour anomaly associated with CV1 is more diffuse. However, I acknowledge that these knobs occupy only a small number of pixels in available WAC images, meaning their spectral properties may not be sufficiently well characterised by MESSENGER.

5.4.1.3 Volcanic interpretation

If CV1 is not a remnant peak-ring element, then it is plausible that it is a volcanic edifice of some kind. As mentioned previously, the thickness of the smooth infill is suggestive of post-impact volcanic activity occurring within Heaney. The red colour anomaly is similar to those of identified pyroclastic deposits in impact craters elsewhere on Mercury (Fig. 5.6; *THOMAS ET AL., 2014A*). Effusion from a dyke underneath CV1 could have contributed to the smooth volcanic plains that cover the crater floor. A volcanic origin for CV1 avoids the problems outlined above for the impact interpretation. Under this scenario, post-impact volcanism erupted directly from the crater floor, burying the original floor morphology, and CV1 was constructed afterward. The red colour anomaly could be due to pyroclasts that

were deposited by an explosive eruption *(THOMAS ET AL., 2015)* that could have contributed to the excavation of the summit crater. If explosive volcanism did occur, this likely represented the final phase of volcanism in Heaney. The northern flank depression is either part of a coincidental secondary impact crater chain or possibly a primary volcanic structure (see Section 5.5.1). MESSENGER data are insufficient to rule out either of these hypotheses, although I have found no immediately obvious primary impact craters that could be responsible for the northern flank depression.

Elsewhere on Mercury, there is a close association between LRM, which is thought to bear surface-darkening carbon in the form of graphite *(PEPLOWSKI ET AL., 2016)*, and sites of explosive volcanism *(THOMAS ET AL., 2015)*. The LRM evident in the southern rim and ejecta blanket of Heaney suggests that LRM is present beneath the crater (e.g. *ERNST ET AL., 2015*). Carbon is suggested to be an important volatile for driving pyroclastic volcanism on Mercury *(WEIDER ET AL., 2016)*. The relatively red colour of explosive volcanic deposits is thought to be due in part to the removal of dark, spectrally blue carbon from the magma that leaves the remaining deposit redder than the effusive plains around it *(WEIDER ET AL., 2016)*. Concentration of volatiles, such as oxised carbon species, in the magma could result either from evolution in a shallow magma chamber or by assimilation of volatiles from the surrounding crust leading to an explosive eruption *(WEIDER ET AL., 2016)*.
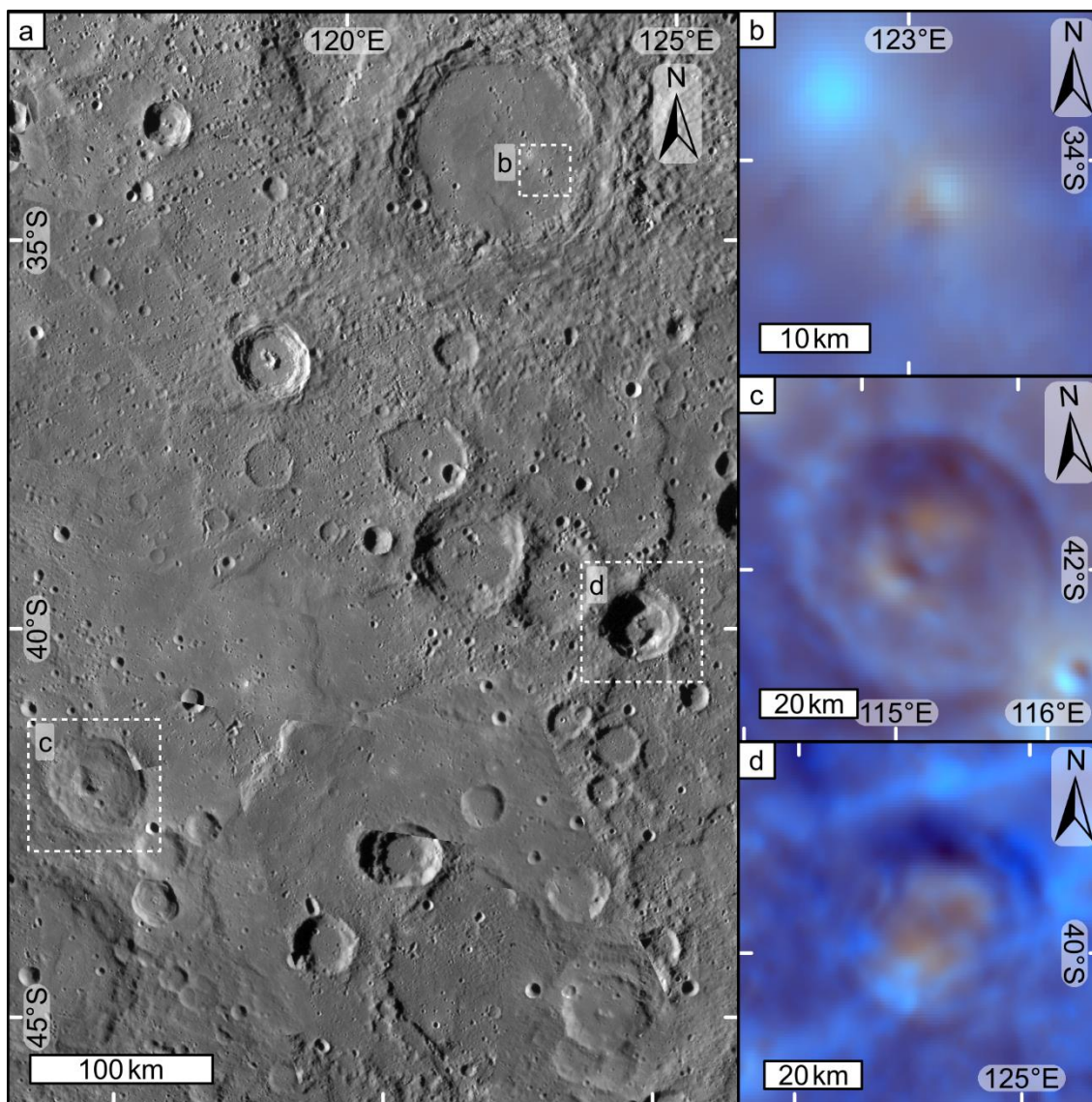
Fig. 5.6 The locations of red colour anomalies near Heaney. *Depressions interpreted as explosive vents are associated with the red colour anomalies in (c) and (d). (a) Context view showing the locations of the colour anomalies (dashed white boxes) in (b–d). ~166 m/pixel monochrome mosaic. (b) Enhanced colour view of the colour anomalies in Heaney. ~665 m/pixel. (c) Red anomaly, interpreted as pyroclastic by THOMAS ET AL. (2014A), within an unnamed crater (at 115.2°E, 42.0°S). ~665 m/pixel. (d) A similar colour anomaly, interpreted as pyroclastic by THOMAS ET AL. (2014A), within an unnamed crater (at 124.6°E, 39.9°S). ~665 m/pixel. All panels show sinusoidal projections centred on 123°E, 34°S.*

However, MESSENGER data are insufficient to establish an unequivocal volcanic origin for CV1. For instance, it is unclear at the available resolution whether CV1 superposes or is embayed by the smooth plains within Heaney. The impact uplift interpretation would be ruled out if CV1 superposes the plains, but if the smooth plains postdate it, then a volcanic origin is not assured. Furthermore, additional

volcanic features (e.g. individual lava flows, a caldera) cannot be seen at CV1. This could be merely due to the lack of resolution, however. For example, identifications of lava flow fronts elsewhere on Mercury based on morphological observations have proven to be equivocal *(HEAD ET AL., 2011; BYRNE ET AL., 2013)*.

The small, red colour anomaly coincident with CV1 is poorly characterised in the available MESSENGER images. Heaney was imaged by WAC (Fig. 5.7) at high incidence angles (>45°) only, which are not ideal for assessing spectral properties, and at low spatial resolution (>600 m/pixel). Under these conditions, nearby Sun-facing slopes, such as parts of the crater wall of Heaney, also appear reddish. I therefore consider the presence of a small explosive volcanic deposit at CV1, supporting its volcanic origin, to be equivocal as the red colour anomaly is plausibly the result of misleading photometric effects. Nevertheless, the smooth infill, interpreted to be the product of post-impact volcanism, makes observations of volcanic colour signatures in the region unsurprising. Moreover, an unequivocal colour anomaly or identified pyroclastic deposit is not prerequisite for CV1 to have a volcanic origin.
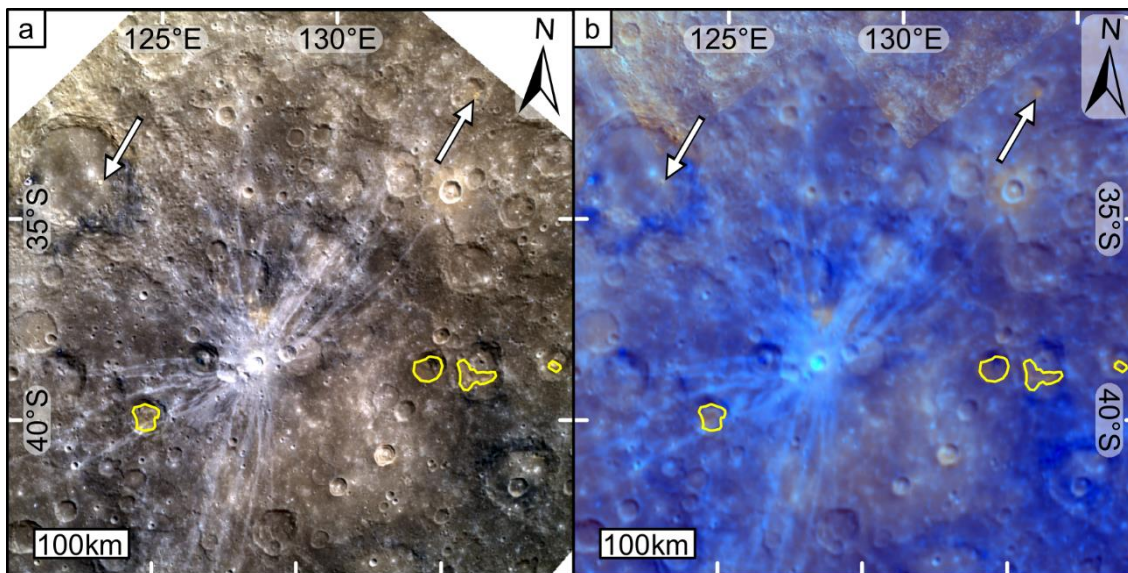
Fig. 5.7 Colour observations of faculae in the region surrounding Heaney. *(a) An RGB-combined colour image featuring faculae previously suggested by* THOMAS ET AL. *(2014A) to be explosive volcanic deposits (yellow outlines) and others not included in that study (white arrows). WAC frames EW1012886465I, EW1012886457G, and EW1012886453F were placed in the red, green and blue channels, respectively. 763 m/pixel. (b) The same view as in (a) but shown in the enhanced global enhanced colour mosaic. The photometric seam masked out in Fig. 5.3c is shown here for completeness. ~665 m/pixel. Both panels show sinusoidal projections centred on 123°E, 34°S.*

5.4.2　Candidate volcano #2

5.4.2.1 Observations

Candidate volcano #2 ('CV2') is located in the northwest of the Caloris basin rim (Fig. 5.8a), at 144°52'24"E, 44°30'49"N, and morphologically resembles CV1 (Fig. 5.8b). MLA data show that it has a convex-up shape and is 12.1 km in diameter, with an elevation above its surroundings of 700 m (Fig. 5.8c). Treating it as a cone, CV2 has an average flank slope of 7°, in close agreement with the point-to-point slope method, which returns a median slope of 8°. Again, there is a summit depression, the internal shadow of which indicates that it is shallower than similarly sized impact craters nearby, as is the case for CV1. The ratio of the summit depression diameter to the basal diameter of CV2 (~0.21) is also similar to that of CV1. Conversely, CV2 has no associated colour anomaly (Fig. 5.9).
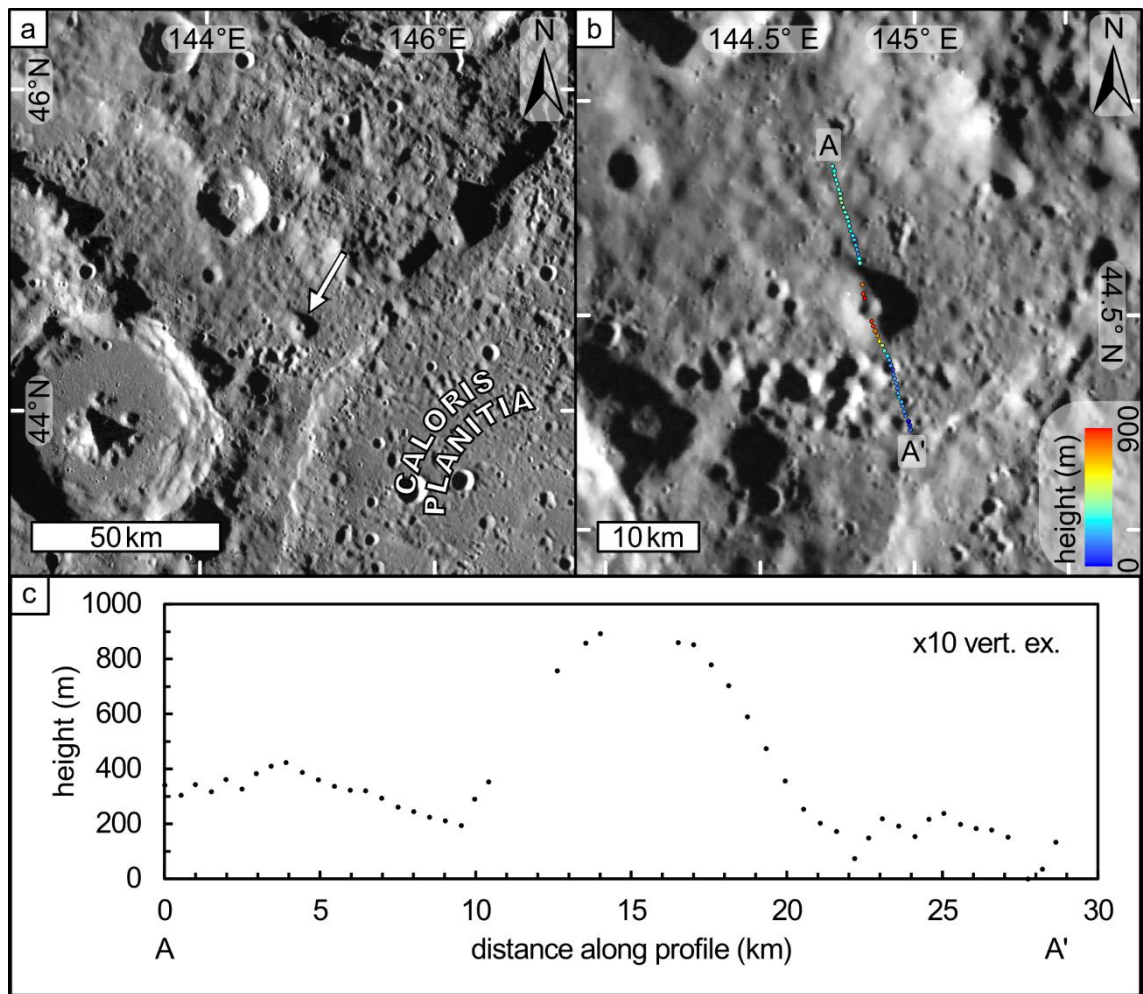
Fig. 5.8 Photogeological and topographical observations of CV2. (a) The location of CV2 (white arrow) 15 km outside Caloris Planitia. ~166 m/pixel monochrome mosaic. Sinusoidal projection centred on 145°E, 44.5°N. (b) A larger-scale view of CV2 with dots marking the locations of MLA data (MLASCIRDRI109302134). The colours indicate the relative elevation. A and A' mark the ends of the topographic profile shown in (c). ~166 m/pixel monochrome mosaic. Sinusoidal projection centred on 145°E, 44.5°N. (c) MLA topographic profile of CV2.
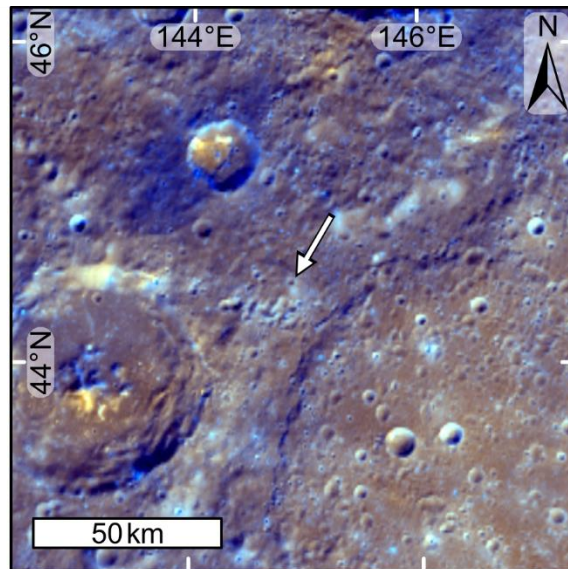
Fig. 5.9 Enhanced colour view of CV2. *CV2 (white arrow) has no associated colour anomaly. ~665 m/pixel. Sinusoidal projection centred on 145°E, 44.5°N.*

5.4.2.2 Interpretation

Other than having a summit depression, CV2 resembles the numerous knobs associated with the Caloris basin (Fig. 5.10a). These 'circum-Caloris knobs' are briefly introduced here, but my full investigation of their origin is contained in Chapter 6. The circum-Caloris knobs are most commonly interpreted as Caloris ejecta blocks, some of which have been embayed by smooth plains *(MCCAULEY ET AL., 1981; DENEVI ET AL., 2009; FASSETT ET AL., 2009)*, although it has been suggested that these features are possibly "small volcanic constructs perhaps directly linked to the emplacement of the circum-Caloris plains" *(FASSETT ET AL., 2009)*. I consider the interpretation of CV2 (Fig. 5.10b) as a volcanic edifice to be a plausible alternative to it being an ejecta block because of its morphological resemblance to CV1. The convex-up 'shield' shape is consistent with a volcanic origin, whereas Caloris rim elements (Caloris Montes) are typically blocky and straight-sided *(MCCAULEY ET AL., 1981; FASSETT ET AL., 2009; ROTHERY ET AL., 2017)*. The Caloris knobs described to the east of Caloris are smaller (i.e. have lower heights and typically smaller diameters) than CV2 *(ACKISS ET AL., 2015)*. Knobs west of Caloris (closer to CV2) have comparable diameters but appear to be characterised by steeper flank slopes (Fig. 5.10c). CV2 is located just 15 km beyond the edge of Caloris Planitia, which was emplaced by smooth plains volcanism *(DENEVI ET AL., 2009)*. The proximity of CV2 to this volcanic province means a volcanic origin for

it must be considered. For example, vents attributed to explosive volcanism are concentrated within about 220 km of the Caloris rim *(MURCHIE ET AL., 2008; ROTHERY ET AL., 2014)* and other impact features on Mercury *(THOMAS ET AL., 2014A)*.
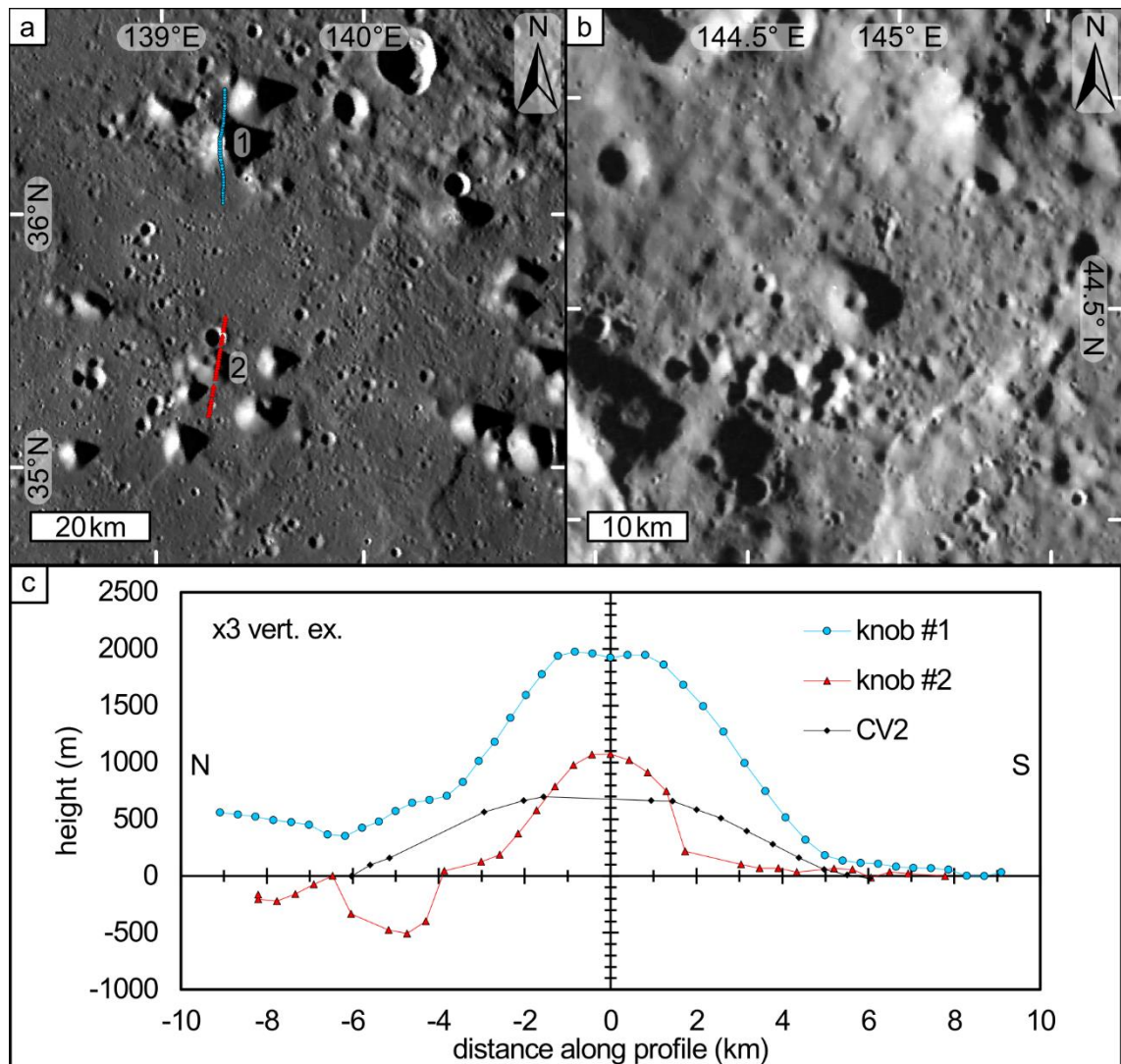
Fig. 5.10 A morphological comparison of CV2 with knobs in the circum-Caloris plains. *(a) An example of typical circum-Caloris knobs. The coloured symbols indicate MLA data points used to construct the profiles shown in (c). Fortuitously placed MLA tracks (knob #1, MLASCIRDR1407230620; knob #2, MLASCIRDR1503132308) cross close to the knobs' peaks. Inspection of the numerous other knobs in this view shows that those crossed by MLA tracks are probably representative of the population as a whole. Mosaic of WAC frames EW0236023591G and EW0235981138G. ~200 m/pixel. Sinusoidal projection centred on 140°E, 35.5°N. (b) CV2 for comparison with the circum-Caloris knobs. ~166 m/pixel. Sinusoidal projection centred on 145°E, 44.5°N. (c) MLA topographic profiles of two knobs shown in (a) as well as CV2. All profiles are aligned N–S and are shown with the same scale and vertical exaggeration. The circum-Caloris knobs have steeper slopes than CV2.*

5.5 Discussion

5.5.1 Comparison with volcanic edifices on other bodies
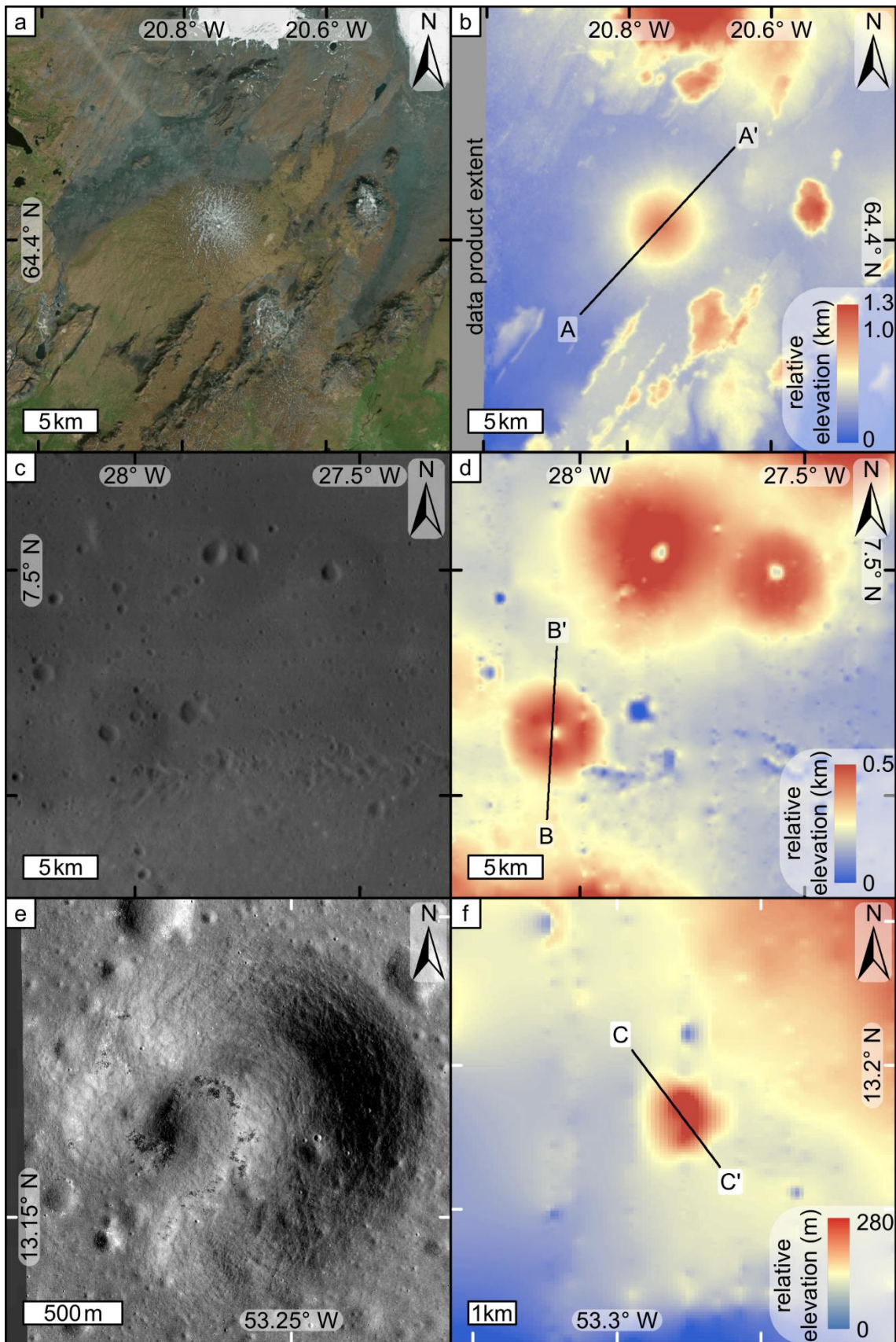
Fig. 5.11 A comparison of select, small volcanic landforms on Earth and the Moon.
(a) Skjaldbreiður, Iceland. Esri World Imagery, ~100 m/pixel. Sinusoidal projection centred on 20.5°W, 64.4°N. (b) The topography of Skjaldbreiður. Same view and projection as in (a). The line marked A–A' indicates the cross section of Skjaldbreiður in Fig. 5.12. ~30 m/pixel. (c) Lunar mare domes in Oceanus Procellarum. 100 m/pixel LROC WAC mosaic. Simple cylindrical projection centred on 0°E, 0°N. (d) Lunar mare dome topography. Same view and projection as in (c). The line marked B–B' indicates the cross section of lunar mare dome Hortensius 5 in Fig. 5.12. ~60 m/pixel. (e) A putative cinder cone in the Marius Hills region on the Moon. Note its smaller size compared with the other volcanoes shown LROC NAC frame M166195459RE, ~43 cm/pixel. Simple cylindrical projection centred on 0°E, 0°N. (f) Marius Hills cinder cone topography. Same projection, but wider context of the view in (e). The line marked C–C' indicates the cross section of the cinder cone in Fig. 5.12. ~60 m/pixel gridded LOLA DEM.

If these landforms are volcanic in origin, then they should compare favourably with other edifices throughout the Solar System that are interpreted as volcanic. Given their sizes, I compare CV1 and CV2 to small volcanic landforms on Earth and the Moon (Fig. 5.11).

There is no evidence that Mercury's lithosphere ever consisted of multiple tectonic plates *(SOLOMON, 1978)*, so other single plate bodies and intraplate settings on Earth provide the most plausible analogues for CV1 and CV2. The most comparable Earth analogues in terms of size are small (<15 km in diameter), monogenetic shields, or cones, such as Mauna Ulu on the Island of Hawai'i *(SWANSON, 1973)*. Even interplate settings, such as Iceland, host monogenetic volcanoes that have formed in a similar manner to Hawaiian examples *(THORDARSON AND LARSEN, 2007)*. Skjaldbreiður (Fig. 5.11a and b) has an axisymmetric shape in plan view, as do CV1 and CV2, and a similar aspect ratio. The main difference between the Mercury landforms and Skjaldbreiður is the relative sizes of the summit craters: Skjaldbreiður has a crater-base diameter ratio of 3.75×10^{-3}, two orders of magnitude fewer than the corresponding ratios of the Mercury landforms. As previously stated, there is some colour evidence for explosive excavation of the summit crater at CV1 that is not evidenced to have occurred at Skjaldbreiður *(THORDARSON AND LARSEN, 2007)*. In any case, eruptions on Mercury are expected

to have featured more vigorous fire-fountaining than those on Earth due to rapid expansion of even a small volatile content within the magma under vacuum *(WILSON AND HEAD, 1981)*. This would allow a wider summit crater to open than might happen on Earth *(KERBER ET AL., 2009)*.

As airless bodies, comparisons of the products of volcanism on the Moon and Mercury are also potentially informative. Lunar mare domes (Fig. 5.11c and d) provide an instructive comparison for the Mercury candidate volcanoes. These landforms are low domes and are interpreted as small (<20 km in diameter) shield volcanoes *(HEAD AND GIFFORD, 1980)*. They are generally located toward the edges of the lunar maria or close to the edges of mare-hosting impact basins *(MCGOVERN AND LITHERLAND, 2011)*. The lunar maria frequently feature sinuous rilles, landforms that suggest that these plains were emplaced by high-effusion-rate lavas, with the mare domes thought to have formed toward the end of maria emplacement as effusion rates waned and lava flow lengths decreased *(WÖHLER ET AL., 2006)*.

As with the Mercury landforms, mare domes are generally circular and host summit craters that are shallower than impact craters of similar diameter *(HEAD AND GIFFORD, 1980)*. Lunar mare dome summit craters are also larger than the terrestrial equivalents with one example, named Hortensius 5, within Mare Insularum, having a crater-base diameter ratio of ~0.33, much closer to those of the Mercury examples than Skjaldbreiður. The large sizes of the lunar mare dome summit depressions have been attributed to magma withdrawal from the conduit, causing the vent to collapse *(WÖHLER ET AL., 2006)*, and to the vigorous nature of eruptions into a vacuum *(HEAD AND GIFFORD, 1980)*. Both of these mechanisms can explain the large summit diameters of the candidate volcanoes on Mercury. If explosive activity did occur at CV1, as the colour data suggest, then this may have contributed to the large size of the summit depression. At CV2, where there is no colour evidence of an explosive volcanic deposit, magma withdrawal may have been the chief driver of summit depression enlargement.

Although mare domes have lower heights and shallower flank slopes than the prospective volcanoes on Mercury, this disparity can be explained by Mercury's higher surface gravity than the Moon. Stronger surface gravity leads to a less dispersed fire fountain where pyroclasts and spatter fall closer to the vent *(KERBER*

ET AL., 2009), resulting in a steeper edifice. Furthermore, there are steeper putative volcanic constructs on the Moon in the Marius Hills region. Here there are steep domes (6–7° slopes) and cones (up to 17° slopes) with summit craters (Fig. 5.11e and f) that are interpreted as constructs of varying degrees of lava and pyroclasts, superposed on lunar mare material *(WEITZ AND HEAD, 1999; S. J. LAWRENCE ET AL., 2013)*. The domes are spectrally indistinct from the mare material, suggesting that eruption mechanics, rather than magma composition, are responsible for the switch from lava plains emplacement to shield construction. Cones in the Marius Hills often superpose steep domes, indicating that they are the youngest volcanic forms in the region. These are interpreted as cinder cones that formed from terminal strombolian eruptions as the eruption rate waned further. Most of the Marius Hills cones are C-shaped in plan view, possibly due to flows that overtopped the summit crater rim at its lowest point, eroding the cone walls *(S. J. LAWRENCE ET AL., 2013)*. It is possible that this cone morphology is analogous to the northern flank depression of CV1. Other Marius Hills cones do not have such a gap, which makes them more similar to CV2 in appearance. The main difference between the Marius Hills cones and the candidate volcanoes on Mercury is size. The Marius Hills cones are generally 1–2 km across, whereas CV1 and CV2 have diameters of ~6 and ~12 km, respectively. These diameters correspond more closely to those of lunar mare domes interpreted as shield volcanoes, although these features are not as steep as the Mercury landforms. Both the candidate volcanoes on Mercury I have described here have flank slopes intermediate between lunar shield volcanoes and lunar cinder cones (Fig. 5.12). This apparent discrepancy can be explained if the landforms on Mercury are composite volcanoes constructed by the accumulation of both lava and pyroclasts *(HEAD, 1975; DAVIDSON AND DE SILVA, 2000)*.
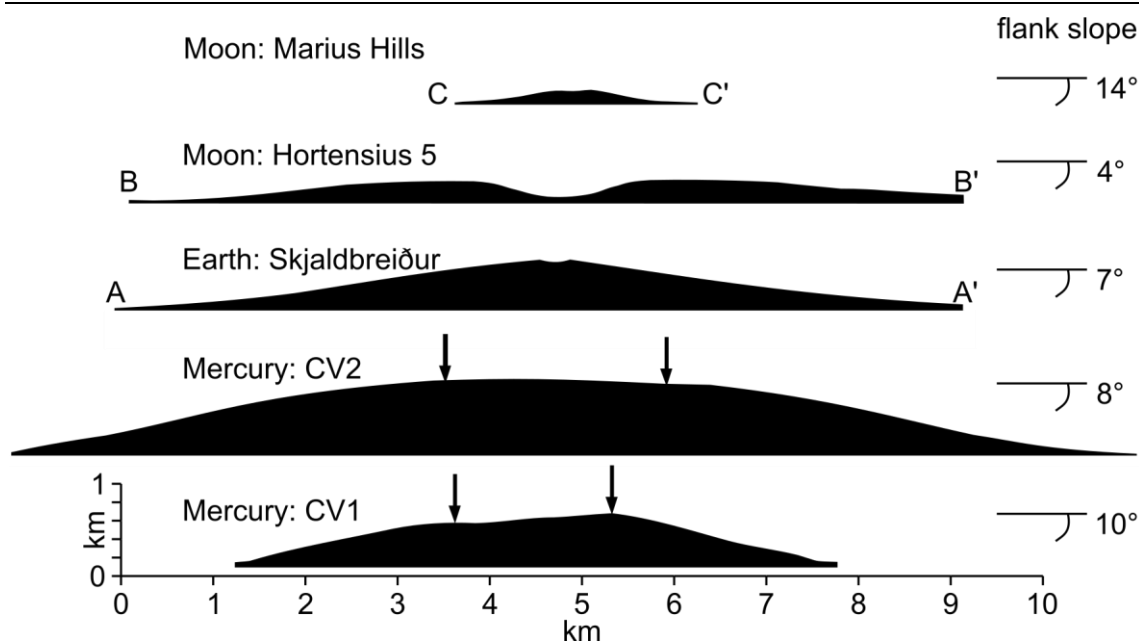
Fig. 5.12 Comparisons of Mercury candidate volcanoes with small, volcanic landforms on Earth and the Moon. *The black arrows indicate the extent of the summit depressions in each example where the topography of the depression cannot be resolved. The Mercury landforms have sizes comparable to an Icelandic shield volcano, and slopes intermediate between the examples of shield volcanoes and a lunar cinder cone shown here. No vertical exaggeration.*

5.5.2 Edifice construction on Mercury

Whether or not CV1 and CV2 are volcanic edifices, it is apparent that Mercury's characteristic eruptive style during its early history overwhelmingly generated widespread volcanic plains, akin to LIPs on Earth, with edifice construction occurring either very rarely or not at all. Borealis Planitia and the Caloris smooth plains, believed to represent the most recent, large-scale effusive activity, have model ages of ~3.7 Ga *(HEAD ET AL., 2011; DENEVI ET AL., 2013; OSTRACH ET AL., 2015)*. Shortly after this time, at about 3.5 Ga, large-scale effusive volcanism on Mercury appears to have ceased across the planet *(BYRNE ET AL., 2016)*. This cessation was probably in response to magma ascent pathways being closed by global contraction *(SOLOMON, 1978; WILSON AND HEAD, 2008; BYRNE ET AL., 2016)*. As cooling and contraction of Mercury's interior continued after the end of widespread effusive volcanism, magma is predicted to have stalled at ever increasing depths beneath the planet's surface *(MENAND ET AL., 2010; MACCAFERRI ET AL., 2011)*. However, impacts remove overburden, promote uplift, temporarily reset the pre-existing

stress regime, propagate fractures *(KLIMCZAK, 2015)*, and deposit heat *(ROBERTS AND BARNOUIN, 2012)*, all of which could facilitate the generation and extraction of magma from the subsurface *(BYRNE ET AL., 2016)*. Therefore, impact craters that formed a sufficiently short time after the end of large-scale effusive volcanism on Mercury are arguably more likely than other locations to host late-stage volcanism.

I therefore propose a sequence of events that led to the formation of CV1 that is both consistent with my observations and explains the paucity of constructional edifices on the planet in general (Fig. 5.13). The late-Calorian/early-Mansurian appearance of Heaney crater means it probably formed toward the end of, or after, large-scale effusive volcanism on Mercury, but probably when crustal magma intrusion was still occurring (~3.5 Ga; *BYRNE ET AL., 2016*). Post-impact volcanism has been recognised in impact features elsewhere on Mercury dating from this time period or later *(PROCKTER ET AL., 2010; BLAIR ET AL., 2013)*. Crustal storage and intrusion permitted the melt to become more evolved (thus increasing magma viscosity) and/or assimilate crustal volatiles *(THOMAS ET AL., 2015)*. Due to the effects of impacts listed above, the crater was filled by late-stage, post-impact effusive volcanism. The erupted volumes of this post-impact volcanism were much lower than during the emplacement of the extensive smooth plains on Mercury because magma stored locally beneath the impact site only could be mobilised. This is similar to the small volumes of magma mobilised from shallow magma chambers theorised to form the domes and cones of the Marius Hills *(HEATHER ET AL., 2003)*.
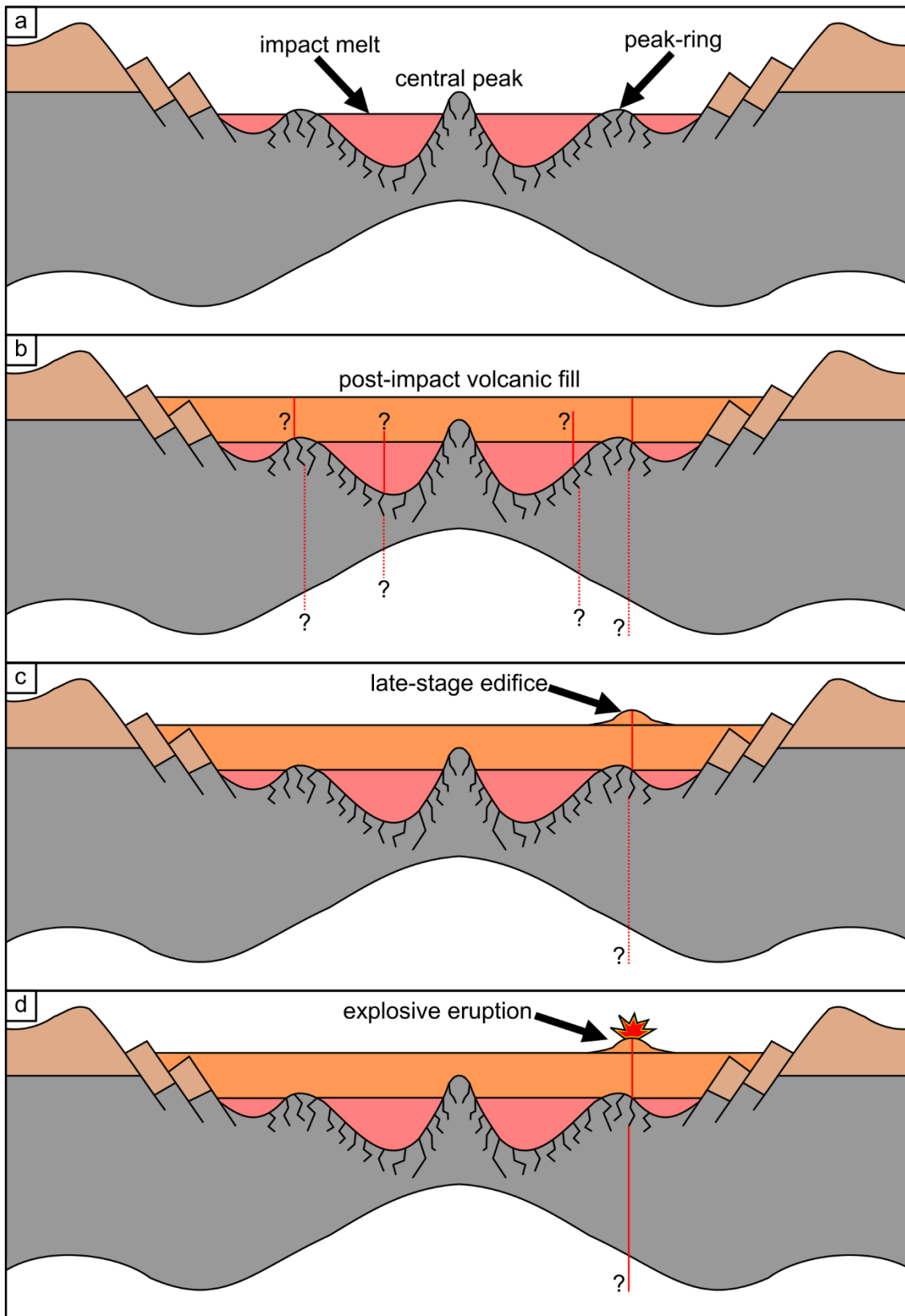
Fig. 5.13 Conceptual formation model of CVI. Heaney is shown as a protobasin, based on evidence discussed in Section 5.4.1.2. This model would also apply to a complex crater morphology. (a) Heaney formed as a crater with a peak-ring after the end of large-scale effusive eruptions on Mercury, but before magmagenesis in the subsurface was inhibited due to secular cooling of the planet's interior. The impact propagated fractures within, and temporarily reset the compressive regime of, the crust. (b) A small volume of mantle-derived magma was liberated from subsurface storage by exploiting fractures opened by the impact. Eruptions may have occurred at multiple locations onto the crater floor. (c) As geological time progressed, the stress regime within the crater became increasingly horizontally compressive, such that later eruptions were concentrated at a single, final location. If Heaney did form with a peak-ring, then deep fractures associated with this structure might have facilitated the ascent of late-stage magmas. CVI was built as a result of these late-stage, small-volume eruptions from a point source. (d) When the magma rise rate became critically low, it is possible that a switch to an explosive eruptive style occurred due to the concentration of volatiles in the magma, causing a terminal deposition of pyroclasts. Cartoon not to scale.

To begin with, eruptions may have occurred at multiple locations within Heaney, but the peak-ring area could have been favoured by the presence of high-angle, deep, bounding normal faults *(KENKMANN ET AL., 2014)*. Lunar mare domes, for example, are also associated with such structural features *(HEAD AND GIFFORD, 1980)*, and explosive vents within craters on Mercury also cluster toward peak elements *(THOMAS ET AL., 2015; JOZWIAK ET AL., 2018)*. Following the initial post-impact volcanism, the effusion rate slowed as Mercury's global horizontally compressive stress regime began to reassert itself. Evidence for this effect comes in the form of small, young lobate scarps elsewhere on Mercury *(WATTERS ET AL., 2016)*. Heaney's smooth infill could be accommodating strain due to Mercury's stress regime similarly, since the infill contains possible incipient wrinkle ridges. Alternatively, these ridges may have formed due to natural subsidence of the smooth infill, evidenced to have occurred to some degree by Heaney's concave-up interior topography (Fig. 5.4b). Subsidence could drive shallow folding and thrust faulting, resulting in wrinkle ridge formation *(BLAIR ET AL., 2013)*. In either case, the stress regime within Heaney would be expected to have become increasingly

horizontally compressive following the impact. If the reassertion of such a stress field upon the interior of Heaney were geologically rapid, then any post-impact volcanism must have commenced relatively quickly after the impact. This is a plausible scenario, since no ghost craters are in the smooth infill of Heaney, suggesting that little geological time passed between crater formation and volcanic infilling. The increasingly horizontally compressive stress regime closed magma ascent pathways until eruptions were concentrated at a single vent at the location of CV1. The lower effusion rate, small erupted volume, and single source vent led to the construction of a prominent volcano toward the end of this sequence. Construction may have been enhanced by the erupted lavas having higher crystallinity, lower eruption temperatures, and more evolved compositions *(NAMUR AND CHARLIER, 2017)* than typical plains-forming lavas on Mercury. Eventually, the effects of the impact that had mobilised the magma diminished and effusion ceased. The final eruption(s) occurred in the style of other explosive eruptions elsewhere on Mercury: the exsolution of volatiles concentrated in the magma by subsurface evolution and/or crustal assimilation caused the last melt to ascend rapidly from depth, leading to a final phase of explosive volcanic activity before the extinction of the volcano *(THOMAS ET AL., 2015)*. This last phase of explosive volcanism must have been short-lived and was possibly a single event of sufficiently small scale to explain the correspondingly small size of the resultant pyroclastic deposit compared with other faculae on Mercury *(THOMAS ET AL., 2014A)* and the preservation of the constructional edifice. No observations I have made of Heaney crater require that significant intervals of geological time separate the impact event, the burial of the crater floor by smooth plains, the construction of the edifice, or the final explosive eruptive phase. Therefore, based on studies of post-impact volcanism elsewhere on Mercury *(PROCKTER ET AL., 2010; CHAPMAN ET AL., 2012; FERRARI ET AL., 2015)*, I tentatively suggest that this whole sequence of events was completed in under 100 million years.

It may be that CV2 formed in a similar manner. In this case, toward the end of the emplacement of the Caloris plains, late-stage, low-volume eruptions ascended along a fracture associated with the rim of the Caloris basin. The known explosive vents within Caloris Planitia are within 220 km of the edge of the basin *(THOMAS ET AL., 2014A; BESSE ET AL., 2015)*. Sites of young lunar volcanism are also

concentrated toward the edges of the lunar maria *(HEAD AND GIFFORD, 1980)*. This is thought to be due to the magma ascent-enhancing stress state found at mare basin margins. Lithospheric loads, such as the lunar maria or Caloris Planitia, can cause extension in an annulus close to the edge of the load, assisting magma ascent *(MCGOVERN AND LITHERLAND, 2011)*. Furthermore, small-volume magmas might preferentially erupt close to the edge of Caloris Planitia, where the basin-filling lavas are thinnest, since their overburden stresses would pose the least obstacle to magma ascent there *(ROTHERY ET AL., 2014)*.

The fact that few prospective constructional volcanic edifices have been reported on Mercury is important. Any small constructional volcanic edifices that do exist on Mercury probably represent only a fraction of those that ever formed, since edifices are subject to erosion, particularly due to destruction by subsequent impacts. However, numerous small volcanic constructs exist on the Moon *(HEAD AND GIFFORD, 1980)*, which has had a similar history of impact erosion to Mercury *(FASSETT AND MINTON, 2013)*, indicating that if small-scale edifice construction is widespread enough, evidence that it occurred can survive billions of years of geological time. On this basis, I argue that edifice construction on Mercury must have been highly spatiotemporally constrained throughout its geological history, assuming such construction occurred at all. I suggest that the scarcity of candidate volcanic edifices on Mercury is not a product of their removal by erosion but instead reflects the limited availability of small-volume, short flow length, high-viscosity eruptions. Eruptions of this kind appear to have been very unusual, since volcanism during Mercury's early history primarily formed widespread plains. Large-scale effusive volcanism came to a geologically abrupt end globally ~3.5 Ga, most likely in response to global contraction *(BYRNE ET AL., 2016)*. This contrasts with the more protracted decline of effusive volcanism on the Moon *(HIESINGER ET AL., 2000)*, which could explain the dearth of volcanic edifices on Mercury.

The first candidate edifice I have described may have been able to form due to the small erupted volume of material capable of ascending into an impact crater post-dating large-scale effusive volcanism. This is similar to how monogenetic volcanoes on Earth and other terrestrial planets are thought to form from small volumes of lava. Assuming Heaney has the minimum diameter required to extract small-

volume melts, I conservatively estimate that there are ~26 impact features on Mercury of sufficient size and youth to host constructional edifices (Table 5.1). Other than Heaney, none of these appears to host edifices with summit depression similar to the candidates I have described here, but they may host less topographically pronounced domes that cannot be identified using MESSENGER data.

My second candidate edifice could be the result of final, small melt volumes erupting toward the end of the emplacement of the Caloris smooth plains, similar to the formation of lunar mare domes after most of the mare basalts were emplaced.

5.6   Conclusions

To date, no constructional volcanic edifices have been unambiguously identified on Mercury. I have appraised two positive-relief landforms on the planet as candidate constructional volcanic edifices, although I cannot rule out non-volcanic hypotheses for their origins with MESSENGER data. My interpretations for these two candidate volcanic edifices lead me to conclude that: (1) volcanic edifices could be found in other impact craters that formed shortly after the end of widespread effusive volcanism on Mercury, controlled by impact-related fractures in the subsurface; (2) edifices are unlikely to be found toward the centre of thick volcanic plateaus, as magmas capable of forming edifices are better able to ascend to the surface through the reduced overburden and favourable stress fields at the edge of plateaus *(MCGOVERN AND LITHERLAND, 2011)*, and; (3) edifices are not expected to be found in more ancient impact craters that formed when large-scale plains emplacement was still occurring globally, as the erupted volumes and effusion rates are predicted to be too high. No edifices have, to date, been recognised in the smooth plains within the Beethoven basin, for example, or other pre-Calorian impact basins and craters *(FASSETT ET AL., 2012)*.

Crater name	Crater diameter (km)	lat., long. (°, +ve east)
Heaney	125	-33.77, 122.29
Unnamed	125	-70.65, 48.50
Ahmad Baba	126	58.33, 231.65
Stravinsky	129	51.95, 281.10
Zeami	129	-2.96, 212.59
Sūr Dās	131	-46.98, 266.43
Chopin	131	-65.45, 236.60
Sousa	138	46.69, 0.63
Bello	139	-18.87, 239.82
Joplin	139	-38.56, 25.51
Verdi	145	64.36, 190.29
Sayat-Nova	146	-27.98, 237.30
Magritte	149	-72.78, 121.63
Alver	151	-66.97, 77.25
Lermontov	166	15.24, 311.06
Nabokov	166	-14.56, 55.76
Derain	167	-9, 19.70
Aksakov	174	34.71, 281.26
Strindberg	189	53.41, 233.33
Larrocha	196	43.29, 290.17
Steichen	196	-12.79, 77.04
Rustaveli	200	52.41, 82.74
Vivaldi	213	13.76, 274.08
Mozart	241	7.75, 169.41
Raditladi	258	27.15, 119.06
Rachmaninoff	305	27.66, 57.37

Table 5.1 Impact features that are at least as young and large as Heaney. These impact features are good candidate hosts of post-impact volcanism that may have constructed low volcanic edifices. They are good targets for high-resolution observations by BepiColombo.

Although MESSENGER data are sufficient to search for features such as those I have described here, the arrival of the BepiColombo spacecraft *(ROTHERY ET AL., 2010)* will enable a new search for prospective small volcanoes on the innermost planet. High-resolution (approaching 5 m/pixel), stereo (~50 m/pixel), and multispectral images *(BENKHOFF ET AL., 2010)* will enable more detailed observations of the surface, facilitating the search for additional volcanoes on Mercury, such as low domes or cones without large summit craters, should they be present. BepiColombo will also be able to test the origin, volcanic or otherwise, of the two landforms described here.

CHAPTER 6
THE CIRCUM-CALORIS KNOBS: LONG-LIVED POST-DEPOSITION MODIFICATION OF CALORIS EJECTA BLOCKS

6.1   Introduction

During the course of my search for constructional volcanoes on Mercury, I encountered the circum-Caloris knobs. These landforms appear to be peculiar to the area surrounding the Caloris basin, and during the preparation of this thesis two competing hypotheses for their formation existed; either by volcanism or as impact ejecta. In this chapter, I introduce the Caloris basin and all the relevant details pertaining to the circum-Caloris knobs (Section 6.2). Following the background details about Caloris, I explain the data and methods I used to study the circum-Caloris knobs (Section 6.4). My results include the first map of the distribution of circum-Caloris knobs >5 km in diameter (Section 6.5.3), detailed observations of their geomorphology (Section 6.5.1) and topography (Section 6.5.5). I discuss the implications of my observations and measurements of the circum-Caloris knobs for their formation and evolution in Section 6.6.1. I conclude that the circum-Caloris knobs are not volcanic edifices, but instead Caloris ejecta blocks. However, the present-day conical shapes of the blocks requires them to have been modified after their original emplacement. I suggest that conical shapes can be achieved and maintained on these ancient landforms only by an advective transport process, such as slope failure, rather than a diffusive erosive process, such as impact gardening (Section 6.6.1.1). Post-impact modification of the knobs might be controlled in part by volatile-loss from their interiors, making these knobs an unrecognised landform formed by a hitherto undescribed process on the surface of Mercury. If so, they would also provide support for a volatile-rich (sulfur/carbon-bearing species in greater than lunar concentrations) deep interior of Mercury.

6.2 The Caloris basin

The Caloris basin (~1,550 km in diameter) is the largest preserved impact structure on Mercury *(MURCHIE ET AL., 2008)*. The associated Caloris Group *(MCCAULEY ET AL., 1981)* consequently contains diverse geology (Section 6.2.1). The Caloris basin is also associated with widespread smooth plains (Section 6.2.2) both within (Caloris Planitia) and without (circum-Caloris plains) it.

6.2.1 The Caloris Group

The Caloris Group (Fig. 6.1) contains the Caloris Montes Formation, the Nervo Formation, the Van Eyck Formation, and the Odin Formation. These formations were imaged by Mariner 10 and are considered to have formed as a result of the Caloris impact *(MCCAULEY ET AL., 1981)*. Since the Odin Formation is characterised by the circum-Caloris knobs, which are the focus of this chapter, it is introduced separately, and in greater detail, in Section 6.2.3.

6.2.1.1 Caloris Montes Formation

The Caloris Montes Formation (Fig. 6.1a) is interpreted as the uplifted rim of the Caloris basin. Typically, the Caloris Montes Formation consists of "a jumbled array of smooth-surfaced but highly segmented rectilinear mountain massifs" *(MCCAULEY ET AL., 1981)*. The formation takes its name from the formally named 'Caloris Montes' that make up the eastern rim of the basin imaged by Mariner 10. When MESSENGER imaged the entirety of the basin during its first flyby *(MURCHIE ET AL., 2008)*, the Caloris Montes Formation was also identified at the western rim of the basin, leaving its definition and interpretation unchanged in the MESSENGER-era. Now that it is has been imaged in full, it is apparent that the Caloris Montes Formation is discontinuous around the circumference of the Caloris basin, which has posed some difficulty in determining the rim position and its diameter *(FASSETT ET AL., 2009)*. The Caloris Montes Formation is more continuous and better exposed in the north and southeast than it is in the west *(GOOSMANN ET AL., 2016; KINCZYK ET AL., 2018B)*.
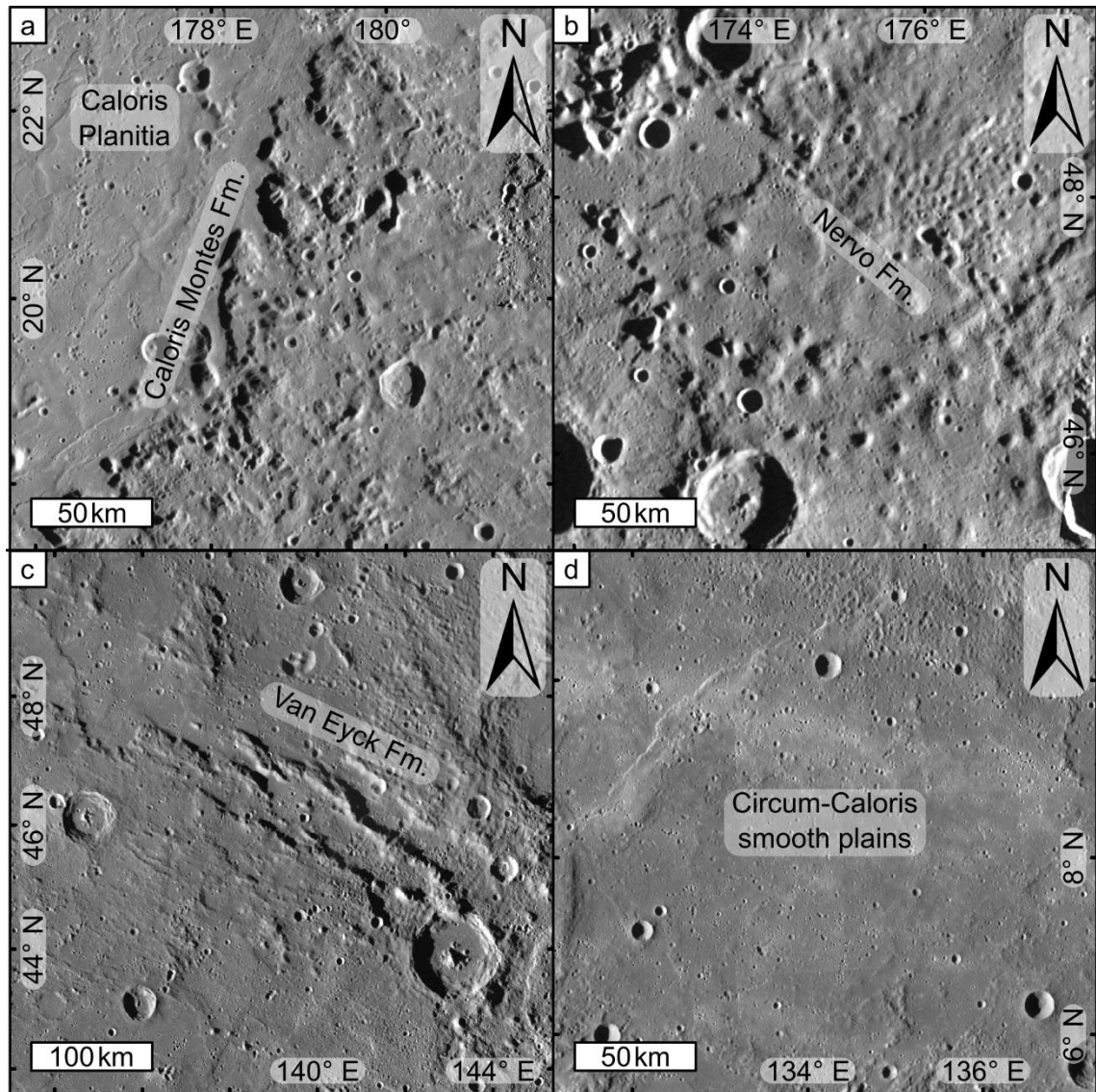
Fig. 6.1 Caloris Group formations. *(a) The Caloris Montes Formation constitutes the rim of the Caloris basin. Caloris Planitia is a region of smooth plains within the Caloris basin. (b) The Nervo Formation appears to be Caloris ejecta mantling the Caloris rim and other surrounding materials. (c) The Van Eyck Formation constitutes scour and lineaments radial to Caloris. (d) The circum-Caloris smooth plains appear to postdate the Caloris impact. All panels show a Mercator projection centred on 167.2°E, 31.5°N of the ~166 m/pixel global monochrome mosaic.*

6.2.1.2 Nervo Formation

The Nervo Formation (Fig. 6.1b), originally the 'intermontane plains' *(TRASK AND GUEST, 1975)*, is characterised by "rolling to locally hummocky plains that lie in inter-massif depressions" *(MCCAULEY ET AL., 1981)*. These plains were observed to drape Caloris Montes Formation massifs, and appeared to lie at elevations above the surroundings. The Nervo Formation was interpreted as fallback ejecta that has

covered some parts of the Caloris basin rim *(TRASK AND GUEST, 1975)*. After the arrival of MESSENGER, some doubts about the observations of the Nervo Formation made using Mariner 10 data were raised. Following the first MESSENGER flyby, no unambiguous exposures of the Nervo Formation as defined above were made, even where MESSENGER data overlapped with identification of the Nervo Formation in Mariner 10 data *(FASSETT ET AL., 2009)*. The three explanations offered for this problem were: (1) Nervo Formation happens to be more poorly exposed in western Caloris (imaged by MESSENGER) compared with eastern Caloris (imaged by Mariner 10); (2) Nervo Formation defined on the basis of Mariner 10 data is actually part of other plains units interior and exterior to the Caloris basin, and; (3) Nervo Formation cannot be resolved in MESSENGER flyby data of the western Caloris rim *(FASSETT ET AL., 2009)*. Subsequent orbital MESSENGER observations have revealed Nervo Formation in western Caloris, although it is poorly exposed in the same regions where Caloris Montes Formation is poorly exposed *(GOOSMANN ET AL., 2016; KINCZYK ET AL., 2018B)*, which suggests exposure of both formations is controlled by the same factors. The Nervo Formation continues to be interpreted as Caloris fallback ejecta that has mantled high-standing regions around its rim, including the Caloris Montes Formation *(GOOSMANN ET AL., 2016)*.

6.2.1.3 Van Eyck Formation

The Van Eyck Formation (Fig. 6.1c), originally 'Caloris lineated terrain' *(TRASK AND GUEST, 1975)*, is considered by *MCCAULEY ET AL. (1981)* to consist of a lineated facies and a secondary crater facies. The lineated facies, which is located proximal to the Caloris rim, is made of radial ridges and grooves that were interpreted to have formed as ballistically emplaced ejecta mixed with pre-basin bedrock *(MCCAULEY ET AL., 1981)*. The secondary crater facies contains numerous secondary crater chains attributable to the Caloris basin *(MCCAULEY ET AL., 1981)*. Both facies of the Van Eyck Formation were identified around the whole of the Caloris basin after MESSENGER's first flyby *(FASSETT ET AL., 2009)*. Radial lineations were observed to transition into the rims of craters in chains, indicating that the lineated and secondary crater facies of the Van Eyck Formation are related and not fully separable *(FASSETT ET AL., 2009)*. The Van Eyck Formation appears to have formed

due to scouring of the pre-impact landscape by Caloris ejecta. This resulted in the sculpted landscape observable today. Impact sculpture radial to Caloris has been observed from the basin rim to over one basin diameter beyond the rim *(FASSETT ET AL., 2009)*.

6.2.2 Smooth plains

As mentioned previously, the Caloris basin is associated with two extensive regions of smooth plains (Chapter 5, Fig. 5.1). The smooth plains that occupy the interior of the basin constitute Caloris Planitia and have buried the basin's original floor (Fig. 6.1a). Smooth plains are found around the outside of the Caloris basin too (informally referred to as the 'circum-Caloris plains'; Fig. 6.1d). Collectively, I refer to Caloris Planitia and the circum-Caloris smooth plains as the 'Caloris smooth plains' and their mutual relationship is discussed in *ROTHERY ET AL. (2017)*. The Caloris smooth plains were initially thought to be volcanic in origin *(TRASK AND GUEST, 1975)*, however at the time when Mariner 10 data were being analysed, results from Apollo 16 indicated that the smooth Cayley Formation (or lunar light plains) were impact ejecta, rather than volcanic lavas *(EGGLETON AND SCHABER, 1972)*. The smooth plains on Mercury, as imaged by Mariner 10, resembled the Cayley Formation, which raised the possibility that some or all of Caloris Planitia and the circum-Caloris plains could be a mixture of impact melt and fluidised impact ejecta *(WILHELMS, 1976)*.

At the time of the first MESSENGER flyby, the debate about the impact or volcanic origin of the smooth plains on Mercury was ongoing. MESSENGER data were used to conclude the debate and established a volcanic origin for most smooth plains on Mercury. Important observations that favour a volcanic origin for the Caloris smooth plains include: the identification of candidate volcanic vents within Caloris Planitia *(HEAD ET AL., 2008)* and the circum-Caloris plains *(BYRNE ET AL., 2013)*; Caloris smooth plains appear to embay the Caloris Montes Formation *(FASSETT ET AL., 2009)*; the Caloris smooth plains have distinct colour signatures from Caloris Group formations *(MURCHIE ET AL., 2008)*, and; multiple studies have shown that the Caloris smooth plains have a younger crater retention age than the Caloris Montes Formation *(FASSETT ET AL., 2009; DENEVI ET AL., 2013; MANCINELLI ET AL., 2016)*.

The established volcanic origin for the Caloris smooth plains raises some further questions, including the matter of the amount of time that passed between the impact and the beginning of post-impact eruptions. There are no ghost craters ≥10 km in diameter within Caloris Planitia. This probably means that either Caloris Planitia is so thick that all craters that formed on the original floor of the Caloris basin are so deeply buried that they have no surface manifestation as ghost craters or that post-Caloris eruptions began shortly after the Caloris impact *(ERNST ET AL., 2015)*.

Another important question about the Caloris smooth plains is whether the circum-Caloris smooth plains, or the smooth plains of Caloris Planitia formed first. Some crater size-frequency distribution studies have suggested that the circum-Caloris plains have fewer superposed craters, and are therefore the younger of the two *(STROM ET AL., 2008; FASSETT ET AL., 2009)*.

6.2.3   The Odin Formation and the circum-Caloris knobs

The Odin Formation (Fig. 6.2a) is the most enigmatic formation within the Caloris Group. It was originally called 'hummocky plains' *(TRASK AND GUEST, 1975)* and was later described as consisting of kilometre-scale knobs (Fig. 6.2b) with intervening smooth plains *(MCCAULEY ET AL., 1981)*. Similar to the Van Eyck Formation, the Odin Formation extends away from the Caloris rim by approximately one basin diameter, but it is more widespread proximal to the rim. In Mariner 10 images, the Odin Formation resembles the Alpes Formation, associated with Imbrium on the Moon *(MCCAULEY ET AL., 1981)*. The Odin Formation was interpreted as high-angle, late-arriving ejecta, with blocks, which have been subsequently embayed by volcanic smooth plains *(MCCAULEY ET AL., 1981)*.

However, MESSENGER-era studies of the Odin Formation raised doubts about its origin as Caloris impact ejecta. The Odin Formation appears to have a younger crater retention age than the Caloris Montes Formation *(FASSETT ET AL., 2009)*. If the Odin Formation did form as Caloris ejecta, then it should have the same crater size-frequency distribution as the Caloris Montes Formation, since the uplifted basin rim and ejecta were generated in the same geological instant. This result has led some workers to suggest that the Odin Formation has different crater

production/retention properties from smooth plains *(DENEVI ET AL., 2013)*. Others have suggested that the Odin Formation must have a volcanic origin and that its low crater density is due to its formation postdating the Caloris impact.

A further enduring difficulty with the Odin Formation is that its Mariner 10 definition refers to both characteristic knobs and intervening smooth plains *(MCCAULEY ET AL., 1981)*. No threshold spatial density of knobs has been prescribed in order to distinguish smooth plains with incidental knobs and exposed Odin Formation *(ROTHERY ET AL., 2017)*. As a result, mappers of the Caloris smooth plains were forced to use approximate or gradational contacts between the smooth plains and the Odin Formation *(DENEVI ET AL., 2013)*.
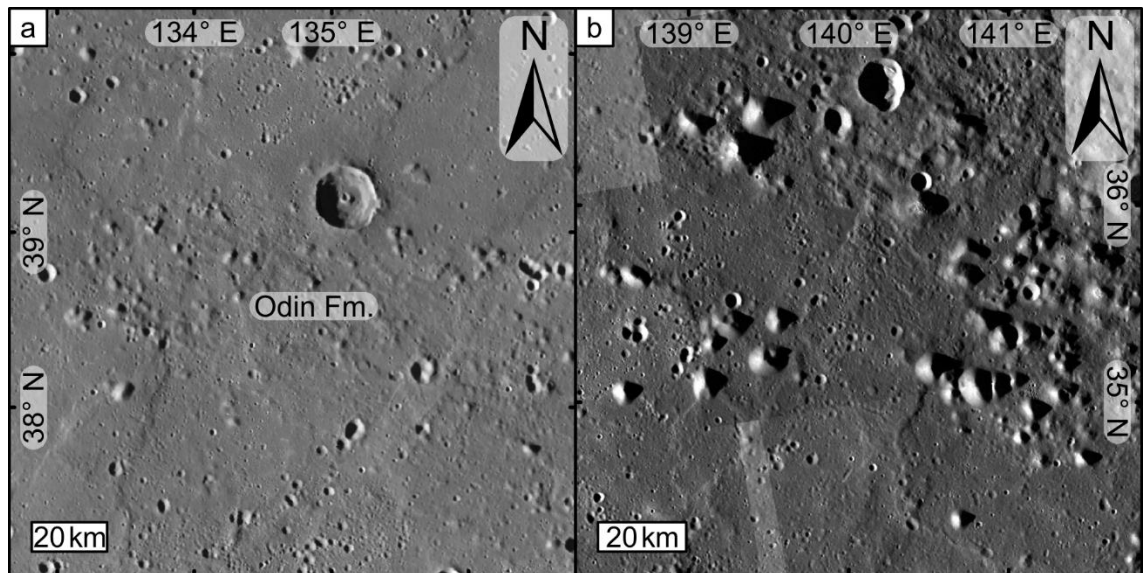
Fig. 6.2 The Odin Formation and the circum-Caloris knobs. *(a) The Odin Formation is the knobby material occupying an east–west strip in the centre of this panel. (b) Examples of larger circum-Caloris knobs proximal to the Caloris rim. Both panels show Mercator projections centred on 167.2°E, 31.5°N of the ~166 m/pixel global monochrome mosaic.*

Interpretations of the circum-Caloris knobs themselves depend on the interpretation of the Odin Formation, which they help define. If the relatively young crater size-frequency distribution of the Odin Formation compared with the Caloris impact leads us to draw the conclusion that the Odin Formation is volcanic in origin, then the circum-Caloris knobs might be small, volcanic constructs *(FASSETT ET AL., 2009; MANCINELLI ET AL., 2016)*. On the other hand, if the Odin Formation is interpreted as a Caloris ejecta facies, then the circum-Caloris knobs

could be either volcanic constructs or remnant Caloris ejecta blocks. *ACKISS ET AL. (2015)* mapped the locations of the circum-Caloris knobs proximal to northeast Caloris. They used shadow-length measurements to calculate the heights of the knobs. They found that the spatial density and height distribution of the knobs is most consistent with their emplacement as Caloris ejecta that was subsequently embayed. However, their study did not map knobs west of Caloris or knobs >600 km from the basin rim at any azimuth.

6.3   Aims and objectives

In this study, I aimed to investigate the origin of the Odin Formation and the circum-Caloris knobs. In particular, I aimed to establish wheher any circum-Caloris knobs are volcanic constructs or if they are all Caloris ejecta. I also hoped that this study would inform the debate about the young crater size-frequency distribution of the Odin Formation.

To do this, I set out to map the locations of the circum-Caloris knobs and make detailed observations of their appearances, contexts, slopes and shapes.

6.4   Data and methods

6.4.1   Photogeological observations of knobs

I used the ~166 m/pixel global MDIS monochrome mosaic to map the locations of circum-Caloris knobs. I mapped the locations of all knobs ≥5 km in diameter. I chose to implement a threshold diameter since knob frequency is strongly anti-correlated with diameter. I quickly established that it would not be feasible to map the locations of knobs <5 km in diameter and also guarantee that the resultant catalogue would be complete.

I used a Mercator projection focussed on the centre of the Caloris basin (162.7°E, 31.5°N) to map the knobs using ArcMap 10.1. I chose this projection because it conserves angles, and thus shapes, over the whole projection. Furthermore, north is toward the top of this projection at all longitudes, which is a property that I knew would simplify my data processing (see Section 6.4.2.2). However, this projection does distort distances, such that at latitudes far away from the latitude of origin (31.5°N) the apparent sizes of objects in the projection are distorted (Fig. 6.3).

Initially, when I measured knob diameters in order to categorise them for my map, I made my measurements using the ArcMap Measure Tool in 'geodesic' mode, which makes distance measurement corrections based on the projection being used. Final knob diameter measurements were made using the three-point circle digitisation functionality in CraterTools *(KNEISSL ET AL., 2011)*. For this method, I selected three points on each knob's perimeter and a circle was digitally fitted to these points. The projection-independent diameter of each circle fitted to a knob was recorded as the diameter of that knob.

I mapped the circum-Caloris knobs in a point feature class. Landforms that I confidently identified as circum-Caloris knobs were included in this feature class along with more ambiguous landforms that in my view conceivably could be unrelated landforms. Some knobs <5 km in diameter were also included in this feature class. This is because many knobs were mapped before I implemented the 5 km diameter threshold. Furthermore, I found it instructive to illustrate regions around Caloris where knobs are abundant but not many are ≥5 km in diameter. Had I excluded these knobs, then my map of the distribution of the knobs would have been misleading. As a result, my catalogue of the circum-Caloris knobs is practically complete for knobs ≥5 km in diameter, but contains many, but by no means all, knobs <5 km in diameter. I felt that this compromise would capture a more informative representation of the distribution of the circum-Caloris knobs. These three knob types (certain, uncertain, <5 km) were given corresponding distinguishing attributes that allowed me to symbolise them differently and separate them as required.
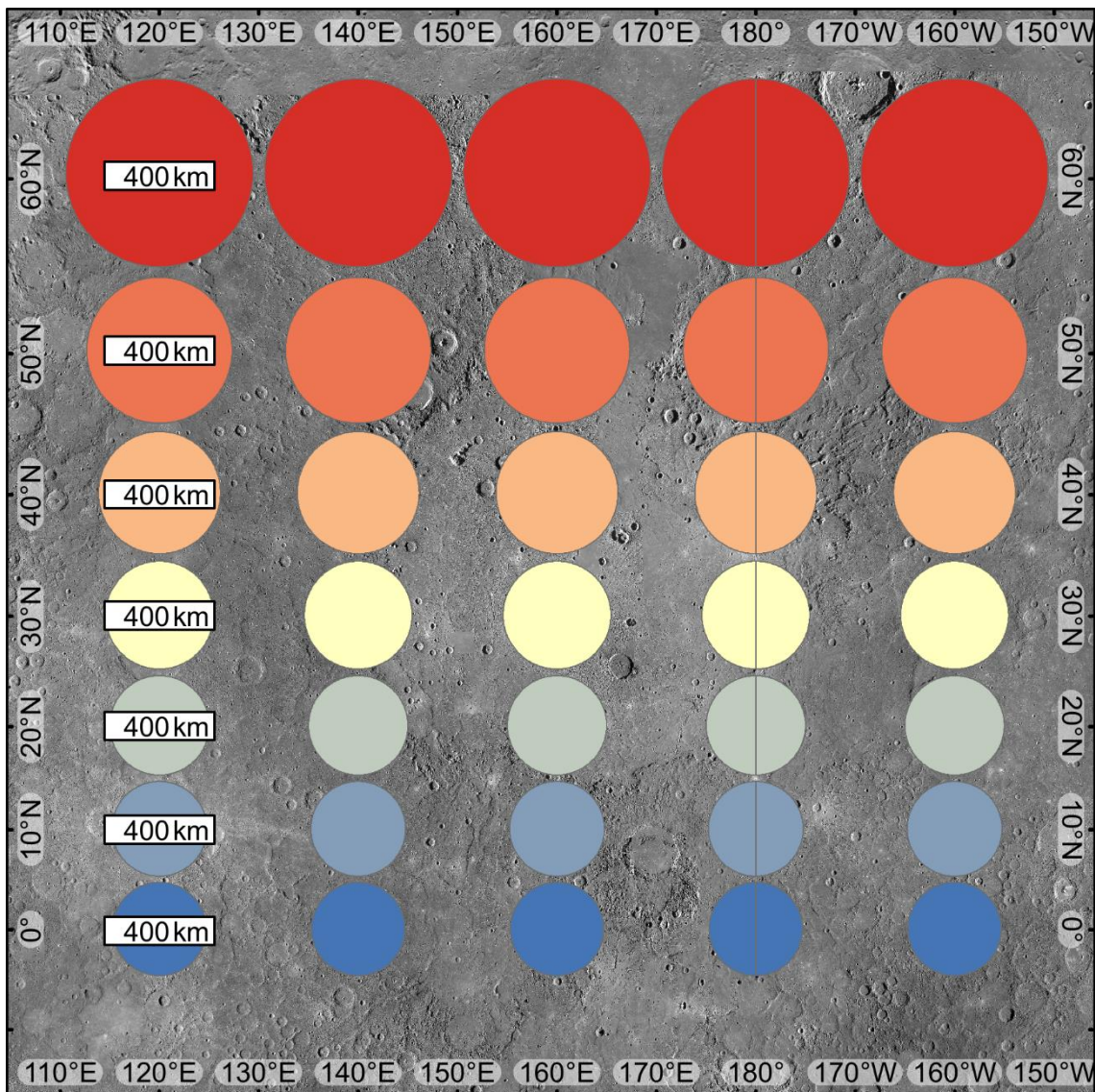
Fig. 6.3 Tissot's indicatrices of deformation for the Mercator projection used throughout this chapter. *The Mercator projection I used when mapping and measuring the circum-Caloris knobs: central meridian 162.7°E, standard parallel 31.5°E. The coloured shapes represent the size and shape distortion of theoretical impact craters, all 400 km in diameter, by the projection at different latitudes and longitudes. All the shapes are circles, since Mercator projections are conformal and preserve shapes. However, only the circles at 30°N, i.e. close to the projection's standard parallel (31.5°N), would be measured as 400 km in diameter using the linear scale bar. The circles at 60°N have apparent diameters of ~680 km, which is ~17× true scale. The circles at Mercury's equator have apparent diameters of ~350 km, which is ~0.87× true scale.*

In order to make photogeological observations of individual knobs, I searched the Planetary Data System (PDS) for MDIS NAC images (with higher spatial resolutions than the ~166 m/pixel global mosaic) that captured knobs ≥5 km in

diameter. The best images for making photogeological observations have spacecraft emission angles close to 0° (Fig. 6.4) and solar illumination angles around 68° *(CHABOT ET AL., 2016)*. I focused on gathering images that met these additional criteria, but when this was not possible I prioritised the highest resolution images. With these images I observed the shapes and surface textures of the knobs in order to gain insight into their origin and evolution.

6.4.2 Topographic measurements of knobs

In order to quantify my photogeological observations of the circum-Caloris knobs, I measured topographic profiles of them using two methods: MLA-derived topography and shadow-derived topography.

6.4.2.1 MLA-derived knob topography

MLA tracks cover the northern hemisphere of Mercury with increasing density toward high northern latitudes *(CAVANAUGH ET AL., 2007; ZUBER ET AL., 2012)*. As Caloris is situated at mid-northern latitudes, I considered the possibility of MLA data coverage of the circum-Caloris knobs to be a very important resource for measuring knob topography. After I completed my map of all the circum-Caloris knobs ≥5 km in diameter, I used the MLA footprint shapefile to search for MLA data tracks that sample the maximum height of knobs. I prioritised MLA data tracks that traversed knobs in the direction of steepest ascent/descent, so that I could use them to measure the flank slopes of knobs. MLA data are archived as tab-separated variable (.tab) files on the Mercury Orbital Data Explorer (http://ode.rsl.wustl.edu/mercury/indexDatasets.aspx).

I downloaded the MLA data for knob-intersecting tracks and converted them to point feature classes for visualising in ArcMap. I did this by using the ArcCatalog 10.1 'Create Feature Class From XY Table' functionality. The inputs required for this functionality are a table of X- and Y-coordinates and their coordinate system. Since the MLA data tables store the locations of the measured points on the surface of Mercury as latitude and longitude pairs, I imported these data as a geographic coordinate system for Mercury (with radius 2,440 km) and used longitudes as X-coordinates and latitudes as Y-coordinates. Z-coordinates can also be generated, so I included the corresponding MLA measurements of Mercury's planetary radius

as the Z-coordinate. Once this processing was complete, I rendered the new point feature classes for each knob in ArcMap.

MLA data tables contain abundant information in addition to the locations and elevations of measured points on the surface, including a measure of the signal-to-noise ratio of the laser pulse return recorded by the spacecraft, which is stored as an integer from 0 (best) to 9 (worst; *CAVANAUGH ET AL., 2007*). MLA data with a channel value of ≤4 were retained, and where multiple returns for the same MLA pulse were recorded, the planetary radius measurement with the quality channel closest to 0 was prioritised. For each MLA point feature class, I selected the elevation data points with the best available quality channels (always ≤4) that lie on a knob, with a few extra points each side of the knob to guarantee the outermost extent of each knob would be retained, using the 'Select by Attributes' function in ArcMap. I exported this selection as a new feature class.

For each of these new feature classes, I calculated the projected map coordinates (units of metres, rather than degrees) of each data point. I used trigonometry to calculate the along profile distance for each point. I then plotted point height vs along profile distance to generate topographic profiles for each knob with MLA data. From these profiles, I used a modification of the point-to-point method (*KRESLAVSKY AND HEAD, 1999*: see Chapter 5) to calculate flank slopes of their respective knobs. The modification and justification are given in Section 6.4.2.2.

6.4.2.2 Shadow-derived knob topography

MLA data were unavailable for most knobs. In order to measure the topography of more knobs than just those with MLA data I decided to use shadow length measurements. Shadow length measurements have been widely deployed on multiple planetary bodies for calculating the heights and depths of landforms (*BASILEVSKY, 2002; BARNOUIN ET AL., 2012)*, particularly where digital elevation models generated from laser altimetry or photogrammetry have been unavailable.

Basic shadow length measurements estimate the maximum height of a shadow-casting landform by exploiting the trigonometric relationship between the length of a landform's shadow cast on a horizontal plane and the height of the landform (Fig. 6.4; *BARNOUIN ET AL., 2012*).
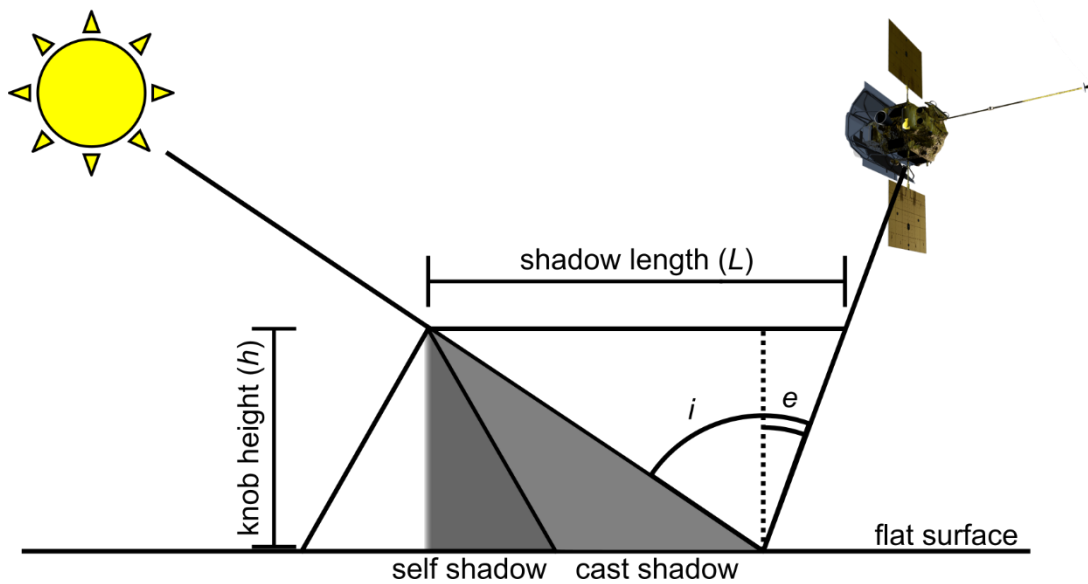
Fig. 6.4 Cartoon of shadow calculation key variables. *i = solar incidence angle. e = spacecraft emission angle. L = length of shadow measured in an image with known illumination conditions. h = knob height, the quantity to be calculated. This cartoon illustrates a positive spacecraft emission, where the spacecraft is looking back toward the Sun. Negative emission angles occur when the Sun is behind the spacecraft. In this cartoon, the Sun, knob and spacecraft are in the same vertical plane. When this is the case, the sum of the incidence angle and emission angle equals the phase angle, φ. Modified from* BARNOUIN ET AL. *(2012). MESSENGER graphic credit: NASA/Johns Hopkins University Applied Physics Laboratory/Carnegie Institute of Washington.*

The height of a landform, h, is given by:

$$h = \frac{L}{\tan i \pm \tan e} \qquad\qquad 6.1$$

where L is the length of the shadow measured from the summit of the landform in the direction of solar illumination, i is the solar incidence angle and e is the spacecraft emission angle. Off-nadir images contain distortions caused by the perspective from which such images were captured. Ideally, emission angle distortions would be removed by producing orthorectified images where image pixels are fixed to their true location on the surface elevation of the planet. This results in the horizontal scale of the orthorectified image being constant. However, this would require a local DEM for each knob image with comparable resolution to its image. Currently, such high-resolution DEMs are largely unavailable for

Mercury. Instead, MDIS images are projected onto a 'flat' sphere approximating Mercury's overall shape. This is achieved by fixing a number of points only in each image onto the sphere, leaving the intervening pixels 'stretched' into position such that the spatial scale across the image is not constant. As such, distortions resulting from the original image perspective remain and have to be accounted for in the shadow length-height relationship. The full derivation of this relationship is shown in *BARNOUIN ET AL. (2012)*.

Since I sought to determine the flank slopes of the circum-Caloris knobs, I decided to employ the method of *BASILEVSKY (2002)*. Rather than employing equation 6.1 on a single shadow length measurement, this method applies a scaling factor derived from the equation to an image of known illumination. The scaled shadows can then be digitised to make topographic profiles of the landforms in the image, as I did in Chapter 5. Here, I modified the method by instead rotating and scaling digitised outlines of the shadows cast by knobs in MDIS frames (Fig. 6.5). By avoiding rotating images, I reduced the computational intensity of this method.
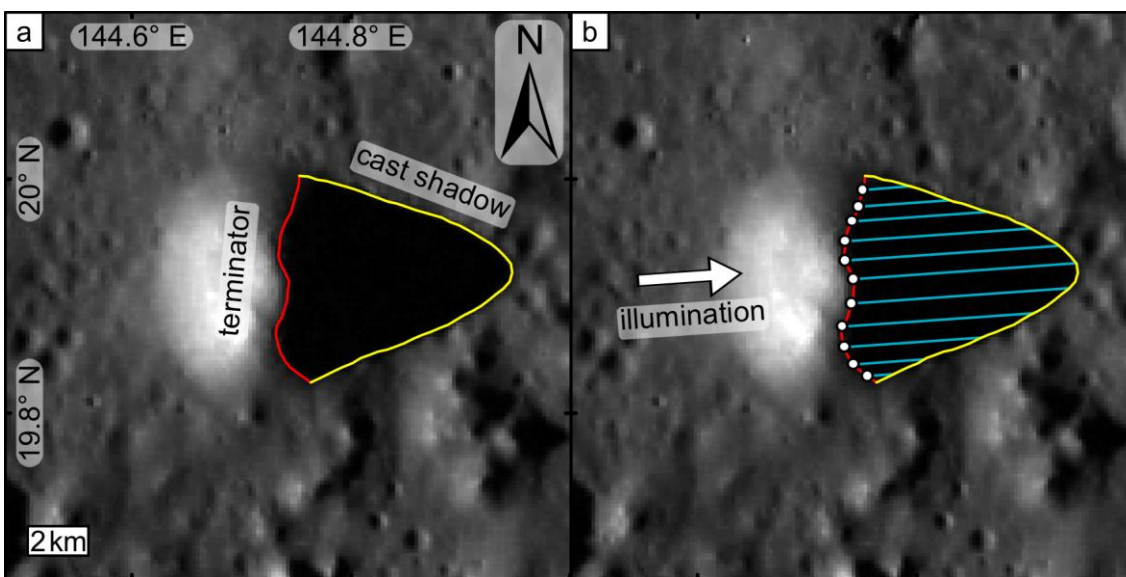
Fig. 6.5 Knob topographic information contained within digitised shadows. *(a) The two critical parts of a knob's shadow are its cast shadow and the shadow terminator on the body of the knob itself. (b) By measuring the distance from multiple points on the terminator (examples marked with white dots) to the cast shadow in the dirction of the solar illumination (measured lengths illustrated with blue lines), the heights of those points on the terminator can be calculated. These heights can be used to generate a topographic profile of the knob along its terminator.*

In order for shadow length measurements to be valid, the cast shadow of a knob must fall on a smooth (at the scale of the shadow), horizontal surface. In practice, this is often not the case. The most important requirement is that the cast shadow does not fall on an obvious slope. I did not digitise any knob shadows where I could see that the shadow was being cast up or down a slope. Minor modification of a knob's shadow due to short wavelength surface roughness, such as that generated by impact craters that are very small compared with the size of the knob, could be ignored during shadow digitisation. This was necessary to allow a large dataset to be generated. Ideally, a knob's terminator is a single, linear, sharp demarcation between the illuminated side of the knob and the shadowed side. However, knob terminators are most often not sharp, due to the Sun acting as an extended light source at Mercury. This means that penumbral shadow blurs the terminator. Penumbral shadow is much less problematic at the edge of the cast shadow. When digitising the terminator and the cast shadow, I deliberately digitised the dark, umbral 'core' of the shadow. This means that all knob heights estimated using this shadow length technique are underestimates, since the shadow lengths the heights were calculated from were under-measurements. Since penumbral shadow significantly blurs the terminator only (penumbral blurring of the cast shadow was very minor by comparison), this effect is the greatest contributor to the underestimate. A consequence of digitising the umbral terminator is that very often the digitised terminator is convex toward the Sun, rather than straight. This means that the topographic profile generated by this method is not a straight line traverse of the knob, such as an ideally placed MLA track profile would be. This means that additional care is required when interpreting my shadow-derived slope measurements. To aid slope interpretation, I always plotted the line of the profile on the knob next to the topographic profile graph. A further problem is that some knob terminators can be segmented due to topographic undulations on the surface of the knob. Since such terminators could not be digitised as a single line, I excluded knobs with segmented terminators from this analysis.

Cognisant of the caveats outlined above, I decided to use MDIS WAC (*HAWKINS ET AL., 2007*) frames with a ground resolution of ~100 m/pixel for shadow digitisation. Data of this type were available for the majority of the circum-Caloris knobs. It

might seem that higher resolution NAC data should be used where possible, but because such data were not available for all the knobs, I thought it would be better to digitise the knobs at the best resolution available for all knobs. WAC data offer several other advantages over NAC data. The larger pixel size of WAC data de-emphasises short-wavelength topographic features that would cause substantial deflections of knob shadows at the NAC scale. The wider field of view of WAC meant that multiple knobs could often be digitised within one WAC frame. This reduced the number of WAC frames that needed to be downloaded, processed and georeferenced, thus reducing the amount of time required to carry out this analysis. WAC images with optimum illumination conditions and viewing geometries for shadow length measurements were deliberately collected during the global mapping campaign of the MESSENGER mission *(CHABOT ET AL., 2016)*. NAC frames that serendipitously imaged circum-Caloris knobs, while useful for high-resolution photogeological observations of knobs, were not necessarily captured under ideal illumination conditions and viewing geometries for shadow length measurements.

For each knob ≥5 km in diameter, I searched the PDS for WAC frames with ~100 m/pixel resolution and ideal illumination conditions. Each image was downloaded and processed in ISIS3 using standard radiometric and photometric corrections. I used ISIS3 to project these images into the Mercator projection centred on Caloris that I introduced in Section 6.4.1 (central meridian = 162.7°E, standard parallel = 31.5°N). I displayed these projected WAC frames in ArcGIS. I then georeferenced these images to the global monochrome mosaic with a manual shift.

Each knob was attributed with the WAC frame that captures it, in addition to the solar azimuth, central solar incidence angle (i), central spacecraft emission angle (e), and the central phase angle (φ). These image metadata were collected from the Planetary Image Locator Tool (PILOT) and were used to calculate each WAC frame's scale factor. An image's scale factor is given by

$$\frac{1}{\tan i + \tan e} \qquad\qquad 6.2$$

if

$$\varphi = i + e \qquad\qquad 6.3$$

or

$$\frac{1}{\tan i - \tan e} \qquad\qquad 6.4$$

if

$$\varphi = i - e \qquad\qquad 6.5$$

This scale factor was then attributed to each knob within the corresponding WAC frame.

In each WAC frame, the shadow of each knob was validated before digitisation. As explained previously, knob shadows were rejected for digitisation if they were cast on obvious slopes or greatly affected by uneven terrain. Cast shadows and terminator shadow were digitised in separate feature classes (Fig. 6.6a). Shadows were digitised as lines with 100 m between each line vertex. This is generally meant that the digitised shadows had a higher vertex resolution than the images they were digitised from. This approach ensured that the digitisation process would be able to capture the maximum amount of detail in the shadows in each WAC frame. Shadows were digitised at the maximum zoom level at which they could be viewed in their entirety on my screen. Again, this approach was used so that each knob was digitised with the maximum possible fidelity. All cast shadows and terminators were digitised from north to south. All cast shadow and terminator pairs were snapped together at their start and end points. At the start point of each knob, I created a point feature class called the 'shadow anchor' (Fig. 6.6).
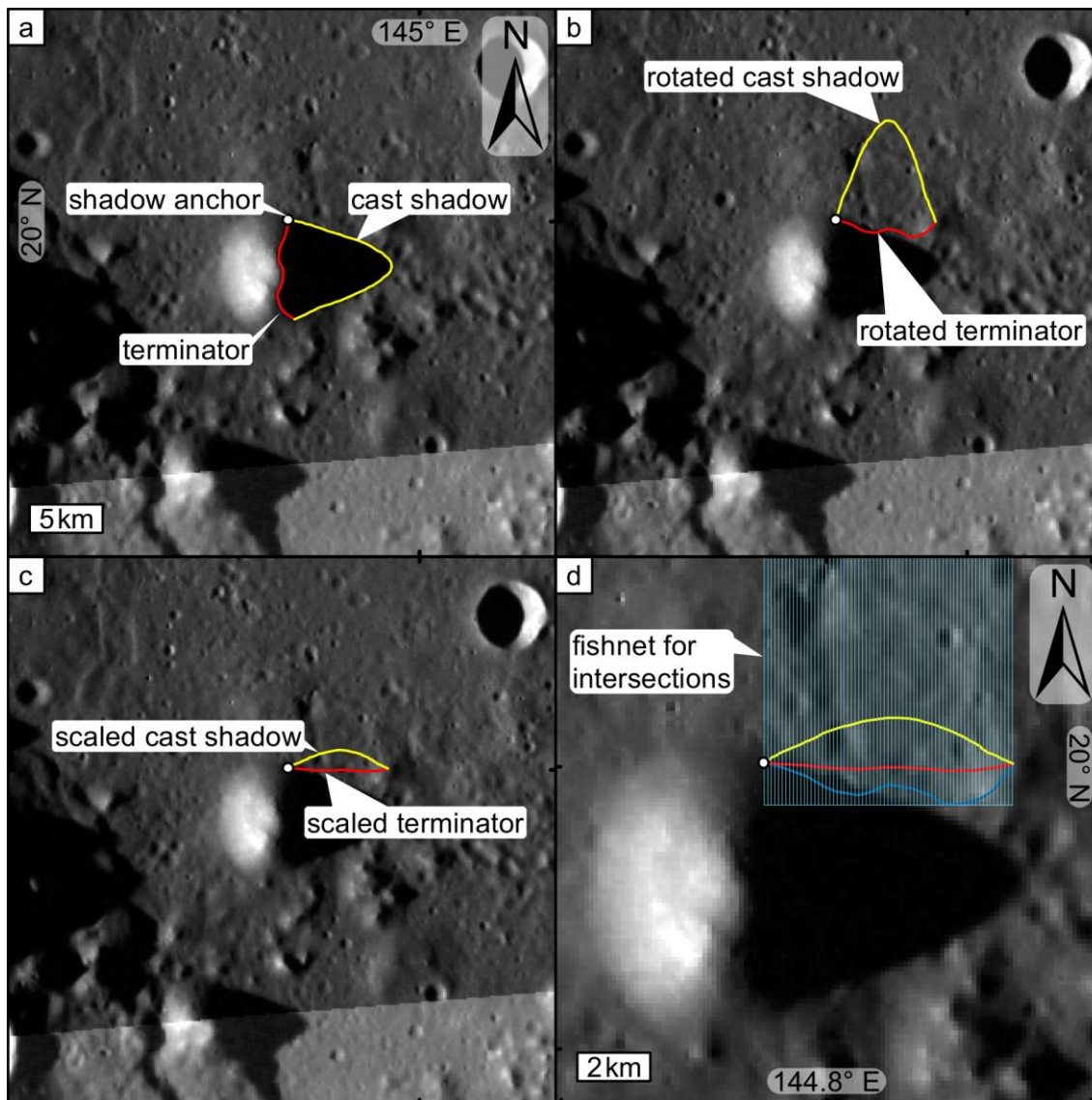
Fig. 6.6 Illustration of the first steps in the method for generating topography data from shadow information. *(a) Example of digitised cast shadow (yellow line) and terminator (red line). The shadow anchor is a point (white dot) created at the northern intersection of each cast shadow and terminator pair. (b) The digitised shadows from (a) after rotation around the shadow anchor. (c) The digitised shadows from (b) after being scaled by the scale factor calculated from equation 6.2 or 6.4 as appropriate. (d) A closer view of the scaled cast and terminator shadows. A grid of parallel, north-south lines (a 'fishnet', in blue), each separated by 100 m, encompassing the rotated and scaled digitised shadows used to measure the height of the knob at several points along the knob's terminator is shown. The rotated, but unscaled terminator (blue line) is also shown to illustrate how the calculated heights can be related back to the knob. All panels show MDIS WAC frame EW0220764090G (~125 m/pixel). Panels (a–c) also show the ~166 m/pixel global monochrome mosaic. All panels show Mercator projections centred on 162.7°E, 31.5°N.*

After all the knobs in all the WAC images were digitised, I implemented my modification of the BASILEVSKY (2002) method. I used the ET GeoWizards add-in for ArcGIS (TCHOUKANSKI, 2017) to rotate each cast shadow and terminator pair by a function of the solar azimuth of the image from which the pair was digitised. The shadow anchor for each cast shadow and terminator pair was used as the rotation fulcrum. This rotated each knob shadow so that it appeared as if the illumination was coming directly from the south (Fig. 6.6b). This essentially achieves the same effect as the image rotation used by BASILEVSKY (2002). Each rotated cast shadow and terminator pair was then scaled in the north–south direction by its scale factor (Fig. 6.6c). Again, this achieves the same effect as scaling the image in the method of BASILEVSKY (2002).

I created a 'fishnet' of polylines over each scaled cast shadow, scaled terminator, and rotated but unscaled terminator belonging to a given knob (Fig. 6.6d). Each fishnet was composed of cells 100 m in width arranged in a single row. I used the intersections between the fishnet lines and the rotated and scaled digitised shadows, as shown in Fig. 6.7a, to measure the elevations of different points on the terminators of each knob. I created points at the intersection between the fishnet lines and the scaled cast shadow line and scaled terminator line for each knob. I calculated the Y-coordinates (in metres) of these intersection points in their native Mercator projection. The absolute spatial location of these intersection points is meaningless, but the distance between points linked by the same fishnet line (i.e. the difference between their Y-coordinates measured in metres) equals the height at the corresponding point on a given knob's terminator. I calculated a height by subtracting the Y-coordinate of each terminator intersection point from the Y-coordinate of its corresponding shadow intersection point. I attributed the height calculated for each scaled cast shadow and terminator pair to the rotated but unscaled terminator-fishnet intersection point. I then rotated these terminator intersection points, replete with height data, back onto their knob. At this stage, each point could be symbolised according to its height, as shown in Fig. 6.7b, similar to MLA data points.
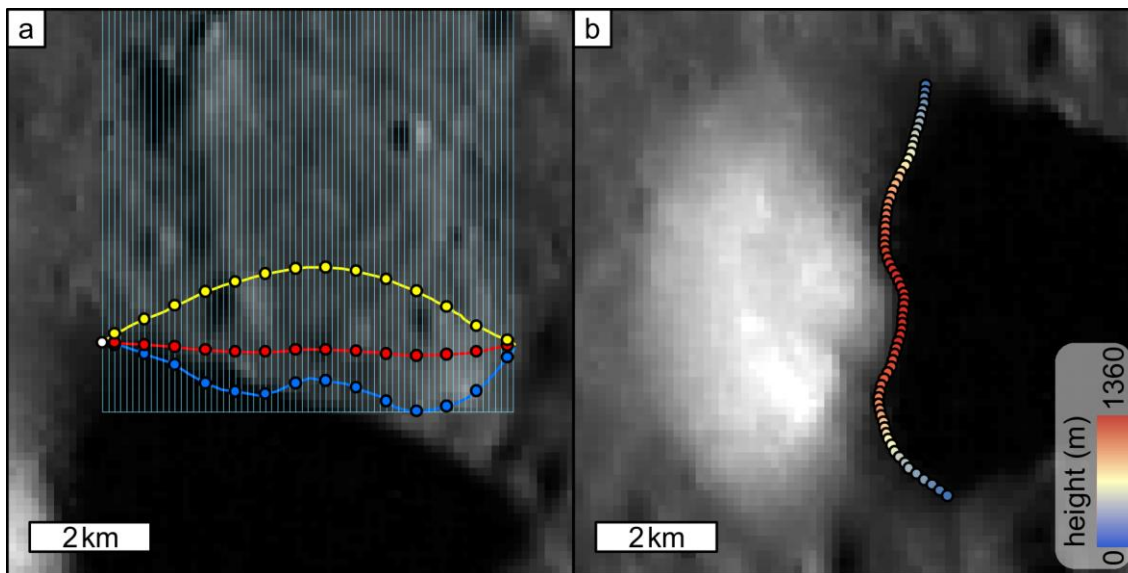
Fig. 6.7 Illustration of how heights are calculated from intersections between the transformed shadows and the measurement fishnet. *(a) A closer view of the knob shown throughout Fig. 6.6. The yellow and red lines represent the scaled cast shadow and terminator, respectively, of the knob. The dark blue line represents the rotated but unscaled terminator of the same knob. Matching coloured dots lie along each line where the lines intersect the fishnet (light blue). For clarity in this panel, only every fifth intersection along each line is rendered. The distance between a red dot and the yellow dot along their shared fishnet line equals the knob height at the corresponding point on the knob's terminator. This height is calculated and attributed to the corresponding blue dot on the rotated, but unscaled terminator. These blue dots with the height values are then rotated back onto the knob to place the height data points at their measurement locations. (b) The final shadow-derived topographic profile points, colourised to indicate their heights. Neither panel is shown with a graticule nor a north arrow so that the fishnet intersections and profile points can be rendered clearly. The location of this knob is clearly labelled in Fig. 6.6. North is at the top of both panels. Both panels show Mercator projections of MDIS WAC frame EW0220764090G (~125 m/pixel) centred on 162.7°E, 31.5°N.*

In order to plot these height data as a topographic profile, I needed to calculate the along profile distance to each point from the start of the profile. Even though the fishnet lines that generated the profile points are 100 m apart, the along profile distance between subsequent profile points is not necessarily 100 m when they are rotated back onto the knob. I used ArcGIS to measure the distance to each profile point of a given knob using the original digitised terminator as the measurement route. This generated a table containing the along profile distance for each profile

point of each knob. These along profile distances were then added to the profile points attribute table. Each knob whose shadow was digitised at the beginning of this process had a feature class of profile points with heights and along profile distances recorded in its attribute table. Since all shadows were digitised from north to south, all the shadow profiles begin at the north point of the knob. I exported the height and along profile distances from each knob's attribute table as a .csv file for plotting in R *(RCoreTeam, 2013)*.

Where both MLA-derived and shadow-derived topographic profiles for a given knob existed, I compared the two profiles to establish the strengths and weaknesses of the shadow technique.

To calculate the slopes of the knobs, I calculated 3-point slopes along their MLA- and shadow-derived topographic profiles (as appropriate). For each point in a topographic profile for a given knob, I calculated the linear gradient at the point using it and the previous and subsequent points in the profile (i.e. a local slope derived from 3 points). I used this modification of the point-to-point slope determination method of *(Kreslavsky and Head, 1999)* in order to smooth away spuriously high point-to-point slopes introduced during manual shadow digitisation. To make a fair comparison, MLA-derived slopes were calculated in the same way. I calculated 3-point slopes over the entirety of all the available topographic profiles of knobs. Since the three points could be either on the ascending or descending sides of the profile, the calculated slopes could be either positive or negative. I report the median of the absolute 3-point slope values for a given topographic profile of a knob as the typical flank slope along that profile.

6.5 Results

I have mapped the locations of 2017 circum-Caloris knobs. I have made detailed observations of the 545 knobs that are ≥5 km in diameter and my map contains all circum-Caloris knobs whose diameters satisfy this criterion (these catalogues are included in the Supporting Digital Media of this thesis). My observations of knobs in MDIS data are detailed in Section 6.5.1, followed by my interpretations in Section 6.5.2. I present my map of the distribution of knobs in Section 6.5.3 and I

explain what I infer from this distribution in Section 6.5.4. My measurements of knob topography are contained in Section 6.5.5.

6.5.1 MDIS observations of knobs

6.5.1.1 Knob appearance

The circum-Caloris knobs ≥5 km in diameter (some examples are shown in Fig. 6.8) are typically domal to conical in shape. This is clearest when they are isolated, however they are commonly closely colocated in chains and clusters such that their lower slopes overlap to form multi-knob landforms (Fig. 6.9). I present my measurements of knob distribution and knob shape in more detail in Sections 6.5.3 and 6.5.5.
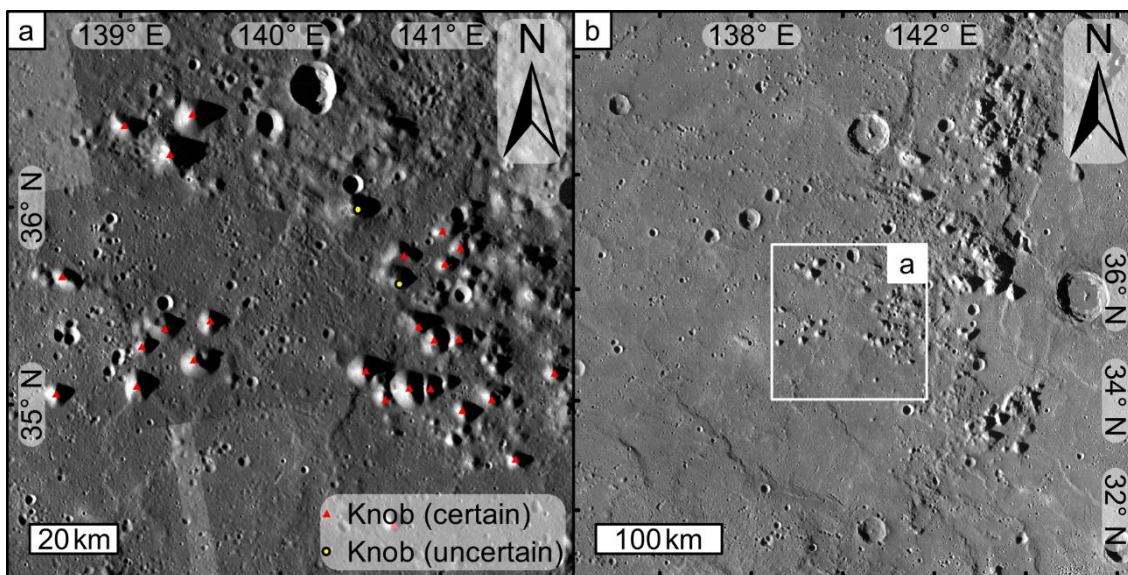
Fig. 6.8 Examples of the circum-Caloris knobs. *(a) Circum-Caloris knobs close to the western rim of the Caloris impact basin. The three knobs in the upper left are situated in the Odin Formation (my interpretation, see Fig. 6.17). The knobs in the centre-left are surrounded by smooth plains. The knobs in the centre-right are closely colocated and overlap with each other, which is common for knobs proximal to Caloris. Mosaic of WAC frames EW0220807059G, EW0220807071G and EW0220763870G (~86 m/pixel) overlain on the ~166 m/pixel global monochrome mosaic. (b) Context view of the west of the Caloris basin. The labelled white box indicates the extent of (a). The Caloris rim runs north–south along the right side of the panel and contains many knobs. Smaller, more distal knobs can be seen in the circum-Caloris plains in the left of the panel. ~166 m/pixel global monochrome mosaic. Both panels show Mercator projections centred on 162.7°E, 31.5°N.*

At the spatial resolution of MDIS WAC frames (~100 m/pixel; Fig. 6.8a), which have full coverage of the circum-Caloris region, knobs appear as featureless cones or domes. They are not characterised by summit craters and are generally devoid of craters at this scale.
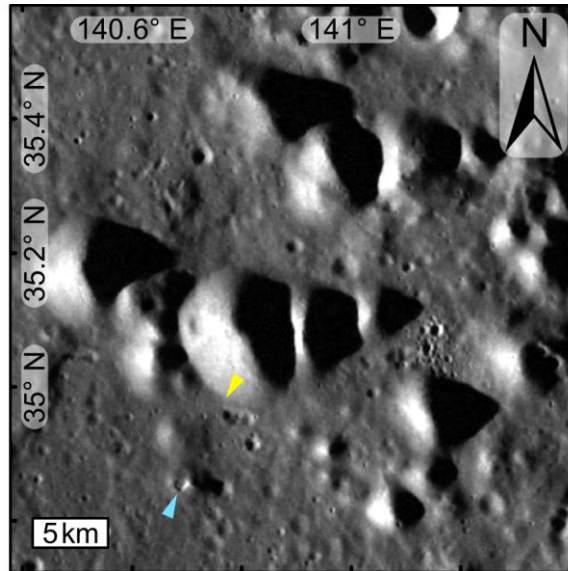
Fig. 6.9 Detail of overlapping knobs. *This knob cluster is shown in the lower-right of Fig. 6.8a. These knobs lie between smooth plains on the left and the Odin Formation on the right. The yellow triangle indicates to a basal point on a knob. To the left of this point, the knob presents a sharp basal contact with smooth plains. To the right of this point the knob basal contact is with the Odin Formation and is more blurred. Knobs toward the right of the panel generally have diffuse basal contacts. The blue triangle indicates a hollow in a low knob (<5 km in diameter) in the Odin Formation. WAC frame EW0220763870G (~88.0 m/pixel). Mercator projection centred on 162.7°E, 31.5°N.*

NAC frames (a few tens of metres resolution), available for 70 knobs only, show that these landforms are substantially less densely cratered than their surroundings (Fig. 6.10). Furthermore, some knobs have a wispy texture. Where this wispy texture has been identified on a knob, its grain does not obviously run directly across or down the slope of the knobs. This wispy texture probably indicates that a mature regolith is present on the circum-Caloris knobs.
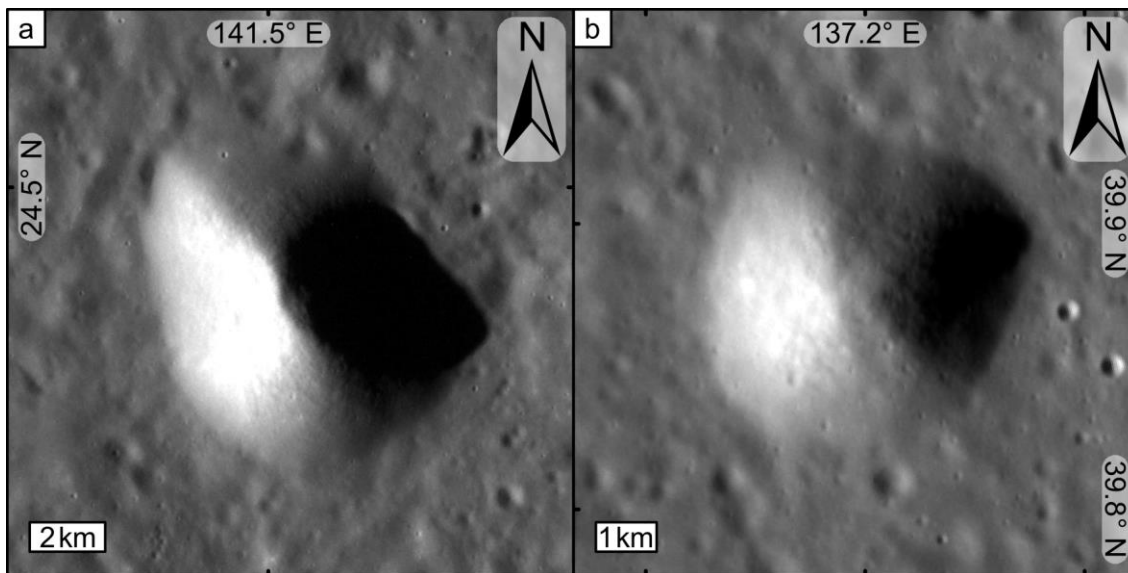
Fig. 6.10 High-resolution images of individual knobs. *(a) A knob located just outside western Caloris Planitia. The visible knob flanks are smoother and qualitatively less cratered than the surrounding Odin Formation. Knobs in this pristine state are typically conical in shape. NAC frame EN1015339337M (~36.1 m/pixel). (b) A knob located ~220 km beyond the western rim of Caloris. This knob is more cratered than the example shown in (a) but still appears to be less cratered than the surrounding plains. This knob is more dome shaped than the pristine example in (a). NAC frame EN1045703411M (~27.4 m/pixel). Both panels show Mercator projections centred on 162.7°E, 31.5°N.*
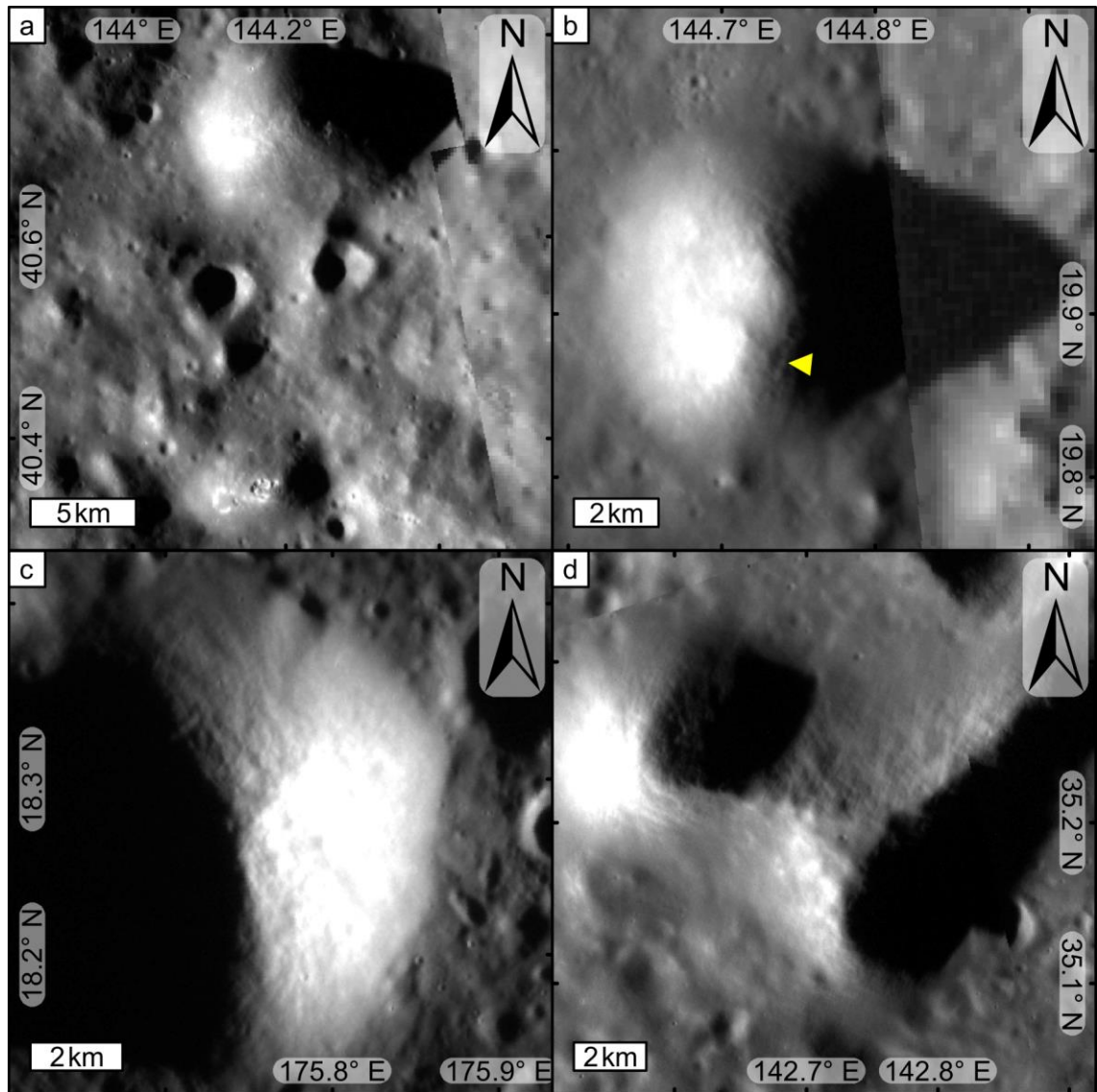
Fig. 6.11 Knob textures. *(a) A knob with a fine-scale mottled and streaky appearance. A knob at the bottom of the panel has hollows. It is unclear if the reflectance variations across the knob at the top of this panel are due to surface roughness or composition. Mosaic of NAC frames EN1015281357M and EN1015281357M (~49.3 m/pixel) overlain on the ~166 m/pixel global monochrome mosaic. (b) This knob also exhibits a mottled appearance. What appears to be an elongate depression on the southern mid-flank of the knob (yellow triangle), close to the terminator of its shadow, suggests that at least some mottling could be due to surface roughness. This elongate depression could be a slump or a degraded impact crater or catena. NAC frame EN1045703971M (~48.4 m/pixel) overlain on the ~166 m/pixel global monochrome mosaic. (c) A knob exhibiting a mottled and streaky appearance. NAC frame EN0258398544M (~43.2 m/pixel). (d) These knobs have streaks that do not obviously run either directly down or across the knob flank slopes. Mosaic of NAC frames EN1015223718M and EN1015223842M (~29 m/pixel) overlain on the ~166 m/pixel global monochrome mosaic. All panels show Mercator projections centred on 162.7°E, 31.5°N.*

6.5.1.2 Knob colour

It is difficult to be conclusive about the colour properties of the circum-Caloris knobs. In general, the best MDIS colour data were gathered when the local time on Mercury was midday and MESSENGER was flying overhead (i.e. $i = 0°$ and $e = 0°$; HAWKINS ET AL., 2007). This meant that the Sun was illuminating Mercury from directly behind the MESSENGER spacecraft and most of the light would reflect back to the spacecraft without being scattered. However, since the circum-Caloris knobs are positive relief features defined by slopes this means that colour data for them is potentially compromised by photometric errors due to unfavourable viewing angles, illumination, and scattering.
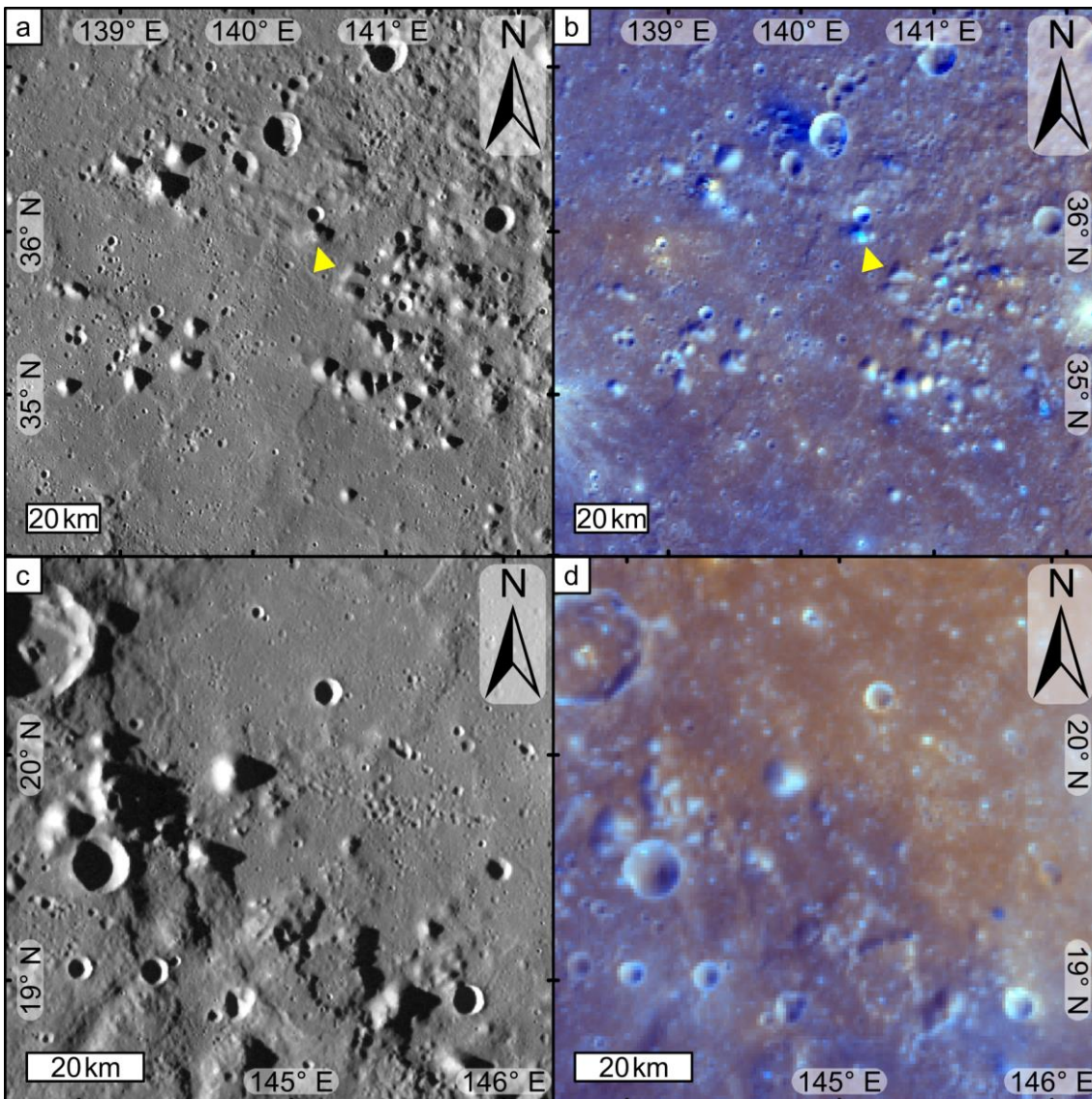
Fig. 6.12 Comparison of knobs in monochrome and enhanced colour. (a) Knobs in monochrome. The view shown is similar to that shown in Fig. 6.8a. The yellow triangle indicates a knob exhibiting pervasive hollowing. ~166 m/pixel global monochrome mosaic. (b) The same view as in (a) shown in the ~665 m/pixel global enhanced colour mosaic. Most knobs in this view are not strongly distinct in colour from the surrounding plains. These plains most closely conform to the definition of the low-reflectance blue plains colour unit (DENEVI ET AL., 2009). Sun-facing slopes on the knobs in this view have a brighter blue colour than their surroundings. Conversely, knob slopes in shadow have a darker blue colour. The yellow triangle indicates the same knob as in (a). The bright blue colour of this knob is characteristic of hollow forming material elsewhere on Mercury (BLEWETT ET AL., 2011). ~665 m/pixel global enhanced colour mosaic. (c) Knobs in southwestern Caloris Planitia. ~166 m/pixel global monochrome mosaic. (d) The same view as in (c) shown in the ~665 m/pixel global enhanced colour mosaic. The smooth plains of Caloris Planitia correspond to the high-reflectance red plains colour unit (DENEVI ET AL., 2009). The knobs in this view have a similar blue appearance in enhanced colour to the knobs surrounded by low-reflectance blue plains in (b). This gives the knobs in Caloris Planitia a stronger colour contrast with their surroundings. Note that Sun-facing slopes of both knobs and impact craters appear brighter and bluer and their shadowed regions are dark blue, as in (b). All panels show Mercator projections centred on 162.7°E, 31.5°N.

In the circum-Caloris plains, which mostly correspond to the low-reflectance blue plains colour unit *(DENEVI ET AL., 2009)*, knobs do not have a strong colour signature (Fig. 6.12b). Sun-facing slopes appear brighter blue than the surroundings and shadowed slopes appear darker, suggesting that these colour variations are most likely due to the photometric effects noted previously.

There is some evidence that the bright blue colouration of the knobs might be real. Knobs within Caloris Planitia, which corresponds to the high-reflectance red plains colour unit *(DENEVI ET AL., 2009)*, do have a blue colour contrast with the surrounding red plains (Fig. 6.12d). Furthermore, I have found many examples of knobs that have hollows on or near them (see Section 6.5.1.6). Hollows are associated with bright blue material elsewhere on Mercury *(BLEWETT ET AL., 2011)*. If knobs potentially host hollow forming materials then it is possible that that material will lend a blue colour to knobs.

6.5.1.3 Knobs and the surrounding plains

Knobs can exhibit both sharp and diffuse boundaries with the surrounding plains (Fig. 6.9). The sharpness of knob basal contacts appears to at least partly controlled by the surrounding plains type. Knobs more commonly present diffuse or gradational contacts with surrounding Odin Formation plains. Conversely, individual knobs can exhibit both sharp and diffuse contacts with surrounding smooth plains.

Sharp contacts with smooth plains could result from embayment of knob bases by smooth plains material, requiring the smooth plains to postdate knob formation and evolution by some amount of geological time. Where knob basal contacts with surrounding smooth plains are diffuse, this suggests that at least some knob evolution has taken place after the local cessation of smooth plains emplacement.

Alternatively, the observation that an individual knob can appear to have both sharp and diffuse contacts with its surroundings may be an observational bias due, for example, to changing illumination conditions around the knob. When the lower angle basal flank slopes of knobs are poorly illuminated they might be unrecognisable within MDIS images, leading me to identify only a sharp distinction between the upper slopes and the surroundings.

6.5.1.4 Knobs and impact craters

I have observed 38 cases of knobs intersecting with impact craters. The basal slopes of some knobs partially obscure impact craters in the surrounding plains (Fig. 6.13). This means that knob evolution, at least in these examples, far outlasted local plains emplacement, such that these plains could accumulate impact craters that subsequently could be encroached upon by knobs. In some examples, knob material appears to have avalanched into an impact crater near the base of the knob. In most of these cases, I cannot be certain if the impactor hit the knob and caused a collapse of knob material into the cavity or if the impact occurred in the plains surrounding the knob and the knob spread laterally to engulf the crater. In either case, the observation of knob material mantling, infilling, and obscuring impact craters suggests that at least the outermost material of these knobs is composed of loose material capable of avalanching.

As mentioned earlier, at the NAC scale, knobs are qualitatively less densely cratered than the surrounding plains. In the cases of small knobs, this could be explained by the fact that impacts of sufficient size would completely remove all traces of a knob. In the case of larger knobs, which have sufficient surface area to accommodate multiple small impact craters (yet they do not often appear to do so), this requires any combination of the following: (1) knobs postdate the local cessation of plains emplacement in geological time; (2) the physical properties of knobs give them a different crater production function from the surrounding plains, or; (3) knobs retain impact craters for a shorter time than the surrounding plains due to some resurfacing process (e.g. volcanic resurfacing or slope failure). Where impact craters are present on knobs, they appear to be spatially concentrated on either the flatter summits of domal knobs or, more commonly, on the lower angle distal flank slopes of knobs in general. Impact craters are nearly entirely absent on the steep mid-flanks of knobs. Where impact craters are present on knob flanks, these are typically more degraded than other impact craters elsewhere on the knob and on the surrounding plains (Fig. 6.14).
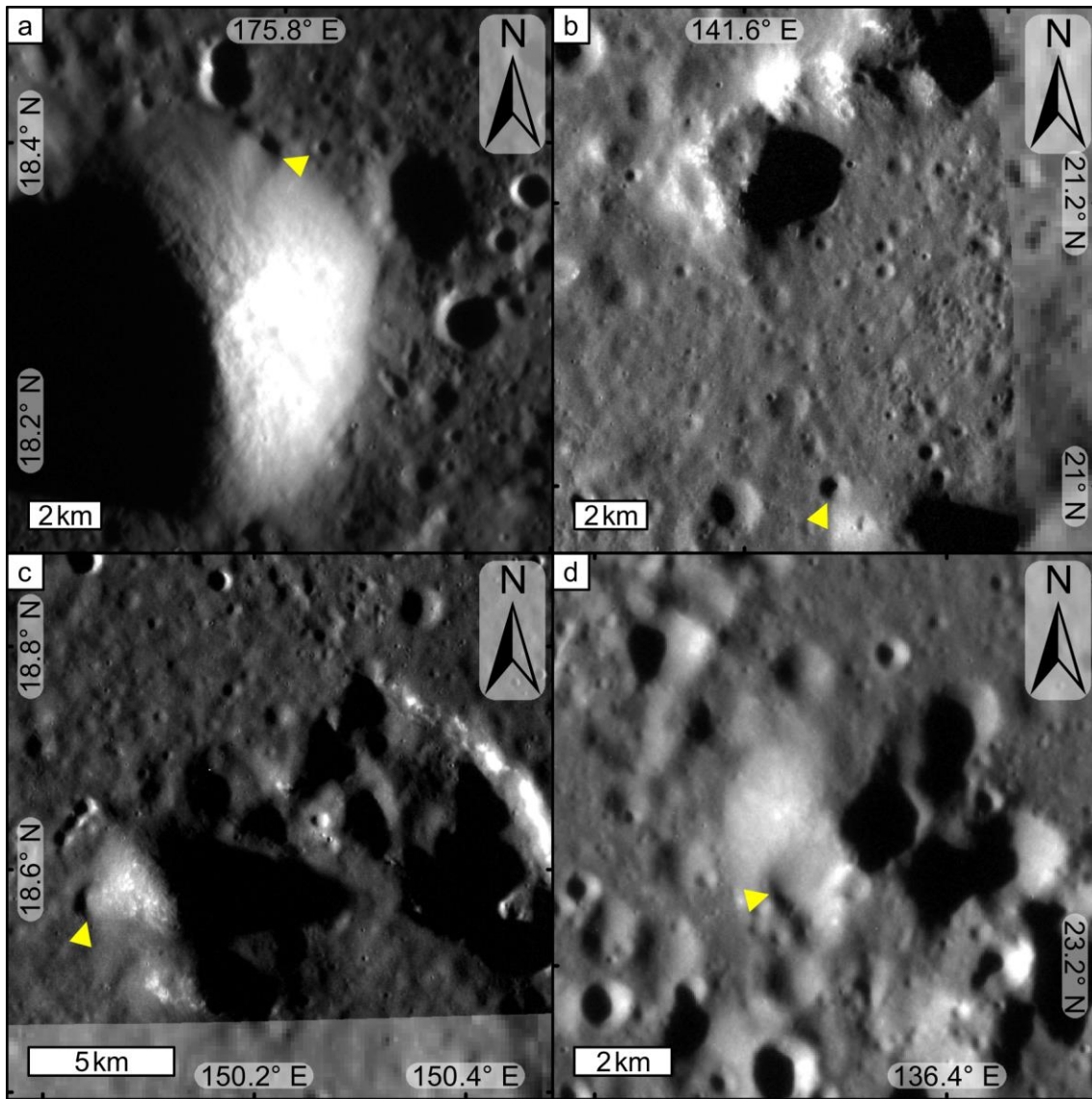
Fig. 6.13 Knob interactions with impact craters. *(a) The same knob shown in Fig. 6.11c. The yellow triangle indicates an impact crater on the smooth plains of Caloris Planitia that is partially obscured by knob material. There is a subtle notch in the knob topographically above this partially obscured impact crater. NAC frame EN0258398544M (~43.2 m/pixel). (b) A knob in the lower-right of this panel is partially obscuring an impact crater (yellow triangle) in the Odin Formation 75 km beyond the southwestern Caloris rim. At the top of the panel, two large knobs show evidence of pervasive hollowing. NAC frame EN0220720878M (~18.8 m/pixel) overlain on the ~166 m/pixel global monochrome mosaic. (c) This knob is partially obscuring an impact crater (yellow triangle) on Caloris Planitia. High albedo streaks and blotches on this knob and the knob adjoining it to the south appear to be due to surface composition variation. The high albedo regions at the right of the panel appear to be due to hollowing in a crater chain wall. NAC frame EN0220764135M (~19.9 m/pixel overlain on the ~166 m/pixel global monochrome mosaic). (d) This knob is situated ~220 km beyond the south-western rim of Caloris in the circum-Caloris smooth plains. The yellow triangle indicates an impact crater that is almost completely buried by knob material. NAC frame EN1015541044M (~39.8 m/pixel). All panels show Mercator projections centred on 162.7°E, 31.5°N.*
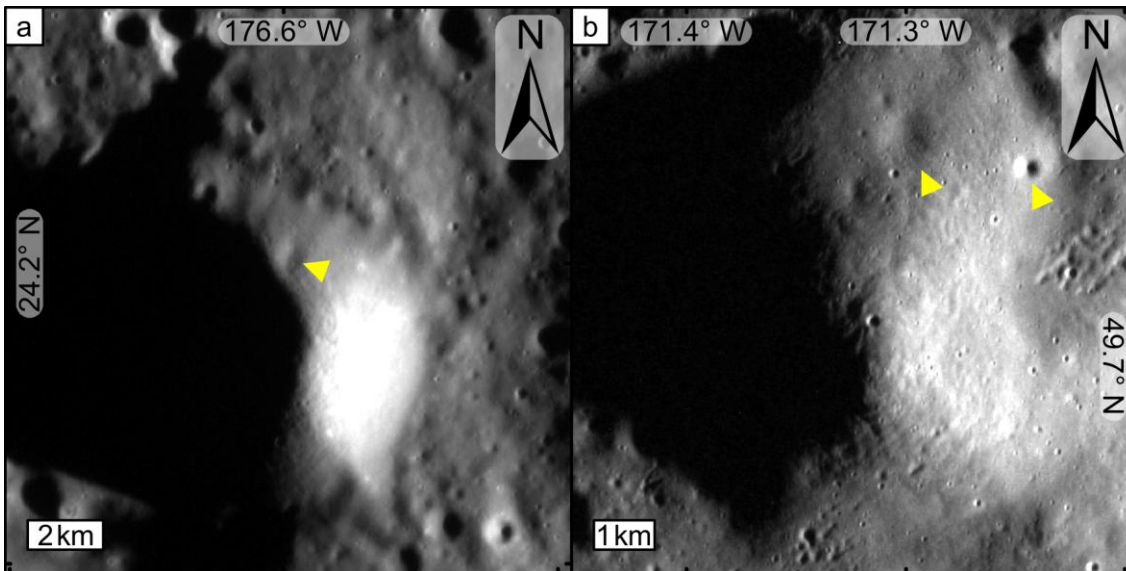
Fig. 6.14 Impact craters on knob flanks. *(a) The yellow triangle indicates an approximately circular depression in the flank slope of a knob in the southeastern rim of Caloris. This depression is probably a degraded impact crater. The knob is less densely cratered than the surrounding smooth plains. NAC frame EN0258283508M (~37.2 m/pixel). (b) A knob with more superposing craters than the example in (a). This knob is located ~550 km beyond the northwestern rim of Caloris. The yellow arrows indicate probable impact craters that have undergone degradation. Smaller impact craters elsewhere on the knob appear to be relatively pristine. NAC frame EN1037605314M (~16.2 m/pixel). Both frames show Mercator projections centred on 162.7°E, 31.5°N.*

6.5.1.5 Knobs and lobate scarps
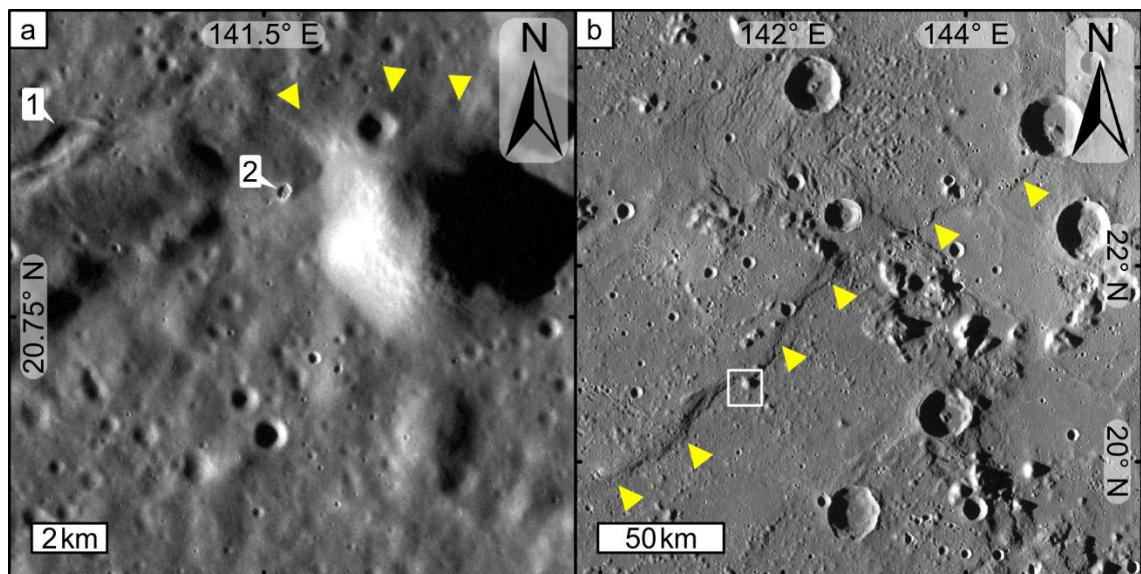
Fig. 6.15 Knob interaction with a lobate scarp. (a) A knob situated ~50 km beyond the southwestern rim of Caloris with flank materials apparently draped on a lobate scarp (yellow triangles). Label (1) indicates a back-scarp graben. The presence of such grabens has been used as evidence for geologically young fault movement on their host lobate scarps elsewhere on Mercury *(WATTERS ET AL., 2016)*. Label (2) indicates a hollow in close association with the knob. Although it is not clear that the hollow has formed in knob material, the local plains type is the Odin Formation. NAC frame EN0220720885M (~19.1 m/pixel). (b) Context view. The extent of (a) is indicated by the white box. The yellow triangles indicate the surface break of the lobate scarp draped by the knob shown in (a). This lobate scarp cuts across the rim of Caloris, the smooth plains of Caloris Planitia, and the circum-Caloris smooth plains. ~166 m/pixel global monochrome mosaic. Both panels show Mercator projections centred on 162.7°E, 31.5°N.

I have made one observation of a knob interacting with a lobate scarp (Fig. 6.15). The wispy northernmost flanks of this knob appear to be draped over the steep front of the lobate scarp. Away from this knob, the surface break of the lobate scarp is sharp and quite obvious, however near the knob the appearance of the break is muted. This lobate scarp cuts across the rim of the Caloris basin, which means some, if not all, of the movement on this fault postdates the Caloris impact. Furthermore, this lobate scarp also deforms the smooth plains of Caloris Planitia and the circum-Caloris plains. The majority of these plains are thought to be

volcanic in origin *(DENEVI ET AL., 2013)* and multiple crater size-frequency distribution studies suggest that these plains are ~100 Myr younger than the Caloris impact *(FASSETT ET AL., 2009; DENEVI ET AL., 2013)*. However, the knob material is not cut by the lobate scarp.

6.5.1.6 Knobs and hollows

I have observed 10 examples of hollows in close association with knobs (Fig. 6.16). These hollows appear to be forming within native knob materials, rather than material that has subsequently been delivered to the region as impact ejecta, as has obviously been the case elsewhere on Mercury *(BLEWETT ET AL., 2013; THOMAS ET AL., 2014C)*. My ability to observe hollows on or nearby knobs will have been limited by the availability of suitable NAC data to resolve the hollows. Furthermore, it is possible that hollows are not uniquely associated with the circum-Caloris knobs, but are in fact abundant in the intervening plains and are colocated with knobs in the cases of my 10 examples by chance. Nevertheless, knobs with resolvable hollows on them are an important observation. Hollowing is thought to be an important surface modification process operating at least until Mercury's very recent past or possibly even in the present day *(BLEWETT ET AL., 2011, 2013)*.
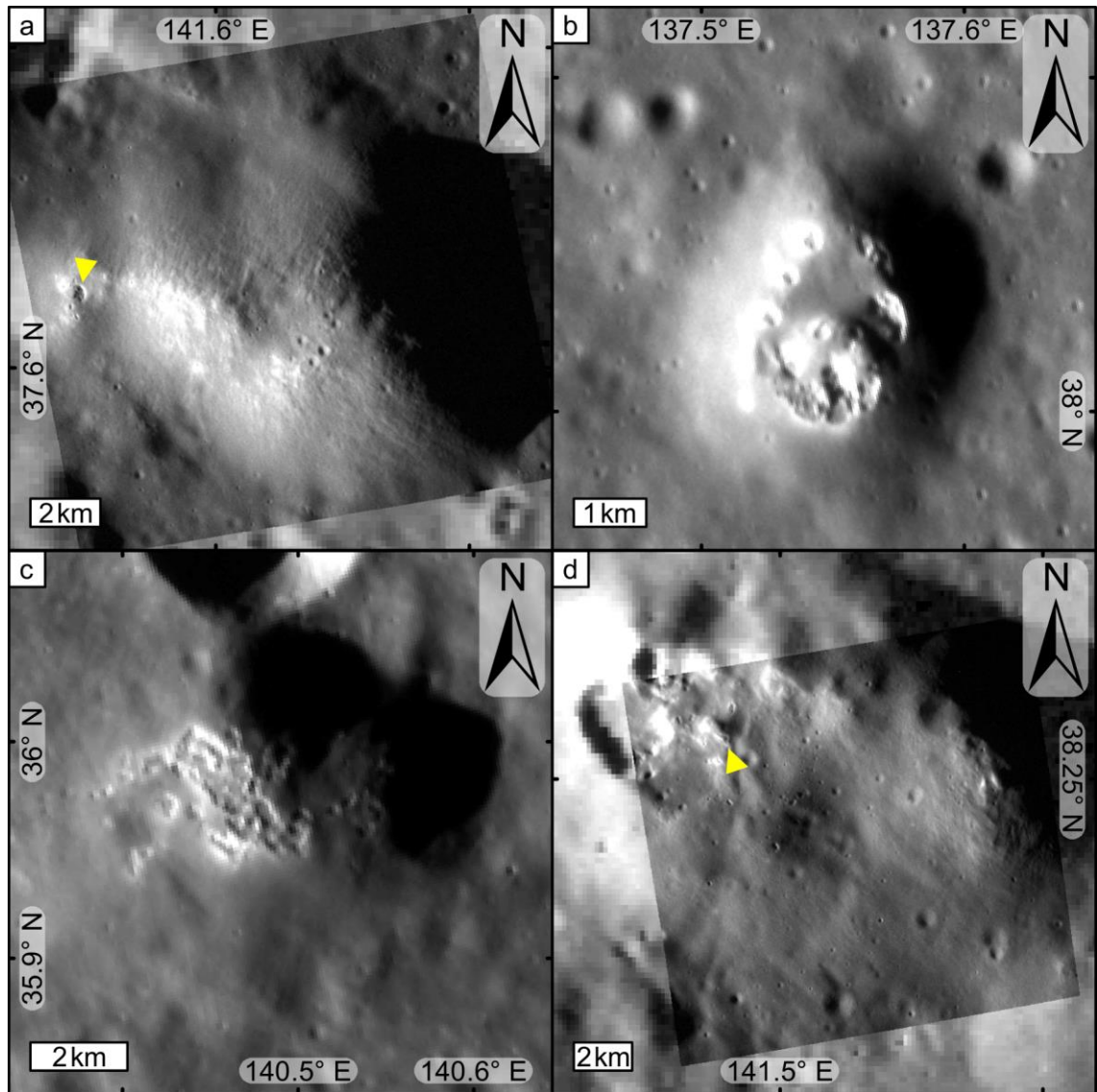
Fig. 6.16 Knobs and hollows. *A high-resolution image of an elongate knob ~70 km beyond the western rim of Caloris. The yellow triangle indicates a hollow on the flank of the knob. NAC frame EN0220720623M (~12.4 m/pixel) overlain on the ~166 m/pixel global monochrome mosaic. (b) A knob in the Odin Formation ~220 km west of the Caloris rim. This knob has hollows in a near-complete ring around its summit. NAC frame EN1045703448M (~28.8 m/pixel). (c) Detail of the knob indicated by the yellow triangle in (panels (a) and (b)). NAC frame EN1045674576M (~61.2 m/pixel). (d) Two overlapping knobs located ~70 km west of the Caloris rim. The left knob contains a depression that has been identified as an explosive volcanic vent (*THOMAS ET AL., 2014A*). East of this depression, and indicated by the yellow triangle, are high albedo materials that have been identified as hollows (*THOMAS ET AL., 2014C*). The knob on the right of the panel appears to have two small, blade-like projections close to its summit.*

6.5.1.7 Odin Formation observations

In making high-resolution observations of the circum-Caloris knobs, I also observed the Odin Formation passively. I found that the inter-knob plains are not smooth, particularly in comparison with the smooth plains, when viewed at WAC resolution (Fig. 6.17).
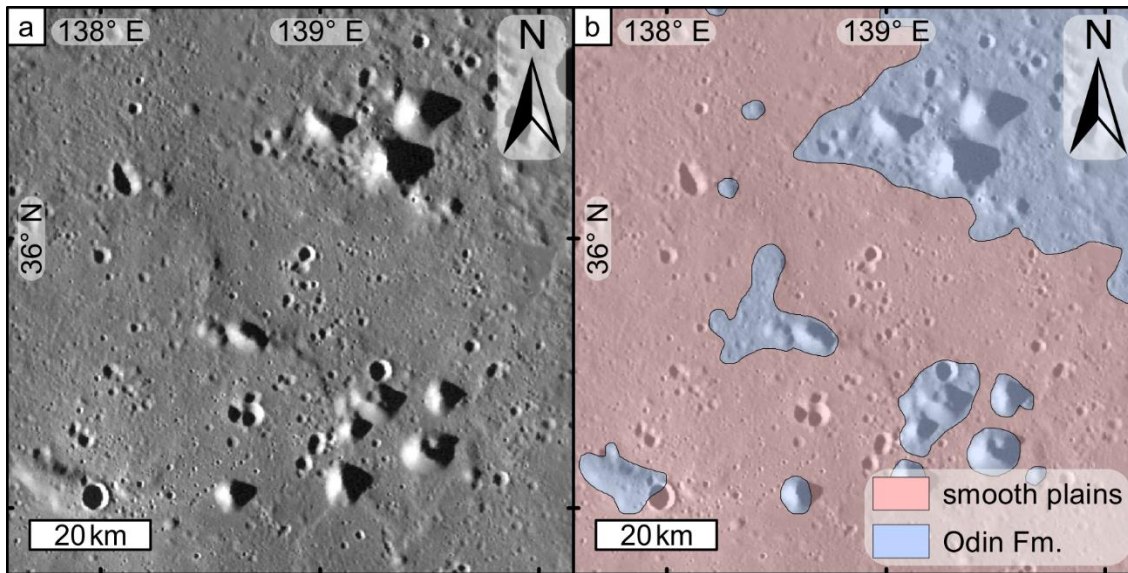
Fig. 6.17 Smooth plains and the Odin Formation. *(a) ~166 m/pixel global monochrome mosaic showing a region west of Caloris with smooth plains in contact with the Odin Formation. (b) Geological interpretation overlain on the ~166 m/pixel global monochrome mosaic. The inter-knob Odin Formation has a hummocky texture that is distinct from the smooth plains. This linework was completed at the 1:200k-scale. Both panels show Mercator projections centred on 162.7°E, 31.5°N.*

6.5.2   Interpretations of MDIS observations

The observations I have described above have led me to the following interpretations of the circum-Caloris knobs.

6.5.2.1 Knobs are not volcanic constructs

As stated previously in Chapter 6, two hypotheses about the origin of the circum-Caloris knobs currently exist. The first is that the knobs are remnants of ejecta blocks from the Caloris impact, and that the Odin Formation, which is characterised by knobs, represents a Caloris ejecta facies. However, doubt is cast on this hypothesis by studies of the Caloris Group, which have consistently returned younger crater size-frequency distributions for the Odin Formation

compared with estimates of the age of the Caloris impact itself *(FASSETT ET AL., 2009; MANCINELLI ET AL., 2016)*. The other suggestion for the formation of the circum-Caloris knobs is that they are small volcanic constructs *(FASSETT ET AL., 2009)*. This is plausible, since the majority of the circum-Caloris smooth plains are volcanic in origin *(DENEVI ET AL., 2009)*. However, several of the observations I have made argue strongly against a volcanic origin for these knobs.

The most important observation that led me to discount a volcanic origin for the circum-Caloris knobs is their lack of any summit crater. As stated in Chapter 5, volcanic eruptions into a vacuum with even a modest gas fraction would be highly explosive *(WILSON AND HEAD, 1981)*. This is because gas expansion within the erupting magma is highly efficient. This explosion would cause a volcanic crater to open *(KERBER ET AL., 2009)*. Such volcanic craters characterise volcanic constructs on the Moon *(HEAD AND GIFFORD, 1980; S. J. LAWRENCE ET AL., 2013)*. Geochemical data returned by the MESSENGER mission suggest that Mercury's crust is rich in volatile species *(NITTLER ET AL., 2011; PEPLOWSKI ET AL., 2011)*. Large volcanic craters elsewhere on Mercury *(KERBER ET AL., 2009; THOMAS ET AL., 2014A; JOZWIAK ET AL., 2018)* appear to have been excavated by explosive eruptions with high gas-fractions *(KERBER ET AL., 2009)*. It is worth noting at this point that this does not require that Mercury's mantle is also volatile rich. Mantle-derived melts would have the opportunity to assimilate crustal volatiles such that their eruptions would have significant explosive character *(THOMAS ET AL., 2015)*. Furthermore, the candidate volcanic edifices I detailed in Chapter 5 have summit craters that are conceivably of volcanic origin *(WRIGHT ET AL., 2018)*. Therefore, the absence of craters, besides those of obvious incidental impact origin, on the circum-Caloris knobs therefore presents a serious obstacle to a volcanic interpretation for their origin.

Another observation that argues against a volcanic origin for the circum-Caloris knobs is that they do not have a red volcanic colour signature resembling those associated with putative volcanism elsewhere on Mercury *(MURCHIE ET AL., 2008; KERBER ET AL., 2009, 2011; GOUDGE ET AL., 2014; THOMAS ET AL., 2014A; JOZWIAK ET AL., 2018)*. The smooth plains of Borealis Planitia and Caloris Planitia mostly correspond to the high-reflectance red plains colour unit *(DENEVI ET AL., 2009)*. The faculae associated with putative pyroclastic volcanism have an even stronger red

colour signature than high-reflectance red plains *(DENEVI ET AL., 2009)*. Most circum-Caloris knobs are situated in low-reflectance blue plains surrounding Caloris *(DENEVI ET AL., 2009)*. If these knobs were formed by volcanism, then any red volcanic colour signature should contrast strongly with these surroundings. However, no knobs that I observed have red colour anomalies. Since the knobs in the circum-Caloris plains are generally indistinct from their low-reflectance blue plains surroundings, I would therefore ascribe the knobs in the circum-Caloris plains to that same colour unit. This is inconsistent with a volcanic interpretation of the knobs.

Most variations in the blue colour of the knobs appear to be due to photometric errors. Where real colour anomalies appear to exist, they are all bright blue, similar to the colour anomaly associated hollow-forming material elsewhere on Mercury *(BLEWETT ET AL., 2011)*. As I have shown, many knobs seen in high-resolution NAC data have resolvable hollows on them. This suggests that at least some knobs contain a volatile component. It is difficult to imagine how these knobs could have formed as volcanic constructs and simultaneously retained volatiles within them in order to facilitate hollow formation later. It is worth remembering at this point that hollows are not often found within the volcanic high-reflectance red plains of Borealis Planitia and Caloris Planitia or in the explosive volcanic deposits elsewhere on Mercury *(THOMAS ET AL., 2014C)*. This means that knobs must be made of different materials from volcanic landscapes on Mercury. The simplest explanation for a difference in materials between the circum-Caloris knobs and the volcanics on Mercury is that the knobs are not volcanic in origin.

As I have shown, the circum-Caloris knobs are characteristic of the Odin Formation, however knobs also occur within the Caloris smooth plains (Fig. 6.17). The association of some knobs with a smooth plains unit, generally regarded to have formed due to voluminous effusive volcanic eruptions *(DENEVI ET AL., 2013)*, means that a volcanic origin for at least some knobs should be considered. However, my observation that the knobs present diffuse margins when hosted by the Odin Formation and sharp contacts when hosted by the smooth plains provides additional evidence of how the knobs are unrelated to the volcanic episode that formed the smooth plains. The sharp basal contact with surrounding

smooth plains suggests that these knobs formed *before* the smooth plains and were subsequently embayed by it. Diffuse basal knob contacts with the Odin Formation suggest that knobs formed within the same span of geological time as the Odin Formation. This is consistent the knobs being the remnants of late-arriving ejecta blocks.

6.5.2.2 Knobs as modified Caloris ejecta blocks

My observations of the circum-Caloris knobs have led me to discount a volcanic origin for these landforms. I have found that my observations are consistent with the circum-Caloris knobs instead having originally formed as Caloris ejecta.

Several of my NAC observations of knobs suggest that the circum-Caloris knobs are piles of unconsolidated material, or at least have unconsolidated surfaces. I have shown examples of knobs that host depressions that I interpret as impact craters. Often these depressions exhibit rounded bounding rims and subdued topography compared with pristine impact craters (Fig. 6.14). The appearances of these craters on the knobs could be explained by degradation of the craters from a pristine state, or these craters may have formed with subdued appearances originally. Both of these mechanisms are consistent with knobs being piles of unconsolidated material. If these impact craters are primarily subdued then this could be because unconsolidated material is less capable of supporting steep and sharp topographic landforms, such as impact crater rims. Furthermore, during the modification stage of impact cratering, unconsolidated target material can flow more readily into the impact cavity, resulting in a topographically subdued crater. If these impact craters were originally pristine, then their degradation may have been enhanced by slumping of unconsolidated knob material *(ASCHAUER AND KENKMANN, 2017)*. The observation that knobs are always less densely cratered than their surroundings suggests that knobs have shorter crater retention times than the surrounding plains. The alternative is that they are substantially younger than the Odin Formation and smooth plains, but this is inconsistent with knob embayment by the smooth plains. Shorter crater retention times require craters on knob surfaces to degrade at a faster rate than on the surrounding plains. On steep knob surfaces this is probably due to mass-wasting *(ASCHAUER AND KENKMANN, 2017)*. Relatively rapid crater degradation by mass-wasting is more consistent with

knobs being piles of unconsolidated material, such as disintegrating ejecta blocks or pyroclastic cones, rather than consolidated volcanic piles. However, I am able to discount the pyroclastic cone hypothesis on the basis of my previous arguments about the absence of a pyroclastic colour signature. Furthermore, numerical modelling has shown that edifices constructed purely from ballistically emplaced pyroclasts cannot realistically achieve the topographic relief exhibited by the circum-Caloris knobs *(BROŽ ET AL., 2018)*. Based on these considerations, I believe an origin for the circum-Caloris knobs as Caloris ejecta is most consistent with my observations.

The interactions between the circum-Caloris knobs and impact craters provide further evidence that these knobs are composed of unconsolidated material. In Fig. 6.13a I showed a knob with an impact crater partially obscured by the knob's outer edge. If the knob were a volcano active long after the cessation of the voluminous eruptions, which generated the smooth plains surrounding the knob, then it would be possible for a volcanic knob to grow and bury nearby impact craters with either lava flows or ballistically emplaced pyroclasts. As I have explained previously, I do not think the circum-Caloris knobs can be pyroclastic constructs due to their lack of a red colour anomaly characteristic of explosive volcanism elsewhere on Mercury *(MURCHIE ET AL., 2008)* and the results from numerical simulations that show that ballistically emplaced pyroclasts on Mercury are probably incapable of constructing the topographic relief of a knob *(BROŽ ET AL., 2018)*. However, my observation of an alcove-like notch upslope of the crater on the knob suggests that this knob is composed of unconsolidated materials, rather than a coherent volcanic pile. If the knob is an ejecta block remnant that is disintegrating then as time passes material will be transported from the top of the knob downwards. This will have the dual effect of lowering the height of the knob and spreading out knob material laterally. Knob material encroaching on an existing impact crater will build up until it overtops the crater rim and begins to infill the crater. This process is conceptually the same as burial of the crater by lava flows. However, if the knob is shedding material when it is struck by an impact near its periphery then it is possible for a great volume of knob material to cascade all at once into the newly formed impact crater. This would result in the formation of a cavity in the knob, such as might

correspond to the notch I have observed in Fig. 6.13a. It is difficult to imagine how a similar notch could be formed by a volcano erupting lavas.

My observation of a knob interacting with a lobate scarp (Fig. 6.15a) provides more information about the nature of the circum-Caloris knobs. This lobate scarp is intriguing because it cuts directly across the rim of the Caloris basin (Fig. 6.15b). This means that at least some, if not all, movement on this fault occurred after the Caloris impact. Evidence of geologically young fault movement at this lobate scarp comes in the form of back-scarp grabens on the topographic crest of the lobate scarp. These grabens are small with respect to their associated lobate scarp. This means that they would be more easily erased by impact gardening following the cessation of activity on the main fault than the large scarp itself. Not all major lobate scarps on Mercury possess recognisable back-scarp grabens, but apparently newly formed lobate scarps have pristine back-scarp grabens *(WATTERS ET AL., 2016)*. This suggests that movement on some portions of the lobate scarp cutting across the Caloris rim could be geologically young. This is important because this lobate scarp also cuts through the Odin Formation and several large circum-Caloris knobs are located in its vicinity. The knob in Fig. 6.15a lies on top of where one would expect the surface break of the lobate scarp to be. This knob is not deformed by the lobate scarp in a brittle fashion. This suggests that the knob formed more recently than the most recent movement on this fault or that knob was originally deformed by the lobate scarp but has since been resurfaced. Two important additional observations are that: (1) material from this knob appears to be located up the steep face of the lobate scarp from the base of the knob, and; (2) a hollow is located near the base of the knob.

The apparent superposition of this knob on this lobate scarp, which has evidently built much of its topography after the formation of Caloris Planitia, could be explained by this knob being a late-stage volcanic construct. However, this is inconsistent with many of my other observations (lack of volcanic crater, lack of volcanic colour signature, and the presence of hollows nearby). However, if this knob formed from a Caloris ejecta block then it must predate some if not all of the fault movement on the lobate scarp it abuts. The fact that the knob does not appear to be cut by the lobate scarp would seem to contradict this requirement, however

if a substantial portion of the knob is composed of unconsolidated material then cascades of loose knob material could have resurfaced any affected regions on the surface of the knob. The knob material observed on the steep scarp face apparently upslope from the base of the knob is more difficult to explain. If the circum-Caloris knobs are the remnants of Caloris ejecta blocks, then I believe the most likely explanation for this knob material being present upslope from the present day location of the knob is that the original ejecta block was much larger than the present day knob. The original ejecta block could have been large enough that it existed on both sides of the lobate scarp's surface break. As the ejecta block evolved into the present day knob, it shed material all around it, including on the existing or growing lobate scarp steep face. At some stage, the 'core' of the shedding ejecta block became located on the footwall side of the lobate scarp, where it is today. After that, shedding of knob material was restricted to the footwall side of the scarp and the material on the steep face of the scarp was deposited when the knob-scarp system was in a different configuration from that observed today.

6.5.3   Knob distribution

In Fig. 6.18, I show my map of the locations of the circum-Caloris knobs. Knobs are not uniformly distributed around the Caloris basin. Knobs are generally densely spaced proximal to the basin rim and more sparsely distributed farther from the basin. I found a small number of knobs within Caloris Planitia, the smooth plains making up the interior of the basin. Knobs located inside the Caloris basin are situated no farther than 100 km inside the basin rim. There are no knobs within the deep interior of the Caloris basin. The knobs most distal from the basin occur ~1,000 km beyond the south-southwestern rim.
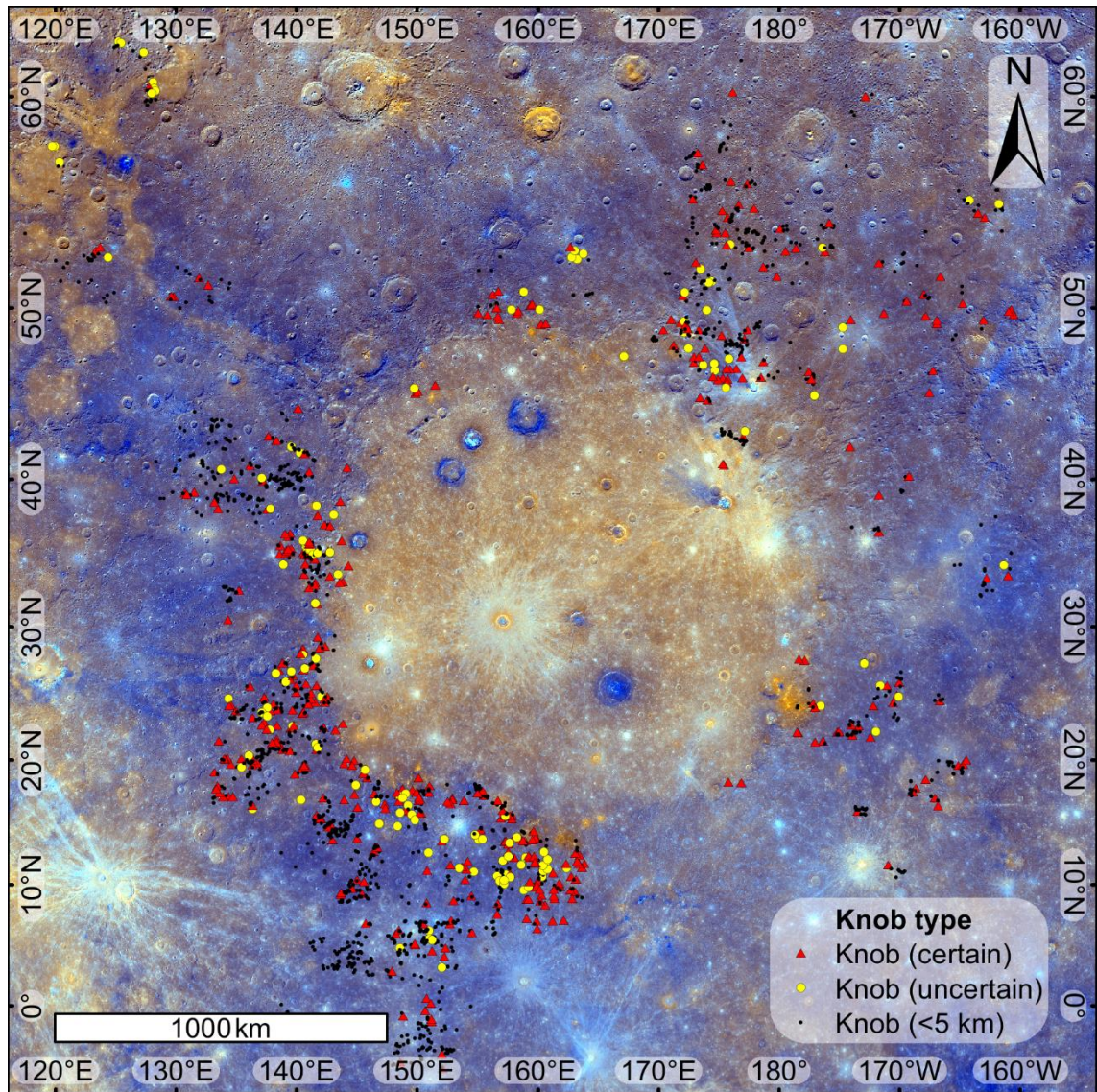
Fig. 6.18 The distribution of the circum-Caloris knobs. *All knobs ≥5 km in diameter are shown. Individual knobs are marked with a red triangle. Landforms tentatively identified as knobs, but could be potentially unrelated landforms, are marked with yellow circles. Knobs marked with small black dots are prominent but <5 km in diameter. Mercator projection centred at 162.7°E, 31.5°N. ~665 m/pixel enhanced colour global mosaic.*

Knobs are occasionally arranged in chains that radiate approximately from the centre of the Caloris impact basin (Fig. 6.19).
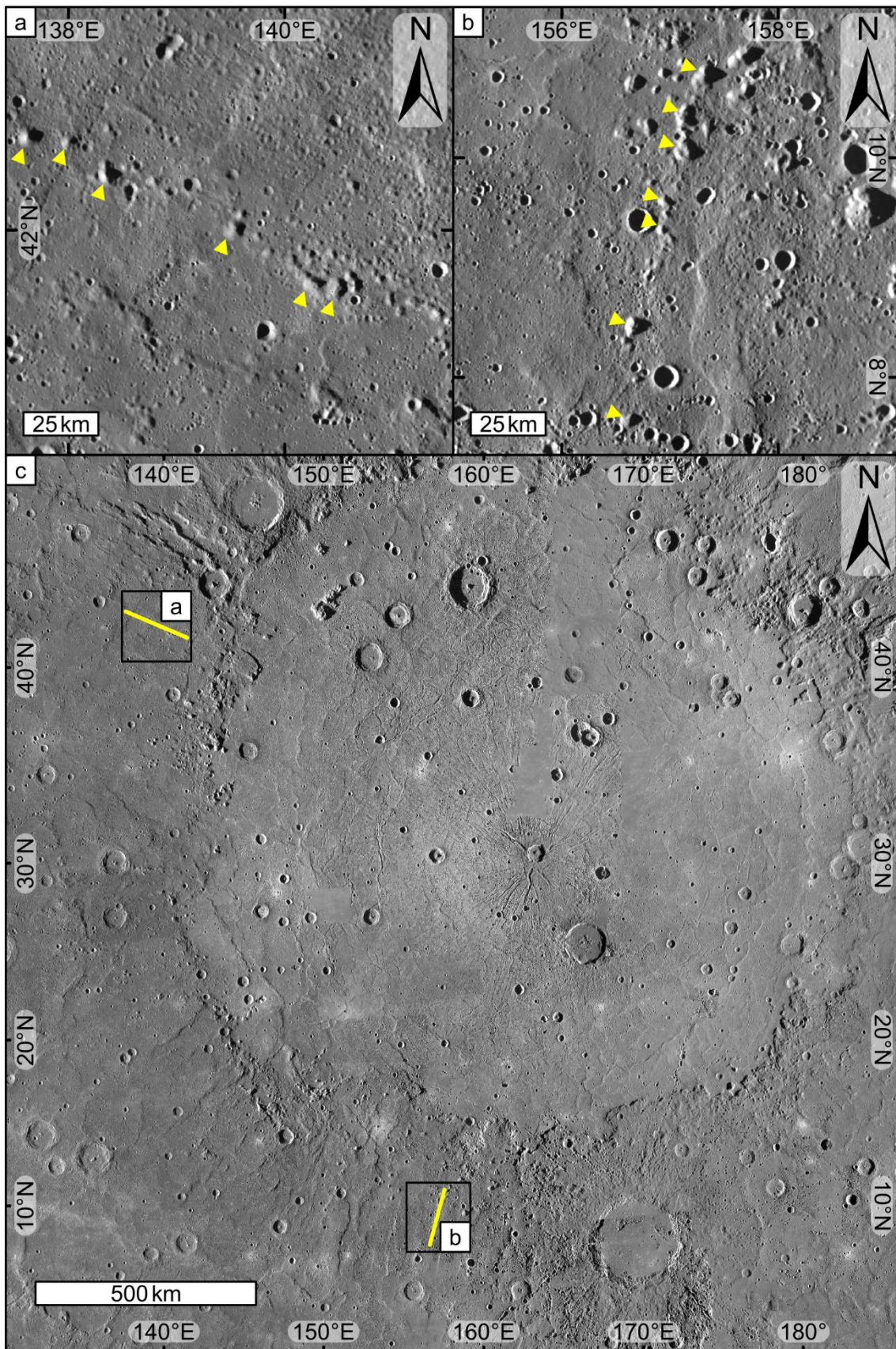
Fig. 6.19 Knob chains. (a) An example of a chain of circum-Caloris knobs. (b) Another example of a chain of knobs. Some single and multi-knob landforms are elongate in the direction of the chain. (c) Context view of Caloris showing the locations of (a) and (b). The yellow lines indicate the trends of the knob chains. All panels show Mercator projections centred on 162.7°E, 31.5°N. All panels show the ~166 m/pixel global monochrome mosaic.

6.5.3.1 Knob distribution with respect to geological setting

Fig. 6.18 also shows that knobs are not found in equal spatial densities at all azimuths around the Caloris basin. The sketch geological map of the Caloris region shown in Fig. 6.20 indicates some probable explanations for this observation.

Knobs most commonly occur within the Odin Formation, as mapped by *DENEVI ET AL. (2013)*, and the Caloris Montes Formation (Caloris rim material). Any future update to the Odin Formation mapping is unlikely to overturn this association. Knobs also occur in the smooth plains, however they typically lie close to the smooth plains contact with the Odin Formation or the Caloris Montes Formation. Knobs occur only rarely within the ejecta blankets of superposing craters within the mapped region. Most knobs within young crater ejecta blankets lie towards the thin outer margins of the ejecta, as can been seen at the Mozart impact basin (Fig. 6.20).
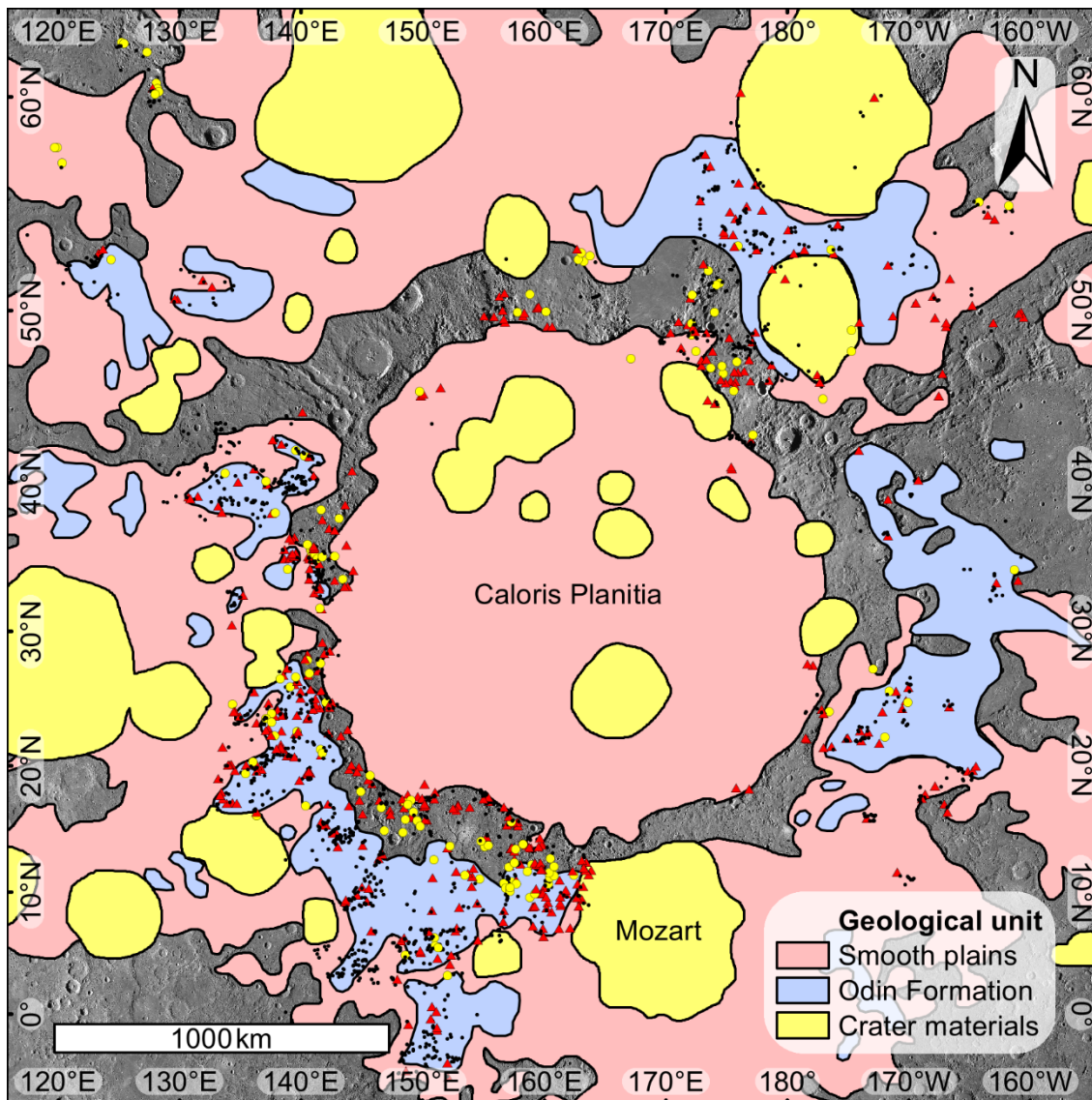
Fig. 6.20 Distribution of the circum-Caloris knobs in relation to key photogeological units. *Knob symbology matches that shown in Fig. 6.18. Geological units redrawn and simplified from DENEVI ET AL. (2013). Mercator projection centred at 162.7°E, 31.5°N. ~166 m/pixel MDIS global monochrome mosaic.*

6.5.3.2 Knob distribution with respect to elevation

In Fig. 6.21 I show my map of knobs with respect to Mercury's surface elevation. I was interested to see if surface elevation had any control on where knobs occur. At the regional scale of Caloris (Fig. 6.21a) there appears to be no obvious relationship between areas with a high spatial density of knobs and either areas of high or low topography. However, any relationship between knob distribution and regional topography might be obscured since this region has long-wavelength topographic

undulations that postdate the emplacement of Caloris and its associated smooth plains units *(ZUBER ET AL., 2012; BYRNE ET AL., 2014)*.

Conversely, at local scales (Fig. 6.21b and Fig. 6.21c) knobs appear more commonly on high-standing topography. Locally low-lying regions are more often occupied by smooth plains than the knobby Odin Formation. I have found examples of individual knobs and knobby plains occurring on the uplifted region above the hangingwalls of lobate scarps. Knobs frequently occur on the rims of apparently pre-Caloris impact craters, but the floors of these craters have been buried by smooth plains.
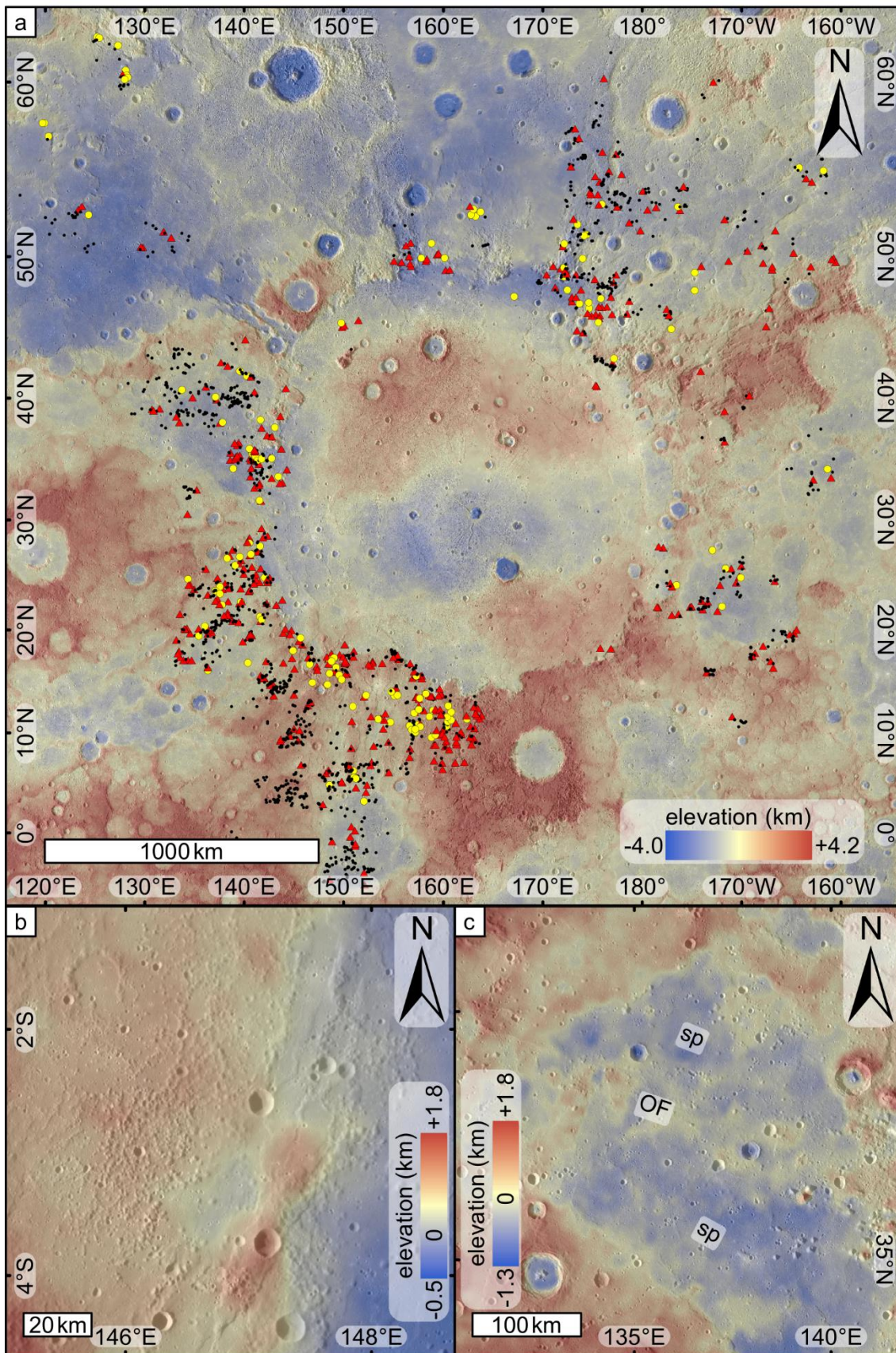
Fig. 6.21 Knob distribution with respect to Mercury's surface elevation. (a) Locations of all mapped knobs overlain on the global stereo-derived DEM of Mercury. At this scale, knob distribution does not appear to be obviously influenced by surface elevation. Knobs appear in both high and low concentrations in regions of high and low absolute elevation. Note the approximately east-northeast–west-southwest trending topographic bulges and troughs within and around Caloris. (b) An example where there appears to be a relationship between local topography and knob distribution. The plains in the centre-left of this panel are knobby and at locally high elevations. West of the knobs, the elevation gently drops and the plains become characterised by smooth floored impact craters with rims, where these are exposed, with knobs on them. The plains east of the knobs are smooth and at lower elevations. The knobs in this panel appear to be situated on the topographically high crests of lobate scarps. (c) Another region where local elevation may control knob exposure. A band of Odin Formation (OF), including small knobs, is exposed on locally high topography in the middle of an otherwise low elevation circular depression just west of the Caloris rim. Large knobs occur on the periphery of this depression, but no knobs occur within the centres of the lobes of smooth plains (sp) that exist north and south of the central band of Odin Formation. All panels show Mercator projections centred on 162.7°E, 31.5°N. All panels show the 665 m/pixel global stereo-derived DEM of Mercury (BECKER ET AL., 2016) overlain on the ~166 m/pixel global monochrome mosaic.

6.5.4 Interpretations of knob distribution

It is apparent from my map of the circum-Caloris knobs that several factors appear to have contributed to their present-day distribution.

6.5.4.1 Knob distribution with respect to geological setting

The overwhelming majority of mapped knobs occur within the Odin Formation, although knobs were found in the other members of the Caloris Group. As previously stated, the knobs within the smooth plains within and without Caloris appear to have been embayed by the smooth plains. This means that the embayed knobs most likely belong to Odin Formation that is stratigraphically below these smooth plains. Examples of knobs on the exposed rims of deeply flooded impact craters north east of Caloris provide corroborating evidence for this hypothesis.

6.5.4.2 Knob distribution with respect to elevation

As stated previously, any relationship between knob distribution and surface elevation has been obscured by long-wavelength topographic undulations than postdate Caloris *(ZUBER ET AL., 2012)*. However, my observations of knobs appearing in higher spatial densities on locally high-standing topography supports my hypothesis that the knobs are native to the Odin Formation, which itself is Caloris ejecta, and that its exposure in the present day is controlled by the presence or absence of thick, post-Caloris volcanic smooth plains. The fact that knobs appear on the uplifted hangingwalls of lobate scarps suggests that these lobate scarps had built significant local topography by the time the volcanic smooth plains were emplaced (~100 Myr after the Caloris impact). If lobate scarp topography postdated smooth plains inundation of the region then smooth plains would be found on both sides of the lobate scarp surface breaks.

6.5.5   Knob topography

Here I present the results of my topographic measurements of knobs.

6.5.5.1 MLA-derived knob topography

Of the 545 knobs ≥5 km in diameter, 22 had MLA tracks with useful data (Fig. 6.22–Fig. 6.27; these figures were separated for convenience and illustrate the knobs in no particular order). These data show that pristine circum-Caloris knobs typically have planar flank slopes, whereas degraded knobs are more likely to have convex-up flanks. Where MLA data tracks appear to pass along lines of steepest ascent and descent of a given knob, the median flank slopes calculated from these data are ~15–23°. Knobs >10 km in diameter are rare, but two such knobs have heights of ~2 km.

MLA data proved to be very useful to me in making confident topographic measurements of the circum-Caloris knobs, however there are several shortfalls with these data that warrant alternative methods for estimating knob topography.

As mentioned in Section 6.4.2, at the outset of this study I knew MLA data would be unavailable for most circum-Caloris knobs. Once I finished mapping the knobs and found all those with useful MLA data, I was left with the 22 knob profiles in this section. 22 out of 545 knobs ≥5 km in diameter represents just over 4% of the

population, which would be a poor sample on which to base all my conclusions. MLA data were particularly sparse over the circum-Caloris knobs since many of them occur at low northern latitudes. As explained in Chapter 3, MLA lateral track spacing increased away from Mercury's northern pole *(CAVANAUGH ET AL., 2007; ZUBER ET AL., 2012).*

Where MLA data did coincide with a knob there was no guarantee that the MLA data would be useful. Seams due to inconsistent image georeferencing in the MESSENGER MDIS mosaics meant that the topography that particular MLA tracks covered could not be ascertained confidently.

In other cases, MLA data clearly did measure knob topography but the returns to MESSENGER were given low signal-to-noise ratio flags (i.e. channel ≥5) and so they could not be used. MLA worked by firing a laser pulse and measuring the two-way travel time in order to calculate the range to Mercury's surface *(CAVANAUGH ET AL., 2007).* A single pulse was capable of producing multiple returns because the laser footprint on Mercury's surface from an altitude of ~200 km is ~16 m across *(CAVANAUGH ET AL., 2007).* Within this 16 m diameter, surface roughness can cause multiple reflections. If the strongest first reflection is scattered by steep slopes, such as can occur at knobs, then it cannot return to the spacecraft, leaving weaker return pulses with lower signal-to-noise ratios, which I could not use in my study, to be recorded by MESSENGER. Off-nadir surface ranging also produced low signal-to-noise MLA data *(CAVANAUGH ET AL., 2007).* Off-nadir ranging also produced MLA tracks that were deflected from a straight line, which meant several tracks that appeared to be summit crossing in fact slightly missed measuring the maximum height of their knob (e.g. Fig. 6.24c). A more serious flaw of off-nadir MLA data was that steep knobs were apparently capable of eclipsing their slopes that faced away from the spacecraft look angle, leading to incomplete data over the knob (Fig. 6.23c).

Even if the MLA data quality for a knob was good, sometimes the distance between MLA data points (typically 400 m) was too great for smaller knobs (e.g. Fig. 6.22g). This meant that the topography of some knobs was under-sampled by MLA, meaning that my slope calculations might be underestimates.

I hoped that by using my shadow measurement technique I might be able to mitigate some of the problems I would have if I based my conclusions entirely on my small sample of knobs with high quality MLA data.
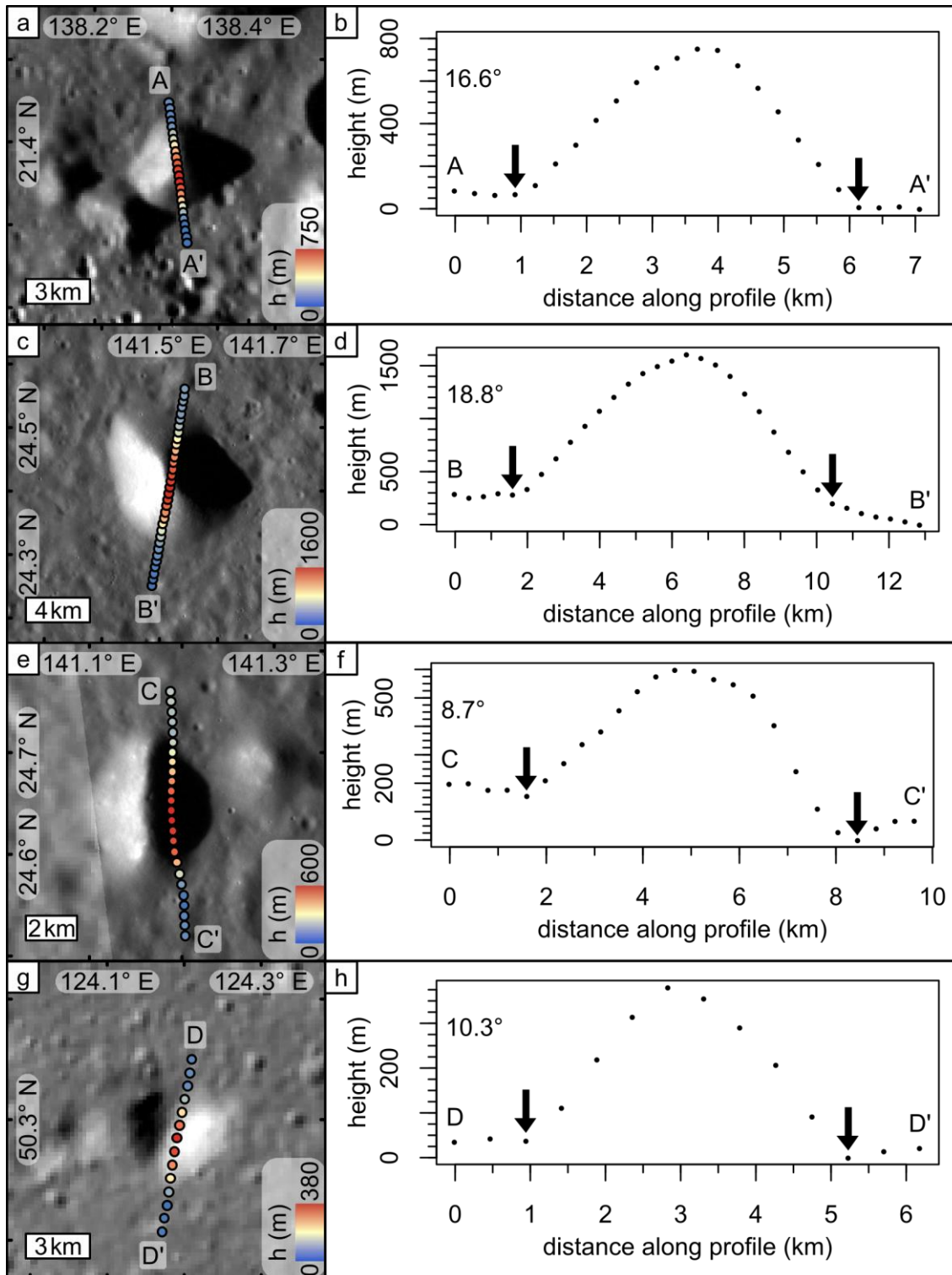
Fig. 6.22 MLA measurements of knob topography (1). *Panels (a), (c), (e) and (g) show MDIS images of knobs and the locations of MLA topography measurements. These panels show Mercator projections centred on 162.7°E, 31.5°N. Panels (b), (d), (f) and (h) show topographic profiles of their corresponding knobs. In the upper-left of each topographic profile I have included the median 3-point slope of each knob that I calculated using the topographic data between the black arrows. All panels indicate the start and end points of each topographic profile with lettering (e.g. A–A'). (a) MDIS WAC frame EW0220893691G (123.9 m/pixel) and MLASCIRDR1108030842 data points. This summit-crossing profile probably measured the maximum height and flank slopes of this knob. (b) Topographic profile from MLASCIRDR1108030842. (c) MDIS NAC frame EN1015339337M (36.1 m/pixel) and MLASCIRDR1503130635 data points. This profile probably measured the maximum height and true maximum southern flank slope. (d) Topographic profile from MLASCIRDR1503130635. (e) MDIS NAC frame EN1015339337M (36.1 m/pixel) and MLASCIRDR1501140941 overlain on the ~166 m/pixel global monochrome mosaic. This profile runs adjacent to the elongate summit of this knob and across, rather than up and down, its flank slopes. The measured height and flank slope are underestimates. (f) Topographic profile from MLASCIRDR1501140941. The broad knob summit apparent in this topographic profile appears to be due to the profile running parallel to, not across, the sharp summit of the knob. (g) MDIS WAC frame EW0231135692G (189.4 m/pixel) and MLASCIRDR1501171132. This summit-crossing profile probably measures the true height and flank slope of this knob. (h) Topographic profile from MLASCIRDR1501171132. This knob's diameter is just above the 5 km threshold for inclusion in my MLA knob topography dataset. The ~475 m MLA data point separation means that this knob's topography is poorly sampled by MLA.*
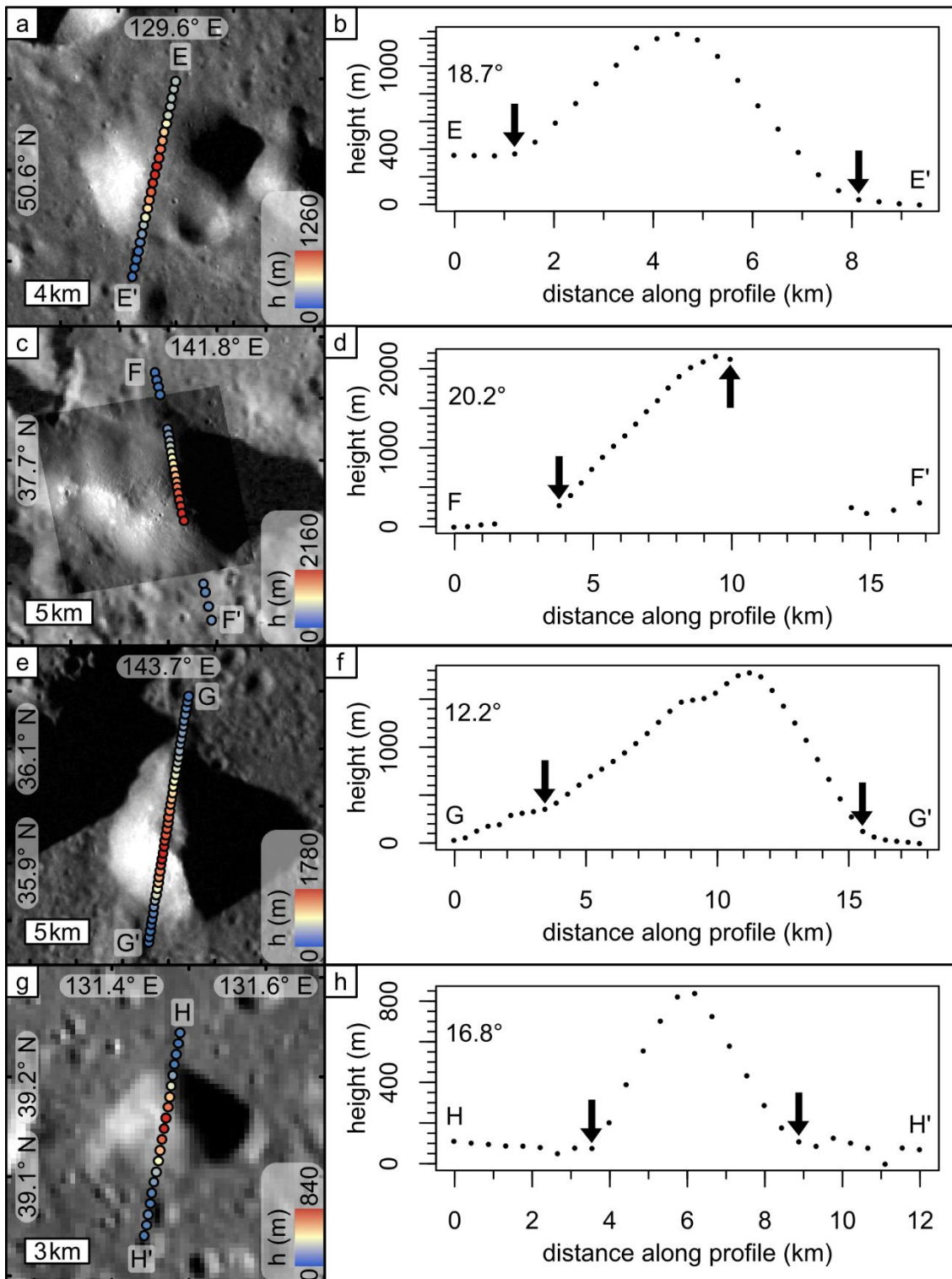
Fig. 6.23 MLA measurements of knob topography (2). Panels (a), (c), (e) and (g) show MDIS images of knobs and the locations of MLA topography measurements. These panels show Mercator projections centred on 162.7°E, 31.5°N. Panels (b), (d), (f) and (h) show topographic profiles of their corresponding knobs. In the upper-left of each topographic profile I have included the median 3-point slope of each knob that I calculated using the topographic data between the black arrows. All panels indicate the start and end points of each topographic profile with lettering (e.g. E–E'). (a) MDIS WAC frame EW0220893257G (~64.8 m/pixel) and MLASCIRDRI403291801 data points. This summit-crossing profile cuts diagonally across the true flank slope of the knob apparent in the image. As a result, the height of the knob is probably accurate, but the flank slope calculated from the profile is an underestimate. (b) Topographic profile from MLASCIRDRI403291801. Despite an oblique MLA track crossing, I calculated a relatively steep median flank slope of 18.7° for this knob. (c) MDIS NAC frame EN0220720623M (12.4 m/pixel) and MLASCIRDRI109300948 data points overlain on the ~166 m/pixel global monochrome mosaic. MLA data are missing at the northern base of the knob and along its southern flank. The gap at the northern base is because no data with a high signal-to-noise channel were available, possibly due to local rough terrain. The gap on the southern flank is probably due to the off-nadir angle of MLA (~32°), which would mean that the northern flank of the knob blocked the southern flank from MLA's view. As a result, the slope of this knob was calculated using a partial profile. (d) Topographic profile from MLASCIRDRI109300948. This knob's northern flank has an approximately planar 20° slope. (e) MDIS WAC frame EW0220763859G (86 4 m/pixel) and MLASCIRDRI503130635 data points. These MLA data sample the narrow plateau at the summit of this knob, meaning that the measured maximum height of the knob is probably accurate. The MLA data track lies obliquely across the southern flank of the knob, meaning that flank slope I calculated for this knob is an underestimate. (f) Topographic profile from MLASCIRDRI503130635. The southern flank of this knob is much steeper than the northern flank. (g) MDIS WAC frame EW0251314775G (233.8 m/pixel) and MLASCIRDRI503150815 data points. The MLA data track passes up the steepest ascent of the knob to the summit, meaning that the maximum height and flank slope measurements I made are accurate. (h) Topographic profile from MLASCIRDRI503150815. The ~445 m spacing of the MLA data points means that the topography of this small knob is poorly sampled.
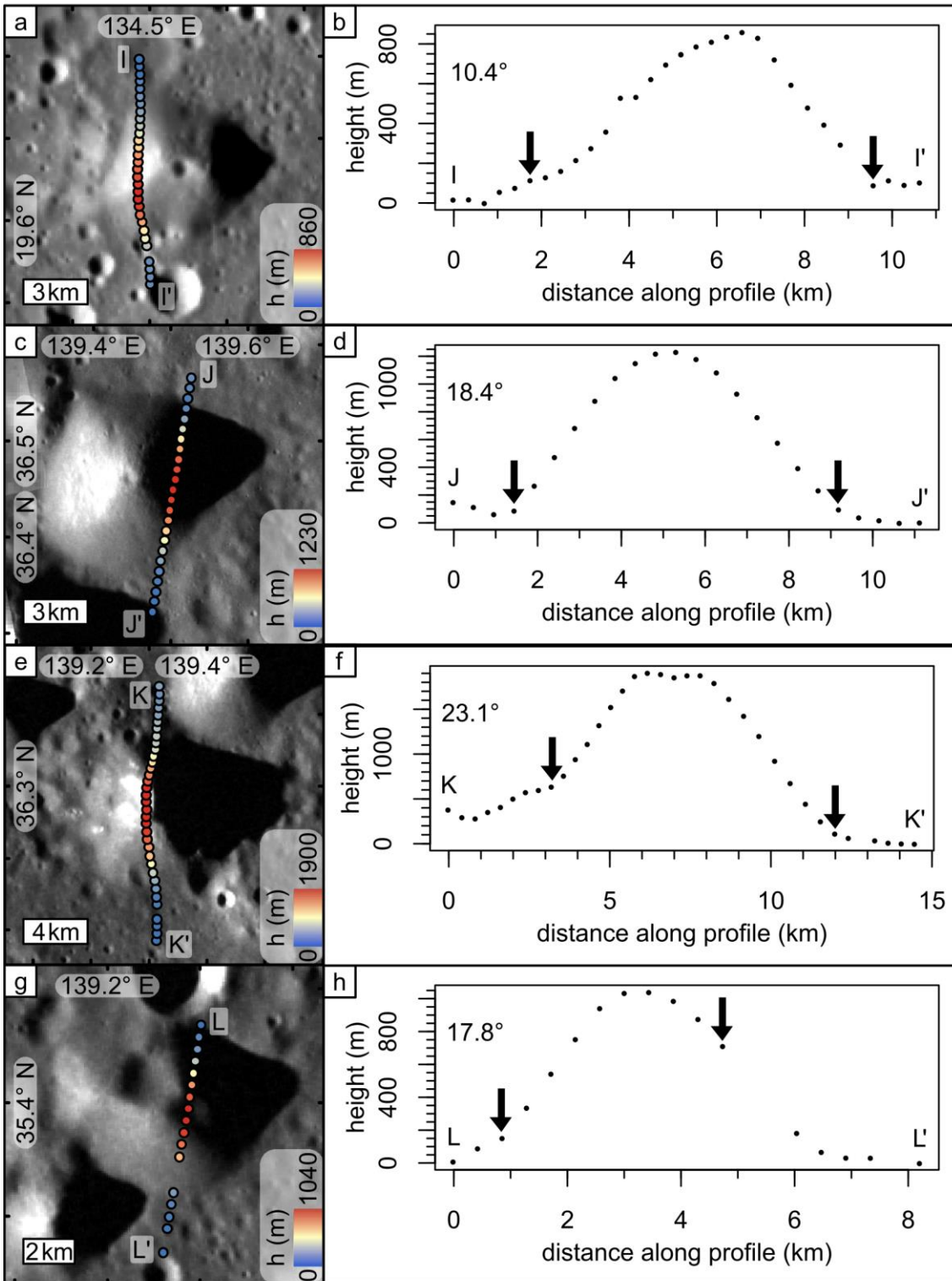
Fig. 6.24 MLA measurements of knob topography (3). Panels (a), (c), (e) and (g) show MDIS images of knobs and the locations of MLA topography measurements. These panels show Mercator projections centred on 162.7°E, 31.5°N. Panels (b), (d), (f) and (h) show topographic profiles of their corresponding knobs. In the upper-left of each topographic profile I have included the median 3-point slope of each knob that I calculated using the topographic data between the black arrows. All panels indicate the start and end points of each topographic profile with lettering (e.g. J–J'). (a) MDIS NAC frame EN1045848643M (101.5 m/pixel) and MLASCIRDR1501151016 data points. These MLA data do not sample the summit of the knob and traverse the knob across, rather than along, its flank slopes. As a result, my calculated slopes and height for this knob are underestimates. (b) Topographic profile from MLASCIRDR1501151016. The trapezoidal shape of this profile is an artefact of the oblique crossing of the knob by the MLA data. The shadow of this knob indicates that this knob has a triangular cross-section in actuality. (c) Mosaic of MDIS NAC frames EN1015339048M (27.1 m/pixel) and EN1015339061M (27.4 m/pixel) with MLASCIRDR1503132308 data points overlain on the ~166 m/pixel global monochrome mosaic. These MLA data do not sample the summit of the knob and traverse the knob across, rather than along, its flank slopes. As a result, my calculated slopes and height for this knob are underestimates. (d) Topographic profile from MLASCIRDR1503132308. Despite an oblique, non-summit-crossing profile, I have measured a height for this knob in excess of 1 km and slopes >18°. The true height and slope of this knob are likely to be even greater. (e) MDIS WAC frame EW0220807059G (86.1 m/pixel) and MLASCIRDR1407230620 data points. This is an ideal profile that crosses the summit of the knob and samples the true slopes of the flanks. (f) Topographic profile from MLASCIRDR1407230620. The knob has planar upper flanks with a concave-up lowermost slope on its southern side. This knob has the steepest flank slope of all the knobs measured using MLA data. (g) MDIS WAC frame EW0220807059G (86.1 m/pixel) and MLASCIRDR1503132308 data points. This profile has a near-ideal geometry that passes close to the knob summit and samples the true slope of the flanks. (h) Topographic profile from MLASCIRDR1503132308.

Fig. 6.25 MLA measurements of knob topography (4). *Panels (a), (c), (e) and (g) show MDIS images of knobs and the locations of MLA topography measurements. These panels show Mercator projections centred on 162.7°E, 31.5°N. Panels (b), (d), (f) and (h) show topographic profiles of their corresponding knobs. In the upper-left of each topographic profile I have included the median 3-point slope of each knob that I calculated using the topographic data between the black arrows. All panels indicate the start and end points of each topographic profile with lettering (e.g. M–M'). (a) MDIS NAC frame EN1015223834M (28.2 m/pixel) and MLASCIRDR1501140941 data points overlain on the ~166 m/pixel global monochrome mosaic. This is a non-ideal profile that does not sample the knob summit or the true slopes of the knob's flanks. My maximum height and flank slope measurements calculated from these data are underestimates. (b) Topographic profile from MLASCIRDR1501140941. Despite the non-ideal MLA track geometry, I have calculated relatively steep flank slopes of 16.1° for this knob. (c) MDIS WAC frame EW0220807059G (86.1 m/pixel) and MLASCIRDR1207182305 data points. This MLA track has ideal knob-crossing geometry but has unevenly distributed data with the requisite signal-to-noise for slope calculations. (d) Topographic profile from MLASCIRDR1207182305. My height measurement of this knob is accurate, but my slope calculation might be affected by the uneven spacing of the MLA data. (e) MDIS NAC frame EN1015339241M (33.0 m/pixel) and MLASCIRDR1409182117 data points. This MLA track has ideal knob-crossing geometry. (f) Topographic profile from MLASCIRDR1409182117. The planar southern flank of this knob appears to terminate with an abrupt break in slope at its base. This knob has relatively steep flank slopes. (g) MDIS WAC frame EW0220849922G (58.9 m/pixel) and MLASCIRDR1405280237 data points. This MLA track samples the northern flank of this knob well, but lacks data on the southern flank. (h) Topographic profile from MLASCIRDR1405280237. This northern flank has a planar surface.*
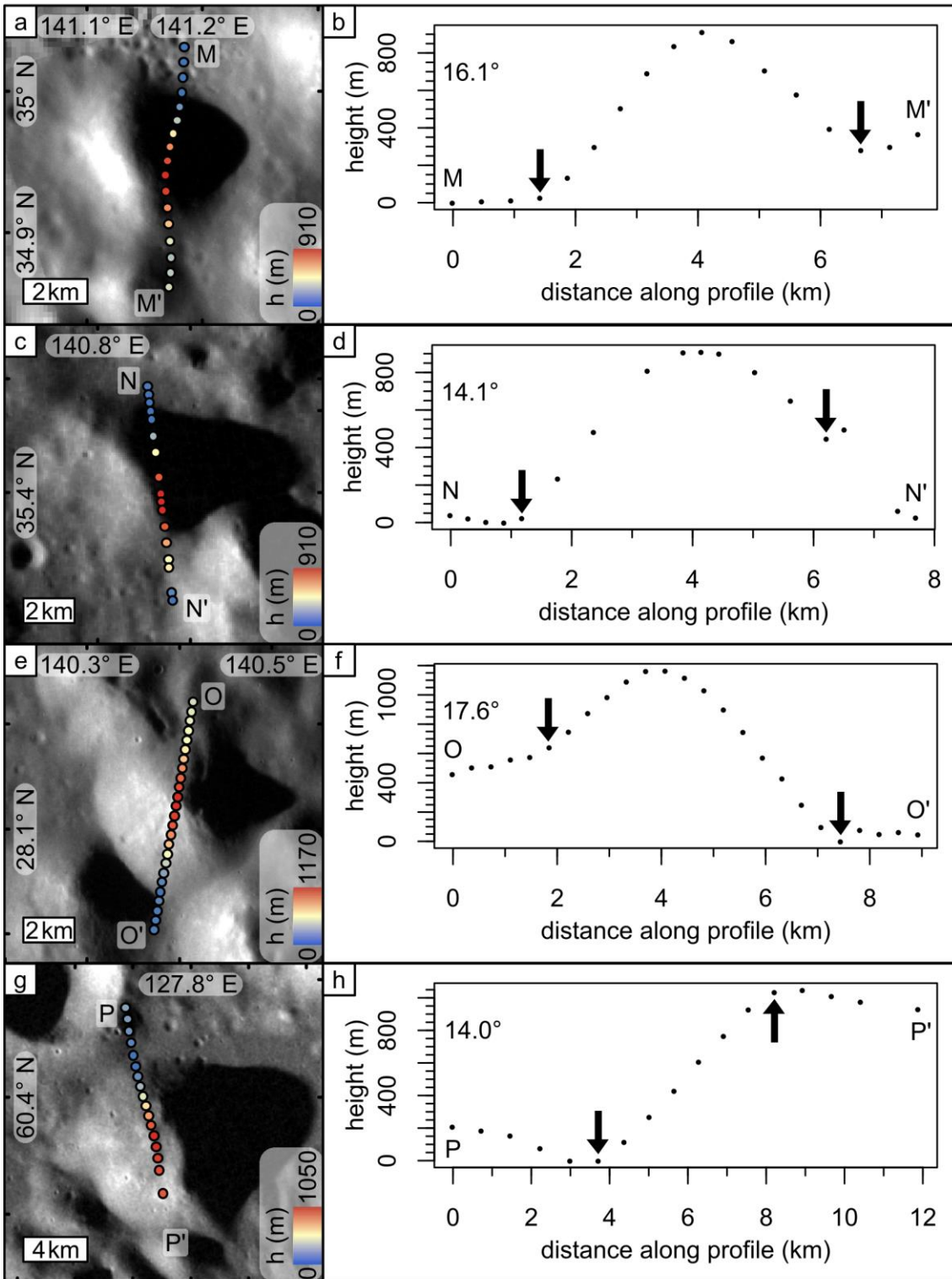
Fig. 6.26 MLA measurements of knob topography (5). *Panels (a), (c), (e) and (g) show MDIS images of knobs and the locations of MLA topography measurements. These panels show Mercator projections centred on 162.7°E, 31.5°N. Panels (b), (d), (f) and (h) show topographic profiles of their corresponding knobs. In the upper-left of each topographic profile I have included the median 3-point slope of each knob that I calculated using the topographic data between the black arrows. All panels indicate the start and end points of each topographic profile with lettering (e.g. Q–Q'). (a) MDIS WAC frame EW0220159587G (78.2 m/pixel) and MLASCIRDR1503081900 data points. The high-resolution MDIS data that capture this knob all have high solar incidence angles. The MLA track has somewhat non-ideal knob-crossing geometry that passes within one kilometre of the summit. (b) Topographic profile from MLASCIRDR1503081900. The non-ideal geometry of the MLA track may mean that the flank slope I calculated based on this profile is an underestimate however the true flank slope of this knob is unlikely to be >>10°. (c) MDIS NAC frame EN0258312801M (23.9 m/pixel) and MLASCIRDR1103290204 data points overlain on the ~166 m/pixel global monochrome mosaic. This MLA track has near-ideal knob crossing geometry. (d) Topographic profile from MLASCIRDR1103290204. The low slopes of this knob are not likely to be due to the imperfect knob-crossing geometry of the MLA data track. (e) MDIS WAC frame EW1000273184G (195.7 m/pixel) and MLASCIRDR1110022037 data points. This MLA track has near-perfect knob-crossing geometry, however the track appears to have been deflected somewhat due to off-nadir pointing of MLA. (f) Topographic profile from MLASCIRDR1110022037. The good knob-crossing geometry of the MLA data track means that my calculated knob height and flank slope are accurate. (g) MDIS WAC frame EW0227853976G (174.0 m/pixel) and MLASCIRDR1407141333 data points. This MLA track has ideal knob-crossing geometry. (h) Topographic profile from MLASCIRDR1407141333. This knob appears to have a broad, relatively flat summit, which appears to have contributed to the low flank slope I calculated for this knob.*
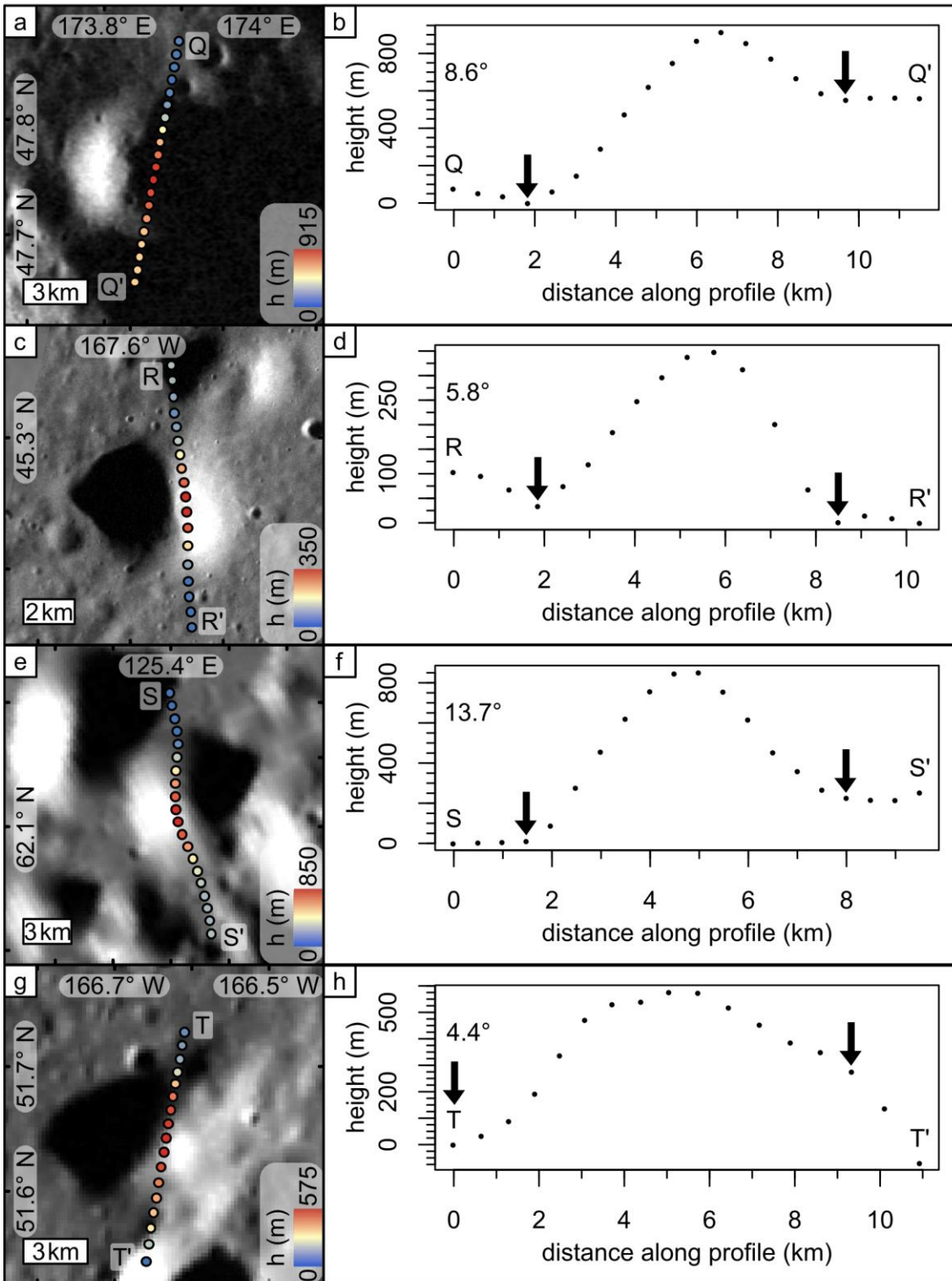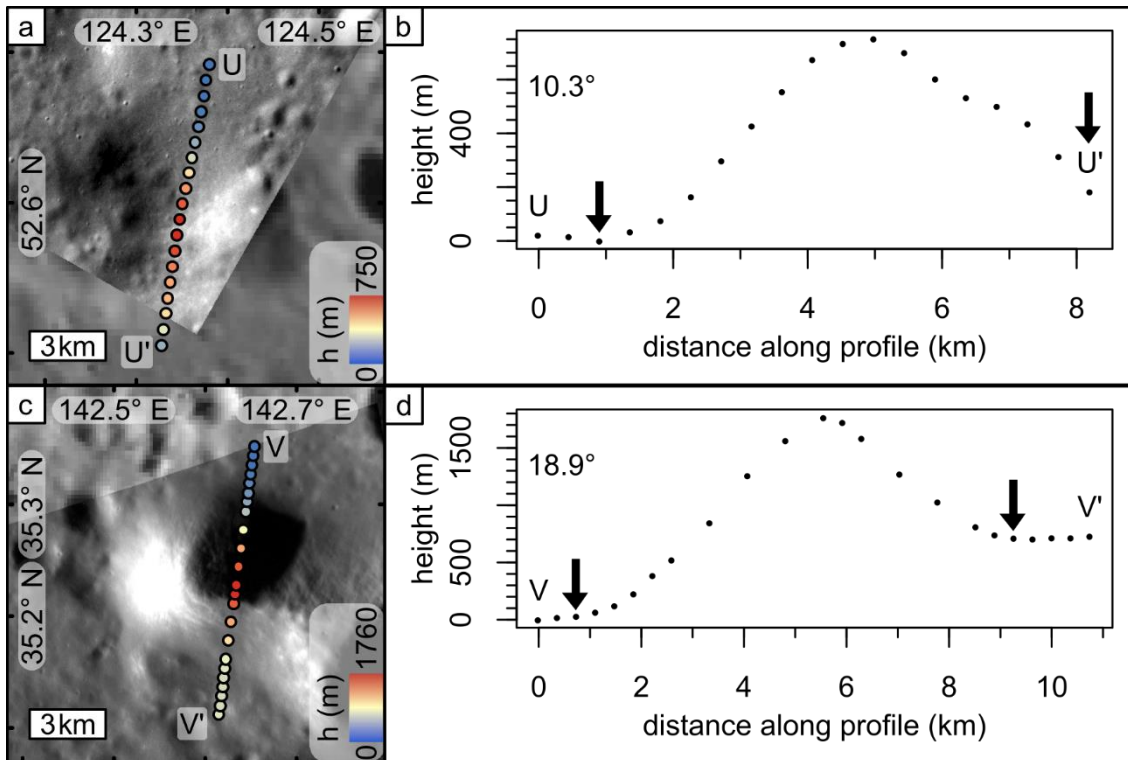
Fig. 6.27 MLA measurements of knob topography (6). *Panels (a) and (c) show MDIS images of knobs and the locations of MLA topography measurements. These panels show Mercator projections centred on 162.7°E, 31.5°N. Panels (b) and (d) show topographic profiles of their corresponding knobs. In the upper-left of each topographic profile I have included the median 3-point slope of each knob that I calculated using the topographic data between the black arrows. All panels indicate the start and end points of each topographic profile with lettering (e.g. U–U'). (a) MDIS NAC frame EN1056021536M (17.7 m/pixel) and MLASCIRDR1407252235 data points overlain on the ~166 m/pixel global monochrome mosaic. This MLA track has good knob-crossing geometry. (b) Topographic profile from MLASCIRDR1407252235. (c) MDIS NAC frame EN1015223718M (26.0 m/pixel) and MLASCIRDR1403270159 data points overlain on the ~166 m/pixel global monochrome mosaic. This MLA track traverses a 'saddle' between the knob in the centre of the frame and a second knob to the southeast. My measurement of the height of this knob is an underestimate, but the geometry of the MLA track is ideal for measurement of the slope on the knob saddle. (d) Topographic profile from MLASCIRDR1403270159. Even though the MLA data do not pass over the summit of either knob, the height of the saddle between the knobs is over 1.5 km high. Furthermore, this saddle has steep flank slopes.*

6.5.5.2 Comparison of MLA and shadow derived knob topography

Of the 545 circum-Caloris knobs ≥5 km in diameter, 134 cast shadows that I was able to digitise. Of these 134, 15 had MLA data for comparison (Fig. 6.28–Fig. 6.31: these figures illustrate the knobs in no particular order).

In order for a straightforward comparison of MLA- and shadow-derived topographic profiles to be made, the lines of the MLA and shadow profiles must follow very similar knob traverses. More often than not MLA profiles and shadow profiles did not closely coincide, but fortunately a few good overlaps occurred (e.g. Fig. 6.28g, Fig. 6.29a, Fig. 6.30c). I found that where MLA- and shadow-derived profiles made similar knob traverses the shapes of the profiles match very well. Furthermore, the 3-point slopes I calculated based on closely coinciding MLA- and shadow-derived topographic profiles also match well. Flank slope was an important morphometric parameter that I aimed to calculate to characterise the knobs. I show plots of shadow-derived knob flank slopes in Section 6.5.5.3.

Single point comparisons can be made between MLA- and shadow-derived topographic profiles of knobs where these profiles intersect near a knob's summit (e.g. Fig. 6.28c and Fig. 6.30a). In these cases, the shapes of the profiles often do not match, which is to be expected if the knobs have a non-uniform shape, but their estimates of the maximum heights of a knob can be compared. I have found that shadow-derived measurements of knob height have a tendency to underestimate knob height compared with MLA measurements. As predicted in Section 6.4.2.2, this most likely arises from the digitisation method I employed. Since I digitised only umbral shadows of knobs, some fraction of the true shadow length of each knob was lost. The effect of measuring shorter shadow lengths for the knobs is that the calculated knob heights are underestimates. The underestimate is typically ~100 m but can be up to 500 m. Furthermore, shadow-derived topographic profiles of knobs also underestimate knob width compared to MLA measurements. This is because lower flank slopes at the outer margins of knobs do not cast umbral shadows under these conditions, meaning that I could not digitise them. This means that the full width of the knobs could not be measured. This also explains why the basal terminations of shadow-derived knob profiles generally have steep angles of attack, rather than the concave-up returns

to the regional slopes seen in the MLA-derived topographic profiles. As a result, I did not analyse my shadow-derived measurements of knob heights and widths further. For shadow-derived height measurements to be made of these knobs to be trustworthy, a different digitisation rationale, where penumbral shadows are carefully digitised, would need to be employed *(ACKISS ET AL., 2015)*.
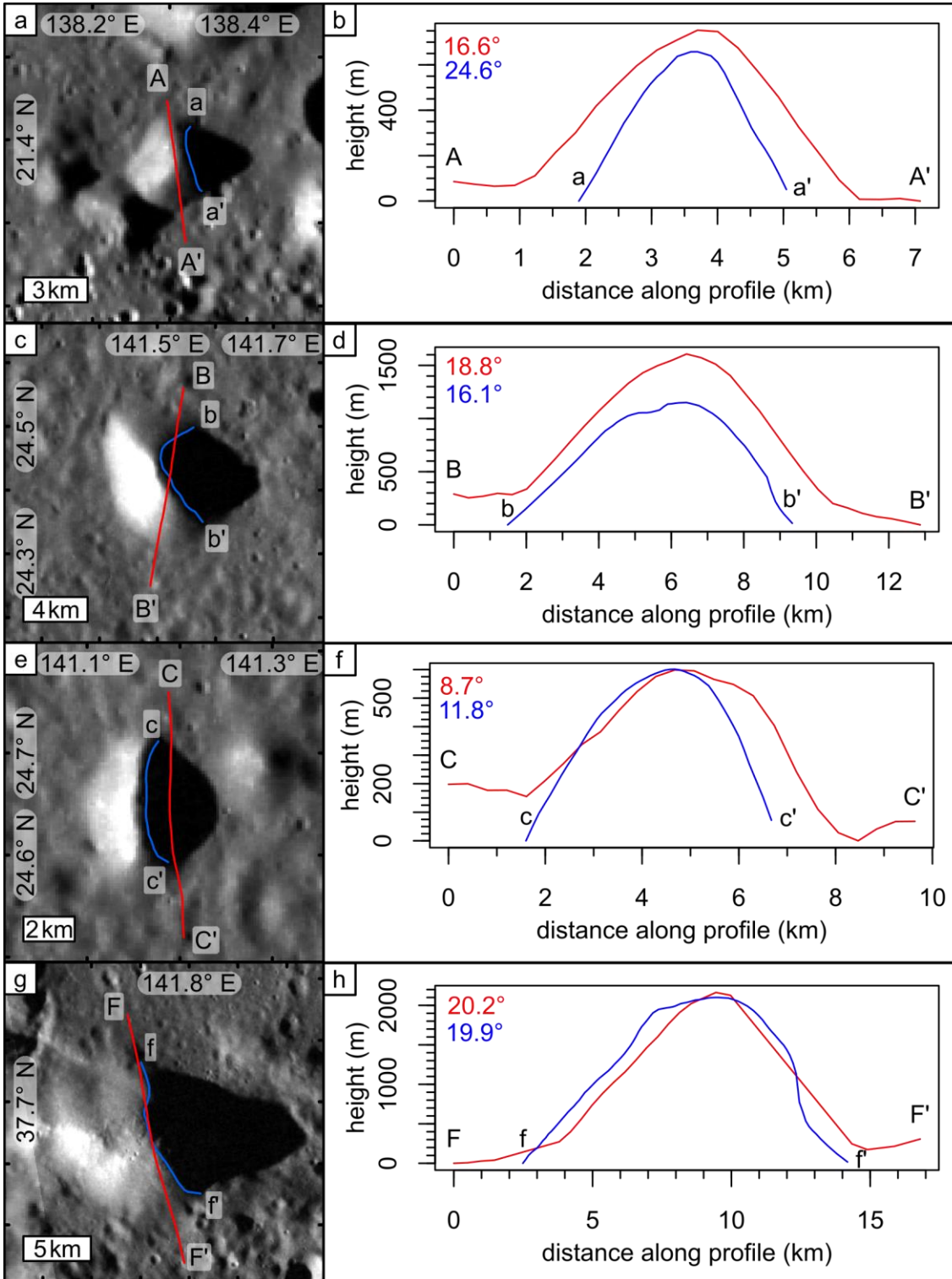
Fig. 6.28 Comparison of MLA- and shadow-derived knob topography (1). Panels (a), (c), (e) and (g) show MDIS images of knobs. The frames shown are the ones I used when I digitised each knob's shadow. MLA tracks are marked as red lines with capital letters marking their start and end points. The blue lines show the digitised shadows of each knob, which also serve as the line of each knob's shadow-derived topographic profile (starts and ends marked with lowercase letters). These panels show Mercator projections centred on 162.7°E, 31.5°N. Panels (b), (d), (f) and (h) show both the MLA- (red) and shadow-derived (blue) topographic profiles on the same axes. These profiles have been aligned so that their maximum height measurements plot at the same X-coordinate. In the upper-left of each plot I have included the median 3-point slope for both types of topographic profile for each knob. The colour of the slope values matches the colour of their profile line. The MLA-derived 3-point slopes were calculated using data in the same range as indicated by the black arrows in Fig. 6.22–Fig. 6.27. Shadow-derived 3-point slopes were calculated using the full range of data for each knob. (a) MDIS WAC frame EW0220893691G (123.9 m/pixel). The shadow-derived profile traverses the knob beneath its summit. Therefore, the maximum height and width of the knob I estimated from its shadow profile are underestimates. (b) Topographic profiles from MLASCIRDR1108030842 and the knob's shadow. The shadow-derived knob height and width are underestimates. The shadow profile qualitatively reproduces the shape measured by the MLA data. (c) MDIS WAC frame EW0220764022G (112.4 m/pixel). The shadow profile line crosses the MLA profile line close to the knob summit, which allows the profiles to be compared at this point. (d) Topographic profiles from MLASCIRDR1503130635 and the knob's shadow. The shadow-derived topographic profile underestimates the height of the knob by 450 m. The calculated flank slopes match well. (e) MDIS WAC frame EW0220764022G (112.4 m/pixel). The shadow profile traverses the summit of the knob, therefore it should provide a better estimate of the knob's height than the MLA track, which has a non-ideal crossing geometry. (f) Topographic profiles from MLASCIRDR1501140941 and the knob's shadow. Both profiles show similar height measurements for the knob, despite the MLA profile not traversing the knob summit. This indicates that my shadow-derived height measurement is an underestimate. However, the shadow-derived slope is greater than the MLA-derived slope, as expected. (g) MDIS WAC frame EW0220763834G (83.0 m/pixel). The MLA and shadow profiles make very similar traverses of the knob, particularly in the north, which means that the shapes of both profiles should match well. (h) Topographic profiles from MLASCIRDR1109300948 and the knob's shadow. As expected, both profiles show similar shapes for the knob. Slope estimates from both profiles correspond well. The difference between the profiles in the south is most likely because the MLA profile had to be interpolated over the southern flank due to the unavailability of data.
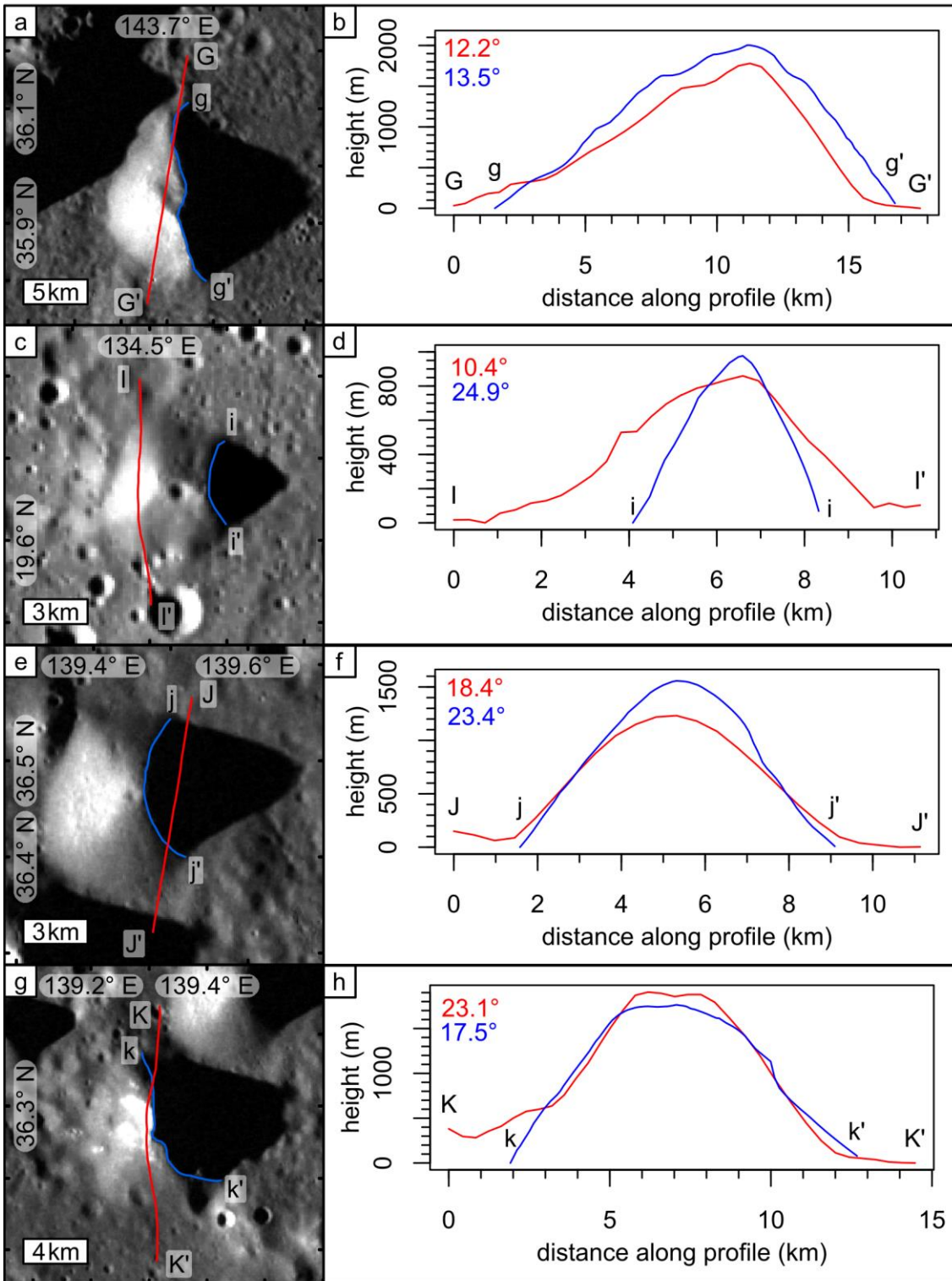
Fig. 6.29 Comparison of MLA- and shadow-derived knob topography (2). *Panels (a), (c), (e) and (g) show MDIS images of knobs. The MDIS frames shown are the ones I used when I was digitising each knob's shadow. MLA tracks are marked as red lines with capital letters marking their start and end points. The blue lines show the digitised umbral shadows of each knob, which also serves as the line of each knob's shadow-derived topographic profile (starts and ends marked with lowercase letters). These panels show Mercator projections centred on 162.7°E, 31.5°N. Panels (b), (d), (f) and (h) show both the MLA- (red line) and shadow-derived (blue line) topographic profiles plotted on the same axes. These profiles have been aligned so that their maximum height measurements plot at the same X-coordinate. In the upper-left of each plot I have included the median 3-point slope I calculated for both types of topographic profile for each knob. The font colour of the slope values matches the colour of their associated profile line. The MLA-derived 3-point slopes were calculated using data in the same range as indicated by the black arrows in Fig. 6.22–Fig. 6.27. Shadow-derived 3-point slopes were calculated using the full range of data for each knob. (a) MDIS WAC frame EW0220763859G (86.4 m/pixel). The MLA and shadow profiles make similar traverses of the knob, which should result in both profiles having similar topography. (b) Topographic profiles from MLASCIRDR1503130635 and the knob's shadow. Both profiles show very similar shapes, sizes and slopes for the knob. (c) MDIS WAC frame EW0220893703G (126.2 m/pixel). The shadow profile traverses the summit of the knob via steepest slopes of approach. The maximum height and flank slope calculated from the shadow profile should be greater and more realistic than those calculated from the MLA profile. (d) Topographic profiles from MLASCIRDR1501115106 and the knob's shadow. As expected, the shadow-derived profile is steeper and taller than the MLA profile. (e) MDIS WAC frame EW0220807059G (86.1 m/pixel). The shadow profile traverses the summit of the knob via steepest slopes of approach. The maximum height and flank slope calculated from the shadow profile should be greater and more realistic than those calculated from the MLA profile. (f) Topographic profiles from MLASCIRDR1503132308 and the knob's shadow. As expected, the shadow-derived profile is steeper and taller than the MLA profile. (g) MDIS WAC frame EW0220807059G (86.1 m/pixel). The MLA and shadow profiles make similar traverses of the knob, which should result in both profiles having similar topography. (h) Topographic profiles from MLASCIRDR1407230620 and the knob's shadow. As expected, both profiles show very similar shapes for the knob. The somewhat lower flank slope calculated from the shadow profile is most likely due to this profile traversing the full extent of the broad summit of the knob.*
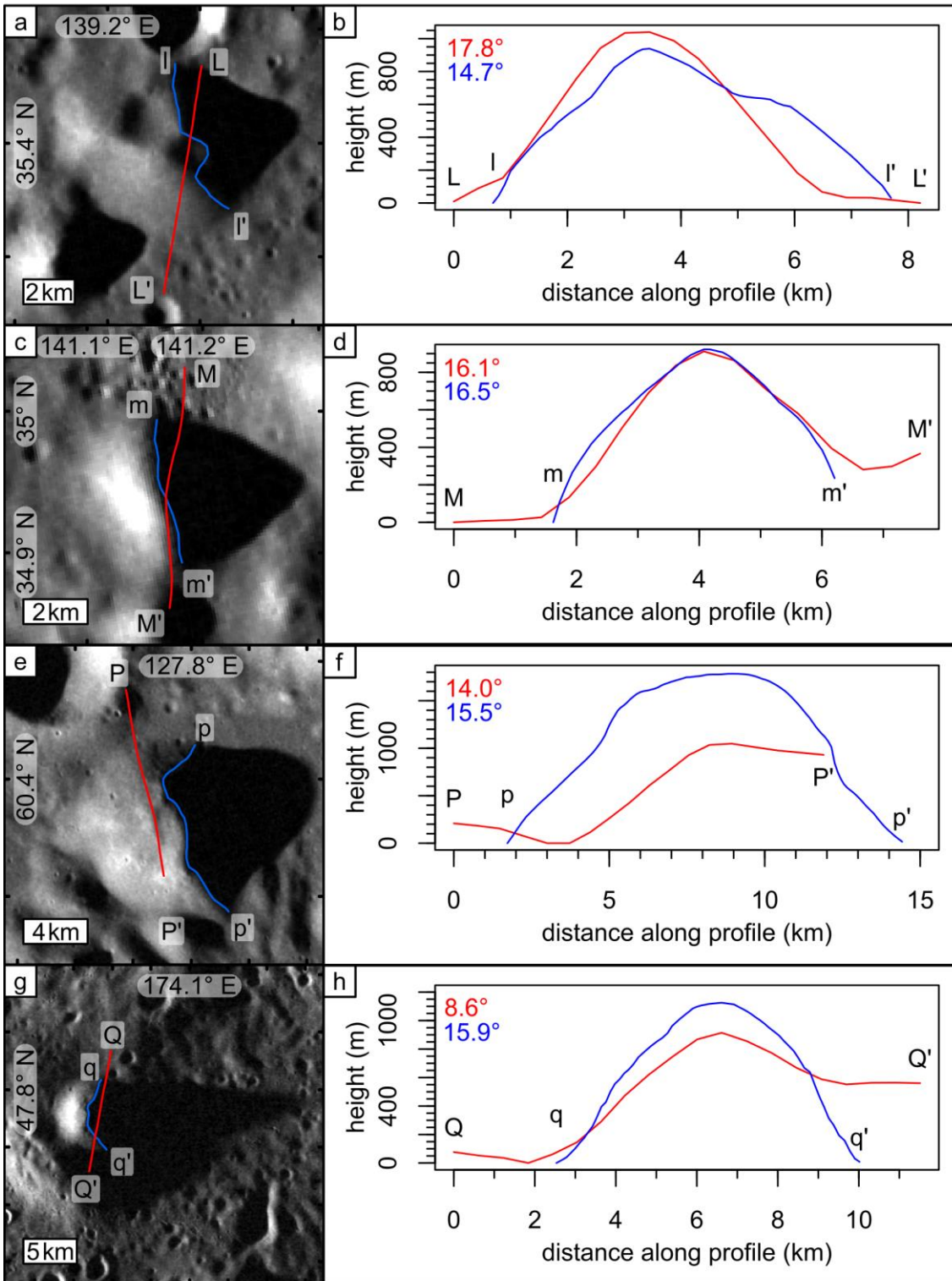
Fig. 6.30 Comparison of MLA- and shadow-derived knob topography (3). *Panels (a), (c), (e) and (g) show MDIS images of knobs. The MDIS frames shown are the ones I used when I digitised each knob's shadow. MLA tracks are shown as red lines with capital letters at their start and end points. The blue lines show the digitised umbral shadows of each knob, which also serves as the line of each knob's shadow-derived topographic profile (beginning and end marked with lowercase letters). These panels show Mercator projections centred on 162.7°E, 31.5°N. Panels (b), (d), (f) and (h) show both the MLA- (red) and shadow-derived (blue) topographic profiles on the same axes. These profiles have been aligned so that their maximum height measurements plot at the same X-coordinate. In the upper-left of each plot I have included the median 3-point slope for both types of topographic profile for each knob. The colour of the slope values matches the colour of their profile line. The MLA-derived 3-point slopes were calculated using data in the same range as indicated by the black arrows in Fig. 6.22–Fig. 6.27. Shadow-derived 3-point slopes were calculated using the full range of data for each knob. (a) MDIS WAC frame EW0220807059G (86.1 m/pixel). The profiles make different traverses of the knob, which means the shapes of the profiles could differ. (b) Topographic profiles from MLASCIRDR1503132308 and the knob's shadow. Both profiles pass close to the knob summit via steepest slopes of approach. The difference in shape between the profiles is probably due to the deflection of the shadow profile by a degraded impact crater on the knob summit. (c) MDIS WAC frame EW0220763870G (88.0 m/pixel). Both profiles make very similar traverses of the knob and intersect very close to the summit of the knob, allowing for a direct comparison of the two profiles at this point. The shapes and slopes of both profiles should match. (d) Topographic profiles from MLASCIRDR1501140941 and the knob's shadow. As expected, both profiles have very similar shapes and flank slopes. Furthermore, both profiles measure the same height for the knob. (e) MDIS WAC frame EW0220849922G (58.9 m/pixel). MLA data are unavailable for the southern portion of the knob. Furthermore, the shadow profile diverges from the MLA profile in the north and south. (f) Topographic profiles from MLASCIRDR1405280237 and the knob's shadow. As expected the MLA- and shadow-derived topographic profiles do not match well. However, both methods return similar flank slopes for the knob. (g) MDIS WAC frame EW0220159587G (78.2 m/pixel). Both profiles make quite similar traverses of the knob, except in the south where they diverge. The MLA data do not measure the summit of the knob. (h) Topographic profiles from MLASCIRDR1503081900 and the knob's shadow. As expected, both profiles have similar shapes in the north but differ greatly in the south. The MLA track covers high terrain adjacent to the knob in the south, whereas the shadow profile runs to the foot of the knob in the southeast. The height and slope calculated from the shadow profile are probably more representative of the true values than those calculated from the MLA data.*
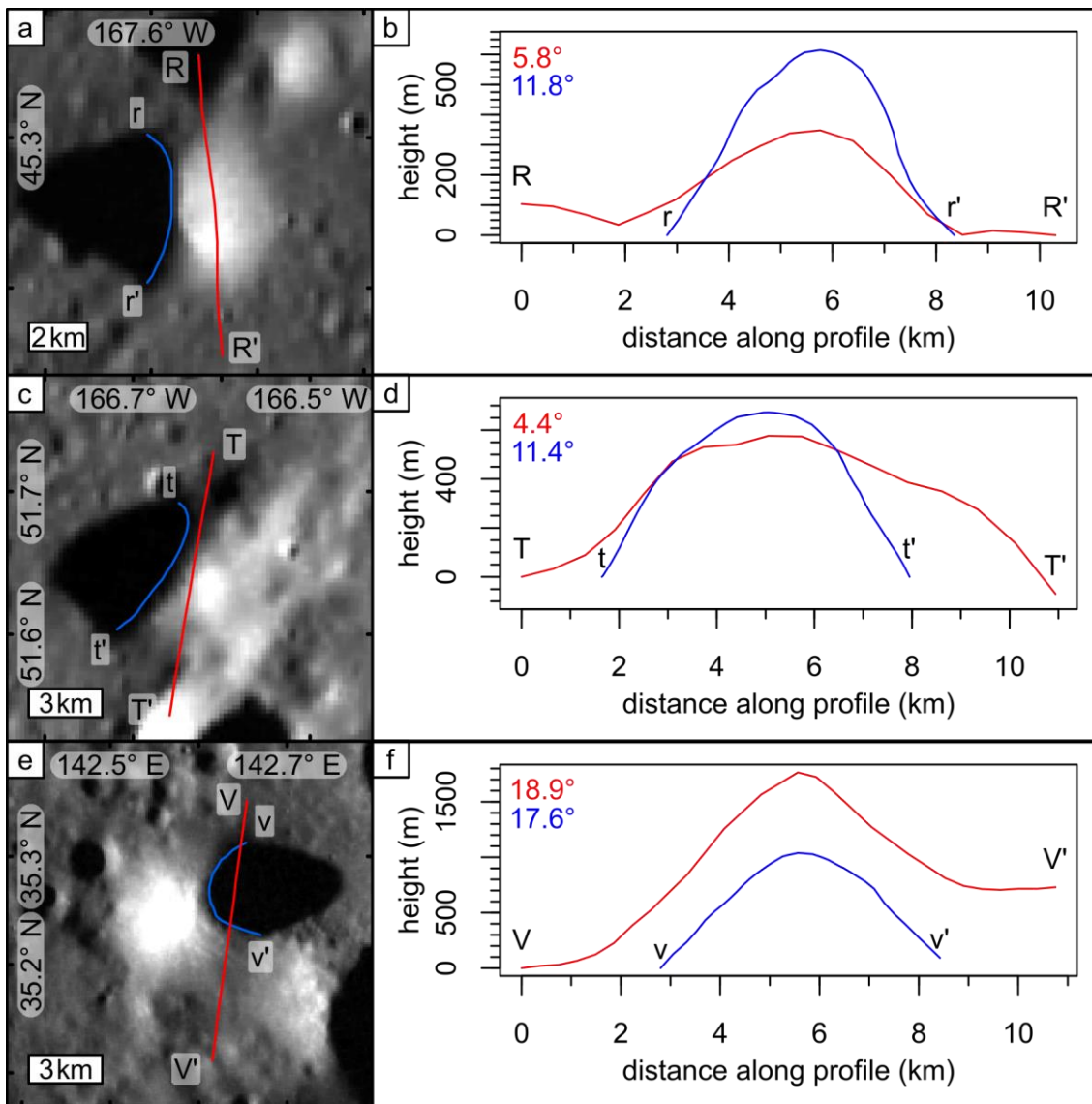
Fig. 6.31 Comparison of MLA- and shadow-derived knob topography (4). *Panels (a), (c), (e) and (g) show MDIS images of knobs. The MDIS frames shown are the ones I used when I was digitising each knob's shadow. MLA tracks are marked as red lines with capital letters marking their start and end points. The blue lines show the digitised umbral shadows of each knob, which also serves as the line of each knob's shadow-derived topographic profile (starts and ends marked with lowercase letters). These panels show Mercator projections centred on 162.7°E, 31.5°N. Panels (b), (d), (f) and (h) show both the MLA- (red line) and shadow-derived (blue line) topographic profiles plotted on the same axes. These profiles have been aligned so that their maximum height measurements plot at the same X-coordinate. In the upper-left of each plot I have included the median 3-point slope I calculated for both types of topographic profile for each knob. The font colour of the slope values matches the colour of their associated profile line. The MLA-derived 3-point slopes were calculated using data in the same range as indicated by the black arrows in Fig. 6.22–Fig. 6.27. Shadow-derived 3-point slopes were calculated using the full range of data for each knob. (a) MDIS WAC frame EW0242923264G (171.5 m/pixel). The shadow profile traverses the knob summit via steep slopes of approach whereas the MLA track crosses the knob's flank approximately halfway up. The MLA-derived profile should underestimate the knob slope and height by about half. (b) Topographic profiles from MLASCIRDR110320204 and the knob's shadow. As expected, the slope and height I calculated from the MLA data are about half the values I calculated from the shadow profile. The shadow-derived values are probably more representative of the true values. (c) MDIS WAC frame EW0227853976G (174.0 m/pixel). Both profiles make similar traverses of the knob in the north and pass close to the summit of the knob. However, the profiles diverge in the south. (d) Topographic profiles from MLASCIRDR1407141333 and the knob's shadow. As expected, the topographic profiles are quite similar in the north but deviate in the south. This shape of the MLA profile might be influenced by irregular knob topography in the southern region due to nearby superposing impact craters.*

6.5.5.3 Knob slopes

Based on my finding in Section 6.5.5.2 that shadow-derived knob flank slopes are trustworthy, I have plotted the flank slopes for the 134 knobs with digitised shadows versus their diameters (measured using CraterTools *(KNEISSL ET AL., 2011)* and the ~166 m/pixel global monochrome mosaic) in Fig. 6.32.
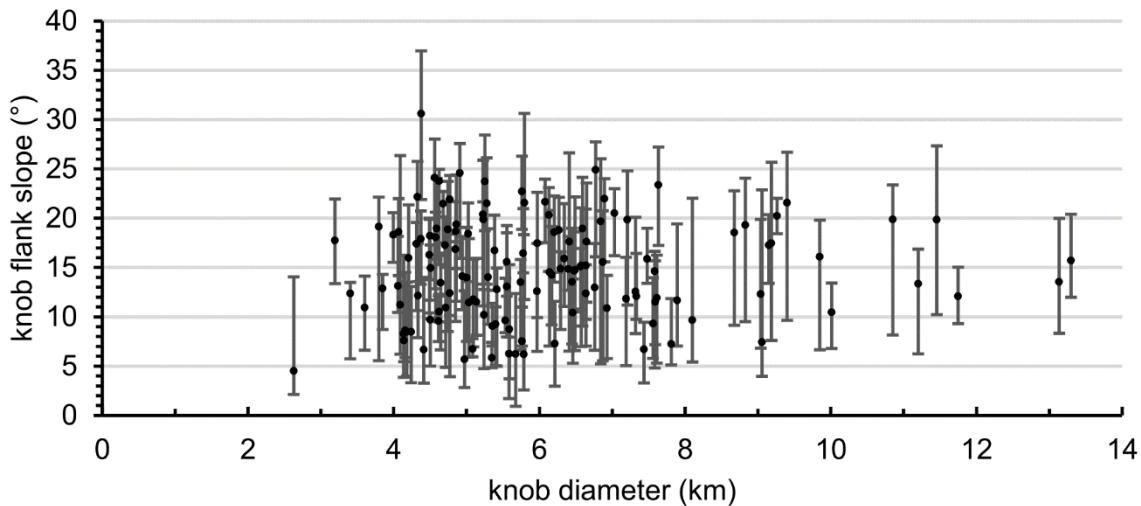
Fig. 6.32 Knob median 3-point flank slope versus knob diameter. *Data for 134 knobs with shadow-derived flank slopes. Upper and lower bars for each data point indicate the upper and lower quartiles for the 3-point slope values for that knob. I measured these knob diameters, using CraterTools (KNEISSL ET AL., 2011), along the shadow profile.*

Fig. 6.32 shows that many (n = 45) of the 134 knobs with digitised shadows are <5 km in diameter. This discrepancy arose because I originally tested if knobs were ≥5 km in diameter by measuring their longest axis. The diameters in Fig. 6.32 were measured after I digitised the knobs' shadows. Often, knobs were illuminated along their long axis, meaning their shadow profiles were of a narrower cross-section. In order for my knob slopes to plot correctly, I needed to measure knob diameters along their shadow profiles, replacing my earlier measurements of their long-axis diameters, resulting in 45 knobs in Fig. 6.32 having diameters <5 km.

More importantly, Fig. 6.32 shows that knob slopes can be very steep. The median slopes of many knobs are ~20°. The 3-point slope calculation I used generated several point estimates for knob slope values along their topographic profiles. Some of these point estimates were unfeasibly steep (>>40°). Such point slopes appear to have arisen due to minor digitisation defects and are easily discounted. However, if I reported only the median 3-point slopes for each knob, I would be glazing over the fact that many knobs are characterised by tracts of their flanks with significantly steeper slopes than the median value. I used the upper quartile of the 3-point slopes for each knob to give an indication of the realistic values for their steep slopes. The upper quartile cuts out the very steepest 3-point slope calculated values that are evidently due to manual digitisation errors. The upper

quartile slopes of many knobs approach, but critically seldom exceed, ~32°.This is an important finding, since the angle of repose of unconsolidated material on Mercury is ~32° *(BARNOUIN ET AL., 2012)*. This provides additional support for my suggestion, based on the photogeological observations in Section 6.5.1, that many of the circum-Caloris knobs have been modified by mass-wasting processes.

6.5.5.4 Knob shapes

In addition to flank slope, I also characterised knobs by their shape. One of the most striking characteristics of apparently pristine knobs is their highly conical shape (Fig. 6.13a). More degraded knobs appear to be more domal. I devised a 'shape factor' in order to quantify the conical–domal spectrum of knob shapes. The basis for my 'shape factor' is explained in Fig. 6.33.
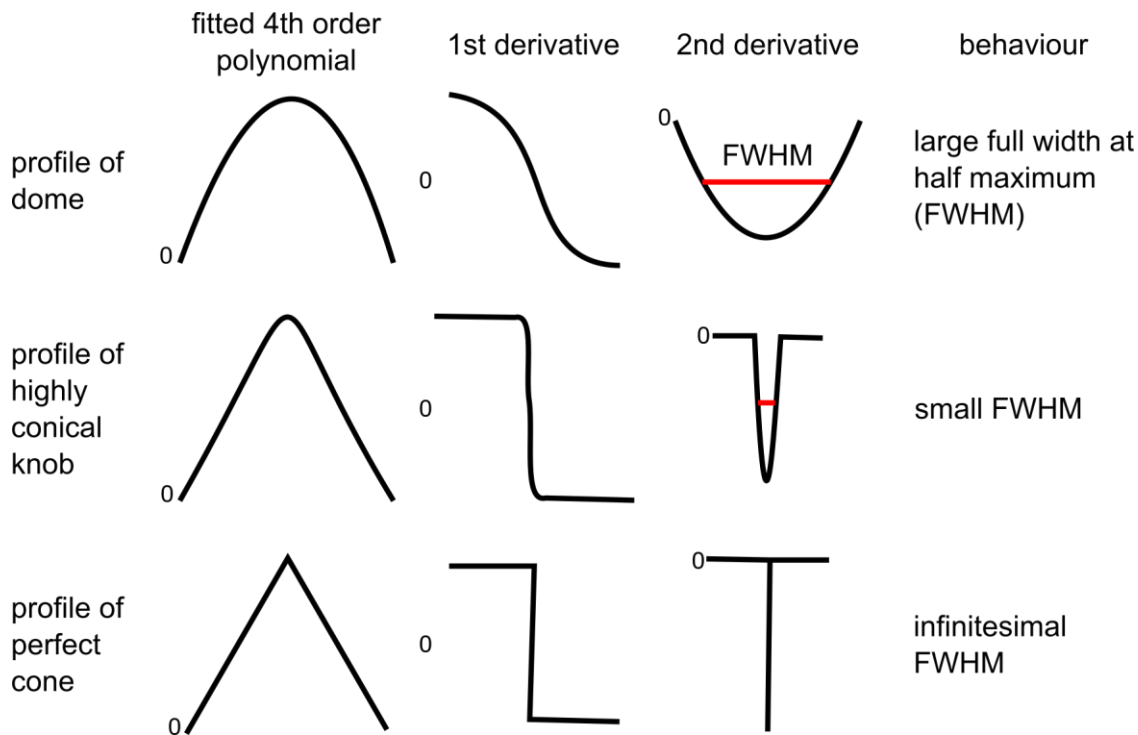
Fig. 6.33 Concept of the 'shape factor' devised to distinguish conical and domal knobs quantitatively. *Left shape column: topographic profiles of three theoretical knobs fitted by a 4th order polynomial. Centre column: general shape of the 1st derivative of the fitted 4th order polynomial. Right shape column: general shape of the 2nd derivative of the fitted 4th order polynomial. The full width at half maximum (FWHM) of each of these shapes is different for each original knob shape. The FWHM is simply the difference of the X-coordinates that both have corresponding Y-coordinates equal to half the maximum depth of the function. As knobs become more conical, the FWHM, or 'shape factor', approaches zero. In order for the shape factors of knobs of different diameters to be comparable, I calculated knob shape factors using topographic profiles for each of the knobs normalised to unit width.*

I wanted a shape factor that could distinguish between conical and domal knobs that is independent of flank slope. A shape factor of this kind could be plotted against flank slope in order to distinguish steep cones, low cones, steep domes and low domes from each other. In order for my shape factor to be independent of flank slope, I decided to devise it from a quantification of sharpness of the summit (effectively the maximum of a mathematical function) of each shadow-derived topographic profile of a knob. Furthermore, I wanted to be able to compare shape factors of knobs with different diameters. Therefore, I calculated shape factors using topographic profiles of the knobs that I had normalised to unit width. I

considered the hypothetical knob end-member morphologies that I wanted the shape factor to distinguish: rounded and sharp triangular profiles. A triangular profile cannot be expressed with a simple polynomial function because a triangular function contains a functional discontinuity. As shown in Fig. 6.33, the general form of a triangular function's 2nd derivative has an infinitesimal full width at half maximum (FWHM), whereas more rounded knob simulating functions have finite FWHMs that become larger as the knob function becomes more rounded. I used this as the basis of my shape factor calculation. I began by fitting 4th order polynomials to each of the 134 shadow-derived topographic profiles of knobs. I used a 4th order polynomial because at least a 4th order polynomial is required if the 2nd derivative of the polynomial is to be a parabola capable of having a FWHM measurement. I found that 4th order polynomials accurately reproduced my shadow-derived knob topographic profiles. I calculated the 2nd derivative of each of the 134 4th order polynomials fitted to my unit width shadow-derived topographic profiles of knobs. I plotted each of the second derivative functions to inspect whether they would produce useful FWHM measurements or not. Useful FWHM measurements of a given 2nd derivative function could be made only when that function's shape approximated a U shape. I found that many 2nd derivative functions instead approximate J shapes, such that their FWHM is undefined. 68 of the 134 4th order polynomials fitted to unit width topographic profiles of knobs yielded 2nd derivative functions of which I could measure FWHMs. I used these FWHM measurements as my shape factors. I have plotted flank slope versus shape factor in Fig. 6.34.
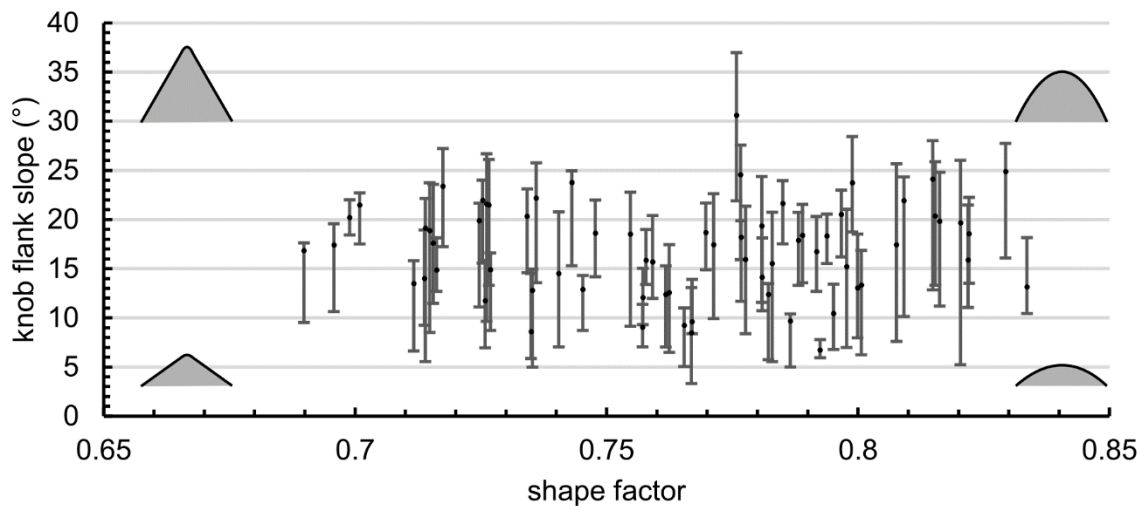
Fig. 6.34 Knob median 3-point flank slope versus knob shape factor. *Data for 68 knobs with shadow-derived slopes and shape factors. Cartoon shapes in the four corners of this graph illustrate conceptually what knobs whose data plot close to the shapes look like. Knobs whose data plot in the upper-left of the graph are characterised by steep slopes and a conical shape. Conversely, knobs whose data plot in the lower-right of the graph are characterised by low slopes and a domal shape. A perfectly triangular knob profile has a shape factor of 0. A knob profile equivalent to a semi-circle has a shape factor of $\sqrt{3}/2$ (~0.87). Upper and lower bars for each data point represent the upper and lower quartiles of that knob's flank slope. For the circum-Caloris knobs there is no obvious relationship between shape factor and flank slope.*

The first thing to note about my shape factor is that the calculation needs to be refined. I was able to calculate shape factors for 68 out of 134 knobs ≥5 km in diameter with digitised shadows. Testing, calibration and refinement of this shape factor is left for future work. Nevertheless, in its present form, my shape factor does impart information when the values for the circum-Caloris knobs are compared with similar shape factor values I determined for knobs on the Moon (see Section 6.6.1.4, Fig. 6.45).

6.6 Discussion

6.6.1 Knob formation and modification

In Sections 6.5.2 and 6.5.4, based on my photogeological observations of individual knobs and the distribution of knobs ≥5 km in diameter respectively, I concluded that the circum-Caloris knobs are Caloris ejecta blocks that have undergone long-

lived modification since their original emplacement. Here, I discuss the processes that might have acted upon on the ejecta blocks over Mercury's geological history to have modified these Caloris ejecta blocks into the circum-Caloris knobs observed today.

Under the hypothesis that the knobs were originally emplaced as Caloris ejecta, the knobs are ~3.9 Gyr old *(FASSETT ET AL., 2009)*. If the Odin Formation, which is the native host of the knobs, is interpreted as Caloris ejecta also, then it should have the same age, although this has been disputed by analyses of its crater size-frequency distribution *(FASSETT ET AL., 2009; DENEVI ET AL., 2013; MANCINELLI ET AL., 2016)*. If the Odin Formation is assumed for the moment to be Caloris ejecta, then the knobs observable today must have formed as late-arriving ejecta blocks (Fig. 6.35a). My observations of the basal contacts of knobs with their surroundings and my observations of the distribution of knobs with respect to geological setting and local elevation suggest that the true extent of the Odin Formation, and hence the circum-Caloris knobs, was obscured when the Caloris smooth plains formed (Fig. 6.35b) ~100 Myr later *(FASSETT ET AL., 2009; DENEVI ET AL., 2013)*.

After their deposition, the Caloris ejecta blocks would be subject to erosion, leading to landform degradation. On an airless body, such as Mercury, physical degradation of landforms is chiefly due to sub-kilometre to kilometre sized impact craters whose formation mobilises material *(FASSETT ET AL., 2017)*. This impact gardening is a diffusive process that transports material up and down slopes (although there is a bias toward downslope transport). Topographic diffusion results in sharp topographic contrasts becoming relaxed over time *(FASSETT ET AL., 2017)*. For example, pristine impact craters on Mercury have sharp uplifted crater rims, whereas impact craters similar in age to the Caloris impact have a more degraded appearance, with lower, more rounded rims and generally lower depth-diameter ratios *(BAKER AND HEAD, 2013; FASSETT ET AL., 2017)*. Therefore, impact gardening of Caloris ejecta blocks of any original shape is most likely to produce rounded landforms after ~3.9 Gyr of erosion (Fig. 6.35c).
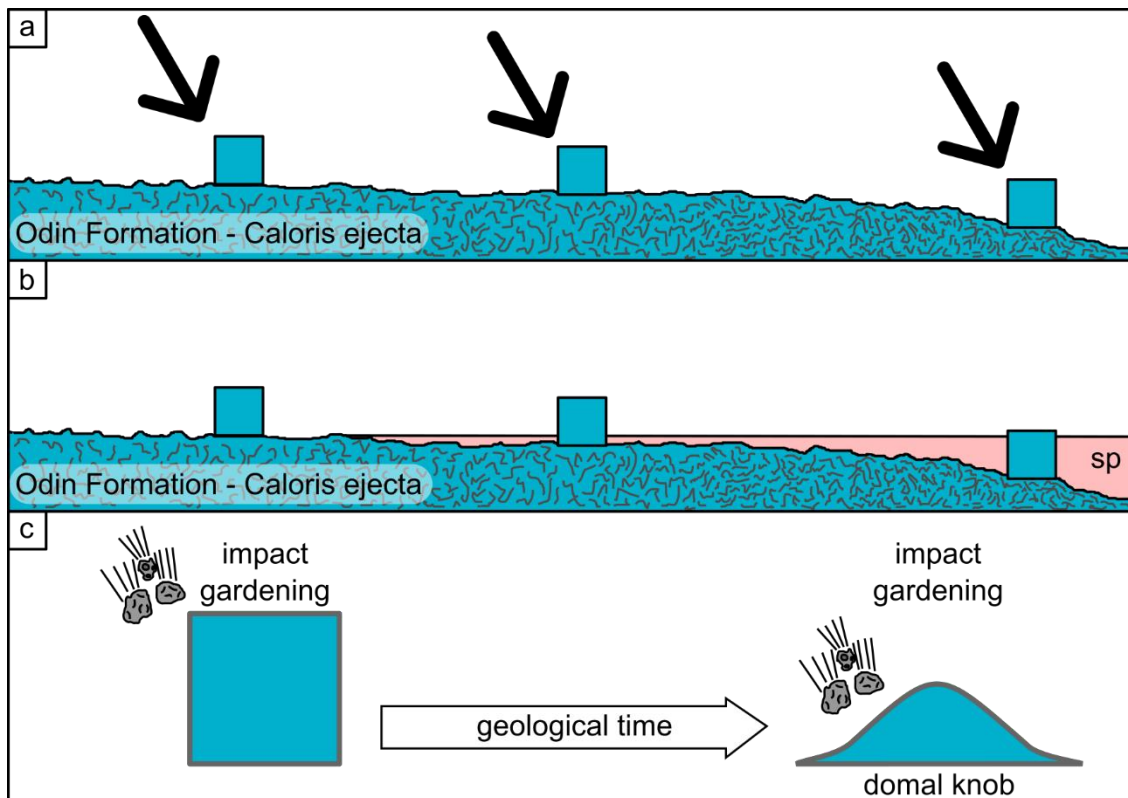
Fig. 6.35 Cartoon illustrating ejecta block formation and modification into knobs.
Cross-section perspective. (a) The Odin Formation formed during the Caloris impact
~3.9 Ga. The circum-Caloris knobs represent late-arriving ejecta blocks excavated from
Mercury's lower crust/upper mantle (ERNST ET AL., 2015). At this stage, the circum-Caloris
knobs had unknown original shapes, represented here arbitrarily by cubes. (b) Sometime
after the Caloris impact, the volcanic smooth plains of Caloris Planitia and the circum-
Caloris smooth plains were emplaced. The smooth plains embayed the Odin Formation and
left it completely buried over much of its original extent. Large Caloris ejecta blocks escaped
complete burial where the smooth plains only shallowly bury the knobs' native Odin
Formation. Embayed knobs are effectively geological inliers with unconformable contacts
with younger smooth plains. (c) Predicted landform evolution of the circum-Caloris knobs if
they remain inert after their original emplacement. Landform evolution on Mercury is
dominated by impact gardening, which diffuses topography such that sharp topographic
contrasts are smoothed and relaxed (FASSETT ET AL., 2017). This scenario can account for
domal knobs, but not conical knobs.

However, I have shown multiple examples of knobs with steep conical shapes,
which are not predicted by erosion of ejecta blocks of arbitrary original shape. In
order to 'sharpen' an arbitrarily shaped ejecta block into a cone, an advective mass
transport mechanism is required; i.e. one that exclusively transports mass

downslope. Furthermore, this mass transport mechanism needs to be faster than erosion due to impact gardening and long-lived in order for conical knobs to be observable today.

6.6.1.1 Volatile-driven knob evolution

When observing the surface of Mercury, rapid and long-lived advective erosional surface processes are not forthcoming. However, hollows present one possibility. These landforms are geologically young and possibly still undergoing formation and growth today *(BLEWETT ET AL., 2011)*. They appear to grow by the loss of some volatile component of the crust into space, which opens a depression. As the volatile component is exposed in the hollow walls, it is lost and the hollow expands laterally by scarp retreat *(BLEWETT ET AL., 2011)*. This is an advective mass movement mechanism where material exclusively moves downslope and it forms sharp-edged, steep-walled hollows with no uplifted rims. If the Caloris ejecta blocks could have undergone modification by scarp retreat and mass movement downslope, then this could explain my observations of steep, highly conical knobs.

In Section 6.5.1.6, I showed several examples of knobs and materials closely associated with knobs that contain hollows. Since it is not apparent that the materials in which the hollows have formed were delivered from elsewhere after the formation of the knobs, I interpreted the hollow-forming material to be native to the knobs and the Odin Formation that hosts them. Where the volatile that forms hollows elsewhere on Mercury occurs close to the surface of a knob, hollows form on the knob. However, if a structurally integral volatile material is located within the interior of the knob then devolatilisation of this component might cause a volatile-rich ejecta block to evolve differently. I illustrate how devolatilisation of Caloris ejecta blocks could modify the blocks in a similar manner to hollow formation in Fig. 6.36
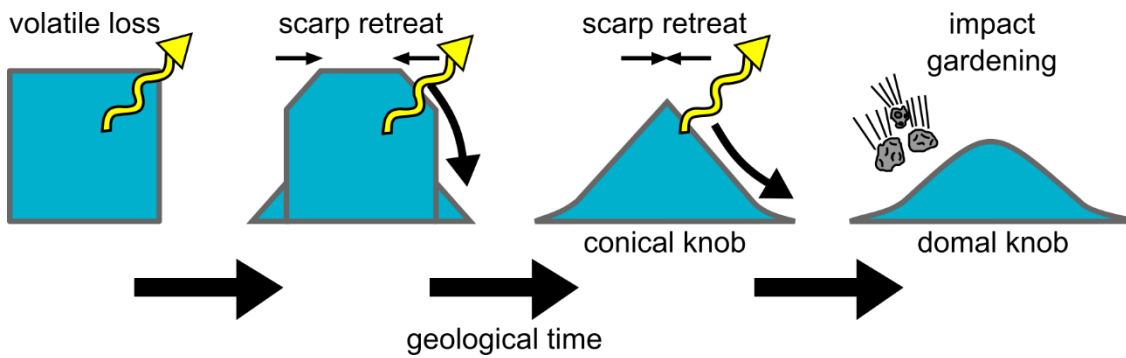
Fig. 6.36 Cartoon illustrating possible volatile-driven modification of Caloris ejecta blocks. Caloris ejecta blocks were excavated from a volatile-bearing stratum. The volatile component of the ejecta block began to sublime, or was otherwise lost, into space (yellow arrows). Loss of structurally integral volatile material caused the ejecta block to disintegrate. Disintegration of the ejecta block led to a build-up of inert material at the block base. Mass wasting exposed fresh material, allowing devolatilisation and scarp retreat to continue. As long as scarp retreat due to devolatilisation outpaced erosion by impact gardening, ejecta blocks continued to be modified into conical knobs. If impact gardening began to dominate, knobs were degraded into domal forms.

The Caloris ejecta blocks were probably excavated from Mercury's lower crust or even its upper mantle *(ERNST ET AL., 2015)*. Given the common occurrence of hollows in impact ejecta globally on Mercury, it appears that there are substantial reservoirs of material within Mercury's subsurface that becomes volatile when exposed on the surface of the planet. Low-reflectance material, which is suspected of being volatile bearing, has been excavated from beneath Caloris *(ERNST ET AL., 2015)*. Therefore, it seems reasonable to suggest that the ejecta blocks that later formed the circum-Caloris knobs contained some volatile component. Exposure at the surface of Mercury would destabilise this volatile component and cause it to be lost into space, perhaps in the same way that volatile-loss appears to cause hollows to form. The devolatilisation process could be insolation driven, such as sublimation, thermal desorption, or photon-stimulated desorption *(DOMINGUE ET AL., 2014; PIETERS AND NOBLE, 2016)*. Alternatively, micrometeorite bombardment, which is independent of the Sun, might provide the necessary energy for devolatilisation *(DOMINGUE ET AL., 2014; PIETERS AND NOBLE, 2016)*.

Loss of a structurally integral volatile component of a Caloris ejecta block would cause the block to disintegrate and inert knob material would build up at the base

of the block to form a slope. The pile of unconsolidated material at the base of the block would be able to build up to the angle of repose (~32°) before becoming oversteepened. If slopes became oversteepened then they would fail and cause material to spread outward from the knob.

As long as mass wasting continued to expose fresh volatile material, devolatilisation of the knob would continue to cause the ejecta block to disintegrate until scarp retreat had modified the ejecta block into a knob or cluster of knobs. Continued devolatilisation of the knob would maintain the knob in a conical form as long as devolatilisation induced slope failures outpaced erosion by impact gardening.

When the volatile component within a knob became exhausted or when it became so deeply entombed by an inert lag deposit then devolatilisation would have ceased. At around this stage of knob evolution, impact gardening would have become the dominant process operating on the knob, which would result in steeper, conical knobs being modified into lower, domal knobs.

This mechanism for knob formation and evolution is consistent with several of the observations I have made of the knobs and has wider implications for the geology of Mercury if it is true. Furthermore, my hypothesis makes some predictions that could falsify it if tested by future studies.

6.6.1.2 Observations supporting volatile-driven knob evolution

As mentioned previously, it is reasonable to assume that many Caloris ejecta blocks originally had a volatile component within them, given the volatile-bearing material excavated by impact craters in Caloris Planitia *(ERNST ET AL., 2015)* and my observations of hollows in knob materials. However, the presence of volatiles in Caloris ejecta does not necessitate their involvement in the degradation of the blocks into knobs. Nevertheless, I have made several observations that support a rapid (for Mercury's surface), advective erosional process capable of turning arbitrarily shaped ejecta blocks into the knobs observed today.

The dearth of impact craters on the flanks of knobs requires efficient surface renewal of the knobs, particularly when an ejecta block origin for the knobs requires them to have been emplaced ~3.9 Ga. My observations of knob material

burying impact craters and abutting lobate scarps that postdate knob emplacement provide evidence that long-lived and voluminous mass wasting has occurred during at least some knobs' histories, which supports an efficient advective mass movement resurfacing process. The steep slopes observed on many knobs cannot be explained by the action of a diffusive erosional process, such as impact gardening.

6.6.1.3 Molards on Earth: an analogous landform?

The volatile-driven knob formation process I have outlined above is conceptually identical to the formation of landforms on Earth known as 'molards' (Fig. 6.37).

Fig. 6.37 Example of a 'molard' in Iceland. *Molards are conical rock piles that can form when ice-cemented permafrost blocks thaw and disaggregate. Image credit: MORINO ET AL. (2019).*

A detailed review of molard formation and evolution has been written by *MORINO ET AL. (2019)*. Briefly, molards are cones of rubble that have been observed in permafrost environments on Earth (*MORINO ET AL. (2019)* and references therein), such as Iceland. Molards can form when permafrost becomes exposed to environmental conditions that initiate thawing. For example, landslides and rock falls can remove permafrost from sheltered cliffsides and expose them to higher daytime temperatures and rainfall, which can cause the permafrost to thaw. The ice in permafrost is structurally integral, such that when it melts the remaining

rock and soil collapse into a mound *(MORINO ET AL., 2019)*. This process is illustrated in Fig. 6.38.
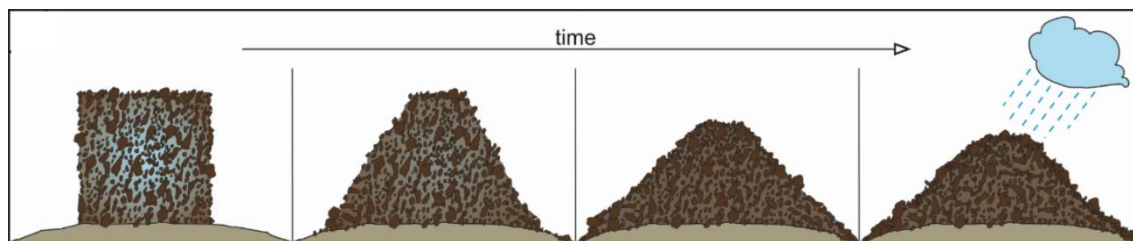
Fig. 6.38 Cartoon illustrating various stages of molard formation from a permafrost block. *This example shows a permafrost block that has been exposed by a rockfall. Exposure initiated melting of the ice on the outside surfaces of the block and uncemented rock and soil began to form an apron around the block. As melting continued, a cone formed. When melting ceased, other erosional processes, such as rainfall, degraded the cone into more dome shape. Reproduced from MORINO ET AL. (2019) with the kind permission of the authors.*

Molards have been observed at the different stages of development shown in Fig. 6.38. Fig. 6.39 shows a permafrost block shortly after its deposition, and again three years later (Fig. 6.40).

Fig. 6.39 An undegraded permafrost block. *This block was deposited during the Móafellshyrna, Iceland landslide and this image was taken in September 2012, shortly after the landslide. A human is in the lower-right of the image for scale. The boulder clasts that make up the rock fraction of the permafrost can clearly be seen throughout the block and a steep slope of rubble has accumulated against the block toward the right of the image. Image credit: MORINO ET AL. (2019).*

Fig. 6.40 A molard formed from a permafrost block. *This mound of rubble is what remained of the permafrost block shown in Fig. 6.39. This image was taken in July 2015, nearly three years after that shown in Fig. 6.39. Image credit: MORINO ET AL. (2019).*

The principle of a volatile-rich ejecta block on Mercury is similar to a thawing permafrost block on Earth. The observation of molards at different stages of their development (i.e. as blocks, cones, and domes) raises the possibility that a similar process could have operated on Caloris ejecta blocks to form the circum-Caloris knobs in the manner I described in Fig. 6.36.

6.6.1.4 Comparison with the lunar Alpes Formation

One important prediction made by my volatile-driven hypothesis of knob modification is that similar landforms should not develop on volatile-poor planetary bodies. As an airless body, the Moon is subject to similar surface conditions and processes to Mercury, however the Moon is not thought to have an interior that is as volatile-rich as Mercury's *(NITTLER ET AL., 2011; PEPLOWSKI ET AL., 2011)*. Therefore, my volatile-driven hypothesis of circum-Caloris knob formation on Mercury predicts that no similarly conical knobs should arise on the Moon by the same mechanism.

As stated previously, the Odin Formation, which hosts the circum-Caloris knobs on Mercury, was originally likened to the Alpes Formation on the Moon *(MCCAULEY ET AL., 1981)*. The Alpes Formation is interpreted as ejecta from the Imbrium impact basin *(WILHELMS AND MCCAULEY, 1971)*. The Imbrium impact has been dated to ~3.9 Ga *(LIU ET AL., 2012; MERLE ET AL., 2014)* and the basin is ~1,300 km in diameter, making the size and age of the basin very similar to those of Caloris *(FASSETT ET AL., 2009)*. Therefore, I chose to compare the knobs in the Alpes Formation on the Moon to the circum-Caloris knobs on Mercury. Fig. 6.41 shows the location of the knobs I measured on the Moon.
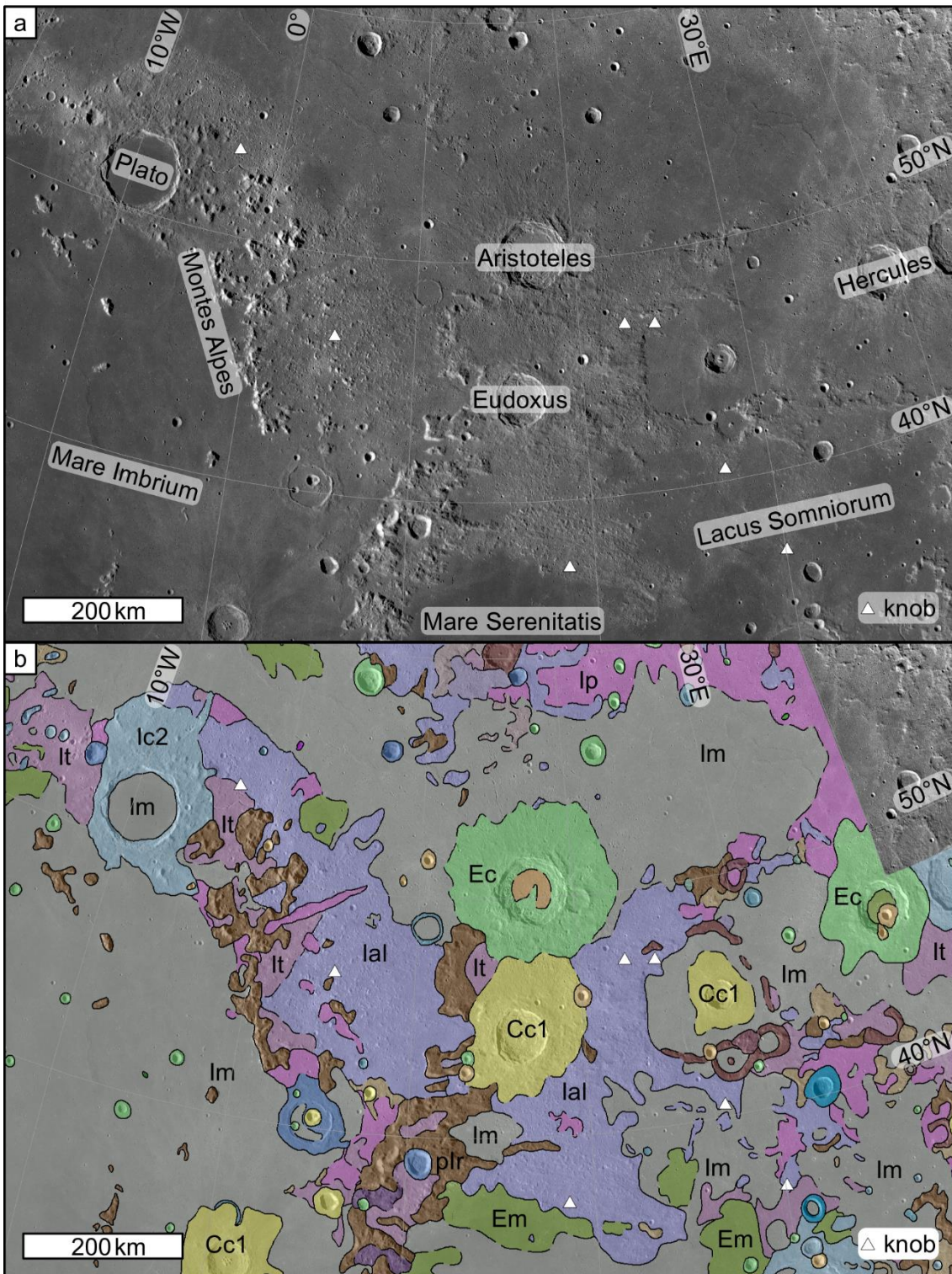
Fig. 6.41 Geography and geology of the lunar Alpes Formation and its knobs. In both panels, the locations of the lunar knobs discussed in this subsection are indicated with white triangles. (a) View of northeast Imbrium on the Moon. The Alpes Formation is the knobby plains unit that is relatively bright compared to the mare material. This unit is named after the Montes Alpes that are labelled in the figure. The Montes Alpes have been interpreted as part of the rim of the Imbrium basin (WILHELMS AND MCCAULEY, 1971), rather than impact ejecta blocks. (b) Geology of northeast Imbrium. Semi-transparent coloured geological units are overlain on LROC imagery. The Alpes Formation is coloured blue-purple and labelled 'Ial'. Lunar geology shapefiles are based on USGS map I-703 by WILHELMS AND MCCAULEY (1971) and were generated by and made publicly available at https://webgis.wr.usgs.gov/pigwad/down/moon_geology.htm. Both panels show orthographic projections of the 100 m/pixel global LROC WAC mosaic centred on 14°E, 50°N.

I used the gridded LOLA ~60 m/pixel global DEM to measure topographic profiles of the largest knobs in the Alpes Formation. I used the lunar geology shapefiles digitised based on the original map of the nearside of the Moon by WILHELMS AND MCCAULEY (1971) to make sure I selected knobs interpreted as ejecta blocks for measurement. The Montes Alpes, which resemble the larger circum-Caloris knobs, are interpreted as the uplifted Imbrium rim (WILHELMS AND MCCAULEY, 1971; WILHELMS ET AL., 1987), rather than ejecta blocks. In order to make my comparison of the lunar and circum-Caloris knobs as fair as possible, I searched for lunar knobs ≥5 km in diameter. For this preliminary comparison, I found seven knobs in northeast Imbrium (Fig. 6.41). The topographic profiles that I measured of these Alpes Formation knobs are shown in Fig. 6.42 and Fig. 6.43 (these figures are split for convenience and show the knobs in no particular order). A shapefile containing the locations of the seven lunar knobs is included in the Supporting Digital Media of this thesis.
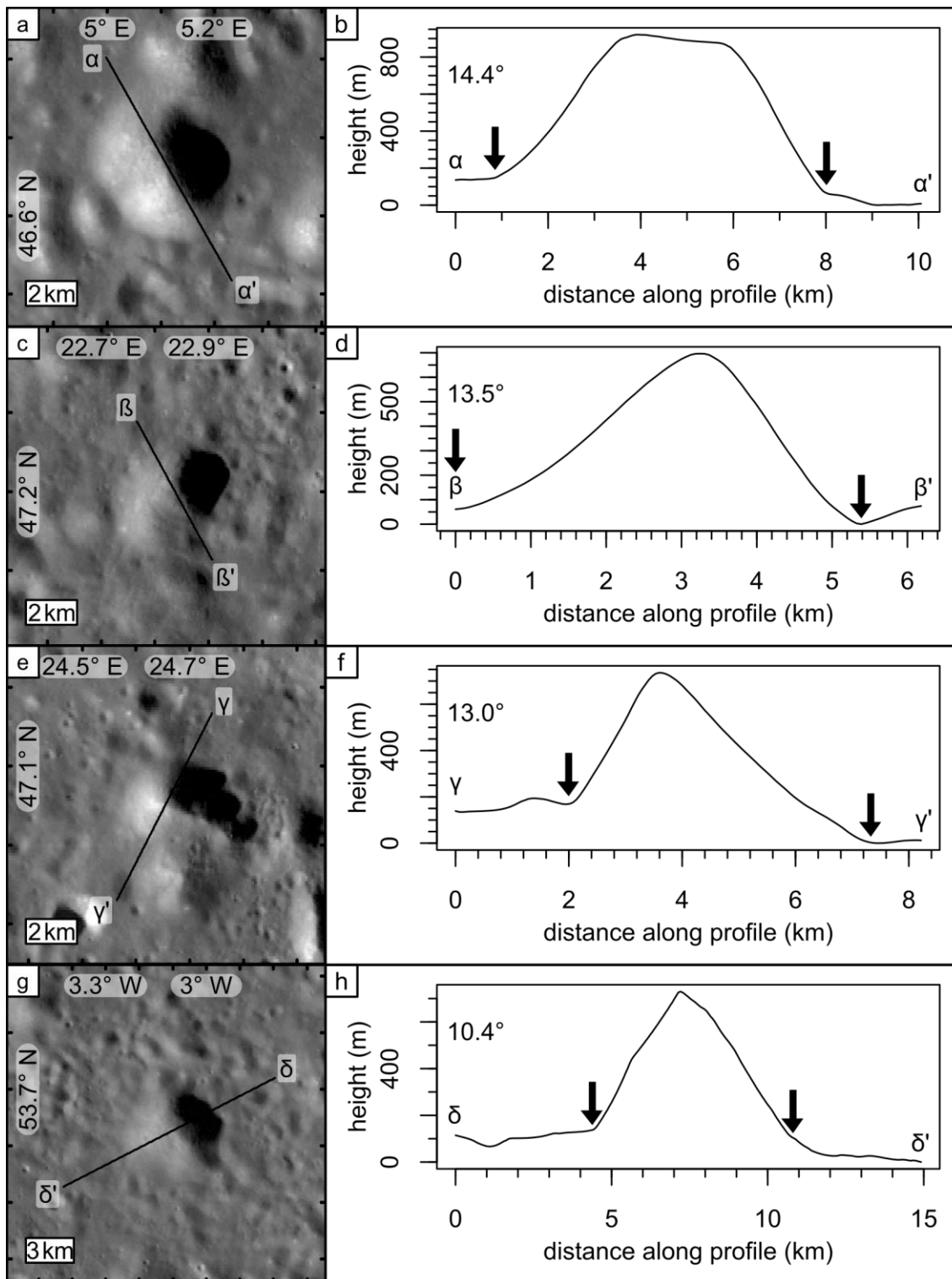
Fig. 6.42 LOLA measurements of lunar Alpes Formation knob topography (1). *Panels (a), (c), (e) and (g) show knobs in the lunar Alpes Formation in the 100 m/pixel global LROC WAC mosaic. These panels show Mercator projections centred on 8°E, 46°N (selenographic coordinates). Panels (b), (d), (f) and (h) show topographic profiles of their corresponding knobs, In the upper-left of each topographic profile I have included the median 3-point slope of the knob that I calculated using the topographic data between the two black arrows.*

278

(Fig. 6.40 cont.) Topographic data were taken from the ~60 m/pixel gridded LOLA DEM. In all panels Greek lettering (e.g. α–α') mark the starts and ends of the topographic profiles.
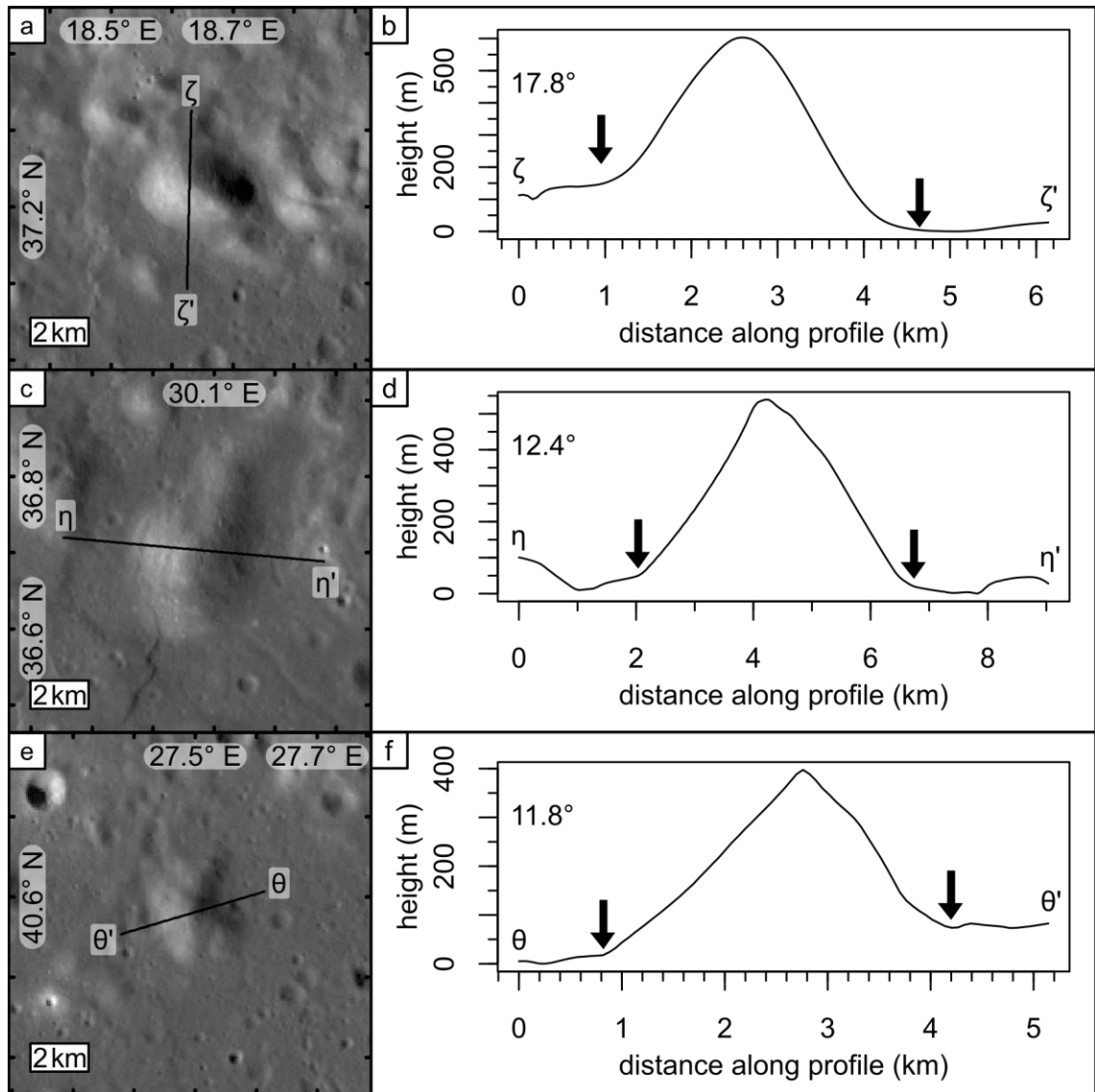
Fig. 6.43 LOLA measurements of lunar Alpes Formation knob topography (2). *Panels (a), (c) and (e) show knobs in the lunar Alpes Formation in the 100 m/pixel global LROC WAC mosaic. These panels show Mercator projections centred on 8°E, 46°N (selenographic coordinates). Panels (b), (d) and (f) show topographic profiles of their corresponding knobs, In the upper-left of each topographic profile I have included the median 3-point slope of the knob that I calculated using the topographic data between the two black arrows. Topographic data were taken from the ~60 m/pixel gridded LOLA DEM. In all panels Greek lettering (e.g. ζ–ζ') mark the starts and ends of the topographic profiles.*

While making topographic measurements of the lunar knobs, I noted some differences between them and the circum-Caloris knobs. I made no observations of lunar knobs partially obscuring impact craters. Furthermore, lunar knob boundaries were more commonly sharp and well-defined than those of the unembayed circum-Caloris knobs.

From these topographic profiles of the lunar knobs, I calculated their median, upper and lower quartile 3-point slopes and shape factors in the same way that I calculated the flank slopes and shape factors of the circum-Caloris knobs. The data for the Alpes Formation knobs are summarised alongside the circum-Caloris knob data in Fig. 6.44 and Fig. 6.45.
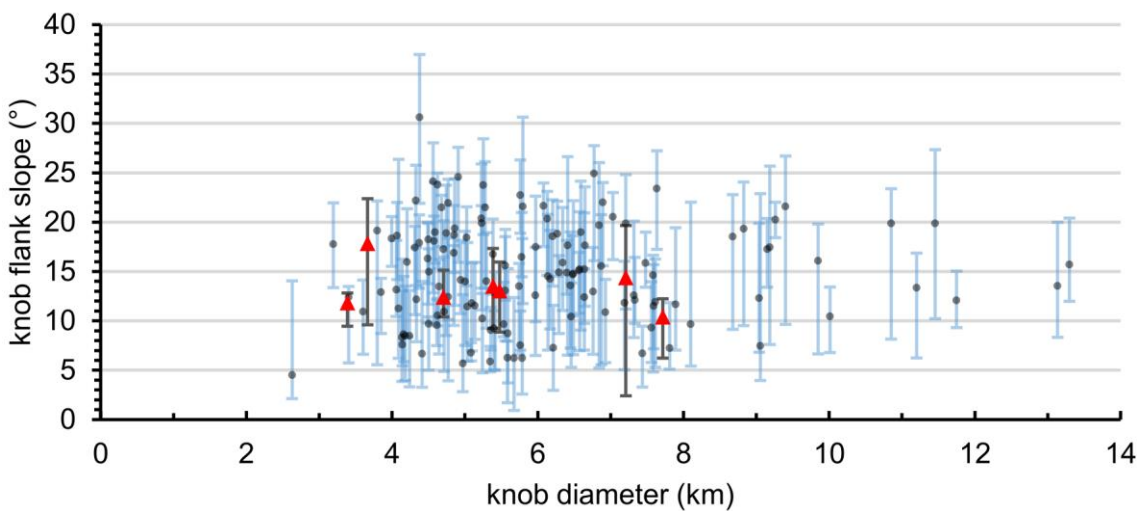
Fig. 6.44 Comparison of Alpes Formation knob slopes and diameters with the circum-Caloris knobs. *The same graph as shown in Fig. 6.32 with data for the Alpes Formation added as red triangles. The data for the circum-Caloris knobs have been made transparent for clarity. The Alpes Formation knobs that I measured do not have examples >8 km in diameter. The Alpes Formation knobs appear not to have slopes as steep as those that characterise many of the circum-Caloris knobs, even when the upper quartile slopes for the lunar knobs are considered. Most lunar knobs have flank slope <<20°.*
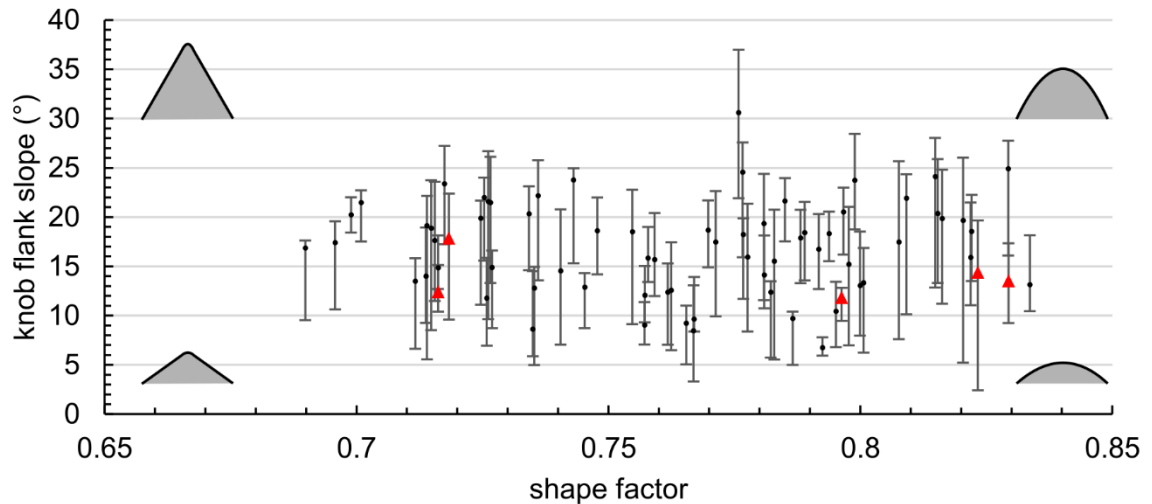
Fig. 6.45 Comparison of Alpes Formation knob slopes and shape factors with the circum-Caloris knobs. *The same graph as shown in Fig. 6.34 with data for the Alpes Formation added as red triangles. Alpes Formation knobs appear to span a similar range of shape factors to that of the circum-Caloris knobs, but the most conical shape factors belong to the circum-Caloris knobs.*

Based on this preliminary comparison between the Alpes Formation knobs and the circum-Caloris knobs, I have made the following observations. The largest knobs in northeast Imbrium (diameter 7–8 km) are still smaller than the largest circum-Caloris knobs (diameter ~13 km). This is a robust finding since I deliberately searched for the largest knobs in the Alpes Formation. Furthermore, six out of seven Alpes Formation knobs that I measured had slopes in the lower range of slopes I obtained for the circum-Caloris knobs. Finally, the Alpes Formation knobs span a similar range of shape factors to the circum-Caloris knobs, but the most conical shape factors belong to the circum-Caloris knobs.

My preliminary comparison between the Alpes Formation knobs and the circum-Caloris knobs suggests that at least some of the circum-Caloris knobs have undergone a different landform evolution from the Alpes Formation knobs. The strength of these observations is limited by the very low number of Alpes Formation knobs that I was able to measure and the uncertainties in the shadow-derived measurements of the circum-Caloris knobs. In the future, a study dedicated to comparing the circum-Caloris knobs and lunar knobs is required.

6.6.2 Wider implications of volatile-rich Caloris ejecta

If the Caloris ejecta blocks that formed the circum-Caloris knobs were volatile-rich, then it follows that other Caloris material could have been volatile-rich too.

Objections have been raised about the interpretation of the Odin Formation as Caloris ejecta based on its younger crater size-frequency distribution compared with other Caloris materials *(DENEVI ET AL., 2013)*. However, if the Odin Formation was emplaced as a volatile-rich ejecta sheet that degraded to produce the knobby appearance that it exhibits today, then it could be possible that its physical properties mean it has unusual crater production/retention properties. This may be a substantial enough effect to give the Odin Formation a young crater size-frequency distribution relative to the Caloris impact itself.

I observed many circum-Caloris knobs along the Caloris rim. It is possible that the blocky, isolated massifs of the Caloris Montes Formation formed as a result of scarp retreat and that these massifs have been modified into clusters of knobs due to volatiles uplifted in the rim from depth. Widespread devolatilisation and degradation of the Caloris rim might be part of the reason why the Caloris rim is so incomplete.

Perhaps the most important implication of volatile-rich Caloris ejecta is that the circum-Caloris knobs could provide insight into the composition and material properties of Mercury's interior. Permafrost degradation produces different landforms depending on the original volume of ice *(MORINO ET AL., 2019)*. If the circum-Caloris knobs formed due to devolatilisation of Caloris ejecta blocks, then careful analysis of the shapes of pristine knobs might be used to estimate the volume fraction of the volatile species in the substratum from which the blocks were excavated. They might represent the most easily observed lower crustal or upper mantle material exposed at the surface of Mercury *(ERNST ET AL., 2015)*, which makes them important targets for the BepiColombo mission *(BENKHOFF ET AL., 2010; ROTHERY ET AL., 2010)*.

6.7 Conclusions

My observations of the circum-Caloris knobs have shown that they are not small volcanic constructs, which was suggested as a solution to their problematic interpretation as Caloris ejecta blocks *(FASSETT ET AL., 2009)*. I have made observations that strengthen the conclusion of others that the circum-Caloris knobs did originate as Caloris ejecta *(ACKISS ET AL., 2015)*. My observations that support an ejecta origin for the knobs include their non-volcanic colour signature, their lack of volcanic craters, their arrangement in cluster proximal to and chains radiating from Caloris, and their apparent preservation on locally high-standing topography. My observations of hollows in association with several knobs also argue against a volcanic interpretation of the knobs.

Regardless of how the Caloris ejecta were modified into the circum-Caloris knobs observed today, my observations have made it clear for the first time that this modification process was long-lived, since knob material has been able to spread out to obscure small, post-Caloris impact craters and abut lobate scarps that cross-cut Caloris.

Furthermore, my measurements of knob slopes approaching the angle of repose, in conjunction with the association of hollows with knobs, suggests that the circum-Caloris knobs might be analogous to molards. If this is true, then the circum-Caloris knobs represent a hitherto unrecognised landform on Mercury, formed by an undocumented physical process on that planet, and they provide evidence that Mercury's deep interior, including at least the upper mantle, is volatile-rich.

CHAPTER 7
SYNTHESIS, FUTURE WORK AND BEPICOLOMBO

7.1   Synthesis

My work has made several valuable contributions to our understanding of the planet Mercury. Here, I place my findings in the wider context of Mercury planetary science.

7.1.1   Geological mapping of Mercury

7.1.1.1   Intermediate plains

As stated in Chapter 2, most of the intercrater plains and smooth plains on Mercury are believed to be the remains of voluminous effusions of lava emplaced >3.5 Ga *(DENEVI ET AL., 2013; WHITTEN ET AL., 2014; OSTRACH ET AL., 2015; BYRNE ET AL., 2016)*. The first global geological map of Mercury currently recognises these widespread units, in addition to probable effusive volcanic units associated with the Caloris and Rembrandt basins *(KINCZYK ET AL., 2018B)*. In Chapter 4, I showed that these unit definitions are inadequate in certain parts of H05. This is most likely due to the scale of digitisation that I used (1:400k). At this large scale, following the rationale employed when making the global map *(KINCZYK ET AL., 2018B)*, the regions I mapped as 'intermediate plains' would require multitudinous, areally small enclosed smooth plains patches to be demarcated. These smooth patches have gradational contacts, which do not lend themselves to mapping, with the surrounding rougher terrain, which in places do not conform to the *TRASK AND GUEST (1975)* definition of the intercrater plains. The global approach is untenable at the quadrangle scale, at least in the case of H05, for the following reasons: (1) the near-fractal complexity of the digitisation required would be time-consuming and in many cases would not render meaningfully at the publication scale (1:3M), and; (2) by shoe-horning the smooth patches into the smooth plains and the rough areas into the intercrater plains, the opportunity to demarcate this physiographic region to assess its stratigraphic position and origin is missed. Therefore, I mapped

these regions as intermediate plains, contrary to the advice of WHITTEN ET AL. (2014). As a result, I determined an origin for the intermediate plains as partially volcanically inundated intercrater plains. This is consistent with the observations and interpretations of similar physiographic regions described by BYRNE ET AL. (2013). This raises the likelihood that more 'intermediate plains-type' regions will be identified elsewhere on Mercury that have otherwise been mapped as intercrater plains and/or smooth plains in the global map. For example, preliminary geological mapping of H10 (MALLIBAND ET AL., 2019B) has identified plains inconsistent with the classical definitions of smooth and intercrater plains (TRASK AND GUEST, 1975), which are most likely contiguous with the intermediate plains in H05. If the intermediate plains are interpreted as late-stage effusive volcanism, then the history of effusive volcanism on Mercury might be extended measurably beyond its apparently abrupt cessation ~3.5 Ga (BYRNE ET AL., 2016).

7.1.2 Implications of deep-interior volatiles

As explained in Chapter 6, it is probable that the circum-Caloris knobs contain volatile materials excavated from the deep interior of Mercury; possibly the upper mantle (ERNST ET AL., 2015). In the sections that follow, I outline briefly the implications of this finding on wider Mercury science.

7.1.2.1 Explosive volcanism

I have remarked throughout this thesis that for explosive volcanism to occur a volatile species within the magma must cause the ascending magma to fragment. Volatiles that drive explosive volcanic eruptions on Earth (e.g. H_2O), can be incorporated into melts at the source region in the mantle, or be assimilated into magmas during their ascent (CASHMAN ET AL., 2000). It is also possible that both primary mantle and assimilated volatiles contribute to a given eruption. On Mercury, it is not clear how and where magmas involved in explosive eruptions acquired their volatiles. Geochemical data from MESSENGER show that Mercury's surface is volatile-rich (NITTLER ET AL., 2011; PEPLOWSKI ET AL., 2011), and hollows (BLEWETT ET AL., 2011), which typically form in material excavated by impact craters (BLEWETT ET AL., 2013; THOMAS ET AL., 2014C), show that Mercury's upper crust is also volatile-rich. This means that crustal assimilation of volatiles into magmas is

certainly possible *(THOMAS ET AL., 2014A)*. So far, the involvement of mantle-derived volatiles in the explosive eruptions on Mercury is uncertain, since crustal volatiles are so much in evidence and the existence of abundant volatiles in the mantle was unproven. However, since the circum-Caloris knobs appear to be volatile-rich, a primary mantle volatile source for explosive eruptions is available. This means that both crustal and mantle volatiles could have contributed to the explosiveness of any given eruption.

7.1.2.2 Formation of Mercury

Perhaps the most important implication of my study of the circum-Caloris knobs is that models of the formation of Mercury must account for how abundant volatiles could be instilled, and retained within, the planet's mantle. The giant impact *(BENZ ET AL., 1988)* and silicate vaporisation *(CAMERON, 1985)* models of formation of Mercury were devised to explain the large iron core of the planet, but the heating that would have been experienced by proto-Mercury during these models would have driven away the crustal volatiles observed *(NITTLER ET AL., 2011)*. Since the deep interior of Mercury appears to contain volatiles as well, perhaps Mercury's entire silicate fraction is volatile-rich and could have been derived from chondritic material. If so, another mechanism for endowing the planet with a large iron core is required. Mantle volatiles may still be consistent with an initially metal-rich accretion of Mercury *(WEIDENSCHILLING, 1978)*, possibly assisted by magnetic fields in the proto-planetary disc *(KRUSS AND WURM, 2018)*, but how and when volatile-undepleted material was accreted by Mercury remains unknown.

7.2   Future work and the role of BepiColombo

My research has addressed some research questions, but it has raised additional ones, some of which may have to wait until the arrival of BepiColombo to be answered.

7.2.1   Geological mapping of Mercury

7.2.1.1 The Hokusai quadrangle

My geological map of the Hokusai (H05) quadrangle (0°–90°E, 22.5°N–65°N) of Mercury is complete. As explained in Chapter 3, I constructed my basemap with 5°

of latitude and longitude overlap with the adjoining quadrangles (Borealis – H01, Victoria – H02, Raditladi – H04, Kuiper – H06, Eminescu – H09, and Derain – H10). My own mapping of the 5° of overlap with these adjoining quadrangles is ongoing. The published MESSENGER-era quadrangle geological maps of Mercury were published upon their completion as standalone maps *(GALLUZZI ET AL., 2016; MANCINELLI ET AL., 2016; GUZZETTA ET AL., 2017)* and the process of merging the quadrangle maps at their edges began afterward *(GALLUZZI ET AL., 2019)*.

My first priority for my geological map of H05 is for it to be published in the *Journal of Maps* alongside the maps of H02 *(GALLUZZI ET AL., 2016)*, H03 *(GUZZETTA ET AL., 2017)* and H04 *(MANCINELLI ET AL., 2016)*. In order to match the existing quadrangle maps, the 3-class crater degradation scheme will have to be published, but I intend to include the 5-class system in the same publication.

Following the publication of my H05 map, the next important step in this work would be for me to complete mapping of the 5° overlap with the adjoining quadrangles. This would allow me to collaborate with the mappers of the adjoining quadrangles in order to fix the geological linework at the boundaries between our quadrangles to allow our maps to be merged *(GALLUZZI ET AL., 2019)*. The highest priority H05 map boundaries are those with H02 and H04, to the west and east of H05 respectively. The maps of H02 *(GALLUZZI ET AL., 2016)* and H04 *(MANCINELLI ET AL., 2016)* have been published already and so their mappers have been awaiting the completion of the H05 map. A geological map of H01, which borders H05 to the north, is underway *(OSTRACH ET AL., 2018)*. Although it is being completed outside the European effort to map the quadrangles of Mercury for the explicit purpose of preparing for BepiColombo *(GALLUZZI ET AL., 2019)*, it will be an important future task to check the boundary linework of my H05 map with the H01 map. Maps of H06 and H10, which are part of the European BepiColombo mapping effort and border southern H05, are currently underway. When these maps have been published, linework fixing along the southern boundary of H05 can begin. In the final stages of the preparation of this thesis, two European mappers were assigned to H09, which borders H05 in the southeast.

The map of H05 naturally points to some future work within that quadrangle. For example, a careful crater size-frequency distribution study of the intermediate

plains in H05 might be able to determine the age of this unit relative to the intercrater plains and the smooth plains. It might be possible to estimate the total thickness of the lavas that generated the intermediate plains by observing if there is any threshold crater diameter below which craters appear to be missing from the size-frequency distribution. The total stack thickness could be estimated by using well-established relationships between crater diameter and depth *(BAKER AND HEAD, 2013)*. Furthermore, observations of the intermediate plains by BepiColombo might be able to determine why the intermediate plains appears where they do. When quadrangle geological mapping of Mercury is complete, and the full extent of the intermediate plains as identified in H05 is known, we can better understand the origin and stratigraphic relationships of this plains type.

My regional mapping also highlighted some interesting locales in H05 that warrant detailed mapping in the future with the highest resolution MESSENGER data available. In particular, the Rachmaninoff crater, as I showed in Chapter 4, would offer an opportunity to examine material exhumed from the thinnest crust on Mercury *(SORI, 2018)* and provide insight into internal effusive post-impact volcanism after the cessation of large-volume effusions *(BYRNE ET AL., 2016)*.

During my geological mapping, work on mapping the crustal magnetic anomalies above Mercury's northern latitudes was undertaken by *HOOD ET AL. (2018)*. They discovered that there is an approximately circular 6 nT magnetic field strength anomaly centred on Rustaveli crater in northeast H05. They attribute the magnetic anomaly to impactor-delivered iron. *HOOD ET AL. (2018)* found that circular magnetic anomalies associated with other impact craters on Mercury are offset from the crater centres. They suggest that this offset could be due to an oblique impact angle in some cases. To test this hypothesis, a follow-up study to *HOOD ET AL. (2018)* is underway. I have been asked to produce a detailed geological map of Rustaveli. I will pay particular attention to the distribution of the crater's ejecta, secondary craters, impact melt and visible peak-ring elements in order to determine what the probable angle and azimuth of the impact were. This study will test the hypothesis of *WIECZOREK ET AL. (2012)* that magnetic anomalies on the Moon could result from an asymmetric distribution of magnetically susceptible impactor material around the South Pole-Aitken Basin due to an oblique impact.

We will use photogeological evidence to determine the probable impact angles and azimuths for all the craters on Mercury identified by *HOOD ET AL. (2018)* that have magnetic anomalies to see if the magnetic anomalies offset from the centre of their associate crater are offset in the downrange direction.

7.2.1.2 Other Mercury quadrangles

Now that my geological map of H05 is complete, geological mapping of the remaining unmapped quadrangles of Mercury must continue in preparation for the arrival of the BepiColombo mission. At the time of writing, maps of H01 *(OSTRACH ET AL., 2018)*, H06, H07, H10 *(MALLIBAND ET AL., 2019B)*, and H14 *(PEGG ET AL., 2019)* were underway, maps of H08, H09, and H11 were assigned mappers, and maps of them remaining quadrangles (H12, H13 and H15) had not been started.

One important task for all the MESSENGER-era quadrangle mappers is to standardise the units between the quadrangles where possible. Some units, such as smooth plains and intercrater plains, are common to all the quadrangles and were predefined from the Mariner 10-era, and so these units do not require standardisation. However, some newly defined units of regional extent do require standardisation across the quadrangles, including the intermediate plains I mapped in H05. The MESSENGER-era maps of H02 and H03 both contain units called 'intermediate plains'. An important task of unit standardisation will be to determine if the intermediate plains in H02, H03 and H05 are too distinct in appearance or probable provenance to be unified. H04 contains a unit called 'bright intercrater plains' not included in the other published quadrangle geological maps of Mercury. Standardisation could result in this unit being identified in more quadrangles or could recombine the bright intercrater plains in H04 with the regular intercrater plains.

7.2.2 Constructional volcanic edifices

In Chapter 5, I described two candidate constructional volcanic edifices. I was unable to demonstrate a volcanic origin for these landforms using MESSENGER data. In particular, the candidate volcano within Heaney crater was poorly characterised by MESSENGER due to its location at 34°S, where the spacecraft was at a high altitude. BepiColombo's Mercury Planetary Orbiter will have an orbit

much more symmetrical about the equator, such that data availability and resolution over the southern hemisphere will be greatly improved. Both the candidate volcanic edifices I identified would be important landforms for targeted data return by SYMBIO-SYS, MERTIS and BELA. Together, these instruments will be able to determine the morphology and composition of the candidate volcanoes. Observations indicative of a volcanic origin for these landforms include, but are not limited to, lava flows and non-impact summit crater morphologies.

After I published the contents of Chapter 5 *(WRIGHT ET AL., 2018)*, I became involved in a numerical modelling study that aimed to investigate how different eruption parameters would affect pyroclast emplacement and edifice construction on Mercury. The results of these numerical simulations are presented in *BROŽ ET AL., (2018)*. In that paper, we showed that purely pyroclastic eruptions on Mercury probably could not have constructed steep volcanic edifices, comparable to pyroclastic cones on Earth, due to the planet's lack of an atmosphere. A natural follow-up to this work would be to consider the topography plausibly due to large, explosive volcanic eruptions on Mercury to investigate under what eruption conditions such topography could have been built. The deposits around most large explosive volcanic vents on Mercury do not have substantial topography when corrections for the effects of regional slopes and other topographic modifiers have been made *(ROTHERY ET AL., 2014; THOMAS ET AL., 2014A)*. However, MLA data indicate topographic rises with slopes of ~3° for some pyroclastic deposits *(THOMAS ET AL., 2014A)*. Our next paper will take measurements of topography attributable to pyroclasts, where present, around large volcanic vents deposited over the course of those vents' activities and estimate the required eruption parameters, such as ejected volume and velocity. One compounding issue is that there is mounting evidence (Chapter 4; see also *ROTHERY ET AL. 2014*) that the large explosive volcanic vents on Mercury were formed by multiple eruptions over a prolonged period of activity. Therefore the topography surrounding such 'compound' vents was generated by multiple eruptions. If the number of eruptions is uncertain, as it is likely to be since subsequent eruptions can overprint earlier ones entirely, then the model will overestimate the amount of material ejected by a single eruption.

7.2.3   Circum-Caloris knobs

In Chapter 6 I suggested that the circum-Caloris knobs have been modified by an unknown devolatilisation process. While it might take high-resolution observations of the knobs by BepiColombo to determine whether this is true or not, it might be possible to find out more about the knobs using MESSENGER data. The geomorphology the knobs might indicate what devolatilisation process has modified them. For example, if devolatilisation proceeded by sublimation, thermal or photon-stimulated desorption, then there might be some asymmetry between the Sun-facing and anti-Sun slopes of the knobs. Furthermore, any asymmetry present might be expected to become more pronounced at higher latitudes, as the contrast in insolation between the Sun-facing and anti-Sun slopes becomes greater. Most of the circum-Caloris knobs that I mapped are in the northern hemisphere and they span latitudes from 5°S to 62°N. This means that most knobs have Sun-facing southern slopes and anti-Sun northern slopes. Since MLA tracks and shadow profiles generally make approximately make north-south traverses of the knobs, it should be possible for me to modify my existing slope analysis of the knobs to test for any north-slope slope asymmetry. If such an asymmetry exists, then not only would this corroborate a volatile-driven degradation of the knobs, but it would narrow down the range of devolatilisation mechanisms by eliminating micrometeorite bombardment. If no such asymmetry exists, then a non-insolation devolatilisation mechanism, such as sputtering by micrometeorite bombardment, might have been responsible. If no asymmetry is observed then the possibility would remain that volatiles are not involved in the modification of Caloris ejecta into the circum-Caloris knobs.

The circum-Caloris knobs would be good observation targets for SYMBIO-SYS, MERTIS, and BELA. High-resolution imaging would be able to identify pitting in the surface of the knobs that might indicate collapses due to devolatilisation. Stereo- and altimetry-derived topography of the knobs would be useful to make more accurate measurements of the shapes of the knobs. High-resolution compositional measurements of the knobs should be a top priority, since these knobs most likely represent lower crustal or upper mantle materials exposed at the surface of Mercury. Furthermore, if the knobs and the plains of the Odin

Formation continue to release volatiles today, it might be possible for the SERENA instruments on BepiColombo to detect them in Mercury's exosphere.

Hydrocode models of the Caloris impact would be useful to determine the depth from which Caloris ejecta blocks were excavated. My map of the circum-Caloris knobs, which gives an indication of the distribution of Caloris ejecta, could be used to constrain the impact model parameters, such as impactor size and velocity.

CHAPTER 8
CONCLUSIONS

8.1   Summary

I have used orbital MESSENGER data to investigate Mercury's geological history from the scale of a mapping quadrangle down to the scale of small cones. As part of my thesis, I have produced the first geological map of the Hokusai quadrangle. I produced this map to be consistent the other quadrangle geological maps of Mercury that were being published during my work *(GALLUZZI ET AL., 2016; MANCINELLI ET AL., 2016; GUZZETTA ET AL., 2017)*. My map of H05 completes geological mapping of Mercury's mid-northern latitudes. The intricate volcanic history of H05 led me to be most interested in the volcanic evolution of the whole planet. I was particularly intrigued by the lack of observations of constructional volcanic edifices on Mercury, despite the planet's surface being composed largely of volcanic plains. I made two serendipitous discoveries of candidate volcanic edifices. While undergoing a concerted global search for volcanic edifices, I investigated the origin and evolution of the circum-Caloris knobs.

8.2   Conclusions

During my research, I have found that:

- The subdivision of Mercury's plains into two global types (smooth and intercrater) is an oversimplification at the quadrangle scale. My inclusion of my intermediate plains unit in my map imparts geological information pertaining to the multi-phase volcanic resurfacing of Mercury that would be lost if the map contained only smooth and intercrater plains. I interpret the intermediate plains as low-volume effusions that occurred either at the beginning or before the end of the emplacement of the smooth plains.

- Impact craters ≥20 km in diameter in H05 can be classified according to the same 5-class crater degradation system in the global MESSENGER geological map of Mercury *(KINCZYK ET AL., 2016, 2018B)*. This gives the map

more temporal resolution than the 3-class system in previous MESSENGER quadrangle maps.

- Volcanic edifice construction on Mercury was probably inhibited by the high volumes, long flow lengths and low viscosities of the lavas that were typical of Mercury's effusions >3.5 Ga. The waning stage of volcanism, which produced many small volcanic constructs on the Moon, might have played out differently on Mercury due to the relatively abrupt end to effusive volcanism in response to Mercury's global contraction.

- The two candidate volcanic edifices that I have described might have formed as composite cones after the end of large-volume effusions (smooth plains) from small melt volumes that were liberated following impacts. These impacts appear to have emulated the effects of the waning stage of volcanism, which formed many small volcanic constructs on the Moon, which apparently did not occur on Mercury due to the relatively abrupt end to effusive volcanism in response to the planet's global contraction. The BepiColombo mission should search for other small volcanic constructs in other impact craters that postdate the smooth plains on Mercury.

- The circum-Caloris knobs are not volcanic constructs but are instead remnants of Caloris ejecta blocks that have been modified into knobs.

- Knob modification certainly took place over a protracted length of time following their original emplacement and is possibly ongoing today.

- It is possible that these knobs are analogous to 'molards' (conic mounds of rubble formed from thawed permafrost blocks) in that the conic shape of the knobs formed as a result of the loss of a structurally integral volatile component from the ejecta block. If so, this would mean the circum-Caloris knobs were formed by a hitherto undocumented volatile-related surface process potentially active on Mercury's present-day surface. This is a new line of evidence regarding the volatile richness of Mercury that suggests that volatiles occur in the deep interior of the planet, as well as the crust.

REFERENCES

Ackiss, S.E., Buczkowski, D.L., Ernst, C.M., McBeck, J.A., Seelos, K.D., 2015. Knob heights within circum-Caloris geologic units on Mercury: Interpretations of the geologic history of the region. Earth Planet. Sci. Lett. 430, 542–550.

Anderson, D.H., Anderson, E.E., Bieman, K., Bell, P.R., Bogard, D.D., Brett, R., Burlingame, A.L., Carrier, W.D., Chao, E.C.T., Costes, N.C., Dahlem, D.H., Dalrymple, G.B., Doell, R., Eldridge, J.S., Favaro, M.S., Flory, D.A., Fryxell, R., Funkhouser, J., Gast, P.W., Greenwood, W.R., Grolier, M.J., Gromme, C.S., Heiken, G.H., Hess, W.N., Johnson, P.H., Johnson, R., King, E.A., Mancuso, N., Menzies, J.D., Mitchell, J.K., Morrison, D.A., Murphy, R., O'Kelley, G.D., Schaber, G.G., Schaeffer, O.A., Schleicher, D., Schmitt, H.H., Schonfeld, E., Schopf, J.W., Scott, R.F., Shoemaker, E.M., Simoneit, B.R., Smith, D.H., Smith, R.L., Sutton, R.L., Taylor, S.R., Walls, F.C., Warner, J., Wilcox, R.E., Wilmarth, V.R., Zähringer, J., 1969. Preliminary examination of lunar samples from Apollo 11. Science (80-.). 165, 1211–1227.

Aschauer, J., Kenkmann, T., 2017. Impact cratering on slopes. Icarus 290, 89–95.

Asphaug, E., Reufer, A., 2014. Mercury and other iron-rich planetary bodies as relics of inefficient accretion. Nat. Geosci. 7, 564–568.

Baker, D.M.H., Head, J.W., 2013. New morphometric measurements of craters and basins on Mercury and the Moon from MESSENGER and LRO altimetry and image data: An observational framework for evaluating models of peak-ring basin formation. Planet. Space Sci. 86, 91–116.

Baker, D.M.H., Head, J.W., Schon, S.C., Ernst, C.M., Prockter, L.M., Murchie, S.L., Denevi, B.W., Solomon, S.C., Strom, R.G., 2011. The transition from complex crater to peak-ring basin on Mercury: New observations from MESSENGER flyby data and constraints on basin formation models. Planet. Space Sci. 59, 1932–1948.

Banks, M.E., Xiao, Z., Braden, S.E., Barlow, N.G., Chapman, C.R., Fassett, C.I.,

References

Marchi, S.S., 2017. Revised constraints on absolute age limits for Mercury's Kuiperian and Mansurian stratigraphic systems. J. Geophys. Res. Planets 122, 1010–1020.

Banks, M.E., Xiao, Z., Watters, T.R., Strom, R.G., Braden, S.E., Chapman, C.R., Solomon, S.C., Klimczak, C., Byrne, P.K., 2015. Duration of activity on lobate-scarp thrust faults on Mercury. J. Geophys. Res. Planets 120, 1751–1752.

Barnouin, O.S., Zuber, M.T., Smith, D.E., Neumann, G.A., Herrick, R.R., Chappelow, J.E., Murchie, S.L., Prockter, L.M., 2012. The morphology of craters on Mercury: Results from MESSENGER flybys. Icarus 219, 414–427.

Basilevsky, A.T., 2002. Morphology of Callisto knobs from photogeologic analysis of Galileo SSI images taken at orbit C21. In: 33rd Lunar and Planetary Science Conference. Houston, p. Abstract #1014.

Becker, K.J., Robinson, M.S., Becker, T.L., Weller, L.A., Edmundson, K.L., Neumann, G.A., Perry, M.E., Solomon, S.C., 2016. First global digital elevation model of Mercury. In: 47th Lunar and Planetary Science Conference. The Woodlands, Houston, p. Abstract #2959.

Benkhoff, J., van Casteren, J., Hayakawa, H., Fujimoto, M., Laakso, H., Novara, M., Ferri, P., Middleton, H.R., Ziethe, R., 2010. BepiColombo—Comprehensive exploration of Mercury: Mission overview and science goals. Planet. Space Sci. 58, 2–20.

Benz, W., Slattery, W.L., Cameron, A.G.W., 1988. Collisional stripping of Mercury's mantle. Icarus 74, 516–528.

Besse, S., Doressoundiram, A., Benkhoff, J., 2015. Spectroscopic properties of explosive volcanism within the Caloris basin with MESSENGER observations. J. Geophys. Res. Planets 120, 2102–2117.

Blair, D.M., Freed, A.M., Byrne, P.K., Klimczak, C., Prockter, L.M., Ernst, C.M., Solomon, S.C., Melosh, H.J., Zuber, M.T., 2013. The origin of graben and ridges in Rachmaninoff, Raditladi, and Mozart basins, Mercury. J. Geophys. Res. Planets 118, 47–58.

Blewett, D.T., Chabot, N.L., Denevi, B.W., Ernst, C.M., Head, J.W., Izenberg, N.R., Murchie, S.L., Solomon, S.C., Nittler, L.R., McCoy, T.J., Xiao, Z., Baker, D.M.H., Fassett, C.I., Braden, S.E., Oberst, J., Scholten, F., Preusker, F., Hurwitz, D.M., 2011. Hollows on Mercury: MESSENGER evidence for geologically recent volatile-related activity. Science (80-.). 333, 1856–1859.

Blewett, D.T., Robinson, M.S., Denevi, B.W., Gillis-Davis, J.J., Head, J.W., Solomon, S.C., Holsclaw, G.M., McClintock, W.E., 2009. Multispectral images of Mercury from the first MESSENGER flyby: Analysis of global and regional color trends. Earth Planet. Sci. Lett. 285, 272–282.

Blewett, D.T., Vaughan, W.M., Xiao, Z., Chabot, N.L., Denevi, B.W., Ernst, C.M., Helbert, J., D'Amore, M., Maturilli, A., Head, J.W., Solomon, S.C., 2013. Mercury's hollows: Constraints on formation and composition from analysis of geological setting and spectral reflectance. J. Geophys. Res. Planets 118, 1013–1032.

Bottke, W.F., Love, S.G., Tytell, D., Glotch, T., 2000. Interpreting the elliptical crater populations on Mars, Venus, and the Moon. Icarus 145, 108–121.

Braden, S.E., Robinson, M.S., 2013. Relative rates of optical maturation of regolith on Mercury and the Moon. J. Geophys. Res. Planets 118, 1903–1914.

Brown, S.M., Elkins-Tanton, L.T., 2009. Compositions of Mercury's earliest crust from magma ocean models. Earth Planet. Sci. Lett. 286, 446–455.

Browne, P.R.L., Lawless, J. V., 2001. Characteristics of hydrothermal eruptions, with examples from New Zealand and elsewhere. Earth Sci. Rev. 52, 299–331.

Brož, P., Čadek, O., Wright, J., Rothery, D.A., 2018. The Apparent Absence of Kilometer-sized Pyroclastic Volcanoes on Mercury: Are We Looking Right? Geophys. Res. Lett. 45, 12171–12179.

Bryan, S.E., Ernst, R.E., 2008. Revised definition of Large Igneous Provinces (LIPs). Earth-Science Rev. 86, 175–202.

Byrne, P.K., Klimczak, C., Şengör, A.. M.C., Solomon, S.C., Watters, T.R., Hauck, S.A., 2014. Mercury's global contraction much greater than earlier estimates.

References

Nat. Geosci. 7, 301–307.

Byrne, P.K., Klimczak, C., Williams, D.A., Hurwitz, D.M., Solomon, S.C., Head, J.W., Preusker, F., Oberst, J., 2013. An assemblage of lava flow features on Mercury. J. Geophys. Res. Planets 118, 1303–1322.

Byrne, P.K., Ostrach, L.R., Fassett, C.I., Chapman, C.R., Denevi, B.W., Evans, A.J., Klimczak, C., Banks, M.E., Head, J.W., Solomon, S.C., 2016. Widespread effusive volcanism on Mercury likely ended by about 3.5 Ga. Geophys. Res. Lett. 43, 7408–7416.

Byrne, P.K., Van Wyk De Vries, B., Murray, J.B., Troll, V.R., 2012. A volcanotectonic survey of Ascraeus Mons, Mars. J. Geophys. Res. Planets 117, 1–25.

Cameron, A.G.W., 1985. The partial volatilization of Mercury. Icarus 64, 285–294.

Carr, M.H., Crumpler, L.S., Cutts, J.A., Greeley, R., Guest, J.E., Masursky, H., 1977. Martian impact craters and emplacement of ejecta by surface flow. J. Geophys. Res. 82, 4055–4065.

Cashman, K. V., Sturtevant, B., Papale, P., Navon, O., 2000. Magmatic fragmentation. In: Sigurdsson, H., Houghton, B.F., McNutt, S.R., Rymer, H., Stix, J. (Eds.), Encyclopedia of Volcanoes. Academic Press, San Diego, California, pp. 421–430.

Cavanaugh, J.F., Smith, J.C., Sun, X., Bartels, A.E., Ramos-Izquierdo, L., Krebs, D.J., McGarry, J.F., Trunzo, R., Novo-Gradac, A.M., Britt, J.L., Karsh, J., Katz, R.B., Lukemire, A.T., Szymkiewicz, R., Berry, D.L., Swinski, J.P., Neumann, G.A., Zuber, M.T., Smith, D.E., 2007. The Mercury Laser Altimeter Instrument for the MESSENGER Mission. Space Sci. Rev. 131, 451–479.

Chabot, N.L., Denevi, B.W., Murchie, S.L., Hash, C.D., Ernst, C.M., Blewett, D.T., Nair, H., Laslo, N.R., Solomon, S.C., 2016. Mapping Mercury: Global imaging strategy and products from the MESSENGER mission. In: 47th Lunar and Planetary Science Conference. The Woodlands, Houston, p. 1256.

Chapman, C.R., Merline, W.J., Marchi, S., Prockter, L.M., Fassett, C.I., Head, J.W., Solomon, S.C., Xiao, Z., 2012. The young inner plains of Mercury's

Rachmaninoff basin reconsidered. In: 43rd Lunar and Planetary Science Conference. The Woodlands, Houston, p. Abstract #1607.

Chin, G., Brylow, S., Foote, M., Garvin, J., Kasper, J., Keller, J., Litvak, M., Mitrofanov, I., Paige, D., Raney, K., Robinson, M.S., Sanin, A., Smith, D.E., Spence, H., Spudis, P.D., Stern, S.A., Zuber, M.T., 2007. Lunar reconnaissance orbiter overview: The instrument suite and mission. Space Sci. Rev. 129, 391–419.

Cintala, M.J., Grieve, R.A.F., 1998. Scaling impact melting and crater dimensions: Implications for the lunar cratering record. Meteorit. Planet. Sci. 33, 889–912.

Collins, G.S., Morgan, J., Barton, P., Christeson, G.L., Gulick, S., Urrutia, J., Warner, M., Wünnemann, K., 2008. Dynamic modeling suggests terrace zone asymmetry in the Chicxulub crater is caused by target heterogeneity. Earth Planet. Sci. Lett. 270, 221–230.

Colombo, G., 1965. Rotational period of the planet Mercury. Nature 208, 575.

Connerney, J.E.P., Ness, N.F., 1988. Mercury's magnetic field and interior. In: Vilas, F., Chapman, C.R., Matthews, M.S. (Eds.), Mercury. pp. 494–513.

Cook, A.H., 1998. Edmond Halley: Charting the heavens and the seas. Oxford University Press.

Crane, K.T., Klimczak, C., 2019. Tectonic patterns of shortening landforms in Mercury's northern smooth plains. Icarus 317, 66–80.

Davidson, J., de Silva, S., 2000. Composite volcanoes. In: Sigurdsson, H., McNutt, S.R., Rymer, H., Stix, J. (Eds.), Encyclopedia of Volcanoes. Academic Press, San Diego, California, pp. 663–681.

Davies, M.E., Dornik, S.E., Gault, D.E., Strom, R.G., 1978. Atlas of Mercury, NASA Special Publication.

Deetz, C.H., Adams, O.S., 1935. Elements of Map Projection with Applications to Map and Chart Construction. US Government Printing Office.

DeHon, R.A., Scott, D.H., Underwood, J.R., 1981. Geologic map of the Kuiper quadrangle of Mercury. USGS Misc. Investig. Ser. Map I–1233.

References

Denevi, B.W., Ernst, C.M., Meyer, H.M., Robinson, M.S., Murchie, S.L., Whitten, J.L., Head, J.W., Watters, T.R., Solomon, S.C., Ostrach, L.R., Chapman, C.R., Byrne, P.K., Klimczak, C., Peplowski, P.N., 2013. The distribution and origin of smooth plains on Mercury. J. Geophys. Res. Planets 118, 891–907.

Denevi, B.W., Robinson, M.S., Solomon, S.C., Murchie, S.L., Blewett, D.T., Domingue, D.L., McCoy, T.J., Ernst, C.M., Head, J.W., Watters, T.R., Chabot, N.L., 2009. The evolution of Mercury's crust: a global perspective from MESSENGER. Science (80-.). 324, 613–618.

Denevi, B.W., Seelos, F.P., Ernst, C.M., Keller, M.R., Chabot, N.L., Murchie, S.L., Domingue, D.L., Hash, C.D., Blewett, D.T., 2016. Final calibration and multispectral map products from the Mercury Dual Imaging System Wide-Angle Camera on MESSENGER. In: 47th Lunar and Planetary Science Conference. The Woodlands, Houston, p. 1264.

Dombard, A.J., Hauck, S.A., 2008. Despinning plus global contraction and the orientation of lobate scarps on Mercury: Predictions for MESSENGER. Icarus 198, 274–276.

Domingue, D.L., Chapman, C.R., Killen, R.M., Zurbuchen, T.H., Gilbert, J.A., Sarantos, M., Benna, M., Slavin, J.A., Schriver, D., Trávníček, P.M., Orlando, T.M., Sprague, A.L., Blewett, D.T., Gillis-Davis, J.J., Feldman, W.C., Lawrence, D.J., Ho, G.C., Ebel, D.S., Nittler, L.R., Vilas, F., Pieters, C.M., Solomon, S.C., Johnson, C.L., Winslow, R.M., Helbert, J., Peplowski, P.N., Weider, S.Z., Mouawad, N., Izenberg, N.R., McClintock, W.E., 2014. Mercury's weather-beaten surface: Understanding Mercury in the context of lunar and asteroidal space weathering studies. Space Sci. Rev. 181, 121–214.

Dunne, J.A., Burgess, E., 1978. The voyage of Mariner 10, NASA Special Publication.

Eggleton, R.E., Schaber, G.G., 1972. Photogeology: Part B: Cayley Formation interpreted as basin ejecta. In: Brett, R., England, A.W., Calkins, J.E., Giesecke, R.L., Holman, D.N., Mercer, R.M., Murphy, M.J., Simkinson, S.H. (Eds.), Apollo 16 Preliminary Science Report. National Aeronautics and Space Administration, Washington D.C.

Ernst, C.M., Chabot, N.L., Barnouin, O.S., 2018. Could the Hokusai Impact Have Delivered Mercury's Water Ice? In: Mercury: Current and Future Science of the Innermost Planet. p. 6094.

Ernst, C.M., Denevi, B.W., Barnouin, O.S., Klimczak, C., Chabot, N.L., Head, J.W., Murchie, S.L., Neumann, G.A., Prockter, L.M., Robinson, M.S., Solomon, S.C., Watters, T.R., 2015. Stratigraphy of the Caloris basin, Mercury: Implications for volcanic history and basin impact melt. Icarus 250, 413–429.

Fassett, C.I., Crowley, M.C., Leight, C., Dyar, M.D., Minton, D.A., Hirabayashi, M., Thomson, B.J., Watters, W.A., 2017. Evidence for rapid topographic evolution and crater degradation on Mercury from simple crater morphometry. Geophys. Res. Lett. 44, 5326–5335.

Fassett, C.I., Head, J.W., Baker, D.M.H., Zuber, M.T., Smith, D.E., Neumann, G.A., Solomon, S.C., Klimczak, C., Strom, R.G., Chapman, C.R., Prockter, L.M., Phillips, R.J., Oberst, J., Preusker, F., 2012. Large impact basins on Mercury: Global distribution, characteristics, and modification history from MESSENGER orbital data. J. Geophys. Res. Planets 117.

Fassett, C.I., Head, J.W., Blewett, D.T., Chapman, C.R., Dickson, J.L., Murchie, S.L., Solomon, S.C., Watters, T.R., 2009. Caloris impact basin: Exterior geomorphology, stratigraphy, morphometry, radial sculpture, and smooth plains deposits. Earth Planet. Sci. Lett. 285, 297–308.

Fassett, C.I., Minton, D.A., 2013. Impact bombardment of the terrestrial planets and the early history of the Solar System. Nat. Geosci. 6, 520–524.

Fegan, E.R., Rothery, D.A., Conway, S.J., Anand, M., 2016. Mercury Catenae: Linear Features and Lighting Bias. In: 47th Lunar and Planetary Science Conference. The Woodlands, Houston, p. Abstract #2945.

Fegan, E.R., Rothery, D.A., Marchi, S.S., Massironi, M., Conway, S.J., Anand, M., 2017. Late movement of basin-edge lobate scarps on Mercury. Icarus 288, 226–234.

Ferrari, S., Massironi, M., Marchi, S.S., Byrne, P.K., Klimczak, C., Martellato, E., Cremonese, G., 2015. Age relationships of the Rembrandt basin and Enterprise

Rupes, Mercury. In: Platz, T., Massironi, M., Byrne, P.K., Hiesinger, H. (Eds.), Volcanism and Tectonism Across the Inner Solar System. Geological Society of London, pp. 159–172.

Freed, A.M., Blair, D.M., Watters, T.R., Klimczak, C., Byrne, P.K., Solomon, S.C., Zuber, M.T., Melosh, H.J., 2012. On the origin of graben and ridges within and near volcanically buried craters and basins in Mercury's northern plains. J. Geophys. Res. Planets 117, 1–15.

Galilei, G., 1610. Sidereus Nuncius.

Galluzzi, V., 2015. Structural analysis of thr Victoria quadrangle (H2) of Mercury based on NASA MESSENGER data. University of Naples Federico II.

Galluzzi, V., Di Achille, G., Ferranti, L., Popa, C., Palumbo, P., 2015. Faulted craters as indicators for thrust motions on Mercury. In: Platz, T., Massironi, M., Byrne, P.K., Hiesinger, H. (Eds.), Volcanism and Tectonism Across the Inner Solar System. Geological Society of London, pp. 313–325.

Galluzzi, V., Giacomini, L., Guzzetta, L., Lewang, A.M., Malliband, C.C., Mancinelli, P., Pegg, D.L., Semenzato, A., Wright, J., Ferranti, L., Massironi, M., Palumbo, P., Pauselli, C., Rothery, D.A., 2019. Geological Mapping of Mercury. In: Geophysical Research Abstracts.

Galluzzi, V., Guzzeta, L., Ferranti, F., Di Achille, G., Rothery, D.A., Palumbo, P., 2016. Geology of the Victoria quadrangle (H02), Mercury. J. Maps 12, 227–238.

Gerlach, T.M., 1986. Exsolution of H_2O , CO_2, and S during eruptive episodes. J. Geophys. Res. Solid Earth 91, 12177–12185.

Giacomini, L., Massironi, M., Marchi, S., Fassett, C.I., Di Achille, G., Cremonese, G., 2015. Age dating of an extensive thrust system on Mercury: Implications for the planet's thermal evolution. In: Platz, T., Massironi, M., Byrne, P.K., Hiesinger, H. (Eds.), Volcanism and Tectonism Across the Inner Solar System. Geological Society of London, pp. 291–311.

Gillis-Davis, J.J., Blewett, D.T., Gaskell, R.W., Denevi, B.W., Robinson, M.S., Strom, R.G., Solomon, S.C., Sprague, A.L., 2009. Pit-floor craters on Mercury:

Evidence of near-surface igneous activity. Earth Planet. Sci. Lett. 285, 243–250.

Golombek, M.P., Tanaka, K.L., Franklin, B.J., 1996. Extension across Tempe Terra, Mars, from measurements of fault scarp widths and deformed craters. J. Geophys. Res. Planets 101, 26119–26130.

Goosmann, E., Buczkowski, D.L., Ernst, C.M., Denevi, B.W., Kinczyk, M.J., 2016. Geologic map of the Caloris Basin, Mercury. In: 47th Lunar and Planetary Science Conference. The Woodlands, Houston, p. Abstract #1254.

Goudge, T.A., Head, J.W., Kerber, L., Blewett, D.T., Denevi, B.W., Domingue, D.L., Gillis-Davis, J.J., Gwinner, K., Helbert, J., Holsclaw, G.M., Izenberg, N.R., Klima, R.L., McClintock, W.E., Murchie, S.L., Neumann, G.A., Smith, D.E., Strom, R.G., Xiao, Z., Zuber, M.T., Solomon, S.C., 2014. Global inventory and characterisation of pyroclastic deposits on Mercury: New insights into pyroclastic activity from MESSENGER orbital data. J. Geophys. Res. Planets 119, 635–658.

Greeley, R., 1982. The Snake River Plain, Idaho - Representative of a new category of volcanism. J. Geophys. Res. Solid Earth 87, 2705–2712.

Grieve, R.A.F., Cintala, M.J., 1992. An analysis of differential impact melt-crater scaling and implications for the terrestrial impact record. Meteoritics 27, 526–538.

Grolier, M.J., Boyce, J.M., 1984. Geologic map of the Borealis region (H-1) of Mercury. USGS Misc. Investig. Ser. Map I–1660.

Guest, J.E., Greeley, R., 1983. Geologic map of the Shakespeare (H-3) quadrangle of Mercury. USGS Misc. Investig. Ser. Map I–1408.

Guzzetta, L., Galluzzi, V., Ferranti, L., Palumbo, P., 2017. Geology of the Shakespeare quadrangle (H03), Mercury. J. Maps 13, 227–238.

Halley, E., 1679. Catalogus Stellarum Australium sive Supplementum Catalogi Tychoni.

Hapke, B., 2001. Space weathering from Mercury to the asteroid belt. J. Geophys.

Res. Planets 106, 10039–10073.

Hapke, B., Danielson, G.E., Klaasen, K., Wilson, L., 1975. Photometric observations of Mercury from Mariner 10. J. Geophys. Res. 80, 2431–2443.

Hauber, E., Bleacher, J., Gwinner, K., Williams, D.A., Greeley, R., 2009. The topography and morphology of low shields and associated landforms of plains volcanism in the Tharsis region of Mars. J. Volcanol. Geotherm. Res. 185, 69–95.

Hawkins, S.E., Boldt, J.D., Darlington, E.H., Espiritu, R., Gold, R.E., Gotwols, B., Grey, M.P., Hash, C.D., Hayes, J.R., Jaskulek, S.E., Kardian, C.J., Keller, M.R., Malaret, E.R., Murchie, S.L., Murphy, P.K., Peacock, K., Prockter, L.M., Reiter, R.A., Robinson, M.S., Schaefer, E.D., Shelton, R.G., Sterner, R.E., Taylor, H.W., Watters, T.R., Williams, B.D., 2007. The Mercury Dual Imaging System on the MESSENGER Spacecraft. Space Sci. Rev. 131, 247–338.

Head, J.W., 1975. Morphology of pyroclastic lunar volcanic deposits: Implications for eruption conditions and localized sources of volatiles. In: 6th Lunar and Planetary Science Conference. p. Abstract #349.

Head, J.W., Chapman, C.R., Strom, R.G., Fassett, C.I., Denevi, B.W., Blewett, D.T., Ernst, C.M., Watters, T.R., Solomon, S.C., Murchie, S.L., Prockter, L.M., Chabot, N.L., Gillis-Davis, J.J., Whitten, J.L., Goudge, T.A., Baker, D.M.H., Hurwitz, D.M., Ostrach, L.R., Xiao, Z., Merline, W.J., Kerber, L., Dickson, J.L., Oberst, J., Byrne, P.K., Klimczak, C., Nittler, L.R., 2011. Flood volcanism in the northern high latitudes of Mercury revealed by MESSENGER. Science (80-.). 333, 1853–1856.

Head, J.W., Gifford, A., 1980. Lunar mare domes: Classification and modes of origin. Earth. Moon. Planets 22, 235–258.

Head, J.W., Murchie, S.L., Prockter, L.M., Robinson, M.S., Solomon, S.C., Strom, R.G., Chapman, C.R., Watters, T.R., McClintock, W.E., Blewett, D.T., Gillis-Davis, J.J., 2008. Volcanism on Mercury: Evidence from the first MESSENGER flyby. Science (80-.). 321, 69–72.

Head, J.W., Murchie, S.L., Prockter, L.M., Solomon, S.C., Chapman, C.R., Strom,

R.G., Watters, T.R., Blewett, D.T., Gillis-Davis, J.J., Fassett, C.I., Dickson, J.L., Morgan, G.A., Kerber, L., 2009. Volcanism on Mercury: Evidence from the first MESSENGER flyby for extrusive and explosive activity and the volcanic origin of plains. Earth Planet. Sci. Lett. 285, 227–242.

Head, J.W., Wilson, L., 1992. Lunar mare volcanism: Stratigraphy, eruption conditions, and the evolution of secondary crusts. Geochim. Cosmochim. Acta 56, 2155–2175.

Heather, D.J., Dunkin, S.K., Wilson, L., 2003. Volcanism on the Marius Hills plateau: Observational analyses using Clementine multispectral data. J. Geophys. Res. 108, 5017.

Herdendorf, C.E., 1986. Captain James Cook and the Transits of Mercury and Venus. J. Pac. Hist. 21, 39–56.

Herrick, R.R., 2014. Protobasins are not part of the normal sequence, target is important, and other musings on the central-peak to peak-ring transition based on Mercury's impact craters. In: 45th Lunar and Planetary Science Conference. The Woodlands, Houston, p. Abstract #1782.

Herrick, R.R., Schenk, P.M., Robbins, S.J., 2012. Surveys of elliptical crater populations on the saturnian satellites, Mercury, and Mars. Icarus 220, 297–304.

Hiesinger, H., Jaumann, R., Neukum, G., Head, J.W., 2000. Ages of mare basalts on the lunar nearside. J. Geophys. Res. Planets 105, 29239–29275.

Hood, L.L., Oliveira, J.S., Galluzzi, V., Rothery, D.A., 2018. Investigating Sources of Mercury's Crustal Magnetic Field: Further Mapping of MESSENGER Magnetometer Data. J. Geophys. Res. Planets 123, 2647–2666.

Howard, K.A., Wilshire, H.G., 1975. Flows of Impact Melt at Lunar Craters. J. Res. United States Geol. Surv. 3, 237–251.

Hutton, C., 1778. An account of the calculations made from the survey and measures taken at Schehallien, in order to ascertain the mean density of the Earth. Philos. Trans. R. Soc. London 68, 1–108.

References

Jacobs, J.A., 1979. Planetary magnetic fields. Geophys. Res. Lett. 6, 213–214.

James, P.B., Zuber, M.T., Phillips, R.J., Solomon, S.C., 2015. Support of long-wavelength topography on Mercury inferred from MESSENGER measurements of gravity and topography. J. Geophys. Res. Planets 120, 287–310.

Jozwiak, L.M., Head, J.W., Wilson, L., 2018. Explosive volcanism on Mercury: Analysis of vent and deposit morphology and modes of eruption. Icarus 302, 191–212.

Kay, J.P., Dombard, A.J., 2019. Long-wavelength topography on Mercury is not from folding of the lithosphere. Icarus 319, 724–728.

Kenkmann, T., Poelchau, M.H., Wulf, G., 2014. Structural geology of impact craters. J. Struct. Geol. 62, 156–182.

Kerber, L., Head, J.W., Blewett, D.T., Solomon, S.C., Wilson, L., Murchie, S.L., Robinson, M.S., Denevi, B.W., Domingue, D.L., 2011. The global distribution of pyroclastic deposits on Mercury: The view from MESSENGER flybys 1-3. Planet. Space Sci. 59, 1895–1909.

Kerber, L., Head, J.W., Solomon, S.C., Murchie, S.L., Blewett, D.T., Wilson, L., 2009. Explosive volcanic eruptions on Mercury: Eruption conditions, magma volatile content, and implications for interior volatile abundances. Earth Planet. Sci. Lett. 285, 263–271.

Kinczyk, M.J., Barnouin, O.S., Ernst, C.M., Byrne, P.K., 2018a. A tale of two craters: Using geological mapping to assess the role of impact melt in the formation of Hokusai crater, Mercury. In: 49th Lunar and Planetary Science Conference. The Woodlands, Houston, p. Abstract #2916.

Kinczyk, M.J., Prockter, L.M., Byrne, P.K., Denevi, B.W., Ostrach, L.R., Skinner, J.A., 2018b. A global geological map of Mercury. In: Mercury: Current and Future Science of the Innermost Planet. Columbia, Maryland, p. Abstract #6123.

Kinczyk, M.J., Prockter, L.M., Chapman, C.R., Susorney, H.C.M., 2016. A

morphological evaluation of crater degradation on Mercury: Revisiting crater classification with MESSENGER data. In: 47th Lunar and Planetary Science Conference. The Woodlands, Houston, p. Abstract #1573.

King, J.S., Scott, D.H., 1990. Geologic map of the Beethoven quadrangle of Mercury. USGS Misc. Investig. Ser. Map I–2048.

King, S.D., 2008. Pattern of lobate scarps on Mercury's surface reproduced by a model of mantle convection. Nat. Geosci. 1, 229–232.

Klimczak, C., 2015. Limits on the brittle strength of planetary lithospheres undergoing global contraction. J. Geophys. Res. Planets 120, 2135–2151.

Klimczak, C., Ernst, C.M., Byrne, P.K., Solomon, S.C., Watters, T.R., Murchie, S.L., Preusker, F., Balcerski, J.A., 2013. Insights into the subsurface structure of the Caloris basin, Mercury, from assessments of mechanical layering and changes in long-wavelength topography. J. Geophys. Res. Planets 118, 2030–2044.

Kneissl, T., Van Gasselt, S., Neukum, G., 2011. Map-projection-independent crater size-frequency determination in GIS environments - New software tool for ArcGIS. Planet. Space Sci. 59, 1243–1254.

Kreslavsky, M.A., Head, J.W., 1999. Kilometer-scale slopes on Mars and their correlation with geologic units: Initial results from Mars Orbiter Laser Altimeter (MOLA) data. J. Geophys. Res. Planets 104, 21911–21924.

Kreslavsky, M.A., Head, J.W., Neumann, G.A., Zuber, M.T., Smith, D.E., 2014. Kilometer-scale topographic roughness of Mercury: Correlation with geologic features and units. Geophys. Res. Lett. 41, 8245–8251.

Kruss, M., Wurm, G., 2018. Seeding the Formation of Mercurys: An Iron-sensitive Bouncing Barrier in Disk Magnetic Fields. Astrophys. J. 869, 1–6.

Lawrence, D.J., Feldman, W.C., Goldsten, J.O., Maurice, S., Peplowski, P.N., Anderson, B.J., Bazell, D., McNutt, R.L., Nittler, L.R., Prettyman, T.H., Rodgers, D.J., Solomon, S.C., Weider, S.Z., 2013. Evidence for Water Ice Near Mercury's North Pole from MESSENGER Neutron Spectrometer Measurements. Science (80-.). 339, 292–296.

Lawrence, S.J., Stopar, J.D., Hawke, B.R., Greenhagen, B.T., Cahill, J.T.S., Bandfield, J.L., Jolliff, B.L., Denevi, B.W., Robinson, M.S., Glotch, T.D., Bussey, D.B.J., Spudis, P.D., Giguere, T.A., Garry, W.B., 2013. LRO observations of morphology and surface roughness of volcanic cones and lobate lava flows in the Marius Hills. J. Geophys. Res. Planets 118, 615–634.

Le Feuvre, M., Wieczorek, M.A., 2011. Nonuniform cratering of the Moon and a revised crater chronology of the inner Solar System. Icarus 214, 1–20.

Liu, D., Jolliff, B.L., Zeigler, R.A., Korotev, R.L., Wan, Y., Xie, H., Zhang, Y., Dong, C., Wang, W., 2012. Comparative zircon U-Pb geochronology of impact melt breccias from Apollo 12 and lunar meteorite SaU 169, and implications for the age of the Imbrium impact. Earth Planet. Sci. Lett. 319–320, 277–286.

Lyttleton, R.A., 1980. History of the mass of Mercury. Pasadena, California.

Maccaferri, F., Bonafede, M., Rivalta, E., 2011. A quantitative study of the mechanisms governing dike propagation, dike arrest and sill formation. J. Volcanol. Geotherm. Res. 208, 39–50.

Malin, M.C., Caplinger, M.A., Davis, S.D., 2001. Observational evidence for an active surface reservoir of solid carbon dioxide on Mars. Science (80-.). 294, 2146–2148.

Malliband, C.C., Conway, S.J., Rothery, D.A., Balme, M.R., 2019a. Potential identification of downslope mass movements on Mercury driven by volatile-loss. In: 50th Lunar and Planetary Science Conference. p. Abstract #1804.

Malliband, C.C., Rothery, D.A., Balme, M.R., Conway, S.J., 2018. Small smooth units ("young" lavas?) abutting lobate scarps on Mercury. In: Mercury: Current and Future Science of the Innermost Planet. Columbia, Maryland, p. Abstract #6092.

Malliband, C.C., Rothery, D.A., Balme, M.R., Conway, S.J., 2019b. 1:3M geological mapping of the Derain (H-10) quadrangle of Mercury. In: 50th Lunar and Planetary Science Conference. The Woodlands, Houston, p. Abstract #1807.

Mancinelli, P., Minelli, F., Pauselli, C., Federico, C., 2016. Geology of the Raditladi

quadrangle, Mercury (H04). J. Maps 5647, 1–13.

Marchi, S., Mottola, S., Cremonese, G., Massironi, M., Martellato, E., 2009. A New Chronology for the Moon and Mercury. Astron. J. 137, 4936–4948.

Margot, J., Peale, S.J., Jurgens, R.F., Slade, M.A., Holin, I. V., 2007. Large longitude libration of Mercury reveals a molten core. Science (80-.). 316, 710–714.

Massironi, M., Di Achille, G., Rothery, D.A., Galluzzi, V., Giacomini, L., Ferrari, S., Zusi, M., Cremonese, G., Palumbo, P., 2015. Lateral ramps and strike-slip kinematics on Mercury. In: Platz, T., Massironi, M., Byrne, P.K., Hiesinger, H. (Eds.), Volcanism and Tectonism Across the Inner Solar System. pp. 269–290.

Mazarico, E., Genova, A., Goossens, S., Lemoine, F.G., Neumann, G.A., Zuber, M.T., Smith, D.E., Solomon, S.C., 2014. The gravity field, orientation, and ephemeris of Mercury from MESSENGER observations after three years in orbit. J. Geophys. Res. Planets 119, 2417–2436.

McCauley, J.F., Guest, J.E., Schaber, G.G., Trask, N.J., Greeley, R., 1981. Stratigraphy of the Caloris basin, Mercury. Icarus 47, 184–202.

McEwen, A.S., Preblich, B.S., Turtle, E.P., Artemieva, N.A., Golombek, M.P., Hurst, M., Kirk, R.L., Burr, D.M., Christensen, P.R., 2005. The rayed crater Zunil and interpretations of small impact craters on Mars. Icarus 176, 351–381.

McGill, G.E., King, E.A., 1983. Geologic map of the Victoria (H-2) quadrangle of Mercury. USGS Misc. Investig. Ser. Map I–1409.

McGovern, P.J., Litherland, M.M., 2011. Lithospheric stress and basaltic magma ascent on the Moon, with implications for large volcanic provinces and edifices. In: 42nd Lunar and Planetary Science Conference. p. Abstract #2587.

Melosh, H.J., 1977. Global tectonics of a despun planet. Icarus 31, 221–243.

Melosh, H.J., Dzurisin, D., 1978. Mercurian global tectonics: A consequence of tidal despinning? Icarus 35, 227–236.

Menand, T., Daniels, K.A., Benghiat, P., 2010. Dyke propagation and sill formation in a compressive tectonic environment. J. Geophys. Res. Solid Earth 115, B08201.

References

Merle, R.E., Nemchin, A.A., Grange, M.L., Whitehouse, M.J., Pidgeon, R.T., 2014. High resolution U-Pb ages of Ca-phosphates in Apollo 14 breccias: Implications for the age of the Imbrium impact. Meteorit. Planet. Sci. 49, 2241–2251.

Morino, C., Conway, S.J., Sæmundsson, Þ., Helgason, J.K., Emmert, A., Kneisel, C., Butcher, F.E.G., Balme, M.R., Hillier, J., Jordan, C., Argles, T., 2019. Molards as an indicator of permafrost degradation and landslide processes. Earth Planet. Sci. Lett. (awaiting moderate reviews).

Morley, C.K., 1988. Out of Sequence Thrusts. Tectonics 7, 539–561.

Murchie, S.L., Klima, R.L., Denevi, B.W., Ernst, C.M., Keller, M.R., Domingue, D.L., Blewett, D.T., Chabot, N.L., Hash, C.D., Malaret, E., Izenberg, N.R., Vilas, F., Nittler, L.R., Gillis-Davis, J.J., Head, J.W., Solomon, S.C., 2015. Orbital multispectral mapping of Mercury with the MESSENGER Mercury Dual Imaging System: Evidence for the origins of plains units and low-reflectance material. Icarus 254, 287–305.

Murchie, S.L., Watters, T.R., Robinson, M.S., Head, J.W., Strom, R.G., Chapman, C.R., Solomon, S.C., McClintock, W.E., Prockter, L.M., Domingue, D.L., Blewett, D.T., 2008. Geology of the Caloris basin, Mercury: a view from MESSENGER. Science (80-.). 321, 73–76.

Murray, B.C., Belton, M.J.S., Danielson, G.E., Davies, M.E., Gault, D.E., Hapke, B., O'Leary, B., Strom, R.G., Suomi, V., Trask, N.J., 1974. Mercury's Surface : Preliminary Description and Interpretation from Mariner 10 Pictures. Science (80-.). 185, 169–180.

Namur, O., Charlier, B., 2017. Silicate mineralogy at the surface of Mercury. Nat. Geosci. 10, 9–13.

Naumann, T., Geist, D., 2000. Physical volcanology and structural development of Cerro Azul Volcano , Isabela Island , Galápagos : implications for the development of Galápagos-type shield volcanoes. Bull. Volcanol. 61, 497–514.

Neil, E.A., Houseman, G.A., 1999. Rayleigh-Taylor instability of the upper mantle and its role in intraplate orogeny. Geophys. J. Int. 138, 89–107.

Ness, N.F., Behannon, K.W., Lepping, R.P., Whang, Y.C., Schatten, K.H., 1974. Magnetic field observations near Venus: Preliminary results from Mariner 10. Science (80-.). 183, 1301–1306.

Neukum, G., Ivanov, B.A., Hartmann, W.K., 2001. Cratering records in the inner solar system in relation to the lunar reference system. In: Kallenbach, R., Geiss, J., Hartmann, W.K. (Eds.), Chronology and Evolution of Mars. Springer Netherlands, pp. 55–86.

Nittler, L.R., Starr, R.D., Weider, S.Z., McCoy, T.J., Boynton, W. V., Ebel, D.S., Ernst, C.M., Evans, L.G., Goldsten, J.O., Hamara, D.K., Lawrence, D.J., McNutt, R.L., Schlemm, C.E., Solomon, S.C., Sprague, A.L., 2011. The major-element composition of Mercury's surface from MESSENGER X-ray spectrometry. Science (80-.). 333, 1847–50.

Oberbeck, V.R., 1971. A mechanism for the production of lunar crater rays. Earth. Moon. Planets 2, 263–278.

Öpik, E., 1960. The lunar surface as an impact counter. Mon. Not. R. Astron. Soc. 120, 404–411.

Orgel, C., Fassett, C.I., Michael, G.G., van der Bogert, C.H., Manske, L., Hiesinger, H., 2019. Re-examination of the population, stratigraphy, and sequence of Mercuryian basins: Implications for Mercury's early impact history and comparison with the Moon. In: 50th Lunar and Planetary Science Conference. The Woodlands, Houston, p. Abstract #2059.

Ostrach, L.R., Mest, S.C., Prockter, L.M., Petro, N.E., Byrne, P.K., 2018. Update on the Geologic Map of the Borealis Quadrangle (H-1) on Mercury. In: 49th Lunar and Planetary Science Conference. The Woodlands, Houston, p. Abstract #1747.

Ostrach, L.R., Robinson, M.S., Whitten, J.L., Fassett, C.I., Strom, R.G., Head, J.W., Solomon, S.C., 2015. Extent, age, and resurfacing history of the northern smooth plains on Mercury from MESSENGER observations. Icarus 250, 602–622.

Pacheco, J.F., Scholtz, C.H., Sykes, L.R., 1992. Changes in frequency–size

relationship from small to large earthquakes. Nature 355, 71.

Pappalardo, R.T., Collins, G.C., 2005. Strained craters on Ganymede. J. Struct. Geol. 27, 827–838.

Pegg, D.L., Rothery, D.A., Balme, M.R., Conway, S.J., 2019. Geological mapping of the Debussy quadrangle (H-14) of Mercury, preliminary results. In: 50th Lunar and Planetary Science Conference. p. Abstract #1271.

Peplowski, P.N., Evans, L.G., Hauck, S.A., McCoy, T.J., Boynton, W. V., Gillis-Davis, J.J., Ebel, D.S., Goldsten, J.O., Hamara, D.K., Lawrence, D.J., McNutt, R.L., Nittler, L.R., Solomon, S.C., Rhodes, E.A., Sprague, A.L., Starr, R.D., Stockstill-Cahill, K.R., 2011. Radioactive Elements on Mercury's Surface from MESSENGER: Implications for the Planet's Formation and Evolution. Science (80-.). 333, 1850–1852.

Peplowski, P.N., Klima, R.L., Lawrence, D.J., Ernst, C.M., Denevi, B.W., Frank, E.A., Goldsten, J.O., Murchie, S.L., Nittler, L.R., Solomon, S.C., 2016. Remote sensing evidence for an ancient carbon-bearing crust on Mercury. Nat. Geosci. 9, 273–276.

Perry, M.E., Neumann, G.A., Phillips, R.J., Barnouin, O.S., Ernst, C.M., Kahan, D.S., Solomon, S.C., Zuber, M.T., Smith, D.E., Hauck, S.A., Peale, S.J., Margot, J.-L., Mazarico, E., Johnson, C.L., Gaskell, R.W., Roberts, J.H., McNutt, R.L., Oberst, J., 2015. The low-degree shape of Mercury. Geophys. Res. Lett. 42, 6951–6958.

Peterson, G.A., Johnson, C.L., Byrne, P.K., Phillips, R.J., Neumann, G.A., 2017. Depth of faulting in Mercury's northern hemisphere from thrust fault morphology. In: 48th Lunar and Planetary Science Conference. p. Abstract #2315.

Pettengill, G.H., Dyce, R.B., 1965. A radar determination of the rotation of the planet Mercury. Nature 206, 1240.

Pieters, C.M., Noble, S.K., 2016. Space weathering on airless bodies. J. Geophys. Res. Planets 121, 1865–1884.

Plescia, J.B., Golombek, M.P., 1986. Origin of planetary wrinkle ridges based on the

study of terrestrial analogs. Geol. Soc. Am. Bull. 97, 1289–1299.

Preusker, F., Oberst, J., Head, J.W., Watters, T.R., Robinson, M.S., Zuber, M.T., Solomon, S.C., 2011. Stereo topographic models of Mercury after three MESSENGER flybys. Planet. Space Sci. 59, 1910–1917.

Prockter, L.M., Ernst, C.M., Denevi, B.W., Chapman, C.R., Head, J.W., Fassett, C.I., Merline, W.J., Solomon, S.C., Watters, T.R., Strom, R.G., Cremonese, G., Marchi, S., Massironi, M., 2010. Evidence for Young Volcanism on Mercury from the Third MESSENGER Flyby. Science (80-.). 329, 668–671.

Prockter, L.M., Kinczyk, M.J., Byrne, P.K., Denevi, B.W., Head, J.W., Fassett, C.I., Whitten, J.L., Thomas, R.J., Buczkowski, D.L., Hynek, B.M., Ostrach, L.R., Blewett, D.T., Ernst, C.M., 2016. The first global geological map of Mercury. In: 47th Lunar and Planetary Science Conference. The Woodlands, Houston, p. Abstract #1245.

Rava, B., Hapke, B., 1987. An analysis of the Mariner 10 color ratio map of mercury. Icarus 71, 397–429.

RCoreTeam, 2013. R: A language and environment for statistical computing.

Roberts, J.H., Barnouin, O.S., 2012. The effect of the Caloris impact on the mantle dynamics and volcanism of Mercury. J. Geophys. Res. Planets 117, E02007.

Robinson, M.S., Brylow, S.M., Tschimmel, M., Humm, D., Lawrence, S.J., Thomas, P.C., Denevi, B.W., Bowman-Cisneros, E., Zerr, J., Ravine, M.A., Caplinger, M.A., Ghaemi, F.T., Schaffner, J.A., Malin, M.C., Mahanti, P., Bartels, A.E., Anderson, J., Tran, T.N., Eliason, E.M., McEwen, A.S., Turtle, E.P., Jolliff, B.L., Hiesinger, H., 2010. Lunar Reconnaissance Orbiter Camera (LROC) Instrument Overview. Space Sci. Rev. 150, 81–124.

Robinson, M.S., Lucey, P.G., 1997. Recalibrated Mariner 10 Color Mosaics: Implications for Mercurian Volcanism. Science (80-.). 275, 197–200.

Robinson, M.S., Murchie, S.L., Blewett, D.T., Domingue, D.L., Hawkins, S.E., Head, J.W., Holsclaw, G.M., McClintock, W.E., McCoy, T.J., McNutt, R.L., Prockter, L.M., Solomon, S.C., Watters, T.R., 2008. Reflectance and color variations on

References

Mercury: regolith processes and compositional heterogeneity. Science (80-.). 321, 66–69.

Rothery, D.A., Mancinelli, P., Guzzetta, L., Wright, J., 2017. Mercury's Caloris basin: Continuity between the interior and exterior plains. J. Geophys. Res. Planets 122, 560–576.

Rothery, D.A., Marinangeli, L., Anand, M., Carpenter, J., Christensen, U., Crawford, I.A., Cristina De Sanctis, M., Epifani, E.M., Erard, S., Frigeri, A., Fraser, G., Hauber, E., Helbert, J., Hiesinger, H., Joy, K., Langevin, Y., Massironi, M., Milillo, A., Mitrofanov, I., Muinonen, K., Näränen, J., Pauselli, C., Potts, P., Warell, J., Wurz, P., 2010. Mercury's surface and composition to be studied by BepiColombo. Planet. Space Sci. 58, 21–39.

Rothery, D.A., Massironi, M., 2010. Beagle Rupes – Evidence for a basal decollement of regional extent in Mercury's lithosphere. Icarus 209, 256–261.

Rothery, D.A., Thomas, R.J., Kerber, L., 2014. Prolonged eruptive history of a compound volcano on Mercury: Volcanic and tectonic implications. Earth Planet. Sci. Lett. 385, 59–67.

Schaber, G.G., McCauley, J.F., 1980. Geologic map of the Tolstoj quadrangle of Mercury (H-8). Map I-1199. USGS Misc. Investig. Ser. Map I–1199.

Schiapparelli, G. V., 1889. Sulla rotazione di Mercurio. Astron. Nachricten 123, 241–250.

Sigurdsson, H., Houghton, B.F., McNutt, S.R., Rymer, H., Stix, J., 2000. The encyclopedia of volcanoes, First. ed. Academic Press, San Diego, California.

Smith, D.E., Zuber, M.T., Jackson, G.B., Riris, H., Neumann, G.A., Sun, X., McGarry, J.F., Cavanaugh, J.F., Ramos-Izquierdo, L.A., Zellar, R., Torrence, M.H., Mazarico, E., Connelly, J., Matuszeski, A., Ott, M., Rowlands, D.D., Zagwodzki, T., Torrence, M.H., Katz, R., Kleyner, I., Peters, C., Liiva, P., Coltharp, C., Schmidt, S., Ramsey, L., Scott, V.S., Unger, G., Krebs, D.C., Novo-Gradac, A.-M.D., Shaw, G.B., Yu, A.W., 2010. The Lunar Orbiter Laser Altimeter investigation on the Lunar Reconnaissance Orbiter mission. Space Sci. Rev. 150, 209–241.

Smith, D.E., Zuber, M.T., Phillips, R.J., Solomon, S.C., Hauck, S.A., Lemoine, F.G., Mazarico, E., Neumann, G.A., Peale, S.J., Margot, J., Johnson, C.L., Torrence, M.H., Perry, M.E., Rowlands, D.D., Goossens, S., Head, J.W., Taylor, A.H., 2012. Gravity Field and Internal Structure of Mercury from MESSENGER. Science (80-.). 336, 214–217.

Solomon, S.C., 1976. Some Aspects of Core Formation in Mercury. Icarus 28, 509–521.

Solomon, S.C., 1978. On volcanism and thermal tectonics on one-plate planets. Geophys. Res. Lett. 5, 461–464.

Solomon, S.C., Head, J.W., 1980. Lunar Mascon Basins: Lava filling, tectonics, and evolution of the lithosphere. Rev. Geophys. Sp. Phys. 18, 107–141.

Solomon, S.C., McNutt, R.L., Gold, R.E., Acuña, M.H., Baker, D.N., Boynton, W. V., Chapman, C.R., Cheng, A.F., Gloeckler, G., Head, J.W., Krimigis, S.M., McClintock, W.E., Murchie, S.L., Peale, S.J., Phillips, R.J., Robinson, M.S., Slavin, J.A., Smith, D.E., Strom, R.G., Trombka, J.I., Zuber, M.T., 2001. The MESSENGER mission to Mercury: Scientific objectives and implementation. Planet. Space Sci. 49, 1445–1465.

Solomon, S.C., McNutt, R.L., Gold, R.E., Domingue, D.L., 2007. MESSENGER mission overview. Space Sci. Rev. 131, 3–39.

Sori, M.M., 2018. A thin, dense crust for Mercury. Earth Planet. Sci. Lett. 489, 92–99.

Soter, S., Ulrichs, J., 1967. Rotation and heating of the planet Mercury. Nature 214, 1315–1316.

Spudis, P.D., Guest, J.E., 1988. Stratigraphy and geologic history of Mercury. In: Vilas, F., Chapman, C.R., Matthews, M.S. (Eds.), Mercury. University of Arizona Press, Tucson, pp. 118–164.

Spudis, P.D., Prosser, J.G., 1984. Geologic Map of the Michelangelo Quadrangle of Mercury. USGS Misc. Investig. Ser. Map I–1659.

Stark, A., Preusker, F., Oberst, J., Matz, K.-D., Gwinner, K., Roatsch, T., 2017. High-

resolution topography from MESSENGER orbital stereo imaging - the H5 quadrangle "Hokusai." In: 48th Lunar and Planetary Science Conference. The Woodlands, Houston, p. Abstract #2287.

Stockstill-Cahill, K.R., McCoy, T.J., Nittler, L.R., Weider, S.Z., Hauck, S.A., 2012. Magnesium-rich crustal compositions on mercury: Implications for magmatism from petrologic modeling. J. Geophys. Res. Planets 117, E00L15.

Strom, R.G., Chapman, C.R., Merline, W.J., Solomon, S.C., Head, J.W., 2008. Mercury cratering record viewed from MESSENGER's first flyby. Science (80-.). 321, 79–81.

Strom, R.G., Malin, M.C., Leake, M.A., 1990. Geologic map of the Bach region of Mercury. USGS Misc. Investig. Ser. Map I–2015.

Strom, R.G., Neukum, G., 1988. The cratering record on mercury and the origin of impacting objects. In: Vilas, F., Chapman, C.R., Matthews, M.S. (Eds.), Mercury. University of Arizona Press, Tuscon, Arizona, pp. 336–373.

Strom, R.G., Trask, N.J., Guest, J.E., 1975. Tectonism and volcanism on Mercury. J. Geophys. Res. 80, 2478–2507.

Swanson, D.A., 1973. Pahoehoe flows from the 1969-1971 Mauna Ulu eruption, Kilauea volcano, Hawaii. Geol. Soc. Am. Bull. 84, 615–626.

Tanaka, K.L., Skinner, J.A., Hare, T.M., 2011. Planetary Geologic Mapping Handbook – 2011. USGS Astrogeology Science Center.

Taylor, S.R., 1987. The unique lunar composition and its bearing on the origin of the Moon. Geochim. Cosmochim. Acta 51, 1297–1309.

Tchoukanski, I., 2017. ET Geo Wizards.

Thomas, P.C., Malin, M.C., Edgett, K.S., Carr, M.H., Hartmann, W.K., Ingersoll, A.P., James, P.B., Soderblom, L.A., Veverka, J., Sullivan, R., 2000. North-south geological differences between the residual polar caps on Mars. Nature 404, 161–164.

Thomas, R.J., Hynek, B.M., Rothery, D.A., Conway, S.J., 2016. Mercury's low-reflectance material: constraints from hollows. Icarus 277, 455–465.

Thomas, R.J., Rothery, D.A., Conway, S.J., Anand, M., 2014a. Mechanisms of explosive volcanism on Mercury: Implications from its global distribution and morphology. J. Geophys. Res. Planets 119, 2239–2254.

Thomas, R.J., Rothery, D.A., Conway, S.J., Anand, M., 2014b. Long-lived explosive volcanism on Mercury. Geophys. Res. Lett. 41, 6084–6092.

Thomas, R.J., Rothery, D.A., Conway, S.J., Anand, M., 2014c. Hollows on Mercury: Materials and mechanisms involved in their formation. Icarus 229, 221–235.

Thomas, R.J., Rothery, D.A., Conway, S.J., Anand, M., 2015. Explosive volcanism in complex impact craters on Mercury and the Moon: Influence of tectonic regime on depth of magmatic intrusion. Earth Planet. Sci. Lett. 431, 164–172.

Thordarson, T., Larsen, G., 2007. Volcanism in Iceland in historical time: Volcano types, eruption styles and eruptive history. J. Geodyn. 43, 118–152.

Tobler, W., 1987. Measuring spatial resolution. In: Proceedings of the Land Resource Information Systems Conference. Beijing, pp. 12–16.

Trask, N.J., Dzurisin, D., 1984. Geologic map of the Discovery (H-11) quadrangle of Mercury. USGS Misc. Investig. Ser. Map I–1658.

Trask, N.J., Guest, J.E., 1975. Preliminary geologic terrain map of Mercury. J. Geophys. Res. 80, 2461–2477.

Vander Kaaden, K.E., Mccubbin, F.M., 2015. Exotic crust formation on Mercury: Consequences of a shallow, FeO-poor mantle. J. Geophys. Res. Planets 120, 195–209.

Vaucher, J., Baratoux, D., Toplis, M.J., Pinet, P., Mangold, N., Kurita, K., 2009. The morphologies of volcanic landforms at Central Elysium Planitia: Evidence for recent and fluid lavas on Mars. Icarus 200, 39–51.

Watters, T.R., Daud, K., Banks, M.E., Selvans, M.M., Chapman, C.R., Ernst, C.M., 2016. Recent tectonic activity on Mercury revealed by small thrust fault scarps. Nat. Geosci. 9, 743–747.

Watters, T.R., Head, J.W., Solomon, S.C., Robinson, M.S., Chapman, C.R., Denevi, B.W., Fassett, C.I., Murchie, S.L., Strom, R.G., 2009. Evolution of the

rembrandt impact basin on Mercury. Science (80-.). 324, 618–621.

Watters, T.R., Robinson, M.S., Bina, C.R., Spudis, P.D., 2004. Thrust faults and the global contraction of Mercury. Geophys. Res. Lett. 31, L04701.

Watters, T.R., Selvans, M.M., Banks, M.E., Hauck, S.A., Becker, K.J., Robinson, M.S., 2015. Distribution of large-scale contractional tectonic landforms on Mercury: Implications for the origin of global stresses. Geophys. Res. Lett. 42, 3755–3763.

Weidenschilling, S.J., 1978. Iron/silicate fractionation and the origin of Mercury. Icarus 35, 99–111.

Weider, S.Z., Nittler, L.R., Murchie, S.L., Peplowski, P.N., McCoy, T.J., Kerber, L., Klimczak, C., Ernst, C.M., Goudge, T.A., Starr, R.D., Izenberg, N.R., Klima, R.L., Solomon, S.C., 2016. Evidence from MESSENGER for sulfur- and carbon-driven explosive volcanism on Mercury. Geophys. Res. Lett. 43, 3653–3661.

Weider, S.Z., Nittler, L.R., Starr, R.D., McCoy, T.J., Stockstill-Cahill, K.R., Byrne, P.K., Denevi, B.W., Head, J.W., Solomon, S.C., 2012. Chemical heterogeneity on Mercury's surface revealed by the MESSENGER X-Ray Spectrometer. J. Geophys. Res. E Planets 117, E00L05.

Weitz, C.M., Head, J.W., 1999. Spectral properties of the Marius Hills volcanic complex and implications for the formation of lunar domes and cones. J. Geophys. Res. Planets 104, 18933–18956.

White, J.D.L., Bryan, S.E., Ross, P.-S., Self, S., Thordarson, T., 2009. Physical Volcanology of Large Igneous Provinces: Update and Review. In: Thordarson, T., Self, S., Larsen, G., Rowland, S.K., Hoskuldsson, A. (Eds.), Studies in Volcanology: The Legacy of George Walker. pp. 291–321.

White, J.D.L., Ross, P.-S., 2011. Maar-diatreme volcanoes: A review. J. Volcanol. Geotherm. Res. 201, 1–29.

Whitten, J.L., Head, J.W., Denevi, B.W., Solomon, S.C., 2014. Intercrater plains on Mercury: Insights into unit definition, characterization, and origin from MESSENGER datasets. Icarus 241, 97–113.

Wieczorek, M.A., Weiss, B.P., Stewart, S.T., 2012. An Impactor Origin for Lunar Magnetic Anomalies. Science (80-.). 335, 1212–1215.

Wilhelms, D.E., 1976. Mercurian volcanism questioned. Icarus 28, 551–558.

Wilhelms, D.E., McCauley, J.F., 1971. Geologic map of the near side of the Moon. U.S. Geol. Surv. Misc. Geol. Inv. Map I–703.

Wilhelms, D.E., McCauley, J.F., Trask, N.J., 1987. The Geologic History of the Moon. US Geol. Surv. Prof. Pap. 1348.

Wilson, L., Head, J.W., 1981. Ascent and eruption of basaltic magma on the Earth and Moon. J. Geophys. Res. 86, 2971–3001.

Wilson, L., Head, J.W., 2008. Volcanism on Mercury: A new model for the history of magma ascent and eruption. Geophys. Res. Lett. 35, L23205.

Wöhler, C., Lena, R., Lazzarotti, P., Phillips, J., Wirths, M., Pujic, Z., 2006. A combined spectrophotometric and morphometric study of the lunar mare dome fields near Cauchy, Arago, Hortensius, and Milichius. Icarus 183, 237–264.

Wood, C.A., Head, J.W., Cintala, M.J., 1977. Crater degradation on Mercury and the Moon: Clues to surface evolution. In: 8th Lunar and Planetary Science Conference. pp. 3503–3520.

Wright, J., Rothery, D.A., Balme, M.R., Conway, S.J., 2018. Constructional Volcanic Edifices on Mercury: Candidates and Hypotheses of Formation. J. Geophys. Res. Planets 123, 952–971.

Xiao, Z., Prieur, N.C., Werner, S.C., 2016. The self-secondary crater population of the Hokusai crater on Mercury. Geophys. Res. Lett. 43, 7424–7432.

Xiao, Z., Strom, R.G., Blewett, D.T., Byrne, P.K., Solomon, S.C., Murchie, S.L., Sprague, A.L., Domingue, D.L., Helbert, J., 2013. Dark spots on Mercury: A distinctive low-reflectance material and its relation to hollows. J. Geophys. Res. Planets 118, 1752–1765.

Zuber, M.T., Smith, D.E., Phillips, R.J., Solomon, S.C., Neumann, G.A., Hauck, S.A., Peale, S.J., Barnouin, O.S., Head, J.W., Johnson, C.L., Lemoine, F.G., Mazarico,

E., Sun, X., Torrence, M.H., Freed, A.M., Klimczak, C., Margot, J., Oberst, J., Perry, M.E., McNutt, R.L., Balcerski, J.A., Michel, N., Talpe, M.J., Yang, D., 2012. Topography of the Northern Hemisphere of Mercury from MESSENGER Laser Altimetry. Science (80-.). 336, 217–221.

APPENDIX 1

Appendix 1 is a publication scale (1:3,000,000) version of my geological map of H05 with three crater degradation classes. A hardcopy can be found in the plastic document wallet accompanying this thesis. A digital copy of the map sheet, and the GIS files used to create it, can be found in the Digital Supporting Media DVD accompanying this thesis.

APPENDIX 2

Appendix 2 is a publication scale (1:3,000,000) version of my geological map of H05 with five crater degradation classes. A hardcopy can be found in the plastic document wallet accompanying this thesis. A digital copy of the map sheet, and the GIS files used to create it, can be found in the Digital Supporting Media DVD accompanying this thesis.